The Stable Chromium Isotope Signatures of Earth's Silicate Reservoirs: Probing the Deep Earth through Time

Dissertation

der Mathematisch-Naturwissenschaftlichen Fakultät

der Eberhard Karls Universität Tübingen

zur Erlangung des Grades eines

Doktors der Naturwissenschaften

(Dr. rer. nat.)

vorgelegt von

M. Sc. Johanna Luise Wagner

aus Duisburg

Tübingen

2023

Gedruckt mit Genehmigung der Mathematisch-Naturwissenschaftlichen Fakultät der Eberhard Karls Universität Tübingen.

Tag der mündlichen Qualifikation:	05.05.2023
Dekan:	Prof. Dr. Thilo Stehle
1. Berichterstatter/-in:	Prof. Dr. Ronny Schoenberg
2. Berichterstatter/-in:	Prof. Dr. Stefan Weyer

Abstract

Chromium is a lithophile, compatible, multivalent element. Its geochemical behavior during partial mantle melting and magmatic differentiation is controlled by temperature and pressure of melting, source mineralogical composition, and oxygen fugacity. Based on the redox sensitive character of Cr, stable Cr isotopic variability may provide insights into the redox conditions of magmatic systems. Decoding the processes driving stable Cr isotopic fractionation is a prerequisite in order to understand the Cr isotopic variability imprinted in the geological rock record of the deep Earth. By studying the Cr and Fe isotopic compositions of mantle derived rocks and melts this thesis aims at deciphering stable Cr isotope signatures of various terrestrial silicate reservoirs to give insights into the processes controlling Cr isotopic fractionation.

At first, two Archean komatiite-tholeiite suites from the Barberton greenstone belt (3.5-3.22 Ga) and Belingwe greenstone Belt (2.9-2.7 Ga) were chosen to be investigated. Komatiites are generated by high degrees of partial mantle melting and thus provide insights into the stable Cr isotopic composition of bulk silicate Earth. Based on the average stable Cr isotopic composition of komatiites only, it was shown that the Cr isotope value of bulk silicate Earth is -0.12 ± 0.06 ‰. This value agrees very well with previous estimates, paving the way for subsequent investigations of Cr isotopic variations of different terrestrial mantle reservoirs. Additionally, the large range of MgO contents in these rock suites enables the investigation of the effect of variable degrees of mineral crystallization on Cr isotopic variability. Fractional crystallization of Cr-bearing minerals, such as clinopyroxene and Cr-spinel, drives the residual melt towards lighter Cr isotopic compositions. In contrast, crystallization and accumulation of olivine has negligible effect on the Cr isotope compositions as shown by the invariant Cr isotope signature of komatiites. Based on the distinct sensitivity of stable Fe isotopes to fractional crystallization of olivine, clinopyroxene and spinel, the coupled investigation of the Cr-Fe isotope proxy can be used to distinguish these mineral phases during fractional crystallization.

To further investigate the effect of magmatic processes at modern terrestrial mantle conditions Cr and Fe isotopic compositions of basaltic glasses from the East-Pacific Rise, Pacific-Antarctic Ridge, and one sample from the Mid-Atlantic Ridge were measured. These samples represent normal mid-ocean ridge basalts depicting a typical depleted upper mantle signature in radiogenic Sr-Nd-Pb and trace element compositions. Magmatic differentiation involving a typical crystallization assemblages of plagioclase, olivine, clinopyroxene and Fe-Ti oxides induces no measurable Cr isotopic fractionation. Normal mid-ocean ridge basalts reveal a small range between -0.278 to -0.186 ‰ with an average Cr isotopic composition of -0.237 ± 0.050 ‰ significantly offset towards lower values compared to bulk silicate

Earth. Forward modeling using a phase equilibria-based mantle melting model and published mineral-melt fractionation factors is applied to investigate Cr isotopic fractionation during partial melting of peridotite at mid-ocean ridge melting conditions. It shows that Cr isotopic fractionation between a peridotite source and the melt is up to 0.07 ‰ during partial melting in the spinel-stability field. In agreement with the recently proposed source mineralogical control on stable Cr isotopic variability involving pyroxenite source components, the low Cr isotopic signature of mid-ocean ridge basalts suggests pyroxene-rich components in the melt source region and highlights stable Cr isotopes as a tracer for mantle source lithological heterogeneities.

Chapter 4 provides the Cr and Fe isotopic compositions of 45 intraplate basalts from five different localities to further investigate the effect of source mineralogical compositions associated with mantle source heterogeneities on the Cr isotope variability. These samples include ocean island basalts and continental intraplate basalts and represent variable mantle sources as defined by the range of radiogenic Sr-Nd-Pb isotopic compositions of these samples. The observed trends between stable Cr isotopic compositions and indices of magmatic differentiation for most ocean island basalts are in conflict with expected trends for fractional crystallization based on published mineral-melt fractionation factors. In contrast, Doros intrusive basalts display Cr isotopic fractionation trends mirroring those of the Barberton komatiite-tholeiite suite. This suggests that factors like temperature and pressure of melting, which are distinct for Archean vs. modern mantle melting regimes, do not control stable Cr isotopic fractionation. Instead, correlations of stable Cr signatures with radiogenic Sr and Nd isotope compositions in ocean island basalts indicate that the composition of the mantle source is a key mechanism controlling Cr isotope variability. Therein, samples displaying a HIMU- and PREMA-like mantle signature in radiogenic Sr-Nd-Pb isotope space show lighter Cr and heavier Fe isotopic compositions compared to bulk silicate Earth. This is tentatively explained by incorporation of recycled oceanic crust components carrying a mid-ocean ridge-like stable Cr and Fe isotopic signature, and which are possibly present as pyroxenite lithologies. In contrast, ocean island basalts with EM2 isotopic affinties from French Polynesia show heavier Cr and lighter Fe isotopic signatures with increasing radiogenic Sr isotopic compositions. Combined with the observed correlations between stable Cr and Fe isotopic compositions with trace element ratios indicative for carbonate metasomatism for these samples, it is hypothesized that EM2 basalts originated from a carbonated source, which imprints its elevated Cr isotopic composition on the melt.

Zusammenfassung

Chrom ist ein lithophiles, kompatibles, mehrwertiges Element. Sein geochemisches Verhalten während der partiellen Aufschmelzung des Mantels und der magmatischen Differenzierung wird von der Temperatur und dem Druck während der Schmelzbildung, der mineralogischen Zusammensetzung der Quelle und der Sauerstofffugazität gesteuert. Aufgrund des redox-empfindlichen Verhaltens von Chrom kann die Variabilität der stabilen Cr-Isotope Aufschluss über die Redox-Bedingungen magmatischer Systeme geben. Die Entschlüsselung der Prozesse, welche die stabile Cr-Isotopenfraktionierung steuern, ist eine Voraussetzung für das Verständnis der Cr Isotopenvariabilität, welche in den geologischen Gesteinsaufzeichnungen der tiefen Erde aufgezeichnet ist. Durch die Untersuchung der stabilen Cr und Fe Isotopenzusammensetzungen von aus dem Erdmantel stammenden Gesteinen und Schmelzen sollen in dieser Arbeit die stabilen Cr-Isotopensignaturen verschiedener terrestrischer silikatisch Mantelreservoire entschlüsselt werden, um somit einen Einblick in die Prozesse zu erhalten, die die stabile Cr-Isotopenfraktionierung steuern.
Zunächst wurden zwei archaische aus Komatiiten und Tholeiiten bestehenden Gesteinsabfolgen aus dem Barberton Grünsteingürtel (3,5-3,22 Ga) und und dem Belingwe Grünsteingürtel (2,9-2,7 Ga) untersucht. Komatiite werden durch hohe partielle Aufschmelzgrade des Mantels gebildet und können somit einen Einblick in die stabile Cr Isotopenzusammensetzung der gesamten silikatischen Erde bieten. Basierend auf der durchschnittlichen stabilen Cr Isotopenzusammensetzung der Komatiite kann gezeigt werden, dass der Cr-Isotopenwert der gesamten silikatischen Erde - $0{,}12 \pm 0{,}06$ ‰ beträgt. Dieser Wert stimmt sehr gut mit früheren Schätzungen überein und ebnete somit den Weg für die folgenden Untersuchungen der Cr-Isotopenvariationen verschiedener terrestrischer Mantelreservoire. Darüber hinaus ermöglicht die große Variation des MgO-Gehalts in diesen Gesteinsabfolgen, die Auswirkungen eines hohen Differenzierungsgrades auf die Cr-Isotopenvariabilität zu untersuchen. Fraktionierte Kristallisation von Cr-haltigen Mineralen wie Klinopyroxen und Cr-Spinell führt zu einer leichteren Cr Isotopenzusammensetzung der Restschmelze. Im Gegensatz dazu hat die Kristallisation und Akkumulation von Olivin vernachlässigbare Auswirkungen auf die Cr Isotopenzusammensetzung, wie die unveränderliche Cr-Isotopensignatur von Komatiiten zeigt. Aufgrund der unterschiedlichen Empfindlichkeit der Fe-Isotope gegenüber der fraktionierten Kristallisation von Olivin, Klinopyroxen und Spinell kann die gekoppelte Untersuchung des Cr-Fe Isotopen-Proxys zur Unterscheidung dieser Mineralphasen während der fraktionierten Kristallisation verwendet werden.
Um die Auswirkungen magmatischer Prozesse unter rezenten Bedingungen während des partiellen Aufschmelzens des Mantels zu untersuchen, wurden die Cr und Fe Isotopenzusammensetzungen basaltischer Gläser vom Ostpazifischen Rücken, dem

Pazifisch-Antarktischen Rücken und einer Probe vom Mittelatlantischen Rücken gemessen. Bei diesen Proben handelt es sich um normale Ozeanrückenbasalte, die eine für sie typische Signatur des verarmten oberen Mantels im Hinblick auf ihre radiogene Sr-Nd-Pb sowie Spurenelement-Zusammensetzungen aufweisen. Die magmatische Differenzierung mit einer typischen Kristallisationsabfolge von Plagioklas, Olivin, Klinopyroxen und Fe-Ti-Oxiden führt zu keiner messbaren Cr-Isotopenvariation. Die normalen Ozeanrückenbasalte weisen eine kleine Spanne zwischen -0,278 und -0,186 ‰ auf, welche mit einer durchschnittlichen Cr Isotopenzusammensetzung von -0,237 $\pm$ 0,050 ‰ deutlich von der gesamten silikatischen Erde abweicht. Eine Vorwärtsmodellierung unter Verwendung eines auf Phasengleichgewichten basierenden Schmelzmodells und veröffentlichter Fraktionierungsfaktoren für Mineral und Schmelze wird angewendet, um die Cr-Isotopenfraktionierung während der partiellen Aufschmelzung von Peridotit unter den Bedingungen, die an mittelozeanischen Rücken vorherrschen, zu untersuchen. Diese zeigt, dass die stabile Cr-Isotopenfraktionierung zwischen dem aufzuschmelzenden Peridotit und der Schmelze bis zu 0,07 ‰ im Spinell-Stabilitätsfeld beträgt. In Übereinstimmung mit der kürzlich vorgeschlagenen Idee, dass die mineralogische Zusammensetzung der Quelle, besonders im Hinblick auf Pyroxenit, eine entscheidenen Rolle für die Variabilität der stabilen Cr-Isotope in der Schmelze spielen kann, deutet die niedrige Cr-Isotopensignatur der ozeanischen Rückenbasalte auf eine pyroxenreiche Komponenten in der Quelle hin und hebt die stabilen Cr-Isotope als Indikator für lithologische Heterogenitäten im Mantel hervor.
Kapitel 4 enthält die Cr und Fe Isotopenzusammensetzungen von 45 Intraplattenbasalten aus fünf verschiedenen Lokalitäten, um die Auswirkungen der mineralogischen Zusammensetzung der Quelle in Verbindung mit Mantelheterogenitäten auf die Cr-Isotopenvariabilität weiter zu untersuchen. Diese Proben umfassen Ozeaninselbasalte und kontinentale Intraplattenbasalte und repräsentieren basierend auf der variablen radiogene Sr-Nd-Pb Isotopenzusammensetzung verschiedene Mantelquellen. Die beobachteten Trends zwischen den stabilen Cr Isotopenzusammensetzungen und Indizes der magmatischen Differenzierung für die meisten Ozeaninselbasalte stehen im Widerspruch zu den erwarteten Trends für die fraktionierte Kristallisation auf der Grundlage der veröffentlichten Mineral-Schmelze Fraktionierungsfaktoren. Im Gegensatz dazu zeigen die Intrusivbasalte vom Doros Complex Cr Isotopentrends, die denen der Komatiit-Tholeiit Gesteinsabfolge vom Barberton Grünsteingürtel ähneln. Dies deutet darauf hin, dass Faktoren wie Temperatur und Druck, vorherrschend während der partiellen Auschmelzung, nicht die Cr-Isotopenfraktionierung steuern, da diese Faktoren sich für archaische und rezente Schmelzbildung im Mantel generell unterscheiden. Stattdessen deuten die Korrelationen zwischen stabilen Cr-Signaturen und radiogenen Sr und Nd Isotopenzusammensetzungen in Ozeaninselbasalten darauf hin, dass die Zusammensetzung der Mantelquelle ein Schlüsselmechanismus zur Steuerung der Cr-Isotopenvariabilität ist. Proben, die im radiogenen Sr-Nd-Pb Isotopenraum eine HIMU- und PREMA-ähnliche Mantelsignatur aufweisen, haben eine leichtere Cr- und schwerere Fe-Isotopenzusammensetzung im Vergleich zur gesamten silikatischen Erde. Dies wird versuchsweise durch die Inkorporation von recyklierten ozeanischen Krustenkomponenten erklärt, die eine stabile Cr- und Fe-Isotopenzusammensetzung ähnlich der mittelozeanischen Rückenbasalte tragen und möglicherweise als Pyroxenit-Lithologien vorliegen. Im Gegensatz dazu weisen Ozeaninselbasalte aus Französisch-Polynesien

mit einer EM2-Mantelsignatur schwerere Cr und leichtere Fe Isotopensignaturen mit zunehmenden radiogenen Sr-Isotopenzusammensetzungen auf. In Verbindung mit den beobachteten Korrelationen zwischen stabilen Cr und Fe Isotopenzusammensetzungen und Spurenelementverhältnissen, die bei diesen Proben auf Metasomatismus durch eine karbonisierte Schmelze hindeuten, wird die Hypothese aufgestellt, dass die EM2-Basalte aus einer karbonisierten Mantelquelle stammen, welche ihre erhöhte Cr-Isotopensignatur auf die Schmelze überträgt.

Erklärung

Ich erkläre hiermit, dass ich die von mir vorgelegte Dissertation mit dem Titel "The stable chromium isotope signatures of Earth's silicate reservoirs: Probing the deep Earth through time" selbständig verfasst, nur die angegebenen Quellen und Hilfsmittel, einschließlich Tabellen, Abbildungen und Karten, benutzt und wörtlich oder inhaltlich übernommene Stellen als solche gekennzeichnet habe. Ich erkläre, dass die Richtlinien zur Sicherung guter wissenschaftlicher Praxis der Universität Tübingen (Beschluss des Senats vom 25.05.2000) beachtet wurden. Ich versichere an Eides statt, dass diese Angaben wahr sind, und dass ich nichts verschwiegen habe. Mir ist bekannt, dass die falsche Angabe einer Versicherung an Eides statt mit Freiheitsstrafe bis zu drei Jahren oder mit Geldstrafe bestraft wird. Die von mir vorgelegte Dissertation ist von Prof. Dr. Ronny Schoenberg betreut worden.

Hannover, 14.12.2022

Acknowledgments

First of all, I am truly grateful to Ronny Schoenberg to give me the opportunity to do my doctoral studies in Tübingen. Thank you for your continuous guidance, support, scientific and analytical discussions whenever needed, providing a well-managed laboratory, and all the many things I could learn from you. Also living in a historic town like Tübingen with all its nature was a real treat. I also would like to thank Prof. Dr. Stefan Weyer for taking the time and effort to read my thesis as an external referee.
I am also very thankful to Ilka Kleinhanns, who gave guidance during lab work, measurements, continuous reading of my paper drafts and all the small details. I appreciate that your door was always open and your ideas and suggestions throughout this project were always helpful and constructive.
I would also like to thank Mike Babechuk, who supported me from St John's during writing my first manuscript. Thank you for your help and guidance during this time and the fun times we had when you were visiting.
I also want to thank all current and former Isotope Geochemistry group members. Special thanks go to the amazing women Lucile Roué, Gülüm Albut, Maria Varas-Réus and Carolina Rosca. I also want to thank Elmar Reitter and Bernd Steinhilber, who I wouldn't want to miss during this journey. Special thanks also go to Benny Eickmann, Clara Zelinsky, Nadja Weber, Stefan Koenig, Julius Havsteen, Markus Gogouvatis, Rachel Bezard, Erpan Airken, Timon Kurzawa, Marie-Laure Pons, Heinrich Taubald and Daniel Schöckle. Without all of you this time would have been half as much fun. I also want to thank Simone Schafflick for preparing thin sections, Manuel Scharrer for helpful discussion during microscopy and Sebastian Staude and Thomas Wenzel for microprobe analyses.
Moreover, I would like to thank Axel Hofmann and Trishya Owen-Smith for hosting us at the University of Johannesburg on our 2018 fieldtrip to South Africa. This has been a very memorable time for me and I appreciate the hospitality throughout this time. I am also grateful to Olivier Rouxel to host me at the Ifremer in Brest and Gerhard Woerner at the University of Goettingen.
Finally, I want to express my deepest gratitude to my family and Nils for their support throughout these years. Your believe in me has been the greatest support of all.

Included manuscripts

The project idea for this thesis was developed by Prof. Dr. Ronny Schoenberg and Dr. Ilka Kleinhanns (University of Tübingen) and funded by the German Research Council (DFG) to Prof. Dr. Ronny Schoenberg.

The scientific contributions of authors for the manuscripts included in this thesis are as follows:

Chapter 2 Published paper

Title: Coupled stable chromium and iron isotopic fractionation tracing magmatic mineral crystallization in Archean komatiite-tholeiite suites.
Authors: Luise J. Wagner, Ilka C. Kleinhanns, Nadja Weber, Michael G. Babechuk, A. Hofmann, R. Schoenberg.
Status: published 2021 (Chemical Geology, 576, 120121).

Overall, 80 % of the data generation, 80 % of scientific ideas, 90 % of analysis and interpretation and 85 % of writing were done by myself. During the field campaign in 2018 in South Africa sampling of the Barberton Drillcore BARB-1 were done by Ronny Schoenberg, Ilka Kleinhanns and myself. Numerous discussions with Ronny Schoenberg, Ilka Kleinhanns, Michael Babechuk helped me to develop scientific ideas and interpret the data. Michael Babechuk helped with analyses of the Fe^{2+}/Fe_{total} ratios and trace element data. Nadja Weber generated the major element data for the Barberton Greenstone Belt rock suite with assistance of Heinrich Taubald during measurements and myself during laboratory work. Ronny Schoenberg, Ilka Kleinhanns, Michael Babechuk and Axel Hofmann reviewed and edited the manuscript at various stages during writing. Axel Hofmann provided samples from the Belingwe Greenstone Belt.

Chapter 3 Submitted paper

Title: Consistently light stable chromium isotopic compositions in mid-ocean ridge basalts: Implications for the mantle source composition.
Authors: Luise J. Wagner, Ilka C. Kleinhanns, Maria I. Varas-Réus, Carolina Rosca, Stephan Koenig, Wolfgang Bach, Ronny Schoenberg.
Status: submitted to Geochimica Cosmochimica Acta.

Overall, 65 % of the data generation, 90 % of scientific ideas, 100 % of analysis

and interpretation and 90 % of writing were done by myself. Numerous discussions with Ronny Schoenberg, Ilka Kleinhanns, Carolina Rosca, Maria Varas-Réus and Stephan Koenig helped me to develop scientific ideas and interpret the data. Ilka Kleinahnns generated 35% of the stable isotope data. Maria Varas-Reus, Carolina Rosca, Ilka Kleinhanns, Ronny Schoenberg, Stephan Koenig and Wolfgang Bach edited and reviewed the manuscript. Wolfgang Bach and Stephan Koenig provided samples from the East-Pacific Rise and Pacific-Antarctic Ridge, respectively.

Chapter 4 in preparation for submission

Title: Heterogeneous stable Cr and Fe isotope compositions of Earth's silicate mantle: Constraints from intraplate basalts.
Authors: this manuscript will be published with Luise J. Wagner, Ilka C. Kleinhanns, Carolina Rosca, Maria I. Varas-Réus, Clara Zelinsky, Stephan Koenig, Gehard Woerner, Olivier Rouxel, Trishya Owen-Smith, Ronny Schoenberg.
Status: in preparation for submission.

Overall, 95 % of the data generation, 95 % of scientific ideas, 95 % of analysis and interpretation and 100% of writing were done by myself. Discussions with Ronny Schoenberg, Ilka Kleinhanns, Carolina Rosca, Maria Varas-Réus helped me to develop scientific ideas and interpret the data. Clara Zelinsky generated 5 % of the included data within her bachelor thesis. Stephan Koenig provided samples from French Polynesia. Gerhard Woerner provided samples from Vogelsberg volcano and La Réunion. Olivier Rouxel provided samples from Lō'ihi seamount. Trishya Owen-Smith provided samples from the Doros complex.

Contents

Chapter 1

Introduction

Metal stable isotopes are a proven, powerful instrument for tracing a variety of geological and geochemical processes. Applications of metal stable isotopes encompass constraining Earth's core formation conditions (Shahar and Young, 2020), Earth's continental crust build-up (McCoy-West et al., 2019), and Earth's oceans' redox conditions (Anbar and Rouxel, 2007). In short, metal stable isotopes contribute to a fundamental understanding of Earth's evolution.

Variations of stable chromium (Cr) isotopes have been used in studies as diverse as characterizing the solar system's building blocks (Rotaru et al., 1992), identifying anthropogenic chromate pollution (Berna et al., 2010; Ellis et al., 2002; Wanner et al., 2012), and acting as a paleo redox tracer for the oxygenation of the Earth's atmosphere (Cole et al., 2016; Crowe et al., 2013; Frei et al., 2009; Gilleaudeau et al., 2016; Planavsky et al., 2014).

On Earth's surface stable Cr isotope fractionation is mainly mediated by partial redox reactions between the two most common redox states of chromium, Cr^{6+} and Cr^{3+}. Tracing and quantifying chromate (CrO_4^{2-}) released to the environment by the pigmenting, automotive or steel industries has been a critical use of stable Cr isotopes due to the highly toxic and carcinogenic behavior of Cr^{6+} (Berna et al., 2010; Ellis et al., 2004; Izbicki et al., 2008). Stable Cr isotopes helped create chromate remediation from the environment by permeable reactive barriers or natural attenuation in groundwater aquifers (Basu and Johnson, 2012; Blowes, 2002). Cr isotope variations in early Earth's sediments, again mediated by partial redox reactions between Cr^{6+} and Cr^{3+}, have been attributed to the existence of free atmospheric oxygen before the Great Oxidation Event at ~2.45 Ga (e.g., Crowe et al., 2013; Frei et al., 2009), although the exact cause of these variations is debated (Albut et al., 2018; Babechuk et al., 2017; Babechuk et al., 2019). Nevertheless, it is accepted that redox reactions mediate isotope fractionation (Schauble et al., 2004).

The level of oxygen in Earth's interior, or oxygen fugacity (fO_2), for different terrestrial silicate reservoirs may in principle be detected by metal stable isotope fractionations mediated by redox reactions. For example, an early study investigating high-temperature stable iron (Fe) isotopes fractionation, found a correlation between stable Fe isotopic compositions and the fO_2 signature of spinel (Williams et al., 2004). In high-temperature, magmatic environments Cr exists as Cr^{2+} and Cr^{3+} (e.g., Berry et al., 2006; Berry and O'Neill, 2004; Li et al., 1995), and may thus be used as a potential proxy for fO_2. Stable Cr isotopic fractionation is expected

due to differences in bonding environments of Cr^{2+} and Cr^{3+} (Sharp, 2007) and the resulting variable partitioning behavior of Cr^{2+} and Cr^{3+} between melt and different silicate minerals (e.g., Mallmann and O'Neill, 2009). Difficulties in constraining the fO_2 with stable Cr isotopes arise from Cr isotopic fractionation that occur during magma generation, wherein subsequent magmatic differentiation potentially masks the stable isotope source signal and thus the recorded fO_2, as has been shown previously for stable Fe isotopes (e.g., Schuessler et al., 2009; Weyer et al., 2005; Williams et al., 2005).

The pioneering study of stable Cr isotopes by Schoenberg et al. (2008) investigating mantle-derived rocks suggested an overall narrow range of -0.124 ± 0.101 ‰, termed Earth's igneous inventory and considered indistinguishable from the compiled average $\delta^{53/52}$Cr (ordinary and carbonaceous) chondrite value ($\delta^{53/52}$Cr = -0.119 ± 0.045 ‰, 2SD, n=18; Schoenberg et al., 2016; $\delta^{53/52}$Cr = -0.115 ± 0.043 ‰, 2SD, n=10; Bonnand et al., 2016b). Studied mantle-derived rocks by Schoenberg et al. (2008) were from various tectonic settings and thus display a variety of sources and/or differentiation histories (i.e., xenoliths, ultramafic rocks and cumulates, oceanic basalts, and one granite; Schoenberg et al., 2008). Therefore, further investigation regarding the variability of Cr isotopic compositions of different terrestrial reservoirs and the possible refinement of the bulk silicate Earth (BSE) value were needed (Jerram et al., 2020; Sossi et al., 2018; Xia et al., 2017). Systematic differences in Cr isotopic compositions of mantle-derived terrestrial rocks (Schoenberg et al., 2016; Xia et al., 2017) as well as inter-mineral Cr isotope variations in silicate minerals (Shen et al., 2018) gave rise to investigations of the effect of magmatic processes such as fractional crystallization and partial melting on Cr isotope fractionation under extra-terrestrial (Bonnand and Halliday, 2018; Bonnand et al., 2016a; Bonnand et al., 2016b; Schoenberg et al., 2016; Sossi et al., 2018; Zhu et al., 2019) and terrestrial mantle conditions (Bai et al., 2019; Bonnand et al., 2020b; Chen et al., 2019a; Jerram et al., 2020; Ma et al., 2022; Shen et al., 2020). Moreover, considerable Cr isotope variations in mantle peridotites and xenoliths indicate the possible influence of metasomatism or refertilization on Cr isotopic composition of these samples and may thus cause some Cr isotope heterogeneity within the mantle (Farkas et al., 2013; Jerram et al., 2022; Xia et al., 2017). Based on the mineralogical control on Cr isotope fractionation, it was recently proposed that the Cr (and Fe) isotope signature of basalts may be used to trace pyroxenite-bearing mantle sources (Soderman et al., 2022). So far, only three only three studies have investigated the Cr isotope variations of unaltered Phanerozoic oceanic basalts (Bonnand et al., 2020b; Ma et al., 2022; Shen et al., 2020), which give supporting evidence that the observed variations are related to source processes such as melt degree or mantle fO_2 (Bonnand et al., 2020b; Shen et al., 2020). However, it remains unclear to which degree specifically Cr isotope, but also Fe isotope variations may record mantle source heterogeneity. The use of Cr isotopes as a tracer for fO_2 or source heterogeneity clearly requires an understanding of processes causing stable Cr isotope fractionation. Thus, this thesis aims for a better understanding of the cause and extent of Cr isotope fractionation in high-temperature environments, with special focus on characterizing different silicate reservoirs of Earth in order to improve our knowledge regarding the influence of source heterogeneities on Cr isotope variations of mantle-derived rocks.

Among transition metals, Cr and Fe, share many geochemical features, making

them a promising isotope couple for investigation. As knowledge about the behavior and fractionation processes of Fe isotopes in high-temperature systems continues to grow, research conducted on Fe isotopes over the past two decades made it a well characterized system (see reviews by Dauphas et al., 2017 and Johnson et al., 2020). In contrast, studies of Cr isotope systematics in high-temperature environments are scarce. Improvement of analytical protocols for high-precision stable Cr isotope measurements via thermal ionization mass spectrometry (TIMS) and multi collector inductively coupled plasma mass spectrometry (MC-ICP-MS) using the double spike method led to resolving small variations in Cr isotope fractionation resulting from magmatic processes (Schiller et al., 2014; Schoenberg et al., 2016; Schoenberg et al., 2008; Trinquier et al., 2008). However, more studies are needed that 1) investigate the specific processes, during which Cr isotopes may fractionate in magmatic systems, in order to 2) characterize and identify variations between different geochemical reservoirs of the deep Earth. Both are an important step towards developing Cr isotopes as redox tracer in high-temperature systems and also use them as a complementary/additional tracer for identifying source lithologies by coupled Cr-Fe proxy studies (Soderman et al., 2021).

1.1 Non-traditional metal stable isotope systematics

The theory and principles underlying stable isotope variations are grounded in the early investigations of the traditional stable isotopes of the elements H, C, N, O, and S since the 1930s (e.g., Urey and Greiff, 1935). Improving measurement techniques, in particular MC-ICP-MS, have expanded the field of stable isotope research to novel stable isotope systems of elements such as Li, Si, Mg, Ca, Fe, Cr, Mo, Ni, Sr and more, also called non-traditional stable isotopes (Johnson et al., 2004). Both traditional and non-traditional stable isotopes underlie the same principles of mass-dependent isotope fractionation and are shortly described in the following Section 1.1.1 This thesis focuses on the stable isotope systems of Cr and Fe during high-temperature, magmatic processes, of which the elemental and isotopic systematics are introduced in Sections 1.1.2 and 1.1.3.

1.1.1 Principles of mass-dependent stable isotope fractionation

Stable isotopic variations may arise from a variety of processes, in which isotopes of a specific element are fractionated based on physicochemical properties varying with different masses (Bigeleisen and Mayer, 1947; Schauble, 2004; Urey, 1947). These isotope variations are usually referred to in the δ-notation, which is the isotope ratio measured relative to a standard and expressed in 'per mil' [‰]. The δ-notation is calculated as follows:

$$\delta_{sample} = \frac{R_{sample}}{R_{standard}} - 1 \times 1000 \tag{1.1}$$

where R is commonly the ratio of the heavy to the lighter isotope.
Mass-dependent stable isotope variations may arise from kinetic or equilibrium processes and the magnitude of isotopic fractionation between two phases A and B, for

example melt and solid, can be described by the fractionation factor α:

$$\alpha_{A-B} = \frac{R_A}{R_B} \tag{1.2}$$

For small isotopic variations, such as usually encountered for transition metal isotopes at high-temperature, the difference between two phases expressed in δ-values can be expressed as Δ and relates to α as follows:

$$\Delta_{A-B} = \delta_A - \delta_B \approx 1000 \times ln\alpha \tag{1.3}$$

Stable isotope fractionation between two phases is based on the differences in bond strength of an element and its isotopes within a molecule. Differences in bond strength arise from different translational, vibrational, and rotational motion energies of atoms with different masses affecting their zero point energy (ZPE) (Urey, 1947). The ZPE is lower for molecules with heavier isotopes, which translates into stronger bonds as a higher dissociation energy is needed (Figure 1.1). This mass dependence of bond strengths can lead to both equilibrium and kinetic isotope effects. Kinetic (non-equilibrium) fractionation is driven by higher velocities of lighter isotopes, which are thus enriched in the product compared to the residue of processes such as diffusion or evaporation (Richter et al., 2009; Richter et al., 2003). Kinetic isotope fractionation is considered a uni-directional, incomplete process and can produce relatively large isotope effects compared to equilibrium isotope fractionation (Schauble et al., 2004).
At equilibrium, stable isotope fractionation follows laws of equilibrium thermodynamics. Equilibrium conditions usually occur in closed systems, but can also be attained during open system processes. Therein, the heavy isotopes prefer the stronger bonds, which relates to higher oxidation states of the element, low coordination number, low-spin electronic configuration and highly covalent bonds (Bigeleisen and Mayer, 1947; Schauble, 2004). In addition to the mass dependence of isotopic fractionation (decreasing with increasing atomic mass, and thereby decreasing relative mass difference between isotopes of a specific element), the magnitude of stable isotope fractionation is also related to temperature and decreases with increasing temperature ($\sim 1/T^2$; Bigeleisen and Mayer, 1947; Urey, 1947). Recent advances in the sensitivity of analytical mass spectrometry enabled the detection of these small, but systematic variations in stable isotopic compositions of various heavy, multivalent elements, such as Cr and Fe, in high-temperature, magmatic systems, of which a short introduction is given in the following.

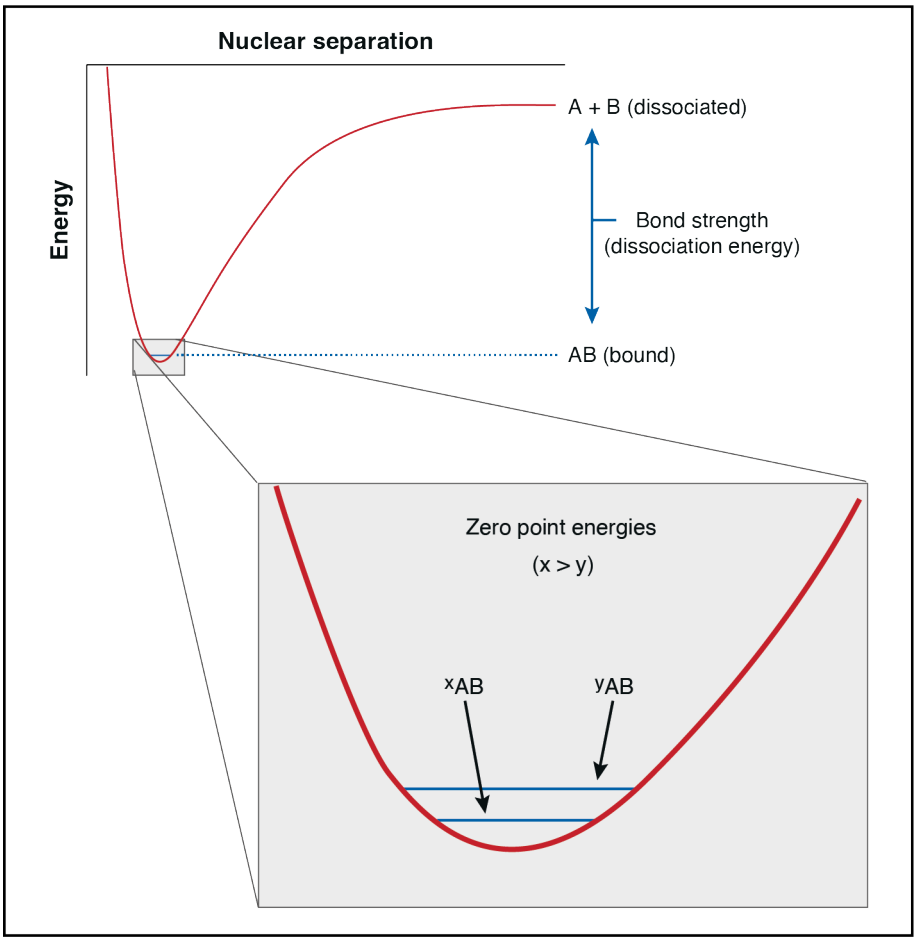

Figure 1.1: The bond strength between two atoms (A and B) is dependent on their zero point energy (ZPE). The lower the ZPE (here ^{x}AB), the higher the energy needed to dissociate these atoms, hence the stronger the bond. Lower ZPE is achieved by incorporating heavier isotopes (x >y). From Anbar and Rouxel, 2007.

1.1.2 Chromium

1.1.2.1 Chromium elemental systematics

Chromium is named after the greek word *chroma* for colour. This hints at one of the main properties of the element, namely its occurrence in various oxidation states (Cr^0 to Cr^{6+}). The main oxidation states on Earth's surface are Cr^{6+} (purple) and Cr^{3+} (green), whereas in high-temperature, magmatic environments Cr also exists as Cr^{2+} (blue). The existence of Cr^{2+} in the terrestrial mantle has been postulated since the 1970s (Burns, 1970, 1975b; Schreiber and Haskin, 1976), and mainly inferred from mineral-melt partitioning studies (Barnes, 1998; Li et al., 1995; Roeder and Reynolds, 1991). These works have been built on by later experimental studies that have fuelled the topic of the multivalence of Cr in silicate melts (Berry et al., 2021a; Berry et al., 2021b; Berry et al., 2006; Berry and O'Neill, 2004; Hanson and Jones, 1998; Jollands et al., 2018; Mallmann and O'Neill, 2009; Sutton et al., 1993). In Earth's mantle Cr is considered a lithophile trace element (Goldschmidt, 1937). However, under the prevalent conditions during core formation, i.e. strongly reducing fO_2 (higher pressure/temperature), Cr is siderophile/chalcophile (e.g., Siebert et al., 2011; Wood et al., 2008), which may explain the relative depletion of Cr in

the BSE (2,500 $\mu g\,g^{-1}$; Salters and Stracke, 2004) compared to the estimated Cr concentration in Earth's core (7790 $\mu g\,g^{-1}$; Allegre et al., 1995) (see also Section 1.1.2.3 for a stable Cr isotope perspective). A viable alternative explanation for the relative depletion of Cr in the silicate mantle is the evaporative loss of Cr during Earth's accretion (Drake et al., 1989; Walter et al., 2000) based on the moderate volatility of Cr (Lodders, 2003; McDonough and Sun, 1995; Palme and O'Neill, 2014), which increases with increasing fO_2 by stabilizing oxidized gaseous species of Cr (O'Neill, 1991; Sossi et al., 2018). These observations imply that the partitioning behavior of Cr is dependent on fO_2, temperature, pressure, and composition of the two phases involved. Under conditions prevailing during present day mantle melting, Cr behaves compatible and is thus depleted in the crust ($\sim$331 $\mu g\,g^{-1}$ in mid-ocean ridge basalt (MORB); White and Klein, 2014; $\sim$92 $\mu g\,g^{-1}$ in the continental crust; Rudnick and Gao, 2014) compared to the terrestrial mantle.
Element partitioning is dependent on the size and charge of an element (Cr^{2+} = 0.80 Å and Cr^{3+} = 0.615 Å; Figure 1.2b; Shannon, 1976). In the case of transition metals, partitioning into the crystal lattice is also influenced by the variable crystal field stabilization energies (CFSE) of reduced and oxidized species, influencing their bonding environment. Differences in CFSE for transition metals and the effect on elemental distribution in the mantle, largely introduced by Burns (1970), is mediated by incompletely filled d-orbitals. Therein, Cr^{2+} and Cr^{3+} have an electron configuration of $[Ar]3d^4 4s^0$ and $[Ar]3d^3 4s^0$, respectively. Crystal field theory predicts that in the case of Cr^{3+} in octahedral coordination, all three electrons of the d-orbitals occupy the three electron orbitals within the lower energy level (t_{2g} group), which results in a particularly high CFSE. For Cr^{2+}, with the presence of four electrons in the d-orbitals, the energetically favourable solution is to place the electrons across the lower (t_{2g} group) and higher (e_g group) energy levels, resulting in a lower octahedral CFSE compared to Cr^{3+}. Based on this non-ideal electron configuration of Cr^{2+}, distortion of its environments is predicted in order to yield a higher stabilization energy by further splitting the electron orbitals according to the Jahn-Teller Theorem (Burns, 1975a). For Cr^{2+} and Cr^{3+} the CFSE in tetrahedral coordination is lower compared to octahedral CFSE, resulting in an overall preference for octahedral coordination. The compatibility of Cr in these minerals depends on the type and composition of each phase (e.g., inverse vs. normal spinel structure) and is described in more detail in Section 1.1.2.2. In general, chromium is very compatible in silicate phases such as spinel, pyroxene, garnet yielding a bulk distribution coefficient ($D^{s/l} = C^s/C^l$) >> 1 during partial melting of peridotite. The significant implications for the latter considerations are, however, that Cr will show variable partitioning behavior depending on its redox state.

1.1.2.2 Chromium partitioning in terrestrial mantle minerals and silicate melts

In spinel Cr is largely considered to be incorporated as Cr^{3+} in octahedral coordination due to its high CFSE (Burns, 1975a), whereas Cr^{2+} is non-preferred due to the absence of distorted sites in the spinel structure. However, the compatibility of Cr^{3+} in spinel may depend on the structural properties of spinel (i.e., normal vs. inverse spinel). Normal spinel has a general formula of $^{[4]}A^{[6]}B_2O_4$, in which the tetrahedral A and octahedral B sites accommodate divalent and trivalent cations, respectively. Chromite ($Fe^{2+}Cr_2^{3+}O_4$) is an example for the normal spinel group,

in which Cr^{3+} is highly compatible in the octahedral site with $D^{spinel/melt}$ >100 (Liu and O'Neill, 2004). In the inverse spinel group, half of the trivalent B cations occupy the tetrahedral sites, whereas the divalent A cations are partitioned into the octahedral B site, such as in magnetite ($^{[4]}Fe^{3+\,[6]}(Fe^{2+},Fe^{3+})O_4$). Although, Cr partitioning into spinel is also dependent on the Cr concentrations of the melt (Barnes, 1998; Murck and Campbell, 1986), it can be anticipated that Cr partitioning as Cr^{3+} is limited in magnetite compared to chromite based on the lower availability of octahedral sites (Roeder and Reynolds, 1991). In clinopyroxene and orthopyroxene Cr^{3+} can easily substitute into the octahedral M1 site, whereas Cr^{2+} can substitute into the larger and slightly distorted M2 site. In clinopyroxene (and orthopyroxene) Cr^{3+} is substantially more compatible ($D^{clinopyroxene/melt}$ ∼8.72) compared to Cr^{2+} ($D^{clinopyroxene/melt}$ ∼0.65) (Mallmann and O'Neill, 2009). Moreover, partitioning of Cr^{3+} in clinopyroxene has been shown to be dependent on composition, as Cr is more compatible in augite compared to pigeonite, due to charge balance constraints (Mallmann and O'Neill, 2009; Papike et al., 2005; Papike et al., 2016). In olivine, Cr^{2+} can easily substitute for octahedral coordinated Mg^{2+} in distorted M2 sites, whereas substitution of Cr^{3+} into the smaller octahedrally coordinated M1 site is accounted for by charge vacancies or coupled substitution of Al^{3+} with Si^{4+} (Burns, 1975a; Hanson and Jones, 1998; Jollands et al., 2018; Papike et al., 2005). The compatibility of Cr^{2+} and Cr^{3+} in olivine were shown to be similar ($D^{olivine/melt}$ = 0.85) (Bell et al., 2014; Hanson and Jones, 1998; Mallmann and O'Neill, 2009). Chromium is also compatible in garnet with partition coefficients varying with the composition of garnet. The Ca-Cr and Mg-Cr garnet endmembers, uvarovite ($Ca_3Cr_2Si_3O_{12}$) and knorringite ($Mg_3Cr_2Si_3O_{12}$) are highly enriched in Cr, but in general rare in occurrence and relatively unstable at mantle conditions (Liu and O'Neill, 2004). Peridotitic garnets mostly consist of pyrope (75 %; $Mg_3Al_2Si_3O_{12}$), grossular (10 %; $Ca_3Al_2Si_3O_{12}$) and almandine components (15 %; $Fe_3^{2+}Al_2Si_3O_{12}$) (Wood et al., 2013). Substitution of Cr in these garnets usually occurs with the octahedral coordinated Al^{3+} (Figowy et al., 2020; Wood et al., 2013) and experimental studies indicate that Cr in garnet remains as Cr^{3+} over a wide range of fO_2 (Righter et al., 2011). Compared to peridotitic garnets, eclogitic garnets have lower Cr contents and consist of an increasing almandine and grossular component, which can be directly related to the mafic origin of eclogites roughly resembling bulk compositions of basalt (van Westrenen et al., 2001; Wood et al., 2013).

In the lower mantle Cr is incompatible in Ca-perovskite and Mg-perovskite with $D^{perovskite/melt}$ approaching one (Corgne et al., 2005), whereas Cr is compatible in (ferro)-periclase ((Mg,Fe)O; Geßmann and Rubie, 1998; Ohtani and Yurimoto, 1996). Trivalent Cr is predicted to remain in octahedral coordination in ferropericlase and perovskite based on its large CFSE (Burns, 1975a). In contrast, Cr^{2+} is predicted to favour the larger distorted [7]- to [12]- coordinated sites of lower mantle phases (Burns, 1975a). Although Cr is predominantly present as Cr^{3+}, the presence of Cr^{2+} has been shown for ferropericlase inclusions in lower mantle diamonds (Odake et al., 2008) and for experimentally synthesized (ferro)periclase and perovskite (Eeckhout et al., 2007; Kagi et al., 2013). Although possibly affected by analytical difficulties, the Cr^{2+}/Cr_{total} ratio in ferropericlase has been shown to range between ∼0.07 and ∼0.12 (Eeckhout et al., 2007; Kagi et al., 2013), but can be up to ∼0.4 in Fe-free periclase with Cr^{2+} suggested to be present in [6]-coordinated

sites (Eeckhout et al., 2007). On the other hand, perovskite was shown to have Cr^{2+}/Cr_{total} of ~0.7 with Cr^{2+} present in the [12]-coordinated site (Eeckhout et al., 2007).

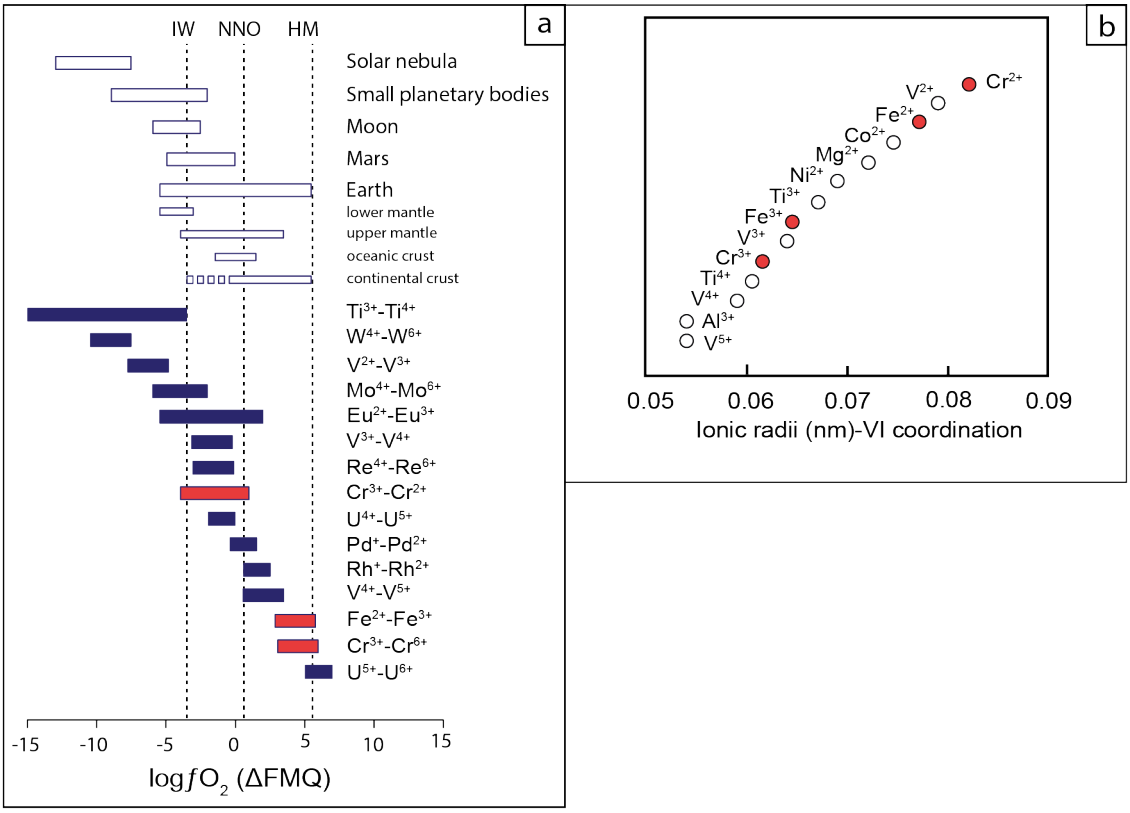

Figure 1.2: **a)** The relative oxygen fugacity conditions (log units relative to FMQ, fayalite-magnetite-quartz buffer) are shown for different planetary reservoirs. Also shown are valence state transition ranges for various multivalent elements. Elements discussed in this chapter are Cr and Fe and are marked in red. Also shown are reference lines for oxygen fugacity buffers, such as IW (Fe-FeO), NNO (Ni-NiO), and HM (hematite-magnetite) (modified after Mallmann et al., 2021); **b)** Ionic raddi for different redox states of multivalent elements in octahedral coordination with relevant elements discussed in this chapter marked in red (modified after Papike et al., 2005).

Experimental studies have shown that in silicate melts Cr can exist as Cr^{6+}, Cr^{3+}, and Cr^{2+} (Berry et al., 2006; Berry and O'Neill, 2004). The occurrence of Cr^{6+} in silicate melts is limited to highly oxidizing conditions (Berry et al., 2006; Berry and O'Neill, 2004), whereas Cr^{2+} and Cr^{3+} are the main oxidation states under representative terrestrial magmatic conditions (Figure 1.2; Berry et al., 2006; Mallmann et al., 2021; Papike et al., 2005). Although the determination of Cr^{2+} is complicated by the electron exchange reaction $Cr^{2+} + Fe^{3+} = Cr^{3+} + Fe^{2+}$ upon cooling, the existence of Cr^{2+} in basaltic melts has been determined by in-situ X-ray absorption near-edge structure (XANES) spectroscopy (Berry et al., 2021b; Berry et al., 2006). This study also demonstrated the dependence of melt Cr^{2+}/Cr_{total} on fO_2, in which Cr^{2+}/Cr_{total} ~0.5 at ΔFMQ = -1.6 (Berry et al., 2006). In addition to the dependence on fO_2, Cr^{2+}/Cr_{total} is dependent on temperature, pressure and composition of the melt (Berry et al., 2021b; Li et al., 1995). Therein, the melt Cr^{2+}/Cr_{total} increases with increasing temperature and decreasing fO_2 (Berry et al., 2006; Li et al., 1995), but significantly decreases with increasing pressure (Berry et al., 2021b).

As Cr^{2+} is expected in distorted sites due to the Jahn-Teller effect, the decreasing Cr^{2+}/Cr_{total} with increasing pressure was attributed to the general increase of regular octahedral sites in melts with increasing pressure (Berry et al., 2021b). At lower pressures coordination freedom in a melt allows for the presence of Cr^{2+} in the preferred distorted coordination. This may result in a Cr^{2+}/Cr_{total} ratio of 0.35 in a basaltic melt at crustal pressures, but Cr^{2+}/Cr_{total} of zero at ~2 GPa corresponding to a depth of ~60 km (Berry et al., 2021b). Berry et al. (2021b) note that this pressure dependence of Cr^{2+}/Cr_{total} should not be extrapolated above 4.5 GPa.
Overall, the behavior of Cr is very different depending on the redox state. Namely, in upper mantle silicate phases Cr^{3+} behaves mostly compatibly except for olivine and Cr^{2+} behaves moderately incompatibly. These differences in partitioning influences stable Cr isotope fractionation between minerals and melts. Generally, heavier isotopes prefer the stronger bonds, which occur with higher oxidation state and at lower coordination numbers. These isotope effects arising from variable partitioning of Cr^{2+} and Cr^{3+} with different coordination environments are described in detail for minerals such as olivine, spinel and pyroxene in Chapter 2 (Section 2.5.3.2) of this thesis.

1.1.2.3 High-temperature stable Cr isotope systematics

Chromium has four stable isotopes ^{50}Cr, ^{52}Cr, ^{53}Cr, and ^{54}Cr, with natural abundances of 4.35 %, 83.79 %, 9.50 %, and 2.36 %, respectively. ^{53}Cr is the decay product of the now extinct ^{53}Mn (half-life of 3.7 Ma), and is used to study early-solar system processes (e.g., Moynier et al., 2007; Trinquier et al., 2008). Stable chromium isotope variations are reported as δ-values (see also Eq. 1.1) relative to the NIST (National Institute of Standards and Technology) SRM979, and will henceforth referred to as $\delta^{53/52}Cr$.
As discussed above, it is clear that variable partitioning of Cr^{2+} and Cr^{3+} between mineral phases and melt may induce Cr isotopic fractionation during magmatic processes. The first study investigating stable Cr isotope variations of high-temperature terrestrial rocks by Schoenberg et al. (2008) reported an average $\delta^{53/52}Cr$ value of -0.124 ± 0.101 ‰ for rocks from various origins, i.e., ultramafic rocks and cumulates, xenoliths, oceanic basalts, and one granite, which was termed the Earth's igneous inventory. This value was mainly proposed as a reference for low-temperature Cr isotope studies. The average (ordinary and carbonaceous) chondrite value ($\delta^{53/52}Cr = -0.119 \pm 0.045$ ‰, n=18; Schoenberg et al., 2016; $\delta^{53/52}Cr = -0.115 \pm 0.043$ ‰, n=10; Bonnand et al., 2016b) was found to be indistinguishable from the igneous inventory suggesting that core formation did not impart any resolvable Cr isotope fractionation onto the silicate portion of the Earth (Bonnand et al., 2016b; Schoenberg et al., 2016). This was supported by metal-silicate experiments showing no resolvable Cr isotope fractionation during conditions of Earth's core formation (Bonnand et al., 2016b). Considerably lower $\delta^{53/52}Cr$ values for chondrites were later found to be the result of analytical difficulties (Moynier et al., 2011). During the course of this project and shortly before, three studies investigating high-temperature Cr isotope systematics aimed at refining the $\delta^{53/52}Cr$ of the BSE and gave values of -0.14 ± 0.12 ‰ based on peridotites (Xia et al., 2017), -0.11 ± 0.06 ‰ based on peridotites and komatiites (Sossi et al., 2018), and -0.12 ± 0.04 ‰ based on komatiites (Jerram et al., 2020).
The slightly higher Cr isotope signature of chromites compared to the igneous inven-

tory reported by Farkas et al. (2013) (-0.079 ± 0.129 ‰; n=42) and Schoenberg et al. (2008) (-0.082 ± 0.058 ‰; n=12) points toward small inter-mineral stable Cr isotopic fractionations. Additionally, ab-initio calculations predict a higher $\delta^{53/52}$Cr for spinel compared to Cr metal, Cr-bearing sulphides, or olivine (Moynier et al., 2011). By focusing on silicate mantle minerals, ionic model calculations predict decreasing $\delta^{53/52}$Cr in the order of spinel > clinopyroxene ≥ orthopyroxene > olivine (Shen et al., 2018). A later study by Bonnand et al. (2020a) experimentally confirmed that Cr-spinel exhibits a heavier Cr isotopic composition compared to silicate melt.
Mass dependent stable Cr isotopic fractionation caused by magmatic differentiation was first observed in lunar rocks, in which Cr-spinel crystallization drives the residual magma towards lower $\delta^{53/52}$Cr values (Bonnand et al., 2016a). Similar trends of $\delta^{53/52}$Cr correlating positively with indices of magmatic differentiation were seen in differentiated meteorites (HED achondrites; Bonnand et al., 2016a; Schoenberg et al., 2016). The heavy isotope signature of iron meteorites was explained by the fractional crystallization of an isotopically light sulphide phase, i.e. daubréelite (Bonnand and Halliday, 2018). In contrast to the interpretation of Bonnand et al. (2016a), the light $\delta^{53/52}$Cr of lunar basalts can be explained by evaporative loss of heavy isotopes associated with the gaseous species $CrO_{2(g)}$ during the Moon forming impact under oxidizing conditions (Sossi et al., 2018). Recently, experimentally determined fractionation factors between silicate melt and a gaseous phase show that during kinetically driven degassing light Cr isotopes are enriched in the gas phase (Klemme et al., 2022).
The continuously increasing number of studies on terrestrial mantle rocks show that the silicate mantle exhibits a considerable range in $\delta^{53/52}$Cr (Jerram et al., 2020; Schoenberg et al., 2016; Schoenberg et al., 2008; Shen et al., 2015; Shen et al., 2018; Xia et al., 2017). Fresh peridotites, bearing no indication of metasomatism, display increasing $\delta^{53/52}$Cr values with increasing melt depletion, interpreted as the result of the preferential partitioning of the light isotope into the melt (Xia et al., 2017). Based on an extensive $\delta^{53/52}$Cr dataset of mantle minerals presented by Shen et al. (2018), the authors used the resulting inter-mineral isotopic fractionations to model the behavior of Cr isotopes during partial melting. The latter study and subsequently published partial melting models showed that the melt would be indeed isotopically lighter compared to the residue (Jerram et al., 2020; Shen et al., 2018; Shen et al., 2020). Yet, it remains an open question if isotopic fractionation increases (Shen et al., 2018) or decreases (Jerram et al., 2020; Shen et al., 2020) with increasing melt degree. Additionally, the effect of partial melting on the $\delta^{53/52}$Cr of the residue remains enigmatic as the increase in $\delta^{53/52}$Cr with increasing melt depletion in peridotites (Xia et al., 2017) contrasts theoretical calculations indicating no significant change in $\delta^{53/52}$Cr of the residual peridotite (Jerram et al., 2020). The negligible effect in the latter model can be largely explained by mass balance considerations. Based on the compatible behavior of Cr during partial melting of peridotite, a large fraction of Cr remains in the residuum.
So far, studies investigating oceanic basalts are scarce and restricted to two ocean island basalt (OIB) locations (Hawaiian Islands and Fangataufa atoll, French Polynesia). Both studies observed $\delta^{53/52}$Cr variations caused by fractional crystallization of Cr-spinel, which dominates the Cr-budget and drives the residual melt towards lower $\delta^{53/52}$Cr (Bonnand et al., 2020b; Shen et al., 2020). The parental magmas of the different localities were estimated to be slightly lower than the BSE caused by

partial melting at variable redox conditions (variable Cr^{2+}/Cr_{total}) (Bonnand et al., 2020b; Shen et al., 2020). Most recently, a study investigated MORBs from various ocean basins (Ma et al., 2022). These authors interpreted the observed positive trend between $\delta^{53/52}$Cr and MgO as the result of fractional crystallization. Although the light $\delta^{53/52}$Cr imparted by fractional crystallization agrees with observations of OIBs, the authors applied the same fractional crystallization model for all their samples despite clearly not following the same liquid lines of descent (for further discussion see Chapter 3 of this thesis).
The large $\delta^{53/52}$Cr variations of mantle peridotites and mantle derived xenoliths were attributed to metasomatism of silicate or carbonatitic melts inducing a shift to heavy $\delta^{53/52}$Cr and suggested an at least locally heterogeneous mantle (Jerram et al., 2022; Xia et al., 2017). Pyroxenitic veins exhibit a very light $\delta^{53/52}$Cr signature, which has been explained by kinetic effects (Jerram et al., 2022; Xia et al., 2017). Most recently, using model calculations, applied to multiple isotope systems, to evaluate the effects of pyroxenitic contributions during mantle melting on the stable isotopic composition of basalts showed that Cr isotopes can be used as tracers for source lithologies such as pyroxenites (Soderman et al., 2022). The model predicts these melts to exhibit a lower $\delta^{53/52}$Cr compared to melts from pure peridotite sources (Soderman et al., 2022). Nonetheless, the extent to which the mantle is heterogeneous, and if this heterogeneity is reflected by basalts erupting on the surface remains rather enigmatic. Moreover, the effect of the variety of recycled components with variable Cr isotopic compositions is so far unresolved (e.g., heavily serpentinized peridotites with $\delta^{53/52}$Cr of up to +1.23 ‰, Farkas et al., 2013; carbonated peridotite, Jerram et al., 2022, and oceanic crust, Chapter 3; Ma et al., 2022).

1.1.3 Iron

1.1.3.1 Iron elemental systematics

Iron is the second most abundant element on Earth (Palme and O'Neill, 2014) and fourth most abundant element in Earth's mantle and crust (Palme and O'Neill, 2014; Rudnick and Gao, 2014). Of special interest is that Fe is the most abundant multivalent transition metal and will thus control the overall fO_2 of silicate melts (Cicconi et al., 2020). Depending on the redox environment, Fe behaves as a siderophile (Fe_0) and is enriched in the core, or as a lithophile (Fe^{2+} and Fe^{3+}), in which it forms a range of silicates and oxides at higher oxygen levels. At fO_2 of ΔFMQ >1, $Fe^{3+}/Fe^{2+} = 0.5$ (Figure 1.2a) whereas under common fO_2 for Earth's mantle conditions ($fO_2 = \Delta$FMQ ± 1) $Fe^{3+}/Fe_{total} = 0.15$ (e.g., Bézos and Humler, 2005). As a major element, Fe is a common constituent in most mantle minerals. Olivine largely incorporates Fe^{2+}, whereas pyroxenes, garnet, and spinel variably incorporate Fe^{2+} and Fe^{3+} into their crystal lattices. Based on crystal field theory, Fe^{2+} acquires only small octahedral CFSE, whereas Fe^{3+} has an octahedral CFSE of zero (Burns, 1970). This may result in a slight preference of Fe^{2+} for octahedral sites, whereas no preference for octahedral or tetrahedral coordination is predicted for Fe^{3+} (Burns, 1970). Based on ionic radius and charge, olivine incorporates Fe^{2+} (0.78 Å) into its octahedral sites, whereas Fe^{3+} (0.645 Å) is considered to be negligible (Figure 1.2b; Shannon, 1976). Similarly, orthopyroxenes only incorporate minor amounts of Fe^{3+} (0.2 to 0.6 wt. % Fe_2O_3; Woodland and Koch, 2003; Yaxley et al.,

2012), whereas Fe^{2+} is regularly partitioned into the octahedral coordinated sites (i.e., endmember ferrosilit $Fe_2Si_2O_6$) and is thus highly compatible in orthopyroxene, in agreement with experimental studies (e.g., Mallmann and O'Neill, 2009). Iron partitioning into clinopyroxene has been shown to be complex, as it depends on the melt composition controlling the composition of pyroxenes (McCanta et al., 2004). Whereas Fe^{2+} is easily incorporated into clinopyroxenes based on its ionic radius and charge, Fe^{3+} incorporation is often charge balanced by the coupled substitution of Al^{3+} or Na^{+} (Papike et al., 2005). As the spinel structure ($^{[4]}A^{[6]}B_2O_4$) is quite adjustable, partitioning of Fe^{2+} and Fe^{3+} is also variable. In Cr-spinel, Fe^{2+} partitions into the tetrahedral coordinated site. For Fe-Ti oxides, ulvöspinel incorporates Fe^{2+} in its tetrahedral A- and octahedral B-site, whereas magnetite preferentially incorporates Fe^{3+} into its tetrahedral coordinated A-site and Fe^{2+} and Fe^{3+} into its octahedral-coordinated B-site. Most garnet varieties ($^{[8]}A_3{}^{[6]}B_2Si_3O_{12}$) incorporate Fe^{2+} in their [8]-coordinated A-site along with Ca and Mg. In contrast, Fe^{3+} is usually partitioned into garnet at its octahedral B site with andradite as an endmember ($Ca_3Fe_2^{3+}Si_3O_{12}$). During partial melting Fe^{3+} is thought to behave more incompatibly than Fe^{2+} (Canil et al., 1994; O'Neill et al., 1993), leading to an Fe^{3+} enrichment in the melt. In silicate melts, X-ray absorption studies indicate that Fe^{2+} prefers the higher coordination compared to Fe^{3+} (Cicconi et al., 2020; Wilke et al., 2004). Moreover, the stabilization of Fe^{3+} or Fe^{2+} in silicate melts depends on melt composition. Increasing melt basicity (i.e., increasing network modifiers such as Na and K) favours the oxidized species, so that for example trachytic melts exhibit a higher Fe^{3+}/Fe_{total} ratio compared to basaltic melts (Cicconi et al., 2020; Kress and Carmichael, 1991).

1.1.3.2 High-temperature stable Fe isotope systematics

Iron has four stable isotopes ^{54}Fe, ^{56}Fe, ^{57}Fe, and ^{58}Fe with natural abundances of 5.845 %, 91.754 %, 2.119 %, and 0.282 %, respectively. As discussed above, the presence of Fe^{2+} and Fe^{3+} in silicate melts and redox exchange reactions during magmatic processes are expected to lead to measurable variations in iron isotopic compositions given as δ-values (see also Eq. 1.1), relative to reference material IRMM-014, henceforth referred to as $\delta^{56/54}Fe$. Among stable transition metal isotope systems, stable Fe isotopes are probably the most well-studied, with most recent reviews specifically on iron isotope geochemistry given by Dauphas et al. (2017) and Johnson et al. (2020). The following paragraphs are a relatively brief overview on the behavior of Fe isotope in high-temperature systems.

Although first investigations on the Fe isotopic composition of igneous rocks could not identify significant variations (Beard and Johnson, 1999), subsequent analytical improvements (e.g., Schoenberg and von Blanckenburg, 2005) led to the resolution of small Fe isotope variations within planetary and silicate Earth reservoirs, including inter-mineral isotope differences (e.g., Beard and Johnson, 2004; Schoenberg and von Blanckenburg, 2006; Weyer et al., 2005; Williams et al., 2004; Williams et al., 2005; Zhu et al., 2002). Various studies investigated the Fe isotopic composition of the BSE and yielded $\delta^{56/54}Fe$ of $+0.015 \pm 0.018$ ‰ (2SD, n=11; Weyer et al., 2005) or 0.02 ± 0.03 ‰ (Weyer and Ionov, 2007) based on terrestrial peridotites from diverse tectonic settings, $+0.025 \pm 0.025$ ‰ based on abyssal peridotites (Craddock et al., 2013), or -0.08 ± 0.033 ‰ based on the 90 Ma Gorgona komatiite suite (Hibbert et al., 2012). These estimates overlap within error, and are indistinguishable from

the average chondrite $\delta^{56/54}$Fe value of -0.011 ± 0.106 ‰ compiled by Johnson et al. (2020) suggesting negligible Fe isotope fractionation during core formation (Weyer et al., 2007; Weyer et al., 2005; Weyer and Ionov, 2007). Bulk rock as well as mineral analyses of mantle peridotites can be highly variable in $\delta^{56/54}$Fe, which has been attributed to kinetic processes associated with metasomatism and melt percolation (Poitrasson et al., 2013; Weyer and Ionov, 2007). At equilibrium, $\delta^{56/54}$Fe of silicate mantle minerals increase from olivine, garnet < pyroxene < spinel (Macris et al., 2015; Weyer and Ionov, 2007; Williams and Bizimis, 2014; Williams et al., 2004; Williams et al., 2005), broadly in agreement with ionic modeling (Macris et al., 2015; Young et al., 2015). Non-metasomatized peridotites have been shown to correlate with indices of melt extraction, during which the $\delta^{56/54}$Fe of the residual peridotite decreases with increasing melt depletion (Weyer and Ionov, 2007; Williams et al., 2005). Based on this observation and the heavier average $\delta^{56/54}$Fe of basalts (+0.107 ± 0.055 ‰; n=119; compiled from Chen et al., 2019b; Richter et al., 2021; Teng et al., 2013; Weyer and Ionov, 2007) compared to peridotites, it was suggested that partial melting fractionates Fe isotopes.
The magnitude of Fe isotopic fractionation is suggested to be dependent on Fe^{3+}/Fe_{total} of the source and melt, the degree of melting, and the source lithology (Dauphas et al., 2009). With increasing partial melting degrees Fe isotopic fractionation decreases (Dauphas et al., 2009; Williams and Bizimis, 2014; Williams et al., 2009; Williams et al., 2005), in agreement with the on average lower $\delta^{56/54}$Fe of large-degree mantle melts such as Archean komatiites (Dauphas et al., 2010; Hibbert et al., 2012; Nebel et al., 2014). Ocean islands basalts are more variable, extending towards higher $\delta^{56/54}$Fe values (up to +0.34 ‰ for Samoan lavas, (Konter et al., 2016), whereas the majority of OIBs has $\delta^{56/54}$Fe between 0.00 and +0.2 ‰ (McCoy-West et al., 2018; Nebel et al., 2019; Peters et al., 2019; Schuessler et al., 2009; Soderman et al., 2021; Teng et al., 2008; Teng et al., 2013; Weyer and Ionov, 2007). The higher $\delta^{56/54}$Fe variability of OIBs has been frequently attributed towards a lithological heterogeneous source consisting of peridotite and pyroxenites. Pyroxenites have been shown to exhibit heavier Fe isotopic compositions compared to peridotites (Macris et al., 2015; Williams and Bizimis, 2014). Combining mineral-specific fractionation factors with a source signature that is initially isotopically heavier than pure peridotite may thus contribute to the heavier and more heterogeneous $\delta^{56/54}$Fe of basalts sampling these sources. Theoretical calculations using a thermodynamical melting model combined with equilibrium fractionation factors showed that Fe isotopes may trace pyroxenitic components driving the $\delta^{56/54}$Fe of basalts towards heavier $\delta^{56/54}$Fe in MORB sources and OIB sources (Gleeson et al., 2020; Soderman et al., 2021; Soderman et al., 2022; Williams and Bizimis, 2014). An additional process influencing Fe isotopic composition of basalts is fractional crystallization, driving $\delta^{56/54}$Fe of the residual melt towards heavier values due to the incorporation of light Fe isotopes into olivine and pyroxenes (Schuessler et al., 2009; Sossi et al., 2012; Teng et al., 2008; Williams et al., 2018). Iron isotopic fractionation during fractional crystallization is dependent on the mineral assemblage, e.g. magnetite or Cr-spinel crystallization would impart a lower $\delta^{56/54}$Fe onto the residual melt (McCoy-West et al., 2018; Sossi et al., 2012; Williams et al., 2018). Moreover, in highly differentiated igneous rocks $\delta^{56/54}$Fe may increase up to +0.3 ‰, proposed to be due to e.g., fluid exsolution during fractional crystallization (Heimann et al., 2008; Telus et al., 2012; Zambardi et al., 2014).

1.2 Scope of this thesis

As shown in the previous sections several factors can influence stable Cr (and Fe) isotopic fractionations. Mediated by the prevailing fO_2, the variable abundances and structural associations of Cr^{2+} and Cr^{3+} (as well as Fe^{2+} and Fe^{3+}) between melts and minerals likely result in Cr isotopic fractionations during magmatic processes, similar to what is observed for Fe isotopes.
Although the numbers of studies concerning the behavior of Cr isotopes during high-temperature processes have increased, it remains an open question to what extent Cr isotopes fractionate during magmatic processes. Thus, a better understanding of Cr isotopic fractionation during magmatic processes is needed to develop stable Cr isotopes as a tracer for mantle fO_2.
This thesis is separated into three main chapters (Chapter 2, 3, and 4), which aim to improve our understanding of stable isotope fractionation under high-temperature conditions. Thereby, different reservoirs of the Earth are explored by investigating mantle derived melts generated at variable conditions and encompassing Archean komatiites and basalt as well as Phanerozoic basalts from a variety of petrogenetic settings including mid-ocean ridges and intraplate volcanism.
Chapter 2 investigates two komatiite-tholeiite suites from Archean Greenstone belts, i.e., the 3.5 Ga Barberton greenstone belt (South Africa and Eswatini) and the 2.9-2.7 Ga Belingwe greenstone belt (Zimbabwe), to evaluate the influence of magmatic processes operating during the Archean before revising the Cr isotope value of the BSE. Using komatiites to constrain the Cr isotope BSE value is particular helpful as large degrees of melting at very high temperatures minimize isotope fractionation during partial melting. Moreover, as komatiite-tholeiite suites from the Archean are typically affected by magmatic differentiation and post-magmatic alteration, the influence of these processes on Cr isotope fractionation will be discussed in detail. This work is published in Chemical Geology (Wagner, L. J., Kleinhanns, I. C., Weber, N., Babechuk, M. G., Hofmann, A., Schoenberg, R. 2021. Coupled stable chromium and iron isotopic fractionation tracing magmatic mineral crystallization in Archean komatiite-tholeiite suites. Chemical Geology, 576, 120121).
Chapter 3 evaluates the effect of partial melting and fractional crystallization during typical fast spreading mid-ocean ridge basalts genesis to constrain the effect of modern terrestrial mantle melting conditions on Cr isotope variations. This chapter focuses on modeling Cr isotopic behavior during partial melting at a mid-ocean ridge setting based on phase equilibria mantle melting models using MELTS. The results show that melting of peridotitic upper depleted mantle produces a melt enriched in light Cr isotopes. However, based on the overall lower Cr isotopic composition of MORBs compared to the model the results are subsequently evaluated in the light of source mineralogical constraints of mid-ocean ridge basalts providing compelling evidence for a pyroxene-rich source sampled by mid-ocean ridge basalts. This chapter has been submitted to Geochimica et Cosmochimica Acta.
Chapter 4 aims to improve our understanding of the controlling processes leading to the observed Cr isotope variations of ocean island basalts and continental intraplate basalts. Fe isotopes have been used extensively to constrain source mineralogical effects, whereas Cr has recently been proposed to trace pyroxenitic source compositions. However, the investigation of Cr isotope systematics of ocean island basalts is so far limited to two locations in the Pacific Ocean (Fangataufa atoll,

French Polynesia (Bonnand et al., 2020b) and Hawaii (Shen et al., 2020)). The focus of this study lies on the effect of mantle source heterogeneity on Cr isotope systematics by studying intraplate basalt suites encompassing a variety of mantle source compositions as defined by radiogenic isotope systematics.

References

Albut, G., Babechuk, M.G., Kleinhanns, I.C., Benger, M., Beukes, N.J., Steinhilber, B., Smith, A.J., Kruger, S.J., Schoenberg, R., 2018. Modern rather than Mesoarchaean oxidative weathering responsible for the heavy stable Cr isotopic signatures of the 2.95 Ga old Ijzermijn iron formation (South Africa). Geochimica et Cosmochimica Acta 228, 157-189.

Allegre, C.J., Poirier, J.-P., Humler, E., Hofmann, A.W., 1995. The chemical composition of the Earth. Earth and Planetary Science Letters 134, 515-526.

Anbar, A.D., Rouxel, O., 2007. Metal stable isotopes in paleoceanography. Annual Review of Earth and Planetary Sciences 35, 717-746.

Babechuk, M., Kleinhanns, I., Schoenberg, R., 2017. Chromium geochemistry of the ca. 1.85 Ga Flin Flon paleosol. Geobiology 15, 30-50.

Babechuk, M.G., Weimar, N.E., Kleinhanns, I.C., Eroglu, S., Swanner, E.D., Kenny, G.G., Kamber, B.S., Schoenberg, R., 2019. Pervasively anoxic surface conditions at the onset of the Great Oxidation Event: New multi-proxy constraints from the Cooper Lake paleosol. Precambrian Research 323, 126-163.

Bai, Y., Su, B.X., Xiao, Y., Chen, C., Cui, M.M., He, X.Q., Qin, L.P., Charlier, E.N.R., 2019. Diffusion-driven chromium isotope fractionation in ultramafic cumulate minerals: Elemental and isotopic evidence from the Stillwater Complex. Geochimica et Cosmochimica Acta 263, 167-181.

Barnes, S.J., 1998. Chromite in komatiites, 1. Magmatic controls on crystallization and composition. Journal of Petrology 39, 1689-1720.

Basu, A., Johnson, T.M., 2012. Determination of hexavalent chromium reduction using Cr stable isotopes: isotopic fractionation factors for permeable reactive barrier materials. Environmental Science & Technology 46, 5353-5360.

Beard, B.L., Johnson, C.M., 1999. High precision iron isotope measurements of terrestrial and lunar materials. Geochimica et Cosmochimica Acta 63, 1653-1660.

Beard, B.L., Johnson, C.M., 2004. Inter-mineral Fe isotope variations in mantle-derived rocks and implications for the Fe geochemical cycle. Geochimica et Cosmochimica Acta 68, 4727-4743.

Bell, A.S., Burger, P.V., Le, L., Shearer, C.K., Papike, J.J., Sutton, S.R., Newville, M., Jones, J., 2014. XANES measurements of Cr valence in olivine and their applications to planetary basalts. American Mineralogist 99, 1404-1412.

Berna, E.C., Johnson, T.M., Makdisi, R.S., Basu, A., 2010. Cr stable isotopes as indicators of Cr (VI) reduction in groundwater: a detailed time-series study of a point-source plume. Environmental Science & Technology 44, 1043-1048.

Berry, A.J., Miller, L.A., O'Neill, H.S.C., Foran, G.J., 2021a. The coordination of Cr^{2+} in silicate glasses and implications for mineral-melt fractionation of Cr isotopes. Chemical Geology 586, 120483.

Berry, A.J., O'Neill, H.S.C., Foran, G.J., 2021b. The effects of temperature and pressure on the oxidation state of chromium in silicate melts. Contributions to Mineralogy and Petrology 176, 40.

Berry, A.J., O'Neill, H.S.C., Scott, D.R., Foran, G.J., Shelley, J.M.G., 2006. The effect of composition on Cr^{2+}/Cr^{3+} in silicate melts. American Mineralogist 91, 1901-1908.

Berry, A.J., O'Neill, H.S.C., 2004. A XANES determination of the oxidation state of chromium in silicate glasses. American Mineralogist 89, 790-798.

Bézos, A., Humler, E., 2005. The $Fe^{3+}/\Sigma Fe$ ratios of MORB glasses and their implications for mantle melting. Geochimica et Cosmochimica Acta 69, 711-725.

Bigeleisen, J., Mayer, M.G., 1947. Calculation of equilibrium constants for isotopic exchange reactions. The Journal of Chemical Physics 15, 261-267.

Blowes, D., 2002. Tracking hexavalent Cr in groundwater. Science 295, 2024-2025.

Bonnand, P., Bruand, E., Matzen, A.K., Jerram, M., Schiavi, F., Wood, B.J., Boyet, M., Halliday, A.N., 2020a. Redox control on chromium isotope behavior in silicate melts in contact with magnesiochromite. Geochimica et Cosmochimica Acta 288, 282-300.

Bonnand, P., Doucelance, R., Boyet, M., Bachelery, P., Bosq, C., Auclair, D., Schiano, P., 2020b. The influence of igneous processes on the chromium isotopic compositions of Ocean Island basalts. Earth and Planetary Science Letters 532, 116028.

Bonnand, P., Halliday, A., 2018. Oxidized conditions in iron meteorite parent bodies. Nature Geoscience 11, 401-404.

Bonnand, P., Parkinson, I.J., Anand, M., 2016a. Mass dependent fractionation of stable chromium isotopes in mare basalts: Implications for the formation and the differentiation of the Moon. Geochimica et Cosmochimica Acta 175, 208-221.

Bonnand, P., Williams, H.M., Parkinson, I.J., Wood, B.J., Halliday, A.N., 2016b. Stable chromium isotopic composition of meteorites and metal-silicate experiments: Implications for fractionation during core formation. Earth and Planetary Science Letters 435, 14-21.

Burns, R.G., 1970. Site preferences of transition metal ions in silicate crystal structures. Chemical Geology 5, 275-283.

Burns, R.G., 1975a. Crystal field effects in chromium and its partitioning in the mantle. Geochimica et Cosmochimica Acta 39, 857-864.

Burns, R.G., 1975b. Occurence and stability of divalent chromium in olivines included in diamonds. Contributions to Mineralogy and Petrology 51, 213-221.

Canil, D., O'Neill, H.S.C., Pearson, D., Rudnick, R.L., McDonough, W.F., Carswell, D., 1994. Ferric iron in peridotites and mantle oxidation states. Earth and Planetary Science Letters 123, 205-220.

Chen, C., Su, B.-X., Xiao, Y., Sakyi, P.A., He, X.-Q., Pang, K.-N., Uysal, I., Avcı, E., Qin, L.-P., 2019a. High-temperature chromium isotope fractionation and its implications: Constraints from the Kızıldağ ophiolite, SE Turkey. Lithos 342, 361-369.

Chen, S., Niu, Y.L., Guo, P.Y., Gong, H.M., Sun, P., Xue, Q.Q., Duan, M., Wang, X.H., 2019b. Iron isotope fractionation during mid-ocean ridge basalt (MORB) evolution: Evidence from lavas on the East Pacific Rise at 10° 30' N and its implications. Geochimica et Cosmochimica Acta 267, 227-239.

Cicconi, M.R., Le Losq, C., Moretti, R., Neuville, D.R., 2020. Magmas are the largest repositories and carriers of earth's redox processes. Elements 16, 173-178.

Cole, D.B., Reinhard, C.T., Wang, X., Gueguen, B., Halverson, G.P., Gibson, T., Hodgskiss, M.S., McKenzie, N.R., Lyons, T.W., Planavsky, N.J., 2016. A shale-hosted Cr isotope record of low atmospheric oxygen during the Proterozoic. Geology 44, 555-558.

Corgne, A., Liebske, C., Wood, B.J., Rubie, D.C., Frost, D.J., 2005. Silicate perovskite-melt partitioning of trace elements and geochemical signature of a deep perovskitic reservoir. Geochimica et Cosmochimica Acta 69, 485-496.

Craddock, P.R., Warren, J.M., Dauphas, N., 2013. Abyssal peridotites reveal the near-chondritic Fe isotopic composition of the Earth. Earth and Planetary Science Letters 365, 63-76.

Crowe, S.A., Døssing, L.N., Beukes, N.J., Bau, M., Kruger, S.J., Frei, R., Canfield, D.E., 2013. Atmospheric oxygenation three billion years ago. Nature 501, 535-538.

Dauphas, N., Craddock, P.R., Asimow, P.D., Bennett, V.C., Nutman, A.P., Ohnenstetter, D., 2009. Iron isotopes may reveal the redox conditions of mantle melting from Archean to Present. Earth and Planetary Science Letters 288, 255-267.

Dauphas, N., John, S.G., Rouxel, O., 2017. Iron isotope systematics. Reviews in Mineralogy and Geochemistry 82, 415-510.

Dauphas, N., Teng, F.Z., Arndt, N.T., 2010. Magnesium and iron isotopes in 2.7 Ga Alexo komatiites: Mantle signatures, no evidence for Soret diffusion, and identification of diffusive transport in zoned olivine. Geochimica et Cosmochimica Acta 74, 3274-3291.

Drake, M.J., Newsom, H.E., Capobianco, C.J., 1989. V, Cr, and Mn in the Earth, Moon, EPB, and SPB and the origin of the Moon: Experimental studies. Geochimica et Cosmochimica Acta 53, 2101-2111.

Eeckhout, S.G., Bolfan-Casanova, N., McCammon, C., Klemme, S., Amiguet, E., 2007. XANES study of the oxidation state of Cr in lower mantle phases: Periclase and magnesium silicate perovskite. American Mineralogist 92, 966-972.

Ellis, A.S., Johnson, T.M., Bullen, T.D., 2002. Chromium isotopes and the fate of hexavalent chromium in the environment. Science 295, 2060-2062.

Ellis, A.S., Johnson, T.M., Bullen, T.D., 2004. Using chromium stable isotope ratios to quantify Cr (VI) reduction: lack of sorption effects. Environmental Science & Technology 38, 3604-3607.

Farkas, J., Chrastny, V., Novak, M., Cadkova, E., Pasava, J., Chakrabarti, R., Jacobsen, S.B., Ackerman, L., Bullen, T.D., 2013. Chromium isotope variations ($\delta^{53/52}$Cr) in mantle-derived sources and their weathering products: Implications for environmental studies and the evolution of $\delta^{53/52}$Cr in the Earth's mantle over geologic time. Geochimica et Cosmochimica Acta 123, 74-92.

Figowy, S., Dubacq, B., Noel, Y., d'Arco, P., 2020. Partitioning of chromium between garnet and clinopyroxene: first-principle modelling versus metamorphic assemblages. European Journal of Mineralogy 32, 387-403.

Frei, R., Gaucher, C., Poulton, S.W., Canfield, D.E., 2009. Fluctuations in Precambrian atmospheric oxygenation recorded by chromium isotopes. Nature 461, 250-253.

Geßmann, C.K., Rubie, D.C., 1998. The effect of temperature on the partitioning of nickel, cobalt, manganese, chromium, and vanadium at 9 GPa and constraints on formation of the Earth's core. Geochimica et Cosmochimica Acta 62, 867-882.

Gilleaudeau, G., Frei, R., Kaufman, A., Kah, L., Azmy, K., Bartley, J., Chernyavskiy, P., Knoll, A.H., 2016. Oxygenation of the mid-Proterozoic atmosphere: clues from chromium isotopes in carbonates. Geochemical Perspectives Letters 2, 178-187.

Gleeson, M.L., Gibson, S.A., Williams, H.M., 2020. Novel insights from Fe-isotopes into the lithological heterogeneity of Ocean Island Basalts and plume-influenced MORBs. Earth and Planetary Science Letters 535, 116114.

Goldschmidt, V.M., 1937. The principles of distribution of chemical elements in minerals and rocks. The seventh Hugo Müller Lecture, delivered before the Chemical Society on March 17th, 1937. Journal of the Chemical Society (Resumed), 655-673.

Hanson, B., Jones, J.H., 1998. The systematics of Cr^{3+} and Cr^{2+} partitioning between olivine and liquid in the presence of spinel. American Mineralogist 83, 669-684.

Heimann, A., Beard, B.L., Johnson, C.M., 2008. The role of volatile exsolution and sub-solidus fluid/rock interactions in producing high $^{56}Fe/^{54}Fe$ ratios in siliceous igneous rocks. Geochimica et Cosmochimica Acta 72, 4379-4396.

Hibbert, K.E.J., Williams, H.M., Kerr, A.C., Puchtel, I.S., 2012. Iron isotopes in ancient and modern komatiites: Evidence in support of an oxidised mantle from Archean to present. Earth and Planetary Science Letters 321, 198-207.

Izbicki, J.A., Ball, J.W., Bullen, T.D., Sutley, S.J., 2008. Chromium, chromium isotopes and selected trace elements, western Mojave Desert, USA. Applied Geochemistry 23, 1325-1352.

Jerram, M., Bonnand, P., Harvey, J., Ionov, D., Halliday, A.N., 2022. Stable chromium isotopic variations in peridotite mantle xenoliths: Metasomatism versus partial melting. Geochimica et Cosmochimica Acta 317, 138-154.

Jerram, M., Bonnand, P., Kerr, A.C., Nisbet, E.G., Puchtel, I.S., Halliday, A.N., 2020. The δ^{53}Cr isotope composition of komatiite flows and implications for the composition of the bulk silicate Earth. Chemical Geology 551, 119761.

Johnson, C., Beard, B., Weyer, S., 2020. Iron geochemistry: an isotopic perspective. Cham, Switzerland, Springer.

Johnson, C.M., Beard, B.L., Albarède, F., 2004. Geochemistry of non-traditional stable isotopes. Reviews in Mineralogy and Geochemistry 55.

Jollands, M., O'Neill, H.S.C., Van Orman, J., Berry, A., Hermann, J., Newville, M., Lanzirotti, A., 2018. Substitution and diffusion of Cr^{2+} and Cr^{3+} in synthetic forsterite and natural olivine at 1200–1500° C and 1 bar. Geochimica et Cosmochimica Acta 220, 407-428.

Kagi, H., Odake, S., Ishibashi, H., Shozugawa, K., Matsuo, M., Satake, W., Mikouchi, T., 2013. Oxygen fugacity and valence state of chromium in ferropericlase: Can Cr^{2+} be a redox indicator for the deep mantle? Journal of Mineralogical and Petrological Sciences 108, 172-177.

Klemme, S., Genske, F., Sossi, P.A., Berndt, J., Renggli, C.J., Stracke, A., 2022. Cr stable isotope fractionation by evaporation from silicate melts. Chemical Geology 610, 121096.

Konter, J.G., Pietruszka, A.J., Hanan, B.B., Finlayson, V.A., Craddock, P.R., Jackson, M.G., Dauphas, N., 2016. Unusual δ^{56}Fe values in Samoan rejuvenated lavas generated in the mantle. Earth and Planetary Science Letters 450, 221-232.

Kress, V.C., Carmichael, I.S., 1991. The compressibility of silicate liquids containing Fe_2O_3 and the effect of composition, temperature, oxygen fugacity and pressure on their redox states. Contributions to Mineralogy and Petrology 108, 82-92.

Li, J.P., Oneill, H.S.C., Seifert, F., 1995. Subsolidus phase-relations in the system MgO-SiO_2-Cr-O in equilibrium with metallic Cr, and their significance for the petrochemistry of chromium. Journal of Petrology 36, 107-132.

Liu, X., O'Neill, H.S.C., 2004. The effect of Cr_2O_3 on the partial melting of spinel lherzolite in the system CaO-MgO-Al_2O_3-SiO_2-Cr_2O_3 at 1.1 GPa. Journal of Petrology 45, 2261-2286.

Lodders, K., 2003. Solar system abundances and condensation temperatures of the elements. The Astrophysical Journal 591, 1220-1247.

Ma, H., Xu, L.-J., Shen, J., Liu, S.-A., Li, S., 2022. Chromium isotope fractionation during magmatic processes: Evidence from mid-ocean ridge basalts. Geochimica et Cosmochimica Acta 327, 79-95.

Macris, C.A., Manning, C.E., Young, E.D., 2015. Crystal chemical constraints on inter-mineral Fe isotope fractionation and implications for Fe isotope disequilibrium in San Carlos mantle xenoliths. Geochimica et Cosmochimica Acta 154, 168-185.

Mallmann, G., Burnham, A.D., Fonseca, R.O., 2021. Mineral-Melt Partitioning of Redox-Sensitive Elements. Magma Redox Geochemistry, 345-367.

Mallmann, G., O'Neill, H.S.C., 2009. The Crystal/Melt Partitioning of V during Mantle Melting as a Function of Oxygen Fugacity Compared with some other Elements (Al, P, Ca, Sc, Ti, Cr, Fe, Ga, Y, Zr and Nb). Journal of Petrology 50, 1765-1794.

McCanta, M.C., Dyar, M.D., Rutherford, M.J., Delaney, J.S., 2004. Iron partitioning between basaltic melts and clinopyroxene as a function of oxygen fugacity. American Mineralogist 89, 1685-1693.

McCoy-West, A.J., Chowdhury, P., Burton, K.W., Sossi, P., Nowell, G.M., Fitton, J.G., Kerr, A.C., Cawood, P.A., Williams, H.M., 2019. Extensive crustal extraction in Earth's early history inferred from molybdenum isotopes. Nature Geoscience 12, 946-951.

McCoy-West, A.J., Fitton, J.G., Pons, M.L., Inglis, E.C., Williams, H.M., 2018. The Fe and Zn isotope composition of deep mantle source regions: Insights from Baffin Island picrites. Geochimica et Cosmochimica Acta 238, 542-562.

McDonough, W.F., Sun, S.-S., 1995. The composition of the Earth. Chemical geology 120, 223-253.

Moynier, F., Yin, Q.-z., Jacobsen, B., 2007. Dating the first stage of planet formation. The Astrophysical Journal 671, L181.

Moynier, F., Yin, Q.Z., Schauble, E., 2011. Isotopic Evidence of Cr Partitioning into Earth's Core. Science 331, 1417-1420.

Murck, B.W., Campbell, I.H., 1986. The effects of temperature, oxygen fugacity and melt composition on the behavior of chromium in basic and ultrabasic melts. Geochimica et Cosmochimica Acta 50, 1871-1887.

Nebel, O., Campbell, I.H., Sossi, P.A., Van Kranendonk, M.J., 2014. Hafnium and iron isotopes in early Archean komatiites record a plume-driven convection cycle in the Hadean Earth. Earth and Planetary Science Letters 397, 111-120.

Nebel, O., Sossi, P.A., Bénard, A., Arculus, R.J., Yaxley, G.M., Woodhead, J.D., Davies, D.R., Ruttor, S., 2019. Reconciling petrological and isotopic mixing mechanisms in the Pitcairn mantle plume using stable Fe isotopes. Earth and Planetary Science Letters 521, 60-67.

O'Neill, H.S.C., 1991. The origin of the Moon and the early history of the Earth - A chemical model. Part 2: The Earth. Geochimica et Cosmochimica Acta 55, 1159-1172.

O'Neill, H.S.C., Rubie, D., Canil, D., Geiger, C., Ross, C., Seifert, F., Woodland, A., 1993. Ferric iron in the upper mantle and in transition zone assemblages: Implications for relative oxygen fugacities in the mantle. Geophysical monograph series 74, 73-88.

Odake, S., Fukura, S., Arakawa, M., Ohta, A., Harte, B., Kagi, H., 2008. Divalent chromium in ferropericlase inclusions in lower-mantle diamonds revealed by micro-XANES measurements. Journal of Mineralogical and Petrological Sciences 103, 350-353.

Ohtani, E., Yurimoto, H., 1996. Element partitioning between metallic liquid, magnesiowustite, and silicate liquid at 20 GPa and 2500°C: A secondary ion mass spectrometric study. Geophysical Research Letters 23, 1993-1996.

Palme, H., O'Neill, H.S.C., 2014. Cosmochemical Estimates of Mantle Composition in: Turekian, K.K., Holland, H.D. (Eds.), Treatise on Geochemistry, 2 ed. Elsevier,

pp. 1-39.

Papike, J.J., Karner, J.M., Shearer, C.K., 2005. Comparative planetary mineralogy: Valence state partitioning of Cr, Fe, Ti, and V among crystallographic sites in olivine, pyroxene, and spinel from planetary basalts. American Mineralogist 90, 277-290.

Papike, J.J., Simon, S.B., Burger, P.V., Bell, A.S., Shearer, C.K., Karner, J.M., 2016. Chromium, vanadium, and titanium valence systematics in Solar System pyroxene as a recorder of oxygen fugacity, planetary provenance, and processes. American Mineralogist 101, 907-918.

Peters, B.J., Shahar, A., Carlson, R.W., Day, J.M., Mock, T.D., 2019. A sulfide perspective on iron isotope fractionation during ocean island basalt petrogenesis. Geochimica et Cosmochimica Acta 245, 59-78.

Planavsky, N.J., Reinhard, C.T., Wang, X., Thomson, D., McGoldrick, P., Rainbird, R.H., Johnson, T., Fischer, W.W., Lyons, T.W., 2014. Low Mid-Proterozoic atmospheric oxygen levels and the delayed rise of animals. Science 346, 635-638.

Poitrasson, F., Delpech, G., Grégoire, M., 2013. On the iron isotope heterogeneity of lithospheric mantle xenoliths: implications for mantle metasomatism, the origin of basalts and the iron isotope composition of the Earth. Contributions to Mineralogy and Petrology 165, 1243-1258.

Richter, F.M., Dauphas, N., Teng, F.-Z., 2009. Non-traditional fractionation of non-traditional isotopes: evaporation, chemical diffusion and Soret diffusion. Chemical Geology 258, 92-103.

Richter, F.M., Davis, A.M., DePaolo, D.J., Watson, E.B., 2003. Isotope fractionation by chemical diffusion between molten basalt and rhyolite. Geochimica et Cosmochimica Acta 67, 3905-3923.

Richter, M., Nebel, O., Schwindinger, M., Nebel-Jacobsen, Y., Dick, H.J.B., 2021. Competing effects of spreading rate, crystal fractionation and source variability on Fe isotope systematics in mid-ocean ridge lavas. Scientific Reports 11, 4123.

Righter, K., Sutton, S., Danielson, L., Pando, K., Schmidt, G., Yang, H., Berthet, S., Newville, M., Choi, Y., Downs, R.T., 2011. The effect of fO_2 on the partitioning and valence of V and Cr in garnet/melt pairs and the relation to terrestrial mantle V and Cr content. American Mineralogist 96, 1278-1290.

Roeder, P., Reynolds, I., 1991. Crystallization of chromite and chromium solubility in basaltic melts. Journal of Petrology 32, 909-934.

Rotaru, M., Birck, J.L., Allègre, C.J., 1992. Clues to early solar system history from chromium isotopes in carbonaceous chondrites. Nature 358, 465-470.

Rudnick, R., Gao, S., 2014. Composition of the continental crust, in: Turekian, K.K., Holland, H.D. (Eds.), Treatise on Geochemistry, 2 ed. Elsevier, pp. 1-51.

Salters, V.J.M., Stracke, A., 2004. Composition of the depleted mantle. Geochemistry, Geophysics, Geosystems 5, Q05B07.

Schauble, E., Rossman, G.R., Taylor Jr, H.P., 2004. Theoretical estimates of equilibrium chromium-isotope fractionations. Chemical Geology 205, 99-114.

Schauble, E.A., 2004. Applying stable isotope fractionation theory to new systems. Reviews in Mineralogy and Geochemistry 55, 65-111.

Schiller, M., Van Kooten, E., Holst, J.C., Olsen, M.B., Bizzarro, M., 2014. Precise measurement of chromium isotopes by MC-ICPMS. Journal of Analytical Atomic Spectrometry 29, 1406-1416.

Schoenberg, R., Merdian, A., Holmden, C., Kleinhanns, I.C., Haßler, K., Wille, M., Reitter, E., 2016. The stable Cr isotopic compositions of chondrites and silicate planetary reservoirs. Geochimica et Cosmochimica Acta 183, 14-30.

Schoenberg, R., von Blanckenburg, F., 2005. An assessment of the accuracy of stable Fe isotope ratio measurements on samples with organic and inorganic matrices by high-resolution multicollector ICP-MS. International Journal of Mass Spectrometry 242, 257-272.

Schoenberg, R., von Blanckenburg, F., 2006. Modes of planetary-scale Fe isotope fractionation. Earth and Planetary Science Letters 252, 342-359.

Schoenberg, R., Zink, S., Staubwasser, M., von Blanckenburg, F., 2008. The stable Cr isotope inventory of solid Earth reservoirs determined by double spike MC-ICP-MS. Chemical Geology 249, 294-306.

Schreiber, H.D., Haskin, L.A., 1976. Chromium in basalts: Experimental determination of redox states and partitioning among synthetic silicate phases, Lunar and planetary science conference proceedings, pp. 1221-1259.

Schuessler, J.A., Schoenberg, R., Sigmarsson, O., 2009. Iron and lithium isotope systematics of the Hekla volcano, Iceland - evidence for Fe isotope fractionation during magma differentiation. Chemical Geology 258, 78-91.

Shahar, A., Young, E.D., 2020. An assessment of iron isotope fractionation during core formation. Chemical Geology 554, 119800.

Shannon, R.D., 1976. Revised effective ionic-radii and systematic studies of interatomic distances in halides and chalcogenides. Acta Crystallographica 32, 751-767.

Sharp, Z., 2007. Principles of Stable Isotope Geochemistry, 1 ed.

Shen, J., Liu, J., Qin, L.P., Wang, S.J., Li, S.G., Xia, J.X., Ke, S., Yang, J.S., 2015. Chromium isotope signature during continental crust subduction recorded in metamorphic rocks. Geochemistry, Geophysics, Geosystems 16, 3840-3854.

Shen, J., Qin, L.P., Fang, Z.Y., Zhang, Y.N., Liu, J., Liu, W., Wang, F.Y., Xiao, Y., Yu, H.M., Wei, S.Q., 2018. High-temperature inter-mineral Cr isotope fractionation: A comparison of ionic model predictions and experimental investigations of mantle xenoliths from the North China Craton. Earth and Planetary Science Letters 499, 278-290.

Shen, J., Xia, J.X., Qin, L.P., Carlson, R.W., Huang, S.C., Helz, R.T., Mock, T.D., 2020. Stable chromium isotope fractionation during magmatic differentiation: Insights from Hawaiian basalts and implications for planetary redox conditions.

Geochimica et Cosmochimica Acta 278, 289-304.

Siebert, J., Corgne, A., Ryerson, F.J., 2011. Systematics of metal–silicate partitioning for many siderophile elements applied to Earth's core formation. Geochimica et Cosmochimica Acta 75, 1451-1489.

Soderman, C.R., Matthews, S., Shorttle, O., Jackson, M.G., Ruttor, S., Nebel, O., Turner, S., Beier, C., Millet, M.-A., Widom, E., 2021. Heavy δ^{57}Fe in ocean island basalts: A non-unique signature of processes and source lithologies in the mantle. Geochimica et Cosmochimica Acta 292, 309-332.

Soderman, C.R., Shorttle, O., Matthews, S., Williams, H.M., 2022. Global trends in novel stable isotopes in basalts: theory and observations. Geochimica et Cosmochimica Acta 318, 388-414.

Sossi, P.A., Foden, J.D., Halverson, G.P., 2012. Redox-controlled iron isotope fractionation during magmatic differentiation: an example from the Red Hill intrusion, S. Tasmania. Contributions to Mineralogy and Petrology 164, 757-772.

Sossi, P.A., Moynier, F., van Zuilen, K., 2018. Volatile loss following cooling and accretion of the Moon revealed by chromium isotopes. Proceedings of the National Acadademy of Science 115, 43, 10920-10925.

Sutton, S.R., Jones, K.W., Gordon, B., Rivers, M.L., Bajt, S., Smith, J.V., 1993. Reduced chromium in olivine grains from lunar basalt 15555 - X-ray absorption near edge structure (XANES). Geochimica et Cosmochimica Acta 57, 461-468.

Telus, M., Dauphas, N., Moynier, F., Tissot, F.L., Teng, F.-Z., Nabelek, P.I., Craddock, P.R., Groat, L.A., 2012. Iron, zinc, magnesium and uranium isotopic fractionation during continental crust differentiation: The tale from migmatites, granitoids, and pegmatites. Geochimica et Cosmochimica Acta 97, 247-265.

Teng, F.Z., Dauphas, N., Helz, R.T., 2008. Iron isotope fractionation during magmatic differentiation in Kilauea Iki Lava Lake. Science 320, 1620-1622.

Teng, F.Z., Dauphas, N., Huang, S.C., Marty, B., 2013. Iron isotopic systematics of oceanic basalts. Geochimica et Cosmochimica Acta 107, 12-26.

Trinquier, A., Birck, J.-L., Allègre, C.J., 2008. High-precision analysis of chromium isotopes in terrestrial and meteorite samples by thermal ionization mass spectrometry. Journal of Analytical Atomic Spectrometry 23, 1565-1574.

Urey, H.C., 1947. The thermodynamic properties of isotopic substances. Journal of the Chemical Society (Resumed), 562-581.

Urey, H.C., Greiff, L.J., 1935. Isotopic Exchange Equilibria. Journal of the American Chemical Society 57, 321-327.

van Westrenen, W., Blundy, J.D., Wood, B.J., 2001. High field strength element/rare earth element fractionation during partial melting in the presence of garnet: Implications for identification of mantle heterogeneities. Geochemistry, Geophysics, Geosystems 2, 2000GC000133.

Walter, M., Newsom, H., Ertel, W., Holzheid, A., 2000. Siderophile elements in the Earth and Moon: metal/silicate partitioning and implications for core formation.

Origin of the Earth and Moon 1, 265-289.

Wanner, C., Zink, S., Eggenberger, U., Mäder, U., 2012. Assessing the Cr (VI) reduction efficiency of a permeable reactive barrier using Cr isotope measurements and 2D reactive transport modeling. Journal of contaminant hydrology 131, 54-63.

Weyer, S., Anbar, A., Brey, G., Münker, C., Mezger, K., Woodland, A., 2007. Fe-isotope fractionation during partial melting on Earth and the current view on the Fe-isotope budgets of the planets (reply to the comment of F. Poitrasson and to the comment of BL Beard and CM Johnson on "Iron isotope fractionation during planetary differentiation" by S. Weyer, AD Anbar, GP Brey, C. Münker, K. Mezger and AB Woodland). Earth and Planetary Science Letters 256, 638-646.

Weyer, S., Anbar, A.D., Brey, G.P., Münker, C., Mezger, K., Woodland, A.B., 2005. Iron isotope fractionation during planetary differentiation. Earth and Planetary Science Letters 240, 251-264.

Weyer, S., Ionov, D.A., 2007. Partial melting and melt percolation in the mantle: The message from Fe isotopes. Earth and Planetary Science Letters 259, 119-133.

White, W., Klein, E., 2014. Composition of the oceanic crust, in: Turekian, K.K., Holland, H.D. (Eds.), Treatise on Geochemistry, 2 ed. Elsevier, pp. 457-496.

Wilke, M., Partzsch, G.M., Bernhardt, R., Lattard, D., 2004. Determination of the iron oxidation state in basaltic glasses using XANES at the K-edge. Chemical Geology 213, 71-87.

Williams, H.M., Bizimis, M., 2014. Iron isotope tracing of mantle heterogeneity within the source regions of oceanic basalts. Earth and Planetary Science Letters 404, 396-407.

Williams, H.M., McCammon, C.A., Peslier, A.H., Halliday, A.N., Teutsch, N., Levasseur, S., Burg, J.-P., 2004. Iron isotope fractionation and the oxygen fugacity of the mantle. Science 304, 1656-1659.

Williams, H.M., Nielsen, S.G., Renac, C., Griffin, W.L., O'Reilly, S.Y., McCammon, C.A., Pearson, N., Viljoen, F., Alt, J.C., Halliday, A.N., 2009. Fractionation of oxygen and iron isotopes by partial melting processes: implications for the interpretation of stable isotope signatures in mafic rocks. Earth and Planetary Science Letters 283, 156-166.

Williams, H.M., Peslier, A.H., McCammon, C., Halliday, A.N., Levasseur, S., Teutsch, N., Burg, J.-P., 2005. Systematic iron isotope variations in mantle rocks and minerals: the effects of partial melting and oxygen fugacity. Earth and Planetary Science Letters 235, 435-452.

Williams, H.M., Prytulak, J., Woodhead, J.D., Kelley, K.A., Brounce, M., Plank, T., 2018. Interplay of crystal fractionation, sulfide saturation and oxygen fugacity on the iron isotope composition of arc lavas: An example from the Marianas. Geochimica et Cosmochimica Acta 226, 224-243.

Wood, B.J., Kiseeva, E.S., Matzen, A.K., 2013. Garnet in the Earth's Mantle. Elements 9, 421-426. Wood, B.J., Wade, J., Kilburn, M.R., 2008. Core formation

and the oxidation state of the Earth: Additional constraints from Nb, V and Cr partitioning. Geochimica et Cosmochimica Acta 72, 1415-1426.

Woodland, A., Koch, M., 2003. Variation in oxygen fugacity with depth in the upper mantle beneath the Kaapvaal craton, Southern Africa. Earth and Planetary Science Letters 214, 295-310.

Xia, J.X., Qin, L.P., Shen, J., Carlson, R.W., Ionov, D.A., Mock, T.D., 2017. Chromium isotope heterogeneity in the mantle. Earth and Planetary Science Letters 464, 103-115.

Yaxley, G.M., Berry, A.J., Kamenetsky, V.S., Woodland, A.B., Golovin, A.V., 2012. An oxygen fugacity profile through the Siberian Craton—Fe K-edge XANES determinations of $Fe^{3+}/\Sigma Fe$ in garnets in peridotite xenoliths from the Udachnaya East kimberlite. Lithos 140, 142-151.

Young, E.D., Manning, C.E., Schauble, E.A., Shahar, A., Macris, C.A., Lazar, C., Jordan, M., 2015. High-temperature equilibrium isotope fractionation of non-traditional stable isotopes: Experiments, theory, and applications. Chemical Geology 395, 176-195.

Zambardi, T., Lundstrom, C.C., Li, X., McCurry, M., 2014. Fe and Si isotope variations at Cedar Butte volcano; insight into magmatic differentiation. Earth and Planetary Science Letters 405, 169-179.

Zhu, K., Sossi, P.A., Siebert, J., Moynier, F., 2019. Tracking the volatile and magmatic history of Vesta from chromium stable isotope variations in eucrite and diogenite meteorites. Geochimica et Cosmochimica Acta 266, 598-610.

Zhu, X., Guo, Y., Williams, R., O'nions, R., Matthews, A., Belshaw, N., Canters, G., De Waal, E., Weser, U., Burgess, B., 2002. Mass fractionation processes of transition metal isotopes. Earth and Planetary Science Letters 200, 47-62.

Chapter 2

Coupled stable chromium and iron isotopic fractionation tracing magmatic mineral crystallization in Archean komatiite-tholeiite suites

Abstract

Chromium exists in the two oxidation states Cr^{2+} and Cr^{3+} during high-temperature magmatic processes and changes in Cr redox are often associated with stable isotopic fractionation. Thus, the stable chromium isotope compositions of mantle-derived magmas bear the potential to trace the oxidation states of their mantle sources as well as any post melting changes in Cr redox (e.g. during magmatic differentiation), in a manner similar to magmatic stable Fe isotopic fractionation. However, these stable isotope fractionation effects are less understood for Cr relative to Fe. Komatiites and tholeiitic basalts represent a wide range of mantle-derived partial melts with variable fractional crystallization of phases with different affinity for Cr^{2+} and Cr^{3+}. Thus, they offer potential archives to better understand high-temperature Cr isotope fractionation processes and mantle redox.

Here, we report major and trace elements as well as coupled stable Cr and Fe isotope compositions of two well-characterized Archean komatiite-tholeiite suites from the Barberton Greenstone Belt, South Africa and Eswatini, and Belingwe Greenstone Belt, Zimbabwe. The sample suites range in MgO concentrations from 3.85 to 34.33 wt. %, which allows investigation of the impact of large degrees of magmatic differentiation in a komatiite-basalt system. Whole-rock $\delta^{53/52}Cr_{SRM979}$ and $\delta^{56/54}Fe_{IRMM014}$ values range from -0.390 ± 0.016 to -0.061 ± 0.016 ‰ and -0.014 ± 0.018 to +0.192 ± 0.018 ‰, respectively. The komatiites have a very narrow range in their Cr isotopic composition with an average $\delta^{53/52}Cr_{SRM979}$ value of -0.122 ± 0.050 ‰ (2SD; n=21), which supports previous estimates of the bulk silicate Earth $\delta^{53/52}Cr_{SRM979}$ value. However, high-Mg tholeiites and basaltic andesites exhibit significantly lighter $\delta^{53/52}Cr_{SRM979}$ and heavier $\delta^{56/54}Fe_{IRMM014}$ values than

komatiites. These variations can be linked to crystallization and accumulation of mineral phases observed from fractionation trends of the two Archean komatiite-tholeiite suites. In detail, during crystallization and accumulation of olivine the Cr isotope compositions of komatiites stay invariant, whereas at the onset of Cr-bearing spinel and pyroxene crystallization the Cr isotope signatures of komatiitic basalts, high-Mg tholeiites and basaltic andesites become progressively lighter, which is attributed to the preferential incorporation of isotopically heavier Cr^{3+} in these mineral phases. The gradual increase of $\delta^{56/54}Fe_{IRMM014}$ with increasing magmatic differentiation, does not allow identifying the crystallization of particular mineral phases using Fe isotopes alone. Ultimately, this study demonstrates the power of combining stable Cr and Fe isotopic analyses to examine the effects of fractional crystallization on modifying melt source values and thus to ensure accurate mantle redox estimations.

2.1 Introduction

Stable isotopes of redox-sensitive transition metals applied to high-temperature magmatic systems are potential proxies of the prevailing oxygen fugacity (fO_2) during magmatic processes (i.e., Dauphas et al., 2009; Prytulak et al., 2016; Shen et al., 2020; Weyer and Ionov, 2007; Williams et al., 2004; Williams et al., 2005). These proxies are grounded in theoretical ab initio calculations of bond strengths between two phases at isotopic equilibrium, which predict that heavier isotopes generally prefer the phase with the higher valence state and/or lower coordination number (Ottonello and Zuccolini, 2005; Schauble et al., 2004).
Among all multivalent stable metal isotope systems applied to study high-temperature magmatic systems so far, the processes and magnitude of fractionation between stable Fe isotopes are arguably the best understood (e.g. Dauphas et al., 2017). Previous studies have invoked a direct relationship between changing fO_2 and mass-dependent Fe isotope fractionation in magmatic systems (Dauphas et al., 2009; Williams et al., 2004; Williams et al., 2005), but many other magmatic processes may also cause Fe isotope fractionation between different phases and reservoirs. For example, partial mantle melting may enrich the magma in heavy Fe isotopes (mid-ocean ridge basalt (MORB) $\delta^{56/54}$Fe $\sim$+0.1 ‰; for definition of $\delta^{56/54}$Fe see equation 2.4) compared to the original mantle reservoir with a chondritic Fe isotopic signature ($\delta^{56/54}$Fe of $\sim$0 ‰; see Dauphas et al., 2009; Poitrasson et al., 2004; Schoenberg and von Blanckenburg, 2005; Schoenberg and von Blanckenburg, 2006; Schuessler et al., 2009; Weyer et al., 2005; Weyer and Ionov, 2007; Williams et al., 2004). Subsequent magmatic differentiation may further fractionate Fe isotopes depending on the associated fractional assemblage (Chen et al., 2019; Poitrasson and Freydier, 2005; Schoenberg et al., 2009; Schoenberg and von Blanckenburg, 2006; Schuessler et al., 2009; Sossi et al., 2012; Williams et al., 2018).
Interest in the application of stable Cr isotopes to study high-temperature magmatic systems has increased in recent years (Bonnand et al., 2020; Bonnand et al., 2016; Schoenberg et al., 2016; Schoenberg et al., 2008; Shen et al., 2015; Shen et al., 2018; Shen et al., 2020; Xia et al., 2017). On Earth the predominant redox state of the compatible element Cr in igneous minerals and rocks is Cr^{3+}. However, studies based on experimental data by Berry and O'Neill (2004), Berry et al. (2006) and Papike et al. (2016) confirmed findings of earlier studies that Cr^{2+} may also play a

significant role in magmatic (basaltic) melts and their crystallization products (Angel et al., 1989; Burns, 1975a; Schreiber and Haskin, 1976). An important result from the aforementioned experimental studies is that the $Cr^{2+}/\Sigma Cr$ ratios of the melt depend on melt composition and significantly increase with decreasing fO_2 and increasing temperature (Berry et al., 2006; Papike et al., 2016). According to crystal field theory Cr^{3+} has a strong preference for octahedral sites, such as the B-site in normal spinel ($A^{2+}B_2^{3+}O_4$), whereas Cr^{2+} preferentially occupies slightly distorted octahedral crystal lattice sites, such as the M_1 site in olivine ($M_1^{2+}M_2^{2+}SiO_4$; Burns, 1975a). Recently, analyses of mineral separates of peridotite xenoliths revealed decreasing $\delta^{53/52}$Cr values (see equation 2.1), in the order spinel >pyroxene >olivine in accordance with ionic modeling (Shen et al., 2018). As such, changes in Cr oxidation states between mantle peridotites and partial melts as well as differences in bonding environments between minerals and melt may bear the potential for Cr isotope fractionation during magmatic processes such as partial melting and fractional crystallization. However, Schoenberg et al. (2008) reported relatively homogenous $\delta^{53/52}$Cr values for mantle rocks and their derivatives (i.e., restites, partial melts and cumulates) with an average of -0.124 ± 0.101 ‰, defined as igneous inventory. Nevertheless, small but significant variations between chromites and the igneous inventory (Farkas et al., 2013; Schoenberg et al., 2008), small variations of $\delta^{53/52}$Cr in peridotites correlating with indices of melt differentiation (Schoenberg et al., 2016; Xia et al., 2017), and heavy isotope-depleted mafic intrusive rocks (Babechuk et al., 2019) have been observed. All of these evidences hint at stable Cr isotope fractionation during high-temperature processes such as different degrees of partial melting or fractional crystallization. Recent studies on ocean island basalts (OIB) (Bonnand et al., 2020; Shen et al., 2020) and komatiitic sample suites (Jerram et al., 2020) confirmed Cr isotope fractionation at mantle fO_2 and temperature conditions. Nevertheless, several details of high-temperature stable Cr isotopic fractionation remain poorly understood whereby especially the influence of certain mineral phases has yet to be investigated in more detail. Ideal archives to examine the impact on the Fe-Cr isotope systems during high-degree melting processes and magmatic fractionation are komatiite-tholeiite sequences to devise a more complete understanding of the controlling mineral phases.

In this study, we applied the combination of stable Cr and Fe isotope systematics to well-studied komatiite-tholeiite suites from the 3.55-3.22 Ga Barberton Greenstone Belt (BaGB) (Figure 2.1a-b), South Africa and Eswatini (Coetzee, 2014; Robin-Popieul et al., 2012; Schneider et al., 2019), and the 2.9-2.7 Ga Belingwe Greenstone Belt (BeGB) (Figure 2.1c), Zimbabwe (Bolhar, 2001; Bolhar et al., 2003; Nisbet et al., 1987; Nisbet et al., 1977; Shimizu et al., 2005). Olivine, Cr-bearing spinel and pyroxene, the major phases that crystallize from komatiitic melts, contain Cr and Fe at significant concentrations. Similar ionic radii at identical charges allows substitution of Cr^{2+} (0.80 Å) with Fe^{2+} (0.78 Å) and Cr^{3+} (0.62 Å) with Fe^{3+} (0.65 Å) in octahedral coordination in the crystal lattice of these minerals (Shannon, 1976), which is likely to induce isotopic fractionation between melt and minerals. The wide range of MgO concentrations (3.85 to 34.33 wt. %) in our BaGB and BeGB komatiite-tholeiite dataset indicates large degrees of magmatic differentiation and a wide range from cumulate dominated to residual melt dominated rocks, which further enhances the range in Cr and Fe substitution between minerals and melt, potentially increasing the extent of isotopic fractionation. This study

specifically addresses the stable Cr and Fe isotopic fractionation that is induced during the differentiation of high-degree ultramafic melts across the transitions of only olivine crystallization (typically with MgO >20 wt. %), to the combined crystallization of olivine, Cr-bearing spinel, pyroxene, and plagioclase (typically with MgO <15 wt. %). We particularly concentrate on (i) the overall Cr and Fe isotope variations observed in such complex komatiite-tholeiite suites as the ones of the BaGB and BeGB, (ii) the potential influence of secondary alteration, crustal assimilation and degree of partial melting on the observed Cr and Fe isotope variations and (iii) the effects of crystallizing minerals (i.e., 'active' minerals) on the Cr and Fe isotopic compositions of the whole rocks along the complex magmatic evolution of the BaGB and BeGB komatiite-tholeiite suites.

2.2 Geological overview and samples

2.2.1 General aspects of komatiite-tholeiite suites

Two major types of komatiites have been identified based on their chemical compositions: Al-depleted and Al-undepleted (Nesbitt et al., 1979). The formation of these has been ascribed to large degrees of partial melting at high pressures and high melting temperatures (Green et al., 1975; Herzberg, 1992; Nisbet et al., 1993) suggesting a plume origin for komatiites (Arndt, 1986; Bickle, 1993; Campbell et al., 1989; Sun and Nesbitt, 1978).
Aluminum-depleted komatiites are characterized by low Al_2O_3/TiO_2, low incompatible trace element concentrations and relative depletion of the heavy rare earth elements (REE) marked by low primitive mantle (PM) normalized $(Gd/Yb)_{PM}$ (Figure 2.2b) indicative for melting of a garnet-bearing source (Nesbitt et al., 1979; Ohtani et al., 1989; Walter, 1998). In combination with $(La/Sm)_{PM}$ ratios of ∼1, these chemical compositions indicate moderate to high degrees of partial melting (∼30 %) of a primitive source at high pressures (>7 GPa) with garnet as a residual phase (Robin-Popieul et al., 2012; Sossi et al., 2016). Aluminum-undepleted komatiites, depicted by higher Al_2O_3/TiO_2 (see also higher absolute abundances of Al_2O_3; Figure 2.3a), flat and unfractionated $(Gd/Yb)_{PM}$ (Figure 2.2b) and slightly depleted light REE (LREE) (Figure 2.4b) are interpreted to be derived from melting of a moderately depleted source at lower pressures (<7 GPa) at which garnet is absent or completely exhausted due to even higher degrees of partial melting (∼40 %) (Sossi et al., 2016).
Komatiites are always associated with basalts, but the genetic relationship between them remains a subject of debate (Arndt et al., 2008). Different models have been proposed for the generation of basalts associated with these plume-derived komatiites: 1) formation by fractional crystallization of a komatiitic parental melt (Jochum et al., 1991; Waterton et al., 2020; Xie et al., 1993); 2) formation by lower melting degrees within the same plume (Campbell et al., 1989; Dostal and Mueller, 2013) or 3) formation by moderate degrees of melting within the upper ambient mantle (Herzberg et al., 2010; Jochum et al., 1991). Irrespective of these different formation models, there is general consensus about the influence of certain mineral phases at certain evolutionary stages of these melts, which is important for our study to allow the characterization of isotopic Fe-Cr fingerprints for specific mineral phases. It is not the goal of this study to use stable Cr and Fe isotope compositions of whole

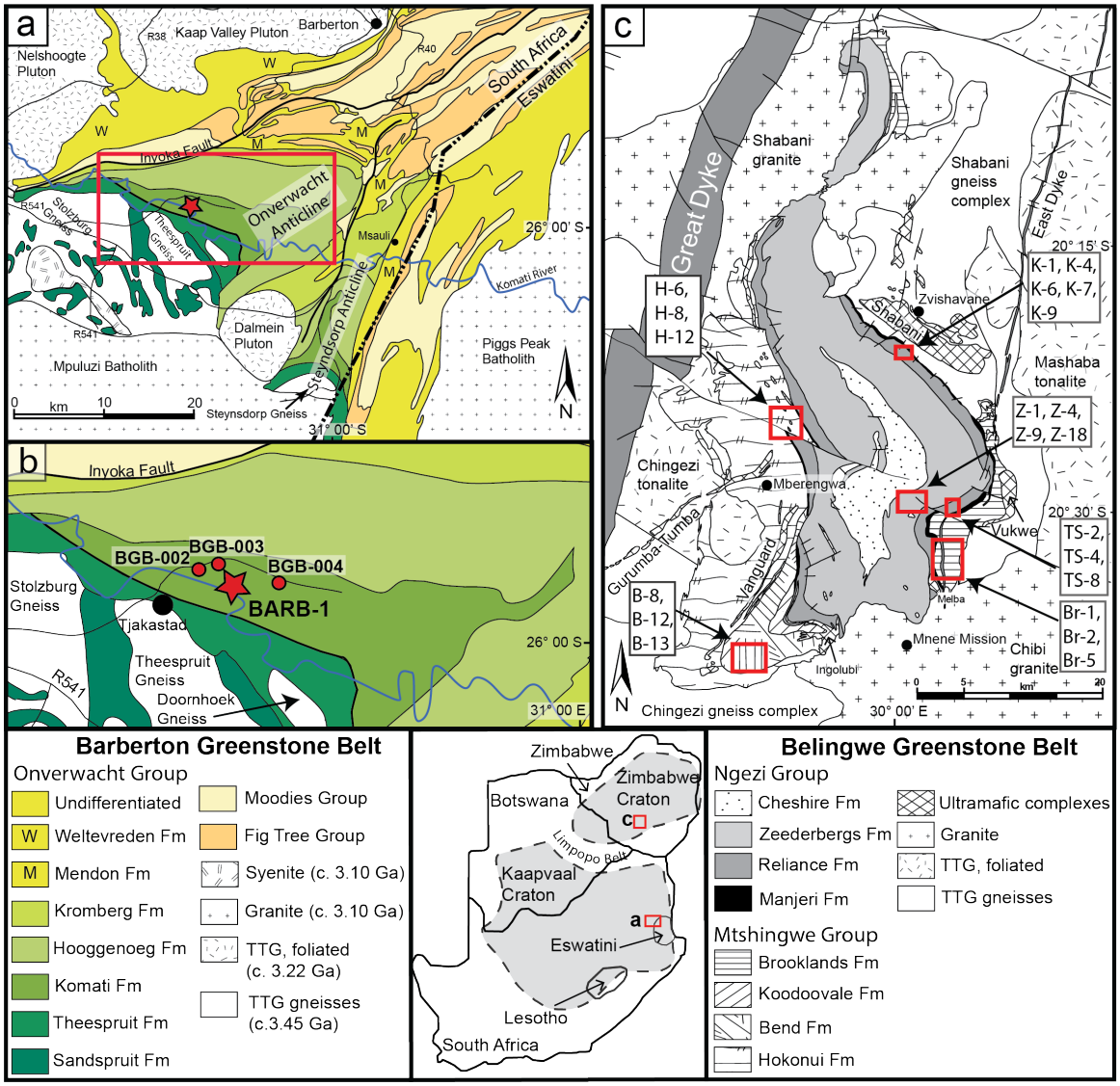

Figure 2.1: **a)** Geological map of the Barberton Greenstone Belt and surrounding granitic terrain (modified after Hofmann (2005) and Kamo and Davis (1994)). Inset **b)** shows the drill core location of BARB-1 (red star) and outcrop sample locations (red circles); **c)** Geological map of the Belingwe Greenstone Belt with surrounding granitic terrain (modified after Hofmann and Kusky (2004) and Martin et al. (1993)).

rocks to enhance the understanding of the highly disputed petrogenetic evolution of these complex melt systems and their products.

2.2.2 Barberton Greenstone Belt

The 3.55 to 3.22 Ga old Barberton Greenstone Belt (BaGB) in South Africa and Eswatini, located at the eastern part of the Kaapvaal Craton (Figure 2.1a), represents one of the oldest and well-preserved supracrustal volcano-sedimentary se-

quences and includes the type locality for komatiites (Viljoen and Viljoen, 1969). The BaGB consist of lithologies of the Barberton Supergroup including the predominantly volcanic Onverwacht Group (3.55-3.26 Ga), the volcano-sedimentary Fig Tree Group (3.26-3.22 Ga) and the terrigenous clastic Moodies Group (3.22 Ga; Armstrong et al., 1990; Heubeck et al., 2013; Heubeck and Lowe, 1994; Kamo and Davis, 1994; Lowe and Byerly, 1999; Lowe and Byerly, 2007). The Onverwacht Group mainly consists of mafic to ultramafic volcanic rocks with minor felsic volcanic and volcaniclastic rocks and chert. The Komati Fault separates the amphibolite-facies Sandspruit and Theespruit formations from the overlying greenschist-facies Komati, Hooggenoeg, Kromberg and Mendon formations (Lowe, 1994; Lowe and Byerly, 2007).

Rock samples studied here originate from the Komati Formation ($3{,}482 \pm 5$ Ma, SHRIMP U-Pb single-grain zircon; Armstrong et al., 1990), which importantly consists of one continuous sequence of submarine volcanic rocks as indicated by the absence of interlayered sediments (Dann, 2000; Viljoen and Viljoen, 1969). It is divided into the Lower Komati (mainly komatiites with minor basalts and komatiitic basalt) and Upper Komati member (mainly pillow basalts and minor komatiite; Dann, 2000). The Komati Formation underwent greenschist facies metamorphism at temperatures of up to 520° C and pressures of up to 4 kbar (Cloete, 1999; Xie et al., 1997).

Formation of BaGB komatiites of the Komati Fm has been attributed to melting of an anhydrous mantle plume (e.g. Chavagnac, 2004; Schneider et al. 2019; Robin-Popieul et al. 2012, Puchtel et al. 2013). Based on parallel trace element pattern (compare Figure 2.4), similar elemental anomalies and similar εHf and εNd isotope values of komatiites, komatiitic basalts, and high Mg-tholeiites, a common mantle source may be inferred (Schneider et al. 2019). Slight differences in $(\mathrm{Gd/Yb})_{\mathrm{PM}}$ ratios between komatiites ($(\mathrm{Gd/Yb})_{\mathrm{PM}} = 1.4$) and komatiitic basalts and high-Mg tholeiites ($(\mathrm{Gd/Yb})_{\mathrm{PM}} = 1.2$) may indicate lower depths of melting and thus derivation by lower melting degrees within the same source (Schneider et al., 2019).

Samples from the BaGB were obtained from the International Continental Scientific Drilling Program (ICDP) drill core BARB-1 (see Figure 2.1a-b), which is stored at the University of Johannesburg (South Africa). Drill core BARB-1 intersected the Lower Komati member and yielded a continuous sequence of differentiated komatiite flows, massive komatiite and komatiitic basalt flows, late stage crystallized gabbro as well as intrusive gabbro and basalt. The upper part of the drill core is a thick differentiated komatiitic flow, referred to as a tumulus unit, representing an inflated and internally strongly differentiated flow (olivine cumulate to pyroxenite/gabbro) produced by resurgence of magma within the same flow (Blichert-Toft et al., 2015; Coetzee, 2014; see also Dann, 2001 for detailed description). In this study, two of the 18 drill core samples are from the tumulus unit (60.70 and 66.70). The other 16 samples cover multiple massive and differentiated komatiitic flows, including cumulate and olivine spinifex textured komatiites, as well as massive komatiitic basalt and basalt flows. Additionally, three outcrop samples were taken from the Komati Formation (see Figure 2.1b and Table 2.3 for sample location).

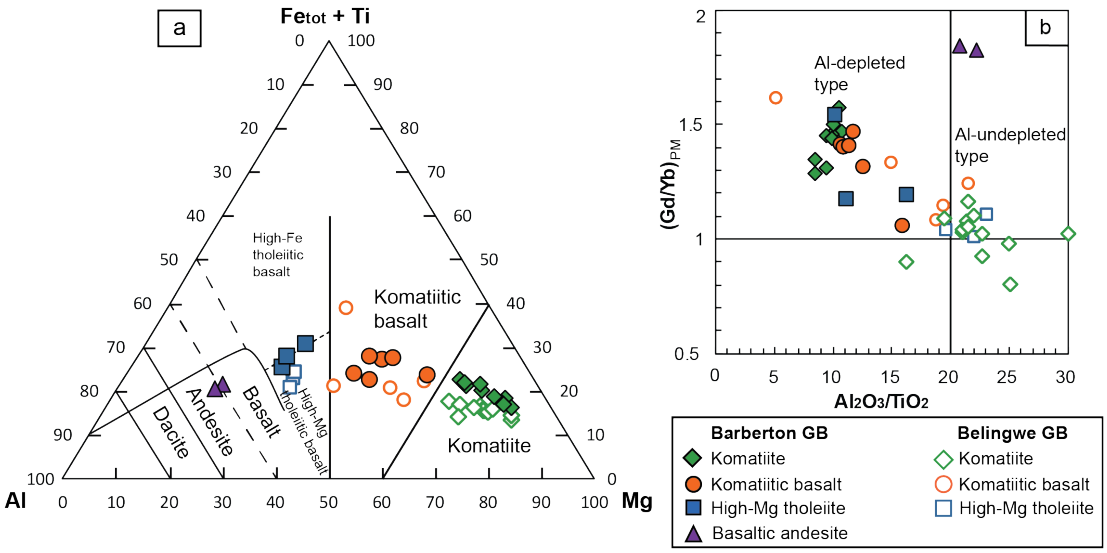

Figure 2.2: Classification diagrams for Barberton and Belingwe komatiites and associated komatiitic basalts, high-Mg tholeiites and basaltic andesites with **a)** (Fe_{tot}+Ti)-Al-Mg cation diagram after Jensen (1976); **b)** Al_2O_3/TiO_2 vs. $(Gd/Yb)_{PM}$ for classification of Al-depleted and Al-undepleted komatiites; normalizing values from Palme and O'Neill (2003). Filled and open symbols refer to BaGB and BeGB samples, respectively.

2.2.3 Belingwe Greenstone Belt

The 2.9 to 2.7 Ga old Belingwe Greenstone Belt (BeGB), Zimbabwe, is located on the south-eastern part of the Zimbabwe Craton (Figure 2.1c). It consists of the Lower Greenstones (Mtshingwe Group) and the Upper Greenstones (Ngezi Group). The Lower Greenstones unconformably overlie the 3.5 Ga old Shabani Gneiss Complex (Bickle et al., 1975; Nisbet et al., 1977) and consist of a series of volcanic units and chemical and clastic sedimentary formations. These are from bottom to top: The Hokonui Formation (mafic to felsic volcanic to volcaniclastic lithotypes), the Bend Formation (komatiites, basalts, iron formations) and the Koodoovale Formation (shales, conglomerates) in the west and the Brookland Formation (sedimentary rocks, komatiites, basalts) in the east (Hofmann and Kusky, 2004). The Lower Greenstones range in age from 2,904 ± 9 Ma (Hokonui Formation; SHRIMP U-Pb single zircon; Wilson et al., 1995) to 2,831 ± 6 Ma (Koodoovale Formation; SHRIMP U-Pb single-grain zircon; Wilson et al., 1995). Metamorphic overprint ranges from lower greenschist facies to amphibolite facies in the vicinity of granitoids (Orpen et al., 1993). The Upper Greenstones unconformably overlie the Shabani gneiss complex as well as the Lower Greenstones (Bickle et al., 1975), and consist of sedimentary units of the Manjeri Formation (clastic sedimentary succession) and Cheshire Formation (shallow marine carbonates) enclosing the volcanic units of the Reliance Formation and the Zeederbergs Formation (Nisbet et al., 1977). The Reliance Formation predominantly consists of komatiite and komatiitic and tholeiitic basalt and transitions into the Zeederbergs Formation, comprising mainly tholeiitic basalt and basaltic andesite, without any distinctive interruption of the magmatic succession (Bickle et al., 1975; Nisbet et al., 1977; Scholey, 1992). A komatiitic basalt of the Reliance Formation yielded an age of 2,692 ± 9 Ma (Pb-Pb on whole rock; Chauvel et al., 1993), while Re-Os dating of whole-rock komatiites as well as olivine and

chromite separates revealed an age of 2,689 ± 16 Ma (Puchtel et al., 2009). The metamorphic overprint in the Upper Greenstones is extremely low and ranges from subgreenschist to greenschist facies and only locally reaches amphibolite facies (Martin, 1978).
The relationship between Lower and Upper Greenstones is still a matter of debate as field evidence shows sheared tectonic contacts between these two units (Blenkinsop et al., 1993; Bolhar et al., 2003; Dirks et al., 1999; Hofmann and Dirks, 2003; Hunter et al., 1998; Kusky et al., 1994). Consequently, a common magmatic origin of the BeGB Lower and Upper Greenstones is disputed. Within each stratigraphic unit a LREE-depleted and LREE-enriched group can be discriminated. Similar major and trace element systematics within each group suggest at least very similar petrogenetic processes being involved for each group (Bolhar et al., 2003). For the BeGB LREE-depleted samples (Figure 2.4b) major and trace element modelling showed that high-Mg tholeiites from the Zeederbergs Formation and komatiitic basalts from the Reliance Fm can be derived by fractional crystallization of a komatiite parental magma from the Reliance Formation with minor crustal assimilation of 1-2 % (Bolhar, 2001; Brake, 1996; Shimizu et al., 2005). The LREE-enriched samples of the BeGB (Figure 2.4b), however, cannot be derived by simple fractional crystallization and require higher degrees (5 to 30 %) of assimilation of continental crust and/or lithospheric components and approximately 70 % fractional crystallization (Bolhar et al., 2003; Shimizu et al., 2005).
Samples from the BeGB are from from the Lower (Bend, Hokonui and Brookland Formations) and Upper Greenstones (Reliance and Zeederberg Formations) and were originally collected for the studies of Bolhar et al. (2003) and Bolhar (2001).

2.3 Methods

Sample selection for the BaGB was based on the petrographic drill core log (Coetzee, 2014) and on-site determinations of Mg, Fe, and Si contents using a portable X-Ray Fluorescence (pXRF) device on rock surfaces to maximize variation in magmatic differentiation (i.e., large spread in MgO content). A comparison of pXRF data and instrumental wavelength dispersive XRF data obtained on fused glass beads at the University of Tuebingen is given in the Supplementary Table A.1.1 and Supplementary Figure A.1.1. Additionally, three outcrop samples were taken from the Komati Formation (see Figure 2.1b and Table 2.3 for sample location). Samples were cut using a diamond-coated saw and crushed to chips with a hydraulic press. Final powdering occurred in an agate ball mill to prevent any contamination from metal. All major and trace element contents as well as stable Fe and Cr isotope compositions for BaGB samples were obtained at the Isotope Geochemistry laboratories of the University of Tuebingen.
Except for one sample (K-1), major element compositions for BeGB samples are from the studies of Bolhar (2001) and Bolhar et al. (2003), and reported again in this study for completeness of the dataset. Trace element concentrations as well as stable Fe and Cr isotope compositions were obtained at the Tuebingen Isotope Geochemistry laboratory on powders (pulverized in agate ball mill) from rock chips prepared by Bolhar et al. (2003). All major and trace element data for BaGB and BeGB are reported in Tables 2.1 and 2.2, respectively, and stable Fe and Cr isotope data are given in Table 2.3.

Table 2.1: Major (wt. %) and trace element (μg/g) compositions of BARB-1 drill core and outcrop samples from the 3.48 Ga Komati Fm, Barberton Greenstone Belt.

	Drill core Barb-1																				**Outcrop**
	Komatiites										Komatiitic basalts				High-Mg tholeiites		Basaltic andesites		High-Mg basalt	Komatiitic basalts	
Sample ID	66.70	109.22	242.47	255.5	261.0	290.65	342.57	345.29	360.23	372.13	60.70	229.40	240.66	262.00	221.64	269.65	315.55	315.91	002	003	004
wt. %																					
SiO_2	48.43	47.95	50.64	49.37	50.93	48.98	49.99	48.44	47.87	47.39	50.35	53.79	51.22	51.68	48.47	50.29	56.23	56.84	49.23	54.93	52.90
TiO_2	0.36	0.38	0.43	0.43	0.45	0.58	0.63	0.56	0.39	0.43	0.83	0.59	0.73	0.79	1.24	0.92	0.79	0.72	1.31	0.79	0.62
Al_2O_3	3.06	4.04	4.53	4.23	4.19	5.44	5.29	5.53	3.86	4.27	8.77	6.42	8.27	9.31	12.57	14.97	16.36	16.08	14.53	9.85	9.84
Fe_2O_3	11.75	12.61	12.36	12.78	12.62	13.05	13.00	13.62	12.70	12.85	13.48	11.75	14.28	13.66	14.39	12.12	8.60	7.84	13.36	10.49	10.78
MnO	0.18	0.21	0.24	0.22	0.22	0.25	0.23	0.24	0.22	0.22	0.23	0.25	0.23	0.21	0.25	0.21	0.20	0.21	0.24	0.22	0.20
MgO	24.33	27.65	22.10	25.61	20.71	20.99	19.08	21.00	31.01	29.54	12.27	14.69	13.15	11.28	7.77	7.36	4.23	3.85	7.37	10.06	11.68
CaO	11.35	6.15	9.48	6.53	9.86	9.13	9.83	8.70	3.10	4.30	8.30	9.39	9.38	9.02	11.04	7.79	4.72	5.42	9.65	9.41	9.50
Na_2O	0.11	0.33	0.26	0.20	0.39	0.52	0.83	0.41	0.30	0.38	2.91	2.73	2.67	3.59	3.22	5.77	8.06	8.22	3.71	3.84	4.01
K_2O	0.01	0.05	0.01	0.01	0.23	0.27	0.50	0.52	0.22	0.18	2.52	0.11	0.08	0.20	0.03	0.77	0.53	0.58	0.09	0.30	0.24
P_2O_5	0.04	0.04	0.04	0.03	0.04	0.05	0.06	0.05	0.03	0.03	0.07	0.06	0.07	0.06	0.10	0.11	0.33	0.31	0.15	0.07	0.06
Sum of	93.61	91.66	96.13	94.14	96.38	95.27	95.88	95.11	92.10	92.94	98.30	98.31	98.03	97.66	96.93	94.77	95.27	95.16	97.43	98.17	97.18
LOI	6.34	8.10	4.17	5.60	3.62	4.29	3.82	4.38	8.00	7.04	1.59	1.79	2.27	2.23	2.28	5.43	4.93	5.14	2.29	1.93	2.66
Al_2O_3/TiO_2	8.50	10.63	10.53	9.84	9.31	9.38	8.40	9.88	9.90	9.93	10.57	10.88	11.33	11.78	10.14	16.27	20.71	22.33	11.09	12.47	15.87
Mg#	78.0	79.0	75.4	77.4	73.8	73.4	71.5	72.5	80.7	79.7	60.9	68.2	61.2	58.6	48.0	51.0	45.7	45.7	48.6	62.2	65.0
in $\mu g/g$																					
Li	20.37	14.0	7.63	18.1	7.77	11.3	11.9	6.34	22.1	28.7	4.74	4.01	5.94	5.37	19.7	14.7	4.82	3.81	36.1	12.2	10.3
Be	0.058	0.139	0.131	0.094	0.118	0.169	0.213	0.185	0.078	0.091	0.246	0.244	0.257	0.193	0.280	0.272	0.872	0.799	0.399	0.277	0.183
Sc	18.9	12.7	19.4	22.3	22.7	26.1	28.2	23.5	17.9	20.4	25.2	28.4	30.8	25.9	34.0	26.0	7.84	8.25	26.1	27.9	32.4
Ti	1878	1349	2272	2251	2296	3136	3505	2984	1961	2149	4882	3247	3649	4517	7088	5216	4459	4088	7291	4602	3345
V	85.9	73.3	121	123	123	153	174	153	106	114	227	156	208	209	369	286	174	156	242	201	233
Cr*	1938	1458	1596	2017	2646	2007	1741	2681	2164	2317	614	2309	901	546	105	133	46.64	34.88	227	720	768
Co	120	71.5	83.7	99.2	90.1	89.9	83.3	101	103	101	66.5	63.3	63.6	57.9	66.9	53.1	24.9	22.8	54.1	53.3	49.6
Ni	1596	904	945	1154	792	832	554	1159	1371	1327	172	285	169	126	127	132	17.47	13.81	127	179	216
Cu	20.5	34.8	124	72.4	84.1	107	193	393	69.8	17.0	41.1	105	204	206	125	108	34.4	40.2	74.6	99.5	88.7
Zn	41.3	48.0	85.4	77.4	79.5	80.9	93.9	97.5	74.6	73.7	92.0	91.5	77.3	81.0	88.7	71.7	93.2	89.4	116	81.2	54.4
Ga	4.32	3.33	5.91	4.93	5.31	6.63	6.29	6.80	4.54	5.05	10.4	7.08	10.4	11.6	17.2	15.0	16.7	15.9	16.3	10.1	11.8

Continued on next page

Table 2.1 – *Continued from previous page*

Sample ID	66.70	109.22	242.47	255.5	261.0	290.65	342.57	345.29	360.23	372.13	60.70	229.40	240.66	262.00	221.64	269.65	315.55	315.91	002	003	004
Rb	0.665	1.22	0.636	0.751	8.24	9.73	18.8	20.9	7.63	6.11	91.1	3.06	1.84	6.46	0.344	27.6	10.3	10.9	1.14	1.78	2.95
Sr	53.9	45.7	16.4	20.2	34.9	39.9	28.5	18.8	20.2	16.9	58.3	21.8	54.5	89.2	165	219	348	355	117	77.4	101
Y	5.50	5.40	7.32	6.34	8.02	11.3	12.0	10.8	6.24	7.16	17.8	12.4	15.5	15.4	17.9	17.6	17.5	18.8	22.4	16.5	14.0
Zr	21.4	16.1	24.1	24.1	25.3	34.8	38.3	30.6	19.2	20.9	62.7	41.4	50.7	50.3	67.7	54.5	121	123	77.7	57.3	40.2
Nb	1.12	1.01	1.27	1.28	1.37	1.93	2.14	1.74	0.99	1.10	3.87	2.46	3.06	2.85	2.07	2.68	7.31	7.70	3.59	2.95	1.98
Cd	0.061	0.037	0.088	0.041	0.065	0.066	0.094	0.158	0.037	0.037	0.075	0.064	0.087	0.093	0.105	0.057	0.129	0.122	0.143	0.070	0.040
Sn	0.580	0.541	0.777	0.227	0.619	0.423	0.596	0.769	0.260	0.553	0.924	0.586	0.702	0.751	0.747	0.490	2.05	2.27	0.737	0.521	0.405
Cs	0.187	0.506	0.383	0.362	1.16	1.55	1.93	2.13	1.73	1.55	5.55	0.357	0.295	0.588	0.082	1.84	1.44	1.51	0.105	0.021	0.243
Ba	8.63	13.6	6.11	10.2	7.35	10.8	9.73	7.88	20.7	21.7	87.0	8.63	14.9	12.7	72.0	76.0	142	138	27.1	51.4	112
La	1.17	1.22	1.17	1.58	1.53	1.69	1.09	1.84	1.11	1.42	4.52	2.84	3.83	3.95	2.34	2.93	21.7	22.7	5.53	3.37	3.09
Ce	3.18	3.48	4.20	4.38	4.72	5.19	4.96	5.95	3.31	4.11	12.4	8.14	10.4	10.8	6.65	8.10	46.7	47.8	14.0	9.21	7.47
Pr	0.488	0.543	0.706	0.684	0.767	0.888	0.925	0.971	0.537	0.651	1.89	1.26	1.58	1.64	1.12	1.26	5.84	5.92	2.06	1.38	1.06
Nd	2.42	2.67	3.59	3.45	3.87	4.68	4.98	4.84	2.78	3.30	9.05	6.13	7.60	7.93	6.21	6.26	23.9	23.9	9.83	6.68	4.87
Sm	0.756	0.805	1.12	1.06	1.20	1.52	1.63	1.51	0.891	1.05	2.66	1.81	2.25	2.37	2.38	1.99	5.17	5.09	2.87	2.09	1.41
Eu	0.095	0.259	0.667	0.223	0.349	0.513	0.712	1.15	0.435	0.531	0.942	0.722	0.764	0.863	0.978	0.808	1.28	1.36	1.09	0.586	0.577
Tb	0.170	0.167	0.234	0.214	0.254	0.331	0.355	0.326	0.192	0.222	0.545	0.378	0.468	0.481	0.573	0.488	0.685	0.676	0.641	0.482	0.361
Gd	0.955	0.969	1.40	1.26	1.50	1.93	2.07	1.91	1.13	1.31	3.20	2.22	2.74	2.81	3.29	2.71	4.65	4.60	3.63	2.75	1.93
Dy	1.09	1.05	1.46	1.34	1.59	2.12	2.26	2.06	1.22	1.40	3.45	2.38	2.94	3.00	3.56	3.25	3.95	3.90	4.18	3.10	2.44
Ho	0.231	0.217	0.303	0.278	0.335	0.453	0.481	0.433	0.255	0.291	0.723	0.505	0.626	0.627	0.744	0.707	0.797	0.786	0.912	0.660	0.542
Er	0.641	0.596	0.819	0.757	0.908	1.27	1.35	1.20	0.702	0.795	2.02	1.40	1.74	1.72	1.99	1.99	2.17	2.16	2.62	1.84	1.57
Tm	0.095	0.088	0.118	0.112	0.137	0.191	0.202	0.175	0.104	0.118	0.294	0.207	0.256	0.254	0.286	0.297	0.324	0.325	0.395	0.273	0.236
Yb	0.603	0.537	0.724	0.705	0.839	1.20	1.25	1.08	0.639	0.710	1.84	1.29	1.58	1.56	1.73	1.85	2.06	2.05	2.51	1.70	1.48
Lu	0.089	0.078	0.105	0.104	0.121	0.173	0.184	0.154	0.093	0.103	0.268	0.188	0.232	0.227	0.248	0.272	0.306	0.303	0.379	0.249	0.219
Hf	0.554	0.424	0.630	0.649	0.678	0.910	0.999	0.817	0.505	0.558	1.61	1.09	1.34	1.32	1.84	1.43	3.02	2.97	2.03	1.48	1.06
Tl	0.007	0.005	0.002	0.005	0.035	0.039	0.078	0.093	0.035	0.025	0.601	0.017	0.009	0.031	0.005	0.125	0.005	0.004	0.008	0.006	0.018
Pb	0.208	0.311	0.165	0.132	0.359	0.188	0.152	0.209	0.345	0.247	0.222	0.262	0.490	0.242	0.635	0.282	3.52	6.02	0.997	0.468	0.703
Th	0.125	0.104	0.144	0.147	0.155	0.196	0.216	0.138	0.079	0.086	0.388	0.278	0.339	0.301	0.223	0.206	3.42	3.62	0.404	0.307	0.231
U	0.031	0.028	0.044	0.038	0.044	0.051	0.054	0.043	0.022	0.026	0.106	0.074	0.092	0.088	0.071	0.057	0.958	0.996	0.104	0.081	0.065

Major element concentrations are recalculated to anhydrous compositions. Trace element concentrations are not corrected for volatile content. Totals are given without LOI. Sample ID of Barberton samples correspond to depths of BARB-1 bore hole. For sample locations of outcrop samples see Table 2.3.
* Cr concentrations obtained via MC-ICPMS. Uncertainties on Cr concentration measurements via isotope dilution method is 0.75 % 2SD.

2.3.1 Major elements

An aliquot of 1.5 g of powdered sample was mixed with 7.5 g of Merck Spectromelt A12, melted at 1,200° C and quenched to a glass bead. Analyses were performed with a wavelength dispersive Bruker AXS S4 Pioneer XRF spectrometer (Rh-tube at 4kW) with 32 standardized samples at the University of Tuebingen. Matrix effects were corrected for using the standard Spectra software provided by Bruker AXS. To complement the determination of major constituents, loss on ignition (LOI) was determined on a separate aliquot of 1 g that was heated to 1,000° C for 1 hour. To allow for comparison of all samples all major oxides are recalculated to a volatile-free basis. United States Geological Survey (USGS) reference material BHVO-2 was analyzed to allow for quality control, and results from this study reproduce the certified USGS values well (Supplementary Table A.1.2).
The determination of the ferrous iron content is based on a standard colorimetric titration technique (Goldich, 1984; Maxwell, 1968) and the detailed procedure is given in Babechuk et al. (2019). USGS reference material BIR-1a yielded a FeO concentration of 7.95 ± 0.20 wt. % (1SD, n=10), which reproduces well with the value of 8.25 ± 0.42 wt. % (1SD, n=8) determined by Babechuk et al. (2019) and those compiled in previous studies (e.g., Saikkonen and Rautiainen, 1993). For the reference material from the International Association of Geoanalysts (IAG) OKUM (= OPY-1 ultramafic rock; Kane, 2015) the obtained FeO concentration of 8.21 ± 0.13 wt. % (1SD, n=6) lies well within the average of 8.47 ± 0.46 wt. % (1SD, n=11) reported by Webb et al. (2007). Single measurements of reference materials are reported in the Supplementary Table A.1.3. Full procedural blanks were $\leq$0.02 wt. % FeO.

2.3.2 Trace element and isotope composition

To ensure complete sample digestion and especially complete dissolution of the refractory Cr-rich spinel phase, closed bomb digestions were carried out. For these, 20 to 30 mg of powdered samples were combined with a 3:1 mixture of HF ($\sim$27 M)-HNO_3 ($\sim$14.5 M) and heated to 200° C in an oven for four days (96 hours). Following evaporation, samples were re-dissolved in 0.5 mL 6 M HCl and heated to 200° C for one day to ensure complete destruction of fluorides. Subsequent evaporation of the sample solutions was followed by the removal of any excess Cl^- by repeated evaporation to incipient dryness with HNO_3 (65 %). The sample residues were re-dissolved in 1 mL 5 M HNO_3 and a stock solution (2 % HNO_3) with a nominal dilution factor of $\sim$1,000 was created gravimetrically. To minimize the effects of possible sample heterogeneity, determination of trace element concentrations as well as Cr and Fe isotope compositions were measured on individual aliquots originating from the same stock solution following the detailed protocol described by Babechuk et al. (2019).

2.3.2.1 Trace elements

Determination of trace element concentration is based on a method originally described by Eggins et al. (1997) and incorporating subsequent modifications (Albut et al., 2018; Babechuk et al., 2010; Kamber et al., 2005), with measurement via solution quadrupole ICP-MS (S-Q-ICP-MS) on a ThermoFisher Scientific iCAP-Qc. This study followed the most recent method adaptation described in detail by Albut

et al. (2018).
In brief, prepared stock solutions (Section 2.3.2) were further diluted to a nominal, gravimetric dilution factor of 10,000 to 15,000, yielding a final 2 % HNO_3 solution ready for measurement. To account for sensitivity and instrumental drift, an internal standard carrying ^{6}Li, In, Re and Bi was added to procedural blanks, calibration standards, quality control reference materials, sample unknowns and external drift monitor samples. Drift-corrected instrument intensities were further corrected for procedural and instrumental background and analytical interferences (e.g. polyatomic and doubly charged species) as described elsewhere (e.g., Ulrich et al.,2010). External calibration was carried out using the averaged intensities at three different dilution factors of the natural USGS reference material W-2a (applying the preferred calibrant concentration values given in Supplementary Table A.1.4). A combination of independent USGS reference materials AGV-2, BIR-1a and BHVO-2 were measured throughout the duration of the study to provide a monitor of method precision and accuracy with data for BHVO-2 and BIR-1a reported in Supplementary Table A.1.4. The mean concentrations determined for each reference material agree well with previous studies applying the same method (i.e., better than 5 %) and with GeoReM preferred values, and the 1 r.s.d suggest a full method precision for mafic-to-andesite volcanic rocks better than 5 % for all of the key elements in this study (e.g., Cr, REE, high field strength elements (HFSE)).

2.3.2.2 Stable Cr and Fe isotope analyses

All stable Cr and Fe isotope data reported in this study were performed on the ThermoFisher Scientific NeptunePlus multicollector inductively coupled plasma mass spectrometer (MC-ICP-MS) housed at the Isotope Geochemistry facilities of the University of Tuebingen using measuring protocols previously published in Schoenberg et al. (2008) and Schoenberg et al. (2016) for Cr and Eroglu et al. (2018), Wu et al. (2017) and Swanner et al. (2015) for Fe.
For Cr isotope determinations aliquots corresponding to 2 to 3 μg of Cr were taken from the dissolved sample stock solutions prepared for trace element analyses and mixed with adequate amounts of the $^{50}Cr - {}^{54}Cr$ double spike to yield 1:1 sample to spike Cr ratios. Purification of sample Cr was achieved using a three-step chromatographic separation described in detail in previous work (Schoenberg et al., 2016; Wille et al., 2018). Samples were introduced to the mass spectrometer using an Aridus II desolvating nebulizer and concentrations of measurement solutions varied between 150 to 200 ng g^{-1} from session to session. Measurements were performed in static mode to simultaneously detect all stable Cr isotope beams as well as $^{49}Ti^{+}$, $^{50}V^{+}$ and $^{56}Fe^{+}$ to monitor and correct isobaric interferences of $^{50}Ti^{+}$ and $^{50}V^{+}$ on $^{50}Cr^{+}$ and $^{54}Fe^{+}$ on $^{54}Cr^{+}$. The use of the medium resolution mode – the resolving power $M/\Delta M$ with ΔM defined as the mass difference between 95 and 5 % beam intensities (Weyer and Schwieters, 2003) was always between 6,000-8,000 for Cr – allowed to resolve any polyatomic interferences such as $^{40}Ar^{12}C^{+}$ on $^{52}Cr^{+}$, $^{40}Ar^{14}N^{+}$ on $^{54}Cr^{+}$ and $^{40}Ar^{16}O^{+}$ on $^{56}Fe^{+}$. Single measurements consisted of 90 to 120 cycles with 4.2 s integration time. Background intensities were corrected by subtraction of on-peak-zero measurements of pure carrier solutions (i.e., average of intensities detected before and after each individual sample unknown) from signals of sample unknowns. Double spike deconvolution assuming exponential fractionation allowed correction of instrumental mass bias and chemical isotopic fractionation

induced by chromatographic Cr purification (Schoenberg et al., 2008). Each sample was determined five times (except samples 315.55 and 315.91 with n=2) as separate measurement including individual background corrections to improve the precision of each sample's measured Cr isotopic composition. The five measurements were neither always performed within the same measurement session nor from the same dilution aliquot of a sample's stock solution. All stable Cr isotope data are reported in the δ-notation relative to NIST SRM979 as:

$$\delta^{53/52}Cr_{SRM979} = \frac{(^{53}Cr/^{52}Cr)_{sample}}{(^{53}Cr/^{52}Cr)_{SRM979}} - 1 \quad (2.1)$$

hereafter referred to as $\delta^{53/52}$Cr. The data are expressed as per mil (‰) difference by multiplication with a factor of 1,000.
The isotopic fractionation factor α observed for a process between two reservoirs is defined as:

$$\alpha_{A-B} = \frac{(^{53}Cr/^{52}Cr)_{reservoirA}}{(^{53}Cr/^{52}Cr)_{reservoirB}} \quad (2.2)$$

And the isotopic fractionation ε is expressed accordingly as:

$$\varepsilon^{53}Cr_{A-B} = (\alpha_{A-B} - 1) \times 1000 \quad (2.3)$$

Over the combined analytical sessions for this study the compiled $\delta^{53/52}$Cr values of NIST SRM979 and in-house Merck Cr(III) standard solutions are 0.000 ± 0.017 ‰ (2SD; n=89) and -0.430 ± 0.020 ‰ (2SD; n=68), respectively. These values are in excellent agreement with previous studies (Albut et al., 2018; Babechuk et al., 2018; Schoenberg et al., 2016; Schoenberg et al., 2008; Zink et al., 2010). The long-term reproducibility of $\delta^{53/52}$Cr values for single measurements of NIST SRM979 and Cr(III) since May 2014 is 0.000 ± 0.022 ‰ (2SD; n=469) and -0.429 ± 0.023 ‰ (2SD; n=292), respectively. Accuracy of natural sample materials was assessed by measuring the USGS rock reference materials BHVO-2 and BIR-1a along with sample unknowns, and which yielded $\delta^{53/52}$Cr values of -0.145 ± 0.023 ‰ (2SD; n=90, 10 digests) and -0.149 ± 0.025 ‰ (2SD; n=86, 9 digests), respectively. These values are in good agreement with previously reported values in the literature (D'Arcy et al., 2016; Li et al., 2016; Sossi et al., 2018; Xia et al., 2017). Following the approach of Schuessler et al. (2009) pooling of all data of the international reference material BHVO-2 into averages of 5 measurements yields a $\delta^{53/52}$Cr value of -0.145 ‰ with a pooled two standard deviation reproducibility (henceforth denoted as 2SD* to distinguish from the 2SD for single analyses) of ± 0.016 ‰ (n=18, Supplementary Table A.1.5). Since nearly all samples of this study have been repeatedly measured 5 times, this pooled 2SD* for BHVO-2 is a reliable estimate for the external reproducibility of repeated measurements (with n=5) of natural samples and is therefore the uncertainty used in plots of this study. Total procedural blanks were 2 to 8 ng, contributing less than 0.26 % to the recovered amount of Cr, and were thus deemed negligible.
For Fe isotope analysis an aliquot corresponding to 15 μg Fe was taken from the prepared stock solution, mixed with a $^{57}Fe - ^{58}Fe$ double spike to yield 1:1 sample-to-spike Fe ratios. Fe purification included a one-step anion exchange chromatography (Schoenberg and von Blanckenburg, 2005). For MC-ICP-MS measurements samples were introduced as solutions of 2.5 $\mu g\,g^{-1}$ Fe in 0.3 M HNO_3 via a dual-glass

spray chamber and a PFA pneumatic nebulizer. The instrument was operated in static mode to simultaneously detect all Fe isotopes and the $^{52}Cr^{+}$ and $^{60}Ni^{+}$ monitors to correct for isobaric interferences of $^{54}Cr^{+}$ on $^{54}Fe^{+}$ and $^{58}Ni^{+}$ on $^{58}Fe^{+}$. Medium-resolution mode with a resolving power $M/\Delta M$ of 6,000-8,000 (Weyer and Schwieters, 2003) enabled the discrimination of polyatomic interferences such as $^{40}Ar^{12}C^{+}$ on $^{52}Cr^{+}$, $^{40}Ar^{14}N^{+}$ on $^{54}Fe^{+}$, $^{40}Ar^{16}O^{+}$ on $^{56}Fe^{+}$, $^{40}Ar^{17}O^{+}$ on $^{57}Fe^{+}$, and $^{40}Ar^{18}O^{+}$ on $^{58}Fe^{+}$. Individual Fe isotope measurements consisted of 90-120 cycles with an integration time of 4.2 s. Background signals were corrected for by subtraction of on-peak-zero measurements on the pure 0.3 M HNO_3 carrier solution before and after each sample and standard measurement. Double-spike deconvolution was carried out based on a method by Compston and Oversby (1969) assuming an exponential mass fractionation law. The Fe isotopic composition of each sample was measured 5 times to improve the measurement precision. All Fe isotope compositions are reported in δ-notation relative to the standard IRMM014 according to equation 2.4 and multiplied by 1,000 to display variations in per mil differences:

$$\delta^{56/54}Fe_{IRMM014} = \frac{(^{56}Fe/^{54}Fe)_{sample}}{(^{56}Fe/^{54}Fe)_{IRMM014}} - 1 \tag{2.4}$$

henceforth referred to as $\delta^{56/54}$Fe. Over the course of this study IRMM-014 yielded a $\delta^{56/54}$Fe value of 0.000 ± 0.029 ‰ (2SD, n=66) matching the long-term reproducibility of 0.000 ± 0.036 ‰ (2SD, n=215) of the Isotope Geochemistry laboratory of Tuebingen since 2015. The in-house standards Han-Fe and Tueb-Fe gave $\delta^{56/54}$Fe values of $+0.290 \pm 0.036$ ‰ (2SD, n=25) and -0.378 ± 0.032 ‰ (2SD, n=16), respectively, being in excellent agreement with previous studies (Babechuk et al., 2019; Eroglu et al., 2018; Kurzweil et al., 2016; Swanner et al., 2015; Wu et al., 2017) and the long-term reproducibility of $+0.289 \pm 0.037$ ‰ (2SD, n=104) and -0.377 ± 0.041 ‰ (2SD, n=67), respectively. Furthermore, analytical accuracy was determined by measuring USGS reference materials BHVO-2 and BIR-1a, which were run together with processed samples, and yielded a $\delta^{56/54}$Fe of $+0.111 \pm 0.030$ ‰ (2SD; n=9, two digests) and $+0.053 \pm 0.011$ ‰ (2SD, n=5, one digest), respectively, agreeing very well with published values (e.g., Barrat et al., 2015; Craddock and Dauphas, 2011; Millet et al., 2012; Nebel et al., 2015). Similar to Cr isotope determinations, pooled averages of five single measurements of the Tueb-Fe standard resulted in a pooled 2SD* external reproducibility of ± 0.018 ‰ (n=13; Supplementary Table A.1.6), which is the uncertainty used in all plots displaying stable Fe isotope compositions. Procedural blanks were <2.7 ng, contributing less than 0.02 % to the processed amount of sample Fe and thus considered to be negligible.

Table 2.2: Major and trace element compositions from the 2.7 Ga Upper Greenstones and 2.9 Ga Lower Greenstones of the Belingwe Greenstone Belt.

	Upper Greenstones									**Lower Greenstones**										
	High-Mg tholeiites			Komatiitic basalts			Komatiites			Komatiites			Komatiitic basalts			Komatiites				
Sample ID	Z-1	Z-4	Z-18	Z-9	K-1a	TS-2	K-4	K-6	K7	K-9	TS-4	TS-8	Br-1	Br-2	Br-5	H-8	H-12	H-6	B-8	B-12	B-13
wt. %																					
SiO_2	49.72	50.15	54.37	51.30	49.10	53.96	44.46	46.61	46.64	46.18	47.33	45.96	51.79	46.35	54.36	55.24	49.10	53.91	45.59	50.09	50.12
TiO_2	0.70	0.75	0.66	1.58	0.43	0.52	0.29	0.30	0.30	0.27	0.35	0.26	0.41	0.31	0.67	0.34	0.66	0.25	0.22	0.15	0.15
Al_2O_3	15.46	14.82	15.28	8.24	8.03	10.10	6.21	6.32	6.30	6.12	6.81	5.59	6.65	9.40	10.12	7.30	14.28	5.50	4.99	3.75	3.77
$Fe_2O_{3\ tot}$	11.50	12.12	9.92	16.99	12.94	9.98	11.77	11.89	11.81	11.68	11.58	12.65	10.19	11.15	9.86	10.75	11.55	10.67	11.50	10.02	10.01
FeO		8.06		11.48			8.02									7.86	7.91	7.69	4.54		
$Fe^{2+}/\Sigma Fe$		0.74		0.75			0.76									0.81	0.76	0.80	0.44		
MnO	0.19	0.18	0.20	0.21	0.25	0.15	0.18	0.19	0.18	0.18	0.16	0.17	0.20	0.13	0.16	0.20	0.18	0.21	0.19	0.19	0.19
MgO	8.81	8.51	8.41	8.24	17.66	14.58	27.72	27.37	27.54	28.57	25.72	29.48	20.79	27.06	16.58	19.98	12.11	23.46	34.33	27.48	27.45
CaO	12.14	11.63	8.18	11.27	10.15	7.59	6.32	6.42	6.33	6.08	7.83	5.65	9.21	5.51	4.35	4.18	10.41	5.17	2.97	8.21	8.19
Na_2O	1.37	1.60	2.80	0.89	0.83	3.09	0.75	0.82	0.80	0.75	0.05	0.16	0.70	0.07	3.71	1.89	1.54	0.70	0.18	0.12	0.12
K_2O	0.01	0.00	0.10	0.97	0.02	0.00	0.00	0.01	0.00	0.12	0.00	0.01	0.04	0.00	0.03	0.09	0.00	0.10	0.02	0.00	0.00
P_2O_5	0.04	0.05	0.06	0.23	0.03	0.03	0.01	0.01	0.01	0.01	0.01	0.00	0.02	0.02	0.05	0.03	0.04	0.02	0.01	0.00	0.00
Sum of	97.15	97.57	95.60	98.01	96.32	96.78	96.93	97.26	97.57	94.55	92.49	91.62	95.95	89.35	94.99	95.80	95.86	94.71	90.00	94.41	93.65
LOI	2.73	1.96	3.88	1.85	3.59	2.95	2.05	2.60	2.44	5.49	6.74	7.58	3.78	9.96	4.46	4.18	4.43	4.61	9.61	5.04	5.78
Al_2O_3/TiO_2	22.09	19.76	23.15	5.22	18.84	19.42	21.41	21.07	21.00	22.67	19.46	21.50	16.22	30.32	15.10	21.47	21.64	22.00	22.68	25.00	25.13
Mg#	56.7	54.6	59.2	45.4	70.0	71.4	80.1	79.8	79.9711	80.7	79.2	80.0	77.7	80.6	74.2	76.1	64.2	79.0	83.6	82.4	82.4
in $\mu g/g$																					
Li	7.38	5.53	18.2	3.53	11.7	3.03	3.08	4.24	4.48	6.96	1.39	3.22	14.5	16.8	2.55	18.6	11.7	12.9	8.38	21.8	19.7
Be	0.181	0.172	0.449	1.31	0.105	0.181	0.078	0.068	0.067	0.062	0.080	0.066	0.189	0.115	0.509	0.210	0.174	0.138	0.047	0.185	0.024
Sc	38.1	34.8	33.0	25.9	41.7	31.9	23.8	20.4	24.8	23.5	23.6	20.9	26.6	22.1	18.1	23.0	33.1	28.4	16.2	44.8	19.5
Ti	3991	4186	3589	8857	2266	3218	1657	1684	1727	1548	1776	1435	2465	1594	2837	1747	3531	1618	1157	2261	826
V	248	233	195	236	176	186	127	128	127	118	127	108	144	123	125	124	193	116	85	198	76
Cr*	339	361	141	453	1461	1355	2399	2380	2954	2346	2085	2734	1417	2427	3468	1764	562	2312	2829	1484	2350
Co	48.3	53.3	46.8	64.0	84.8	63.7	102	98.3	102	98.4	90.6	108	65.5	83.9	64.1	65.1	61.4	71.3	103	67.0	79.4
Ni	155	171	110	111	416	391	1365	1305	1540	1356	1162	1333	777	1263	879	279	308	591	1634	305	532
Cu	122	132	76.5	161	55.0	89.7	52.5	52.2	52.4	48.9	44.2	32.6	21.6	0.730	27.8	43.2	123	26.1	24.4	1.99	25.6
Zn	73.6	78.1	74.1	101.1	71.3	69.3	66.1	65.5	67.2	62.2	50.8	62.9	70.3	57.1	72.6	92.8	68.7	60.6	57.3	75.2	51.2
Ga	13.2	13.4	13.1	13.9	8.39	9.25	6.32	6.36	6.42	5.96	6.50	5.29	6.88	7.32	8.52	6.99	12.5	5.53	3.86	7.68	3.25

Continued on next page

Table2.2 – *Continued from previous page*

Sample ID	Z-1	Z-4	Z-18	Z-9	K-1[a]	TS-2	K-4	K-6	K7	K-9	TS-4	TS-8	Br-1	Br-2	Br-5	H-8	H-12	H-6	B-8	B-12	B-13
Rb	0.292	0.720	2.82	13.1	0.528	0.238	1.15	1.08	0.985	2.23	0.471	2.24	2.14	1.35	0.426	6.26	0.138	5.26	3.95	2.50	1.81
Sr	157	106	78.8	432	10.7	31.9	30.6	29.4	30.3	23.9	21.7	12.1	15.1	23.8	36.6	18.8	84.5	31.3	5.54	15.2	8.47
Y	14.2	14.8	18.0	37.5	7.91	10.5	6.59	6.29	6.29	5.88	6.63	5.11	11.1	5.90	9.82	7.22	13.1	5.59	4.27	8.28	2.62
Zr	32.3	36.1	68.4	180	16.4	36.8	12.7	12.7	13.6	12.0	15.8	10.7	23.2	14.6	53.5	27.6	32.2	18.7	9.13	17.9	4.38
Nb	1.41	1.54	3.20	11.7	0.688	2.13	0.510	0.515	0.552	0.483	0.675	0.445	1.13	0.550	2.73	1.04	1.35	0.775	0.397	0.779	0.205
Cd	0.067	0.073	0.080	0.151	0.029	0.028	0.041	0.040	0.043	0.032	0.012	0.019	0.027	0.033	0.084	0.083	0.053	0.036	0.017	0.042	0.032
Sn	0.394	0.404	0.669	1.96	0.237	1.13	0.192	0.278	0.207	0.236	0.142	0.913	0.389	0.271	0.892	0.276	0.452	0.210	0.077	0.336	0.112
Cs	0.133	0.140	0.116	0.286	0.045	0.028	0.100	0.091	0.071	0.243	0.097	0.402	0.331	0.264	0.054	1.64	0.102	1.83	1.84	0.831	0.845
Ba	10.3	13.1	65.2	237	12.2	6.14	7.22	7.45	6.68	15.9	2.51	9.86	44.9	46.5	36.8	18.2	10.8	39.0	13.8	6.83	8.54
La	1.79	1.88	7.22	20.9	0.884	3.24	0.665	0.678	0.666	0.586	0.953	0.515	1.373	0.586	6.35	5.49	1.84	2.20	0.495	0.901	0.259
Ce	4.99	5.31	15.5	47.4	2.48	7.16	1.78	1.83	1.83	1.66	2.40	1.54	3.44	1.89	12.4	10.3	4.98	4.77	1.40	2.47	0.68
Pr	0.817	0.864	2.01	6.40	0.413	0.965	0.305	0.311	0.308	0.280	0.375	0.259	0.551	0.332	1.58	1.18	0.806	0.623	0.230	0.459	0.118
Nd	4.25	4.50	8.54	27.8	2.23	4.35	1.65	1.65	1.66	1.51	1.93	1.40	2.91	1.75	6.38	4.63	4.16	2.68	1.19	2.43	0.638
Sm	1.46	1.53	2.32	6.86	0.804	1.27	0.605	0.597	0.609	0.557	0.673	0.506	1.03	0.588	1.58	1.05	1.37	0.691	0.402	0.846	0.220
Eu	0.701	0.593	0.663	2.07	0.337	0.474	0.242	0.242	0.241	0.218	0.068	0.208	0.339	0.217	0.572	0.353	0.557	0.230	0.173	0.993	0.100
Tb	0.383	0.399	0.511	1.21	0.215	0.288	0.168	0.168	0.165	0.155	0.181	0.139	0.275	0.150	0.296	0.200	0.359	0.155	0.108	0.214	0.063
Gd	2.09	2.18	2.90	7.54	1.18	1.63	0.918	0.910	0.884	0.838	1.00	0.751	1.51	0.841	1.76	1.19	2.28	0.880	0.580	1.18	0.337
Dy	2.56	2.62	3.32	7.19	1.43	1.88	1.12	1.12	1.11	1.04	1.20	0.910	1.84	1.01	1.83	1.29	2.37	0.995	0.736	1.45	0.435
Ho	0.568	0.593	0.731	1.49	0.314	0.417	0.253	0.248	0.247	0.234	0.263	0.200	0.421	0.230	0.390	0.282	0.521	0.219	0.165	0.321	0.102
Er	1.69	1.73	2.14	4.13	0.917	1.176	0.739	0.720	0.713	0.680	0.760	0.578	1.28	0.668	1.08	0.820	1.50	0.638	0.485	0.945	0.310
Tm	0.257	0.266	0.329	0.609	0.138	0.179	0.112	0.109	0.108	0.103	0.117	0.089	0.207	0.104	0.167	0.125	0.228	0.101	0.076	0.150	0.049
Yb	1.69	1.72	2.15	3.80	0.894	1.16	0.725	0.710	0.693	0.668	0.745	0.581	1.36	0.674	1.08	0.833	1.50	0.648	0.508	0.984	0.341
Lu	0.251	0.260	0.319	0.545	0.132	0.173	0.109	0.107	0.105	0.099	0.110	0.086	0.209	0.102	0.159	0.127	0.222	0.099	0.075	0.148	0.053
Hf	0.943	1.03	1.88	4.58	0.476	1.01	0.380	0.383	0.396	0.362	0.459	0.321	0.653	0.352	1.38	0.734	0.921	0.526	0.276	0.516	0.134
Tl	0.004	0.006	0.020	0.063	0.005	0.003	0.006	0.006	0.005	0.014	0.013	0.009	0.011	0.012	0.003	0.031	0.006	0.039	0.005	0.032	0.009
Pb	0.555	0.438	1.84	3.61	0.435	0.321	0.205	0.251	0.202	0.298	0.256	0.664	1.65	1.28	2.19	1.34	0.339	0.652	0.772	0.360	0.291
Th	0.135	0.155	2.39	4.02	0.073	1.00	0.062	0.063	0.072	0.057	0.219	0.046	0.203	0.118	1.96	0.925	0.161	0.541	0.042	0.093	0.021
U	0.047	0.050	0.685	1.11	0.026	0.290	0.022	0.024	0.025	0.022	0.072	0.019	0.044	0.033	0.396	0.241	0.050	0.159	0.007	0.021	0.008

All major element concentrations are recalculated to anhydrous compositions. Trace element concentrations are not corrected for volatile content. Totals are given without LOI. Except for sample K-1, major element compositions are reported from Bolhar (2001). [a] Major element compositions of sample K-1 were obtained at the Tuebingen Isotope Geochemistry Laboratory. * Cr concentrations were obtained via MC-ICP-MS, except samples K-7 and TS-2, for which Cr concentrations were obtained via S-Q-ICP-MS. Uncertainties on Cr concentration measurements via isotope dilution method is 0.75 % 2SD.

Table 2.3: Iron and Cr isotopic compositions of Barberton and Belingwe igneous rocks.

Sample ID	Formation	Lithology	$\delta^{56/54}$Fe [‰]	2SD	n	$\delta^{53/52}$Cr [‰]	2SD	n
BARB-1	***Barberton greenstone belt***							
66.70	Komati	Komatiite	0.192	± 0.047	5	-0.094	± 0.026	5
109.22	Komati	Komatiite	0.085	± 0.019	5	-0.112	± 0.019	5
242.47	Komati	Komatiite	0.029	± 0.018	3	-0.115	± 0.020	5
255.50	Komati	Komatiite	0.029	± 0.009	5	-0.118	± 0.013	5
261.02	Komati	Komatiite	0.015	± 0.031	5	-0.124	± 0.028	5
290.65	Komati	Komatiite	0.038	± 0.030	5	-0.129	± 0.012	5
342.57	Komati	Komatiite	0.066	± 0.046	4	-0.114	± 0.006	5
345.29	Komati	Komatiite	0.024	± 0.022	4	-0.115	± 0.016	5
360.23	Komati	Komatiite	0.015	± 0.012	5	-0.130	± 0.019	5
372.13	Komati	Komatiite	0.045	± 0.026	5	-0.126	± 0.017	5
60.70	Komati	Komatiitic basalt	0.162	± 0.032	5	-0.173	± 0.020	5
229.40	Komati	Komatiitic basalt	0.077	± 0.055	5	-0.100	± 0.013	5
240.66	Komati	Komatiitic basalt	0.071	± 0.028	5	-0.115	± 0.012	5
262.00	Komati	Komatiitic basalt	0.083	± 0.024	5	-0.061	± 0.005	5
221.64	Komati	High-Mg tholeiite	0.094	± 0.023	5	-0.204	± 0.035	5
269.65	Komati	High-Mg tholeiite	0.053	± 0.036	5	-0.204	± 0.013	5
315.55	Komati	Basaltic andesite	0.123	± 0.021	5	-0.243	± 0.005	2
315.91	Komati	Basaltic andesite	0.129	± 0.031	5	-0.233	± 0.026	2
Outcrop								
BGB-002[a]	Komati	High-Mg tholeiite	0.087	± 0.032	5	-0.172	± 0.027	5
BGB-003[b]	Komati	Komatiitic basalt	0.061	± 0.018	5	-0.140	± 0.027	5
BGB-004[c]	Komati	Komatiitic basalt	0.111	± 0.015	5	-0.230	± 0.011	5
	Belingwe greenstone belt							
Z-1	Zeederbergs	High-Mg tholeiite	0.055	± 0.019	5	-0.196	± 0.015	5
Z-4	Zeederbergs	High-Mg tholeiite	0.052	± 0.046	5	-0.180	± 0.022	5
Z-18	Zeederbergs	High-Mg tholeiite	-0.009	± 0.043	5	-0.390	± 0.015	5
Z-9	Zeederbergs	Komatiitic basalt	0.095	± 0.032	5	-0.124	± 0.019	5
K-1	Reliance	Komatiitic basalt	0.012	± 0.027	5	-0.170	± 0.045	5
TS-2	Reliance	Komatiitic basalt						
K-4	Reliance	Komatiite	0.032	± 0.031	5	-0.136	± 0.015	5
K-6	Reliance	Komatiite	0.026	± 0.024	5	-0.130	± 0.019	5
K-7	Reliance	Komatiite						
K-9	Reliance	Komatiite	0.025	± 0.018	5	-0.129	± 0.029	5
TS-4	Reliance	Komatiite	0.091	± 0.015	5			
TS-8	Reliance	Komatiite	0.035	± 0.011	5	-0.106	± 0.025	5
Br-5	Brookland	Komatiitic basalt	0.046	± 0.020	5	-0.109	± 0.018	5
Br-1	Brookland	Komatiite	0.067	± 0.025	5	-0.124	± 0.026	5
Br-2	Brookland	Komatiite	0.050	± 0.024	5	-0.128	± 0.020	5
H-12	Hokonui	Komatiitic basalt	0.059	± 0.031	5	-0.198	± 0.009	5
H-6	Hokonui	Komatiite	0.054	± 0.015	5	-0.189	± 0.021	5
H-8	Hokonui	Komatiite	0.063	± 0.024	5	-0.111	± 0.020	5
B-12	Bend	Komatiite	-0.014	± 0.036	5	-0.169	± 0.030	5
B-13	Bend	Komatiite	0.055	± 0.022	5	-0.062	± 0.018	5
B-8	Bend	Komatiite	0.029	± 0.019	5	-0.107	± 0.018	5

Sample ID of Barberton samples correspond to depths of BARB-1 drill core in m. Sampling locations of [a] BGB-002: S 25° 58' 25.0, E 030° 49' 36.4; [b] BGB-003: S 25° 58' 17.8, E 030° 50' 10.7; [c] BGB-004: S 25° 58' 15.2, E 030° 51' 47.1. Uncertainties of isotopic compositions are given as two standard deviations (2SD) of replicate measurements n.

2.4 Results

2.4.1 Major Elements

Barberton samples range in geochemical composition (according to Jensen (1976)) from komatiite, komatiitic basalt to high-Mg tholeiitic basalt and basaltic andesite (Figure 2.2a) and agree very well to compositions presented in former studies (Figure 2.3; Coetzee, 2014; Jahn et al., 1982; Puchtel et al., 2013; Robin-Popieul et al., 2012; Schneider et al., 2019). MgO concentrations of samples in this study range from 3.85 to 31.01 wt. % MgO (Table 2.1, Figure 2.3, 2.5a), but values up to

45 wt. % MgO have been reported. Al_2O_3 and TiO_2 concentrations range from 3.06 to 16.36 wt. % and 0.36 to 1.31 wt. %, respectively, and both increase with decreasing MgO concentrations (Figure 2.3). Exceptions are the two basaltic andesites, which show lower TiO_2 concentration compared to high-Mg tholeiites. Chromium and Ni concentrations range from 34.88 to 2681 $\mu g\,g^{-1}$ and from 13.81 to 1596 $\mu g\,g^{-1}$ respectively, and overall decrease with decreasing MgO. Barberton komatiites have small variation in Al_2O_3/TiO_2 ranging between 8.40 and 10.63 characterizing them as being Al-depleted (Figure 2.2b). Associated komatiitic basalts and high-Mg tholeiites display higher variability in Al_2O_3/TiO_2 of 10.14 to 16.27. Exceptions are the two basaltic andesites (315.55 and 315.91) displaying Al_2O_3/TiO_2 of 20.71 and 22.33, respectively.
Belingwe samples vary in composition similar to the BaGB suite and include komatiites, komatiitic basalt and high-Mg tholeiitic basalts (Figure 2.2a) with MgO contents ranging between 8.24 to 34.33 wt. % (Table , Figure 2.3, 2.5a) corresponding also to chemical compositions presented by earlier publications (Bolhar, 2001; Bolhar et al., 2003; Nisbet et al., 1987; Nisbet et al., 1977; Shimizu et al., 2005). Al_2O_3 and TiO_2 concentrations range from 3.75 to 15.46 wt. % and 0.15 to 1.58 wt. %, respectively, and both increase with decreasing MgO concentrations similar to BaGB samples (Figure 2.3). Chromium and Ni concentrations range from 141 to 3468 $\mu g\,g^{-1}$ and from 110 to 1634 $\mu g\,g^{-1}$, respectively, and decrease overall with decreasing MgO (Figure 2.3). Belingwe komatiites and associated rocks are classified as Al-undepleted komatiites with Al_2O_3/TiO_2 ranging between 15.10 and 30.32, except for sample Z-9 displaying an Al_2O_3/TiO_2 of 5.22 (Figure 2.2b) and thus showing larger variation than BaGB samples. A subset of samples covering the whole range of degrees of melt differentiation (MgO from 8.24 to 34.33 wt. %) was analyzed for their $Fe^{2+}/\Sigma Fe$ ratios and revealed high and constant ratios of 0.74 to 0.81, except for cumulate sample B-8 ($Fe^{2+}/\Sigma Fe = 0.44$).

2.4.2 Trace Elements

Komatiites, komatiitic basalts and high-Mg tholeiites from the BaGB sample suite show strikingly homogenous and flat primitive mantle (PM) normalized trace element patterns agreeing well with literature data (Figure 2.4a; Chavagnac, 2004; Puchtel et al., 2013; Robin-Popieul et al., 2012; Schneider et al., 2019; Sossi et al., 2016). Komatiites display trace element patterns that are up to three times enriched relative to PM (values after Palme and O'Neill, 2003) with slightly positive Nb anomalies (Nb/Nb* = 1.06 to 1.73; $Nb/Nb^* = Nb_{PM}/(0.5 \times (Th_{PM}+La_{PM}))$; modified from Schneider et al., 2019) and negative Ti anomalies (Ti/Ti* = 0.67 to 0.92; $Ti/Ti^* = Ti_{PM}/0.5 \times (Gd_{PM}+Tb_{PM})$). All komatiites display slightly LREE-depleted patterns with $(La/Sm)_{PM}$ of 0.43 to 0.99. Komatiitic basalts and high-Mg tholeiites show higher enrichment in trace elements of up to eight times relative to PM and flat to variable LREE abundances, respectively. Both these rock types display small positive Nb anomalies (Nb/Nb* = 1.03 to 1.34, except samples BGB-002 = 0.94 and BGB-004 = 0.92). Komatiitic basalts show negative Ti anomalies (Ti/Ti* of 0.70 to 0.91) reminiscent to komatiites and high-Mg tholeiites, however, show slightly positive Ti anomalies (Ti/Ti* = 1.03 to 1.17). In general, BaGB samples show depletions of heavy REE (HREE) relative to middle REE (MREE) with $(Gd/Yb)_{PM}$ of 1.29 to 1.58 (Figure 2.2b). However, two high-Mg tholeiites as well

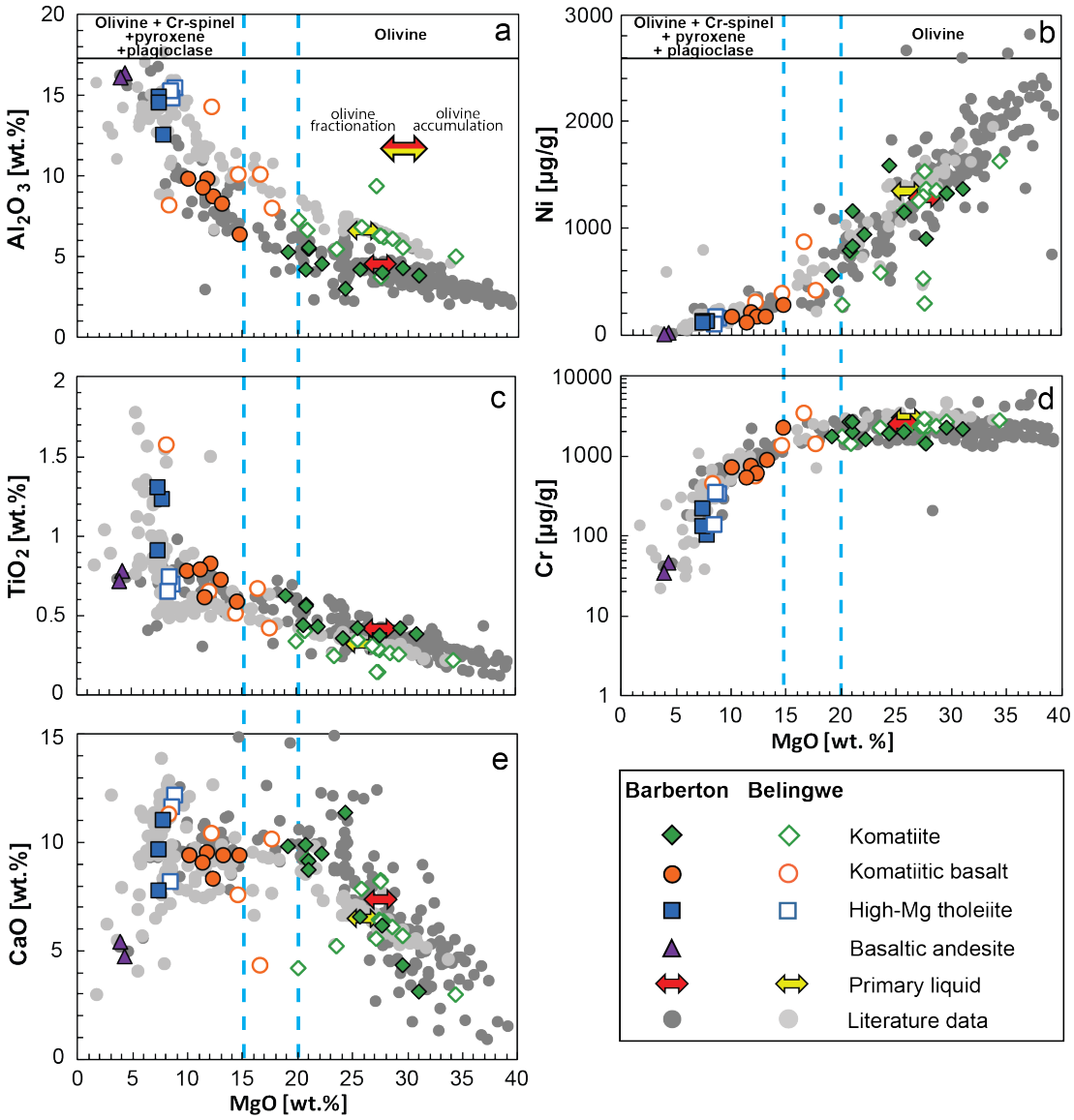

Figure 2.3: MgO variation diagrams for some major and trace elements for BaGB and BeGB samples. Blue dashed lines indicate a change of slope in variation diagrams and indicating the onset of Cr-spinel, pyroxene, and plagioclase crystallization from 20 to 15 wt. % MgO onwards. Above 20 wt. % MgO komatiites are controlled by olivine fractionation/accumulation only. For symbol reference see Figure 2.2. Literature data for Barberton: Coetzee (2014); Jahn et al. (1982); Puchtel et al. (2013); Robin-Popieul et al. (2012); Schneider et al. (2019); Sossi et al. (2016). Literature data for Belingwe: Bolhar (2001); Nisbet et al. (1977); Nisbet et al. (1987); Shimizu et al. (2005); Sossi et al. (2016).

as one komatiitic basalt have lower $(Gd/Yb)_{PM}$ (269 and outcrop samples BGB-002 and BGB-004) coinciding with higher Al_2O_3/TiO_2 of up to 16.27. The two basaltic andesites display enrichments of Th-U and LREE of up to 40-fold relative to PM, and strong depletions of Nb ($Nb/Nb^* = 0.34$) and Ti ($Ti/Ti^* = 0.52$ to 0.56) (Figure 2.4a) resulting in low $(Nb/Th)_{PM}$ of 0.30 to 0.31 (Figure 2.8d).

In general, the BeGB suite shows a more variable trace element pattern relative to PM compared to the BaGB suite (Figure 2.4b). As previously reported by Bolhar et al. (2003) LREE-enriched and LREE-depleted samples can be discriminated within each stratigraphic unit. LREE-depleted samples display trace element

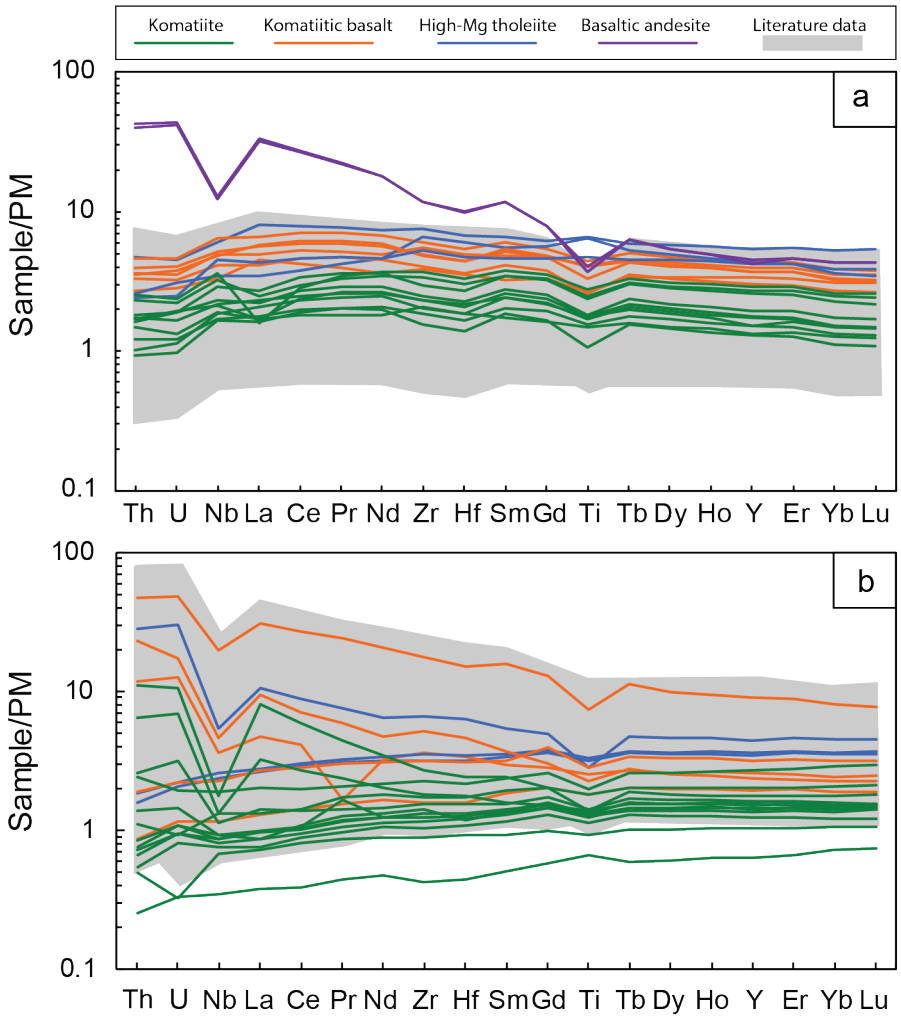

Figure 2.4: Primitive mantle (PM) normalized trace element pattern of **a)** the Barberton sample suite and **b)** the Belingwe sample suite. Literature data are shown as grey fields and derived from Chavagnac (2004); Schneider et al. (2019); Robin-Popieul et al. (2012); Puchtel et al. (2013) for Barberton and from Shimizu et al. (2005) and Bolhar et al. (2003) for the Belingwe Greenstone Belt. Primitive mantle values after Palme and O'Neill (2003).

patterns that are up to two times enriched relative to PM and mainly consist of komatiites with minor komatiitic basalts and high-Mg tholeiites. All LREE-depleted samples show positively sloping LREE with $(La/Sm)_{PM}$ of 0.63 to 0.90 and flat HREE with $(Gd/Yb)_{PM}$ between 0.81 and 1.24 (Figure 2.2b, Figure 2.4b). The LREE-enriched sample group with $(La/Sm)_{PM}$ between 1.62 to 3.33 is characterized by high abundances of highly incompatible elements (up to 50 times PM) with more crustal-type multi-element pattern evidenced by enrichments of Th and U combined with distinct negative Nb ($Nb/Nb^* = 0.18$ to 0.51) and Ti ($Ti/Ti^* = 0.58$ to 0.93) anomalies (Figure 2.4b). These samples can further be depicted by low $(Nb/Th)_{PM}$ ratios ranging between 0.16 to 0.42 (Figure 2.8d). Two enriched samples (Br-5 and Z-9) additionally display peculiar high $(Gd/Yb)_{PM}$ rather resembling Al-depleted komatiites (Figure 2.2b).

2.4.3 Stable chromium and iron isotope compositions

Barberton komatiites cluster around a narrow range with $\delta^{53/52}$Cr values between -0.094 ‰ and -0.130 ‰ with an average value of -0.118 ± 0.021 ‰ (2SD; n=10) (Table 2.3 and Figure 2.5a-d). Chromium isotopic compositions of Barberton komatiites reported by Sossi et al. (2018) agree well with our results (Figure 2.5a-d). The $\delta^{53/52}$Cr of komatiitic basalt, high-Mg tholeiites and basaltic andesites are in general more variable and range between -0.061 and -0.243 ‰ (average of -0.171 ± 0.120 ‰, n=11). There is, however, a general trend to lighter $\delta^{53/52}$Cr values of komatiitic basalts and high-Mg tholeiites with decreasing MgO, Cr and Ni and increasing Al_2O_3 concentrations (Figure 2.5a-d). The two LREE-enriched basaltic andesites display the lightest $\delta^{53/52}$Cr values of -0.243 and -0.233 ‰, respectively. Stable Fe isotope compositions of BaGB komatiites range between +0.015 to +0.085 ‰ in $\delta^{56/54}$Fe (Figure 2.5e-h), with the exception of sample 66.70, which has a $\delta^{56/54}$Fe of +0.192 ‰. Komatiitic basalts and high-Mg tholeiites become slightly heavier in their Fe isotope composition with $\delta^{56/54}$Fe between +0.053 ‰ to +0.162 ‰ showing weak correlations with decreasing MgO and Cr content. However, no correlation of $\delta^{56/54}$Fe with total iron content, also an indicator of magma differentiation (Schoenberg and von Blanckenburg, 2006; Schuessler et al., 2009), is observed. Furthermore, LREE-enriched basaltic andesites with the lowest MgO contents of all BaGB rocks exhibit isotopically heavy $\delta^{56/54}$Fe values of +0.123 and +0.129 ‰.
Stable Cr and Fe isotope compositions of BeGB samples show similar trends as BaGB samples albeit with higher scatter (Figure 2.5). Belingwe komatiites have an average $\delta^{53/52}$Cr value of -0.127 ± 0.066 ‰ (2SD, n=11) (Table 2.3). Komatiitic basalts and high-Mg tholeiites show a higher variation, but similar to BaGB samples, a broad trend of decreasing $\delta^{53/52}$Cr values with decreasing MgO and Cr is observed (Figure 2.5a-d). Similar to BaGB samples, BeGB samples show only weak correlations in $\delta^{56/54}$Fe with decreasing MgO, Cr and Ni contents as well as increasing Al_2O_3 contents (Figure 2.5e-h).

2.5 Discussion

2.5.1 Alteration and crustal assimilation

Although both BaGB and BeGB are well known as sites of well-preserved rocks, all of the studied samples have experienced post-magmatic alteration to various extents. Element mobility during post-magmatic processes may influence the chemical and isotopic composition of rocks and minerals (e.g., (Arndt et al., 1989; Lahaye and Arndt, 1996; Lahaye et al., 1995; Polat and Hofmann, 2003; Polat et al., 2002) and it is therefore important to evaluate the effects of alteration on (isotope) geochemical data. Post-magmatic processes for the BaGB and BeGB may involve low-grade metamorphic overprint and hydrothermal fluid infiltration caused by seafloor alteration (Brake, 1996; Hofmann and Harris, 2008; Lahaye et al., 1995; Puchtel et al., 2013).

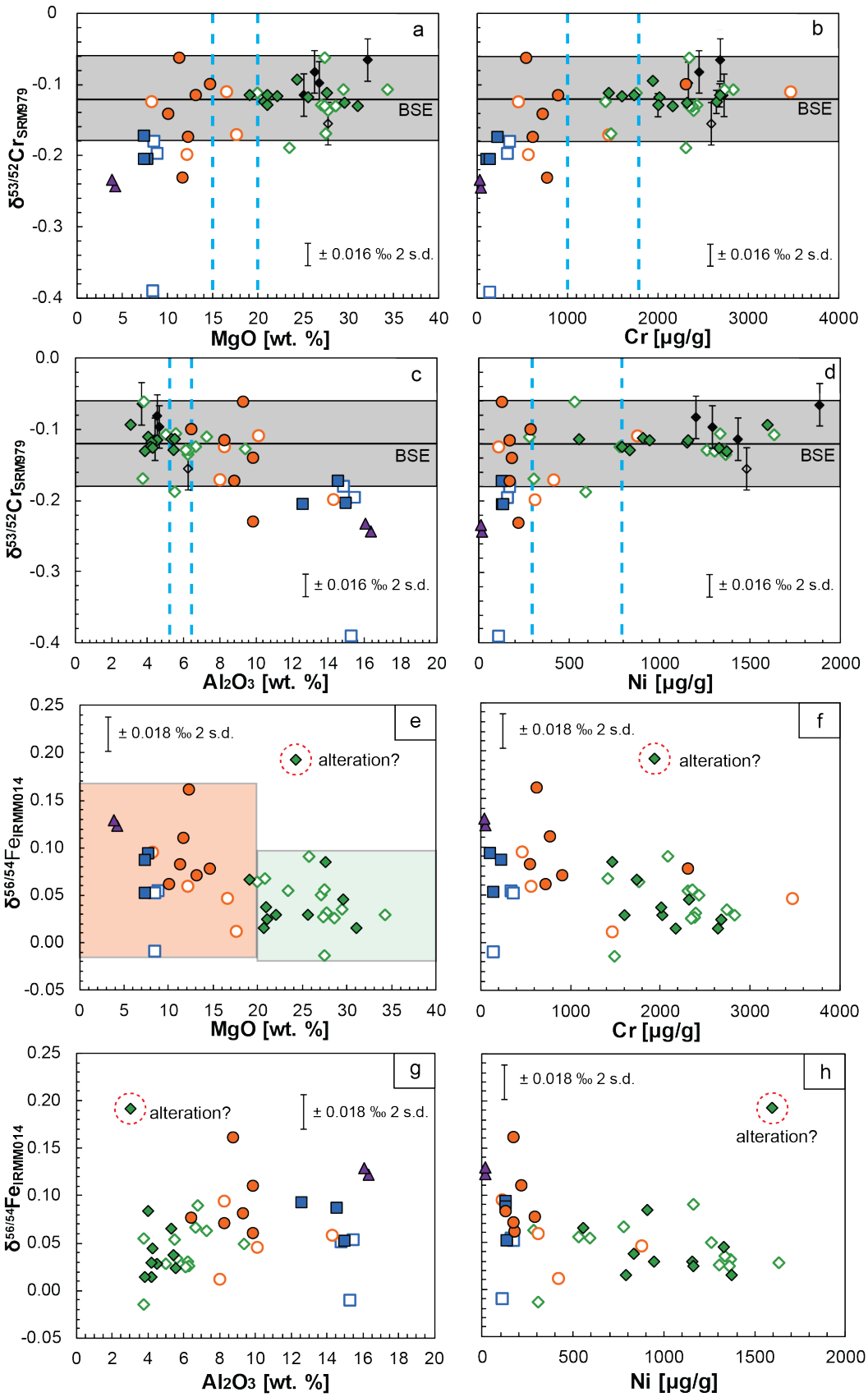

Figure 2.5: **a-d)** Chromium isotope compositions ($\delta^{53/52}$Cr) and **e-h)** iron isotope compositions ($\delta^{56/54}$Fe) versus major and trace element concentrations. Uncertainties on $\delta^{53/52}$Cr and $\delta^{56/54}$Fe correspond to a 2SD of 0.016 ‰ and 0.018 ‰, respectively, which is the pooled 2SD* of repeated measurements of reference material BHVO-2 ($\delta^{53/52}$Cr) and standard material Tueb-Fe ($\delta^{56/54}$Fe). This uncertainty is shown as a bar for reference in all panels. For symbol description see Figure 2.2. The shaded grey area in a-d corresponds to the ($\delta^{53/52}$Cr) average value for BSE of -0.12 ± 0.06 ‰ (this study). a-d) also show literature data with associated 2SD of Sossi et al. (2018): open diamonds: Belingwe Greenstone Belt and filled black diamonds: Barberton Greenstone Belt. Vertical dashed lines correspond to 15 to 20 wt. % MgO indicating a change in the fractionating assemblage (see Figure 2.3).

2.5.1.1 The effect of alteration on major and trace element concentrations

Generally, rocks with high abundance of olivine are more susceptible to alteration (Arndt, 2008) as is evident from the high degree of serpentinization of komatiites, which is mirrored by LOI of up to 9.96 wt. % (Figure 2.8a). Consistently, less Mg-rich rocks (i.e., less abundant in olivine) have lower LOI values and more often preserve fresh pyroxene crystal cores. The majority of studied samples have LOI values less than 6 wt. % (Table 2.1, 2.2 and Figure 2.8a). Samples of the BaGB generally show complete serpentinization and chloritization in thin sections with primary phases being replaced by secondary phases, but nonetheless preserve magmatic textures (Figure 2.6). Serpentinization of komatiites is evident by the light green to colorless appearance of olivine pseudomorphs and green to green-brownish colored groundmass in plane polarized light (Figure 2.6a). Oxides (magnetite/Cr-bearing spinel) cluster along olivine plates. The matrix is made up of devitrified glass completely altered to an assemblage of plumose to fan-shaped serpentine and chlorite/actinolite. Komatiitic basalts are depicted by high degrees of chloritization and actinolite alteration. Komatiitic basalts often show twinned pyroxene crystals completely altered to chlorite sitting in a matrix altered to actinolite/tremolite (Figure 2.6c, d). Cr-bearing spinel and/or magnetite are concentrated within the pyroxene crystals. High-Mg tholeiites and basaltic andesites (Figure 2.6e-h) are characterized by the appearance of olivine altered to serpentine, pyroxene altered to actinolite and relatively unaltered plagioclase. Opaque phases, perhaps Cr-bearing spinel and/or magnetite are disseminated throughout the fine-grained matrix.

Systematic and well-defined correlations of REE and HFSE with the immobile element Zr ($0.93 > R^2 > 0.75$; only Sm is shown, Figure 2.7a) are indicative of primary geochemical signatures of these element groups during low-grade metamorphism and alteration. Correlations of MgO with Zr contents show good correlations with R^2 of 0.74 for the BaGB suite and R^2 of 0.41 for the BeGB suite (Figure 2.7b). Chromium vs. Zr contents show similarly good correlations with R^2 of 0.61 for the BaGB suite and R_2 of 0.23 for the BeGB suite (Figure 2.7e). The lower R_2 for MgO and Cr can at least partially be attributed to the compatible behavior of these elements. The incompatible behavior of the redox-sensitive transition metal V can be observed by the positive correlation with Zr contents in both suites. Excluding the two basaltic andesites, BaGB samples display a good correlation with R_2 of 0.76, but the BeGB suite is less well correlated with a R_2 of 0.32 (Figure 2.7c). Vanadium variations in the BeGB suite can be attributed to variable enrichments by crustal assimilation in the LREE-enriched group (Figure 2.4; Bolhar et al., 2003). In Fe_2O_3 vs. Zr space no clear correlation for the BaGB or BeGB rock suite is observed. However, komatiites, which experienced the highest degree of serpentinization, display relatively narrow range of Fe_2O_3 contents while komatiitic basalts, high-Mg tholeiites and basaltic andesites show very variable Fe_2O_3 contents with increasing Zr concentration. Fe_2O_3 contents in the BeGB suite is equally variable in Mg-rich and Mg-poor rocks (Figure 2.7d).

The mobility of Cr is strongly dependent on the oxidation state. Hexavalent chromium is soluble and therefore mobile, whereas Cr^{3+} is commonly regarded as insoluble and immobile. In contrast, experimental and observational studies have shown that Cr^{3+} can be soluble in Cl- and C-rich aqueous solutions at upper lithospheric mantle and crustal conditions (Babechuk et al., 2017; Huang et al., 2019; Klein-BenDavid et al.,

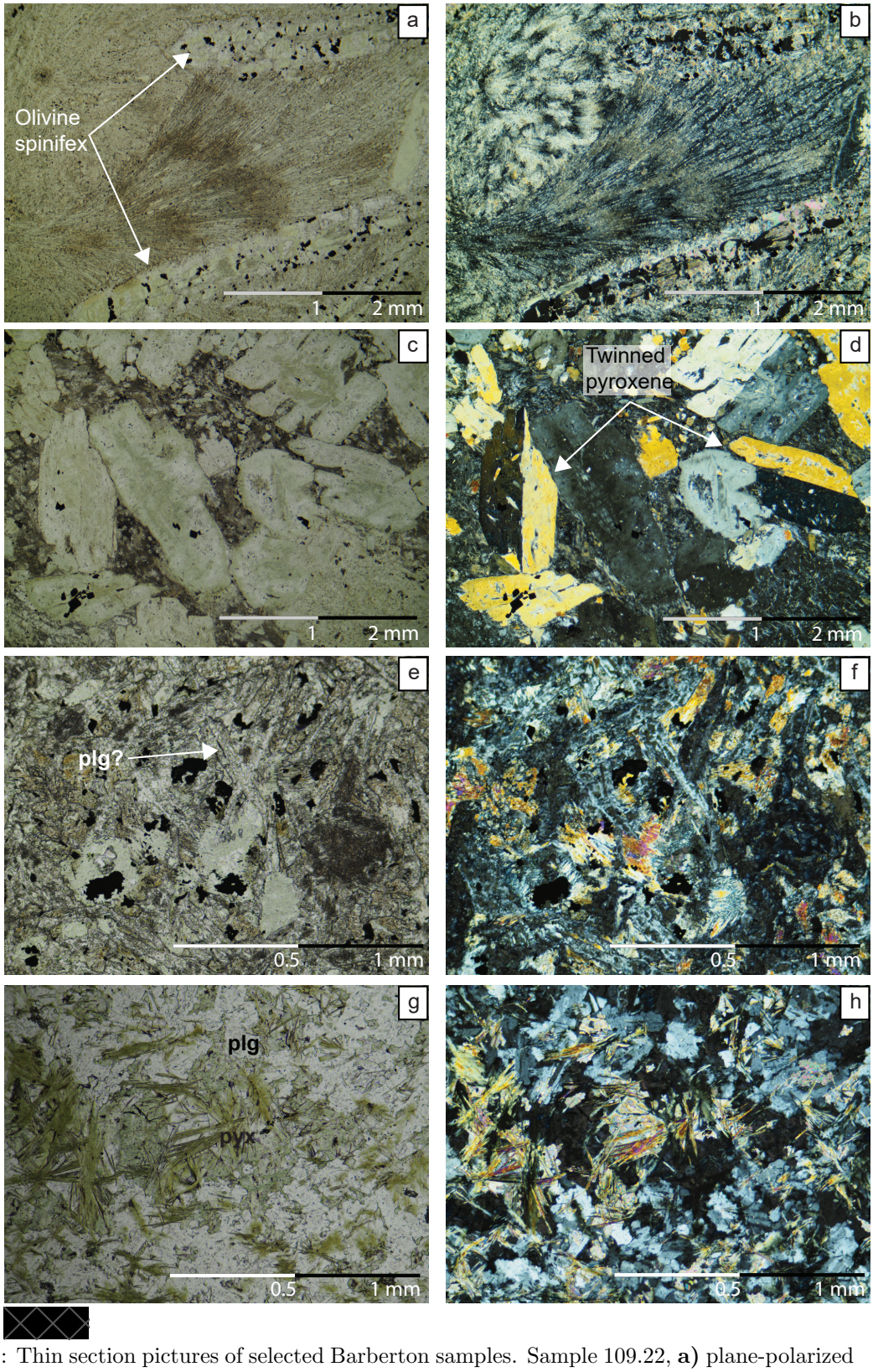

Figure 2.6: Thin section pictures of selected Barberton samples. Sample 109.22, **a)** plane-polarized light and **b)** cross-polarized light. Parallel plate-like olivine crystals altered to serpentine and chlorite sit in a feathery matrix of serpentine. Sample 229.40, **c)** plane-polarized light and **d)** cross-polarized light. Twinned pyroxenes altered to actinolite and chlorite sit in a fine-grained matrix altered to actinolite/tremolite. Sample BGB-002, **e)** plane-polarized light and **f)** cross-polarized light. Sample 315.55, **g)** plane-polarized light and **h)** cross-polarized light. Both, BGB-002 and 315.55 are characterized by relatively fresh plagioclase. Pyroxenes are altered to actinolite/chlorite, whereas the groundmass consists of serpentine minerals. In e) and f) opaque phases (Cr-spinel and/or magnetite) are disseminated throughout the fine-grained matrix.

2011; McClain and Maher, 2016; Watenphul et al., 2014). However, we emphasize that the typical magmatic signatures observed in MgO variation diagrams (Figure 2.3) suggest minor, if any, mobilization of immobile major and trace elements during postmagmatic processes. This is furthermore supported by coherent trace element patterns (Figure 2.4) and the absence of coupled SiO_2 and K_2O enrichments with Na_2O, Sr and Y depletions (Table 2.1, 2.2), which are indicators for Archean seafloor alteration processes (Hofmann and Harris, 2008).

2.5.1.2 The effect of alteration on Cr and Fe isotopic compositions

The concentration of Cr shows negligible evidence for alteration-induced mobility, as discussed above, but the isotopic composition of Cr deserves special attention due to the documented fractionation effects accompanying serpentinization and other forms of fluid-rock alteration. For example, it has been shown that hydration and serpentinization can strongly alter (ultra)mafic samples towards much higher $\delta^{53/52}$Cr values (Farkas et al., 2013; Wang et al., 2016) than that of the igneous inventory of -0.124 ± 0.101 ‰ (Schoenberg et al., 2008) (Figure 2.8a, b), with no clear correlation between $\delta^{53/52}$Cr values and Cr contents (Farkas et al., 2013). Chromium isotope data of this study, however, exclusively trend towards more negative $\delta^{53/52}$Cr values compared to the igneous inventory for both, the BaGB and BeGB suites of rocks (compare with Figure 2.5a-d), suggesting a different process responsible for the observed Cr isotope fractionation. The absence of a correlation between $\delta^{53/52}$Cr and LOI (Figure 2.8a) and the uniform $\delta^{53/52}$Cr signatures of komatiites (Figure 2.5a-d) – especially those of the BaGB – displaying the largest degrees of serpentinization (highest and variable degrees of LOI, Figure 2.8), support the robustness of original $\delta^{53/52}$Cr signatures during post-magmatic alteration for the samples studied here. Furthermore, the absence of correlations between $\delta^{53/52}$Cr values and other indices of seafloor alteration and metamorphism, e.g. increasing K_2O concentrations (Hofmann and Harris, 2008) in komatiites (Figure 2.8c) or Sr/Sr* (not shown), supports that Cr isotopes of the BaGB and BeGB komatiite-tholeiite suites are not fractionated during serpentinization and greenschist metamorphic overprint.
The reason for the very light Cr isotopic composition of -0.390 ‰ in $\delta^{53/52}$Cr for one sample from the BeGB (high-Mg tholeiite Z-18) is unclear. We have tested all possible secondary alteration mechanisms (e.g., serpentinization, seafloor alteration, albitization), but find no coherent explanation for the extraordinary negative $\delta^{53/52}$Cr value. Iron, as a major element, may behave relatively resistant to alteration processes, but also has been shown to be mobilized during post-magmatic alteration processes (e.g., Arndt et al., 1989). The poor correlations of Fe_2O_3 with Zr (Figure 2.7d) might indeed indicate small-scale iron mobility. Associated kinetic isotope fractionation during fluid-rock interaction of serpentinizing fluids could therefore alter the original $\delta^{56/54}$Fe values of komatiites, with a preferential loss of light isotopes by the alteration process (Dauphas et al., 2010; Rouxel et al., 2003). However, this would result in a negative correlation of $\delta^{56/54}$Fe values with total Fe_2O_3 concentrations (Hibbert et al., 2012), which is not observed for the BeGB and BaGB komatiite-tholeiite suites. Such fluid alteration processes may also be depicted by negative correlations of $\delta^{56/54}$Fe values with Fe_2O_3/TiO_2 ratios as demonstrated for altered MORBs by Rouxel et al. (2003). The weak negative correlation between $\delta^{56/54}$Fe values and Fe_2O_3/TiO_2 ratios observed for the BaGB and BeGB suites (Table 2.1, 2.2, 2.3), can however be attributed to the differentiation of the komati-

itic magmas, since the decrease of Fe_2O_3/TiO_2 is controlled by an increase in TiO_2 concentrations while Fe_2O_3 contents remain constant. During serpentinization, a process that includes the formation of magnetite, Fe^{2+} becomes oxidized to Fe^{3+}, which would lead to a decrease in the whole rock $Fe^{2+}/\Sigma Fe$ ratios (Dauphas et al. 2010). The consistently high $Fe^{2+}/\Sigma Fe$ ratios between 0.74 and 0.81 of BeGB samples suggest that oxidation of Fe^{2+} due to serpentinization is minor in at least the BeGB suite of rocks and that associated Fe isotopic fractionation is negligible. As the original silicate mineralogy of Barberton samples has not been preserved as well as that of Belingwe samples, higher degrees of Fe oxidation might be expected. As mentioned above, komatiites with high abundance of olivine would be most affected by serpentinization. However, Barberton komatiites display a relatively small range in Fe_2O_3 contents between 11.75 and 13.62 wt. %. Additionally, Fe speciation of BaGB komatiitic basalts by Cloete (1999) show similarly high $Fe^{2+}/\Sigma Fe$ ratios between 0.76 and 0.9 than rocks of the BeGB komatiite-tholeiite suite. An exception is komatiite sample 66.70 from the BaGB, which displays an exceptionally high $\delta^{56/54}$Fe value of +0.192 ‰. High CaO concentration of this sample combined with abundant serpentine veining indicates stronger alteration compared to other BaGB samples with similar MgO (Figure 2.3, 2.5e-h, Table 2.1) possibly affecting its Fe isotopic composition.

2.5.1.3 The effect of crustal assimilation on Cr and Fe isotopic compositions

During the ascent of komatiitic magma through the lithosphere and crust, assimilation of crustal material might potentially obscure their primitive Cr and Fe isotopic signatures. The two basaltic andesites from the BaGB show enrichments of Th-U and LREE combined with negative anomalies of Nb and Ti (Figure 2.4) potentially indicating crustal contamination. In general, BaGB samples show no signs of crustal contamination and, consistently, exhibit positive Nb anomalies with high $(Nb/Th)_{PM}$ (Figure 2.8d) agreeing well with former studies (Puchtel et al., 2013; Robin-Popieul et al., 2012; Schneider et al., 2019). However, variable degrees of assimilation of crustal/lithospheric material of up to 30 % have been used to explain the trace element enriched pattern of some of the BeGB samples, and is consistent with the inferred continental emplacement and associated interaction with pre-existing Archean crust (Bolhar et al., 2003; Shimizu et al., 2005). Nevertheless, the BeGB komatiite-tholeiite suite does not show a correlation of $\delta^{53/52}$Cr and $\delta^{56/54}$Fe with indices of crustal assimilation such as $(Nb/Th)_{PM}$ (Figure 2.8d), $(La/Yb)_{PM}$, $(Nb/La)_{PM}$ or Nb/U (not shown). Assimilation of crustal/lithospheric material is expected to have a minor to negligible impact on the bulk $\delta^{53/52}$Cr signature of the ascending komatiitic magma, because of the expected similarity in the stable Cr isotopic compositions of assimilated crust and komatiitic magma, and the large difference in Cr concentrations between komatiitic magma (>453 $\mu g\,g^{-1}$ Cr for samples of this study) and continental crust (continental crust = 92 $\mu g\,g^{-1}$; Rudnick and Gao, 2003; Archean Continental Crust = 162 $\mu g\,g^{-1}$; Rudnick and Fountain, 1995). Discrimination between crustal assimilation and fractional crystallization in regard to the Fe isotopic composition of basaltic/komatiitic melt is complicated because both processes lead towards heavier values of $\delta^{56/54}$Fe. Barberton samples are not influenced by assimilation, except for the two LREE-enriched basaltic andesites. However, the trends observed for Barberton and Belingwe, the latter including sam-

ples having experienced considerable assimilation, are very similar in magnitude suggesting that the influence of crustal assimilation on the $\delta^{56/54}$Fe is minor (Figure 2.5e-h).

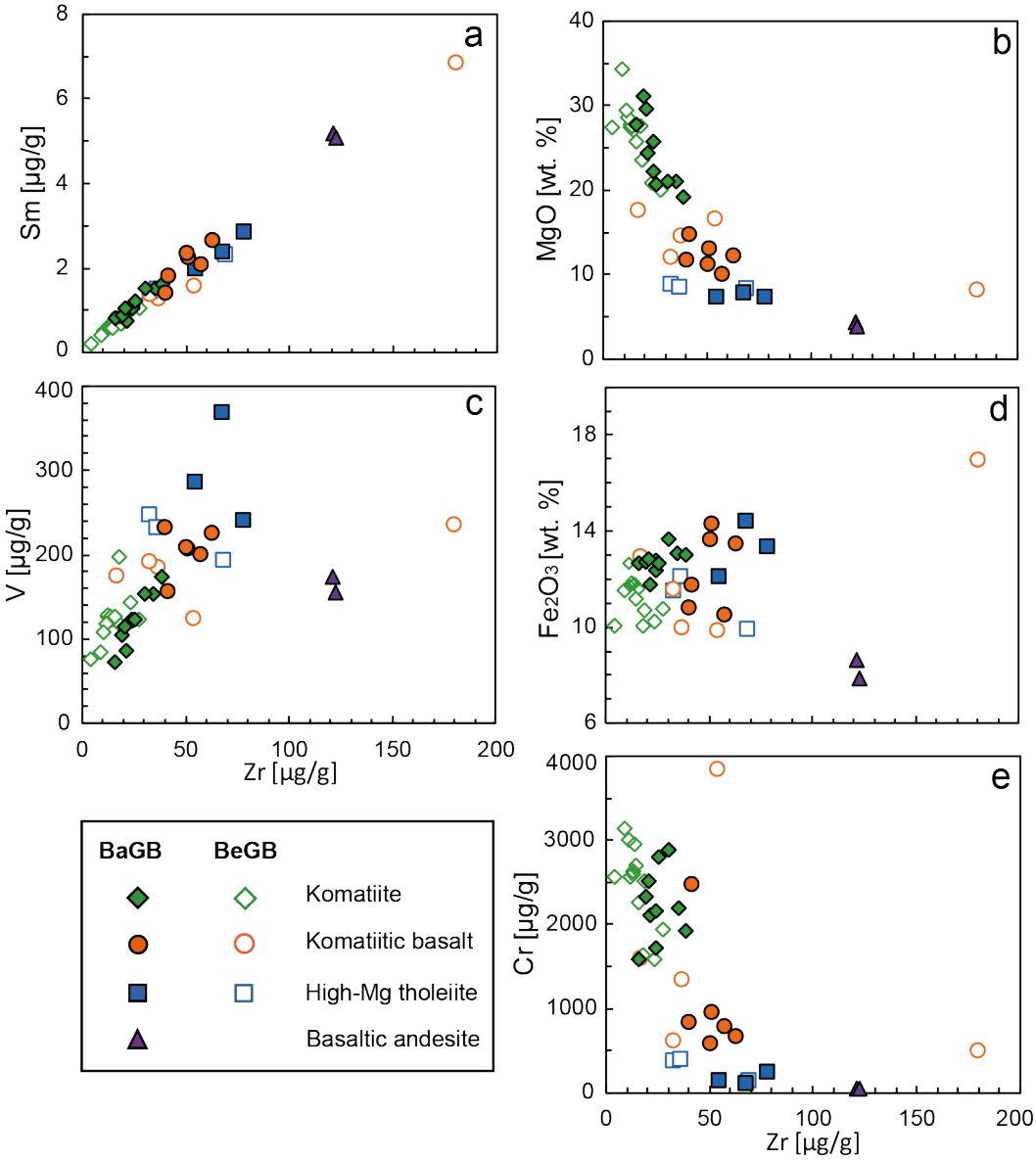

Figure 2.7: Element vs. Zr concentration plots of BaGB and BeGB samples.

2.5.2 The effect of partial melting on Cr and Fe isotopic evolution of komatiitic melts

Iron isotopes are known to be fractionated during partial melting with the heavier Fe isotopes preferentially entering the melt (Weyer et al., 2005; Weyer and Ionov, 2007; Williams et al., 2004; Williams et al., 2005). This effect has been attributed to the incompatible behavior of Fe^{3+}, with the heavier isotopes preferentially being associated with Fe^{3+}-complexes.
Chromium concentrations and $Cr^{2+}/\Sigma Cr$ ratios of mafic melts are dependent on

temperature, pressure, prevailing fO_2 and bulk composition of the melt (Berry et al., 2006; Hanson and Jones, 1998; Papike et al., 2016; Schreiber and Haskin, 1976). At low fO_2 (e.g., iron-wuestite (IW) redox buffer) and high temperatures, the Cr content and $Cr^{2+}/\Sigma Cr$ ratio in the melt will be higher than at higher fO_2 (e.g., fayalite-magnetite-quartz (FMQ) redox buffer) and lower temperatures (Delano, 2001; Murck and Campbell, 1986; Schreiber and Haskin, 1976). Furthermore, experimental data show that under conditions relevant for komatiite generation, i.e. eruption temperatures of up to 1,600° C (Herzberg, 1992; Nisbet et al., 1993) and fO_2 of FMQ $\pm$ 1 log units (Asafov et al., 2018; Canil, 1997; Nicklas et al., 2018), the $Cr^{2+}/\Sigma Cr$ ratio in basaltic melts may vary from 0.60 (FMQ -1 log unit) to 0.30 (FMQ +1 log unit). Therefore, Cr^{2+} represents a significant oxidation state in partial melts at terrestrial mantle fO_2 conditions (Berry et al., 2006; Papike et al., 2016). Consequently, partial melting may lead to the enrichment of light Cr isotopes in the melt in accordance with a negative trend of $\delta^{53/52}$Cr vs. Al_2O_3 in restitic peridotites observed by Xia et al. (2017). Independent of the magnitude of the Cr isotopic fractionation ε during melting, high degree melts (i.e., komatiitic melts) can approximate the Cr isotopic composition of the source (Section 2.5.4), while lower degrees of partial melting (i.e., generating basaltic melt compositions) could lead to a difference in the Cr isotopic composition between melt and source with the melt having lower $\delta^{53/52}$Cr values than the source.

2.5.3 Effects of crystal fractionation on the Cr and Fe isotopic evolution of komatiitic melts

Fractional crystallization of minerals with an isotopically light or heavy Fe isotope signature is known to effectively modify the Fe isotope composition of the residual melt (Schuessler et al., 2009; Sossi et al., 2012; Teng et al., 2008; Williams et al., 2018). Recent studies showed that fractional crystallization of spinel and pyroxene in OIBs can also affect the Cr isotopic composition of the residual melt driving it towards lighter $\delta^{53/52}$Cr values (Bonnand et al., 2020; Shen et al., 2020). In contrast, Jerram et al. (2020) observed an increase of $\delta^{53/52}$Cr values during komatiitic melt evolution, which these authors attributed to the fractional crystallization of olivine. For samples, for which minor crustal assimilation is observed (see above), MgO variation diagrams and coherent trace element patterns of BaGB and BeGB komatiite-tholeiite suites indicate that olivine, Cr-bearing spinel, pyroxene, and plagioclase are the main driving phases of magmatic differentiation of these ancient crustal segments (Figure 2.3; Bolhar et al., 2003; Coetzee, 2014; Schneider et al., 2019). These diagrams, however, may be somewhat misleading in that the observed trends do not reflect the continuous evolution of a single parental melt but represent the complexity between interacting processes such as different degrees of partial melting, crystal fractionation and/or accumulation, magma mixing and minor crustal assimilation within each individual sample. As samples from the BaGB and BeGB are derived from numerous flows (massive and differentiated) the observed variations in chemical composition on MgO variation diagrams need to be taken as an average of the evolution of numerous batches of parental melts of similar composition. Nevertheless, the BaGB and BeGB MgO variation diagrams still reveal which mineral phases are actively controlling the chemical composition of whole rock samples by fractional crystallization and/or accumulation. As the scope

of this study is to interpret the variations of Cr and Fe stable isotopes in the light of bonding environment in crystals, a brief summary of the activity of certain minerals in the komatiitic-tholeiitic suites is provided.

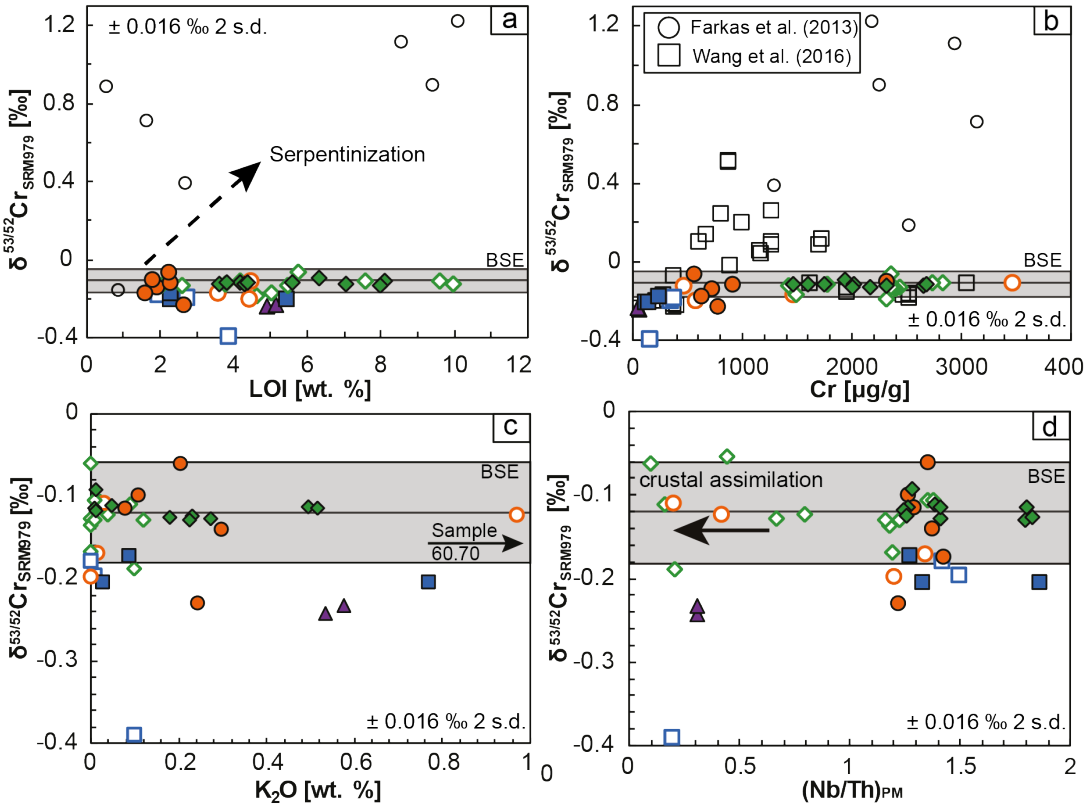

Figure 2.8: Chromium isotope variations ($\delta^{53/52}$Cr) as a function of different alteration and crustal assimilation indices, such as **a)** $\delta^{53/52}$Cr vs. Loss on ignition (LOI), **b)** $\delta^{53/52}$Cr vs. Cr concentration, **c)** $\delta^{53/52}$Cr vs. K_2O concentrations and **d)** $\delta^{53/52}$Cr vs. $(Nb/Th)_{PM}$. Normalizing values for primitive mantle (PM) are after Palme and O'Neill (2003). In addition, a) and b) show literature data of Wang et al. (2016) (open black circles) and/or Farkas et al. (2013) (open black squares), which present ultramafic rocks with variable degree of aqueous and chemical alteration. Please note the change in scale of the y-axis in c) and d). Grey shaded area in a)-d) represents the BSE range of -0.12 ± 0.06 ‰ (this study). Symbols for BaGB and BeGB komatiite-tholeiite suites are as used in Figure 2.2.

2.5.3.1 Active (i.e., crystallizing and/or accumulating) mineral phases along MgO trends

The whole-rock chemical compositions of BaGB and BeGB komatiite-tholeiite suites displayed on MgO variation diagrams are in excellent agreement with literature data (Figure 2.3). Previous studies determined the composition of the parental melt of komatiites from the Komati Formation (BaGB) and the Reliance Formation (BeGB) and suggested MgO concentrations of 26 - 29 wt. % and 24.5 - 27.5 wt. %, respectively. We adopt these ranges in MgO concentrations for the approximate composition of the parental melts of BaGB and BeGB komatiites for the respective rock suites studied here (Figure 2.3). Komatiites with comparable MgO concentrations therefore approximate liquid compositions (sample 109.22 for the BaGB and samples K6, K7 and TS-4 for the BeGB). The positive correlation of Ni with MgO (Figure 2.3b) and

negative correlations of Al_2O_3 and TiO_2 with MgO (Figure 2.3a, c) indicates olivine fractionation for komatiites with MgO smaller than their parental melts and olivine accumulation for komatiites with MgO greater than their parental melts (Figure 2.3a). The accumulation of olivine is in agreement with petrographic observations showing cumulus olivine in thin sections of BaGB samples 360.23 and 372.13 (MgO of 31.01 and 29.54 wt. %, respectively). The flat to slightly negative trend of Cr vs. MgO (Figure 2.3d) suggests that olivine fractionation in komatiites has little influence on the Cr budget (testifying to the moderately compatible behavior of Cr in olivine), and reflects that olivine is the sole cumulus phase in komatiites with MgO higher than their respective parental melts (Barnes, 1998). Another phase that might be active at high-Mg contents and thus might accompany early olivine crystallization is Cr-bearing spinel. Chromium-spinel crystallization is controlled by temperature and fO_2 and experimental studies have shown that a komatiite magma with Fo93 olivine control, fractionating along the FMQ buffer, starts to crystallize Cr-bearing spinel at ∼24 wt. % MgO (Barnes, 1998; Murck and Campbell, 1986). However, BaGB komatiites in this study exhibit a maximum Cr concentration at 20.71 wt. % MgO (Figure 2.3c). Importantly, none of the samples plot at high MgO and high Cr contents, indicating the lack of combined olivine and Cr-bearing spinel accumulation (Barnes, 1998).

A change of the fractional assemblage in BaGB and BeGB suites can be inferred from a change in slope in Al_2O_3, TiO_2, Cr and Ni vs. MgO at 15 to 20 wt. % MgO content indicating the co-crystallization of Cr-bearing spinel, pyroxene and minor olivine (Figure 2.3; Blichert-Toft et al., 2015; Bolhar et al., 2003; Coetzee, 2014; Nisbet et al., 1987; Nisbet et al., 1977; Schneider et al., 2019; Shimizu et al., 2005). Strongly decreasing Cr concentrations below 15 to 20 wt. % MgO are the result of Cr-bearing spinel and pyroxene crystallization. The onset of pyroxene crystallization is further inferred from a change in the slope in CaO vs. MgO space at 20 wt. % MgO and a subsequent decrease of CaO contents below MgO of 15 wt. % (Figure 2.3e). Komatiitic basalts are characterized by abundant pyroxene and the apparent early crystallization of pyroxene can be partially attributed to pyroxene accumulation in these high MgO komatiitic basalts (Arndt et al., 2008; Arndt and Fleet, 1979). High-Mg tholeiites show high Al_2O_3 and TiO_2 contents indicating the absence of appreciable plagioclase or Fe-Ti oxide fractionation (Figure 2.3a, c). The high Al_2O_3 contents are the result of plagioclase accumulation, which, together with pyroxene, is the most abundant phase observed in thin sections of BaGB high-Mg tholeiites (Figure 2.6e-f). The BaGB enriched basaltic andesites show also enrichments in Al_2O_3, agreeing well with the observed cumulus plagioclase (Figure 2.6g-h). However, in contrast to the later crystallizing phases of Cr-bearing spinel and pyroxene, relative to olivine, fractionating or accumulating plagioclase can be neglected regarding Cr and Fe element partitioning and therefore also for interpreting Cr and Fe isotopic variations.

2.5.3.2 Theoretical effects of olivine-spinel-pyroxene crystal fractionation on residual melt Cr and Fe isotope composition

In the following, we will discuss potential effects of crystallization and/or accumulation of the major phases (olivine, Cr-bearing spinel and pyroxene) in a komatiitic melt system on the Cr and Fe isotope signatures of whole rocks on the basis of crystal field theory and the data of natural rocks obtained for this study.

Olivine: Crystal field theory predicts a particular high octahedral crystal field stabilization energy (CFSE) for Cr^{3+}, whereas Cr^{2+} has a lower octahedral site preference and favors slightly distorted crystal lattice sites (Jahn-Teller theorem; Burns (1970); Burns (1975a)). Olivine with the general formula $M_1^{2+}M_2^{2+}SiO_4$ offers tetragonally distorted octahedral positions, M_1, and trigonally distorted octahedral positions, M_2, with M_1 being smaller than M_2. Olivine would therefore prefer Cr^{2+} (0.80 Å) over Cr^{3+} (0.62 Å) inducing no charge imbalance. Moreover, Cr^{2+} is potentially distributed equally between M_1 and M_2 accommodating the Jahn-Teller distortion criterion (slightly higher CFSE) on the M_1 site and the size criterion on the M_2 site (Burns, 1975a; Burns, 1975b; Li et al., 1995). Thus, olivine will preferentially incorporate the isotopically light Cr, which is in agreement with ionic modelling predicting olivine to be lighter than spinel and pyroxene when in equilibrium (Shen et al., 2018) (Figure 2.9a).
Similarly, olivine preferentially incorporates Fe^{2+} (0.76 Å) over Fe^{3+} (0.64 Å) with a slight preference of Fe^{2+} for the olivine M_2 site (Burns, 1970). The preferential incorporation of the isotopically light Fe^{2+} into olivine is in agreement with ionic modelling (Macris et al., 2015; Young et al., 2015) as well as a lighter Fe isotopic composition of olivine separates compared to their respective komatiitic whole-rocks (Dauphas et al., 2010; Hibbert et al., 2012) or compared to other mantle minerals such as spinel, garnet and pyroxene in peridotitic xenoliths (Williams et al., 2005). However, it has been shown that also Mg-Fe diffusion processes based on compositional gradients between olivine and coexisting melt can drive $\delta^{56/54}$Fe in olivine towards lighter Fe isotope compositions compared to the corresponding whole rock (Dauphas et al., 2010; Teng et al., 2011).
In summary, crystal field theory and ionic modelling (Macris et al., 2015; Shen et al., 2018; Young et al., 2015) predict fractional crystallization of olivine to drive the residual melt towards both higher $\delta^{53/52}$Cr and higher $\delta^{56/54}$Fe values (see Figure 2.9a).
Cr-Spinel: Cr-spinel, with the general formula $A^{2+}B_2^{3+}O_4$, exhibits a normal spinel structure and therefore offers two octahedral sites (B-site) generally occupied by trivalent ions and one tetrahedral site (A-site) generally occupied by divalent ions. Due to its large octahedral CFSE Cr^{3+} is incorporated into the octahedral B site, while Cr^{2+} does not fit into the tetrahedral A site (Burns, 1975a) leading to the crystallization of isotopically heavy Cr-spinel. Thus, fractional crystallization of Cr-spinel is expected to lead to the removal of heavy Cr isotopes driving the residual melt towards lower $\delta^{53/52}$Cr values (Figure 2.9a). This is in agreement with studies on lunar mare and ocean islands basalts (Bonnand et al., 2020; Bonnand et al., 2016; Shen et al., 2020) as well as ab initio (Moynier et al., 2011) and ionic modeling (Shen et al., 2018). This observation, however, is in disagreement with the study of Jerram et al. (2020), who did not find a difference in $\delta^{53/52}$Cr values between chromite separates and their host komatiites.

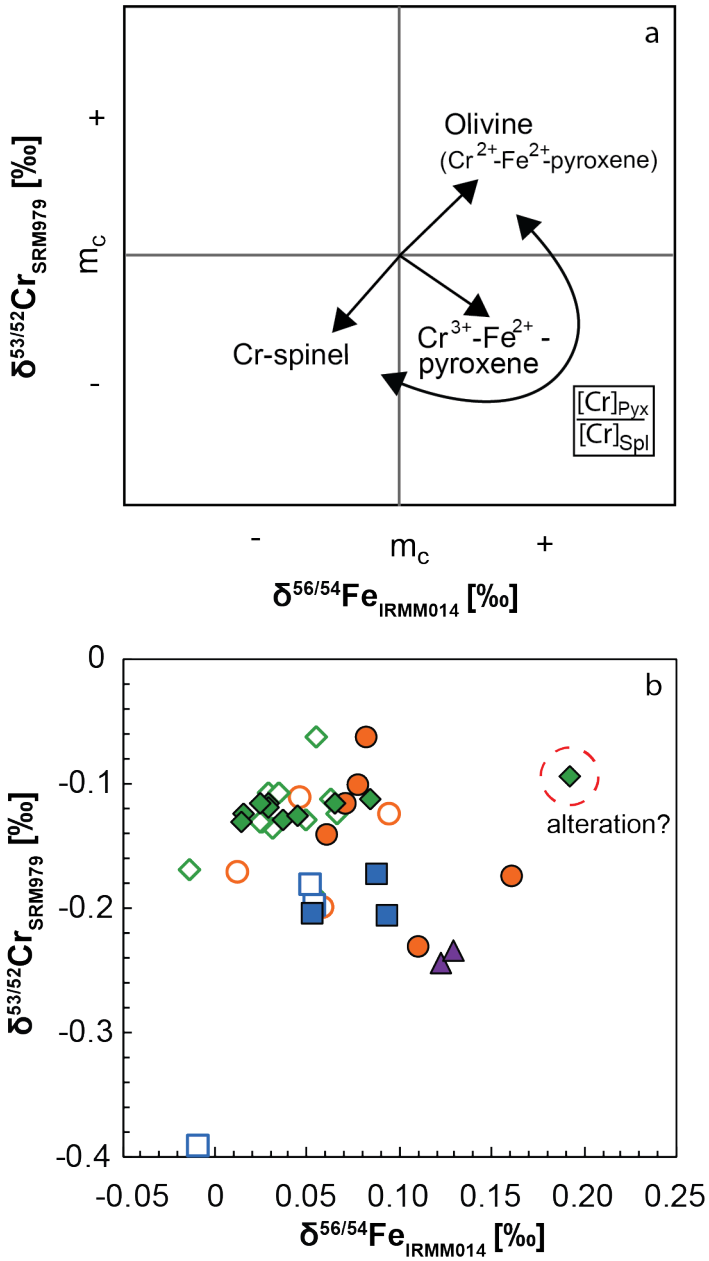

Figure 2.9: Chromium isotope compositions ($\delta^{53/52}$Cr) vs. Fe isotope compositions ($\delta^{56/54}$Fe). **a)** Expected change in Fe and Cr isotope compositions by different fractionating phases from a melt composition (m_c) is indicated by arrows. Major controlling phases are given next to the arrows. See text for further discussion. **b)** $\delta^{53/52}$Cr vs. $\delta^{56/54}$Fe for the BaGB and BeGB komatiite-tholeiite suites. Symbols are as used in Figure 2.2.

The structure of Cr-spinel implies that Fe^{2+} is tetrahedrally coordinated despite its usual preference for octahedral crystal lattice sites. An experimental study by Sossi and O'Neill (2017) showed that the lower coordination of Fe^{2+} in Cr-spinel leads to the enrichment of the heavy Fe isotopes in Cr-spinel despite incorporating the reduced Fe species, which is in agreement with ionic modelling by Macris et al. (2015). The incorporation of Fe^{3+} would even enhance the effect of removing isotopically heavy Fe from the melt during Cr-spinel crystallization. These observations are consistent with, on average, 0.09 ‰ heavier $\delta^{56/54}$Fe of spinel separates compared to associated komatiitic whole-rock samples and olivine separates (Hibbert et al., 2012)

as well as on average heavier $\delta^{56/54}$Fe compositions in spinel compared to whole-rock Fe isotopic compositions of peridotites (Williams et al., 2005). Additionally, picrites (high-Mg lavas) from Baffin Island show decreasing $\delta^{56/54}$Fe with magmatic differentiation during combined fractionation of Cr-spinel and olivine, thus supporting the postulation that Cr-spinel rather incorporates heavy Fe leaving behind an isotopically lighter melt (McCoy-West et al., 2018). The removal of heavy Fe and Cr isotopes during the crystallization of Cr-spinel would thus lead to a decrease in $\delta^{53/52}$Cr and $\delta^{56/54}$Fe values in the residual melt (Figure 2.9a).

Pyroxene: Pyroxene with the general formula $M_1^{2+,(3+)}M_2^{2+,(1+)}Si_2O_6$ offers, similarly to olivine, two energetically different M-sites, with $M_1 < M_2$. M-sites are usually occupied by one divalent ion each or one monovalent ion (M_2) and one trivalent ion (M_1). Additionally, the M_1 sites are octahedrally coordinated, while the M_2 sites are octahedrally to hexahedrally coordinated and considerably distorted (Angel et al., 1989; Burns, 1970). The distorted M_2 site thus offers Cr^{2+} to be incorporated into pyroxene, while the smaller Cr^{3+} ion preferentially partitions into the smaller and more regular octahedrally coordinated M_1 crystal lattice site. The partitioning of Cr^{3+} into pyroxene, however, must be accompanied by coupled substitutions to balance charges. Experimental studies showed that substantial amounts of Cr^{2+} can be incorporated into pyroxene under reducing conditions (Angel et al., 1989; Li et al., 1995), which is further corroborated by ionic modelling predicting inter-mineral equilibrium fractionation, with pyroxene having lighter Cr isotopic composition than spinel (Shen et al., 2018). However, no Cr^{2+} was detected by X-ray adsorption near-edge structure (XANES) spectroscopy in pyroxenes from mantle xenoliths (Shen et al., 2018) as well as lunar and martian basalts (Karner et al., 2007; Sutton et al., 1993). As already noted by Berry et al. (2006) the absence of Cr^{2+} can be the result of the electron exchange reaction $Fe^{3+} + Cr^{2+} = Fe^{2+} + Cr^{3+}$ due to the presence of Fe^{3+} in basaltic melts during cooling from mantle temperatures to their equilibration temperatures. Pyroxenes equilibrated under more reducing conditions than the terrestrial mantle, i.e. iron-wuestite (IW) $\pm$ 1 log units, showed increasing D_{Cr} (pyroxene/melt) with increasing fO_2, which was attributed to a higher compatibility of Cr^{3+} relative to Cr^{2+} in pyroxene. Additionally, D_{Cr} seems to be dependent not only on fO_2, but also on mineral composition with Cr being more compatible in high-Ca pyroxene (augite) compared to low-Ca pyroxenes (pigeonite), which was attributed to the higher availability of elements needed for coupled substitutions (e.g. Na or Al) (Karner et al., 2007; Papike et al., 2016). Pyroxene compositions in komatiites are usually regarded as relatively Al-rich (Cameron and Papike, 1981; Nisbet et al., 1977), which in turn could indicate the importance for the coupled substitutions of the $^{M1}Cr^{3+}$-$^{4}Al^{3+}$ pair in komatiitic pyroxenes, which is known to be a common substitution couple in pyroxene at terrestrial mantle conditions (FMQ $\pm$ 1 log unit) (Karner et al., 2007; Papike et al., 2005). Hence, the fractionation of Cr^{3+}-bearing pyroxene might be more probable and would thus leave a lighter residual melt (Figure 2.9a).

Both M-sites in pyroxene offer Fe^{2+} to acquire octahedral CFSE, but the energy gain is larger for the distorted M_2 site (Burns, 1970). In Ca-pyroxene the majority of M_2 sites is occupied by the larger Ca2+ ion, whereas Fe^{2+} would be incorporated into the smaller and octahedral M_1 site (Macris et al., 2015). Fe^{3+} acquires zero octahedral CFSE in both M-sites in pyroxene, therefore probably preferring the smaller M_1 site (size criterion). However, due to the overall low energy acquirement of

Fe^{3+} during partitioning into solid minerals (Orgel, 1966), Fe^{3+} is usually regarded as incompatible until magnetite becomes saturated when higher SiO_2 contents are reached. Additionally, as the silicate melt offers both octahedral and tetrahedral sites, the partitioning of Fe^{2+} into the octahedrally to hexahedrally coordinated M_1 and M_2 pyroxene sites suggest the preferential incorporation of the isotopically light Fe into pyroxene relative to the melt (Figure 2.9a). This is in agreement with ionic modelling predicting Fe^{2+}-bearing pyroxenes to be similar in $\delta^{56/54}$Fe compared to olivine (Macris et al., 2015).

2.5.3.3 Observed trends – mineral control on Cr and Fe isotope compositions

The large MgO variation from ∼34 to ∼4 wt. % of the BaGB and BeGB sample suites gives the opportunity to investigate Cr and Fe isotopic fractionation during magmatic differentiation. MgO variation diagrams (Figure 2.3) illustrate a changing fractional assemblage from only olivine (fractionation and accumulation) in samples with MgO >20 wt. % to the combined crystallization of olivine, Cr-bearing spinel, pyroxene, and plagioclase in samples with MgO <20 wt. % (Section 2.5.3.1), seemingly correlating with shifts in Cr isotopic composition (Figure 2.5).
Overall, the BaGB komatiite-tholeiite suite shows increasing $\delta^{56/54}$Fe and decreasing $\delta^{53/52}$Cr with indices of magmatic differentiation (Figures 2.5 and 2.9). The BeGB komatiite-tholeiite suite is characterized by a larger scatter in $\delta^{56/54}$Fe and $\delta^{53/52}$Cr values compared to those of the BaGB, with $\delta^{56/54}$Fe values not clearly showing any trend while the $\delta^{53/52}$Cr values also decrease with ongoing magmatic differentiation (Figure 2.5).
In detail, during fractionation and accumulation of olivine BaGB komatiites show invariant $\delta^{53/52}$Cr (Figure 2.5a-d) although the removal of isotopically light Cr^{2+}-bearing olivine would predict the $\delta^{53/52}$Cr of the residual melt to increase (see above; Jerram et al. 2020). However, even though olivine in komatiitic melts can contain up to 0.2 wt. % Cr (Nisbet et al., 1987; Puchtel et al., 2013; Renner et al., 1994), the partition coefficient D_{Cr} between olivine and melt is ≤ 1 and the crystallization of olivine leads to a small relative enrichment of Cr in the residual melt as indicated by the slightly negative trend of Cr with MgO above 20 wt. % MgO (Figure 2.3b). The constant $\delta^{53/52}$Cr above 20 wt. % MgO shows that olivine fractionation or accumulation for the BaGB suites of rocks has no effect on the $\delta^{53/52}$Cr values of the residual melt (Figure 2.5b). Belingwe komatiites (MgO >20 wt. %) display more variable $\delta^{53/52}$Cr and do not show such clear trends in $\delta^{53/52}$Cr vs. MgO, Al_2O_3, Cr and Ni space (Figure 2.5). We attribute this to the fact that BeGB komatiites do not represent one continuous sequence and thus have possibly different parental melt compositions. However, major element systematics indicate that the same phases as observed for the Barberton suite are actively controlling the whole rock compositions of Belingwe samples, namely olivine followed by olivine + Cr-bearing spinel + pyroxene (Figure 2.3).
There is a general increase in $\delta^{56/54}$Fe values from -0.014 to +0.091 ‰ with decreasing MgO, Ni and Cr and increasing Al_2O_3 of the BaGB and BeGB komatiites being consistent with fractionation and accumulation of isotopically light Fe^{2+}-bearing olivine and studies on mantle peridotites and komatiites from Gorgona Island (Colombia, 89 Ma) and Vetreny (Baltic Shield, 2.4 Ga) (Figure 2.5e-h; Hibbert et al., 2012; Weyer and Ionov, 2007; Williams et al., 2004; Williams et al., 2005). As

such, olivine fractionation or accumulation influences the $Fe^{2+}/\Sigma Fe$ ratio but seems not to significantly change the $Cr^{2+}/\Sigma Cr$ ratio of the residual melt, thus driving it towards higher $\delta^{56/54}$Fe values while not influencing its $\delta^{53/52}$Cr signature (Figure 2.9b).

A change of the fractional assemblage can be inferred from changes in slope in MgO variation diagrams with Al_2O_3, CaO, Cr, Ni at MgO <20 wt. % (Figure 2.3, Section 2.5.3.1). The Cr isotopic compositions of BaGB and BeGB komatiitic basalts, high-Mg tholeiites and basaltic andesites appear to correlate with these changes in major and trace element variations as the $\delta^{53/52}$Cr compositions shift to lower values at MgO concentrations <20 wt. % (Figure 2.5). Ab initio calculations presented by Moynier et al. (2011) show that at temperatures of 1,200° C equilibrium isotope fractionation $\varepsilon^{53}Cr_{(magnesiochromite-olivine)}$ between Cr^{3+}-bearing chromite and olivine are 0.18 ‰ for Cr^{2+} occupying the M_1 site and 0.14 ‰ for Cr^{2+} occupying the M_2 site in olivine. The size and mode of these calculated stable Cr isotope effects are consistent with our data, which also imply that Cr^{3+}-bearing spinel is isotopically heavier than olivine and whole rock komatiitic basalts are up to 0.12 ‰ lower in $\delta^{53/52}$Cr than komatiites. Although Cr-bearing spinel is an accessory mineral within komatiitic suites, it is the most important Cr carrier with 30 to 54 wt. % of Cr_2O_3 (Jerram et al., 2020; Nisbet et al., 1977). Therefore, even small amounts of Cr-bearing spinel crystallization can affect the $\delta^{53/52}$Cr signature of the residual melt. Furthermore, magmatic differentiation in the BaGB and BeGB komatiitic-tholeiite suites is additionally governed by pyroxene fractionation or accumulation (Figure 2.3a-c, e), which can contain up to 1.15 wt. % Cr (Renner et al., 1994) and on average ∼0.4 wt. % Cr for Belingwe and Barberton pyroxenes (Bickle et al., 1975; Nisbet et al., 1987; Nisbet et al., 1977; Parman et al., 1997; Parman et al., 2003; Renner et al., 1994; Shimizu et al., 2005). The incorporation of isotopically light Cr^{2+} into pyroxene would lead to a heavier Cr isotopic signature in the residual magma, therefore competing with the effects of Cr-bearing spinel crystallization. However, based on Al-rich pyroxene compositions in komatiites the incorporation of Cr^{3+} might be more favorable to balance charges. Moreover, as mentioned above, Cr^{3+} exhibits a large preference for octahedral sites (high octahedral CFSE) and discriminates against tetrahedral sites (low tetrahedral CFSE) resulting in a high octahedral site preference energy (Orgel, 1966). The discrepancy for Cr^{2+} to enter tetrahedral or octahedral sites is much lower, resulting in an overall lower octahedral site preference energy. As a silicate melt offers octahedral and tetrahedral sites, but the availability of octahedral sites decreases with increasing melt evolution, Cr^{3+} might partition more readily into the octahedral M_1 site in pyroxene with increasing melt evolution. The overall decrease in $\delta^{53/52}$Cr with decreasing MgO contents (Figure 2.5a) is in accordance with recent observations from OIB, which also show a decrease in $\delta^{53/52}$Cr during combined olivine, Cr-bearing spinel and pyroxene fractional crystallization (Bonnand et al. 2020, Shen et al. 2020). The accumulation of Cr^{3+}-bearing pyroxene in some high-Mg komatiitic basalts could however modify the $\delta^{53/52}$Cr evolution towards higher values. Figure 2.9 shows that Cr-bearing spinel and Cr^{3+}-bearing pyroxene fractionation dominate over olivine and Cr^{2+}-bearing pyroxene regarding the Cr-budget.

Barberton and Belingwe samples with less than 20 wt. % MgO show increasing $\delta^{56/54}$Fe with decreasing MgO concentrations, suggesting that combined Cr-bearing spinel and pyroxene fractionation leads toward overall heavier $\delta^{56/54}$Fe in the resid-

ual magma (Figure 2.5e-h). This is supported by the statistical difference in $\delta^{56/54}$Fe between the two groups evaluated by a two-tailed Student t-test. As the sole crystallization of Cr-bearing spinel (FeO = ∼20 wt. %; Nisbet et al. (1977)) would result towards lighter $\delta^{56/54}$Fe in the residual magma, pyroxene (Fe = ∼7 wt. %; (Bickle et al., 1975; Nisbet et al., 1987; Nisbet et al., 1977; Parman et al., 1997; Parman et al., 2003; Renner et al., 1994; Shimizu et al., 2005)) is largely incorporating the light Fe^{2+} isotopes and dominates the Fe isotope composition overall. Figure 2.9 shows that with the combination of $\delta^{53/52}$Cr and $\delta^{56/54}$Fe most samples <20 wt. % MgO lie along a trend of Cr^{3+}-Fe^{2+}-bearing pyroxene fractionation. This, firstly, demonstrates the combined crystallization of Cr-bearing spinel and pyroxene, but also signals the predominance of Cr-bearing spinel (Cr_2O_3 = 30 to 50 wt. %) compared to pyroxene (Cr_2O_3 = ∼0.4 wt. %) on the Cr budget leading towards overall lighter $\delta^{53/52}$Cr during melt evolution and the dominance of pyroxene on the Fe isotope budget leading towards overall heavier $\delta^{56/54}$Fe during melt evolution.

2.5.4 The Cr isotope composition of the Bulk Silicate Earth

Knowledge of bulk Earth's (BE) and bulk silicate Earth's (BSE) Cr isotopic compositions are fundamental for understanding potential fractionation processes for Cr isotopes between and within terrestrial igneous reservoirs. Schoenberg et al. (2008) were the first to show that the variation in Cr isotopic compositions of ultramafic (including cumulates) to felsic igneous rocks with $\delta^{53/52}$Cr = -0.124 ± 0.101 ‰ is very limited. The intention of these authors to determine the Cr isotopic range of igneous rocks was (1) to assess potential Cr isotopic fractionation during intra-crustal differentiation processes and (2) to provide a weathering background $\delta^{53/52}$Cr signature for low-temperature Cr redox studies (Babechuk et al., 2017; Babechuk et al., 2019; Frei et al., 2009; Wille et al., 2018). Schoenberg et al. (2008) therefore dubbed this range in $\delta^{53/52}$Cr as the 'igneous inventory' rather than the BSE value.
Komatiites with their extremely high melting temperatures of >1500° C compared to ∼1300-1400° C for modern mid-ocean ridge basalts (Lee et al., 2009) are likely to be an excellent proxy for the Cr isotope composition of the BSE, because equilibrium isotope fractionation decreases with increasing temperature (α is directly proportional to $1/T^2$). Furthermore, the high degrees of partial mantle melting of up to 35 % for komatiitic melts significantly diminishes the difference in $\delta^{53/52}$Cr values between mantle source and melt. Following this logic, recent studies have turned to komatiites (Jerram et al., 2020) or a combination of komatiites and peridotites (Sossi et al., 2018) to examine the $\delta^{53/52}$Cr signature of the BSE and compare the signature to the igneous inventory reported by Schoenberg et al. (2008) and other estimates of the BSE derived from mantle peridotites (Xia et al., 2017). The existing BSE $\delta^{53/52}$Cr estimates based on the Cr isotopic composition of komatiites are at -0.11 ± 0.06 ‰ (Sossi et al., 2018) and -0.12 ± 0.04 ‰ (Jerram et al., 2020).
Here we follow suit in further assessing the BSE $\delta^{53/52}$Cr value using the komatiite data reported in this work, which includes the use of a pooled Cr stable isotopic measurement approach to each sample (n=5), which reduces analytical scatter (Section 2.3.2.2). The average $\delta^{53/52}$Cr value for all 21 komatiite samples from the BaGB and BeGB suites from this study is -0.122 ± 0.050 ‰ (2 SD). The two suites of samples, with MgO concentrations ranging from 19.08-34.33 wt. %, represent compositions only controlled by the fractionation and accumulation of olivine, which

observations from this study suggest does not induce any Cr isotopic fractionation (Section 2.5.3.3). Although the Belingwe and Barberton komatiite-tholeiite suites show similar Cr isotope systematics during differentiation, the Belingwe komatiites display a significantly larger overall scatter in $\delta^{53/52}$Cr values. The reason for this is unclear, but it is noted that the BeGB sample suite is not derived from one parental melt and $\delta^{53/52}$Cr variations of komatiites might reflect small differences in initial source compositions. This value agrees well with the previously reported BSE estimate of Jerram et al. (2020) with $\delta^{53/52}$Cr = -0.12 ± 0.04 ‰, which was calculated using the weighted averages of komatiite data from five different localities, three of which reported by these authors themselves and two more published by (Sossi et al., 2018). Combining all single komatiite stable Cr isotopic data reported in our study with previously reported ones (Jerram et al., 2020; Sossi et al., 2018) gives a composite komatiite-based BSE $\delta^{53/52}$Cr value of -0.12 ± 0.06 ‰ (2 SD; n=52). This value agrees well with previously published ones (Jerram et al., 2020; Sossi et al., 2018) and indicates the robustness of estimating the BSE $\delta^{53/52}$Cr value using komatiites.

2.6 Conclusions

The impact of large degrees of magmatic differentiation (MgO = ∼4 to ∼34 wt. %) on stable Cr and Fe isotopic compositions has been investigated in Archean komatiites-tholeiite suites from the Barberton Greenstone Belt, South Africa and Eswatini, and the Belingwe Greenstone Belt, Zimbabwe. In total, 21 samples from the Barberton Greenstone Belt and 21 samples from the Belingwe Greenstone Belt, including komatiites, komatiitic basalts, high Mg-tholeiites and basaltic andesites, were analyzed for their major and trace element concentrations as well as stable Cr and Fe isotopic compositions.
From major and trace element data combined with stable Cr and Fe isotopic systematics we conclude that:

- Serpentinization does not seem to affect the stable Cr and Fe isotopic compositions of BaGB and BeGB komatiites, which display the highest influence from this alteration process (i.e. highest LOI) of all BaGB and BeGB rocks.
- Significant Fe and Cr isotopic variations are observed for the BaGB and BeGB komatiite tholeiites whole-rock suite. $\delta^{53/52}$Cr and $\delta^{56/54}$Fe vary systematically with MgO, Al_2O_3, Cr and Ni contents, which can be linked to magmatic processes, such as crystal fractionation being responsible for these variations observed in BaGB and BeGB komatiite-basalt suites.
- Significant amounts of Cr^{2+} (up to 2000 $\mu g\, g^{-1}$) can be incorporated into the olivine crystal structure, and thus in theory olivine crystallization depletes the residual melt in light Cr isotopes. Increasing Cr concentrations with decreasing MgO contents (up to 20 wt. %) for the BaGB and BeGB komatiites, however, indicate that Cr still behaves incompatibly during fractional crystallization of olivine. Furthermore, olivine fractionation does not influence the stable Cr isotopic composition of the melt, as indicated by the constant $\delta^{53/52}$Cr

signatures of komatiites. Cr-bearing spinel and pyroxene crystallization, on the other hand, preferentially remove heavy Cr isotopes from the melt, leading to the observed decrease of $\delta^{53/52}$Cr values of the residual liquid with ongoing melt differentiation.

- The combination of stable Cr and Fe isotope analyses may allow for the distinction between olivine, Cr-bearing spinel and pyroxene fractionations during melt differentiation. Further testing of these coupled trajectories in various magmatic systems will help to improve our understanding of the Cr (and possibly Fe) isotopic fractionation during magmatic differentiation.
- Studies investigating low-temperature redox of Earth-surface reservoirs should use the igneous inventory of -0.124 ± 0.101 ‰ in $\delta^{53/52}$Cr (Schoenberg et al., 2008) as a baseline, because this compilation encloses the full range of potential magmatic bedrock compositions during weathering processes. For high-temperature geo- and cosmochemical studies we suggest to use the BSE $\delta^{53/52}$Cr value of 0.12 ± 0.04 ‰ reported by Jerram et al. (2020), which is based on the weighted averages of Cr isotopic data from different komatiite localities. Alternatively, one may use the more conservative BSE $\delta^{53/52}$Cr estimate of -0.12 ± 0.06 ‰, reflecting the mean of all single komatiite stable Cr isotopic data published so far (Jerram et al. (2020); Sossi et al. (2018); this study).

Acknowledgements

LJW acknowledges financial support from the German Research Council (DFG) project SCHO1071/9-1 to RS. ICK acknowledges financial support from the DFG project SCHO1071/7-1 under priority program SPP-1833 “Building a habitable Earth”. AH acknowledges the support of the Department of Geology, University Zimbabwe. Drilling in the Barberton Greenstone Belt was supported by the International Continental Scientific Drilling Program (ICDP). We thank Elmar Reitter, Simone Schafflick and Bernd Steinhilber for technical and analytical support. Three anonymous reviewers are thanked for constructive comments, which greatly helped improving the quality of this work. Thomas Pettke (guest editor) and Balz Kamber (handling editor) are thanked for editorial handling and helpful comments.

References

Albut, G., Babechuk, M.G., Kleinhanns, I.C., Benger, M., Beukes, N.J., Steinhilber, B., Smith, A.J.B., Kruger, S.J., Schoenberg, R., 2018. Modern rather than Mesoarchaean oxidative weathering responsible for the heavy stable Cr isotopic signatures of the 2.95 Ga old Ijzermijn iron formation (South Africa). Geochimica et Cosmochimica Acta, 228, 157-189.

Angel, R.J., Gasparik, T., Finger, L.W., 1989. Crystal structure of a Cr-2+-bearing pyroxene. American Mineralogist, 74 (5-6), 599-603.

Armstrong, R.A., Compston, W., De Wit, M.J., Williams, I.S., 1990. The stratigraphy of the 3.5-3.2 Ga Barberton Greenstone Belt revisited: a single zircon ion

microprobe study. Earth and Planetary Science Letters, 101 (1), 90-106.

Arndt, N.T., Lesher, C.M., Barnes, S.J., 2008. Komatiite. Cambridge University Press, Cambridge.

Arndt, N.T., 1986. Differentiation of komatiite flows. Journal of Petrology, 27 (2), 279-301.

Arndt, N.T., Fleet, M.E., 1979. Stable and metastable pyroxene crystallization in layered komatiite lava flows. American Mineralogist, 64 (7-8), 856-864.

Arndt, N.T., Teixeira, N.A., White, W.M., 1989. Bizarre geochemistry of komatiites from the Crixas greenstone belt, Brazil. Contributions to Mineralogy and Petrology, 101 (2), 187-197.

Asafov, E.V., Sobolev, A.V., Gurenko, A.A., Arndt, N.T., Batanova, V.G., Portnyagin, M.V., Garbe-Schonberg, D., Krasheninnikov, S.P., 2018. Belingwe komatiites (2.7 Ga) originate from a plume with moderate water content, as inferred from inclusions in olivine. Chemical Geology, 478, 39-59.

Babechuk, M.G., Kamber, B.S., Greig, A., Canil, D., Kodolányi, J., 2010. The behaviour of tungsten during mantle melting revisited with implications for planetary differentiation time scales. Geochimica et Cosmochimica Acta, 74 (4), 1448-1470.

Babechuk, M.G., Kleinhanns, I.C., Reitter, E., Schoenberg, R., 2018. Kinetic stable Cr isotopic fractionation between aqueous Cr(III)-Cl-H_2O complexes at 25° C: Implications for Cr(III) mobility and isotopic variations in modern and ancient natural systems. Geochimica et Cosmochimica Acta, 222, 383-405.

Babechuk, M.G., Kleinhanns, I.C., Schoenberg, R., 2017. Chromium geochemistry of the ca. 1.85 Ga Flin Flon paleosol. Geobiology, 15 (1), 30-50.

Babechuk, M.G., Weimar, N.E., Kleinhanns, I.C., Eroglu, S., Swanner, E.D., Kenny, G.G., Kamber, B.S., Schoenberg, R., 2019. Pervasively anoxic surface conditions at the onset of the Great Oxidation Event: New multi-proxy constraints from the Cooper Lake paleosol. Precambrian Research, 323, 126-163.

Barnes, S.J., 1998. Chromite in komatiites, 1. Magmatic controls on crystallization and composition. Journal of Petrology, 39 (10), 1689-1720.

Barrat, J.-A., Rouxel, O., Wang, K., Moynier, F., Yamaguchi, A., Bischoff, A., Langlade, J., 2015. Early stages of core segregation recorded by Fe isotopes in an asteroidal mantle. Earth and Planetary Science Letters, 419, 93-100.

Berry, A.J., O'Neill, H.St.C., Scott, D.R., Foran, G.J., Shelley, J.M.G., 2006. The effect of composition on Cr^{2+}/Cr^{3+} in silicate melts. American Mineralogist, 91 (11-12), 1901-1908.

Berry, A.J., O'Neill, H.S.C., 2004. A XANES determination of the oxidation state of chromium in silicate glasses. American Mineralogist, 89 (5-6), 790-798.

Bickle, M.J., 1993. Plume origin for komatiites. Nature, 365 (6445), 390-391.

Bickle, M.J., Martin, A., Nisbet, E.G., 1975. Basaltic and peridotitic komatiites and stromatolites above a basal unconformity in the Belingwe greenstone belt, Rhodesia. Earth and Planetary Science Letters, 27, 155-162.

Blenkinsop, T.G., Fedo, C.M., Bickle, M.J., Eriksson, K.A., Martin, A., Nisbet, E.G., Wilson, J.F., 1993. Ensialic origin for the Ngezi Group, belingwe Greenstone belt, Zimbabwe. Geology, 21 (12), 1135-1138.

Blichert-Toft, J., Arndt, N.T., Wilson, A., Coetzee, G., 2015. Hf and Nd isotope systematics of early Archean komatiites from surface sampling and ICDP drilling in the Barberton Greenstone Belt, South Africa. American Mineralogist, 100 (11-12), 2396-2411.

Bolhar, R., 2001. Archaean mafic magmatism and crust formation in the eastern Pilbara craton (Western Australia) and Belingwe greenstone belt (Zimbabwe). Docotor of Philosophy Thesis, University Melbourne, Melbourne.

Bolhar, R., Woodhead, J.D., Hergt, J.M., 2003. Continental setting inferred for emplacement of the 2.9-2.7 Ga Belingwe Greenstone Belt, Zimbabwe. Geology, 31 (4), 295-298.

Bonnand, P., Doucelance, R., Boyet, M., Bachèlery, P., Bosq, C., Auclair, D., Schiano, P., 2020. The influence of igneous processes on the chromium isotopic compositions of Ocean Island basalts. Earth and Planetary Science Letters, 532, 116028.

Bonnand, P., Parkinson, I.J., Anand, M., 2016. Mass dependent fractionation of stable chromium isotopes in mare basalts: Implications for the formation and the differentiation of the Moon. Geochimica et Cosmochimica Acta, 175, 208-221.

Brake, C., 1996. Tholeiitic magmatism in the Belingwe greenstone belt, Zimbabwe.

Burns, R.G., 1970. Site preference of transition metal ions in silicate crystal structures. Chemical Geology, 5 (4), 275-283.

Burns, R.G., 1975a. Crystal-field effects in chromium and its partitioning in the mantle Geochimica et Cosmochimica Acta, 39 (6-7), 857-864.

Burns, R.G., 1975b. On the occurrence and stability of divalent chromium in olivines included in diamonds. Contributions to Mineralogy and Petrology, 51 (3), 213-221.

Cameron, M., Papike, J.J., 1981. Structural and chemical variations in pyroxenes. American Mineralogist, 66 (1-2), 1-50.

Campbell, I.H., Griffiths, R.W., Hill, R.I., 1989. Melting in an Archean Mantle Plume - Heads its basalts, tails its komatiites. Nature, 339 (6227), 697-699.

Canil, D., 1997. Vanadium partitioning and the oxidation state of Archaean komatiite magmas. Nature, 389 (6653), 842-845.

Chauvel, C., Dupre, B., Arndt, N.T., 1993. Pb and Nd isotopic correlation in Belingwe komatiites and basalts, in: Bickle, M.J., Nisbet, E.G. (Eds.), The Geology of the Belingwe Greenstone Belt, Zimbabwe: Geological Society of Zimbabwe Special Publication pp. 167-174.

Chavagnac, V., 2004. A geochemical and Nd isotopic study of Barberton komatiites (South Africa): implication for the Archean mantle. Lithos, 75 (3-4), 253-281.

Chen, S., Niu, Y.L., Guo, P.Y., Gong, H.M., Sun, P., Xue, Q.Q., Duan, M., Wang, X.H., 2019. Iron isotope fractionation during mid-ocean ridge basalt (MORB) evolu-

tion: Evidence from lavas on the East Pacific Rise at 10° 30' N and its implications. Geochimica et Cosmochimica Acta, 267, 227-239.

Cloete, M., 1999. Aspects of volcanism and metamorphism of the Onverwacht group lavas in the South-Western portion of the Barberton greenstone belt. Memoir Geological Survey of South Africa, 84. Council for Geoscience, Pretoria.

Coetzee, G., 2014. Petrology and geochemistry of the Tjakastad (Barberton) ICDP cores. University of the Witwatersrand, Faculty of Science, School of Geology.

Compston, W., Oversby, V.M., 1969. Lead isotopic analysis uysing a double spike. Journal of Geophysical Research, 74 (17), 4338-4348.

Craddock, P.R., Dauphas, N., 2011. Iron isotopic compositions of geological reference materials and chondrites. Geostandards and Geoanalytical Research, 35 (1), 101-123.

D'Arcy, J., Babechuk, M.G., Døssing, L.N., Gaucher, C., Frei, R., 2016. Processes controlling the chromium isotopic composition of river water: constraints from basaltic river catchments. Geochimica et Cosmochimica Acta, 186, 296-315.

Dann, J.C., 2000. The 3.5 Ga Komati Formation, Barberton greenstone belt, South Africa, part I: new maps and magmatic architecture. South African Journal of Geology, 103 (1), 47-68.

Dann, J.C., 2001. Vesicular komatiites, 3.5-Ga Komati Formation, Barberton Greenstone Belt, South Africa: inflation of submarine lavas and origin of spinifex zones. Bulletin of Volcanology, 63 (7), 462-481.

Dauphas, N., Craddock, P.R., Asimow, P.D., Bennett, V.C., Nutman, A.P., Ohnenstetter, D., 2009. Iron isotopes may reveal the redox conditions of mantle melting from Archean to Present. Earth and Planetary Science Letters, 288 (1-2), 255-267.

Dauphas, N., John, S.G., Rouxel, O., 2017. Iron Isotope Systematics, in: Teng, F.-Z., Watkins, J., Dauphas, N. (Eds.), Non-Traditional Stable Isotopes. Reviews in Mineralogy & Geochemistry, pp. 415-510.

Dauphas, N., Teng, F.-Z., Arndt, N.T., 2010. Magnesium and iron isotopes in 2.7 Ga Alexo komatiites: Mantle signatures, no evidence for Soret diffusion, and identification of diffusive transport in zoned olivine. Geochimica et Cosmochimica Acta, 74 (11), 3274-3291.

Delano, J.W., 2001. Redox history of the Earth's interior since ∼3900 Ma: implications for prebiotic molecules. Origins of Life and Evolution of the Biosphere, 31 (4-5), 311-341.

Dirks, P.H.G.M., Jelsma, H.A., Hofmann, A., 1999. Continental extensional setting for the Archean Belingwe Greenstone Belt, Zimbabwe: Comment. Geology, 27 (7), 667-667.

Dostal, J., Mueller, W.U., 2013. Deciphering an Archean mantle plume: Abitibi greenstone belt, Canada. Gondwana Research, 23 (2), 493-505.

Eggins, S.M., Woodhead, J.D., Kinsley, L.P.J., Mortimer, G.E., Sylvester, P., McCulloch, M.T., Hergt, J.M., Handler, M.R., 1997. A simple method for the precise

determination of ≥ 40 trace elements in geological samples by ICPMS using enriched isotope internal standardisation. Chemical Geology, 134 (4), 311-326.

Eroglu, S., Schoenberg, R., Pascarelli, S., Beukes, N.J., Kleinhanns, I.C., Swanner, E.D., 2018. Open ocean vs. continentally-derived iron cycles along the Neoarchean Campbellrand-Malmani Carbonate platform, South Africa. American Journal of Science, 318 (4), 367-408.

Farkas, J., Chrastny, V., Novak, M., Cadkova, E., Pasava, J., Chakrabarti, R., Jacobsen, S.B., Ackerman, L., Bullen, T.D., 2013. Chromium isotope variations ($\delta^{53/52}$Cr) in mantle-derived sources and their weathering products: Implications for environmental studies and the evolution of $\delta^{53/52}$Cr in the Earth's mantle over geologic time. Geochimica et Cosmochimica Acta, 123, 74-92.

Frei, R., Gaucher, C., Poulton, S.W., Canfield, D.E., 2009. Fluctuations in Precambrian atmospheric oxygenation recorded by chromium isotopes. Nature, 461 (7261), 250-253.

Goldich, S.S., 1984. Determination of ferrous iron in silicate rocks. Chemical Geology, 42 (1-4), 343-347.

Green, D.H., Nicholls, I.A., Viljoen, M., Viljoen, R., 1975. Experimental demonstration of the existence of peridotitic liquids in earliest Archean magmatism. Geology, 3 (1), 11-14.

Hanson, B., Jones, J.H., 1998. The systematics of Cr^{3+} and Cr^{2+} partitioning between olivine and liquid in the presence of spinel. American Mineralogist, 83 (7-8), 669-684.

Herzberg, C., 1992. Depth and degree of melting of komatiites. Journal of Geophysical Research: Solid Earth, 97 (B4), 4521-4540.

Herzberg, C., Condie, K., Korenaga, J., 2010. Thermal history of the Earth and its petrological expression. Earth and Planetary Science Letters, 292 (1-2), 79-88.

Heubeck, C., Engelhardt, J., Byerly, G.R., Zeh, A., Sell, B., Luber, T., Lowe, D.R., 2013. Timing of deposition and deformation of the Moodies Group (Barberton Greenstone Belt, South Africa): Very-high-resolution of Archaean surface processes. Precambrian Research, 231, 236-262.

Heubeck, C., Lowe, D.R., 1994. Depositional and tectonic setting of the Archean Moodies Group, Barberton greenstone belt, South Africa. Precambrian Research, 68 (3-4), 257-290.

Hibbert, K.E.J., Williams, H.M., Kerr, A.C., Puchtel, I.S., 2012. Iron isotopes in ancient and modern komatiites: Evidence in support of an oxidised mantle from Archean to present. Earth and Planetary Science Letters, 321, 198-207.

Hofmann, A., 2005. The geochemistry of sedimentary rocks from the Fig Tree Group, Barberton greenstone belt: implications for tectonic, hydrothermal and surface processes during mid-Archaean times. Precambrian Research, 143 (1-4), 23-49.

Hofmann, A., Dirks, P.H.G.M., 2003. Continental setting inferred for emplacement of the 2.9–2.7 Ga Belingwe Greenstone Belt, Zimbabwe: Comment and Reply. Geology, 31 (1), 30-31.

Hofmann, A., Harris, C., 2008. Silica alteration zones in the Barberton greenstone belt: A window into subseafloor processes 3.5-3.3 Ga ago. Chemical Geology, 257 (3-4), 224-242.

Hofmann, A., Kusky, T.M., 2004. The Belingwe greenstone belt: ensialic or oceanic?, in: Kusky, T.M. (Ed.), Precambrian Ophiolites and Related Rocks. Elsevier, Amsterdam, pp. 487-537.

Huang, J., Hao, J., Huang, F., Sverjensky, D., 2019. Mobility of chromium in high temperature crustal and upper mantle fluids. Geochemical Perspectives Letters, 12, 1-6.

Hunter, M.A., Bickle, M.J., Nisbet, E.G., Martin, A., Chapman, H.J., 1998. Continental extensional setting for the Archean Belingwe Greenstone Belt, Zimbabwe. Geology, 26 (10), 883-886.

Jahn, B.-M., Gruau, G., Glikson, A.Y., 1982. Komatiites of the Onverwacht Group, S. Africa: REE geochemistry, Sm/Nd age and mantle evolution. Contributions to Mineralogy and Petrology, 80 (1), 25-40.

Jensen, L., 1976. A new cation plot for classifying subalkalic volcanic rocks, 66. Ministry of Natural Resources.

Jerram, M., Bonnand, P., Kerr, A.C., Nisbet, E.G., Puchtel, I.S., Halliday, A.N., 2020. The $\delta^{53}Cr$ isotope composition of komatiite flows and implications for the composition of the bulk silicate Earth. Chemical Geology, 119761.

Jochum, K.P., Arndt, N.T., Hofmann, A.W., 1991. Nb-Th-La in komatiites and basalts: constraints on komatiite petrogenesis and mantle evolution. Earth and Planetary Science Letters, 107 (2), 272-289.

Kamber, B.S., Greig, A., Collerson, K.D., 2005. A new estimate for the composition of weathered young upper continental crust from alluvial sediments, Queensland, Australia. Geochimica et Cosmochimica Acta, 69 (4), 1041-1058.

Kamo, S.L., Davis, D.W., 1994. Reassessment of Archean crustal development in the Barberton Mountain Land, South Africa, based on U-Pb dating. Tectonics, 13 (1), 167-192.

Kane, J.S., 2015. A Review of the IAG GeoPT™ and Certification Programmes, their Protocols, and the Differences between the Original and Potential Modifications to the Certification Protocol. Geostandards and Geoanalytical Research, 39 (4), 419-432.

Karner, J.M., Papike, J.J., Sutton, S.R., Shearer, C.K., McKay, G., Le, L., Burger, P.V., 2007. Valence state partitioning of Cr between pyroxene-melt: Effects of pyroxene and melt composition and direct determination of Cr valence states by XANES. Application to Martian basalt QUE 94201 composition. American Mineralogist, 92 (11-12), 2002-2005.

Klein-BenDavid, O., Pettke, T., Kessel, R., 2011. Chromium mobility in hydrous fluids at upper mantle conditions. Lithos, 125 (1-2), 122-130.

Kurzweil, F., Wille, M., Gantert, N., Beukes, N.J., Schoenberg, R., 2016. Manganese oxide shuttling in pre-GOE oceans–evidence from molybdenum and iron isotopes.

Earth and Planetary Science Letters, 452, 69-78.

Kusky, T.M. et al., 1994. Ensialic origin for the Ngezi Group, Belingwe greenstone belt, Zimbabwe: Comment and Reply. Geology, 22 (8), 766-768.

Lahaye, Y., Arndt, N.T., 1996. Alteration of a komatiite flow from Alexo, Ontario, Canada. Journal of Petrology, 37 (6), 1261-1284.

Lahaye, Y., Arndt, N.T., Byerly, G.R., Chauvel, C., Fourcade, S., Gruau, G., 1995. The influence of alteration on the trace-element and Nd isotopic compositions of komatiites. Chemical Geology, 126 (1), 43-64.

Lee, C.-T.A., Luffi, P., Plank, T., Dalton, H., Leeman, W.P., 2009. Constraints on the depths and temperatures of basaltic magma generation on Earth and other terrestrial planets using new thermobarometers for mafic magmas. Earth and Planetary Science Letters, 279 (1-2), 20-33.

Li, C.-F., Feng, L.-J., Wang, X.-C., Chu, Z.-Y., Guo, J.-H., Wilde, S.A., 2016. Precise measurement of Cr isotope ratios using a highly sensitive Nb^2O_5 emitter by thermal ionization mass spectrometry and an improved procedure for separating Cr from geological materials. Journal of Analytical Atomic Spectrometry, 31 (12), 2375-2383.

Li, J.P., O'Neill, H.St.C., Seifert, F., 1995. Subsolidus phase relations in the system MgO-SiO_2-Cr-O in equilibrium with metallic Cr, and their significance for the petrochemistry of chromium. Journal of Petrology, 36 (1), 107-132.

Lowe, D.R., 1994. Accretionary history of the Archean Barberton greenstone belt (3.55-3.22 Ga), southern Africa. Geology, 22 (12), 1099-1102.

Lowe, D.R., Byerly, G.R., 1999. Stratigraphy of the west-central part of the Barberton Greenstone Belt, South Africa, in: Lowe, D.R., Byerly, G.R. (Eds.), Geologic Evolution of the Barberton Greenstone Belt, South Africa. Geological Society of America Special Papers, 329, 1-36.

Lowe, D.R., Byerly, G.R., 2007. An overview of the geology of the Barberton Greenstone Belt and vicinity: implications for early crustal development, in: Van Kranendonk, M.J., Smithies, H., Bennett, V.C. (Eds.), Earth's oldest rocks. Elsevier, Amsterdam, pp. 481-526.

Macris, C.A., Manning, C.E., Young, E.D., 2015. Crystal chemical constraints on inter-mineral Fe isotope fractionation and implications for Fe isotope disequilibrium in San Carlos mantle xenoliths. Geochimica et Cosmochimica Acta, 154, 168-185.

Martin, A., 1978. The Geology of the Belingwe-Shabani Shist Belt. Rhodesia Geological Survey Bulletin, 83.

Martin, A., Nisbet, E.G., Bickle, M.J., Orpen, J.L., 1993. Rock units and stratigraphy of the Belingwe Greenstone Belt: the complexity of the tectonic setting, in: M.J. Bickle, A. Martin, E.G. Nisbet, J.L. Orpen (Eds.). The geology of the Belingwe Greenstone Belt, Zimbabwe: A study of the evolution of Archean continental crust. CRC Press, London, pp. 13-37.

Maxwell, J.A., 1968. Rock and mineral analysis.

McClain, C.N., Maher, K., 2016. Chromium fluxes and speciation in ultramafic catchments and global rivers. Chemical Geology, 426, 135-157.

McCoy-West, A.J., Fitton, J.G., Pons, M.L., Inglis, E.C., Williams, H.M., 2018. The Fe and Zn isotope composition of deep mantle source regions: Insights from Baffin Island picrites. Geochimica et Cosmochimica Acta, 238, 542-562.

Millet, M.-A., Baker, J.A., Payne, C.E., 2012. Ultra-precise stable Fe isotope measurements by high resolution multiple-collector inductively coupled plasma mass spectrometry with a ^{57}Fe–^{58}Fe double spike. Chemical Geology, 304, 18-25.

Moynier, F., Yin, Q.Z., Schauble, E.A., 2011. Isotopic Evidence of Cr Partitioning into Earth's Core. Science, 331 (6023), 1417-1420.

Murck, B.W., Campbell, I.H., 1986. The effects of temperature, oxygen fugacity and melt composition on the behaviour of chromium in basic and ultrabasic melts. Geochimica et Cosmochimica Acta, 50 (9), 1871-1887.

Nebel, O., Sossi, P.A., Benard, A., Wille, M., Vroon, P.Z., Arculus, R.J., 2015. Redox-variability and controls in subduction zones from an iron-isotope perspective. Earth and Planetary Science Letters, 432, 142-151.

Nesbitt, R.W., Sun, S.-S., Purvis, A.C., 1979. Komatiites: geochemistry and genesis. The Canadian Mineralogist, 17 (2), 165-186.

Nicklas, R.W., Puchtel, I.S., Ash, R.D., 2018. Redox state of the Archean mantle: Evidence from V partitioning in 3.5-2.4 Ga komatiites. Geochimica et Cosmochimica Acta, 222, 447-466.

Nisbet, E.G. et al., 1987. Uniquely fresh 2.7 Ga komatiites from the Belingwe greenstone belt, Zimbabwe. Geology, 15 (12), 1147-1150.

Nisbet, E.G., Bickle, M.J., Martin, A., 1977. The mafic and ultramafic lavas of the Belingwe greenstone belt, Rhodesia. Journal of Petrology, 18 (4), 521-566.

Nisbet, E.G., Cheadle, M.J., Arndt, N.T., Bickle, M.J., 1993. Constraining the potential temperature of the Archaean mantle: a review of the evidence from komatiites. Lithos, 30 (3-4), 291-307.

Ohtani, E., Kawabe, I., Moriyama, J., Nagata, Y., 1989. Partitioning of elements between majorite garnet and melt and implications for petrogenesis of komatiite. Contributions to Mineralogy and Petrology, 103 (3), 263-269.

Orgel, L.E., 1966. An introduction to transition-metal chemistry: ligand-field theory. Taylor & Francis.

Orpen, J.L., Martin, A., Bickle, M.J., Nisbet, E.G., 1993. The Mtshingwe Group in the west: Andesites, basalts, komatiites and sediments of the Hokonui, Bend and Koodoovale Formations, in: Bickle, M.J., Nisbet, E.G. (Eds.), The Geology of the Belingwe Greenstone Belt, Zimbabwe. Geological Society of Zimbabwe Special Publication, pp. 69-86.

Ottonello, G., Zuccolini, M.V., 2005. Ab-initio structure, energy and stable Cr isotopes equilibrium fractionation of some geochemically relevant H-O-Cr-Cl complexes. Geochimica et Cosmochimica Acta, 69 (4), 851-874.

Palme, H., O'Neill, H.St.C., 2003. Cosmochemical estimates of mantle composition., in: Turekian, K., Holland, H. (Eds.), Treatise on Geochemistry. Elsevier, pp. 1-39.

Papike, J.J., Karner, J.M., Shearer, C.K., 2005. Comparative planetary mineralogy: Valence state partitioning of Cr, Fe, Ti, and V among crystallographic sites in olivine, pyroxene, and spinel from planetary basalts. American Mineralogist, 90 (2-3), 277-290.

Papike, J.J., Simon, S.B., Burger, P.V., Bell, A.S., Shearer, C.K., Karner, J.M., 2016. Chromium, vanadium, and titanium valence systematics in Solar System pyroxene as a recorder of oxygen fugacity, planetary provenance, and processes. American Mineralogist, 101 (4), 907-918.

Parman, S.W., Dann, J.C., Grove, T.L., De Wit, M.J., 1997. Emplacement conditions of komatiite magmas from the 3.49 Ga Komati Formation, Barberton Greenstone Belt, South Africa. Earth and Planetary Science Letters, 150 (3-4), 303-323.

Parman, S.W., Shimizu, N., Grove, T.L., Dann, J.C., 2003. Constraints on the premetamorphic trace element composition of Barberton komatiites from ion probe analyses of preserved clinopyroxene. Contributions to Mineralogy and Petrology, 144 (4), 383-396.

Poitrasson, F., Freydier, R., 2005. Heavy iron isotope composition of granites determined by high resolution MC-ICP-MS. Chemical Geology, 222 (1-2), 132-147.

Poitrasson, F., Halliday, A.N., Lee, D.C., Levasseur, S., Teutsch, N., 2004. Iron isotope differences between Earth, Moon, Mars and Vesta as possible records of contrasted accretion mechanisms. Earth and Planetary Science Letters, 223 (3-4), 253-266.

Polat, A., Hofmann, A.W., 2003. Alteration and geochemical patterns in the 3.7-3.8 Ga Isua greenstone belt, West Greenland. Precambrian Research, 126 (3-4), 197-218.

Polat, A., Hofmann, A.W., Rosing, M.T., 2002. Boninite-like volcanic rocks in the 3.7-3.8 Ga Isua greenstone belt, West Greenland: geochemical evidence for intra-oceanic subduction zone processes in the early Earth. Chemical Geology, 184 (3-4), 231-254.

Prytulak, J., Sossi, P.A., Halliday, A.N., Plank, T., Savage, P.S., Woodhead, J.D., 2016. Stable vanadium isotopes as a redox proxy in magmatic systems? Geochemical Perspectives Letters, 3 (1), 75-84.

Puchtel, I.S., Blichert-Toft, J., Touboul, M., Walker, R.J., Byerly, G.R., Nisbet, E.G., Anhaeusser, C.R., 2013. Insights into early Earth from Barberton komatiites: Evidence from lithophile isotope and trace element systematics. Geochimica et Cosmochimica Acta, 108, 63-90.

Puchtel, I.S., Walker, R.J., Brandon, A.D., Nisbet, E.G., 2009. Pt-Re-Os and Sm-Nd isotope and HSE and REE systematics of the 2.7 Ga Belingwe and Abitibi komatiites. Geochimica et Cosmochimica Acta, 73 (20), 6367-6389.

Renner, R., Nisbet, E.G., Cheadle, M.J., Arndt, N.T., Bickle, M.J., Cameron, W.E., 1994. Komatiite flows from the reliance formation, Belingwe Belt, Zimbabwe: I.

Petrography and mineralogy. Journal of Petrology, 35 (2), 361-400.

Robin-Popieul, C.C.M., Arndt, N.T., Chauvel, C., Byerly, G.R., Sobolev, A.V., Wilson, A., 2012. A New Model for Barberton Komatiites: Deep Critical Melting with High Melt Retention. Journal of Petrology, 53 (11), 2191-2229.

Rouxel, O., Dobbek, N., Ludden, J., Fouquet, Y., 2003. Iron isotope fractionation during oceanic crust alteration. Chemical Geology, 202 (1-2), 155-182.

Rudnick, R.L., Fountain, D.M., 1995. Nature and composition of the continental crust: a lower crustal perspective. Reviews of Geophysics, 33 (3), 267-309.

Rudnick, R.L., Gao, S., 2003. Composition of the continental crust., in: Turekian, K., Holland, H. (Eds.), Treatise on Geochemistry, 3, 1-64 pp.

Saikkonen, R.J., Rautiainen, I.A., 1993. Determination of ferrous iron in rock and mineral samples by three volumetric methods. Bulletin Geological Society of Finland, 65, 59-63.

Schauble, E.A., Rossman, G.R., Taylor Jr, H.P., 2004. Theoretical estimates of equilibrium chromium-isotope fractionations. Chemical Geology, 205 (1-2), 99-114.

Schneider, K.P., Hoffmann, J.E., Munker, C., Patyniak, M., Sprung, P., Roerdink, D., Garbe-Schonberg, D., Kroner, A., 2019. Petrogenetic evolution of metabasalts and metakomatiites of the lower Onverwacht Group, Barberton Greenstone Belt (South Africa). Chemical Geology, 511, 152-177.

Schoenberg, R., Marks, M.A.W., Schuessler, J.A., von Blanckenburg, F., Markl, G., 2009. Fe isotope systematics of coexisting amphibole and pyroxene in the alkaline igneous rock suite of the Ilímaussaq Complex, South Greenland. Chemical Geology, 258 (1-2), 65-77.

Schoenberg, R., Merdian, A., Holmden, C., Kleinhanns, I.C., Hassler, K., Wille, M., Reitter, E., 2016. The stable Cr isotopic compositions of chondrites and silicate planetary reservoirs. Geochimica et Cosmochimica Acta, 183, 14-30.

Schoenberg, R., von Blanckenburg, F., 2005. An assessment of the accuracy of stable Fe isotope ratio measurements on samples with organic and inorganic matrices by high-resolution multicollector ICP-MS. International Journal of Mass Spectrometry, 242 (2-3), 257-272.

Schoenberg, R., von Blanckenburg, F., 2006. Modes of planetary-scale Fe isotope fractionation. Earth and Planetary Science Letters, 252 (3-4), 342-359.

Schoenberg, R., Zink, S., Staubwasser, M., von Blanckenburg, F., 2008. The stable Cr isotope inventory of solid Earth reservoirs determined by double spike MC-ICP-MS. Chemical Geology, 249 (3-4), 294-306.

Scholey, S.P., 1992. The geology and geochemistry of the Ngezi group volcanics, Belingwe Greenstone Belt, Zimbabwe, University of Southampton.

Schreiber, H.D., Haskin, L.A., 1976. Chromium in basalts: Experimental determination of redox states and partitioning among synthetic silicate phases, Lunar and Planetary Science Conference Proceedings, pp. 1221-1259.

Schuessler, J.A., Schoenberg, R., Sigmarsson, O., 2009. Iron and lithium isotope systematics of the Hekla volcano, Iceland - Evidence for Fe isotope fractionation during magma differentiation. Chemical Geology, 258 (1-2), 78-91.

Shannon, R.D., 1976. Revised effective ionic-radii and systematic studies of interatomic distances in halides and chalcogenides. Acta Crystallographica 32 (5), 751-767.

Shen, J., Liu, J., Qin, L.P., Wang, S.J., Li, S.G., Xia, J.X., Ke, S., Yang, J.S., 2015. Chromium isotope signature during continental crust subduction recorded in metamorphic rocks. Geochemistry, Geophysics, Geosystems, 16 (11), 3840-3854.

Shen, J. et al., 2018. High-temperature inter-mineral Cr isotope fractionation: A comparison of ionic model predictions and experimental investigations of mantle xenoliths from the North China Craton. Earth and Planetary Science Letters, 499, 278-290.

Shen, J., Xia, J.X., Qin, L.P., Carlson, R.W., Huang, S., Helz, R.T., Mock, T.D., 2020. Stable chromium isotope fractionation during magmatic differentiation: Insights from Hawaiian basalts and implications for planetary redox conditions. Geochimica et Cosmochimica Acta, 278, 289-304.

Shimizu, K., Nakamura, E., Maruyama, S., 2005. The geochemistry of ultramafic to mafic volcanics from the Belingwe greenstone belt, Zimbabwe: Magmatism in an Archean continental large Igneous Province. Journal of Petrology, 46 (11), 2367-2394.

Sossi, P.A., Eggins, S.M., Nesbitt, R.W., Nebel, O., Hergt, J.M., Campbell, I.H., O'Neill, H.St.C., Van Kranendonk, M.J., Davies, D.R., 2016. Petrogenesis and Geochemistry of Archean Komatiites. Journal of Petrology, 57 (1), 147-184.

Sossi, P.A., Foden, J.D., Halverson, G.P., 2012. Redox-controlled iron isotope fractionation during magmatic differentiation: an example from the Red Hill intrusion, S. Tasmania. Contributions to Mineralogy and Petrology, 164 (5), 757-772.

Sossi, P.A., Moynier, F., Van Zuilen, K., 2018. Volatile loss following cooling and accretion of the Moon revealed by chromium isotopes. Proceedings of the National Academy of Science, 115 (43), 10920-10925.

Sossi, P.A., O'Neill, H.St.C., 2017. The effect of bonding environment on iron isotope fractionation between minerals at high temperature. Geochimica Et Cosmochimica Acta, 196, 121-143.

Sun, S.-S., Nesbitt, R.W., 1978. Petrogenesis of Archaean ultrabasic and basic volcanics: evidence from rare earth elements. Contributions to Mineralogy and Petrology, 65 (3), 301-325.

Sutton, S.R., Jones, K.W., Gordon, B., Rivers, M.L., Bajt, S., Smith, J.V., 1993. Reduced Chromium in olivine grains from Lunar basalt 15555 - X-ray adsorption near edge structure (XANES). Geochimica et Cosmochimica Acta, 57 (2), 461-468.

Swanner, E.D., Wu, W., Schoenberg, R., Byrne, J., Michel, F.M., Pan, Y., Kappler, A., 2015. Fractionation of Fe isotopes during Fe (II) oxidation by a marine photoferrotroph is controlled by the formation of organic Fe-complexes and colloidal Fe

fractions. Geochimica et Cosmochimica Acta, 165, 44-61.

Teng, F.-Z., Dauphas, N., Helz, R.T., 2008. Iron isotope fractionation during magmatic differentiation in Kilauea Iki Lava Lake. Science, 320 (5883), 1620-1622.

Teng, F.-Z., Dauphas, N., Helz, R.T., Gao, S., Huang, S., 2011. Diffusion-driven magnesium and iron isotope fractionation in Hawaiian olivine. Earth and Planetary Science Letters, 308 (3-4), 317-324.

Ulrich, T., Kamber, B.S., Woodhead, J.D., Spencer, L.A., 2010. Long-term observations of isotope ratio accuracy and reproducibility using quadrupole ICP-MS. Geostandards and Geoanalytical Research, 34 (2), 161-174.

Viljoen, M.J., Viljoen, R.P., 1969. The geology and geochemistry of the lower ultramafic unit of the Onverwacht Group and a proposed new class of igneous rocks. Geological Society of South Africa Special Publication, 2, 55-86.

Walter, M.J., 1998. Melting of garnet peridotite and the origin of komatiite and depleted lithosphere. Journal of Petrology, 39 (1), 29-60.

Wang, X.L., Planavsky, N.J., Reinhard, C.T., Zou, H.J., Ague, J.J., Wu, Y.B., Gill, B.C., Schwarzenbach, E.M., Peucker-Ehrenbrink, B., 2016. Chromium isotope fractionation during subduction-related metamorphism, black shale weathering, and hydrothermal alteration. Chemical Geology, 423, 19-33.

Watenphul, A., Schmidt, C., Jahn, S., 2014. Cr(III) solubility in aqueous fluids at high pressures and temperatures. Geochimica et Cosmochimica Acta, 126, 212-227.

Waterton, P., Pearson, D.G., Mertzman, S.A., Mertzman, K.R., Kjarsgaard, B.A., 2020. A fractional crystallisation link between komatiites, basalts, and dunites of the Palaeoproterozoic Winnipegosis Komatiite Belt, Manitoba, Canada. Journal of Petrology, 61 (5), egaa052.

Webb, P.C., Thompson, M., Potts, P.J., Burnham, M., 2007. GeoPT20 - an international proficiency test for analytical geochemsitry laboratories - report on round 20/ Jan 2007 (Ultramafic rock, OPY-1). International Association of Geoanalysts, Report.

Weyer, S., Anbar, A.D., Brey, G.P., Munker, C., Mezger, K., Woodland, A.B., 2005. Iron isotope fractionation during planetary differentiation. Earth and Planetary Science Letters, 240 (2), 251-264.

Weyer, S., Ionov, D.A., 2007. Partial melting and melt percolation in the mantle: The message from Fe isotopes. Earth and Planetary Science Letters, 259 (1-2), 119-133.

Weyer, S., Schwieters, J.B., 2003. High precision Fe isotope measurements with high mass resolution MC-ICPMS. International Journal of Mass Spectrometry, 226 (3), 355-368.

Wille, M., Babechuk, M.G., Kleinhanns, I.C., Stegmaier, J., Suhr, N., Widdowson, M., Kamber, B.S., Schoenberg, R., 2018. Silicon and chromium stable isotopic systematics during basalt weathering and lateritisation: A comparison of variably weathered basalt profiles in the Deccan Traps, India. Geoderma, 314, 190-204.

Williams, H.M., McCammon, C.A., Peslier, A.H., Halliday, A.N., Teutsch, N., Levasseur, S., Burg, J.P., 2004. Iron isotope fractionation and the oxygen fugacity of the mantle. Science, 304 (5677), 1656-1659.

Williams, H.M., Peslier, A.H., McCammon, C.A., Halliday, A.N., Levasseur, S., Teutsch, N., Burg, J.P., 2005. Systematic iron isotope variations in mantle rocks and minerals: The effects of partial melting and oxygen fugacity. Earth and Planetary Science Letters, 235 (1-2), 435-452.

Williams, H.M., Prytulak, J., Woodhead, J.D., Kelley, K.A., Brounce, M., Plank, T., 2018. Interplay of crystal fractionation, sulfide saturation and oxygen fugacity on the iron isotope composition of arc lavas: an example from the Marianas. Geochimica et Cosmochimica Acta, 226, 224-243.

Wilson, J.F., Nesbitt, R.W., Fanning, C.M., 1995. Zircon geochronology of Archaean felsic sequences in the Zimbabwe craton: a revision of greenstone stratigraphy and a model for crustal growth. Geological Society, London, Special Publications, 95 (1), 109-126.

Wu, W., Swanner, E.D., Kleinhanns, I.C., Schoenberg, R., Pan, Y., Kappler, A., 2017. Fe isotope fractionation during Fe (II) oxidation by the marine photoferrotroph Rhodovulum iodosum in the presence of Si–Implications for Precambrian iron formation deposition. Geochimica et Cosmochimica Acta, 211, 307-321.

Xia, J., Qin, L.P., Shen, J., Carlson, R.W., Ionov, D.A., Mock, T.D., 2017. Chromium isotope heterogeneity in the mantle. Earth and Planetary Science Letters, 464, 103-115.

Xie, Q., Kerrich, R., Fan, J., 1993. HFSE/REE fractionations recorded in three komatiite-basalt sequences, Archean Abitibi greenstone belt: Implications for multiple plume sources and depths. Geochimica et Cosmochimica Acta, 57 (16), 4111-4118.

Xie, X., Byerly, G.R., Ferrell Jr, R.E., 1997. IIb trioctahedral chlorite from the Barberton greenstone belt: crystal structure and rock composition constraints with implications to geothermometry. Contributions to Mineralogy and Petrology, 126 (3), 275-291.

Young, E.D., Manning, C.E., Schauble, E.A., Shahar, A., Macris, C.A., Lazar, C., Jordan, M., 2015. High-temperature equilibrium isotope fractionation of non-traditional stable isotopes: Experiments, theory, and applications. Chemical Geology, 395, 176-195.

Zink, S., Schoenberg, R., Staubwasser, M., 2010. Isotopic fractionation and reaction kinetics between Cr(III) and Cr(VI) in aqueous media. Geochimica et Cosmochimica Acta, 74 (20), 5729-5745.

Chapter 3

Consistently light stable chromium isotopic compositions in mid-ocean ridge basalts: Implications for the mantle source composition

Abstract

Stable isotopes of chromium (Cr) and iron (Fe), both multivalent elements in silicate melts, are valuable proxies of redox conditions in magmatic systems. Partial melting and fractional crystallization were identified as the dominant fractionation processes for Cr and Fe isotopes in high-temperature reservoirs that can lead to small but detectable isotope variations in igneous rocks. More recently, however, the source mineralogy was suggested to additionally play an important role, since small but measurable differences in the stable Cr and Fe isotopic compositions of source rock minerals and non-modal partial melting may influence the magnitude of Cr and Fe isotopic fractionation during partial melting and thus the Cr and Fe isotopic composition of the originating melt.

With the aim to investigate the role of magmatic processes and the source Cr and Fe isotope signatures on the isotope composition of these transition metals in normal mid-ocean ridge basalt (N-MORB), we analyzed 21 well-characterized MORB glasses from the southern East-Pacific Rise, Pacific-Antarctic Ridge and Mid-Atlantic Ridge. The Cr isotope compositions of N-MORBs show a narrow range from -0.278 to -0.186 ‰ in $\delta^{53/52}$Cr (i.e., difference of a sample's $^{53}Cr/^{52}Cr$ ratio relative to the international reference material NIST SRM979), with an average value of -0.237 $\pm$ 0.050 ‰ (2SD; n=19). As such, the average N-MORB $\delta^{53/52}$Cr value is significantly lower than that of Bulk Silicate Earth of -0.12 $\pm$ 0.06 ‰ and the Cr isotope compositions that have been observed for most ocean island basalts ranging from $\sim$ -0.23 to 0.00 ‰. Iron isotopic compositions of these MORBs range from +0.032 to +0.137 ‰ and are within the range of previously published MORB data. The lack of correlations between N-MORB Cr isotope signatures and indices of magmatic differentiation suggests a negligible control of this process on Cr stable isotopes. Partial melting modeling using pMELTS provides evidence that the

significant offset towards lower $\delta^{53/52}$Cr values of N-MORBs cannot be produced by decompression partial melting of a lherzolithic source such as the depleted upper mantle alone. Instead, we suggest that the lower $\delta^{53/52}$Cr values of MORBs could be linked to intrinsic small-scale ^{53}Cr-depleted pyroxene-rich domains in the upper mantle that influence the melt's Cr isotopic budget during partial melting.

3.1 Introduction

The stable isotopic composition of multivalent elements, such as chromium (Cr) and iron (Fe), in magmatic rocks may provide valuable insight into the prevailing oxygen fugacity (fO_2) of silicate reservoirs within our planet Earth (Dauphas et al., 2009; Shen et al., 2020; Williams et al., 2005). Chromium is a minor element in the upper mantle with an average concentration of 2500 $\mu g\, g^{-1}$ (Salters and Stracke, 2004), and with spinel and pyroxene as the major Cr-bearing phases (Liu and O'Neill, 2004; Mallmann and O'Neill, 2009). As a compatible element with a bulk partition coefficient $\gg 1$ for typical upper mantle compositions (Liu and O'Neill, 2004), Cr concentrations of primary melts vary little over a relatively large range of melting degrees (Zou, 2007). Under terrestrial mantle conditions, it has been experimentally demonstrated that Cr occurs as trivalent (Cr^{3+}) and divalent (Cr^{2+}) species in silicate melts (Berry et al., 2006). However, the presence of Cr^{2+} in mantle minerals is based on theoretical models, and so far, its existence has only been confirmed in olivine due to the presence of Fe^{3+} and the electron exchange reaction $Cr^{2+} + Fe^{3+} = Fe^{2+} + Cr^{3+}$ upon cooling (Berry and O'Neill, 2004; Shen et al., 2018). The relative proportions of Cr^{2+} and Cr^{3+} in the melt, expressed as Cr^{2+}/Cr_{total} ratio ($Cr_{total} = Cr^{2+} + Cr^{3+}$), depend on fO_2, pressure, temperature as well as melt composition, particularly the ratio of non-bridging oxygen to tetrahedral cations (known as NBO/T) and melt basicity (Berry et al., 2021b; Berry et al., 2006; O'Neill and Berry, 2021). As theory predicts that heavy isotopes favor stronger bonds associated with the higher oxidation state (e.g., Schauble, 2004), the stable Cr isotope compositions ($\delta^{53/52}$Cr; reported as the deviation of $^{53}Cr/^{52}Cr$ relative to NIST SRM979; Equation 3.1) of igneous rocks, bear the potential to trace the prevailing fO_2 of the associated magmatic system.

Igneous processes such as partial melting or fractional crystallization may further influence the Cr isotopic composition of magmatic rocks. Studies on natural samples and theoretical predictions indicate that partial melting may fractionate stable Cr isotopes, generating lower $\delta^{53/52}$Cr values in the melt compared to its source (Bonnand et al., 2020b; Shen et al., 2018; Shen et al., 2020; Xia et al., 2017). It has been argued that light Cr isotopes preferentially enter the melt based on the less compatible behavior of Cr^{2+} compared to Cr^{3+}, again, governed by the weaker bonding of the reduced Cr^{2+} species. However, based on the overall compatible behavior of Cr during igneous processes and mass balance considerations, partial melting will most likely not produce any resolvable increase of $\delta^{53/52}$Cr in the residue (Jerram et al., 2022). The magnitude of isotope fractionation during partial melting may change with melting degree and the Cr^{2+}/Cr_{total} of the source (Shen et al., 2018; Shen et al., 2020) and a decrease in Cr isotopic fractionation with increasing degree of melting is proposed (Jerram et al., 2022; Shen et al., 2020). At equilibrium and mantle conditions under which Cr^{2+} is present, inter-mineral isotope fractionations show an increase in $\delta^{53/52}$Cr in the order of olivine $<$ orthopyroxene $\leq$ clinopyrox-

ene < spinel (Shen et al., 2018). A melt in equilibrium with peridotite is inferred to be isotopically light compared to the source rock composition based on mass balance considerations, in which spinel controls the Cr budget and is isotopically heavy relative to a silicate melt (Berry et al., 2021a; Shen et al., 2020). Thus, Cr isotopic fractionation during partial melting driven by mineral-melt specific fractionations may depend additionally on the melting and residual assemblages and the associated Cr fractions involved. Jerram et al. (2022), for example, proposed a difference in the magnitude of Cr isotopic fractionation during melting of garnet- vs. spinel-bearing peridotite. Moreover, a multi-element approach by Soderman et al. (2022) demonstrated that stable isotope systems such as Mg, Ca, Cr and Fe can potentially be sensitive tracers for source lithology. These authors modeled partial melting of pyroxenitic or mixed peridotite-pyroxenite sources and showed that this process could generate basalts with $\delta^{53/52}$Cr values significantly lower than that of their sources.

Fractional crystallization, similar to partial melting, can also result in small Cr isotope fractionation as proposed for different suites of terrestrial mafic to ultramafic igneous rocks (Bonnand et al., 2020b; Jerram et al., 2020; Shen et al., 2020; Wagner et al., 2021). These isotopic variations are mainly induced through variable partitioning behavior of Cr^{2+} and Cr^{3+} between the melt and the crystallizing mineral phases and the associated change in the Cr coordination environment affecting bond strengths, but can also be caused by kinetic processes such as diffusion (Bai et al., 2019; Bonnand et al., 2020b; Shen et al., 2020; Wagner et al., 2021). As such, ionic model calculations for spinel and clinopyroxene, in addition to ab-initio calculations and experimental studies for spinel, have shown that these minerals preferentially incorporate Cr^{3+} over Cr^{2+}, leading to a preferential removal of the heavy isotopes from the melt during fractional crystallization (Berry et al., 2021a; Bonnand et al., 2020a; Moynier et al., 2011; Shen et al., 2018). In contrast, similar partitioning behavior of Cr^{2+} and Cr^{3+} into olivine (Mallmann and O'Neill, 2009), yet an associated difference in bond strengths in olivine compared to the melt should theoretically lead to the preferential removal of the light Cr isotopes (Berry et al., 2021a; Shen et al., 2020). Similarly, stable Fe isotopes ($\delta^{56/54}$Fe; reported as the deviation of $^{56}Fe/^{54}Fe$ relative to IRMM-014; Equation 3.4) are fractionated during magma differentiation with olivine and clinopyroxene removing the light Fe isotopes that are associated with Fe^{2+} species from the melt, whereas oxides such as magnetite or spinel preferentially incorporate the heavy Fe isotopes (Shahar et al., 2008; Teng et al., 2008; Williams et al., 2005). Consequently, coupled stable isotope systems can be used to distinguish between different crystallizing phases as already shown for stable Fe-V isotopes in an oceanic arc setting (Williams et al., 2018) and stable Cr-Fe isotopes in two Archean komatiite-tholeiite suites (Wagner et al., 2021).

Although recent analytical advances have improved our knowledge of the stable Cr isotope system in high-temperature reservoirs, only a few studies are available for mantle derived rocks. Thus, to which extent the different modern Earth's mantle silicate reservoirs show resolvable Cr isotopic differences diverging from the Bulk Silicate Earth (BSE) value remains to be further investigated. Currently, the Cr isotope value for BSE has been constrained by a number of studies based on komatiites (Jerram et al., 2020; Wagner et al., 2021), peridotites (Xia et al., 2017), or a combination of both (Sossi et al., 2018) and yield similar values within uncertainties (e.g., -0.12 $\pm$ 0.06 ‰; Wagner et al., 2021). Hence, the Cr isotope BSE

composition is indistinguishable from the combined average $\delta^{53/52}$Cr composition of ordinary and carbonaceous chondrites (-0.119 ± 0.045 ‰, n=18; Schoenberg et al., 2016; and -0.115 ± 0.043 ‰, n=10; Bonnand et al., 2016). Considerable $\delta^{53/52}$Cr variations have been observed for mantle xenoliths, in which pyroxenite veins exhibit very light $\delta^{53/52}$Cr values of up to -1.36 ‰, advocating for small-scale Cr isotopic mantle heterogeneities in the lithospheric mantle (Jerram et al., 2022; Xia et al., 2017). Studies of Phanerozoic ocean island basalts (OIB), including Fangataufa atoll (French Polynesia; $\delta^{53/52}$Cr = -0.226 to -0.169 ‰; Bonnand et al., 2020b) and three different Hawaiian volcanoes $\delta^{53/52}$Cr = -0.21 to 0.00 ‰; Shen et al., 2020), show slightly lower $\delta^{53/52}$Cr values compared to BSE. These values were inferred to result from partial melting, followed by fractional crystallization that acted towards a $\delta^{53/52}$Cr decrease of the melt with increasing degree of magmatic differentiation (Bonnand et al., 2020b; Shen et al., 2020). Much less is known about the Cr isotope systematics of mid-ocean ridge basalts (MORB) with a single recent study pointing to light $\delta^{53/52}$Cr compositions (-0.27 to -0.07 ‰; Ma et al., 2022) compared to the BSE. The $\delta^{53/52}$Cr variations of these MORBs from various ocean basins show a correlation with MgO contents, which was interpreted as the result of fractional crystallization (Ma et al., 2022).

To explore in depth the Cr isotope fractionation during MORB petrogenesis, including setting-specific attributions, and expand our understanding of Cr isotopes as tracers of mantle source composition, thereby elucidating the Cr isotope heterogeneity of silicate reservoirs of the Earth, we present stable Cr and Fe isotope compositions for 21 fresh MORB glasses collected from different divergent plate boundaries. These samples show mostly geochemical characteristics typical for normal MORB (N-MORB) and are derived from ridge sections with varying spreading rates ranging from superfast- to slow-spreading, including the southern East-Pacific Rise (EPR), the Pacific-Antarctic Ridge (PAR) and one sample from the Mid-Atlantic Ridge (MAR). Since the EPR and PAR MORBs represent a continuous suite generated under similar conditions of melt supply and subsequent fractional crystallization (Standish and Sims, 2010), they are excellent targets for investigating the effect of fractional crystallization on their $\delta^{53/52}$Cr variations. Moreover, these MORBs erupted on-axis, thus providing insights into the $\delta^{53/52}$Cr variations of the Pacific upper mantle and its intrinsic heterogeneity.

3.2 Geological overview and samples

Samples from the EPR were collected during the GEOMETEP (Geothermal Metallogenesis East Pacific) cruises between 7° to 29° S and are described in detail by Bach et al. (1994). The southern EPR belongs to the superfast-spreading class of mid-ocean ridges with full spreading rates > 150 mm/yr and is interrupted by the Easter Microplate, extending from 23 to 28° S and flanked by two hotspot tracks (Sinton et al., 1991). Major elements are available for all EPR samples of this study, whereas REE and Sr, Nd, Pb isotope data are available for a sub-set of these samples (Bach et al., 1994). All samples are fresh glassy rinds of on-axis basaltic lava flows with MgO concentrations typical for MORB varying between 4.87 and 9.00 wt. % (Figure 3.2, Table 3.1). With the exception of sample G412G, all EPR MORBs display N-MORB compositions (defined by $(La/Sm)_{PM} < 1$) with $(La/Sm)_{PM}$ from 0.39 to 0.90 (normalized to Primitive Mantle (PM); Palme and O'Neill, 2014). Sample

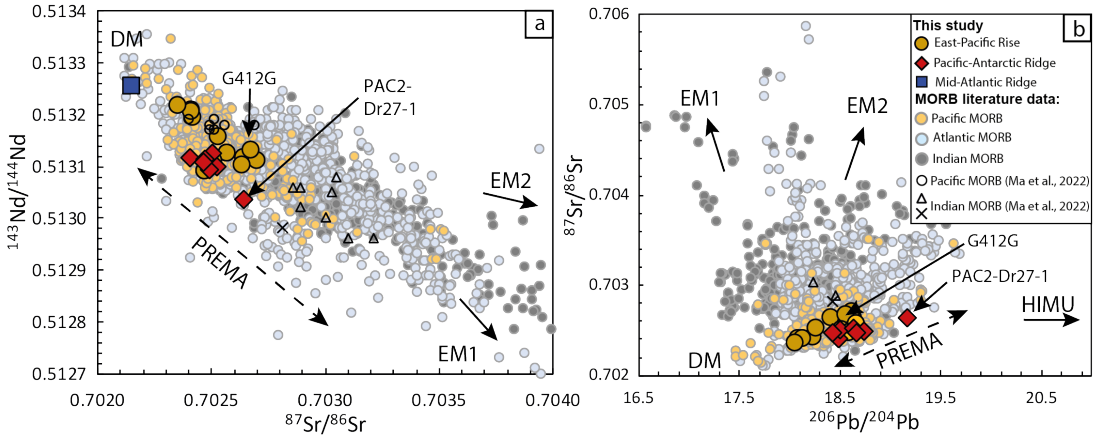

Figure 3.1: **a)** $^{143}Nd/^{144}Nd$ vs. $^{87}Sr/^{86}Sr$ and **b)** $^{87}Sr/^{86}Sr$ vs. $^{206}Pb/^{204}Pb$ for mid-ocean ridge basalts (MORB) from this study as well as literature data for Pacific (orange), Atlantic (blue) and Indian (black) MORB compositions from Stracke (2012). Also shown are radiogenic isotope compositions for MORBs as used in Ma et al. (2022): East-Pacific Rise MORBs (open circles) represent Pacific MORB and Carlsberg ridge (open triangles) and Southwest Indian Ridge (cross) MORBs both represent Indian-type MORB. $^{87}Sr/^{86}Sr$ and $^{143}Nd/^{144}Nd$ are reported by Ma et al. (2022), and where available, $^{206}Pb/^{204}Pb$ ratios are from (Chen et al., 2017). Radiogenic isotope compositions for one sample from the Southwest Indian ridge are from Standish (2006). DM = Deplete mantle, PREMA = Prevalent mantle, EM1 = enriched mantle 1 and EM2 = enriched mantle 2. The stippled arrow indicates the approximate array of compositions for DM-PREMA after Stracke (2012).

G412G displays a transitional MORB (T-MORB; defined by $1 < (La/Sm)_{PM} < 1.7$; Sun et al., 1979) composition with $(La/Sm)_{PM}$ of 1.01 and an elevated K_2O/TiO_2 ratio at moderately evolved MgO concentrations of 7.05 wt. % (Supplementary Table B.4.2).

The PAR is the southern continuation of the EPR. PAR glasses were collected during two cruises PACANTARCTIC 1 (PAC1; 56° to 66° S; Vlastelic et al., 2000) and PACANTARCTIC 2 (PAC2; 53° to 41° S; Hamelin et al., 2010). The total spreading rate along the PAR increases from south to north. The southern ridge segment represented by PAC1 samples displays full spreading rates of 54 to 74 mm/yr (intermediate-spreading ridge; Vlastelic et al., 2000) and the northern ridge segment represented by PAC2 samples displays full spreading rates of 92 to 100 mm/yr (fast-spreading ridge; Hamelin et al., 2010). Major and trace element (including Cl) concentrations as well as radiogenic Sr, Nd, Pb and stable S isotope compositions are available for all samples (Hamelin et al., 2010; Hamelin et al., 2011; Labidi et al., 2014; Vlastelic et al., 2000; Yierpan et al., 2019). Apart from sample PAC2-Dr27-1, all PAR samples represent on-axis erupted magmas with N-MORB compositions ($(La/Sm)_{PM}$ of 0.60 to 0.98). Sample PAC2-Dr27-1 displays the most evolved composition with MgO content of 4.52 wt. %, accordingly high alkali content, and $(La/Sm)_{PM}$ of 1.25, thus representing T-MORB composition following the definition by Sun et al. (1979). This sample originated from a seamount ridge transition zone with less robust melt supply and possibly limited mixing, thus, resulting in different trace element and radiogenic isotope compositions compared to PAR N-MORBs (Figure 3.1; Hamelin et al., 2010). In general, the MgO content varies from 4.52 to 8.57 wt. %, with three samples diverging from the typical early tholeiitic Fe enrichment indicating fractionation of titanomagnetite (Figure 3.2c; Labidi et al.,

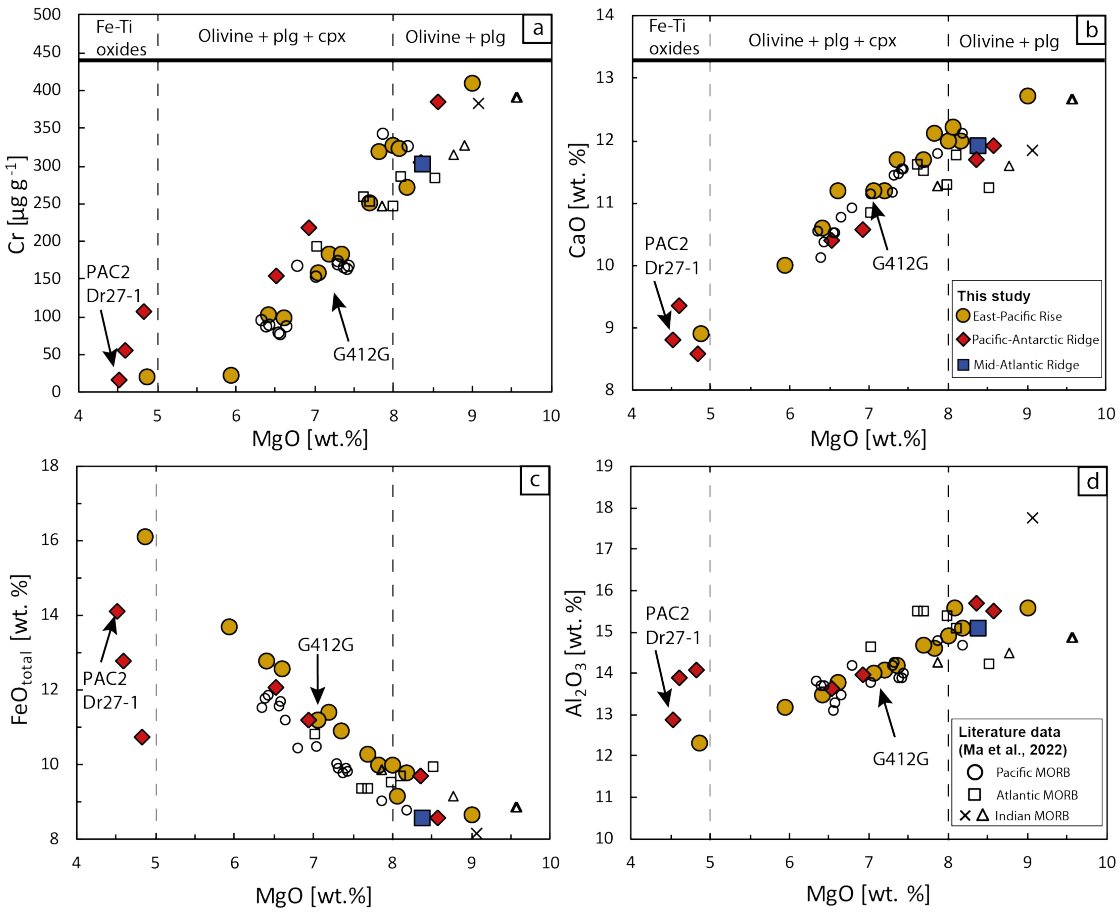

Figure 3.2: Major element variations of mid-ocean ridge basalts (MORBs) from the East-Pacific Rise (EPR), Pacific-Antarctic Ridge (PAR) and Mid-Atlantic Ridge (MAR) in this study. **a)** Cr vs. MgO concentrations; **b)** CaO vs. MgO concentration; **c)** FeO_{total} vs. MgO and **d)** Al_2O_3 vs. MgO concentrations. Stippled lines indicate a change of the fractional assemblage in MORBs from the EPR and PAR from olivine + plagioclase for samples with MgO > 8 wt. % to olivine + plagioclase + clinopyroxene for samples 5 wt. % < MgO < 8 wt. % and to Fe-Ti oxides for samples with MgO < 5 wt. % Plg = plagioclase and cpx = clinopyroxene. Also shown are MORB compositions from the EPR (open circles) representing Pacific-type MORB, from the northern and southern MAR representing Atlantic-type MORB and from the Carlsberg ridge (open triangles) and Southwest Indian Ridge (cross) both representing Indian-type MORB from Ma et al. (2022). We note here that the indicated fractional assemblages are representative for EPR and PAR samples from this study and not necessarily for MORBs from Ma et al. (2022).

2014; Yierpan et al., 2019).

Samples from each ridge section, PAR and EPR, plot along similar liquid lines of descent that indicate an overall uniform mantle source regarding their major element composition (Figure 3.2; Bach et al., 1994; Hamelin et al., 2010). Radiogenic Sr-Nd-Pb isotope compositions of PAR and EPR samples of this study lie within the range of previously published MORBs representative of the Pacific upper mantle, which form binary trends between the depleted mantle (DM) and the prevalent mantle (PREMA) in $^{143}Nd/^{144}Nd$ vs. $^{87}Sr/^{86}Sr$ (Figure 3.1a) and $^{87}Sr/^{86}Sr$ vs. $^{206}Pb/^{204}Pb$ space (Figure 3.1b). This trend is generally interpreted as a mixture between DM and small amounts of a recycled oceanic crustal component (Stracke, 2012; Stracke et al., 2005) that changes progressively with a maximum contribution

of the recycled component at ∼ 38° S, as shown by a statistical approach using Sr-Nd-Pb-Hf isotope compositions of samples covering the PAR and southern EPR ridge sections (Hamelin et al., 2011). Small amounts of ancient enriched material are responsible for relatively less radiogenic Nd and more radiogenic Sr and Pb isotope compositions between ∼ 16° and 21° S (Bach et al., 1994; Mahoney et al., 1994; Niu et al., 1996). The origin of T-MORBs along the EPR, represented by sample G412G in this study, is attributed to cyclic mixing of a two-component mantle involving recently formed K-enriched mantle heterogeneities (Bach et al., 1994).
Sample 267ROV-5 was originally collected on-board the R/V Meteor during the expedition M78/2 in 2009 to the slow-spreading southern MAR between 5° and 11° S (Seifert and Party, 2009), displaying a total spreading rate of ∼ 32 mm/yr (DeMets et al., 1990). The ridge section exhibits a typical slow-spreading ridge morphology and sample 267ROV-5 is derived from a pronounced axial high within a deep, central axial rift valley at 4° 48' S (Haase et al., 2007; Seifert and Party, 2009). The sample location is characterized by fresh, unsedimented pillow lavas indicating recent volcanic activity (Haase et al., 2007). Geochemical studies of MORBs from the southern MAR (4° 48' to 11° S) revealed a heterogeneous mantle (Hoernle et al., 2011; Paulick et al., 2010). Therein, MORBs from 4° 48' to 7° 35' S, closest to the sample location of sample 267ROV-5, reflect the most depleted radiogenic isotope compositions and strong LREE depletions with $(La/Sm)_{PM}$ of ∼ 0.5 to 0.75, which was attributed to a common depleted mantle component (Hoernle et al., 2011). In contrast, trends formed by most southern Atlantic or Indian MORBs have been shown to deviate towards enriched mantle (EM1) components (Figure 3.1; Dupré and Allègre, 1983; Stracke, 2012; White, 2015).

3.3 Methods

The complete set of new and published major element, trace element and radiogenic isotope compositions are given in Supplementary Tables B.4.1 and B.4.2. For sample 267ROV-5, major and trace element and radiogenic Sr-Nd isotope compositions were determined at the Isotope Geochemistry laboratories of the University of Tuebingen and are further outlined in Appendix B and given together with published data in the Supplementary Table B.4.1.

3.3.1 Cr and Fe isotope compositions

Basalt glasses were repeatedly cleaned ultrasonically with MQ water, handpicked under a microscope, and ground to fine powders in an agate mill as described in Bach et al. (1994) and Yierpan et al. (2019). Subsequently, samples were digested in closed 15 mL Savillex PFA beakers using concentrated HF:HNO_3 mixtures on hotplates at 120° C. The samples were then dried down and repeatedly dissolved in 6 M HCl until clear of precipitates. Aliquots for stable Cr and Fe isotope analyses were taken from one common digest.
All stable Cr and Fe isotope data reported in this study were obtained on a ThermoFisher Scientific NeptunePlus multicollector inductively coupled plasma mass spectrometer (MC-ICP-MS) housed at the Isotope Geochemistry facilities of the

Table 3.1: Stable Cr and Fe isotopic compositions alongside Cr and Fe concentrations acquired via isotope dilution for MORB glasses in this study, all of which represent N-MORBs, except sample G412G and PAC2-DR27-1, which represent T-MORBs based on trace element compositions (see text for further information). Also listed are compiled sample locations, eruption depths and MgO concentrations from the literature.

Sample	Latitude [S]	Longitude [W]	Depth [mbsl]	$\delta^{53/52}$Cr [‰]	Uncertainty[a]	n[b]	Cr [μg g^{-1}]	$\delta^{56/54}$Fe [‰]	Uncertainty[a]	n[b]	Fe [μg g^{-1}]	MgO[c] [wt. %]
Mid-Atlantic Ridge												
267ROV-5	04°48.161'	12°22.330'	2987	-0.242	±0.01	7 (2)	303	0.051	±0.03	1 (1)	67279	8.37
East-Pacific Rise												
G128G	*22°59.35'*	*114°30.77'*	*3003*	-0.253	±0.02	7 (2)	411	0.045	±0.037	5 (1)	62389	*9*
G148G	*21°29.44'*	*114°16.75'*	*2764*	-0.248	±0.012	7 (2)	183	0.1	±0.026	5 (1)	82094	*7.19*
G243G	*27°46.08'*	*113°16.40'*	*1983*	-0.233	±0.02	7 (2)	99	0.106	±0.041	5 (1)	100627	*6.61*
G258G	*48°45.26'*	*112°59.24'*	*2350*	-0.202	±0.006	5 (1)	20	0.123	±0.017	5 (1)	108615	*4.87*
G264G	*29°46.35'*	*111°43.61'*	*2500*	-0.242	±0.021	6 (2)	184	0.11	±0.035	5 (1)	78077	*7.35*
G287G	*17°23.39'*	*113°11.64'*	*2610*	-0.259	±0.015	7 (2)	320	0.119	±0.025	5 (1)	75601	*7.82*
G312G	*16°42.51'*	*113°04.10'*	*2651*	-0.272	±0.024	7 (2)	272	0.046	±0.025	1 (1)	70899	*8.17*
G319G	*16°26.39'*	*113°03.01'*	*2674*	-0.248	±0.021	7 (2)	328	0.032	±0.024	1 (1)	74333	*8*
G324G	*15°46.39'*	*112°56.90'*	*2627*	-0.241	±0.013	8 (3)	103	0.121	±0.021	1 (1)	93363	*6.41*
G343G	*13°59.12'*	*112°28.79'*	*2637*	-0.207	±0.023	7 (2)	251	0.096	±0.023	1 (1)	74941	*7.69*
G371G	*11°52.44'*	*110°43.40'*	*2598*	-0.222	±0.024	7 (2)	324	0.073	±0.023	1 (1)	69339	*8.07*
G407G	*07°23.71'*	*107°47.44'*	*2740*	-0.278	±0.019	6 (2)	24	0.067	±0.023	1 (1)	100424	*5.94*
G412G	*07°23.69'*	*107°47.43'*	*2717*	-0.085	±0.024	9 (3)	159	0.088	±0.025	1 (1)	82170	*7.05*
Pacific-Antarctic-Ridge												
PAC1-CV03-g	*64°31.8'*	*171°52.8'*	*2576*	-0.208	±0.011	1 (1)	385	0.098	±0.025	1 (1)	62901	*8.57*
PAC1-DR06-g	*60°56.4'*	*153°12.6'*	*2527*	-0.186	±0.011	1 (1)	218	0.106	±0.024	1 (1)	84097	*6.93*
PAC1-DR10-1g	*57°53.4'*	*148°30.0'*	*2319*	-0.258	±0.011	1 (1)	108	0.109	±0.022	1 (1)	82506	*4.83*
PAC2-DR05-2g	*50°58.8'*	*117°54.0'*	*2784*	-0.207	±0.01	1 (1)	155	0.076	±0.029	1 (1)	87684	*6.52*
PAC2-DR20-1	*49°43.98'*	*113°46.98'*	*2441*	-0.254	±0.014	6 (2)	56	0.137	±0.023	1 (1)	95584	*4.6*
PAC2-DR27-1	*48°10.92'*	*113°20.52'*	*2359*	-0.185	±0.011	1 (1)	16	0.072	±0.024	1 (1)	101957	*4.52*
PAC2-DR38-1	*41°48.0'*	*111°20.4'*	*2524*	-0.237	±0.011	1 (1)	305	0.086	±0.026	1 (1)	70916	*8.35*

Note: All literature data are shown in italics. [a] Uncertainty as 2SD if n > 1 and as 2SE if n = 1. [b] n = Number of analyses. The bracketed number corresponds to the number of digestions. [c] The MgO concentrations for East-Pacific Rise samples are from Bach et al. (1994) and for Pacific-Antarctic Ridge samples from Vlastélic et al. (2000) and Hamelin et al. (2010).

University of Tuebingen. Detailed descriptions of the Cr and Fe purification methods are given in previous studies (Schoenberg et al., 2016; Wagner et al., 2021) and details on the analytical accuracy and reproducibility are given in Appendix B.

All stable Cr isotope data are reported in the δ-notation relative to NIST SRM979 as:

$$\delta^{53/52}Cr_{SRM979} = \frac{(^{53}Cr/^{52}Cr)_{sample}}{(^{53}Cr/^{52}Cr)_{SRM979}} - 1 \quad (3.1)$$

hereafter referred to as $\delta^{53/52}$Cr. The data are expressed as per mil (‰) difference by multiplication with a factor of 1000.
The isotopic fractionation factor α observed for a process between two reservoirs is defined as:

$$\alpha_{A-B} = \frac{(^{53}Cr/^{52}Cr)_{reservoirA}}{(^{53}Cr/^{52}Cr)_{reservoirB}} \quad (3.2)$$

and the isotopic difference Δ between two reservoirs is expressed accordingly as:

$$\Delta^{53}Cr_{A-B} = \delta^{53/52}Cr_A - \delta^{53/52}Cr_B \approx (\alpha_{A-B} - 1) \times 1000 \quad (3.3)$$

All Fe isotope compositions are reported in δ-notation relative to the standard IRMM-014 according to equation 3.4 and multiplied by 1000 to display variations in per mil differences:

$$\delta^{56/54}Fe_{IRMM014} = \frac{(^{56}Fe/^{54}Fe)_{sample}}{(^{56}Fe/^{54}Fe)_{IRMM014}} - 1 \quad (3.4)$$

henceforth referred to as $\delta^{56/54}$Fe.

3.4 Results

Chemical compositions of EPR and PAR MORBs have been described in detail in previous studies (Bach et al., 1994; Hamelin et al., 2010; Hamelin et al., 2011; Vlastelic et al., 2000) and are reported in Supplementary Tables B.4.1 and B.4.2 for completeness of the dataset. For this reason, only major element, trace element and radiogenic isotope compositions of MAR sample 267ROV-5 are described shortly in the following. Sample 267ROV-5 displays major element compositions typical for MORBs with a relatively primitive MgO concentration of 8.37 wt. %, K_2O of 0.05 wt. % and TiO_2 of 1.17 wt. % (Figure 3.2, Supplementary Table B.4.1). The N-MORB-like $(La/Sm)_{PM}$ ratio of 0.51 mirrors low trace element concentrations on normalized REE patterns compared to EPR and PAR MORBs, as well as average N-MORB (Figure B.1.1; Yierpan et al. (2019) and Bach et al. (1994)). In radiogenic Nd vs. Sr isotope space, 267ROV-5 lies near the upper end of the Atlantic MORB array (Figure 3.1a and Supplementary Table B.4.1). The depleted trace element and radiogenic isotope signature is in accordance with the compositions derived for samples from the southern MAR at 4° 48' S published by Hoernle et al. (2011).

3.4.1 Cr and Fe isotopic composition of MORB glasses

All $\delta^{53/52}$Cr and $\delta^{56/54}$Fe data are presented in Table 3.1. Stable Cr isotopic compositions of all N-MORBs analyzed in this study range from -0.278 to -0.186 ‰,

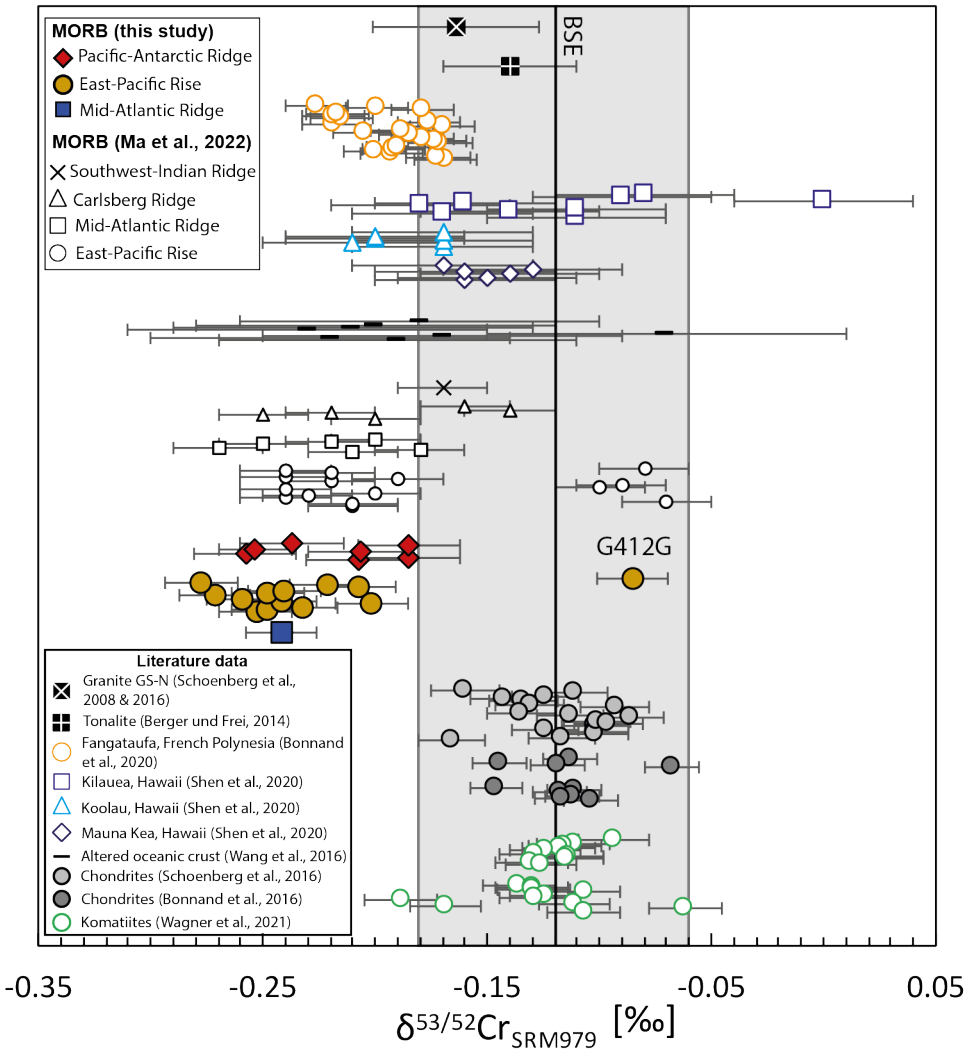

Figure 3.3: Compilation of Cr isotope compositions of MORBs from this study and Ma et al. (2022). Also shown are literature data of one granite (i.e., rock reference material GS-N; Schoenberg et al., 2016; Schoenberg et al., 2008), one tonalite (Berger and Frei, 2014) as well as oceanic basalts from different localities such as Hawaii (Shen et al., 2020), Fangataufa (French Polynesia; Bonnand et al., 2020b) and altered oceanic crust (Wang et al., 2016). For comparison, komatiite data (green open circles) defining the Cr isotope value of the Bulk Silicate Earth (BSE) of -0.12 $\pm$0.06 ‰ (indicated by the grey field; Wagner et al., 2021) and Cr isotope compositions of ordinary and carbonaceous chondrites published by Schoenberg et al. (2016) and Bonnand et al. (2016) are also shown. Error bars for MORBs in this study display the 2SD external reproducibility for pooled ($\delta^{53/52}$Cr = $\pm$0.016 ‰ and $\delta^{56/54}$Fe = $\pm$0.015 ‰) or single measurements ($\delta^{53/52}$Cr = $\pm$0.023 ‰ and $\delta^{56/54}$Fe = $\pm$0.038 ‰; Table 3.1) of standard reference materials BHVO-2 ($\delta^{53/52}$Cr) and Tueb-Fe ($\delta^{56/54}$Fe); see Appendix B for details.

spanning Cr contents ranging from 20 to 411 μg g^{-1} (Figures 3.2a, 3.3 and 3.4a, b). The $\delta^{53/52}$Cr values of the EPR N-MORB glasses range from -0.202 to -0.278 ‰ with an average of -0.242 $\pm$0.047 ‰ (2SD, n=12). Sample G412G (T-MORB composition) exhibits a $\delta^{53/52}$Cr value of -0.085 $\pm$0.024 ‰ (2SD, n=9; three digests), and shows a resolvable offset to the average $\delta^{53/52}$Cr of the EPR N-MORBs. The PAR N-MORB glasses display $\delta^{53/52}$Cr values ranging from -0.186 to -0.258 ‰, with an average of -0.225 $\pm$0.058 ‰ (2SD, n=6), which is identical within uncertainty to the average $\delta^{53/52}$Cr value of EPR N-MORBs. The southern and northern sections of

the PAR (PAC1 and PAC2) are identical within uncertainty displaying averages of -0.217 ± 0.074 ‰ (2SD, n=3) and -0.221 ± 0.061 ‰ (2SD, n=4), respectively. The most evolved PAR sample (PAC2-Dr27-1; MgO = 4.52 wt. %) exhibits a $\delta^{53/52}$Cr value of -0.185 ± 0.011 ‰ (2SE, n=1), representing the heaviest $\delta^{53/52}$Cr within the PAR suite. The N-MORB from the slow-spreading MAR (267ROV-5) displays a $\delta^{53/52}$Cr value of -0.242 ± 0.010 ‰ (2SD, n=7, two digests), identical within uncertainty to EPR and PAR average $\delta^{53/52}$Cr values. The Cr isotope compositions of fresh MORB glasses from this study match very well the recently reported $\delta^{53/52}$Cr values for MORBs ranging from -0.27 to -0.14 ‰ (n=24; Ma et al., 2022), in particular for MORBs from the EPR and MAR. Ma et al. (2022) observed a group of EPR MORBs with $\delta^{53/52}$Cr values between -0.10 to -0.07 ‰ (n=4). Interestingly, our dataset validates the observed $\delta^{53/52}$Cr bimodality of EPR MORBs (Ma et al., 2022), in which T-MORB sample G412G displays a similar $\delta^{53/52}$Cr value within uncertainty (-0.085 ± 0.024 ‰; 2SD, n=9, 3 digests). Furthermore, the Cr isotope compositions of fresh MORB glasses from this study overlap with previously reported $\delta^{53/52}$Cr values for altered oceanic crust from ODP hole 771 ranging from -0.23 to -0.07 ‰ (Figure 3.3; Wang et al., 2016).
All N-MORBs (i.e., T-MORB samples G412G and PAC2-Dr27-1 are excluded) show a significant offset towards lighter $\delta^{53/52}$Cr values with an average of -0.237 ± 0.050 ‰ (2SD, n=19) when compared to the komatiite-based $\delta^{53/52}$Cr BSE value of -0.12 ± 0.06 ‰ (Wagner et al., 2021) and $\delta^{53/52}$Cr values of ordinary and carbonaceous chondrites of -0.119 ± 0.045 ‰ (n=18; Schoenberg et al., 2016) and -0.115 ± 0.043 ‰ (n=10; Bonnand et al., 2016). MORBs exhibit lighter $\delta^{53/52}$Cr than OIBs from Mauna Kea and Kilauea Iki, Hawaii, but overlap with basalts from Koolau, Hawaii, and Fangataufa island ranging from -0.21 to -0.17 ‰ and from -0.226 to -0.169 ‰, respectively (Figure 3.3; Bonnand et al., 2020b; Shen et al., 2020).
Stable Fe isotopic compositions of EPR N-MORBs range from +0.032 to +0.123 ‰ and for PAR N-MORBs from +0.076 to +0.137 ‰ (Figure 3.4c, d). The average $\delta^{56/54}$Fe of the EPR N-MORBs (+0.086 ± 0.065 ‰; 2SD, n=12) is identical within uncertainty to the average $\delta^{56/54}$Fe of the PAR N-MORBs (+0.102 ± 0.042 ‰; 2SD, n=6). Similarly, the average $\delta^{56/54}$Fe of the two PAR sections are indistinguishable: +0.093 ± 0.060 ‰ (2SD, n=4) for the northern section and +0.105 ± 0.011 ‰ (2SD, n=3) for the southern section. MORB glasses from the EPR and PAR with T-MORB compositions show indistinguishable $\delta^{56/54}$Fe values compared to N-MORBs: +0.088 ‰ and +0.072 ‰, respectively. The MAR N-MORB (267ROV-5) displays a $\delta^{56/54}$Fe of +0.051 ‰. The range observed for all MORBs in this study (from +0.032 to +0.137 ‰; n=21) is largely identical to previously published MORB data (ranging from +0.050 to +0.190 ‰; average $\delta^{56/54}$Fe = +0.107 ± 0.055 ‰; 2SD, n=119; Chen et al., 2019; Richter et al., 2021; Teng et al., 2013; Weyer and Ionov, 2007) and systematically heavier than the BSE $\delta^{56/54}$Fe value of ∼ +0.02 ± 0.03 ‰ (Weyer and Ionov, 2007).

3.5 Discussion

Fresh MORB glasses investigated in this study show significantly lighter $\delta^{53/52}$Cr values than BSE (Figures 3.3, 3.4a, b; Jerram et al., 2020; Sossi et al., 2018; Wagner et al., 2021; Xia et al., 2017). Multiple processes may lead to the observed deviation, including partial melting and magmatic differentiation, which are discussed in the

following sections. Low-temperature seafloor alteration can be ruled out for EPR samples due to the fresh state of the volcanic glasses investigated here. In contrast, PAR glasses have been shown to be influenced by hydrothermal brines as well as assimilation of altered crust (comprising sulfides) leading to an increase in Cl/K ratios and δ^{34}S, respectively (Clog et al., 2013; Labidi et al., 2014). The effect of both processes on D/H ratios as well as stable Mo and Se isotopes is negligible (Bezard et al., 2016; Clog et al., 2013; Yierpan et al., 2019) and, as discussed in the Supplementary Material (Appendix B), does not affect stable Cr or Fe isotopes.

3.5.1 Potential effect of magmatic differentiation

Investigation of fresh glasses enables us to evaluate the role of fractional crystallization on Cr and Fe isotopes as they represent quenched melts and are unaffected by potential phenocryst accumulation. In particular, basalts from the superfast-spreading to intermediate-spreading ridges of the EPR and PAR are well suited to test the effect of fractional crystallization on the $\delta^{53/52}$Cr of MORBs as they are characterized by a robust melt supply beneath the axial high into shallow melt lenses within a crystal mush (e.g., Herzberg, 2004; Sinton and Detrick, 1992). Thus, MORBs generated at fast-spreading ridges are generally thought to produce a broader range of compositions by fractional crystallization with a larger proportion of evolved liquids than in slow-spreading ridges (Rubin and Sinton, 2007). This is indeed evident from the wide range of MgO concentrations of EPR and PAR glasses (4.87 to 9.00 and 4.52 to 8.57 wt. %, respectively; Figure 3.2), which display well-defined liquid lines of descent that are consistent with shallow level fractionation of olivine, plagioclase and clinopyroxene (Bach et al., 1994), typical for MORB magmas (Bryan, 1983). Furthermore, the PAR suite offers the unique opportunity to investigate the impact of Fe-Ti oxide crystallization, which only forms late in the MORB crystallizing sequence and is exemplified in three PAR samples (Figure 3.2; Hamelin et al., 2010; Labidi et al., 2014; Yierpan et al., 2019). In detail, olivine and plagioclase fractionation are evident from the decrease of Ni and Al_2O_3 with decreasing MgO (Figure 3.2d), respectively (Bach et al., 1994; Hamelin et al., 2010; Vlastelic et al., 2000). Clinopyroxene joins the fractionating assemblage at ~ 8 wt. % MgO as shown by the decrease in CaO content (Figure 3.2b) and CaO/Al_2O_3 ratios, especially visible for the EPR sample suite (Bach et al., 1994; Sinton et al., 1991). The steep positive correlation between Cr and MgO indicates the compatible behavior of Cr, which partitions into crystallizing clinopyroxene and possibly Cr-spinel before the melts reach Fe-Ti oxide saturation (at MgO < 5 wt. %; Figure 3.2a). Cr-spinel usually crystallizes very early during differentiation, commonly alongside olivine. Experimental studies have shown that at low pressure, Cr-spinel disappears as a liquidus phase when clinopyroxene joins the crystallizing assemblage (Feig et al., 2010; Hill and Roeder, 1974). The PAR samples with MgO < 5 wt. % have experienced titanomagnetite fractionation, as evidenced by a pronounced decrease in TiO_2 and FeO_{total} contents (Figure 3.2c; Hamelin et al., 2010; Labidi et al., 2014; Vlastelic et al., 2000; Yierpan et al., 2019).
The effect of magmatic differentiation on the $\delta^{56/54}$Fe is well-known and attributed to differences in bond strengths between silicate melts and minerals (Schauble, 2004). Generally, the incorporation of the isotopically light Fe^{2+} into olivine and clinopyroxene is expected to increase Fe^{3+} in the residual melt and thus, result in a melt

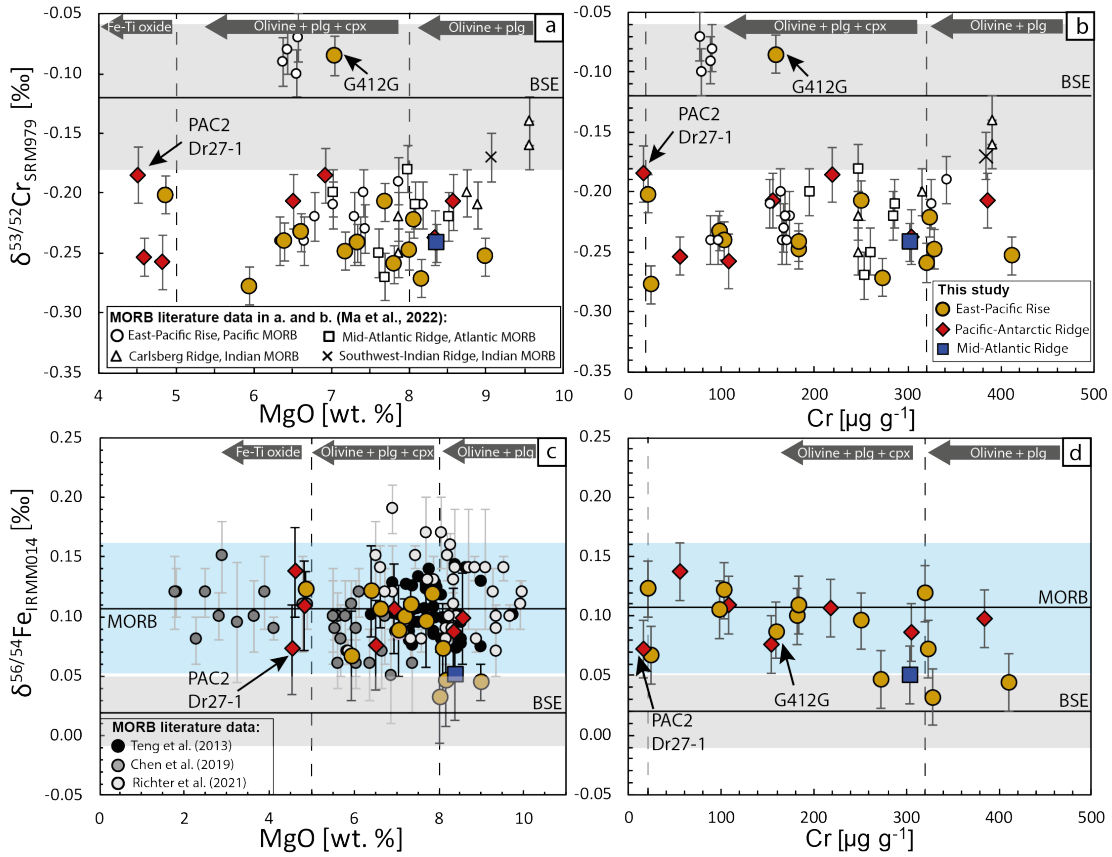

Figure 3.4: Stable Cr isotope compositions ($\delta^{53/52}$Cr) vs. **a)** MgO and **b)** Cr concentrations as well as stable Fe isotope compositions ($\delta^{56/54}$Fe) vs. **c)** MgO and **d)** Cr concentrations. In a) and b) the Bulk Silicate Earth (BSE) $\delta^{53/52}$Cr range is indicated by the grey field and equal to -0.12 $\pm$ 0.06 ‰ (2SD; Wagner et al., 2021). Also shown are $\delta^{53/52}$Cr data of MORBs published by Ma et al. (2022) with the same symbols as used in Figures 3.1-3.3. In c) and d) the BSE $\delta^{56/54}$Fe range as indicated by the grey field and equal to +0.02 $\pm$ 0.03 ‰ (Weyer and Ionov, 2007), whereas the light blue field indicates the $\delta^{56/54}$Fe range for mid-ocean ridge basalts compiled from the literature and equal to +0.107 $\pm$ 0.055 ‰ (n=119; Chen et al., 2019; Richter et al., 2021; Teng et al., 2013; Weyer and Ionov, 2007). Literature MORB $\delta^{56/54}$Fe values with corresponding 2SD reproducibility are shown in c) as black (Teng et al., 2013), grey (Chen et al., 2019) and light grey circles (Richter et al., 2021). The inferred fractional crystallization assemblages for EPR and PAR MORBs from this study is indicated on top of each panel. Stippled lines in a) and c) at 8 wt. % MgO indicate the change of the crystallizing phase assemblage from olivine + plagioclase to olivine + plagioclase + clinopyroxene. This change corresponds to ~320 μg g^{-1} Cr content in b) and d) taken from Figure 3.2a. Stippled lines in a) and c) at 5 wt. % MgO and in b) and d) at ~20 μg g^{-1} Cr indicate the onset of Fe-Ti oxide crystallization for, in particular, the three most differentiated PAR samples. Note the increasing Cr content during Fe-Ti oxide crystallization in Figure 3.2a. Error bars on Cr and Fe isotope measurements for MORBs in this study as in Figure 3.3 (see Appendix B for details). Plg = plagioclase, cpx = clinopyroxene.

with higher $\delta^{56/54}$Fe values. The effect of Fe-Ti oxide fractionation on the $\delta^{56/54}$Fe of the residual melt depends on the composition of the oxides. If the crystallizing Fe-Ti oxide is mineralogically close to magnetite, $\delta^{56/54}$Fe of the residual melt should decrease (Shahar et al., 2008), as shown for MORBs from the EPR at 10° 30' N (Chen et al., 2019). By contrast, the fractionation of ulvöspinel-rich titanomagnetite can increase the $\delta^{56/54}$Fe of the residual melt (Schuessler et al., 2009). Consistent with the fractionation caused by crystallization of Mg-Fe silicates, the most primitive MORBs display the lowest $\delta^{56/54}$Fe (Figure 3.4c, d). However, there is no tight

trend of increasing $\delta^{56/54}$Fe values with decreasing MgO contents within the EPR MORBs, and the PAR MORBs affected by clinopyroxene or Fe-Ti oxide cannot be distinguished within uncertainty. The lack of a clear fractional crystallization-related signature in Fe isotopes agrees with the rather uniform $\delta^{56/54}$Fe variations for global MORBs irrespective of the degree of magmatic differentiation as reported by Teng et al. (2013).

The impact of magmatic differentiation on $\delta^{53/52}$Cr of MORBs derived from a continuous ridge and displaying similar liquid lines of descent in major element variation diagrams (Bach et al., 1994; Hamelin et al., 2010; Mahoney et al., 1994; Vlastelic et al., 2000), has not yet been investigated in detail. The average $\delta^{53/52}$Cr values of samples in this study possibly affected by Cr-spinel crystallization (8 wt. % < MgO wt. % < 9 wt. %) and samples affected by clinopyroxene crystallization (5 wt. % < MgO < 8 wt. %) are identical within uncertainties (-0.240 ± 0.046 ‰, n=6, and -0.219 ± 0.108 ‰, n=10, respectively; Figure 3.4a). If T-MORB G412G with a MgO content of 7.05 wt. % is excluded from the average $\delta^{53/52}$Cr, a much lower variability for samples with MgO contents between 5 and 8 wt. % is obtained ($\delta^{53/52}$Cr = -0.233 ± 0.058 ‰, n=9). The relatively heavy Cr isotopic composition of this sample compared to the rest of N-MORBs in this study is similar to a group of EPR MORBs recently published by Ma et al. (2022) displaying an average $\delta^{53/52}$Cr of -0.09 ± 0.03 ‰ (2SD, n=4) (Figures 3.3, 3.4). This apparent bimodal $\delta^{53/52}$Cr distribution within EPR-MORBs is further discussed in Section 3.5.4. In general, the absence of systematic correlations between $\delta^{53/52}$Cr and MgO or Cr contents indicates that fractional crystallization has a negligible control on the $\delta^{53/52}$Cr variations of EPR and PAR MORBs. Although theory predicts lower $\delta^{53/52}$Cr values for olivine compared to the melt (Berry et al., 2021a; Shen et al., 2020), measurements of Archean komatiitic rock suites have shown that large ranges of olivine accumulation or fractionation do not induce any $\delta^{53/52}$Cr variations (Wagner et al., 2021). The overall lower Cr concentration in olivine in mafic systems and the uniform $\delta^{53/52}$Cr observed during MORB differentiation for a range of MgO contents between 4.52 and 9.00 wt. % in this study support the negligible impact of olivine-induced Cr isotopic fractionation.

The limited effect of clinopyroxene and Cr-spinel crystallization during MORB differentiation on the $\delta^{53/52}$Cr reported here (Figure 3.4a, b) needs to be further explored, as it contrasts with recent studies. Observations from Archean komatiitic rocks suites (Wagner et al., 2021), OIBs from Fangataufa (Bonnand et al., 2020b), Kilauea Iki lava lake, Hawaii (Shen et al., 2020), and recently MORBs from various ocean basins (Ma et al., 2022), showed a general decrease in $\delta^{53/52}$Cr with decreasing MgO, which was attributed to the crystallization of isotopically heavy Cr-spinel dominating the Cr budget. However, the extent of Cr-spinel crystallization is much higher (e.g., up to 5 % in Fangataufa basalts; Bonnand et al., 2020b) in these samples when compared to MORBs as indicated from their MgO content ranges (e.g., from ∼ 8 to 18 wt. % for komatiitic basalts or from ∼ 8 to 11.5 wt. % for Hawaiian basalts). In fact, the absence of negative correlations between $\delta^{53/52}$Cr and MgO or Cr contents argues for the negligible amounts of Cr-spinel on the liquidus of EPR and PAR MORBs for the range of MgO contents of samples from this study. Hence, variations in Cr concentrations are rather attributed to clinopyroxene crystallization. These observations are similar to those emerging from cumulate rocks resulting from magmatic differentiation of MORB such as gabbros (olivine, plagioclase and clinopy-

roxene) or troctolites (olivine and plagioclase). Whereas the former generally have low modal Cr-spinel abundance (White and Klein, 2014), the latter often contain Cr-spinel but rarely occur in the lower oceanic crust (Hekinian et al., 1993; MacLeod et al., 2017; Perk et al., 2007). It is noteworthy, that two samples from the slow-spreading Carlsberg Ridge (MgO = 9.56 to 9.57 wt. %) and one sample from the ultraslow-spreading Southwest Indian Ridge (SWIR; MgO = 9.07 wt. %) reported by Ma et al. (2022) exhibit $\delta^{53/52}$Cr values in the BSE range (Figures 3.4a, b). Ma et al. (2022) interpreted these samples to represent the $\delta^{53/52}$Cr value of the parental melt of all MORBs in their study. Compared to the lower $\delta^{53/52}$Cr of MORBs from ridge segments with slow- to fast-spreading rates (i.e., Carlsberg Ridge, MAR and EPR; Ma et al., 2022), the resulting trend with MgO was used as evidence of a fractional crystallization control on $\delta^{53/52}$Cr for global MORBs (i.e., MORBs derived from various ocean basins). As noted above the three samples largely defining this trend are, however, derived from the Carlsberg Ridge and SWIR, both sampling an Indian-type MORB mantle source that potentially influences the $\delta^{53/52}$Cr of these samples (see also Section 3.5.4). Moreover, our most primitive EPR MORB (sample G128G, MgO = 9.00 wt. % and Mg# = 0.65; calculated on molar oxide basis) displays a $\delta^{53/52}$Cr value of -0.253 ‰, significantly lower than the sample from the ultraslow-spreading SWIR with a $\delta^{53/52}$Cr value of -0.17 ‰ at very similar MgO content of 9.07 wt. % (Figure 3.4a; Ma et al., 2022). These contrasting values may suggest that a fractional crystallization control on $\delta^{53/52}$Cr during MORB differentiation, proposed to induce a decrease in $\delta^{53/52}$Cr with increasing degree of magmatic differentiation, may not be globally encountered as recently suggested by Ma et al. (2022).

For the EPR glasses with MgO concentrations < 7.5 wt. %, the proportions of crystallizing liquidus phases have been shown to vary little, and, as augitic pyroxene makes up 40 % of the crystallizing phases by mass (Bach et al., 1994), this indicates that clinopyroxene crystallization dominates the Cr budget of the EPR MORBs. On the other hand, the impact of pyroxene crystallization on the $\delta^{53/52}$Cr of MORBs may be composition-dependent. The crystallization of Al-rich pyroxenes, typically observed for komatiitic suites, enhances the partitioning of Cr^{3+} into the crystal lattice due to charge balance effects (Mallmann and O'Neill, 2009; Papike et al., 2005), contributing to the overall decrease in $\delta^{53/52}$Cr with decreasing MgO observed in komatiitic basalts (Wagner et al., 2021). However, pyroxenes crystallizing at low pressures from MORB magmas are commonly Ca-pyroxenes and augitic in composition, so the substitution of Cr^{2+} for Ca^{2+} in the 6-8 coordinated M2 site may be prevalent (Shen et al., 2018). Nevertheless, as Cr^{2+} is approximately one order of magnitude less compatible in pyroxenes than Cr^{3+}, experimentally determined at 1300° C and 1 bar (Mallmann and O'Neill, 2009), Cr isotopic fractionation due to the incorporation of Cr^{2+} into pyroxene is rather limited. This also agrees with calculated isotopic differences between clinopyroxene and melt of +0.046 ‰ in $\delta^{53/52}$Cr (Shen et al., 2018).

So far, pressure-dependent Cr isotope fractionation during clinopyroxene fractional crystallization has not been confirmed experimentally. However, this process may account for the variations between $\delta^{53/52}$Cr and MgO observed for MORBs from different ridges, as different average crystallizing pressures are inferred for fast-spreading compared to slow-spreading ridges. For example, crustal pressures corresponding to $\sim$ 0.2 GPa were inferred for the EPR (Bach et al., 1994) compared to crystalliza-

tion pressures ranging from 0.4 to 0.8 GPa for the slow-spreading Carlsberg Ridge (Zong et al., 2020). Furthermore, differences in crystallizing pressures may involve different liquid lines of descent, as exemplified by the contrasting modeled fractional assemblages of the EPR suite provided by Bach et al. (1994) (Figure 3.2) compared to the one modeled by Ma et al. (2022). In the latter, the most primitive MORB from the slow-spreading Carlsberg Ridge was set as a parental melt from which spinel and clinopyroxene were the first phases to crystallize, followed by plagioclase and then olivine (Ma et al., 2022).
Finally, compared to the most primitive samples from all three ridge sections, the PAR samples affected by Fe-Ti oxide crystallization cannot be distinguished in $\delta^{53/52}$Cr within uncertainty. The characteristic decrease of Fe and Ti contents is accompanied by an increase in Cr (Figure 3.2a), Al_2O_3 (Figure 3.2d), and SiO_2 content (not shown). Sample PAC1-Dr10-1g, which exhibits the highest degree of Fe-Ti oxide fractionation, shows the highest Cr content of all samples with MgO < 5 wt. %, indicating that Cr does not partition heavily into Fe-Ti oxides and is in agreement with compositions reported for Fe-Ti oxides typical for MORBs (Barnes and Roeder, 2001).
Ultimately, MORB differentiation is likely more complex than simple closed-system fractional crystallization and may instead be controlled by magma recharge, mixing, and subsequent crystallization processes, in addition to melt-rock reactions induced by replenishment and porous flow of melt through a crystal mush (Coogan and Dosso, 2016; Lissenberg and MacLeod, 2016). Indeed, when plotted versus Zr, the Cr concentrations of EPR MORBs (not shown) do not display the tight hyperbolic trend predicted for fractional crystallization but instead display considerable scatter, which could point to mixing or other open-system processes (Bach et al., 1994). It should be further noted that EPR MORBs represent derivatives of similar, primary magmas at various stages of differentiation along similar liquid lines of descent (Bach et al., 1994). Therefore, mixing of magmas at various stages of differentiation might mask a systematic relationship between MgO and $\delta^{53/52}$Cr. However, we would like to reiterate that the most primitive sample in our study (G128G; MgO = 9.00 wt. %) displays one of the lowest $\delta^{53/52}$Cr value of -0.253 ‰ and thus suggests that neither fractional crystallization nor mixing can account for the light Cr isotope signature. Here, we propose that the consistently light $\delta^{53/52}$Cr signature of MORBs in this study over a large range of MgO concentrations points at a source-related process that controls the Cr isotope composition of MORBs.

3.5.2 Influence of partial melting of a lherzolitic source on $\delta^{53/52}$Cr of MORBs

Chromium isotopic fractionation during partial melting has been predicted by model calculations, where light Cr isotopes are preferentially incorporated into the melt (Shen et al., 2018; Shen et al., 2020). These variations would be dependent on the fO_2 of the source and the degree of partial melting (Shen et al., 2018; Shen et al., 2020), similar to predictions made for Fe isotopic fractionation (Dauphas et al., 2009). Partial melting was proposed to explain Cr isotopic variations of OIBs (Bonnand et al., 2020b) and peridotites (Xia et al., 2017). However, theoretical calculations indicate that the partial melting induced $\delta^{53/52}$Cr variations in the source are currently below the detection limit (Jerram et al., 2022).

The $\delta^{53/52}$Cr data of all N-MORBs from three different ridge sections (MAR, EPR and PAR) yield an average of -0.237 $\pm$ 0.050 ‰ (2SD; n=19), which is below the BSE Cr isotopic value of -0.12 $\pm$ 0.06 ‰ (Figure 3.3; Wagner et al., 2021) and as such, supports preferential enrichment of the light Cr isotopes in a resulting partial mantle melt. In general, MORBs are generated via decompression partial melting of a depleted peridotite source at $\sim$ 1350° C and depths < 60 km, corresponding to pressures < 2 GPa in the spinel stability field (Lee et al., 2009). The major host minerals for Cr in the MORB source are spinel, clinopyroxene and orthopyroxene (Mallmann and O'Neill, 2009). Although the modal abundance of spinel is low, its high Cr concentration makes it a mineral phase as crucial as clino- and orthopyroxene in controlling the Cr budget during partial melting. Furthermore, the non-modal nature of partial peridotite melting, with clinopyroxene being preferentially consumed (Hirschmann et al., 1998), makes the mineral-melt specific isotopic fractionation critical for the resulting Cr isotopic compositions of residual peridotites and corresponding melts.

Consequently, a non-modal melting model in the spinel-stability field is applied to quantify the effect of partial melting during MORB genesis on the Cr isotopic composition of the melt and to test if it can account for the lower $\delta^{53/52}$Cr value of MORBs compared to the BSE. For this, a simplified model of isothermal decompression melting (1350° C and starting pressures of 2.0 GPa) using the thermodynamic model pMELTS (Ghiorso et al., 2002) was applied to a source with a DM-like starting composition (Salters and Stracke, 2004). The resulting mineral modes were used to calculate Cr concentrations of the melt and residue and, ultimately, the Cr isotopic compositions of the melt during batch and accumulated fractional melting for melting degrees from 1 to 20 %. Partition coefficients between minerals and melt were assumed to be constant with ongoing melting (Mallmann and O'Neill, 2009). The Cr isotope composition of the source was set at $\delta^{53/52}$Cr = -0.12 ‰ (Wagner et al., 2021). The equilibrium mineral-melt isotopic differences ($\Delta^{53/52}Cr_{mineral-melt}$) are from Shen et al. (2020) for a melt Cr^{2+}/Cr_{total} ratio of 0.55, and from Berry et al. (2021a) for a melt Cr^{2+}/Cr_{total} ratio of 0.50 determined for temperatures of 1150° C. As mantle melting usually occurs at higher temperatures (1350° C; see above), the calculated isotopic fractionations (see below) represent upper estimates. The calculated isotopic difference between source and melt ($\Delta^{53/52}Cr_{source-melt}$) decreases with increasing degree of melting and is thus highest at low melting degrees (i.e., $\sim$ 0.08 ‰ at 1 % melting using mineral-melt isotopic differences of Berry et al. (2021a) (Figure 3.5a). This is in agreement with previous model results (Jerram et al., 2022; Shen et al., 2020) as well as $\delta^{53/52}$Cr compositions of natural samples representing low- and high-degree partial melts (Bonnand et al., 2020b; Jerram et al., 2020; Wagner et al., 2021). The magnitude of $\Delta^{53/52}Cr_{source-melt}$ obtained here is comparable to that of Jerram et al. (2022), but larger than model results at similar fO_2 conditions presented by Shen et al. (2020). Considering that Cr^{2+}/Cr_{total} ratios between 0.15 and 0.35 may be more realistic for MORB melts (Berry et al., 2021a), the modeled Cr isotopic fractionation during partial melting calculated in this study using $\Delta^{53/52}Cr_{mineral-melt}$ deduced from a melt Cr^{2+}/Cr_{total} of 0.55 and 0.50 (see above) represents an upper limit. The applied model is sensitive to source modal composition and Cr isotopic differences between minerals and melt due to the non-modal nature of partial melting. Hence, the greater Cr isotope fractionation during partial melting using mineral-melt isotopic differences by Berry et al. (2021a)

can be attributed to the larger $\Delta^{53/52}Cr_{spinel-melt}$ and $\Delta^{53/52}Cr_{clinopyroxene-melt}$ compared to estimates given by Shen et al. (2020) (Figure 3.5a, Supplementary Table B.3.1).

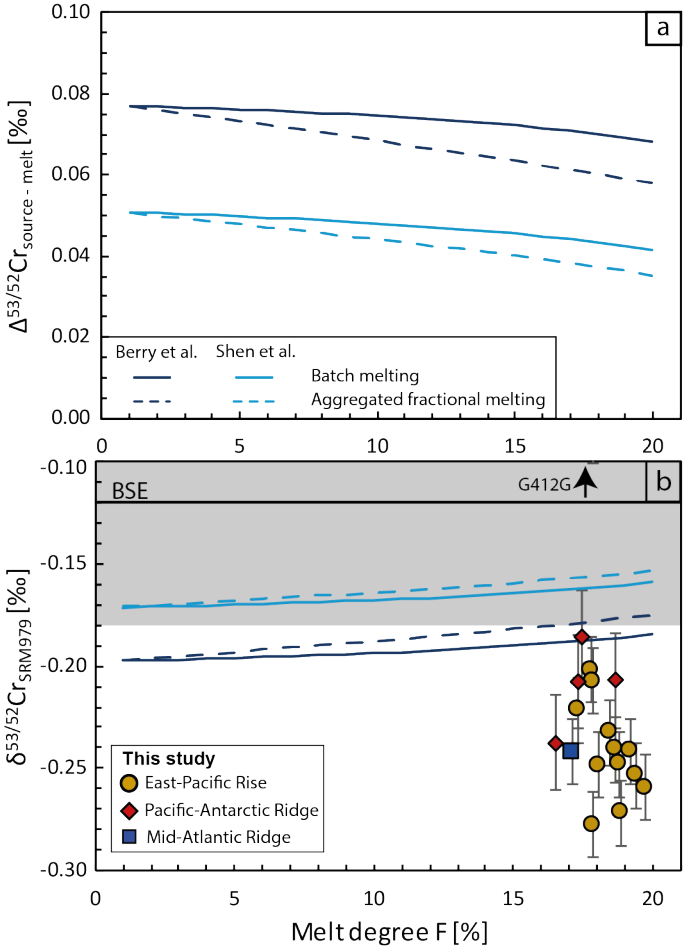

Figure 3.5: **a)** The modeled bulk isotopic differences between source and melt ($\Delta^{53/52}Cr_{source-melt}$) varies with melting degree F. $\Delta^{53/52}Cr_{source-melt}$ are modeled using $\Delta^{53/52}Cr_{mineral-melt}$ by Shen et al. (2020) and Berry et al. (2021a) and are shown in light blue and dark blue, respectively. Only slight differences are seen between different melting models of batch and aggregated fractional melting within the first 20 % of partial melting due to the compatible behavior of Cr; **b)** Modeled chromium isotopic compositions ($\delta^{53/52}$Cr) of the melt are shown with varying melt degree. $\delta^{53/52}$Cr increases with increasing degree of melting and approaches the starting composition of -0.12 $\pm$ 0.06 ‰ representing the Bulk Silicate Earth (BSE) $\delta^{53/52}$Cr value (Wagner et al., 2021). Melting degree for MORBs from this study with MgO $>$ 5 wt. % are calculated after Niu and Batiza (1991). Sample PAC1-Dr06-g from the Pacific-Antarctic Ridge fits on the trend of the partial melting model, whereas the majority of MORBs is significantly lighter compared to the modeled $\delta^{53/52}$Cr. A more detailed outline of the partial melting model is given in Appendix B.

Except for the PAR sample PAC1-Dr06-g, most of the analyzed MORBs display significantly lower $\delta^{53/52}$Cr values than the model predicts (Figure 3.5b). In this context, the slightly lower $\delta^{53/52}$Cr of OIBs compared to the BSE (Figure 3.3) have been interpreted to result from a combination of low-degree melting (Bonnand et al., 2020b) and more reducing melting conditions (Koolau, Hawaii; Shen et al., 2020). Due to their higher degrees of melting, this interpretation is difficult to reconcile

with the lower $\delta^{53/52}$Cr of MORBs compared to OIBs, suggesting an additional process that influences the Cr isotope composition of MORB and OIB melts other than partial melting.
The strong sensitivity to modal composition and associated mineral-melt fractionations, make the source mineralogy a key mediator of Cr isotope fractionation. Theoretical calculations by Jerram et al. (2022) showed that melting of garnet peridotite should generate heavier melts compared to spinel peridotite. Also, recent experimental studies report a strong effect of pressure on the Cr^{2+}/Cr_{total} ratio of partial melts, which decreases with increasing melting pressure and is zero at depths $>$ 60 km (Berry et al., 2021b). In this context, our non-modal melting model of a spinel lherzolite at low pressures could account for a $\Delta^{53/52}Cr_{source-melt}$ of $\sim 0.08\,‰$ at 1 % melting degree. However, the isotopic difference between the inferred source and MORBs ($\Delta^{53/52}Cr_{source-melt}$) is on average 0.117 ‰ (up to 0.158 ‰), and thus by $\sim 0.05\,‰$ larger than the modeled $\Delta^{53/52}Cr_{source-melt}$ of only $\sim 0.066\,‰$ for an average MORB melting degree (F = 18 %) and under the model parameters outlined above.

3.5.3 Light $\delta^{53/52}$Cr as a result of mantle heterogeneity

As discussed in the previous sections, the offset of MORBs towards lower $\delta^{53/52}$Cr values compared to the BSE value and other basaltic suites investigated so far requires a process other than fractional crystallization (Section 3.5.1) or partial melting of a pure lherzolitic source (Section 3.5.2).
One way to lower the $\delta^{53/52}$Cr values of the melt is to lower the $\delta^{53/52}$Cr of the source. Based on the compatible behavior of Cr and the resulting Cr depletion in melts relative to the source, large amounts of Cr would be required to be extracted during partial melting to significantly impact the $\delta^{53/52}$Cr of the source based on mass balance considerations. This is supported by model results suggesting that melting degrees of up to 20 % do not significantly alter the $\delta^{53/52}$Cr of the source (Jerram et al., 2022), while large degree melts such as komatiites (Jerram et al., 2020; Sossi et al., 2018; Wagner et al., 2021) are equal to $\delta^{53/52}$Cr of chondrites (Bonnand et al., 2016; Schoenberg et al., 2016) and thus are representative of the BSE (Figure 3.3). Given that the light Cr isotopes are preferentially incorporated into a silicate melt, melt depletion would in fact result in an increase in $\delta^{53/52}$Cr in the residual source. Therefore, lowering the MORB source $\delta^{53/52}$Cr value by long-term melt depletion seems unlikely.
The large variations of $\delta^{53/52}$Cr reported in mantle xenoliths, including pyroxenite, suggest a certain, small-scale $\delta^{53/52}$Cr mantle heterogeneity (Jerram et al., 2022; Xia et al., 2017). A chemically and isotopically heterogeneous mantle has been proposed previously as part of the MORB source and has often been ascribed to a depleted peridotite source admixed with a pyroxenite component representing recycled oceanic crust (Allegre and Turcotte, 1986; Hamelin et al., 2011; Soderman et al., 2021; Soderman et al., 2022; Stracke, 2012; Stracke and Bourdon, 2009; Yang et al., 2020). Likewise, a lower stable Mo isotope composition of MORB compared to BSE has recently been attributed to oceanic crust recycling generating an upper mantle heterogeneity (Hin et al., 2022). A pyroxenite component in the MORB source will contribute significantly to the generation of primary melts and impact their $\delta^{53/52}$Cr due to its lower solidus and higher melt productivity compared to a pure peridotite

source (Lambart et al., 2016 and references therein). Although the available pyroxenite Cr isotope data are from pyroxenites formed by melt-peridotite interaction and thus do not represent recycled oceanic crust, their isotopic variations with $\delta^{53/52}$Cr values ranging from -1.36 ‰ to -0.05 ‰ (Jerram et al., 2022; Xia et al., 2017) suggest that mantle pyroxenites could be an additional/alternative source of light Cr isotopes, even in the source of MORBs. Moreover, a comprehensive equilibrium melting model exploring multiple isotope systems (Mg-Ca-V-Cr-Fe) showed that a pyroxenite component in the MORB source would significantly decrease $\delta^{53/52}$Cr and increase $\delta^{56/54}$Fe in the resulting melt compared to a pure peridotite source (Soderman et al., 2022). These calculations are based on mineral-melt specific fractionation factors, but also assume that the pyroxenite component exhibits an already fractionated isotopic composition compared to BSE, which is lower for $\delta^{53/52}$Cr and higher for $\delta^{56/54}$Fe, as it is expected to be derived from recycled MORB.

Similar to stable Cr isotopes, the Fe isotopic composition of MORB is offset from the BSE value ($\delta^{56/54}$Fe = $\sim$ +0.02 $\pm$ 0.03 ‰; Weyer and Ionov, 2007). The consistently heavier Fe isotope compositions of MORB have been mainly attributed to partial melting and fractional crystallization (Sossi et al., 2016; Weyer and Ionov, 2007; Williams et al., 2005). However, even after correction for fractional crystallization (Sossi et al., 2016), some MORB samples show a wide range of Fe isotope compositions that mantle melting models cannot explain (Soderman et al., 2022). Based on a quantitative model (combining thermodynamically self-consistent mantle melting and equilibrium isotope fractionation models), Soderman et al. (2022) show that the range of Fe isotope ratios of MORBs, in addition to Mg and possibly Cr isotope ratios, could be derived from equilibrium isotope fractionation during partial melting of a MORB source with a contribution of a pyroxenite component. These authors, however, also point out that disequilibrium and/or low-temperature processes may also be required to explain all the available stable isotopic data. We note here that some EPR MORBs and the MAR MORB display $\delta^{56/54}$Fe values that plot at the lower end of previously published MORBs (Figure 3.4c, d), whereas the remaining samples show $\delta^{56/54}$Fe values typical for N-MORB.

Despite the lack of published MORB data at the time, Soderman et al. (2022) predicted that partial melting of a source consisting of peridotite mixed with 40 % pyroxenite at potential temperatures of 1300° C could generate a melt with $\delta^{53/52}$Cr values that are up to 0.04 ‰ lower than pure lherzolithic peridotite melts. Although this offset could balance the isotopic difference between our peridotite melting model and the $\delta^{53/52}$Cr measured in MORBs (Section 3.5.2), the proportion of pyroxenite is exceptionally high compared to estimates based on major and trace element compositions ranging between 2 and 17 % (Lambart et al., 2016 and references therein). However, if the pyroxenite component in the MORB source has as light Cr isotope signature as that reported in pyroxenite veins (Jerram et al., 2022; Xia et al., 2017), no such high fractions of pyroxenite contribution would be needed to lower $\delta^{53/52}$Cr of the melt. A two-endmember mass balance calculation between the MORB PAC1-Dr06-g straddling the melting model (Section 3.5.2, Figure 3.5b) and two exemplary pyroxenites with $\delta^{53/52}$Cr of -1.36 ‰ and -0.77 ‰ (Xia et al., 2017) suggest that 1 to 2 % of pyroxenite mixed with the MORB melt is sufficient to account for the low $\delta^{53/52}$Cr values of MORBs in this study. Mixing with the pyroxenite P6 ($\delta^{53/52}$Cr = -0.35 ‰; Jerram et al., 2022) would increase the pyroxenite component to $\sim$ 20 %. More Cr isotope data for different pyroxenites lithologies are required to explore

further the type and magnitude of pyroxenite admixture in the source of MORBs.

3.5.4 Local vs. global signature of light $\delta^{53/52}$Cr of MORB

The light Cr isotopic compositions displayed by MORBs in this study are mostly derived from mid-ocean ridges representative of the sub-Pacific mantle domain (EPR and PAR). Although the MAR sample 267ROV-5 displays similarly low $\delta^{53/52}$Cr, as most of the recently published MORB data covering the Pacific-, Atlantic and Indian-type mantle (Ma et al., 2022), further investigation is needed to determine whether this light Cr isotope signature corresponds to a global $\delta^{53/52}$Cr signature. Based on radiogenic Sr-Nd-Hf-Pb isotope compositions, MORBs from the EPR and PAR are derived from a heterogeneous Pacific mantle consisting of variable amounts of recycled oceanic crust within a depleted mantle (Hamelin et al., 2011). A similar heterogeneous mantle has been proposed as the source for Atlantic MORBs (Debaille et al., 2006; Donnelly et al., 2004; Dosso et al., 1999; Hoernle et al., 2011; Paulick et al., 2010; Stracke et al., 2005) and is supported by the general array formed by Atlantic and Pacific MORBs between DM and PREMA (Figure 3.1; Stracke, 2012). In contrast, Indian-type MORBs show arrays in radiogenic isotope space, which deviate towards more radiogenic Sr isotopic compositions, indicative of an EM component (Figure 3.1; Dupré and Allègre, 1983; Escrig et al., 2004; Hamelin et al., 1986; Hanan et al., 2004; Hart, 1984; Nauret et al., 2006). When comparing the $\delta^{53/52}$Cr data of Pacific MORBs from this study (southern EPR and PAR) and those presented by Ma et al. (2022), it becomes evident that the Pacific MORBs display a homogenous $\delta^{53/52}$Cr, which is lighter than the BSE. Similar observations are made for Atlantic MORBs (sample 267ROV-5, this study) which, together with Atlantic MORBs from Ma et al. (2022) including two samples from the northern MAR, are indistinguishable from Pacific MORBs.
However, MORBs from the SWIR and Carlsberg Ridge, so far the only representative samples for Indian-type MORB, extend towards higher $\delta^{53/52}$Cr positioned in the BSE range (Figures 3.3 and 3.4a, b; Ma et al., 2022). It is noteworthy that these samples with $\delta^{53/52}$Cr values from -0.17 ‰ to -0.14 ‰ also display high MgO concentrations (9.07 to 9.57 wt. %, n=3; Figure 3.4a, b), and the most primitive sample (MgO = 9.57 wt. %) was used as the parental melt for the fractional crystallization model in the study by Ma et al. (2022). This Cr isotopic signature is slightly higher than that of Pacific and Atlantic MORBs and mostly higher than the values predicted by < 10 % partial melting of a homogenous peridotitic source (Figure 3.5). A study featuring three identical Carlsberg Ridge samples (CR01-1, CR02-1, CR03-1) to the ones used by Ma et al. (2022) has identified a heterogeneous source for Carlsberg Ridge MORBs and, based on radiogenic Sr-Nd-Pb isotopic compositions, suggested that this source consists of DM and a upper continental crust component (Chen et al., 2017). Moreover, except for sample CR03-1 (Ma et al., 2022), MORBs from the Carlsberg Ridge display a correlation between $\delta^{53/52}$Cr and ^{87}Sr/^{86}Sr, which can be taken as evidence for a source-related process controlling the $\delta^{53/52}$Cr of Carlsberg Ridge MORBs. We thus suggest that the source of Carlsberg Ridge MORBs exhibits an initially heavier $\delta^{53/52}$Cr, which may be related to the EM component distributed within the Indian MORB source mantle (e.g., Hamelin et al., 1986).
The four EPR MORBs reported by Ma et al. (2022) with an average $\delta^{53/52}$Cr of -0.09

± 0.03 ‰ (2SD, n=4) and derived from 3.10983° S; 102.54462° W (Chen et al., 2020) are remarkably similar to the $\delta^{53/52}$Cr of T-MORB G412G from this study (-0.85 ± 0.024 ‰; n=9, 3 digests) and suggest a non-arbitrary process that accounts for the relatively high $\delta^{53/52}$Cr values. However, the high K/Ti ratio of T-MORB G412G (= 0.14) that has been attributed to a K-rich source heterogeneity and inferred for many T-MORBs from the EPR (Bach et al., 1994; Mahoney et al., 1994; Sinton et al., 1991) is in contrast to the low K/Ti (< 0.08) of the four EPR MORBs reported by Ma et al. (2022). Furthermore, MORBs from 3.1° S have been explained by a highly depleted mantle component within a heterogeneous mantle (Li et al., 2020). Therefore, the cause for the observed local $\delta^{53/52}$Cr bimodality in EPR MORBs remains ambiguous and requires further examination of MORBs with endmember chemical compositions.

3.6 Conclusions

In this study, we show that the Cr isotope composition of N-MORB glasses, with an average of -0.237 ± 0.050 ‰ (n=19), displays a significant offset compared to the $\delta^{53/52}$Cr BSE value of -0.12 ± 0.06 ‰. Variations in $\delta^{53/52}$Cr within the sample set cannot be attributed to fractional crystallization- or alteration-induced isotopic fractionation. In addition, conducted models show that the clear offset towards lower values cannot be produced by decompression partial melting of a source alike the depleted mantle. Based the proposed sensitivity of stable Cr isotopes to source mineralogy, especially in the presence of pyroxenites (Soderman et al., 2022), plus the low $\delta^{53/52}$Cr values of down to -1.36 ‰ of pyroxenitic veins in lithospheric mantle xenoliths (Jerram et al., 2022; Xia et al., 2017), we suggest that the lower $\delta^{53/52}$Cr values of MORBs may be linked to partial melting of a source with intrinsic small-scale heterogeneities in the form of pyroxene-rich domains. This is further supported by the variable $\delta^{56/54}$Fe values of MORBs, which extend towards higher $\delta^{56/54}$Fe values than expected for melting of a homogenous peridotite shown by previously published melting models and have been explained by a pyroxenite component (Soderman et al., 2022).

Acknowledgments

We thank Elmar Reitter and Bernd Steinhilber for technical support, Jabrane Labidi and Cedric Hamelin for providing samples from the Pacific-Antarctic Ridge and Juergen Koepke for providing sample 267ROV-5 from the Mid-Atlantic Ridge. Maria Kirchenbaur and Yierpan Airken are thanked for valuable discussions on the partial melting model. LJW acknowledges financial support from the German Research Foundation (DFG) grant [SCHO1071/9-1] funded to RS, and MIVR acknowledges funding from the DFG project [VA1568/1-1]. ERC Starting Grant project O2RIGIN [636808] and Ramón y Cajal contract RYC2020-030014-I to SK is acknowledged.

References

Allegre, C.J. and Turcotte, D.L. 1986. Implications of a 2-component marble-cake mantle. Nature. 323, 123-127.

Bach, W., Hegner, E., Erzinger, J. and Satir, M. 1994. Chemical and isotopic variations along the superfast spreading East Pacific Rise from 6 to 30° S. Contrib. Mineral. Petrol. 116, 365-380.

Bai, Y., Su, B.X., Xiao, Y., Chen, C., Cui, M.M., He, X.Q., Qin, L.P. and Charlier, E.N.R. 2019. Diffusion-driven chromium isotope fractionation in ultramafic cumulate minerals: Elemental and isotopic evidence from the Stillwater Complex. Geochim. Cosmochim. Ac. 263, 167-181.

Barnes, S.J. and Roeder, P.L. 2001. The range of spinel compositions in terrestrial mafic and ultramafic rocks. J. Petrol. 42, 2279-2302.

Berger, A. and Frei, R. 2014. The fate of chromium during tropical weathering: A laterite profile from Central Madagascar. Geoderma. 213, 521-532.

Berry, A.J., Miller, L.A., O'Neill, H.S.C. and Foran, G.J. 2021a. The coordination of Cr^{2+} in silicate glasses and implications for mineral-melt fractionation of Cr isotopes. Chem. Geol. 586, 120483.

Berry, A.J. and O'Neill, H.S.C. 2004. A XANES determination of the oxidation state of chromium in silicate glasses. Am. Miner. 89, 790-798.

Berry, A.J., O'Neill, H.S.C. and Foran, G.J. 2021b. The effects of temperature and pressure on the oxidation state of chromium in silicate melts. Contrib. Mineral. Petrol. 176, 40.

Berry, A.J., O'Neill, H.S.C., Scott, D.R., Foran, G.J. and Shelley, J.M.G. 2006. The effect of composition on Cr^{2+}/Cr^{3+} in silicate melts. Am. Miner. 91, 1901-1908.

Bezard, R., Fischer-Gödde, M., Hamelin, C., Brennecka, G.A. and Kleine, T. 2016. The effects of magmatic processes and crustal recycling on the molybdenum stable isotopic composition of Mid-Ocean Ridge Basalts. Earth Planet. Sc. Lett. 453, 171-181.

Bonnand, P., Bruand, E., Matzen, A.K., Jerram, M., Schiavi, F., Wood, B.J., Boyet, M. and Halliday, A.N. 2020a. Redox control on chromium isotope behaviour in silicate melts in contact with magnesiochromite. Geochim. Cosmochim. Ac. 288, 282-300.

Bonnand, P., Doucelance, R., Boyet, M., Bachelery, P., Bosq, C., Auclair, D. and Schiano, P. 2020b. The influence of igneous processes on the chromium isotopic compositions of Ocean Island basalts. Earth Planet. Sc. Lett. 532, 116028.

Bonnand, P., Williams, H.M., Parkinson, I.J., Wood, B.J. and Halliday, A.N. 2016. Stable chromium isotopic composition of meteorites and metal-silicate experiments: Implications for fractionation during core formation. Earth Planet. Sc. Lett. 435, 14-21.

Bryan, W. 1983. Systematics of modal phenocryst assemblages in submarine basalts: petrologic implications. Contrib. Mineral. Petrol. 83, 62-74.

Chen, C., Ciazela, J., Li, W., Dai, W., Wang, Z., Foley, S.F., Li, M., Hu, Z. and Liu, Y. 2020. Calcium isotopic compositions of oceanic crust at various spreading rates. Geochim. Cosmochim. Ac. 278, 272-288.

Chen, L., Tang, L., Yu, X. and Dong, Y. 2017. Mantle source heterogeneity and magmatic evolution at Carlsberg Ridge (3.7° N): constrains from elemental and isotopic (Sr, Nd, Pb) data. Mar. Geophys. Res. 38, 47-60.

Chen, S., Niu, Y.L., Guo, P.Y., Gong, H.M., Sun, P., Xue, Q.Q., Duan, M. and Wang, X.H. 2019. Iron isotope fractionation during mid-ocean ridge basalt (MORB) evolution: Evidence from lavas on the East Pacific Rise at 10° 30' N and its implications. Geochim. Cosmochim. Ac. 267, 227-239.

Clog, M., Aubaud, C., Cartigny, P. and Dosso, L. 2013. The hydrogen isotopic composition and water content of southern Pacific MORB: A reassessment of the D/H ratio of the depleted mantle reservoir. Earth Planet. Sc. Lett. 381, 156-165.

Coogan, L.A. and Dosso, S.E. 2016. Quantifying Parental MORB Trace Element Compositions from the Eruptive Products of Realistic Magma Chambers: Parental EPR MORB are Depleted. J. Petrol. 57, 2105-2126.

Dauphas, N., Craddock, P.R., Asimow, P.D., Bennett, V.C., Nutman, A.P. and Ohnenstetter, D. 2009. Iron isotopes may reveal the redox conditions of mantle melting from Archean to Present. Earth Planet. Sc. Lett. 288, 255-267.

Debaille, V., Blichert-Toft, J., Agranier, A., Doucelance, R., Schiano, P. and Albarede, F. 2006. Geochemical component relationships in MORB from the Mid-Atlantic Ridge, 22–35° N. Earth Planet. Sc. Lett. 241, 844-862.

DeMets, C., Gordon, R.G., Argus, D.F. and Stein, S. 1990. Current plate motions. Geophys. J. Int. 101, 425-478.

Donnelly, K.E., Goldstein, S.L., Langmuir, C.H. and Spiegelman, M. 2004. Origin of enriched ocean ridge basalts and implications for mantle dynamics. Earth Planet. Sc. Lett. 226, 347-366.

Dosso, L., Bougault, H., Langmuir, C., Bollinger, C., Bonnier, O. and Etoubleau, J. 1999. The age and distribution of mantle heterogeneity along the Mid-Atlantic Ridge (31–41° N). Earth Planet. Sc. Lett. 170, 269-286.

Dupré, B. and Allègre, C.J. 1983. Pb–Sr isotope variation in Indian Ocean basalts and mixing phenomena. Nature. 303, 142-146.

Escrig, S., Capmas, F., Dupré, B. and Allègre, C. 2004. Osmium isotopic constraints on the nature of the DUPAL anomaly from Indian mid-ocean-ridge basalts. Nature. 431, 59-63.

Feig, S.T., Koepke, J. and Snow, J.E. 2010. Effect of oxygen fugacity and water on phase equilibria of a hydrous tholeiitic basalt. Contrib. Mineral. Petrol. 160, 551-568.

Ghiorso, M.S., Hirschmann, M.M., Reiners, P.W. and Kress, V.C. 2002. The pMELTS: A revision of MELTS for improved calculation of phase relations and major element partitioning related to partial melting of the mantle to 3 GPa. Geochem. Geophys. Geosyst. 3, 5, 1-36.

Haase, K., Petersen, S., Koschinsky, A., Seifert, R., Devey, C.W., Keir, R., Lackschewitz, K., Melchert, B., Perner, M. and Schmale, O., et al. 2007. Young vol-

canism and related hydrothermal activity at 5° S on the slow-spreading southern Mid-Atlantic Ridge. Geochem. Geophys. Geosyst. 8, Q11002.

Hamelin, B., Dupré, B. and Allègre, C.J. 1986. Pb-Sr-Nd isotopic data of Indian Ocean ridges: new evidence of large-scale mapping of mantle heterogeneities. Earth Planet. Sc. Lett. 76, 288-298.

Hamelin, C., Dosso, L., Hanan, B., Barrat, J.A. and Ondreas, H. 2010. Sr-Nd-Hf isotopes along the Pacific Antarctic Ridge from 41 to 53° S. Geophys. Res. Lett. 37, L10303.

Hamelin, C., Dosso, L., Hanan, B.B., Moreira, M., Kositsky, A.P. and Thomas, M.Y. 2011. Geochemical portray of the Pacific Ridge: New isotopic data and statistical techniques. Earth Planet. Sc. Lett. 302, 154-162.

Hanan, B.B., Blichert-Toft, J., Pyle, D.G. and Christie, D.M. 2004. Contrasting origins of the upper mantle revealed by hafnium and lead isotopes from the Southeast Indian Ridge. Nature. 432, 91-94.

Hart, S.R. 1984. A large-scale isotope anomaly in the Southern Hemisphere mantle. Nature. 309, 753-757.

Hekinian, R., Bideau, D., Francheteau, J., Cheminee, J.L., Armijo, R., Lonsdale, P. and Blum, N. 1993. Petrology of the East Pacific Rise crust and upper manle exposed in Hess Deep (Eastern equatorial Pacific). J. Geophys. Res.-Sol. Ea. 98, 8069-8094.

Herzberg, C. 2004. Partial crystallization of mid-ocean ridge basalts in the crust and mantle. J. Petrol. 45, 2389-2405.

Hill, R. and Roeder, P. 1974. Crystallization of spinel from basaltic liquid as a function of oxygen fugacity. J. Geol. 82, 709-729.

Hin, R.C., Hibbert, K.E., Chen, S., Willbold, M., Andersen, M.B., Kiseeva, E.S., Wood, B.J., Niu, Y., Sims, K.W. and Elliott, T. 2022. The influence of crustal recycling on the molybdenum isotope composition of the Earth's mantle. Earth Planet. Sc. Lett. 595, 117760.

Hirschmann, M.M., Ghiorso, M.S., Wasylenki, L.E., Asimow, P.D. and Stolper, E.M. 1998. Calculation of peridotite partial melting from thermodynamic models of minerals and melts. I. Review of methods and comparison with experiments. J. Petrol. 39, 1091-1115.

Hoernle, K., Hauff, F., Kokfelt, T.F., Haase, K., Garbe-Schönberg, D. and Werner, R. 2011. On-and off-axis chemical heterogeneities along the South Atlantic Mid-Ocean-Ridge (5–11° S): shallow or deep recycling of ocean crust and/or intraplate volcanism? Earth Planet. Sc. Lett. 306, 86-97.

Jerram, M., Bonnand, P., Harvey, J., Ionov, D. and Halliday, A.N. 2022. Stable chromium isotopic variations in peridotite mantle xenoliths: Metasomatism versus partial melting. Geochim. Cosmochim. Ac. 317, 138-154.

Jerram, M., Bonnand, P., Kerr, A.C., Nisbet, E.G., Puchtel, I.S. and Halliday, A.N. 2020. The $\delta^{53}Cr$ isotope composition of komatiite flows and implications for the composition of the bulk silicate Earth. Chem. Geol. 551, 119761.

Labidi, J., Cartigny, P., Hamelin, C., Moreira, M. and Dosso, L. 2014. Sulfur isotope budget (^{32}S, ^{33}S, ^{34}S and ^{36}S) in Pacific-Antarctic ridge basalts: A record of mantle source heterogeneity and hydrothermal sulfide assimilation. Geochim. Cosmochim. Ac. 133, 47-67.

Lambart, S., Baker, M.B. and Stolper, E.M. 2016. The role of pyroxenite in basalt genesis: Melt-PX, a melting parameterization for mantle pyroxenites between 0.9 and 5GPa. J. Geophys. Res.-Sol. Ea. 121, 5708-5735.

Lee, C.T.A., Luffi, P., Plank, T., Dalton, H. and Leeman, W.P. 2009. Constraints on the depths and temperatures of basaltic magma generation on Earth and other terrestrial planets using new thermobarometers for mafic magmas. Earth Planet. Sc. Lett. 279, 20-33.

Li, W., Tao, C., Liang, J., Liao, S. and Yang, W. 2020. Heterogeneous mantle melting and magmatic processes at the East Pacific Rise (2.6–3.1°S): Evidence from mid-ocean ridge basalt geochemistry and Sr–Nd–Pb isotopes. Int. Geol. Rev. 62, 1387-1405.

Lissenberg, C.J. and MacLeod, C.J. 2016. A Reactive Porous Flow Control on Mid-ocean Ridge Magmatic Evolution. J. Petrol. 57, 2195-2219.

Liu, X. and O'Neill, H.S.C. 2004. The Effect of Cr_2O_3 on the partial melting of spinel lherzolite in the system CaO–MgO–Al_2O_3–SiO_2–Cr_2O_3 at 1.1 GPa. J. Petrol. 45, 2261-2286.

Ma, H., Xu, L.-J., Shen, J., Liu, S.-A. and Li, S. 2022. Chromium isotope fractionation during magmatic processes: Evidence from mid-ocean ridge basalts. Geochim. Cosmochim. Ac. 327, 79-95.

MacLeod, C., Dick, H., Blum, P., Abe, N., Blackman, D., Bowles, J., Cheadle, M., Cho, K., Ciazela, J. and Deans, J. 2017. Site U1473, in: MacLeod, C., Dick, H., Blum, P. (Eds.), Proceedings of the International Ocean Discovery Program. IODP Publication Services, Texas A&M University.

Mahoney, J.J., Sinton, J.M., Kurz, M.D., Macdougall, J.D., Spencer, K.J. and Lugmair, G.W. 1994. Isotope and trace-element characterisitics of a super-fast spreading ride - East Pacific Rise, 13-23°S. Earth Planet. Sc. Lett. 121, 173-193.

Mallmann, G. and O'Neill, H.S.C. 2009. The Crystal/Melt Partitioning of V during Mantle Melting as a Function of Oxygen Fugacity Compared with some other Elements (Al, P, Ca, Sc, Ti, Cr, Fe, Ga, Y, Zr and Nb). J. Petrol. 50, 1765-1794.

Moynier, F., Yin, Q.Z. and Schauble, E. 2011. Isotopic Evidence of Cr Partitioning into Earth's Core. Science. 331, 1417-1420.

Nauret, F., Abouchami, W., Galer, S., Hofmann, A., Hémond, C., Chauvel, C. and Dyment, J. 2006. Correlated trace element-Pb isotope enrichments in Indian MORB along 18–20° S, Central Indian Ridge. Earth Planet. Sc. Lett. 245, 137-152.

Niu, Y.L. and Batiza, R. 1991. An empirical-method for calculating melt compositions produced beneath midocean ridges - application for axis and off-axis (seamounts) melting. J. Geophys. Res.-Sol. Ea. 96, 21753-21777.

Niu, Y.L., Waggoner, D.G., Sinton, J.M. and Mahoney, J.J. 1996. Mantle source heterogeneity and melting processes beneath seafloor spreading centers: The East Pacific Rise, 18-19°S. J. Geophys. Res.-Sol. Ea. 101, 27711-27733.

O'Neill, H.S.C. and Berry, A.J. 2021. The oxidation state of chromium in basaltic silicate melts. Geochim. Cosmochim. Ac. 306, 304-320.

Palme, H. and O'Neill, H.S.C. 2014. Cosmochemical Estimates of Mantle Composition., in: Turekian, K., Holland, H. (Eds.), Treatise on Geochemistry, 2 ed. Elsevier, pp. 1-39.

Papike, J.J., Karner, J.M. and Shearer, C.K. 2005. Comparative planetary mineralogy: Valence state partitioning of Cr, Fe, Ti, and V among crystallographic sites in olivine, pyroxene, and spinel from planetary basalts. Am. Miner. 90, 277-290.

Paulick, H., Münker, C. and Schuth, S. 2010. The influence of small-scale mantle heterogeneities on Mid-Ocean Ridge volcanism: evidence from the southern Mid-Atlantic Ridge (7° 30′ S to 11° 30′ S) and Ascension Island. Earth Planet. Sc. Lett. 296, 299-310.

Perk, N.W., Coogan, L.A., Karson, J.A., Klein, E.M. and Hanna, H.D. 2007. Petrology and geochemistry of primitive lower oceanic crust from Pito Deep: implications for the accretion of the lower crust at the Southern East Pacific Rise. Contrib. Mineral. Petrol. 154, 575-590.

Richter, M., Nebel, O., Schwindinger, M., Nebel-Jacobsen, Y. and Dick, H.J.B. 2021. Competing effects of spreading rate, crystal fractionation and source variability on Fe isotope systematics in mid-ocean ridge lavas. Sci. Rep. 11, 4123.

Rubin, K.H. and Sinton, J.M. 2007. Inferences on mid-ocean ridge thermal and magmatic structure from MORB compositions. Earth Planet. Sc. Lett. 260, 257-276.

Salters, V.J.M. and Stracke, A. 2004. Composition of the depleted mantle. Geochem. Geophys. Geosyst. 5, Q05B07.

Schauble, E.A. 2004. Applying stable isotope fractionation theory to new systems, in: Johnson, C.M., Beard, B.L., Albarede, F. (Eds.), Geochemistry of Non-Traditional Stable Isotopes. Mineralogical Society America, Washington, pp. 65-111.

Schoenberg, R., Merdian, A., Holmden, C., Kleinhanns, I.C., Hassler, K., Wille, M. and Reitter, E. 2016. The stable Cr isotopic compositions of chondrites and silicate planetary reservoirs. Geochim. Cosmochim. Ac. 183, 14-30.

Schoenberg, R., Zink, S., Staubwasser, M. and von Blanckenburg, F. 2008. The stable Cr isotope inventory of solid Earth reservoirs determined by double spike MC-ICP-MS. Chem. Geol. 249, 294-306.

Schuessler, J.A., Schoenberg, R. and Sigmarsson, O. 2009. Iron and lithium isotope systematics of the Hekla volcano, Iceland - Evidence for Fe isotope fractionation during magma differentiation. Chem. Geol. 258, 78-91.

Seifert, R. and Party, S.S. 2009. Mantle to ocean on the southern Mid-Atlantic Ridge (5° S - 11° S) (MAR-SÜD V); cruise report M78/2. Institut für Biogeochemie

und Meereschemie, Universität Hamburg.

Shahar, A., Young, E.D. and Manning, C.E. 2008. Equilibrium high-temperature Fe isotope fractionation between fayalite and magnetite: An experimental calibration. Earth Planet. Sc. Lett. 268, 330-338.

Shen, J., Qin, L.P., Fang, Z.Y., Zhang, Y.N., Liu, J., Liu, W., Wang, F.Y., Xiao, Y., Yu, H.M. and Wei, S.Q. 2018. High-temperature inter-mineral Cr isotope fractionation: A comparison of ionic model predictions and experimental investigations of mantle xenoliths from the North China Craton. Earth Planet. Sc. Lett. 499, 278-290.

Shen, J., Xia, J.X., Qin, L.P., Carlson, R.W., Huang, S.C., Helz, R.T. and Mock, T.D. 2020. Stable chromium isotope fractionation during magmatic differentiation: Insights from Hawaiian basalts and implications for planetary redox conditions. Geochim. Cosmochim. Ac. 278, 289-304.

Sinton, J.M. and Detrick, R.S. 1992. Mid-ocean ridge magma chambers. J. Geophys. Res.-Sol. Ea. 97, 197-216.

Sinton, J.M., Smaglik, S.M., Mahoney, J.J. and Macdonald, K.C. 1991. Magmatic processes at superfast spreading midocean ridges - glass compositional variations along the East Pacific Rise 13°-23° S. J. Geophys. Res.-Solid. 96, 6133-6155.

Soderman, C.R., Matthews, S., Shorttle, O., Jackson, M.G., Ruttor, S., Nebel, O., Turner, S., Beier, C., Millet, M.A., Widom, E., Humayun, M. and Williams, H.M. 2021. Heavy $\delta^{57}Fe$ in ocean island basalts: A non-unique signature of processes and source lithologies in the mantle. Geochim. Cosmochim. Ac. 292, 309-332.

Soderman, C.R., Shorttle, O., Matthews, S. and Williams, H.M. 2022. Global trends in novel stable isotopes in basalts: theory and observations. Geochim. Cosmochim. Ac. 318, 388-414.

Sossi, P.A., Moynier, F. and van Zuilen, K. 2018. Volatile loss following cooling and accretion of the Moon revealed by chromium isotopes. Proc. Natl. Acad. Sci. USA. 115, 10920-10925.

Sossi, P.A., Nebel, O. and Foden, J. 2016. Iron isotope systematics in planetary reservoirs. Earth Planet. Sc. Lett. 452, 295-308.

Standish, J.J. 2006. The influence of ridge geometry at the ultraslow-spreading Southwest Indian Ridge (9°- 25° E): Basalt composition sensitivity to variations in source and process. Massachussetts Institute of Technology.

Standish, J.J. and Sims, K.W. 2010. Young off-axis volcanism along the ultraslow-spreading Southwest Indian Ridge. Nat. Geosci. 3, 286-292.

Stracke, A. 2012. Earth's heterogeneous mantle: A product of convection-driven interaction between crust and mantle. Chem. Geol. 330, 274-299.

Stracke, A. and Bourdon, B. 2009. The importance of melt extraction for tracing mantle heterogeneity. Geochim. Cosmochim. Ac. 73, 218-238.

Stracke, A., Hofmann, A.W. and Hart, S.R. 2005. FOZO, HIMU, and the rest of the mantle zoo. Geochem. Geophys. Geosyst. 6, Q05007.

Sun, S.-S., Nesbitt, R.W. and Sharaskin, A.Y. 1979. Geochemical characteristics of mid-ocean ridge basalts. Earth Planet. Sc. Lett. 44, 119-138.

Teng, F.Z., Dauphas, N. and Helz, R.T. 2008. Iron isotope fractionation during magmatic differentiation in Kilauea Iki Lava Lake. Science. 320, 1620-1622.

Teng, F.Z., Dauphas, N., Huang, S.C. and Marty, B. 2013. Iron isotopic systematics of oceanic basalts. Geochim. Cosmochim. Ac. 107, 12-26.

Vlastelic, I., Dosso, L., Bougault, H., Aslanian, D., Geli, L., Etoubleau, J., Bohn, M., Joron, J.L. and Bollinger, C. 2000. Chemical systematics of an intermediate spreading ridge: The Pacific-Antarctic Ridge between 56° S and 66° S. J. Geophys. Res.-Sol. Ea. 105, 2915-2936.

Wagner, L.J., Kleinhanns, I.C., Weber, N., Babechuk, M.G., Hofmann, A. and Schoenberg, R. 2021. Coupled stable chromium and iron isotopic fractionation tracing magmatic mineral crystallization in Archean komatiite-tholeiite suites. Chem. Geol. 576, 120121.

Wang, X.L., Planavsky, N.J., Reinhard, C.T., Zou, H.J., Ague, J.J., Wu, Y.B., Gill, B.C., Schwarzenbach, E.M. and Peucker-Ehrenbrink, B. 2016. Chromium isotope fractionation during subduction-related metamorphism, black shale weathering, and hydrothermal alteration. Chem. Geol. 423, 19-33.

Weyer, S. and Ionov, D.A. 2007. Partial melting and melt percolation in the mantle: The message from Fe isotopes. Earth Planet. Sc. Lett. 259, 119-133.

White, W. and Klein, E. 2014. Composition of the oceanic crust, in: Turekian, K., Holland, H. (Eds.), Treatise on Geochemistry, 2 ed. Elsevier, pp. 457-496.

White, W.M. 2015. Probing the Earth's deep interior through geochemistry. Geochem. Perspect. 4, 95-251.

Williams, H.M., Peslier, A.H., McCammon, C., Halliday, A.N., Levasseur, S., Teutsch, N. and Burg, J.P. 2005. Systematic iron isotope variations in mantle rocks and minerals: The effects of partial melting and oxygen fugacity. Earth Planet. Sc. Lett. 235, 435-452.

Williams, H.M., Prytulak, J., Woodhead, J.D., Kelley, K.A., Brounce, M. and Plank, T. 2018. Interplay of crystal fractionation, sulfide saturation and oxygen fugacity on the iron isotope composition of arc lavas: An example from the Marianas. Geochim. Cosmochim. Ac. 226, 224-243.

Xia, J.X., Qin, L.P., Shen, J., Carlson, R.W., Ionov, D.A. and Mock, T.D. 2017. Chromium isotope heterogeneity in the mantle. Earth Planet. Sc. Lett. 464, 103-115.

Yang, S., Humayun, M. and Salters, V.J. 2020. Elemental constraints on the amount of recycled crust in the generation of mid-oceanic ridge basalts (MORBs). Sci. Adv. 6, eaba2923.

Yierpan, A., König, S., Labidi, J. and Schoenberg, R. 2019. Selenium isotope and S-Se-Te elemental systematics along the Pacific-Antarctic ridge: Role of mantle processes. Geochim. Cosmochim. Ac. 249, 199-224.

Zong, T., Han, X., Liu, J., Wang, Y., Qiu, Z. and Yu, X. 2020. Fractional crystallization processes of magma beneath the Carlsberg Ridge (57–65° E). J. Oceanol. Limn. 38, 75-92.

Zou, H. 2007. Quantitative geochemistry. Imperial College Press, London.

Chapter 4

Heterogeneous Cr and Fe isotope compositions of Earth's silicate mantle: Constraints from intraplate basalts

Abstract

Differentiation and recycling during the evolution of planet Earth has led to a heterogeneous terrestrial mantle. Ocean island basalts (OIB) representing mantle partial melts provide a window into the deep mantle and radiogenic isotope compositions are traditionally applied as a tracer for identifying and characterizing the sampled mantle heterogeneities. While mid-ocean ridge basalts (MORB) are traditionally thought to sample the upper depleted mantle, OIBs and their deep-rooted continental counterparts display mixing signatures between the depleted mantle and at least three enriched endmember compositions. Stable chromium (Cr) and iron (Fe) isotope ratios have been invoked recently as a tracer for source lithologies potentially associated with mantle heterogeneities, yet a large stable Cr isotope dataset encompassing these variable mantle source compositions is missing. Here we report stable Cr and Fe isotope compositions of in total 45 intraplate basalts, including ocean island basalts (n=27) and continental intraplate basalts (n=18). These samples are representative for variable enriched signatures in radiogenic Sr-Nd-Pb isotope space encompassing prevalent mantle, high-μ, and enriched mantle 1 and 2 compositions. The Cr isotope compositions of intraplate basalts range from -0.227 to -0.094 ‰ in $\delta^{53/52}$Cr (i.e., difference of a sample's ^{53}Cr/^{52}Cr ratio relative to the international reference material NIST SRM979) extending from MORB-like values towards the Cr isotope composition of bulk silicate Earth of -0.12 ± 0.06 ‰, although the majority of intraplate basalts is indistinguishable from the BSE range. Excluding samples affected by fractional crystallization, $\delta^{53/52}$Cr values of intraplate basalts correlate with radiogenic Sr and Nd isotopic compositions and highlight the role of source heterogeneity on the Cr isotope compositions of basalts sampling the non-depleted mantle. Thereby, sources with more radiogenic Sr and less radiogenic Nd isotope compositions show higher $\delta^{53/52}$Cr (continental crust/lithospheric

mantle/sediments), whereas basalts with radiogenic isotopic affinities of high-μ or prevalent mantle sources show lower $\delta^{53/52}$Cr in line with incorporation of oceanic crust with a MORB-like Cr isotope composition. For two locations such as Lō'ihi seamount and Vogelsberg volcano there is compelling evidence that the low $\delta^{53/52}$Cr is derived from melting pyroxene-rich lithologies, whereas pyroxenite contributions for Vogelsberg basanites probably originate from the lithospheric mantle, which has been previously modified by subduction zone processes. Moreover, strong correlations between stable Cr and Fe isotopic compositions with radiogenic Sr signatures and trace element ratios such as Nb/La and La/Yb suggest a carbonated source for EM2-related basalts from French Polynesia imprinting their higher source $\delta^{53/52}$Cr on the melt.

4.1 Introduction

The heterogeneous nature of Earth's mantle is traditionally inferred from incompatible trace element and radiogenic isotope compositions and reflects to some extent the interior evolution of a tectonically active planet over time. Oceanic basalts are the most informative tracers of the Earth's mantle composition as their geochemistry mirrors that of their source, namely the possible geochemical imprint of a thick overlying crust is avoided. Thereby, mid-ocean ridge basalts (MORB) sample the depleted mantle (DM), and ocean island basalts (OIB) are thought to sample primarily variable enriched mantle components, which are referred to as enriched mantle 1 (EM1), enriched mantle 2 (EM2) and high-μ (HIMU, μ being defined as $\mu = (^{238}U/^{204}Pb)$; Hofmann, 1997; Stracke, 2012; White, 2015). Additionally, a mantle component with a range of radiogenic isotopic compositions extending from enriched MORBs towards more radiogenic Pb isotope compositions has been called the Prevalent Mantle (PREMA) and represents enriched compositions along a DM-PREMA array (Stracke, 2012; Stracke et al., 2005; Zindler and Hart, 1986). The main driver of this large-scale element cycling is thought to be subduction recycling, which re-introduces oceanic as well as continental lithosphere along with related sediments back into the mantle. However, the exact nature and proportions of these enriched components in the sources of oceanic basalts has been a long-standing debate and the connection to related lithological heterogeneity in the mantle is still shadowed by contrasting results from major and trace element as well radiogenic isotope proxies (Allègre and Turcotte, 1986; Herzberg, 2011; Hofmann, 1997; Hofmann and White, 1982; Sobolev et al., 2007; Sobolev et al., 2005; Stracke et al., 2005).

Recently, an increasing number of non-traditional stable isotope systems such as Fe, Mg, Ca and Cr, have been used to investigate mantle heterogeneity with special application towards tracing different source lithologies (Gleeson et al., 2020; Kang et al., 2019; Konter et al., 2016; Soderman et al., 2022; Stracke et al., 2018; Williams and Bizimis, 2014). Based on theoretical models using phase equilibria Soderman et al. (2022) showed that stable Cr isotopes, reported in ‰ units as $\delta^{53/52}$Cr ($\delta^{53/52}Cr = (^{53}Cr/^{52}Cr_{sample})/(^{53}Cr/^{52}Cr_{SRM979})$-1; Equation 4.1), and stable Fe isotopes, reported in ‰ units as $\delta^{56/54}$Fe ($\delta^{56/54}Fe = (^{56}Fe/^{54}Fe_{sample})/(^{56}Fe/^{54}Fe_{IRMM014})$-1; Equation 4.2), are especially useful for identifying pyroxenite components in the melt source regions. For Fe isotopes, identifying lithological heterogeneity has been inferred from mineral-specific equilibrium isotope fractionation factors of mantle

minerals during partial melting such as pyroxene and olivine, resulting in greater isotopic fractionation during partial melting of pyroxenite compared to peridotite (Soderman et al., 2021; Williams and Bizimis, 2014). Additionally, pyroxenite components have been constrained to exhibit a higher $\delta^{56/54}$Fe than peridotite, which contributes to the heavy Fe isotope signature of a pyroxenite-derived melts (Williams and Bizimis, 2014). Similarly, model calculations showed that greater Cr isotope fractionation is induced by partial melting of pyroxenite than for peridotite lithologies (Soderman et al., 2022). Assuming that pyroxenite formation is related to recycling of oceanic crust, pyroxenitic components may have a MORB-like $\delta^{53/52}$Cr signature, which recently has been shown to be consistently light ($\delta^{53/52}$Cr = -0.0237 ± 0.050 ‰, Chapter 3; and Ma et al., 2022) compared to the bulk silicate Earth (BSE, $\delta^{53/52}$Cr = -0.12 ± 0.06 ‰; Wagner et al., 2021). On the other hand, pyroxenitic lithologies unrelated to oceanic crust recycling exhibit even lighter Cr isotope composition of down to -1.36 ‰ (Jerram et al., 2022; Xia et al., 2017). Independent of the formation mechanism, it is anticipated that the presence of pyroxenite components in the melt source of OIBs results in lighter $\delta^{53/52}$Cr of the melt compared to homogenous peridotite-derived melt. So far, the range observed for $\delta^{53/52}$Cr in OIBs overlaps with the value for BSE and extends towards slightly lower values (Bonnand et al., 2020b; Shen et al., 2020).

Tracing recycled components in the source regions of OIBs are potentially bedevilled by high Cr concentrations in the mantle. Estimated Cr concentrations of the mantle vary within a small range depending on the used model. Therein, Cr concentrations of the primitive mantle (PM) range between 2520 and 2620 $\mu g\,g^{-1}$ (McDonough and Sun, 1995; Palme and O'Neill, 2014) and of the upper DM between 2,500 ± 1000 $\mu g\,g^{-1}$ (Salters and Stracke, 2004) and 2688 to 3900 $\mu g\,g^{-1}$ (Workman and Hart, 2005). In contrast, the continental crust and global subducting sediments (GLOSS) display low Cr concentration with 92 $\mu g\,g^{-1}$ (Rudnick and Gao, 2014) and 68 $\mu g\,g^{-1}$ (Plank, 2014), respectively. The upper oceanic crust (estimated from MORB) has comparatively elevated Cr contents with averaged values ranging between 249 to 326 $\mu g\,g^{-1}$ (Arevalo Jr and McDonough, 2010; Gale et al., 2013). Combined with the contrasting light Cr isotope composition of normal MORBs (N-MORBs) with an average $\delta^{53/52}$Cr value of -0.237 ± 0.050‰ (Chapter 3), subduction recycling of oceanic crust back into the mantle may be traced by the stable Cr isotope composition of OIBs.

In general, and similar to Fe occurring as Fe^{2+} and Fe^{3+} under terrestrial conditions, Cr is a compatible, redox sensitive, transition metal. In terrestrial magmatic systems, Cr is present as Cr^{2+} and Cr^{3+} (Berry and O'Neill, 2004; Berry et al., 2021b; Berry et al., 2006; O'Neill and Berry, 2021), whereas Cr^{3+} and Cr^{6+} are the major oxidation states in terrestrial surface environments (Bartlett and James, 1988; Elderfield, 1970). For mantle minerals, it has been shown that $\delta^{53/52}$Cr increases in the order of $\delta^{53/52}Cr_{olivine} < \delta^{53/52}Cr_{clinopyroxene} \leq \delta^{53/52}Cr_{orthopyroxene} < \delta^{53/52}Cr_{spinel}$ at equilibrium (Shen et al., 2018b), bearing in mind that the Cr concentrations of theses phases are variable and thus have a different impact on Cr isotope fractionation during magmatic processes. During melting, Cr^{2+} behaves more incompatible than Cr^{3+} (Mallmann and O'Neill, 2009), which preferentially drives the light Cr isotopes into the melt (Chapter 3; Jerram et al., 2022; Shen et al., 2018b; Shen et al., 2020; Xia et al., 2017). Moreover, based on model calculations it has been suggested that melting a spinel-bearing peridotite imparts a relatively greater Cr

isotope fractionation compared to melting a garnet-bearing peridotite (Jerram et al., 2022), which is largely associated to Cr^{3+}-bearing spinel controlling the Cr budget. In general, considerable $\delta^{53/52}$Cr variations have been reported for subcontinental lithospheric mantle xenoliths suggesting Cr isotopic mantle heterogeneities at least to some extent (Jerram et al., 2022; Xia et al., 2017).
Magmatic differentiation has been shown to affect $\delta^{53/52}$Cr in various magmatic suites, such as Phanerozoic OIBs (Bonnand et al., 2020b; Shen et al., 2020) and Archean komatiitic suites (Jerram et al., 2020; Wagner et al., 2021). The investigation of MORBs has led to contradictory observations, in which Ma et al. (2022) suggested that fractional crystallization induces Cr isotope fractionation leading towards lower $\delta^{53/52}$Cr with increasing degree of magmatic differentiation. On the other hand, a continuous MORB suite from the East-Pacific Rise and Pacific-Antarctic Ridge did not show a relationship between $\delta^{53/52}$Cr and MgO, advocating that fractional crystallization plays a subordinate role in controlling $\delta^{53/52}$Cr variability (Chapter 3). Hence, it is important to screen $\delta^{53/52}$Cr variations carefully for effects of magmatic differentiation prior to interpreting any potential source signal. Previous studies investigating different OIBs, i.e., volcanoes of the Hawaiian-Emperor seamount chain (Koolau, Mauna Kea, Kilauea; Shen et al., 2020) as well as Fangataufa atoll (French Polynesia; Bonnand et al., 2020b) (Figure 4.1), observed Cr isotopic fractionation during magmatic differentiation. Therein, accumulation of olivine + Cr-spinel lead towards higher $\delta^{53/52}$Cr and fractional crystallization of olivine + spinel (Kilauea) or olivine + clinopyroxene + spinel (Fangataufa atoll) lead to lower $\delta^{53/52}$Cr values with increasing magmatic differentiation. This effect is deduced from the preferential incorporation of heavy Cr isotopes into clinopyroxene and spinel, which together control the Cr budget relative to olivine based on mass balance considerations. Moreover, the lower $\delta^{53/52}$Cr of Koolau basalts has been attributed to partial melting under slightly more reducing conditions compared to melting conditions of Mauna Kea and Kilauea basalts and may also be associated with recycling of altered oceanic crust (Shen et al., 2020). At the same time, Bonnand et al. (2020b) observed a negative correlation of εNd with $\delta^{53/52}$Cr in Fangataufa volcanic rocks with HIMU-like radiogenic isotope compositions, which they ascribed to the effect of low degree melting preferentially sampling the more fertile component carrying a lower εNd signature.
Although these studies provided first insights into the $\delta^{53/52}$Cr variability of OIBs, this study aims on providing a more comprehensive view on the possible impact of source heterogeneity on $\delta^{53/52}$Cr. Following, new stable Cr and Fe isotope data for 45 intraplate basalts encompassing OIBs and continental intraplate basalts are presented. These samples display considerable variability in their radiogenic Sr-Nd-Pb isotope composition and are thus good targets to illuminate the impact of source heterogeneity on the melt $\delta^{53/52}$Cr. Moreover, it will be tested, if Cr isotopes may be used as a tracer for lithologically distinct mantle source components.

4.2 Geological settings and samples

Ocean island basalt samples are derived from French Polynesia (Schiller, 2019), Piton de la Fournaise (Réunion) and Lō'ihi seamount (Hawaii). Continental intraplate settings include volcanic rocks from the Vogelsberg volcano (Germany; Bogaard and Wörner, 2003) and mafic intrusive rocks from the Doros Complex

(Namibia; Owen-Smith and Ashwal, 2015a, b; Owen-Smith et al., 2017) (Figure 4.1). As shown in Figure 4.2, these rock suites represent various isotopic signatures including HIMU (French Polynesia), enriched mantle EM1 (Doros Complex, French Polynesia) and EM2 (French Polynesia) as well as the ubiquitously present mantle signature of PREMA. PREMA is characterized by a range of isotopic compositions displaying enriched signatures in a variably depleted mantle, and defining an array between DM and HIMU in Pb isotope space, which is referred to as the DM-PREMA array (Stracke, 2012; Stracke et al., 2005). In this study, one sample from Rurutu Island (French Polynesia) represents PREMA compositions (i.e., Austral-Cook-PREMA; Stracke, 2012), whereas one sample from the EM1-related Pitcairn-Gambier island chain (French Polynesia) and all Vogelsberg volcanics show high affinities with PREMA in Sr-Nd-Pb radiogenic isotope space. The Hawaiian plume is generally thought to be related to EM1, whereas a specific Lō'ihi component has been identified based on its radiogenic Pb (Abouchami et al., 2005) and He isotopic signature ($^3He/^4He$ up to 32 R_A; Kurz et al., 1983). High $^3He/^4He$ ratios are taken as evidence for the contribution of a primordial undegassed reservoir, possibly entrained from the lower mantle. Compositions of La Réunion lavas show typical DUPAL signature, named after Dupré and Allègre (1983), which denotes high $^{208}Pb/^{204}Pb$ and $^{207}Pb/^{204}Pb$ at a given $^{206}Pb/^{204}Pb$ (Hart, 1984). This enriched mantle component is characteristic for lavas erupted in the Indian Ocean and thought to be related to an EM1 component (e.g., White, 2015). However, an EM1 contribution in La Réunion lavas is regarded to be small and the Réunion hotspot is typically considered to represent a deep and possibly ancient primitive source, which is free of subduction components (Gleeson and Gibson, 2019; Peters et al., 2018; Vlastélic et al., 2006).
In general, samples are alkaline to tholeiitic in composition (Figure 4.3) and have MgO contents > 7.5 wt. % (exceptions are two samples from Lō'ihi, two samples from La Réunion, one sample from Rurutu Island, and three samples from the Doros Complex having MgO < 7.5 wt. %). Accordingly, samples mostly experienced fractional crystallization of olivine (± Cr-spinel) and clinopyroxene. Details on the geological background of each locality and the samples are given in Section 4.2.1 to 4.2.5, also including a short description of the chemical composition of samples from French Polynesia (Schiller, 2019), Vogelsberg volcano (Bogaard and Wörner, 2003) and Doros intrusive rocks (Owen-Smith and Ashwal, 2015a; Owen-Smith et al., 2017). New chemical compositions for samples from Piton de la Fournaise, La Réunion, and Lō'ihi, Hawaii, are described in the Result Section 4.4 as these are published for the first time.

4.2.1 Piton de la Fournaise, La Réunion

All samples studied here are from the active volcano Piton de la Fournaise, at which volcanic activity started ∼527 ka ago (Albarède et al., 1997). Samples include peripheral and central eruptions. The volcanic island La Réunion, is situated in the Indian Ocean east of Madagascar and is considered to be related to the hotspot track that originates in western India and initially formed the Deccan flood basalt province at ∼65 Ma (Duncan et al., 1989). La Réunion is built on late Cretaceous to Paleocene oceanic crust and rises 7 km above the ocean floor. The seismic Moho discontinuity is thought to be located 10-13 km below sea level (Fontaine et al.,

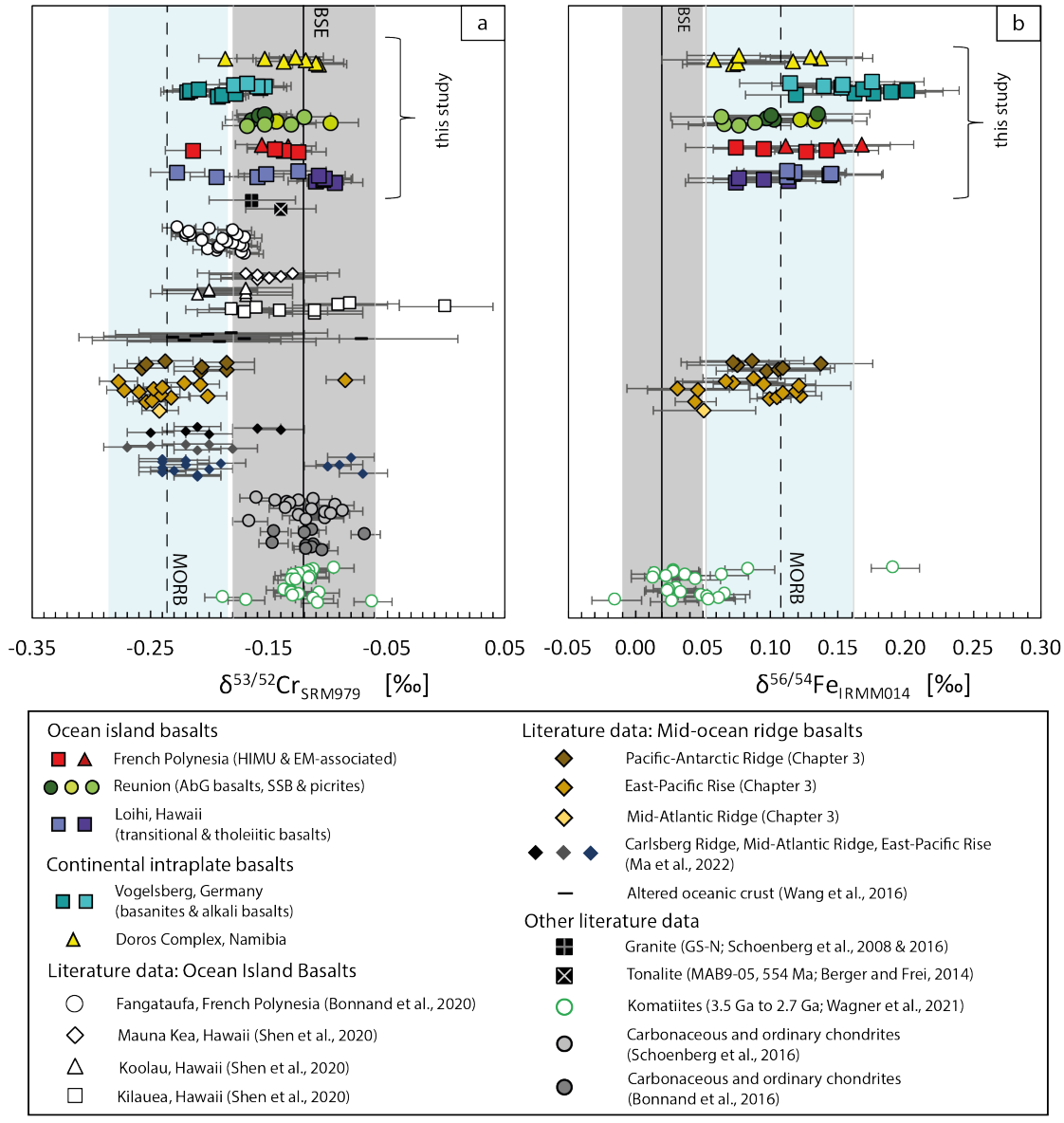

Figure 4.1: Compilation of **a)** stable Cr isotope compositions ($\delta^{53/52}$Cr) and **b)** stable Fe isotope compositions ($\delta^{56/54}$Fe) of intraplate basalts presented in this study. Also shown are $\delta^{53/52}$Cr and $\delta^{56/54}$Fe for mid-ocean ridge basalts (MORBs; Chapter 3) and komatiites (Chapter 2; (Wagner et al., 2021). The grey field indicates the estimated range for bulk silicate Earth (BSE) for $\delta^{53/52}$Cr of -0.12 ± 0.06 ‰ (Wagner et al., 2021) and $\delta^{56/54}$Fe of +0.02 ± 0.03 ‰ (Weyer and Ionov, 2007). The light blue fields indicate the average N-MORB $\delta^{53/52}$Cr value (-0.237 ± 0.050 ‰; Chapter 3) and $\delta^{56/54}$Fe value (+0.107 ± 0.055 ‰; compiled from Chen et al., 2019; Richter et al., 2021; Teng et al., 2013; Weyer and Ionov, 2007). Literature $\delta^{53/52}$Cr data in a) include OIBs (Bonnand et al., 2020b; Shen et al., 2020), MORBs (Ma et al., 2022) and altered oceanic crust (Wang et al., 2016). Cr isotope data of chondrites (Bonnand et al., 2016; Schoenberg et al., 2016), one granite (reference material GS-N, Schoenberg et al., 2016; Schoenberg et al., 2008) and one tonalite (554 Ma, Madagascar; Berger and Frei, 2014) are also shown for comparison. Error bars show the 2SD external reproducibility of ± 0.022 ‰ for $\delta^{53/52}$Cr and ± 0.038 ‰ for $\delta^{56/54}$Fe and based on the long-term reproducibility of single measurements of BHVO-2 ($\delta^{53/52}$Cr) and Tueb-Fe ($\delta^{56/54}$Fe). AbG = Abnormal Group basalts, SSB = steady state basalts.

2015). At the crust-mantle interface a jump in seismic wave velocity indicates the presence of a < 3 km thick layer of dense material resembling ultramafic magmatic underplating (Fontaine et al., 2015). Most of the volcanic activity of Piton de la

Fournaise is confined to its central cone (Enclos Fouqué), whereas less activity is attributed to peripheral eruptions along the major rift zones, located in the NE, SE and NW (i.e., NERZ, SERZ, NWRZ; Lénat et al., 2012; Michon et al., 2015; Villeneuve and Bachèlery, 2006). The central cone is thought to be fed by a central magma plumbing system composed of multiple reservoirs at variable depths within the crust, indicated by shallow seismic activity (Boivin and Bachèlery, 2009; Michon et al., 2015). The central magma plumbing system may also feed peripheral eruptions along the mostly aseismic NE and SE rift zones by shallow lateral migration (Michon et al., 2015), which is supported by similar chemical and mineralogical lava compositions (Boivin and Bachèlery, 2009; Boudoire et al., 2019). Deep seismicity (>11 km below sea level) beneath the NW rift zone indicates that eruptions forming adventive cones on the NW rift zone have a deeper origin and bypass the crustal plumbing system (Michon et al., 2015).

Based on geochemical characteristics of transitional basalts from Piton de la Fournaise three major groups have been identified: 1) Cotectic basalts (or steady-state basalt, SSB) with MgO content between 6-7 wt. % and high CaO/Al_2O_3 ratios of ∼0.8; 2) picritic (olivine-rich) basalts with MgO contents up to 30 wt. %, which formed by olivine accumulation within a SSB-type magma; and 3) abnormal group basalts (AbG), which are characterized by slightly more alkaline compositions (higher K_2O content) and lower CaO/Al_2O_3 ratios (<0.8) at higher MgO contents (8-10 wt. %) and were linked to deep-level fractional crystallization of clinopyroxene (Albarède et al., 1997; Boivin and Bachèlery, 2009; Salaün et al., 2010). Moreover, a detailed study of basalts erupted in the peripheral area showed that the NW rift zone comprises two types of AbG basalts: olivine-bearing and clinopyroxene-bearing basalts, each of which were linked to a characteristic multi-depth differentiation (Boudoire et al., 2019). In detail, olivine-bearing basalts are proposed to be generated by a polybaric evolution process starting with a primary melt at 8 to 10 kbar, at which stage fractionating phases include olivine and clinopyroxene. Following ascent, the now more evolved magma (after ca. 4 % olivine and 12 % clinopyroxene fractionation; Boudoire et al., 2019) ponds within the proposed underplating layer between 3.9 and 4.2 kbar, during which it experiences clinopyroxene resorption and contamination by low-degree melts from cumulate dunites and wehrlites as indicated by incompatible trace element enrichment (Boudoire et al., 2019). The plume related to La Réunion volcanism has been shown to be relatively homogeneous over time and represents a deep isolated mantle reservoir with Hadean origin carrying a moderately high $^3He/^4He$ signature ($12.9 \pm 0.4\ R_A$; 2SD; Graham et al., 1990; Peters et al., 2018; Vlastélic et al., 2006). Limited heterogeneity of radiogenic Sr-Nd-Pb isotope compositions reported for Piton de la Fournaise lavas (e. g., Bosch et al., 2008; Valer et al., 2017; Vlastélic et al., 2009) has been attributed to ∼10 % partial melting of a PM-like source, and limited degrees of crustal contamination (Fretzdorff and Haase, 2002; Pietruszka et al., 2009; Valer et al., 2017).

Samples in this study cover a range of subaerial eruption events, including prehistoric and historic eruptions (precise age data are not available), and encompass central eruptions and associated peripheral eruptions within the NE and SE rift zones, as well as peripheral eruptions along the NW rift zone (Table 4.1). Samples are aphyric to olivine-phyric, whereas olivines vary in size and abundance. Major element analyses for all ten samples and trace element analyses for 8 out of 10 samples have been carried out at the Geochemistry laboratories of the University of Goettingen and

are presented in the Result Section 4.4 as well as in Supplementary Table C.2.6.

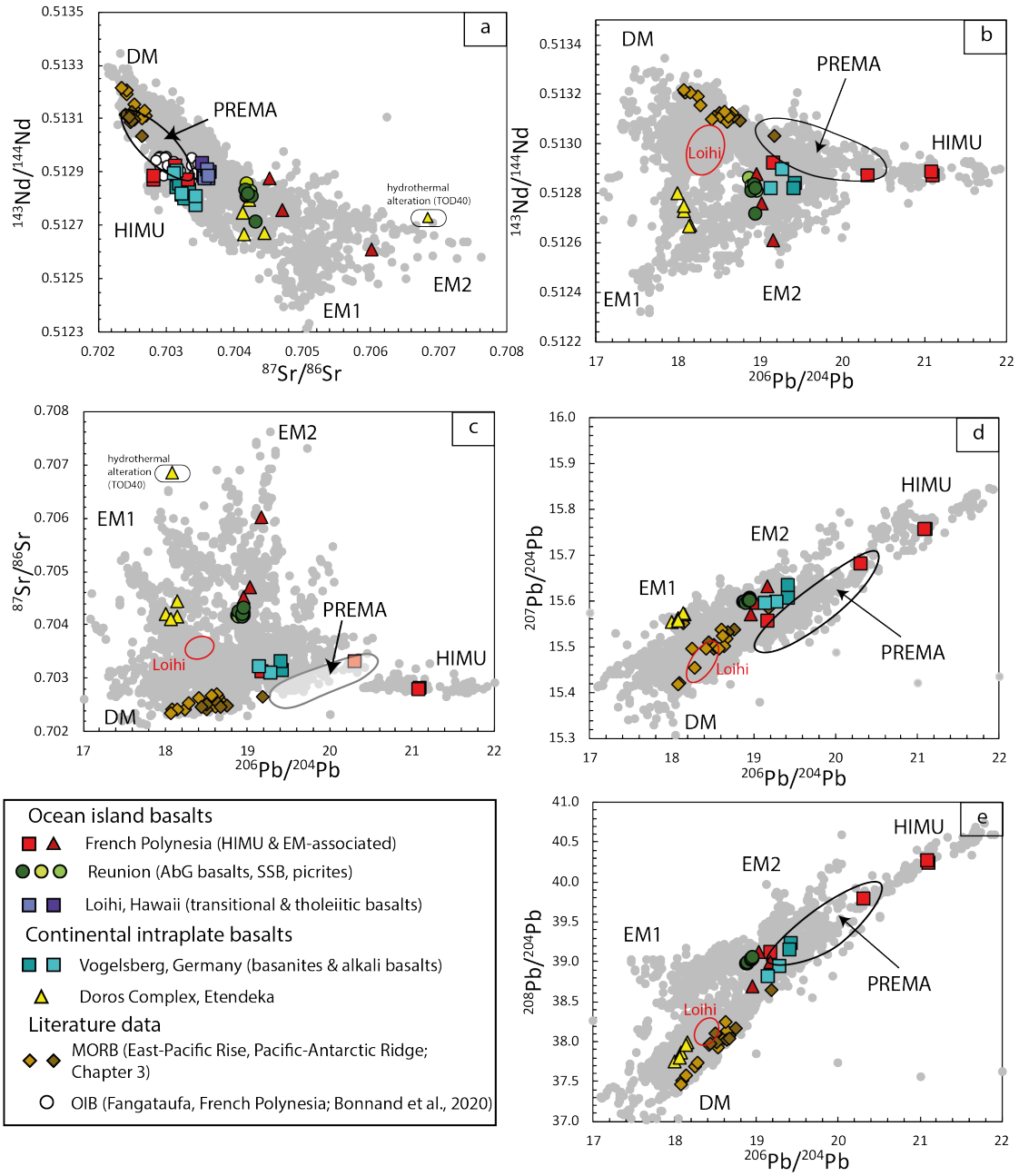

Figure 4.2: Radiogenic Sr, Nd and Pb isotope data for intraplate basalts determined in this study (La Réunion and Lō'ihi seamount) and from the literature (Vogelsberg volcano; Bogaard and Wörner, 2003; French Polynesia; Schiller, 2019; Doros Complex; Owen-Smith et al., 2017) highlighting the different mantle components. Pb isotope data for Lō'ihi samples are not available, but indicated by the red eclipse in b)-e) using the compilation for Lō'ihi basalts by Stracke (2012). Also shown are mid-ocean ridge basalts from the East-Pacific Rise and Pacific-Antarctic Ridge (Chapter 3) and in a) OIBs from Fangataufa (Bonnand et al., 2020b). Literature data for oceanic basalts in grey are from the compilation given in Stracke (2012). PREMA as defined by Stracke et al. (2005) and Stracke (2012). AbG = Abnormal Group basalts, SSB = steady state basalts.

4.2.2 Lō'ihi, Hawaii

Lō'ihi seamount is located 35 km southeast of Big Island of Hawaii and represents the youngest volcano of the Hawaiian-Emperor hotspot track. The active volcano

rises 3 to 5 km from 105 Ma old Pacific oceanic crust (Garcia et al., 2006) and its summit is located 960 m below sea level (Rouxel et al., 2018). Main geological features involve a northern and southern rift zone as well as three pit craters located on the summit platform (Garcia et al., 2006). Lō'ihi seamount is considered the type example of the early plume-related growth phase of ocean island volcanoes. It is thought to represent the transition between the pre-shield stage and shield stage as magma compositions range between alkaline to tholeiitic (Moore et al., 1982). The general evolution from alkaline to tholeiitic magma compositions is thought to be marked by the transition between small degree melting in the peripheral regions of the plume conduit (early stages) and higher degrees of melting as temperatures increase as the volcano moves towards the centre of the plume (later stages) (Garcia et al., 1995). However, coeval alkaline and tholeiitic magmas were observed near the summit (Garcia et al., 1993). Partial melting degrees are estimated to vary between 6 to 10 % of a common, mostly peridotitic, slightly heterogeneous source (Garcia et al., 1995). In general, Hawaiian lavas tap a source varying greatly in Sr and Nd isotope compositions extending from MORB-like compositions towards EM1-like compositions and are further distinguished based on their Pb isotope composition defining Loa- and Kea-trend lavas (e.g., Abouchami et al., 2005). The distinct isotopic compositions of Lō'ihi lavas have been attributed to the Loa-trend of Hawaiian volcanoes, which are marked by high $^{208}Pb/^{204}Pb$ at given $^{206}Pb/^{204}Pb$ compared to Kea-trend lavas (Abouchami et al., 2005; Hanyu et al., 2001). Additionally, Lō'ihi lavas are characterized by high $^{3}He/^{4}He$ of 20.0 to 32.2 R_A (Kurz et al., 1983), and anomalous $\mu^{182}W$ (-9.7 to -18.4; Mundl et al., 2017) indicating a deep mantle origin, possibly related to a large low shear velocity province (LLSVP; Weis et al., 2011; Weis et al., 2020) or an ultralow-velocity zone (ULVZ; Mundl et al., 2017).

4.2.2.1 Petrography of Lō'ihi whole rock samples

Based on their petrography Lō'ihi whole-rock samples in this study can be divided into two types: Highly olivine-phyric basalts (Transitional basalts; Figure C.2.1) and sparsely olivine-phyric to aphyric basalts (Tholeiitic basalt, Figure C.2.2, Table 4.1), similar to what has been observed by Garcia et al. (1995). Vesicularity in highly olivine-phyric samples ranges from vesicle-rich in samples J2-244-1-R2 and J2-309-R1 to vesicle-free in sample J2-246-R3D and J2-307-R2C. Highly olivine-phyric basalts contain large olivine phenocrysts, which are also incorporated in the glassy rinds. Cr-spinel was not observed as a phenocryst phase, but is an abundant microphenocryst and also occurs as inclusions in olivines as observed under the binoclular. Sparsely olivine-phyric to aphyric basalts are usually massive with vesicles $< \sim$10 % (e.g., Figure C.2.2B).

4.2.3 French Polynesia

The islands of French Polynesia are located in the South Pacific Ocean and are grouped in different island chains belonging to the South Pacific Superswell. Samples investigated in this study are derived from the Austral islands (Rurutu, Tubuai), Gambier islands (Mangareva), Marquesas islands (Nuku Hiva) and Society islands (Huahine). Rurutu and Tubuai are part of the northeast alignment of the Austral islands and are associated with the Cook-Austral island chain. At Rurutu two different volcanic stages were identified, one at 13 to 10.8 Ma and a younger stage at

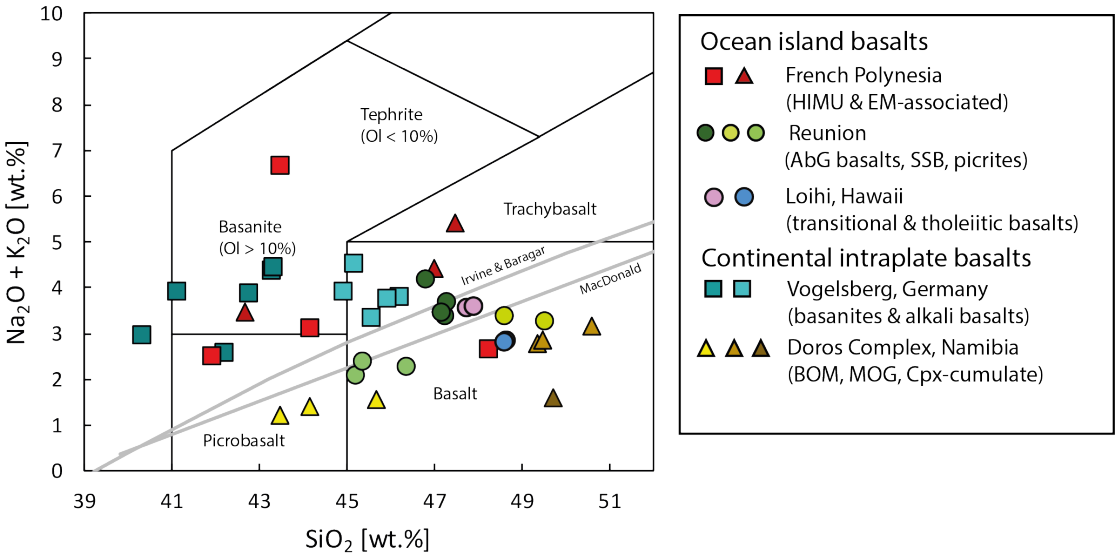

Figure 4.3: Total alkalis vs. silica (TAS) diagram after Le Bas et al. (1986). Note that intrusive rocks from the Doros complex are not classified as basalts and picrobasalts, but as their intrusive counterparts, which is based on their mineralogic compositions (see text for classifications; after Owen-Smith and Ashwal, 2015b). Compositions of Lō'ihi samples are from in-situ electron microprobe analyses (EPMA; Section 4.3.1.1). Discriminating lines for subdivision of alkaline and sub-alkalic rocks are after Macdonald and Katsura (1964) and Irvine and Baragar (1971). AbG = Abnormal Group basalts, SSB = steady state basalts, BOM= basal olivine melagabbro, MOG = massive olivine gabbro, cpx = clinopyroxene.

1.8 to 1.1 Ma, whereas volcanic activity at Tubuai started at ∼12 Ma (Chauvel et al., 1997). The Gambier islands (Mangareva) are associated with the Gambier-Pitcairn island chain and volcanic activity has been dated to range between ∼7.1 Ma and 5.8 Ma (Caroff et al., 1993). Volcanic activity on Nuku Hiva started ∼4.0 Ma ago (Desonie et al., 1993), whereas the sample from Huahine (Society islands) represents the youngest volcanic activity with 2.58 Ma (Duncan and McDougall, 1976). The underlying Pacific plate varies in age between ∼29 to ∼82 Ma (Dupuy et al., 1993). Erupted lavas are known for their heterogeneous radiogenic isotope compositions and are interpreted to relate to different mantle components in the sources feeding the volcanism of French Polynesian islands linked to the so-called South Pacific Isotopic and Thermal Anomaly (SOPITA; Hart, 1984; Staudigel et al., 1991).
Samples in this study have been analyzed for major and trace element as well as radiogenic isotope compositions by Schiller (2019) and are, for completeness of the dataset, presented in Table C.2.8 and described shortly in the following. French Polynesian samples consist of fresh subaerial lavas (LOI < 1.21 wt. %; Schiller, 2019) with mostly transitional to alkaline compositions (Figure 4.3). SiO_2 and MgO contents range between 41.90 to 46.99 wt. % and 6.08 to 17.80 wt. % (Figure 4.3 and 4.4), respectively, thus representing picrites, basanites/tephrites, basalts as well as one trachybasalt (Figure 4.3). The presence of olivine, Ti-augite and magnetite phases and the large range of MgO concentrations indicate magmatic differentiation and/or olivine accumulation to some scale (Schiller, 2019). However, the samples do not display clear fractional crystallization trends in most MgO variation diagrams, which may be due to the variable source and/or initial melt compositions for each island. However, the absence of plagioclase and presence of olivine fractionation is indicated by increasing Al_2O_3 and decreasing Ni and Cr concentrations with decreas-

ing MgO, respectively (Figure 4.4c-e). Most samples with MgO contents < 11 wt.% display CaO/Al_2O_3 ratios < 0.8 indicating the onset of clinopyroxene fractionation in line with decreasing Sc/Yb ratios (Figure 4.4a-b). High MgO contents > 10 wt. % and relatively low Sc concentrations (not shown) may be due to accumulation of olivine, although primary magmas in OIB settings can have up to 16 wt. % MgO (Norman and Garcia, 1999). However, high CaO/Al_2O_3 of these samples cannot be achieved by olivine accumulation only and thus may be an indicator of an additional source effect (Figure 4.4a, b). Primitive mantle normalized trace element patterns (normalizing values after Palme and O'Neill, 2014) show that French Polynesian samples have negatively sloping patterns with highly incompatible elements enriched relative to the rare earth elements (REE), typical for intra-plate basalts (Figure 4.5a). All samples show near parallel REE patterns with $(Gd/Yb)_{PM} > 1$ indicating the presence of residual garnet (Schiller, 2019). Interestingly, samples with HIMU affinity in radiogenic isotope space, show distinct trace element normalized patterns compared to samples with EM affinity. In detail, HIMU samples show negative K and Sr as well as a pronounced negative Zr and Hf and positive Th-U, Nb anomalies and Nd anomalies. In contrast, samples wit EM-type radiogenic isotope compositions display slightly negative Th-U anomalies, less pronounced positive Nd and Nb anomalies and no Zr-Hf anomalies (Figure 4.5a).
Radiogenic isotope compositions are highly heterogeneous for samples from French Polynesia and in agreement with literature data (Figure 4.2; Schiller, 2019; Stracke, 2012). Two samples from Tubuai represent HIMU-type compositions with highly radiogenic $^{206}Pb/^{204}Pb$, $^{207}Pb/^{204}Pb$ and $^{208}Pb/^{204}Pb$ ratios (Figure 4.2d, e). In contrast, the tephrite from Rurutu Island (FP2RU2) shows radiogenic isotope compositions typical for the younger volcanic stage at Rurutu with lower radiogenic Pb, but higher Sr isotopic compositions compared to Tubuai (Figure 4.2c; Chauvel et al., 1997), also defined as Austral-Cook-PREMA signature (Stracke, 2012; Stracke et al., 2005). The EM2 component is represented by the alkali basalts from the islands of Nuku Hiva (Marquesas islands) and Huahine (Society islands) with $^{87}Sr/^{86}Sr > 0.704521$ (Figure 4.2a, c). It should be noted, however, that in $^{208}Pb/^{204}Pb$ vs. $^{206}Pb/^{204}Pb$ isotope space Society and Marquesas samples display lower $^{208}Pb/^{204}Pb$ ratios than expected for EM2-like compositions (Schiller, 2019). Sample FP15GA7 from Mangareva Island is a transitional to tholeiitic basalt and plots close to PREMA compositions in radiogenic isotope space (Figure 4.2c) overlapping with low $^{87}Sr/^{86}Sr$ compositions of the characteristic hotspot-specific mantle array of the Gambier-Pitcairn island chain trending towards EM1 mantle compositions (Stracke et al., 2005).

4.2.4 Vogelsberg, Germany

The Vogelsberg volcano is located to the east of the Rhenish Massif and belongs to the Cenozoic Central European Volcanic Province (CEVP). Samples analyzed in this study are from the study of Bogaard and Wörner (2003) and range in composition from basanites to alkali basalts (Figure 4.3). They are derived from the two youngest volcanic stages: stage III (alkali basalts and basanites; 16.6 to 14.7 Ma, ^{40}Ar-^{39}Ar age dating; Bogaard, 2000) and stage II (alkali basalt VB96-40; minimum age $\sim$16.7 Ma, ^{40}Ar-^{39}Ar age dating; Bogaard, 2000). Included are also four outcrop samples (alkali basalts and basanites). For detailed descriptions see Bogaard and

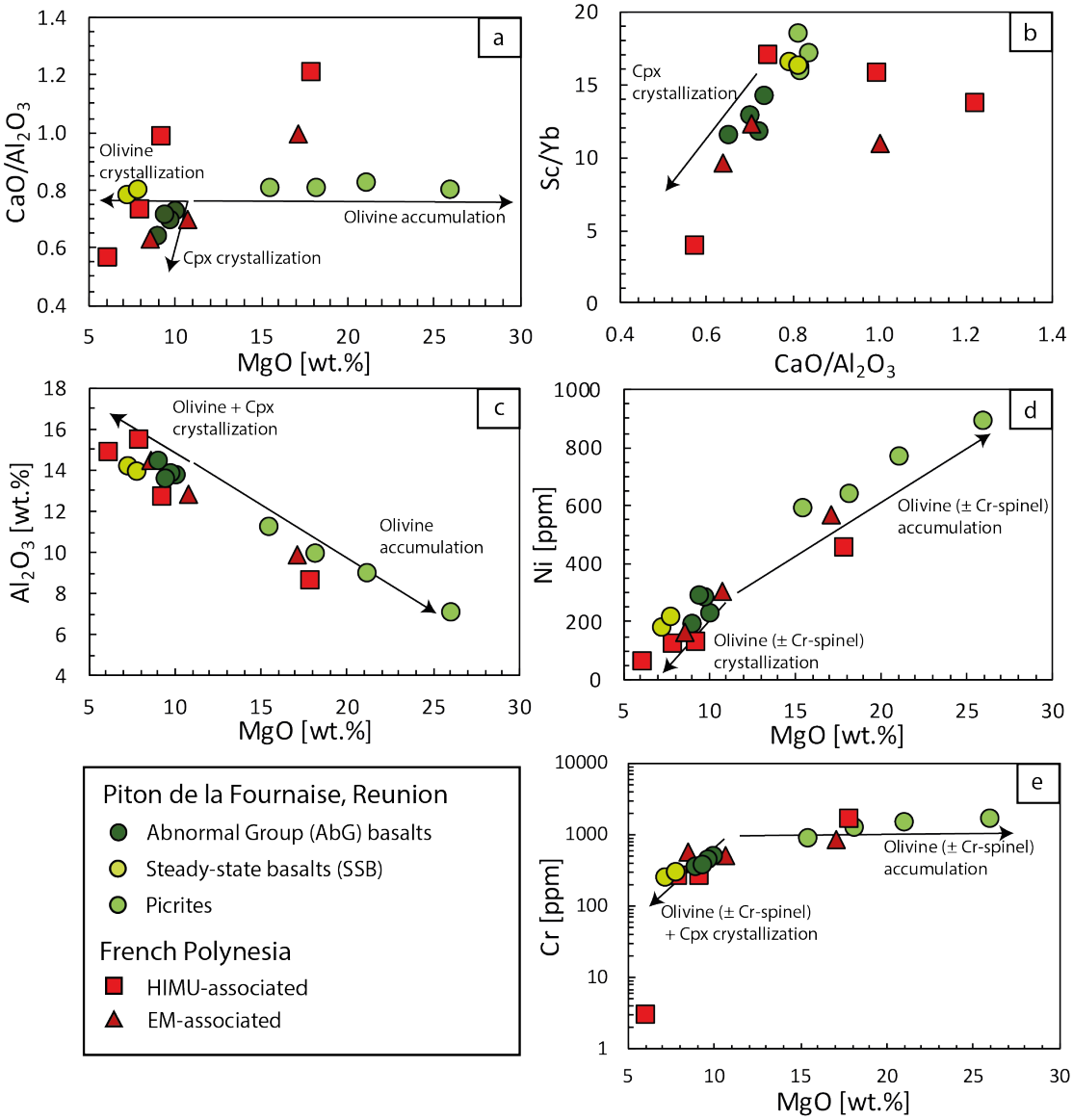

Figure 4.4: Major element variations for ocean island basalts from Piton de la Fournaise (Réunion) and French Polynesia. **a)** Réunion Abnormal Group (AbG) basalts can be easily distinguished from picrites and steady-state basalts (SSB) based on their low CaO/Al_2O_3 ratios < 0.8 at relatively high MgO contents compared to SSB basalts. The parental melt of Réunion basalts has been suggested to have ~10 wt. % MgO (Boudoire et al., 2019). Picrites (MgO > 10 wt. %) and SSB (MgO < 10 wt. %) are mostly controlled by accumulation and fractional crystallization of olivine, respectively, based on their constant CaO/Al_2O_3 ratios at variable MgO contents. Lower CaO/Al_2O_3 ratios of AbG basalts are generated from clinopyroxene fractionation, which is also suggested for some French Polynesia samples; **b)** Fractional crystallization of clinopyroxene is also evident from decreasing Sc/Yb ratios at low CaO/Al_2O_3 displayed by AbG basalts and some French Polynesia samples; **c)** Plagioclase fractionation is negligible as indicated by continuously increasing Al_2O_3 with decreasing MgO; **d)** Ni vs. MgO and **e)** Cr vs. MgO variations indicate olivine (± Cr-spinel) accumulation for samples with MgO > 10 wt. % and olivine (± Cr spinel) + clinopyroxene fractionation for samples with MgO < 10 wt. %. Cpx= clinopyroxene.

Wörner (2003). Chemical alteration is considered to be of minor influence and overall coherent variations for major and trace elements testify the immobile behavior of elements other than the alkali elements. Furthermore, basanites and alkali basalts are devoid of crustal contamination (Bogaard and Wörner, 2003). In general, high Mg#, Cr and Ni concentrations of all samples indicates their primitive composition, whereas the common occurrence of mantle xenoliths in basanites suggest these rocks to be near-primary melts. Basanites have higher MgO (13.5 to 12.1 wt. %) and lower SiO_2 concentrations (42.0 to 44.0 wt. %) than alkali basalts with MgO and SiO_2 between 11.1 to 9.9 wt. % and 45.7 to 46.9 wt. %, respectively (Figure 4.3 and S5). Based on decreasing Ni, Cr and Sc contents with decreasing MgO, and increasing Al_2O_3 with decreasing MgO alkali basalts are thought to be affected by fractional crystallization of olivine and clinopyroxene (Figure C.2.7). The lower incompatible trace element abundances on PM-normalized trace element patterns of alkali basalts compared to basanites argue against a relationship through fractional crystallization of a basanitic parental melt (Figure 4.5b). In contrast, trace element partial melting models indicate that primitive alkali basalts are generated by higher degrees of partial melting (∼10 %) compared to basanites (2 to 6 %) within the garnet-spinel transition zone (Figure 4.12; Bogaard and Wörner, 2003).
Basanites and alkali basalts are highly enriched in incompatible trace elements relative to PM and depict negatively sloping trace element patterns reminiscent of normalized OIB trace element patterns (Figure 4.5) and are characterized by positive Nb-Ta anomaly, slight depletions in Th-U, Zr-Hf and Ti and strong depletions in K. Based on the presence of mantle xenoliths and the homogeneous radiogenic Sr-Nd-Pb isotope compositions, Bogaard and Wörner (2003) proposed that the source of basanites and alkali basalts is dominated by an asthenospheric component closely matching the composition of the European Asthenospheric Reservoir (EAR; Cebria and Wilson, 1995) and PREMA (Stracke, 2012) (Figure 4.2). Additionally, melting within a hydrated amphibole-bearing metasomatized lithospheric mantle has been suggested based on the strong depletions in K, indicating residual, hydrous K-bearing phases (Bogaard and Wörner, 2003; Jung et al., 2011). The metasomatic overprint of the lithospheric mantle beneath the CEVP has been linked to subduction recycling during the Variscan orogeny (Lustrino and Wilson, 2007; Wilson and Downes, 1991). Moreover, in order to combine OIB-like radiogenic Sr-Nd-Hf-Os-Pb isotope compositions with lithospheric K-depleted signatures a multi-stage melting model in the presences of hydrous phlogopite-amphibole-bearing pyroxenite- and/or carbonatite-veins was proposed (Jung et al., 2011; Pfänder et al., 2012).

4.2.5 Doros complex, Namibia

The 130 Ma Doros complex is a shallow-level layered mafic intrusion within the Damaraland Intrusive Suite. It is associated with the Paraná-Etendeka Large Igneous Province (Botha and Hodgson, 1976; Marsh et al., 2008), in which magmatism has been attributed to the earliest impingement of the Tristan mantle plume subsequently creating the Tristan-Gough hotspot track (Renne et al., 1996). Its geology, stratigraphy, petrography and geochemistry has been described in detail in previous studies providing also detailed descriptions of samples from this study (Owen-Smith and Ashwal, 2015a, b; Owen-Smith et al., 2017) and is therefore only shortly described below. The Doros Complex consists of three zones comprising olivine-

rich melagabbros (Lower Zone), more plagioclase-rich olivine gabbros (Intermediate Zone) and a series of mineralogically variable foliated gabbros (Upper Zone). These units are thought to be derived from multiple, small-volume, crystal-bearing magma pulses emplaced as sill-like bodies with an estimated depth of intrusion of 1.5 km (Owen-Smith and Ashwal, 2015a).
Samples from this study exclusively originate from the lower stratigraphic units, i.e., the basal olivine melagabbro (BOM) and the overlying massive olivine gabbro (MOG) (Figure 4.3 and C.2.8). Additionally, one clinopyroxene-cumulate from the upper foliated gabbros is included (TOD-77; this sample displays MgO of ~10 wt. % and markedly lower Al_2O_3 content, in line with > 65 % cumulus clinopyroxene; Figure C.2.8a). Consistently, MgO contents of Doros samples in this study range from 4.17 to 21.26 wt. %, where high MgO contents (> 15 wt. %) reflect the high proportions of olivine accumulation in BOM. Massive olivine gabbros are characterized by small positive Eu-anomalies (Eu/Eu*) and positive Ba and Sr spikes on PM normalized trace element patterns reflecting an increase in cumulus plagioclase up-

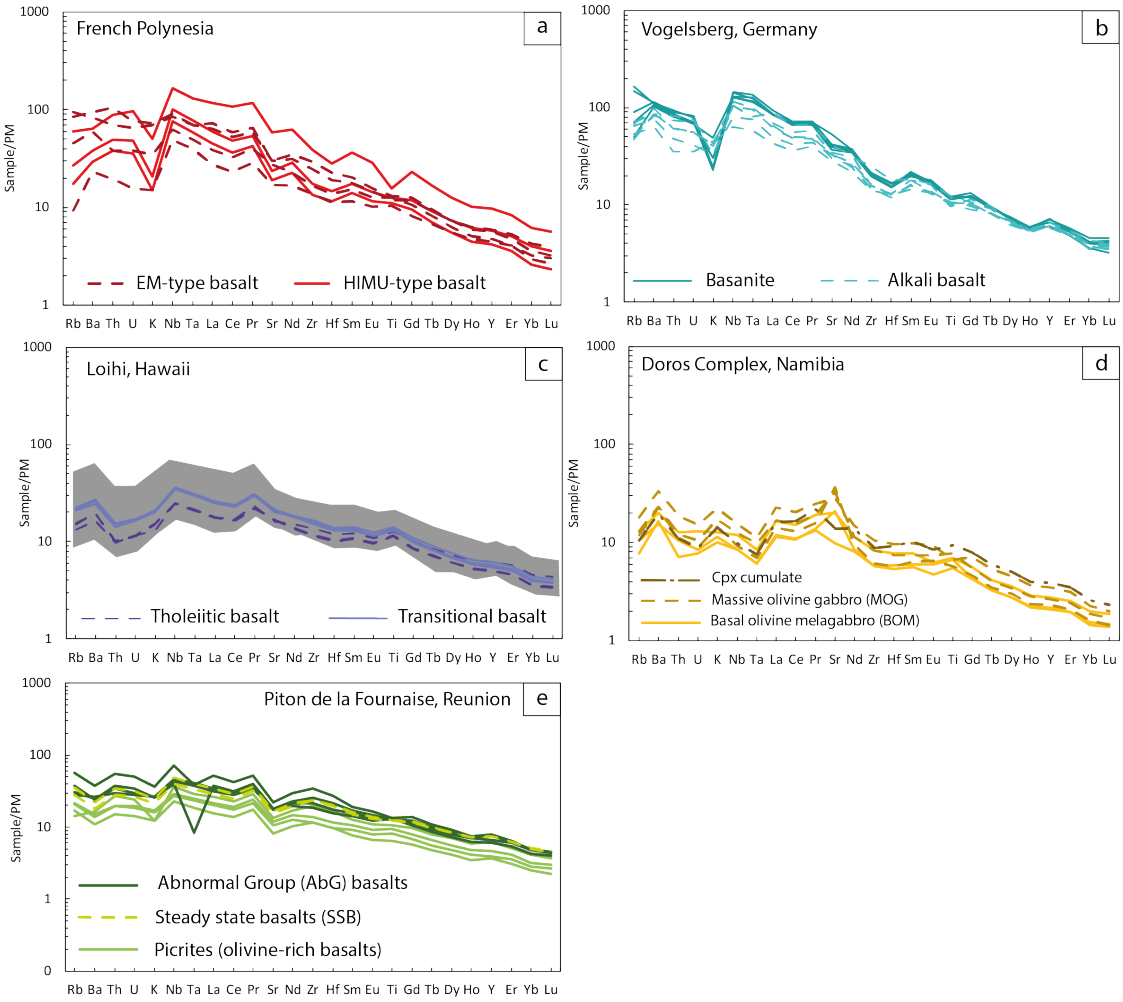

Figure 4.5: Trace element patterns normalized to primitive mantle (PM) values (Palme and O'Neill, 2014). Ocean island basalts in **a)** French Polynesia (Schiller, 2019); **c)** Lō'ihi, Hawaii; **e)** Piton de la Fournaise, Réunion; Continental intraplate basalts in **b)** Vogelsberg volcano, Germany (Bogaard and Wörner, 2003); **d)** Doros Complex, Namibia (Owen-Smith and Ashwal, 2015a). Grey field in c) denotes compiled trace element data for Lō'ihi glasses (Garcia et al., 1995; Garcia et al., 1993; Garcia et al., 1998).

stratigraphy (Figure 4.5d). All samples show uniform REE patterns as well as extended trace element patterns with slight light REE (LREE) enrichments. Moreover, based on the absence of orthopyroxene and relatively depleted and homogeneous Sr-Nd-Pb isotope compositions crustal contamination is considered negligible (Owen-Smith and Ashwal, 2015a; Owen-Smith et al., 2017). Excluding one sample, which has been affected by hydrothermal alteration (TOD-40) initial radiogenic isotope compositions show a narrow range ($^{143}Nd/^{144}Nd$ = 0.512669 to 0.512799, $^{87}Sr/^{86}Sr$ = 0.704115 to 0.704449, $^{206}Pb/^{204}Pb$ = 17.996 to 18.142; Figure 4.2). Accordingly, Sr-Nd-Pb isotope signatures have been attributed to a mixture of 60 to 80 % of depleted shallow asthenospheric mantle component and 20-40 % of an enriched deeper mantle component (EM1), free of lithospheric mantle contribution (Owen-Smith et al., 2017).

4.3 Methods

Major and trace element as well as radiogenic Sr, Nd and Pb isotope compositions for samples from the Doros Complex and Vogelsberg volcano have been reported previously (Owen-Smith and Ashwal 2015a; Owen-Smith et al. 2017 and Bogaard and Wörner, 2003; respectively). French Polynesia samples were fully characterized by Schiller (2019) for major and trace element as well as radiogenic Sr, Nd and Pb isotope compositions performed at the Isotope Geochemistry laboratories of the University of Tuebingen, and therefore follow protocols given below.
Major element compositions for all Réunion samples and trace element compositions for 8 out of 10 Réunion samples were analyzed at the University of Goettingen and the data are described in Section 4.4.1.1 and 4.4.2.1, respectively. Réunion samples REU14-45 and REU14-48, together with samples REU14-31 and REU14-32 used for quality reference, were analyzed for their trace element compositions at the University of Tuebingen after protocols given in Section 4.3.2.1 (Figure C.2.9. Radiogenic Sr, Nd and Pb isotope compositions for Réunion samples were performed at the University of Tuebingen after protocols described in Section 4.3.2.2 and 4.3.2.3.
All samples, but glassy basalts from Lō'ihi, Hawaii, were provided as powders. Lō'ihi glass chips were removed from basalt blocks, repeatedly cleaned with MQ water, and carefully handpicked under a binocular to avoid alteration and minimize the effects of phenocrysts incorporation (Figure C.2.3). These glassy chips were then used for determination of major (Section 4.3.1) and trace element concentrations (Section 4.3.2.1) as well as radiogenic Sr-Nd (Section 4.3.2.2) and stable Cr and Fe isotope compositions (Section 4.3.2.4) carried out at the University of Tuebingen.
All stable Cr and Fe isotope data were obtained at the Isotope Geochemistry facilities of the University of Tuebingen as described in 3.2.4 and are reported in Table 4.1. The complete set of all published and newly acquired data are reported in Appendix C (Supplementary Tables C.2.6 to C.2.10).

4.3.1 Major element compositions

A subset of four Lō'ihi samples were analyzed for their major element compositions using two different methods, electron probe micro analysis (EPMA) and solution quadrupole inductively coupled plasma mass spectrometer (Q-ICP-MS; Table C.2.7). These four samples include both petrographic types, highly olivine-phyric

(samples J2-307-R2C, J2-246-R3D) and sparsely olivine-phyric basalts (samples J2-243-1C-R6 and J2-243-1B-R3).

4.3.1.1 Electron probe micro analyses

Major element compositions were determined using an electron probe micro analyzer JEOL JXA-8230 in wavelength-dispersive mode with an accelerating voltage of 15 kV and a beam current of 20 nA at the University of Tuebingen. The reported values, described in further detail in Section 4.4.1.2, are averages of three spot analyses of at least 5 glass chips per sample using a 20 μm beam size. Major and minor/trace element oxides included in the measurement protocol were SiO_2, Al_2O_3, CaO, MgO, Na_2O, K_2O, FeO, TiO_2, MnO, Ba, Cl, F and SrO. Concentrations of SrO and F were always below the detection limit. Backscattered electron image was used to check for the presence and mineralogy of microphenocrysts (Figures C.2.4 to C.2.6). Scanning electron microscopy (SEM) was used to analyse mineral compositions (Section 4.4.1.2.1).
We note that analyses oxide totals are below 100 %, ranging from 97.52 to 98.03 %. It could be assumed that the missing fractions present volatiles (H_2O + CO_2), but this might be an overestimation of volatile content in Lō'ihi glasses. Schipper et al. (2010) investigated lapilli deposits of so-called 'poseidic' eruptions and measured H_2O and CO_2 contents ranging from ∼0.3 to 0.8 wt. % and ∼0 to 500 $\mu g\,g^{-1}$, respectively. Dixon and Clague (2001), however, observed higher volatile contents of up to 1.55 wt. % in Lō'ihi glasses. On the other hand, P_2O_5, and the presences of Fe as Fe_2O_3 are not included in the measurement protocol, although presumably displaying relevant constituents in Lō'ihi glasses (Section 4.4.1.2).

4.3.1.2 Solution quadrupole ICP-MS

All Lō'ihi glasses were analyzed for their major element compositions using a ThermoFisher Scientific iCap-Qc Q-ICP-MS. Measurements were performed based on a method previously published in Albut et al. (2018) and similar to the protocol outlined for trace element analyses (Section 4.3.2.1). Adequate aliquots were taken from the same sample stock solution as prepared for trace element and isotopic composition analyses (Section 4.3.2) and diluted to a nominal, gravimetric dilution factor of ∼100,000 yielding a 2 % HNO_3 solution ready for measurement. External calibration was carried out by measuring different dilutions of USGS reference material W-2a. Method precision and accuracy was checked by measuring USGS reference materials AGV-2, BHVO-2 and BIR-1a. Due to the HF-HNO_3 digestion procedure used in this method and the subsequent evaporative loss of SiF_4, SiO_2 concentrations may only be approximated by normalizing to 100. Based on uncertainties over constituents, which were not included in the measurement method performed via EPMA (e.g., volatile content; Section 4.3.1.1), this approach may be rather inaccurate. In general, averaged major element concentrations of reference materials measured over the course of this study agree well with recommended values (Table C.2.1), and suggest a general method precision of < 2 % RSD. We note that K_2O and P_2O_5 show higher uncertainties in USGS reference material BIR-1a compared to BHVO-2, which is attributed to their very low concentrations in reference material BIR-1a. Moreover, a comparison of major element data for mid-ocean ridge basalt 267ROV-5 determined by Q-ICP-MS and standard x-ray fluorescence

(XRF) show good agreement (Table C.2.1).

4.3.2 Trace element and isotope compositions

For samples from Lō'ihi, 60 to 90 mg of the handpicked glassy chips (Figure C.2.3) were grinded by hand to fine powders in an agate mortar, which was carefully cleaned between samples using MQ water and then low molar HCl. Sample powders were digested in closed Savillex PFA beakers using adequate amounts of concentrated HF (∼27 M):HNO_3 (∼14.5 M) mixtures and heated to 120° C for four days on a hotplate. Following evaporation, samples were re-dissolved in 6 M HCl and heated to 120° C for one day to ensure complete destruction of fluorides. Subsequent removal of any excess Cl^- was achieved by repeated evaporation to incipient dryness with HNO_3 (65 %). The sample residue was re-dissolved in 1 mL 5 M HNO_3 and a stock solution (2 % HNO_3) with a nominal dilution factor of ∼1,000 was created gravimetrically. All analyses, including Cr and Fe isotope analyses, were determined on individual aliquots from the same digest following a protocol described in Babechuk et al. (2019).
For samples from the Vogelsberg volcano, Doros Complex, French Polynesia and Réunion 30 mg of rock powder was digested via closed bomb digestion after a protocol described in Wagner et al. (2021) and aliquots for stable Cr and Fe analyses were taken from the dissolved sample solution. Additionally, an aliquot from four Réunion samples (REU14-31, REU14-32, REU14-45, REU14-48) was taken for trace element analyses (Section 4.3.2.1) enabling the possibility to compare the trace element data obtained from the University Tuebingen to the trace element data analyzed in the facilities of the University Goettingen (Figure C.2.9 and Table C.2.3). As for Lō'ihi samples, all analyses were determined on individual aliquots from the same digest following a protocol described in Babechuk et al. (2019).

4.3.2.1 Trace element compositions

Trace element determinations were performed via solution Q-ICP-MS on a ThermoFisher Scientific iCAP-Qc housed at the Isotope Geochemistry facilities of the University of Tuebingen applying a method adopted from Albut et al. (2018) and previously described in Wagner et al. (2021). In brief, prepared stock solutions (Section 4.3.2) were further diluted to a nominal, gravimetric dilution factor of ∼10,000 yielding a final 2 % HNO_3 solution ready for measurement. Sensitivity and instrumental drift were corrected for by adding an internal standard (^{6}Li, In, Re and Bi) to procedural blanks, calibration standards, quality control reference materials, sample unknowns and external drift monitor samples. External calibration was carried out using the averaged intensities at three different dilution factors of the natural USGS reference material W-2a. A combination of independent USGS reference materials AGV-2, BIR-1a and BHVO-2 were measured to provide a monitor of method precision and accuracy. Mean trace element concentrations for reference material BIR-1a and BHVO-2, which underwent the same geochemical procedure, agree well with previous studies applying the same method (i.e., better than 5 %), and the 1 r.s.d suggest a full method precision better than 5 % (Table C.2.2). Comparison of trace element data for samples REU14-31 and REU14-32 analyzed at the University Tuebingen and the University of Goettingen show good agreement on PM-normalized trace element patterns (Figure C.2.9, Table C.2.3). However, Zr

and Hf concentrations are lower in samples measured in the facilities of the University of Tuebingen compared to the University of Goettingen.

4.3.2.2 Radiogenic Sr and Nd isotopes

Determination of Sr and Nd isotope compositions were performed using a thermal ionization mass spectrometry (TIMS) at the University of Tuebingen following a protocol described in Wagner et al. (under review; Appendix B, Chapter 3). For Réunion samples, 20 mg of whole-rock powder was digested on a hotplate as described for Lō'ihi samples in Section 4.3.2. For Lō'ihi samples an adequate aliquot was taken from the prepared stock solutions (Section 4.3.2) and converted to chloride form. Separation of Sr and Nd from the sample matrix was achieved by ion-exchange procedures and measured on a Finnigan MAT 262. Total procedural blanks were < 183 pg for Sr and < 22 pg for Nd contributing less than 0.1 % to the total processed Sr and Nd, and thus deemed negligible. A $^{88}Sr/^{86}Sr$ ratio of 8.375209 and exponential law were used to correct for mass fractionation. During the course of this study, measurements of NBS SRM 987 yielded an $^{87}Sr/^{86}Sr$ of 0.710262 $\pm$ 0.000020 (2SD; n=12), which is in good agreement with the long-term reproducibility of 0.710251 $\pm$ 0.000019 (2SD; n=334). Analytical accuracy was assessed by measuring USGS rock reference materials BHVO-2 and BIR-1a, which gave $^{87}Sr/^{86}Sr$ ratios of 0.703497 $\pm$ 0.000010 (2SD, n=2, two digests) and 0.703115 $\pm$ 0.000010 (2SE, n=1; Table C.2.4), respectively, agreeing well with literature data (Fourny et al., 2016; Weis et al., 2006). A $^{146}Nd/^{144}Nd$ ratio of 0.7219 and the exponential law were used to correct for analytical mass fractionation. Epsilon Nd values were calculated using a present-day $^{143}Nd/^{144}Nd_{CHUR}$ of 0.512630 (Bouvier et al., 2008). Repeated measurements of the LaJolla Nd and J-Ndi standards gave $^{143}Nd/^{144}Nd$ ratios of 0.511817 $\pm$ 0.000016 (2SD; n=14) and 0.512073 $\pm$ 0.000020 (2SD; n=18), respectively. These values are in good agreement with the long-term reproducibility of 0.511830 $\pm$ 0.000041 (2SD; n=172) and 0.512075 $\pm$ 0.000073 (2SD; n=71), respectively. Rock reference materials BHVO-2 and BIR-1a were measured to provide a monitor for method accuracy and yielded $^{143}Nd/^{144}Nd$ ratios of 0.512918 $\pm$ 0.000020 (2SD, n=2, two digests) and 0.513030 $\pm$ 0.000011 (2SE, n=1; Table C.2.4), respectively, which are in good agreement with previously reported values (Li et al., 2007; Raczek et al., 2003).

4.3.2.3 Radiogenic Pb isotope compositions

Pb isotope compositions of Réunion samples were determined on 50 mg of sample powder digested on a hotplate using the protocol described in Section 4.3.2. Purification of Pb was achieved by ion-exchange chromatography using anion exchange resin AG1-X8 and measurements were carried out on a ThermoFisher Scientific Neptune-Plus multicollector inductively coupled plasma mass spectrometer (MC-ICP-MS) housed at the Isotope Geochemistry laboratories of the University of Tuebingen. Samples were introduced as solutions of $\sim$200 ng g^{-1} Pb via an Aridus II desolvating nebulizer. Mass fractionation correction was performed using the Tl-doping method, in which the $^{205}Tl/^{203}Tl$ was artificially adjusted to 2.388077 to reach the correct $^{206}Pb/^{204}Pb$ value for NBS 981 of 16.941 as proposed by Collerson et al. (2002). Consequently, repeated measurement of the standard material NBS 981 yielded mean ratios of $^{206}Pb/^{204}Pb$ = 16.9410 $\pm$ 50 (n=13), $^{207}Pb/^{204}Pb$ = 14.4985

± 75 (n=13) and $^{208}Pb/^{204}Pb$ = 36.7210 ± 89 (n=13). Mean ratios obtained for standard material NBS 982 were $^{206}Pb/^{204}Pb$ = 36.7496 ± 36 (n=6), $^{207}Pb/^{204}Pb$ = 17.1642 ± 26 (n=6) and $^{208}Pb/^{204}Pb$ = 36.7522 ± 28 (n=6). These values are in excellent agreement with previously reported values (Collerson et al., 2002; White et al., 2000). Analytical accuracy was assessed by measuring USGS reference material BHVO-2 yielding $^{206}Pb/^{204}Pb$ = 18.681 ± 289 (n=1), $^{207}Pb/^{204}Pb$ = 15.536 ± 315 (n=1) and $^{208}Pb/^{204}Pb$ = 38.260 ± 358 (n=1), which are in good agreement with previously reported values (Fourny et al., 2016; Weis et al., 2006; Woodhead and Hergt, 2000; Wu et al., 2017). Total procedural blanks were 11 pg g^{-1} contributing less than 0.5 % to the total processed Pb and thus deemed negligible.

4.3.2.4 Stable Cr and Fe isotope compositions

Analyses of stable Cr and Fe isotope compositions were carried out on a ThermoFisher Scientific NeptunePlus MC-ICP-MS at the University of Tuebingen. Chemical purification and measurement protocols for Cr and Fe were carried out after protocols previously described in Wagner et al. (2021). For Cr and Fe isotope determinations aliquots corresponding to 2 μg Cr and 15 μg Fe, respectively, were taken from the prepared sample stock solutions (Lō'ihi) or dissolved bomb digest sample solutions (Réunion, French Polynesia, Vogelsberg and Doros Complex; Section 4.3.2) such as described in Babechuk et al. (2019). Cr and Fe isotope analyses for all samples were always performed on the same sample digest.
Cr isotope compositions are reported in δ-notation relative to NIST SRM979 and expressed in ‰ by multiplication with a factor of 1000:

$$\delta^{53/52}Cr_{SRM979} = \frac{(^{53}Cr/^{52}Cr)_{sample}}{(^{53}Cr/^{52}Cr)_{SRM979}} - 1 \quad (4.1)$$

henceforth referred to as $\delta^{53/52}$Cr.
Over the course of this study, repeated measurements of NIST SRM979, with a long-term reproducibility of 0.000 $\pm$ 0.021 ‰ (2SD; n=594), yielded an average $\delta^{53/52}$Cr value of 0.000 $\pm$ 0.021 ‰ (2SD; n=75). In-house standard Merck Cr(III), displaying a long-term reproducibility of -0.430 $\pm$ 0.023 ‰ (2SD; n=372), yielded an average $\delta^{53/52}$Cr value of -0.430 $\pm$ 0.024 ‰ (2SD; n=46). Accuracy of natural sample materials was assessed by measuring the USGS rock reference materials BHVO-2 and BIR-1a along with sample unknowns, which yielded $\delta^{53/52}$Cr values of -0.140 $\pm$ 0.016 ‰ (2SD; n=11, 5 digests) and -0.155 $\pm$ 0.028 ‰ (2SD; n=13, 6 digests), respectively, and are thus in excellent agreement with the long-term averages of -0.144 $\pm$ 0.022 ‰ (2SD; n=103, 17 digests) and -0.150 $\pm$ 0.025 ‰ (2SD; n=100, 16 digests), respectively. As most samples were measured one time only, external reproducibility of sample unknowns is represented by long-term reproducibility of single measurements of natural rock reference material BHVO-2, which is equal to $\pm$ 0.022 ‰ and used in all plots displaying $\delta^{53/52}$Cr values. Total procedural blanks were usually contributing < 0.5 % to the amount of Cr processed (see Appendix C for details on Cr blank contribution).
Fe isotope compositions are reported in in δ-notation relative to NIST IRMM-014 and expressed in ‰:

$$\delta^{56/54}Fe_{IRMM014} = \frac{(^{56}Fe/^{54}Fe)_{sample}}{(^{56}Fe/^{54}Fe)_{IRMM014}} - 1 \quad (4.2)$$

henceforth referred to as $\delta^{56/54}$Fe.
During the course of this study multiple measurements of IRMM-014 gave an average value of 0.000 ± 0.035 ‰ (2SD; n=25) in agreement with long-term reproducibility of 0.000 ± 0.035 ‰ (2SD; n=299). Similarly, the compiled values of in-house standards HanFe and TuebFe gave an average of +0.301 ± 0.043 ‰ (2SD; n=14) and -0.378 ± 0.022 ‰ (2SD; n=3) agreeing well with the long-term reproducibility achieved in our lab of +0.289 ± 0.039 ‰ (2SD; n=131) and -0.377 ± 0.038 ‰ (2SD; n=96), respectively, and values given in previous studies (Babechuk et al., 2019; Kurzweil et al., 2016; Wu et al., 2017). Method accuracy was determined by measuring rock reference materials BHVO-2 (+0.122 ± 0.057 ‰, 2SD; n=6, 5 digests) and BIR-1a (+0.077 ± 0.051 ‰, 2SD; n=7, 6 digests) yielding consistent results with the long-term average obtained during the course of this PhD project (+0.110 ± 0.042 ‰, 2SD; n=21, 9 digests and +0.067 ± 0.042 ‰, 2SD; n=14, 8 digests, respectively; Table C.2.5) and values given in the literature (McCoy-West et al. 2018; Williams et al. 2021; Weyer and Ionov 2007). External reproducibility of Fe isotope measurements is assessed by the long-term reproducibility of single measurements of standard material TuebFe, which is equal to ± 0.038 ‰ and used in all plots displaying $\delta^{56/54}$Fe values. Total procedural blanks were always lower than 0.05 % of the total processed Fe and thus deemed negligible.

4.4 Results

4.4.1 Major element compositions

4.4.1.1 Piton de la Fournaise, La Réunion

In this study, Réunion samples vary in MgO concentrations from 7.19 to 25.94 wt. % (Figure 4.4) encompassing the three compositional groups typical for La Réunion lavas, which are steady-state basalts (SSB), picrites and abnormal group (AbG) basalts. Overall, geochemical compositions agree well with the literature data (e.g., Albarède et al., 1997; Boudoire et al., 2019; Salaün et al., 2010). Two samples erupted within the central area represent SSB with low MgO contents of 7.19 and 7.76 wt. %, K_2O contents < 0.78 wt. % and CaO/Al_2O_3 ratios of 0.79 and 0.81 (Figure 4.4a, Table 4.1). Samples with picritic compositions have high MgO contents between 15.42 and 25.94 wt. % at similar CaO/Al_2O_3 ratios and are derived from the central area and associated SERZ or NERZ as well as from the peripheral NWRZ (Table 4.1). Abnormal group basalts are represented by four samples, which have MgO contents between 8.97 and 9.99 wt. %, K_2O contents > 0.8 wt. % and markedly lower CaO/Al_2O_3 ratios between 0.63 and 0.73 (Figure 4.4a). All AbG basalts were exclusively sampled within the NWRZ. In accordance with previous studies, SSB and picrites are transitional in character (Upton and Wadsworth, 1966), whereas AbG basalts display a mildly alkaline affinity (Figure 4.3; Boudoire et al., 2019; Salaün et al., 2010). Abnormal Group basalts REU14-45, REU14-67 and REU14-76 are olivine-bearing, whereas AbG basalt REU14-48 is aphyric. It is important to note, however, that none of the AbG basalts in this study are clinopyroxene-bearing basalts. Based on the presence of olivines, low CaO/Al_2O_3 ratios, low SiO_2 contents and alkaline enrichments as well as sampling locations within the NWRZ, AbG basalts in this study are similar to "olivine-bearing basalts" from peripheral

eruptions reported in Boudoire et al. (2019) (see also Section 4.2.1 and 4.4.2.1).

4.4.1.2 Lō'ihi, Hawaii

4.4.1.2.1 Mineralogy

Sparsely olivine-phyric basalts Sample J2-243-1C-R6 (Figure C.2.4) carries abundant olivine microphenocrysts. Microphenocrysts of clinopyroxene and Cr-spinel (< 30 μm) are less abundant. Where present, simultaneous growth of clinopyroxene with generally augitic composition and Cr-spinel (34-41 wt. % Cr_2O_3) is observed, but Cr-spinel can also occur as inclusions in olivine. Sometimes clinopyroxene growth structure indicates that further crystallization was terminated by quenching. Very small sulfide crystals/melt droplets (< 10 μm) are frequently observed throughout the glass matrix.
Sample J2-243-1B-R3 contains microphenocrysts of olivine, clinopyroxene and Cr-spinel, whereas the latter occurs also as inclusions in olivine. Clinopyroxene and Cr-spinels display Cr_2O_3 contents ranging from 0.99 to 1.04 wt. % and ∼41 to 46 wt. %, respectively.

Highly olivine-phyric basalts Sample J2-307-R2 (Figure C.2.6) consists of homogeneous glass with minor presence of clinopyroxene and olivine microphenocrysts (10 μm). Olivine microphenocrysts are sometimes idiomorphic. Clinopyroxene phenocrysts are augitic in composition with 0.72 to 0.97 wt. % Cr_2O_3 and can be up to 80 μm in size. Very small sulfide droplets ($< 1\,\mu$m) are frequently observed, whereas the individual occurrence of a large sulfide melt droplet ($< 150\,\mu$m) is unique. Cr-spinel is present as inclusions in olivine or associated with sulfides with variable Cr_2O_3 contents ranging between 24 and 39.48 wt. %.
Sample J2-246-R3D (Figure C.2.5) appears similar compared to sample J2-307-R2 with the glass matrix carrying idiomorphic olivine microphenocrysts ($< 150\,\mu$m), pyroxenes ($< 50\,\mu$m) with Cr_2O_3 contents ranging between 0.36 to 0.45 wt. % and very small sulphide droplets ($< 1\,\mu$m). Pyroxene grows on surfaces of olivine, which indicates that olivine is the first phase to crystallize followed by clinopyroxene. Cr-spinel is overall rare in occurrence and usually $< 10\,\mu$m. It is observed as inclusions in olivines as well in association with sulfide or clinopyroxene and can be up to 50 μm (33 wt. % Cr_2O_3). One glass chip contains Cr-spinel (28 wt. % Cr_2O_3) present as skeletal crystals ($< 10\,\mu$m) indicating non-equilibrium and fast growth.
Generally, Cr contents of Cr-spinel measured in this study agree well with previously reported Cr contents ranging between 41 and 48 wt. % within tholeiitic or alkali basalts (Garcia et al., 1995). Chromium contents in clinopyroxenes also agree well with previously reported values although the literature data show a larger variability with Cr contents ranging between 0.1 to 1.1 wt. % (Garcia et al., 1995).

4.4.1.2.2 Glass composition (EPMA and Q-ICP-MS)

Major element compositions of Lō'ihi glasses determined in-situ (EPMA) and via solution Q-ICP-MS are displayed in MgO variations diagrams and compared to

available literature data covering the two alternate methods in Figure 4.6 (Table

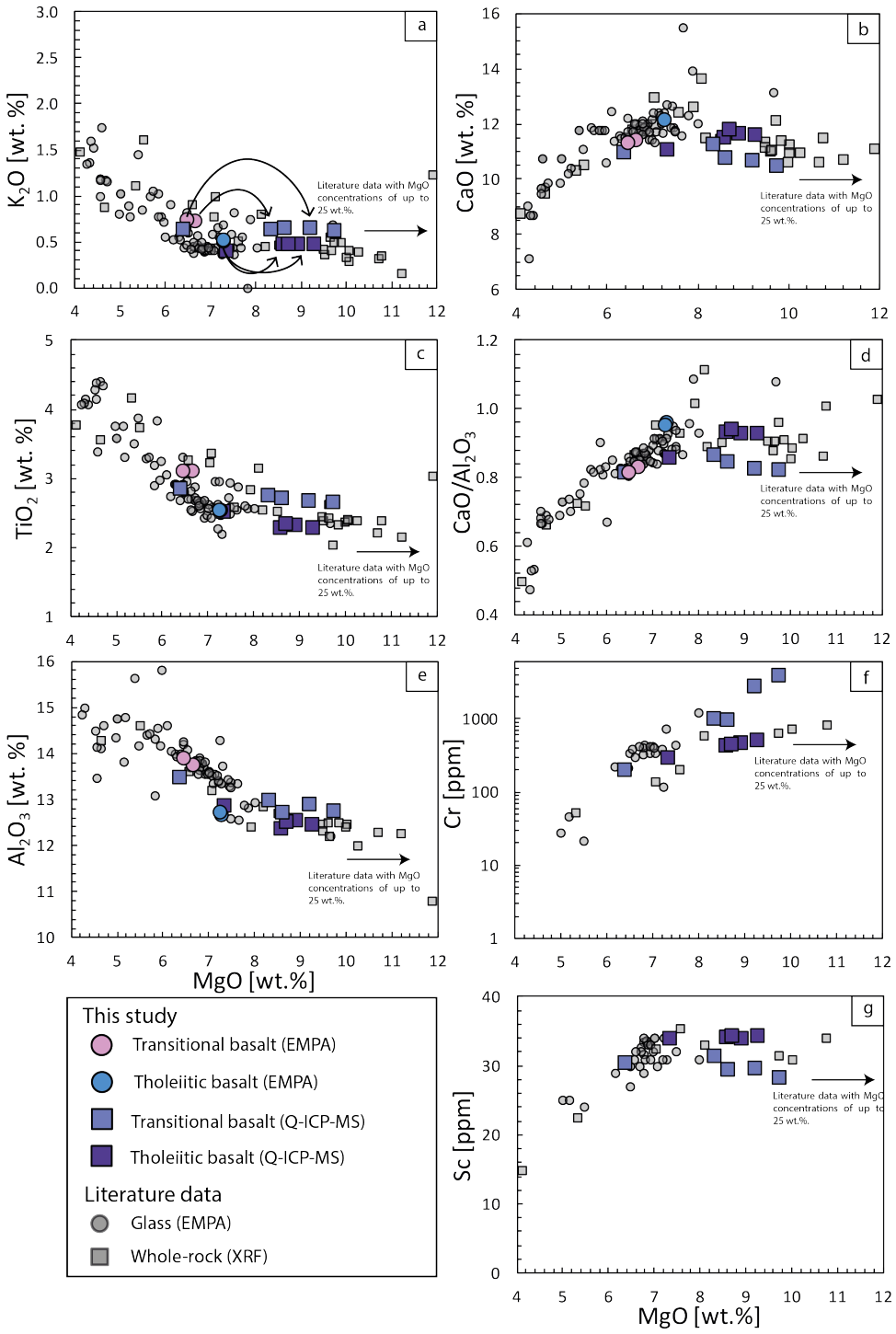

Figure 4.6: Major element vs. MgO shown for transitional and tholeiitic basalts from Lō'ihi, Hawaii, as determined from two alternate methods, i.e., EPMA (circles) and Q-ICP-MS (squares). **a)** the sub-set of four Lō'ihi samples that were analyzed for major element compositions by both methods are connected by curved arrows. Compiled literature data for glass compositions determined by EPMA (grey circles; Garcia et al., 1995; Garcia et al., 1993; Garcia et al., 1998; Hawkins and Melchior, 1983; Pietruszka et al., 2011; Yi et al., 2000) and whole-rock compositions determined by XRF (grey squares; Frey and Clague, 1983; Garcia et al., 1995; Garcia et al., 1998; Hawkins and Melchior, 1983) are shown for comparison.

C.2.7)(Garcia et al., 1995; Garcia et al., 1993; Garcia et al., 1998; Hawkins and Melchior, 1983; Pietruszka et al., 2011).
The subset of four samples from Lō'ihi analyzed for their major element compositions using in-situ EPMA show very homogeneous glass compositions, especially within their two petrographic groups (Figure 4.3). In the total alkalis vs. silica (TAS) diagram sparsely olivine-phyric basalts display tholeiitic compositions, whereas glass compositions of highly olivine-phyric basalts display a transitional composition with mild alkaline affinity (Figure 4.3). Hereinafter, the terms tholeiitic and transitional basalts will be used to distinguish between the two groups. Concentrations of MgO range between 6.47 and 7.28 wt. % and overlap well with literature data of Lō'ihi glasses determined via EPMA (Figure 4.6). Transitional basalts have lower MgO (6.47 to 6.66 wt. %) and SiO_2 contents (47.77 to 47.90 wt. %) compared to tholeiitic samples (∼7.28 and ∼48 wt. %, respectively; Figure 4.6). Lower CaO concentrations and higher K_2O, Al_2O_3 and TiO_2 concentrations at lower MgO abundances in transitional basalts may suggest a higher degree of differentiation compared to the melt compositions of tholeiitic samples (Figure 4.6a, c, e). However, lower SiO_2 contents of transitional basalts (Figure 4.3) are in contrast with a higher degree of differentiation. In general, high CaO concentrations of transitional and tholeiitic basalts (11.34 to 11.44 and 12.16 to 12.18 wt. %, respectively; Figure 4.6b) and resulting higher CaO/Al_2O_3 ratios between 0.81 and 0.96 (Figure 4.6d) are in agreement with higher CaO contents of Lō'ihi basalts compared to other Hawaiian volcanoes (Jackson et al., 2012).
It is noteworthy, that the major element compositions determined via solution Q-ICP-MS are not entirely consistent with glass compositions determined by EPMA (Figure 4.6). Tholeiitic and transitional basalts have higher MgO contents (8.33 to 9.20 wt. %) compared to in-situ analyses of the same samples (Figure 4.6a). As Q-ICP-MS analyses were performed on dissolved glasses, this offset in MgO contents (and also other major elements such as TiO_2, Al_2O_3) may be due to the incorporation of olivine microphenocrysts in the analyzed powders compared to the 'pure' glass compositions analyzed via EPMA. The transitional (highly olivine-phyric) basalts may additionally be affected by incorporation of Cr-spinel microphenocrysts, as shown by the unusual high Cr contents ranging from 969 to 3917 $\mu g\, g^{-1}$ (Figure 4.6f). This may be supported by petrographic observations that Cr-spinel frequently occurs as inclusions in olivine, but cannot be unambiguously demonstrated based on the four samples described above. In general, samples analyzed via Q-ICP-MS extend towards higher MgO contents and fill the gap between the majority of published glass compositions with MgO contents < 8 wt. % (EPMA; Figure 4.6) and sample 187-1 (MgO = 9.68 wt. %; EPMA) taken from the literature (Garcia et al., 1995). Furthermore, these samples overlap well with published whole-rock data analyzed by x-ray fluorescence (XRF) (Frey and Clague, 1983; Garcia et al., 1995; Garcia et al., 1998; Hawkins and Melchior, 1983), although whole-rock MgO concentrations from the literature are as high as 25 wt. % (Figure 4.6). Two samples, J2-241-2-R9 and J2-316-R1, display MgO concentrations < 8 wt. % and are accompanied by low concentrations of compatible trace elements such as Cr and Ni (217-317 $\mu g\, g^{-1}$ and 87.9-115 $\mu g\, g^{-1}$, respectively), which is well within the range of previously published values (Figure 4.6d, f). Generally, Lō'ihi glass compositions fit the trend in MgO variation diagrams defined by previously published data (Figure 4.6): TiO_2 and Al_2O_3 and K_2O increase with decreasing MgO (Figure 4.6a, c, e). For sam-

ples with MgO >8 wt. %, invariant CaO/Al_2O_3 ratios and low Sc contents indicate olivine control, whereas samples with <8 wt. % MgO show decreasing CaO and Sc concentrations and CaO/Al_2O_3 ratios with decreasing MgO indicating fractional crystallization of clinopyroxene (Figure 4.6b, d).
Despite the fact that relatively high MgO and Cr contents may be due to incorporation of microphenocrysts of olivine and Cr-spinel, the two petrographic groups have distinct compositional characteristics as already indicated by EPMA of pure glass compositions. These differences cannot be reconciled with microphenocrysts incorporation in transitional basalts alone. In detail, at similar MgO contents, transitional basalts have higher TiO_2, V, K_2O and slightly higher Al_2O_3 contents and lower FeO, Sc, CaO contents and CaO/Al_2O_3 ratios. Although, olivine incorporation may lower CaO and Sc content (similar to an olivine accumulation trend), it cannot account for the higher K_2O contents in transitional basalts as higher proportion of olivine incorporation would only mute this signal. Although we note, that major element abundances of individual samples may be affected to different extents by incorporation of olivine microphenocrysts, we suggest that higher alkali contents in transitional (highly olivine-phyric) basalts are a primary feature. This is further supported by EPMA, which show the same systematic variations in major element compositions within the two petrographic groups. Moreover, ratios of CaO/Al_2O_3 should not be affected by olivine incorporation or removal, indicating that the generally lower CaO/Al_2O_3 of transitional basalts may be attributed to a higher degree of clinopyroxene fractionation or alternatively mirror variable source compositions for the two petrographic groups.

4.4.2 Trace element compositions

4.4.2.1 Piton de la Fournaise, La Réunion

Trace element patterns of Réunion lavas are roughly parallel and represent typical OIB compositions with enriched incompatible trace elements relative to PM (Figure 4.5e; PM normalizing values from Palme and O'Neill, 2014). Picritic (olivine-rich) basalts show lowest trace element concentrations that continuously increase towards SSB basalts, which is in agreement with fractional crystallization/accumulation of olivine. All samples are characterized by negative Sr and positive Th-U anomalies on PM normalized trace element patterns. The apparent depletion of Sr cannot be explained by plagioclase fractionation since Eu/Eu* of ~1 ($Eu/Eu^* = Eu_{PM}/(Sm_{PM} \times Gd_{PM})^{0.5}$) indicates this process to be negligible. Abnormal Group basalts show similar or higher incompatible trace element concentrations, also shown by higher Th/Yb, $(Ce/Yb)_{PM}$ and $(Sm/Yb)_{PM}$, compared to SSB basalts (compare Figure 4.5), in which AbG basalt REU14-76 shows the highest incompatible element enrichment. Generally, AbG basalts show higher Ni and Cr, but lower Sc concentrations compared to SSB basalts (Figure 4.4d-e). As Sc is compatible in clinopyroxene, low Sc contents and especially decreasing Sc/Yb with decreasing CaO/Al_2O_3 ratios record clinopyroxene fractionation in these samples in agreement with previous studies (Figure 4.4a-b; Boudoire et al., 2019; Pichavant et al., 2016). The enrichment of incompatible trace element concentrations, such as Th, low Sc contents and CaO/Al_2O_3 ratios <0.75 point towards an apparent resemblance with 'olivine-bearing basalts', shown to be associated with the NWRZ (Boudoire et al., 2019).

4.4.2.2 Lō'ihi, Hawaii

Lō'ihi glasses show very homogeneous PM normalized trace element patterns with maximum enrichment of 35x PM (Figure 4.5c). With decreasing incompatibility PM-normalized concentrations decrease as typical for OIB. All samples are enriched in highly incompatible trace elements and LREE with $(Ce/Yb)_{PM}$ between 3.79 and 5.99 and $(La/Yb)_{PM}$ between 3.90 and 6.55. In agreement with published trace element abundances for Lō'ihi, all samples are characterized by depletions in Th and U as well as small positive anomalies in Ti and Nb and the absence of K- and Eu-depletions (Garcia et al., 1995; Garcia et al., 1998). Notably, transitional basalts are more enriched in incompatible trace elements ($(La/Yb)_{PM}$ = 5.62 to 6.28) than tholeiitic basalts ($(La/Yb)_{PM}$ = 3 to 5), which together with lower MgO contents of transitional basalts based on EPMA may be the result of fractional crystallization. However, lower SiO_2 contents of transitional basalts compared to tholeiitic basalts are in contrast with a fractional crystallization control (Figure 4.3).
All Lō'ihi glasses exhibit Eu/Eu* ratios ∼1, indicating the absence of plagioclase fractionation. Moreover, they show fractionated $(Gd/Yb)_{PM} > 2$, indicating melting in the presence of garnet (Figure 4.11). In agreement with previous observations (Garcia et al., 1995), the linear correlation between La/Yb vs. La/Sm suggests variable degrees of partial melting of a common source (not shown). Lō'ihi glasses display Zr/Nb ratios in the range from 7.4 to 9.5, similar to Zr/Nb ratios in Réunion lavas and thus lower than MORB, which has typically Zr/Nb > 20. In Zr/Nb vs. Nb space, Lō'ihi transitional basalts show higher Nb concentrations at lower Zr/Nb in agreement with lower melting degrees generating transitional basalts. However, these trends may also be generated by melting of a slightly heterogeneous source, which is supported by radiogenic Sr isotope compositions presented in Section 4.4.3.2. Moreover, transitional and tholeiitic basalts show distinct ratios of highly incompatible elements, such as Ce/Pb, La/Ce or Ba/Rb, whereas Nb/U ratios overlap for Lō'ihi transitional and tholeiitic basalts.

4.4.3 Radiogenic Sr-Nd-Pb isotope compositions

4.4.3.1 Piton de la Fournaise, La Réunion

Radiogenic Sr, Nd and Pb isotope compositions of Réunion whole-rock samples are generally consistent with literature data reported for central and peripheral eruptions (Bosch et al., 2008; Boudoire et al., 2019; Pietruszka et al., 2009) with $^{87}Sr/^{86}Sr$ and $^{143}Nd/^{144}Nd$ ranging from 0.704154 to 0.704253 and from 0.512810 to 0.512861, respectively (Figure 4.2a). One exception is AbG basalt REU14-76 displaying the highest $^{87}Sr/^{86}Sr$ (0.704317) and lowest $^{143}Nd/^{144}Nd$ (0.512717), which is outside the range reported for AbG basalts by Boudoire et al. (2019). This sample has possibly been subject to contamination and will be excluded from further discussion. Picrites and SSBs overlap in their $^{87}Sr/^{86}Sr$ and $^{143}Nd/^{144}Nd$ with AbG basalts, and AbG basalts show both most depleted and enriched isotopic compositions. Pb isotopic compositions are very homogeneous with $^{206}Pb/^{204}Pb$ between 18.867 and 18.974, $^{207}Pb/^{204}Pb$ of 15.596 to 15.608 and $^{208}Pb/^{204}Pb$ ranging from 38.974 to 39.057 (Figure 4.2b-e) and are in agreement with literature data (e.g., Vlastélic et al., 2009). Moreover, when excluding sample REU14-76, no or only weak ($R^2 = 0.21$) correlations between $^{87}Sr/^{86}Sr$ and incompatible trace element ratios, such as Th/Yb,

$(Sm/Yb)_{PM}$ and $(Ce/Yb)_{PM}$ are observed.

4.4.3.2 Lō'ihi, Hawaii

Lō'ihi glasses are very homogeneous in their radiogenic $^{87}Sr/^{86}Sr$ and $^{143}Nd/^{144}Nd$ isotope compositions and display a narrow range varying between 0.703518 and 0.703634 and between 0.512877 and 0.512935, respectively (Figure 4.2a-c). They are thus in very good agreement with previously reported data for Lō'ihi ranging from 0.703350 to 0.703700 and from 0.512880 to 0.513064 for Sr and Nd isotope signatures, respectively (compilation by Stracke (2012)). Lō'ihi transitional glasses have on average higher $^{87}Sr/^{86}Sr$ ratios compared to tholeiitic glasses, whereas both groups overlap in their Nd isotope compositions, and as such may be an indicator for a slightly heterogeneous source. When compared to Hawaiian lavas in general, which extend from MORB towards EM1 compositions, Lō'ihi glasses display intermediate compositions. Pb isotope ratios for Lō'ihi are not yet available for samples from this study, but literature data is indicated in Figure 4.2 based on the compilation by Stracke (2012). Previous studies have shown that Lō'ihi basalts extend from Mauna Loa-like Pb isotope compositions towards higher $^{206}Pb/^{204}Pb$ and $^{208}Pb/^{204}Pb$ ratios, and are distinguished from the Kea-trend by distinctly higher $^{208}Pb/^{204}Pb$ at a given $^{206}Pb/^{204}Pb$ (Abouchami et al., 2005; Weis et al., 2020).

4.4.4 Stable Cr and Fe isotope compositions

Cr isotope compositions of continental and oceanic intraplate basalts in this study range from $\delta^{53/52}Cr$ values of -0.227 to -0.094 ‰ (Figure 4.1). With an average $\delta^{53/52}Cr$ of -0.152 ± 0.070 ‰ (2SD; n=45) intraplate basalts are heavier compared to N-MORB (average $\delta^{53/52}Cr$= -0.237 ± 0.050 ‰, 2SD; n=19; Chapter 3), display a slightly larger variation compared to N-MORB, and in contrast to N-MORB overlap with the BSE value of -0.12 ± 0.06 ‰ (Wagner et al., 2021). The range of $\delta^{53/52}Cr$ reported for intraplate basalts in this study agrees well with available OIB $\delta^{53/52}Cr$ values ranging from ∼-0.23 to 0.00 ‰ (Figure 4.1; Bonnand et al., 2020b; Shen et al., 2020).
In detail, Vogelsberg volcanic rocks display the lowest average $\delta^{53/52}Cr$ of -0.184 ± 0.047 ‰ (2SD; n=11), whereas alkali basalts exhibit a higher average $\delta^{53/52}Cr$ of -0.164 ± 0.020 ‰ (2SD; n=5) than basanites with an average $\delta^{53/52}Cr$ of -0.201 ± 0.033 ‰ (2SD; n=6). Réunion samples range from -0.168 to -0.098 ‰ with an average $\delta^{53/52}Cr$ of -0.144 ± 0.044 ‰ (2SD; n=10). Doros mafic intrusive rocks display a $\delta^{53/52}Cr$ range between -0.186 and -0.107 ‰ with an average of -0.134 ± 0.056 ‰ (2SD; n=7). Both French Polynesia basalts and Lō'ihi glasses display a large range of $\delta^{53/52}Cr$ with averages of -0.151 ± 0.059 ‰ (2SD; n=7) and -0.138 ± 0.090 ‰ (2SD; n=10), respectively. The average $\delta^{53/52}Cr$ of French Polynesian samples with HIMU- or PREMA-affinity (-0.155 ± 0.080 ‰, 2SD; n=4) compared to samples with EM2-affinity (-0.145 ± 0.022 ‰, 2SD; n=3) cannot be distinguished within uncertainty. We note, however, that samples from French Polynesia with HIMU- or PREMA-affinity display the lowest (FP5TU1, $\delta^{53/52}Cr$ = -0.214 ‰) and highest $\delta^{53/52}Cr$ value (FP2RU2, $\delta^{53/52}Cr$ = -0.125 ‰) within the French Polynesia suite. For Lō'ihi glasses, the average $\delta^{53/52}Cr$ of transitional basalts with -0.172 ± 0.080 ‰ (2SD; n=5) cannot be distinguished from the average $\delta^{53/52}Cr$ of tholeiitic basalts with -0.104 ± 0.013 ‰ (2SD; n=5) within uncertainty. However, whereas tholeiitic basalts

Table 4.1: Stable Cr and Fe isotopic compositions alongside with Cr concentrations acquired by isotope dilution for all samples in this study. If available coordinates of sampling locations are given.

Sample	Rock type	Characteristics/ Location	Latitude	Longitude	$\delta^{53/52}$Cr [‰]	2SD/2SE if n= 1	n	Cr [μg g^{-1}] MC-ICP-MS	$\delta^{56/54}$Fe [‰]	2SD/2SE if n= 1	n
Reunion[a]											
REU 14-28	Picrite	NWRZ	21° 11.345' S	55° 38.560' E	-0.168	0.015	1	873.48	0.077	0.027	1
REU 14-31	Picrite	NERZ	21° 09.647' S	55° 49.243' E	-0.153	0.010	1	1515.35	0.066	0.027	1
REU 14-32	Picrite	NERZ	21° 13.175' S	55° 48.420' E	-0.132	0.010	1	1256.17	0.089	0.025	1
REU 14-33	SSB	Central	21° 14.259' S	55° 47.977' E	-0.098	0.005	3	254.76	0.133	0.025	1
REU 14-36	SSB	SERZ	21° 18.056' S	55° 48.047' E	-0.144	0.011	3	308.70	0.123	0.024	1
REU 14-45	AbG basalt	NWRZ	21° 11.948' S	55° 34.287' E	-0.164	0.012	1	512.37	0.103	0.026	1
REU 14-48	AbG basalt	NWRZ	21° 10.931' S	55° 35.543' E	-0.153	0.011	1	358.93	0.098	0.024	1
REU 14-57	Picrite	Central	21° 15.724' S	55° 47.647' E	-0.119	0.030	3	1728.46	0.064	0.026	1
REU 14-67	AbG basalt	NWRZ	21° 12.615' S	55° 38.589' E	-0.158	0.014	1	442.30	0.101	0.028	1
REU 14-76	AbG basalt	NWRZ	21° 13.227' S	55° 40.401' E	-0.154	0.014	1	377.23	0.135	0.025	
Lō'ihi, Hawaii[b]											
J2-243-1A-R2	Tholeiite	-	-	-	-0.094	0.017	1	523.12	0.075	0.026	1
J2-243-1B-R3,R4	Tholeiite	-	-	-	-0.110	0.017	1	443.59	0.114	0.024	1
J2-243-1C-R6	Tholeiite	-	-	-	-0.104	0.019	1	475.41	0.095	0.030	1
J2-243-1J-R20	Tholeiite	-	-	-	-0.102	0.016	1	452.44	0.077	0.026	1
J2-244-1-R2	Trans. basalt	-	-	-	-0.160	0.018	1	969.47	0.113	0.026	1
J2-246-R3D	Trans. basalt	-	-	-	-0.194	0.019	1	1012.48	0.144	0.021	1
J2-241-2-R9	Tholeiite	-	-	-	-0.108	0.017	1	299.18	0.117	0.021	1
J2-316-R1	Trans. basalt	-	-	-	-0.152	0.020	1	204.19	0.146	0.022	1
J2-309-R1	Trans. basalt	-	-	-	-0.227	0.018	1	3920.47	0.118	0.025	1
J2-307-R2-C	Trans. basalt	-	-	-	-0.124	0.016	1	2852.91	0.113	0.027	1
French Polynesia[c]											
FP2RU2	Tephrite	PREMA	22° 29.530' S	151° 19.760' W	-0.125	0.019	3	3.08	0.127	0.024	1
FP5TU1	Picrobasalt	HIMU	23° 21.343' S	149° 27.602' W	-0.214	0.040	3	273.73	0.142	0.026	1
FP8TU4	Picrobasalt	HIMU	23° 22.033' S	149° 28.520' W	-0.137	0.022	3	1694.52	0.096	0.027	1
FP15GA7	Basalt	PREMA/EM1	23° 07.365' S	134° 58.560' W	-0.145	0.009	3	272.60	0.075	0.026	1
FP24NU5	Trachybasalt	EM2	08° 53.890' S	140° 05.977' W	-0.145	0.015	1	555.91	0.151	0.027	1
FP26HU1	Basalt	EM2	15° 46.370' S	151° 02.470' W	-0.133	0.012	1	490.49	0.112	0.026	1

Continued on next page

Table 4.1 – *Continued from previous page*

Sample	Rock type	Characteristics/ Location	Latitude	Longitude	$\delta^{53/52}$Cr [‰]	2SD/2SE if n= 1	n	Cr [μg g^{-1}] MC-ICP-MS	$\delta^{56/54}$Fe [‰]	2SD/2SE if n= 1	n
FP27HU2	Basanite	EM2	16° 47.255' S	150° 57.523' W	-0.155	0.016	1	857.84	0.168	0.026	1
Vogelsberg[d]											
VB96-08	Basanite	20.86	-	-	-0.193	0.012	1	367.58	0.120	0.022	1
VB96-14	Basanite	49.88	-	-	-0.190	0.014	1	446.91	0.162	0.025	1
VB96-23	Basanite	77.1	-	-	-0.178	0.013	1	490.36	0.176	0.027	1
VB96-26	Basanite	94.4	-	-	-0.219	0.010	1	445.88	0.190	0.026	1
VB97-100	Basanite	Taufstein	-	-	-0.216	0.013	1	497.05	0.202	0.025	1
VB97-101	Basanite	Ortenberg	-	-	-0.209	0.012	1	528.25	0.169	0.028	1
VB96-16	Alkali basalt	55.91	-	-	-0.157	0.012	1	509.67	0.153	0.022	1
VB96-18	Alkali basalt	64.54	-	-	-0.154	0.011	1	625.09	0.139	0.024	1
VB96-40	Alkali basalt	229	-	-	-0.160	0.012	1	366.98	0.154	0.028	1
VB97-102	Alkali basalt	Ortenheim	-	-	-0.179	0.012	1	302.32	0.115	0.027	1
VB97-103	Alkali basalt	Bergheim	-	-	-0.168	0.013	1	361.52	0.176	0.025	1
Doros Complex[e]											
TOD-39	BOM	-	-	-	-0.107	0.012	1	1537.20	0.073	0.025	1
TOD-40	BOM	-	-	-	-0.110	0.013	1	1720.80	0.076	0.025	1
TOD-43	MOG	-	-	-	-0.138	0.014	1	421.61	0.118	0.027	1
TOD-63	BOM	-	-	-	-0.119	0.014	1	1747.00	0.058	0.028	1
TOD-68A	MOG	-	-	-	-0.154	0.010	1	886.41	0.138	0.028	1
TOD-71	MOG	-	-	-	-0.186	0.013	1	341.77	0.130	0.030	1
TOD-77	Cpx cumulate	-	-	-	-0.127	0.013	1	998.88	0.077	0.029	1

[a] Major element, trace element and radiogenic isotopic compositions given in Table C.2.6. Also given are eruption locations, i.e., central, NERZ (North east rift zone) and SERZ (South east rift zone) as well as NWRZ (North west rift zone).
[b] Major element, trace element and radiogenic isotopic compositions given in Table C.2.7.
[c] Major element, trace element and radiogenic isotopic compositions given in Table C.2.8. Also given are mantle components based on radiogenic Sr-Nd-Pb isotopic compositions.
[d] Major element, trace element and radiogenic isotopic compositions given in Table C.2.9. Also given are sampling depths and locations for drill core and outcrop samples, respectively.
[e] Major element, trace element and radiogenic isotopic compositions given in Table C.2.10. BOM = basal olivine melagabbro; MOG = Massive olivine gabbro; Cpx = clinopyroxene.

display a narrow range in $\delta^{53/52}$Cr, Lō'ihi transitional basalts extend towards significantly lower $\delta^{53/52}$Cr, and are thus comparable to $\delta^{53/52}$Cr values of Vogelsberg basanites and MORBs. The effect of olivine and Cr-spinel incorporation as the cause for the observed $\delta^{53/52}$Cr signatures in Lō'ihi samples is discussed in section 4.5.1.1. Stable Fe isotopic compositions of intraplate basalts range from $\delta^{56/54}$Fe values of +0.058 to +0.202 ‰, higher than the $\delta^{56/54}$Fe BSE value of $+0.02 \pm 0.03$ ‰ (Weyer and Ionov, 2007). The $\delta^{56/54}$Fe values of intraplate basalts in this study thus overlap with the average $\delta^{56/54}$Fe value of MORB ($+0.107 \pm 0.055$ ‰, 2SD; n=119; Figure 4.1; Chen et al., 2019; Richter et al., 2021; Teng et al., 2013; Weyer and Ionov, 2007) and extend towards higher values in agreement with literature data (Soderman et al., 2021; Soderman et al., 2022; Teng et al., 2008; Teng et al., 2013; Weyer and Ionov, 2007). In detail, $\delta^{56/54}$Fe of intrusive basalts from the Doros complex (Namibia) and Réunion range from +0.058 to +0.138 ‰ and +0.064 to +0.135 ‰, respectively. Together they display the lowest $\delta^{56/54}$Fe averages with $+0.096 \pm 0.064$ ‰ (2SD; n=7) and $+0.099 \pm 0.052$ ‰ (2SD; n=10), respectively. Low $\delta^{56/54}$Fe values for Réunion lavas are in agreement with previously published data (Peters et al., 2019). Samples from Lō'ihi (Hawaii) show similar $\delta^{56/54}$Fe values ranging from +0.075 to +0.146 ‰ with an average of $+0.111 \pm 0.048$ ‰ (2SD, n=10). They thus overlap with previously reported data, but extend towards higher $\delta^{56/54}$Fe values compared to the range reported by Teng et al. (2013) (+0.05 to +0.09 ‰, n=4). Lō'ihi transitional basalts cannot be distinguished within uncertainty from Lō'ihi tholeiitic basalts, but tend towards heavier values with an average $\delta^{56/54}$Fe of $+0.127 \pm 0.034$ ‰ (2SD; n=5) compared to $+0.096 \pm 0.040$ ‰ (2SD; n=5). Samples from French Polynesia extend towards slightly higher $\delta^{56/54}$Fe values ranging from +0.075 to +0.168 ‰ displaying an average of $+0.124 \pm 0.065$ ‰ (2SD; n=7), which is in the range of previously published data for French Polynesia (Teng et al., 2013). Moreover, the average $\delta^{56/54}$Fe value for samples from French Polynesia with HIMU- or PREMA-affinity ($+0.110 \pm 0.060$ ‰, 2SD; n=4) cannot be distinguished within uncertainty from those with EM2-affinity ($+0.144 \pm 0.058$ ‰, 2SD; n=3), although the latter trend towards heavier $\delta^{56/54}$Fe values. Basanites from the Vogelsberg volcano are on average higher ($+0.170 \pm 0.057$ ‰, 2SD; n=6) than alkali basalts ($+0.147 \pm 0.044$ ‰, 2SD; n=5), thus representing the heaviest Fe isotope compositions in this study and are comparable to rejuvenated samples from Samoa at similar MgO contents. However, Samoan samples extent to overall higher $\delta^{56/54}$Fe values of up to +0.3 ‰ (Konter et al., 2016).

4.5 Discussion

In order to use stable Cr and Fe isotope compositions of basalts to evaluate source characteristics and ultimately trace different source lithologies or recycled components, the isotopic fractionation during processes that may alter the $\delta^{53/52}$Cr and $\delta^{56/54}$Fe source signatures need to be addressed. Therefore, OIBs and continental intraplate basalts will be screened for stable Cr and Fe isotopic fractionation associated with fractional crystallization (Section 4.5.1). The influence of partial melting of a heterogeneous source will be addressed subsequently in order to evaluate potential $\delta^{53/52}$Cr and $\delta^{56/54}$Fe source signatures (Section 4.5.2).

4.5.1 Fractional crystallization

As evidenced by their compositional variability (MgO = 8 to 21 wt. %), OIBs, continental intraplate basalts of the Vogelsberg volcano, and intrusive basalts from the Doros complex have experienced variable differentiation histories that may have influenced the Cr and Fe isotope compositions to variable degrees and are discussed in detail in the following.

4.5.1.1 Ocean island basalts

The major crystallizing phases in OIBs are typically olivine and clinopyroxene with minor plagioclase fractionation as exemplified by the continuous increase in Al_2O_3 with decreasing MgO and the absence of Eu anomalies (Eu/Eu* $\sim$ 1) in Réunion, Lō'ihi and French Polynesia samples (Figure 4.4c, 4.5a, c, e, 4.6e). Samples from Réunion have been shown to exhibit typical fractionation trends of olivine accumulation for picrites with MgO > 10 wt. %, and olivine fractional crystallization for SSB basalts with < 10 wt. % MgO as indicated by constant CaO/Al_2O_3 ratios of $\sim$0.8 and continuously increasing Al_2O_3 concentrations (Figure 4.4a, c). Abnormal group basalts displaying CaO/Al_2O_3 ratios of < 0.8 (Figure 4.4a) are additionally affected by deep-level fractional crystallization of clinopyroxene (< 6 to 4 kbar, Boudoire et al., 2019), which is in agreement with the mild alkali enrichment (Figure 4.3), low Sc contents (Table C.2.6), and low Sc/Yb ratios (Figure 4.4b; Boudoire et al., 2019). Although Réunion basalts display an overall small range in $\delta^{56/54}$Fe at variable MgO contents, the tendency towards heavier $\delta^{56/54}$Fe values with decreasing MgO is in good agreement with fractional crystallization of olivine and clinopyroxene driving the residual melt towards higher $\delta^{56/54}$Fe as has been observed previously for Kilauea Iki lava lake basalts (Figure 4.7a; Teng et al., 2008). Similarly, the accumulation of olivine has been shown to lead to a decrease in $\delta^{56/54}$Fe in Kilauea Iki lava lake basalts (Teng et al., 2008). Here, Réunion picrites lie on the olivine accumulation trend of decreasing $\delta^{56/54}$Fe with increasing MgO as defined by Kilauea Iki lavas (Figure 4.7a). Discriminating the effects of olivine and clinopyroxene crystallization on $\delta^{56/54}$Fe, can be achieved by plotting $\delta^{56/54}$Fe vs. CaO/Al_2O_3 and Sc/Yb ratios (Figure 4.8a, c). Therein, increasing $\delta^{56/54}$Fe with decreasing CaO/Al_2O_3 (Figure 4.8a) and Sc/Yb (Figure 4.8c) indicates clinopyroxene control, whereas increasing or decreasing $\delta^{56/54}$Fe at constant CaO/Al_2O_3 ratios indicate olivine crystallization and accumulation, respectively. Hence, the slightly higher $\delta^{56/54}$Fe values at constant CaO/Al_2O_3 observed for the two Réunion SSB basalts can be mainly attributed to olivine crystallization. On the other hand, Réunion AbG basalts and samples from French Polynesia with CaO/Al_2O_3 ratios < 0.8 show slightly increasing $\delta^{56/54}$Fe with decreasing CaO/Al_2O_3 and Sc/Yb ratios suggesting that some of the $\delta^{56/54}$Fe variations seen in these samples may be due to clinopyroxene fractionation, although variations are small (Figure 4.8a). One EM2-type sample (FP27HU2) from French Polynesia has high CaO/Al_2O_3, but low Sc/Yb (Figure 4.4b) and shifts on an apparent clinopyroxene fractionation trend (Figure 4.8c). In general, the observed trends for French Polynesian samples are in agreement with a previous study investigating the effect of magmatic differentiation on $\delta^{56/54}$Fe for samples from Society and Cook Austral islands (not shown here; Teng et al., 2013).

Based on theoretical calculations and natural data of minerals in mantle xenoliths, it has been suggested that $\delta^{53/52}$Cr increases from $\delta^{53/52}Cr_{olivine} < \delta^{53/52}Cr_{pyroxene} <$

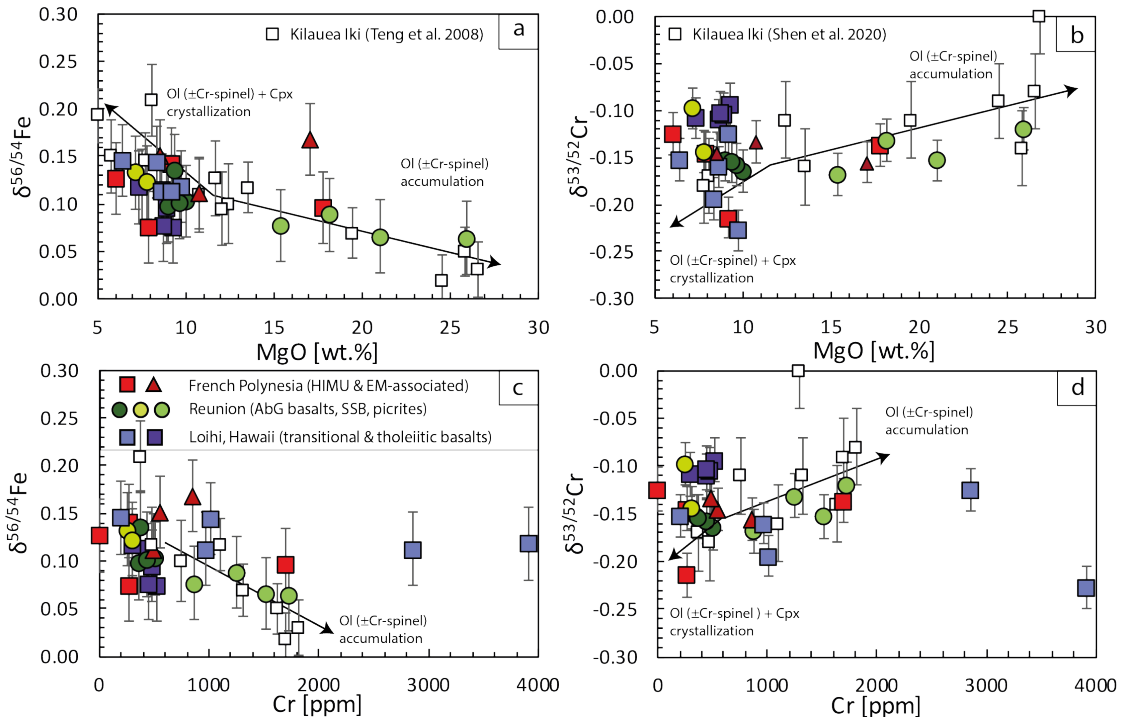

Figure 4.7: Fe and Cr isotopic compositions vs. **a)** and **b)** MgO and **c)** and **d)** Cr contents of ocean island basalts from French Polynesia, Réunion and Lō'ihi. Kilauea Iki lava lake basalts are shown for comparison for which Fe and Cr isotope compositions are from Teng et al. (2008) and Shen et al. (2020), respectively. Kilauea fractional assemblage: Olivine + Cr-spinel accumulation for samples with MgO > 11.5 wt. %; Olivine + Cr-spinel fractionation for samples with MgO < 11.5 wt. %; Clinopyroxene starts to crystallize at MgO < 7.5 wt. % (Shen et al., 2020). Arrows indicate the direction of isotopic fractionation during mineral crystallization and accumulation as suggested by theoretical calculations and trends of Kilauea Iki samples (Shen et al., 2018b; Shen et al., 2020; Teng et al., 2008). Errors on $\delta^{56/54}$Fe and $\delta^{53/52}$Cr as in Figure 4.1. Ol = olivine, Cpx = clinopyroxene, AbG = abnormal Group basalts, SSB= steady state basalts.

$\delta^{53/52}Cr_{spinel}$ (Shen et al., 2018b). Compared to a silicate melt, pyroxene and spinel are predicted to be isotopically heavy, whereas olivine is predicted to incorporate preferentially light Cr isotopes (Berry et al., 2021a; Shen et al., 2020). So far, studies on OIB suites from Fangataufa and Hawaii have shown that $\delta^{53/52}$Cr generally decreases with increasing magmatic differentiation (Bonnand et al., 2020b; Shen et al., 2020). This decrease in $\delta^{53/52}$Cr has been mainly attributed to the crystallization of Cr-spinel, which preferentially incorporates Cr^{3+} and thus the heavy Cr isotopes, and based on mass balance considerations dominates the Cr-budget.

Here, Réunion picrites that have been affected by olivine accumulation (MgO = 15.42 to 25.94 wt. %) show slightly increasing $\delta^{53/52}$Cr with increasing MgO and Cr (Figure 4.7b, d). The observed weak trends of $\delta^{53/52}$Cr with MgO (R^2=0.58) and Cr concentrations (R^2=0.57) are similar to those observed for Kilauea Iki Lava lake basalts, that have been attributed to the concurrent accumulation of olivine and Cr-spinel (Figure 4.7b, d; Shen et al., 2020). In contrast, komatiites show constant $\delta^{53/52}$Cr over large degrees of olivine accumulation (and crystallization) (see also Figure 4.10b, d, f; Wagner et al., 2021). This may suggest that in addition to olivine, Cr-spinel accumulation is prevalent for Réunion picrites, which in turn dominates the Cr budget and thus leads to slightly increasing $\delta^{53/52}$Cr with increasing MgO. Moreover, olivine accumulation in Réunion picrites has been ascribed to a

xenocrystic origin (Albarède et al., 1997) and may thus contribute to some variation in $\delta^{53/52}$Cr whole-rock compositions.

Analogous to $\delta^{56/54}$Fe, samples from Réunion and French Polynesia give the opportunity to discriminate for the effects of clinopyroxene and olivine crystallization on $\delta^{53/52}$Cr. Compared to the average $\delta^{53/52}$Cr of -0.136 ± 0.050 ‰ (2SD; n=6) for Réunion picrites and SSBs, AbG basalts display a restricted range in $\delta^{53/52}$Cr with an average of -0.157 ± 0.011 ‰ (2SD; n=4), that is indistinguishable within uncertainty. However, the on average lower $\delta^{53/52}$Cr value of AbG basalts compared to picrites and SSB would be in agreement with theoretical predictions that clinopyroxene preferentially incorporates the heavy Cr isotopes compared to a silicate melt (Shen et al., 2020). On the other hand, slightly increasing to invariant $\delta^{53/52}$Cr values with decreasing CaO/Al_2O_3 ratios within AbG basalts and of samples from French Polynesia with $CaO/Al_2O_3 < 0.8$ are in contrast with clinopyroxene preferentially removing the heavy Cr isotopes from the melt (Figure 4.8b, d). Noteworthy, variations of $\delta^{53/52}$Cr within AbG basalts and French Polynesian basalts are small and mostly defined by sample FP2RU2 from French Polynesia with MgO of 6.08 wt. %. Negligible effect of fractional crystallization on $\delta^{53/52}$Cr has been recently observed for MORBs from the East-Pacific Rise and Pacific-Antarctic Ridge, which reflect different degrees of fractional crystallization of olivine + plagioclase + clinopyroxenes at low pressures (Chapter 3). Moreover, it has been suggested that low pressure clinopyroxene fractionation could lead towards higher $\delta^{53/52}$Cr in the residual melt

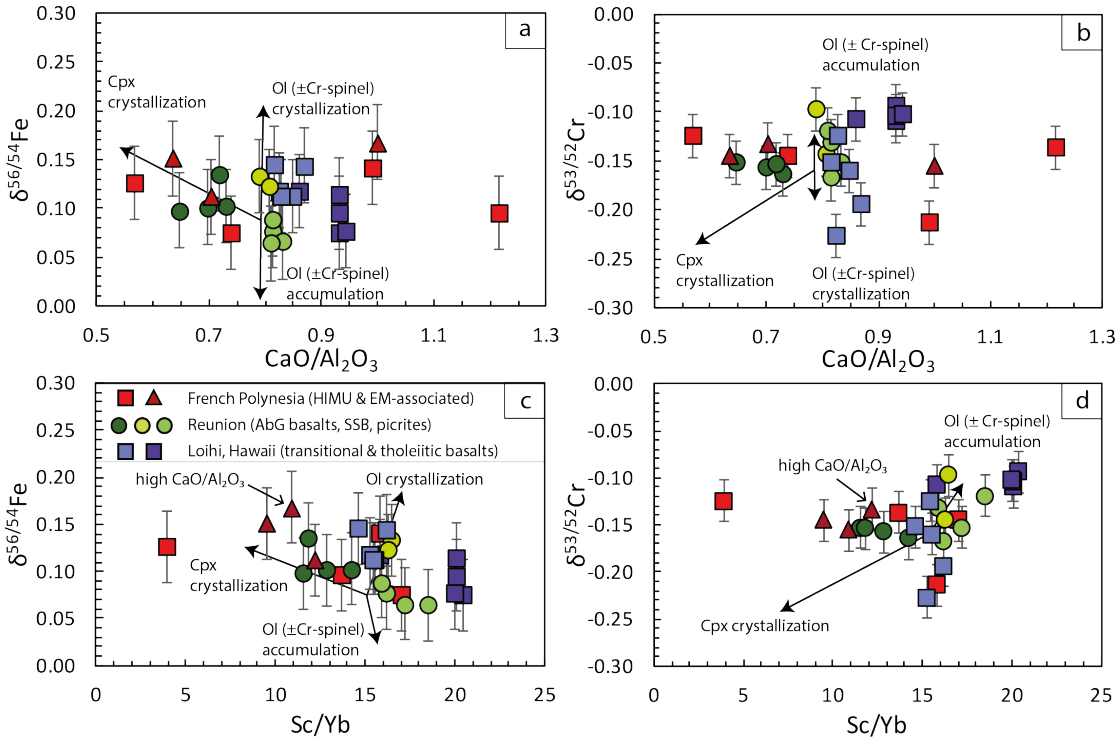

Figure 4.8: Fe and Cr isotopic compositions vs. **a)** and **c)** CaO/Al_2O_3 ratios and **b)** and **d)** Sc/Yb ratios, both used as indicators for clinopyroxene crystallization of ocean island basalts from French Polynesia, Réunion and Lō'ihi. Arrows indicate the direction of Fe and Cr isotopic fractionation induced by mineral crystallization based on theoretical calculations and previous works (e.g., Berry et al., 2021a; Bonnand et al., 2020a; Shen et al., 2018b; Shen et al., 2020; Teng et al., 2008; Teng et al., 2013). Errors on $\delta^{56/54}$Fe and $\delta^{53/52}$Cr as in Figure 4.1. Ol = olivine, Cpx = clinopyroxene, AbG = abnormal Group basalts, SSB= steady state basalts.

(Ma et al., 2022). However, Réunion AbG basalts experienced clinopyroxene fractionation at high pressures (e.g., Boudoire et al., 2019). It has been shown that an increase in crystallization depth leads towards higher Al contents in [4]-coordination in clinopyroxene (Adam and Green, 1994; Boudoire et al., 2019; Pichavant et al., 2016), which in turn increases the compatibility of Cr^{3+} due to charge balance effects (Karner et al., 2007; Papike et al., 2005; Papike et al., 2016). Hence, fractional crystallization of Al-rich clinopyroxenes, frequently occurring in komatiites, lead towards a decrease in $\delta^{53/52}$Cr with increasing degree of differentiation as has been observed for komatiitic basalts from the Barberton Greenstone Belt (Wagner et al., 2021). This is in contrast to the invariant $\delta^{53/52}$Cr with decreasing CaO/Al_2O_3 and Sc/Yb for AbG basalts and French Polynesia samples. AbG basalts may additionally be affected by clinopyroxene resorption and contamination of small degree melts ($< 5\,\%$) from dunitic or wehrlitic cumulates during ponding at intermediate depths, supposedly within the underplating layer (Boudoire et al., 2019). Based on the assumption that clinopyroxene crystals exhibit a higher $\delta^{53/52}$Cr compared to the melt at equilibrium, clinopyroxene resorption would result in an increase of both $\delta^{53/52}$Cr and CaO/Al_2O_3, thus resulting in a positive correlation between $\delta^{53/52}$Cr and CaO/Al_2O_3, which is not observed.

Interestingly, the two types of Lō'ihi glasses display two distinct groups in Cr and Fe isotopic compositions. Transitional basalts display low $\delta^{53/52}$Cr and high $\delta^{56/54}$Fe, whereas tholeiitic glasses display high $\delta^{53/52}$Cr and low $\delta^{56/54}$Fe (Figure 4.1). As described in Section 4.3.1.2 and 4.4.1.2 transitional and tholeiitic glasses display higher MgO abundances in Q-ICP-MS analyses compared to in-situ analyses via EPMA attributed to olivine incorporation, which may thus affect the $\delta^{53/52}$Cr and $\delta^{56/54}$Fe. Incorporation of solely olivine should lead towards negative correlations between both $\delta^{53/52}$Cr and $\delta^{56/54}$Fe and MgO, which is not observed. Although the sample with highest MgO and Ni contents (J2-309-R1) displays the lightest $\delta^{53/52}$Cr, the wide range of $\delta^{53/52}$Cr (and $\delta^{56/54}$Fe) values are accompanied by a relatively small range in MgO abundances, which suggest overall limited olivine incorporation/accumulation (Figure 4.7a-b). Following, these small degrees of olivine incorporation should have negligible effect on the Cr isotopic compositions based on the commonly incompatible behavior of Cr in olivine (Mallmann and O'Neill, 2009). Similarly, Cr-spinel incorporation, which may play a role for Lō'ihi transitional basalts (based on high Cr contents; Figure 4.6f), should increase the $\delta^{53/52}$Cr and decrease $\delta^{56/54}$Fe with increasing Cr as exemplified by the combined Cr-spinel and olivine accumulation trends of Kilauea Iki lava lake basalts (Shen et al., 2020; Teng et al., 2008). However, these relationships are not observed for Lō'ihi glasses (Figure 4.7c-d). Moreover, it could be argued that lower Sc/Yb and CaO/Al_2O_3 ratios of transitional basalts than observed for tholeiitic basalts may signal higher degrees of clinopyroxene fractionation (e.g., Figure 4.6d). This interpretation would be in line with the overall higher $\delta^{56/54}$Fe and lower $\delta^{53/52}$Cr of transitional basalts compared to tholeiitic basalts (Figure 4.8c, d). Additionally, the magnitude of Fe isotopic fractionation from tholeiitic to transitional Lō'ihi glasses is similar to the increase in $\delta^{56/54}$Fe from Réunion picrites to Réunion AbG basalts (Figure 4.8a, c) and supports clinopyroxene control on the Fe isotopic composition of these samples. However, the large range of $\delta^{53/52}$Cr values at very similar CaO/Al_2O_3 and Sc/Yb ratios observed for transitional basalts may point to an additional process influencing $\delta^{53/52}$Cr of transitional Lō'ihi glasses.

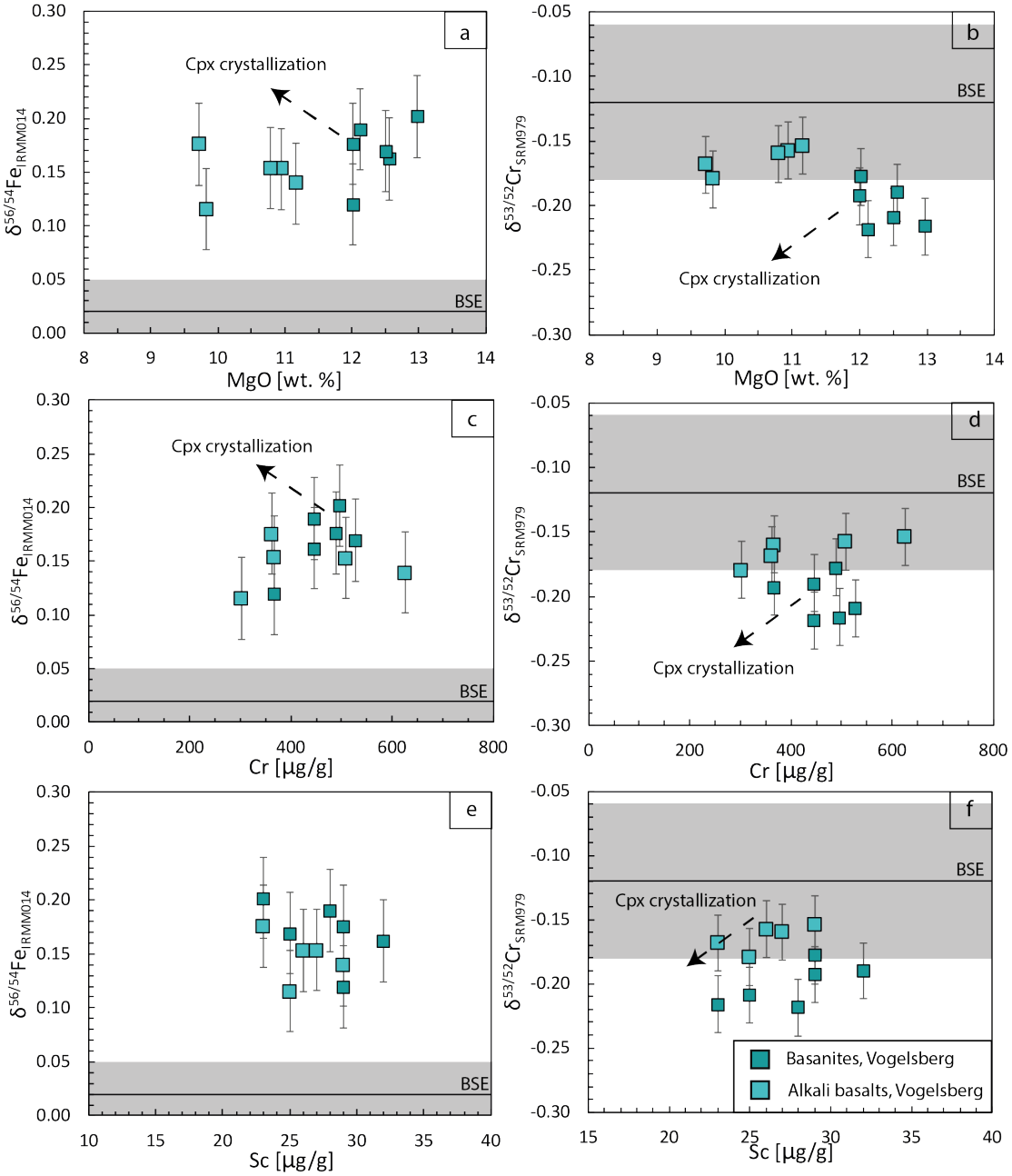

Figure 4.9: Fe and Cr isotopic compositions vs. major and trace element concentrations for Vogelsberg basanites and alkali basalts. In contrast to the expected trends for fractional crystallization of clinopyroxene as indicated by stippled arrows, alkali basalts exhibit higher $\delta^{53/52}$Cr and lower $\delta^{56/54}$Fe. The isotopic range for Bulk Silicate Earth (BSE) is indicated by the grey field ($\delta^{56/54}$Fe; Weyer and Ionov, 2007; $\delta^{53/52}$Cr; Wagner et al., 2021). Errors on $\delta^{56/54}$Fe and $\delta^{53/52}$Cr as in Figure 4.1. Major and trace elements from Bogaard and Wörner (2003). Cpx = clinopyroxene.

4.5.1.2 Vogelsberg, Germany

Vogelsberg basanites with an average $\delta^{53/52}$Cr of -0.201 $\pm$ 0.033 ‰ (2SD; n=6) lie outside the range of the $\delta^{53/52}$Cr BSE value of -0.12 $\pm$ 0.06 ‰ and also show lower $\delta^{53/52}$Cr compared to Vogelsberg alkali basalts having an average $\delta^{53/52}$Cr of -0.164 $\pm$ 0.033 ‰ (2SD; n=5; Figure 4.1a). The opposite is observed for stable Fe isotopes, in which basanites display a higher average $\delta^{56/54}$Fe (+0.170 $\pm$ 0.057 ‰, 2SD; n=6)

compared to alkali basalts (+0.147 ± 0.044 ‰; 2SD, n=5; Figure 4.1b).
The Vogelsberg volcanic suite comprises near-primary basanites and alkali basalts and major element variations indicate typical differentiation trends of olivine and Ti-rich clinopyroxene as major fractionating phases (Figure C.2.7; Bogaard and Wörner, 2003). Two samples VB96-08 and VB96-16 display elevated Fe_2O_3 contents and correspondingly low FeO contents, indicating the oxidation of Fe, which, however did not result Fe loss as indicated by similarly high FeO_{total} contents (Figure C.2.7). Eu/Eu* ratios close to 1 denote the absence of plagioclase fractionation (Figure 4.5b) and therefore suggest that fractional crystallization probably occurred at depths > 15 km (possibly at the crust-mantle boundary; Bogaard and Wörner, 2003). In comparison to near-primary basanites, alkali basalts experienced a higher degree of olivine and clinopyroxene fractionation as indicated by their overall lower MgO and Ni and higher Al_2O_3 (Figure C.2.7) and SiO_2 contents (not shown) (Bogaard and Wörner, 2003). Clinopyroxene fractionation is particularly important in alkali basalts as evident from decreasing Sc with decreasing MgO concentrations, whereas the opposite is observed for basanites (Figure C.2.7f). Despite the relatively good correlations of $\delta^{53/52}$Cr and $\delta^{56/54}$Fe with MgO (Figure 4.9a-b), the observed trends are opposite to what has been observed previously in ultramafic-mafic systems, where $\delta^{53/52}$Cr is generally lowest in most evolved samples (Bonnand et al., 2020b; Shen et al., 2020; Wagner et al., 2021) and $\delta^{56/54}$Fe increases with increasing crystallization of olivine and pyroxene (Schuessler et al., 2009; Sossi et al., 2012; Teng et al., 2008; Teng et al., 2013). As discussed in Section 4.5.1.1 high-pressure clinopyroxene fractionation is predicted to result in lower $\delta^{53/52}$Cr with increasing fractionation (mainly based on the preferential incorporation of the substitution couple Al^{3+}-Cr^{3+} in clinopyroxene at high pressure; Karner et al., 2007; Papike et al., 2016), similar to theoretically calculated heavy $\delta^{53/52}$Cr of pyroxene (Shen et al., 2018b). However, this is inconsistent with the observed trends. We note that the slight decrease of $\delta^{53/52}$Cr vs. MgO in the most evolved alkali basalts (MgO < 10 wt. %) may be due to clinopyroxene fractionation, which is also evident from decreasing $\delta^{53/52}$Cr with decreasing Sc content (Figure 4.9b, f). However, in general the more primitive samples of the Vogelsberg suite, display the heavy $\delta^{56/54}$Fe and light $\delta^{53/52}$Cr (Figure 4.9), and thus preclude crystal fractionation as the cause for the observed stable isotopic signatures. It is thus suggested that $\delta^{53/52}$Cr and $\delta^{56/54}$Fe systematics of basanites and alkali basalts are primarily controlled by partial melting and/or source composition.

4.5.1.3 Doros complex, Namibia

The composition of the intrusive rocks from the shallow-level Doros intrusive complex are affected by both fractional crystallization and crystal accumulation. As described in detail by Owen-Smith and Ashwal (2015b), the main mineralogy of the lower stratigraphic rocks consists of olivine, plagioclase, calcic clinopyroxene and titanomagnetite, whereas Cr-spinel has not been observed. Mineral analyses of Fe-Ti oxides in the BOM and MOG show that these are relatively Ti-poor (15 to 38 % ulvöspinel content), with ilmenite-rich lamellae formed by oxy exsolution (non-primary ilmenite; Owen-Smith and Ashwal, 2015b). The Cr content of Fe-Ti oxides are highest in BOM (up to 7 wt. %) and decreases from BOM to MOG (Owen-Smith and Ashwal, 2015b). The high MgO contents of BOM reflect olivine accumulation (30 to 60 %), whereas MOG are dominated by plagioclase accumu-

lation (45 to 60 %), the latter being indicated by the steep increase of Al_2O_3 for samples with MgO < 10 wt. % (Figure C.2.8a; Owen-Smith and Ashwal, 2015b). Together, both units display an upward differentiation trend supported by more evolved olivine compositions of BOM (Fo_{75}) than MOG (Fo_{62}) (Owen-Smith and Ashwal, 2015a). In general, this upward differentiation trend is accompanied by increasing $\delta^{56/54}$Fe and decreasing $\delta^{53/52}$Cr from BOM to MOG (Figure 4.10). The effect of olivine accumulation on whole-rock $\delta^{56/54}$Fe has been discussed in detail by previous studies (e.g., Teng et al., 2008) and is generally thought to decrease the $\delta^{56/54}$Fe due to the preferential incorporation of light Fe isotopes into olivine. This is in agreement with the slight decrease of $\delta^{56/54}$Fe with increasing MgO and Ni contents for Doros intrusive rocks, although $\delta^{56/54}$Fe variations are less pronounced compared to Kilauea Iki basalts or komatiites from the Barberton Greenstone Belt (Figure 4.10a, c). Theoretical calculations showed that olivine also preferentially incorporates the light Cr isotopes (Berry et al., 2021a; Moynier et al., 2011; Shen et al., 2018b). However, based on invariant $\delta^{53/52}$Cr of komatiites, which display large amounts of olivine crystallization and accumulation (Wagner et al., 2021), olivine has been shown to have negligible control on $\delta^{53/52}$Cr during fractionation and accumulation at terrestrial mantle conditions (Figure 4.10b). In cases, where olivine accumulation is accompanied by Cr-spinel accumulation an increase of $\delta^{53/52}$Cr with increasing MgO has been observed (e.g., Réunion picrites, Section 4.5.1.1; Kilauea Iki basalts, Shen et al., 2020). Invariant $\delta^{53/52}$Cr with decreasing MgO and Ni contents in Doros rocks with MgO > 15 wt. % (Figure 4.10b, d) support the observations made from komatiitic rocks and are in line with Cr-free olivine and absence of Cr-spinel observed for BOMs of the Doros suite (Owen-Smith and Ashwal, 2015b).
Fractionating minerals in Doros rocks include clinopyroxene and Fe-Ti oxides (Owen-Smith and Ashwal, 2015a). Similar to olivine, clinopyroxene is generally thought to incorporate light Fe^{2+} resulting in a low $\delta^{56/54}$Fe compared to their host rock (e.g., Weyer and Ionov, 2007; Williams et al., 2005). Thus, fractional crystallization of clinopyroxene has been suggested to lead towards higher $\delta^{56/54}$Fe with increasing differentiation (e.g., Teng et al., 2008; Teng et al., 2013). Theoretical calculations show that clinopyroxene preferentially incorporates the heavy Cr isotopes (Shen et al., 2018b) displaying an isotopic difference between clinopyroxene and melt of +0.046 ‰ when at equilibrium (Shen et al., 2020). The effect of fractional crystallization of Fe-Ti oxides with the general formula $^{[4]}A^{[6]}B_2O_4$ on $\delta^{56/54}$Fe is dependent on Fe-Ti oxide compositions. Fe-Ti oxides such as magnetite and ulvöspinel belong to the inverse spinel group, in which half of the B cations partition into the tetrahedrally coordinated A site (e.g., magnetite with $^{[4]}Fe^{3+}{}^{[6]}(Fe^{2+}Fe^{3+})O_4$). In detail, magnetite has been shown to lead towards a decrease in $\delta^{56/54}$Fe (Shahar et al., 2008; Sossi et al., 2012), whereas the fractionation of ulvöspinel ($^{[4]}Fe^{2+}{}^{[6]}(Fe^{2+}Ti^{4+})O_4$) has been shown to increase the $\delta^{56/54}$Fe of the residual magma with increasing differentiation (Schuessler et al., 2009). Similarly, solid solutions along the hematite-ilmenite mixing line specifically fractionate Fe isotopes, i.e., ilmenite preferentially incorporates the light Fe isotopes, whereas hematite preferentially incorporates the heavy Fe isotopes (Polyakov et al., 2007; Polyakov and Mineev, 2000). In contrast to Cr-spinel (Berry et al., 2021a; Bonnand et al., 2020a; Moynier et al., 2011; Shen et al., 2018b), there are no experimental data or theoretical predictions concerning Cr isotopic fractionations between Fe-Ti oxides and melt. Moreover, a systematic change of $\delta^{53/52}$Cr with Fe-Ti oxide fractionation could not be resolved in a re-

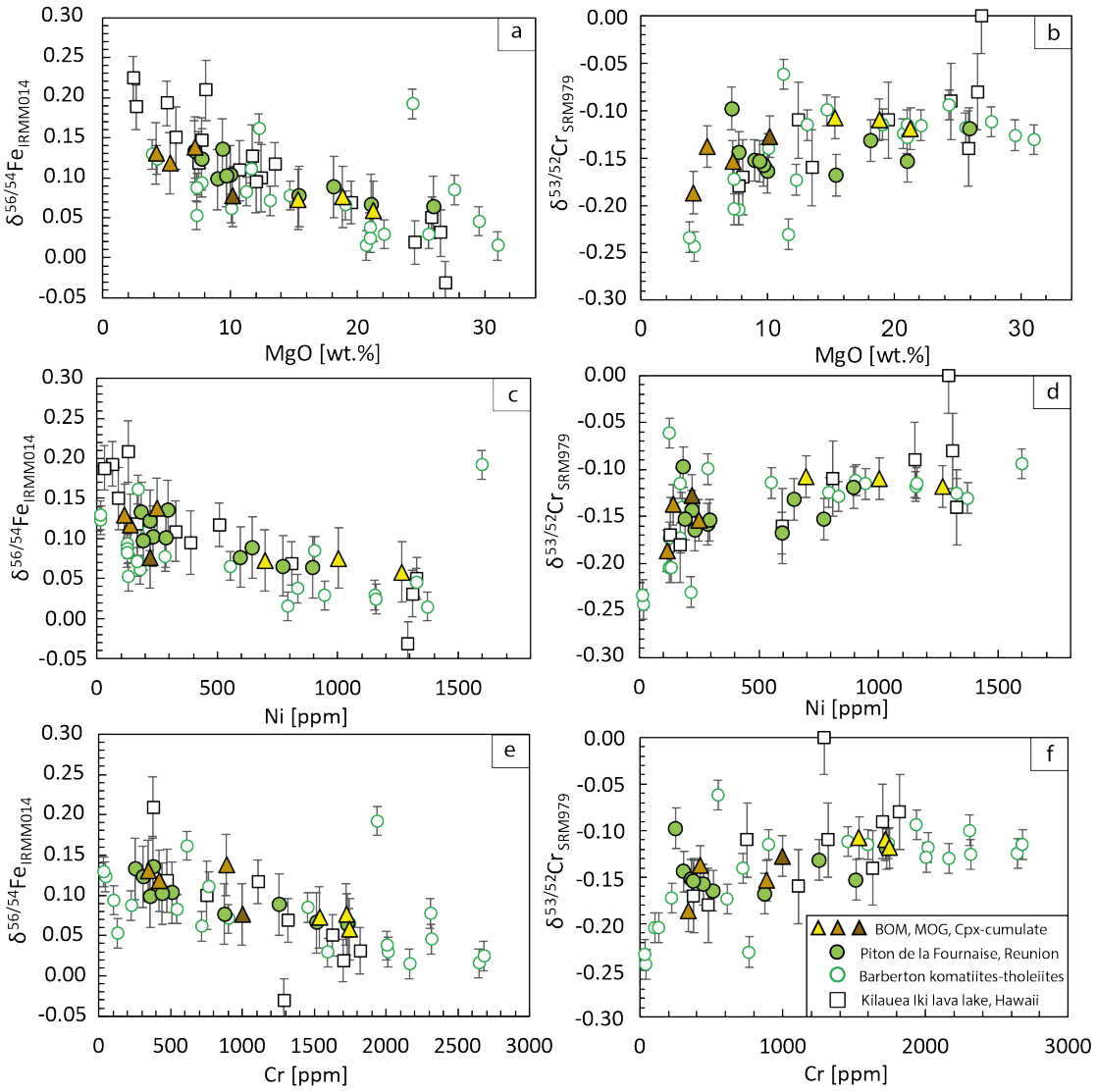

Figure 4.10: Fe and Cr isotopic compositions vs. **a)** and **b)** MgO, **c)** and **d)** Ni, and **e)** and **f)** Cr contents for intrusive rocks from the Doros complex. Also shown are Réunion basalts (this study), komatiites from the ~3.5 Ga Barberton Greenstone Belt (Wagner et al., 2021) and Kilauea Iki lava lake basalts ($\delta^{53/52}$Cr, Shen et al., 2020; $\delta^{56/54}$Fe, Teng et al., 2008). Errors on $\delta^{56/54}$Fe and $\delta^{53/52}$Cr as in Figure 4.1. BOM= basal olivine melagabbro; MOG = massive olivine gabbro, Cpx = clinopyroxene.

cently investigated MORB suite of the Pacific-Antarctic Ridge and was ascribed to relatively low Cr contents in MORB-like Fe-Ti oxides (Chapter 3). The inverse structure of magnetite offers only one trivalent site in octahedral coordination (e.g., $^{[4]}Fe^{3+}{}^{[6]}(Fe^{2+}Cr^{3+})O_4$) and based on the strong octahedral site preference of Cr^{3+} (Burns, 1975) limits its partitioning into magnetite compared to normal Cr-spinel. As Cr^{2+} is generally thought to prefer distorted crystal lattice sites its partitioning into spinel minerals in general is thought to be negligible (Moynier et al., 2011; Shen et al., 2018b). Therefore, the Cr isotopic composition of Fe-Ti oxides would be expected to be heavier compared to the melt, but the magnitude of isotopic fractionation may be smaller based on the overall lower compatibility of Cr in Fe-Ti oxides compared to Cr-spinel.

In order to explain the overall trend towards higher $\delta^{56/54}$Fe and lower $\delta^{53/52}$Cr with

decreasing MgO contents multiple scenarios can be envisaged applying to the Doros intrusive rocks. Firstly, as outlined above the evolution towards higher $\delta^{56/54}$Fe and lower $\delta^{53/52}$Cr can be attributed towards a continuously evolving basaltic magma, in which crystallization of olivine, clinopyroxene and ulvöspinel lead to an increase in $\delta^{56/54}$Fe such as observed for Kilauea Iki basalts (Figure 4.10). On the other hand, increasing magnetite component would preferentially remove the heavy isotopes from the residual melt (Sossi et al., 2012), and correspondingly mask the overall increase in $\delta^{56/54}$Fe. Regarding $\delta^{53/52}$Cr, clinopyroxene and Fe-Ti oxide crystallization would still dominate the Cr budget based on mass balance considerations and thus lead towards the overall decrease in $\delta^{53/52}$Cr during combined crystallization of olivine, clinopyroxene and Fe-Ti oxides similar to observations made from Kilauea Iki basalts (Figure 4.10b, d, f). Secondly, both, fractionation and accumulation, play a role in Doros intrusive rocks. The main accumulating phase for samples < 15 wt. % MgO is plagioclase, whereas Fe-Ti oxide accumulation is insignificant for both BOM and MOG (Owen-Smith and Ashwal, 2015a). Plagioclase accumulation in MOG is evident by small positive Eu anomalies (Eu/Eu*) and pronounced peaks of Sr in PM-normalized trace element patterns (Figure 4.5d). Neither $\delta^{56/54}$Fe nor $\delta^{53/52}$Cr correlate clearly with Eu/Eu* (not shown), which is expected based on extremely low partition coefficients of both Cr and Fe in plagioclase (e.g., $D_{Cr}^{anorthite/melt} = \sim 0.01$; Leitzke et al., 2016). Thus, the effect of plagioclase accumulation is negligible for $\delta^{56/54}$Fe and $\delta^{53/52}$Cr. Accumulation of clinopyroxene would lead towards an overall smaller bulk isotopic fractionation between melt and crystals, and thus may obscure the variations observed for $\delta^{56/54}$Fe and $\delta^{53/52}$Cr in samples with MgO content < 15 wt. % compared to a pure fractional crystallization trend. Due to the difficulty of estimating the exact proportion of accumulating and fractionating phases, further exploration is inhibited. The clinopyroxene cumulate TOD-77 with ~60 % of cumulus clinopyroxene, however, fits roughly on the trend defined by BOM and MOG in $\delta^{56/54}$Fe and $\delta^{53/52}$Cr vs. MgO space (Figure 4.10). Moreover, the continuously increase of $\delta^{56/54}$Fe with increasing magmatic differentiation is in contrast with previous studies of layered mafic intrusions such as the Bushveld Complex (Bilenker et al., 2016) and Baima intrusion, China (Chen et al., 2014; Liu et al., 2014), in which no systematic variations of $\delta^{56/54}$Fe with increasing magmatic differentiation were observed.

The magnitude of isotopic fractionation during melt differentiation depends on many variables including temperature, pressure, oxygen fugacity, melt composition and associated mineral chemistry, and amount of fractionating or accumulating phases. Although slow cooling may lead to large isotopic differences between different mineral phases through diffusion such as shown for $\delta^{56/54}$Fe (e.g., Kilauea Iki lava lake; Teng et al., 2011) and $\delta^{53/52}$Cr (e.g., Stillwater complex; Bai et al., 2019) the isotopic composition of whole-rocks may still reflect isotopic fractionation due to progressive magmatic differentiation (Teng et al., 2008). Despite the difficulties of assessing the effect of accumulating and fractionating mineral phases on the $\delta^{56/54}$Fe and $\delta^{53/52}$Cr in the intrusive rocks of the Doros complex, we note that there is striking resemblance of $\delta^{56/54}$Fe and $\delta^{53/52}$Cr with indicators of magmatic differentiation between the Doros intrusive rocks compared to those observed in volcanic systems such as the historic Kilauea Iki lava lake (Shen et al., 2020; Teng et al., 2008) and the ~3.5 Ga komatiite-tholeiite suite from the Barberton Greenstone Belt (Figure 4.10) (Wagner et al., 2021). Moreover, Doros intrusive rocks show $\delta^{56/54}$Fe values com-

parable to Réunion samples (Figure 4.10). Similar to Doros rocks, komatiitic rocks from the Barberton greenstone belt are variably affected by accumulation of olivine (with MgO > 18 wt. %), whereas Barberton rocks with MgO < 18 wt. % are affected by fractionation and accumulation of clinopyroxene and subsequently plagioclase (Wagner et al., 2021). The similarities of $\delta^{56/54}$Fe and $\delta^{53/52}$Cr evolution within the three locations are remarkable as they are not only different in their age, but also in size and related timescales of crystallization as well as mode and conditions of magma emplacement (e.g., open vs. closed magmatic systems). Overall, despite differences in melting regimes of Archean and modern magmatic systems (e.g., pressure and temperature of melting, degree of melting and hence parental magma composition) the striking resemblance of the komatiite-tholeiite suite compared to the Doros intrusive rocks suggests that these differences do not primarily control Cr, and possibly Fe, isotope fractionation.

4.5.2 Partial melting of a heterogeneous mantle

As shown above and in previous studies, fractional crystallization can fractionate Cr isotopes (e.g., Bonnand et al., 2020b; Jerram et al., 2020; Shen et al., 2020; Wagner et al., 2021). Some of the lower $\delta^{53/52}$Cr values of samples in this study, such as the Doros massive olivine gabbros, can be attributed to fractional crystallization (Section 4.5.1.3). However, the low $\delta^{53/52}$Cr values of Vogelsberg basanites, Lō'ihi transitional basalts or one HIMU-type basalt from French Polynesia are not in accordance with fractional crystallization control (Section 4.5.1.1 and 4.5.1.2). In order to minimize the effects of fractional crystallization the following discussion on partial melting and source effects will be based on samples with MgO > 7.5 wt. %, as the effect of fractional crystallization on $\delta^{53/52}$Cr has been observed to be strongest in samples with MgO < 7.24 wt. % (Doros suite). This filtering approach is similar to that used in Soderman et al. (2022) who applied a filtering of 7.2 wt. % < MgO < 16 wt. % to further avoid cumulates. In detail, the filtering approach used in this study applies to three samples of the Doros suite, one SSB from Piton de la Fournaise, one Lō'ihi transitional basalt and the PREMA-type sample from Rurutu Island (FP2RU2).

4.5.2.1 The effect of melting of garnet- vs. spinel-bearing peridotite

Compared to MORBs with an average $\delta^{53/52}$Cr value of -0.237 ± 0.050 ‰ (2SD; Chapter 3), OIBs extend from BSE-like values or slightly heavier (average $\delta^{53/52}$Cr of -0.104 ± 0.013 ‰ for Lō'ihi tholeiitic basalts, 2SD; n=5) towards $\delta^{53/52}$Cr values as low as -0.227 ± 0.018 ‰ (2SE; Lō'ihi transitional basalt J2-309-R1). During partial melting of the mantle, the silicate melt is enriched in the heavier Fe and lighter Cr isotopes. Hence, the melt exhibits a higher $\delta^{56/54}$Fe (Dauphas et al., 2009; Weyer and Ionov, 2007; Williams et al., 2005) and lower $\delta^{53/52}$Cr (Shen et al., 2018b; Shen et al., 2020; Xia et al., 2017) compared to the source. Thereby, the isotopic fractionation is thought to be greatest at small degrees of melting, and with increasing melting degree the $\delta^{56/54}$Fe and $\delta^{53/52}$Cr values of the melts approach that of their source (Dauphas et al., 2009; Jerram et al., 2022; Chapter 3). As OIBs are generally thought to be generated at lower degrees of melting (∼10 %) compared to MORBs (∼20 %), they should, in theory, exhibit lower $\delta^{53/52}$Cr and higher $\delta^{56/54}$Fe values than MORBs. However, for $\delta^{53/52}$Cr the opposite is observed and the overall higher

$\delta^{53/52}$Cr of OIBs compared to MORBs cannot be reconciled by different degrees of partial melting of a homogeneous source.
In contrast to MORBs, which are mostly generated in the stability field of spinel, melting of OIBs occurs at greater depths and higher pressures in the garnet stability field. This is shown by $(Gd/Yb)_{PM} > 2$ for all samples in this study (Figure 4.11; PM normalizing values after Palme and O'Neill, 2014)). The sensitivity of stable Fe isotopes to lithological variations, i.e., garnet- vs. spinel-bearing peridotite, has been proposed previously (Gleeson et al., 2020; Konter et al., 2016; Soderman et al., 2021; Soderman et al., 2022; Sossi and O'Neill, 2017; Williams and Bizimis, 2014) and recently also invoked for stable Cr isotopes by theoretical calculations (Jerram et al., 2022).
For Fe, experimental work determining equilibrium fractionation factors and natu-

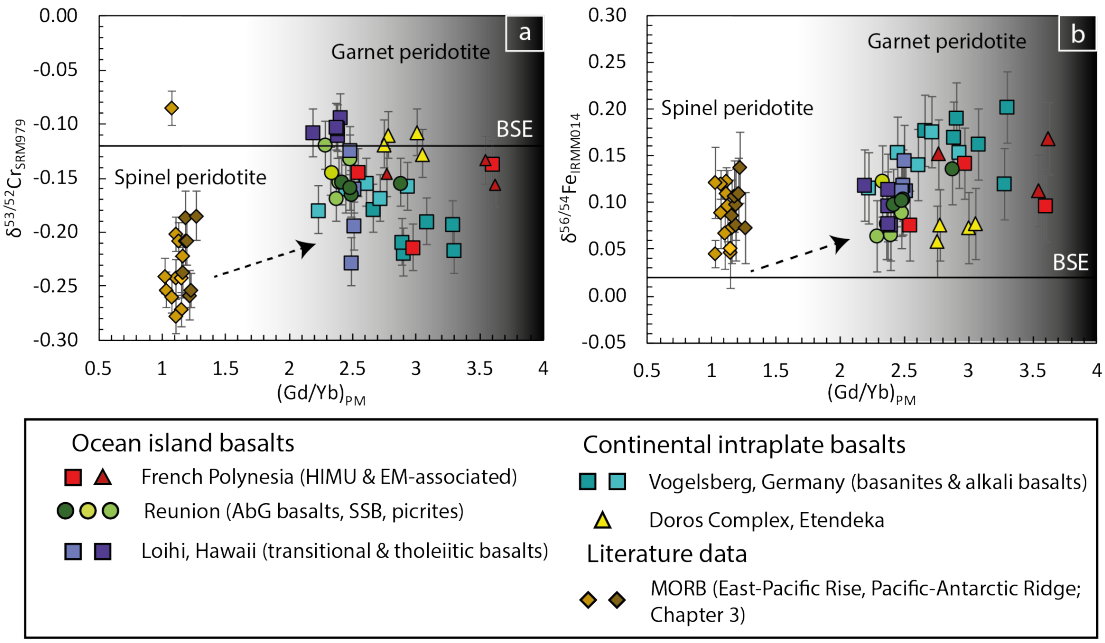

Figure 4.11: **a)** Cr isotopic compositions ($\delta^{53/52}$Cr) and **b)** Fe isotope compositions ($\delta^{56/54}$Fe) vs. $(Gd/Yb)_{PM}$ to illustrate the influence of garnet during partial melting of OIBs compared to MORBs (Chapter 3). $(Gd/Yb)_{PM}$ ratios of ~1 are consistent with melting in the presence of spinel, whereas $(Gd/Yb)_{PM}$ ratios > 2 highlight melting in the garnet stability field. Shaded area is supposed to illustrate qualitatively the increasing influence of garnet. The higher $\delta^{53/52}$Cr and higher $\delta^{56/54}$Fe compared to MORB is qualitatively consistent with partial melting models (indicated by the stippled arrow) which suggest greater Fe isotopic fractionation and lower Cr isotopic fractionation from the BSE during partial melting when compared to melting in the spinel stability field. Estimates for $\delta^{53/52}$Cr and $\delta^{56/54}$Fe BSE values as used in Figure 4.1. Errors on $\delta^{53/52}$Cr and $\delta^{56/54}$Fe as used in 4.1.

ral data showed that garnets preferentially incorporate the light Fe isotopes (Beard and Johnson, 2004; Sossi and O'Neill, 2017; Williams and Bizimis, 2014; Williams et al., 2009; Williams et al., 2005), which can be largely attributed to the differences in coordination environment of Fe^{2+} changing from [4]- to [6]-coordinated in spinel, [6]-coordinated in pyroxene and olivine to [8]-coordinated Fe^{2+} in garnet (Sossi and O'Neill, 2017; Young et al., 2015). Hence, the retention of light Fe isotope in garnet has been proposed to result in a greater Fe isotopic fractionation during melting of garnet peridotite compared to spinel-bearing peridotite. Assuming a BSE-like $\delta^{56/54}$Fe for both lithologies, i.e., identical isotopic starting composition, the iso-

topic differences between a melt generated by partial melting of a garnet-bearing peridotite compared to a spinel-bearing peridotite are small ($< \sim 0.01$ ‰ at 10 % melt degree; Gleeson et al., 2020; Sossi and O'Neill, 2017). Moreover, considering a BSE-like $\delta^{56/54}$Fe source composition modeling results by Sossi and O'Neill (2017) show a melt generated by 1 % melting of a garnet-peridotite would exhibit a $\delta^{56/54}$Fe of ~0.07 ‰. Therefore, the on average higher $\delta^{56/54}$Fe values of OIBs in this study compared to MORBs are qualitatively in agreement with differences in the degree and depth of melting (Figure 4.11). However, the $\delta^{56/54}$Fe variations within single OIB rock suites are too large and the absolute $\delta^{56/54}$Fe values of OIBs are too high to be generated by lower melting degrees and the presence of garnet alone, which has been also highlighted by previous studies (e.g., Gleeson et al., 2020; Soderman et al., 2021; Sossi and O'Neill, 2017).

The effect of garnet on $\delta^{53/52}$Cr during mantle melting is less well studied and $\delta^{53/52}$Cr data on garnet separates are sparse. So far, mineral analyses of two garnet pyroxenites showed that garnets have consistently lower $\delta^{53/52}$Cr compared to coexisting clinopyroxene (Shen et al., 2015), which may indicate substantial incorporation of light Cr isotopes into garnet. However, variable isotopic differences between the two clinopyroxene-garnet pairs suggest disequilibrium (Shen et al., 2015). Besides, garnet pyroxenites are not representative for garnet-peridotite melting. In particular, garnet pyroxenites studied by Shen et al. (2015) are derived from a subarc mantle being affected by a variety of complex processes, such as metasomatism by fluids and melts from the subducted slab (Shen et al., 2018a). Metasomatism especially by melts has been shown to promote $\delta^{53/52}$Cr disequilibrium between minerals and melts (Jerram et al., 2022; Xia et al., 2017) and may thus account for the light $\delta^{53/52}$Cr of garnet in these particular samples. On the other hand, the Cr isotopic composition of garnet-bearing peridotites derived from subcontinental lithospheric mantle show a considerable range between -0.35 and +0.03 ‰ (Xia et al., 2017). However, these samples have experienced variable degrees of melt extraction and metasomatism (Xia et al., 2017). Moreover, a recent study by Jerram et al. (2022) revealed no systematic difference in $\delta^{53/52}$Cr between spinel- and garnet-bearing lherzolites, with the latter displaying a $\delta^{53/52}$Cr range between -0.17 and -0.08 ‰. Nevertheless, based on a similar approach used by Sossi and O'Neill (2017), model calculations by Jerram et al. (2022) suggest lower Cr isotopic fractionation ($\Delta^{53/52}Cr_{source\text{-}melt}$) during melting of garnet peridotite compared to spinel peridotite, which in theory should result in higher $\delta^{53/52}$Cr values of OIBs compared to MORBs. These authors use the same potential energies to calculate $\delta^{53/52}$Cr of garnet as used for olivine and spinel, because Cr^{3+} occurs in octahedral coordination in all these minerals. This is supported by experimental data, which showed that garnet preferentially incorporates Cr^{3+} over Cr^{2+} over a wide range of oxygen fugacities (ΔIW-2 to ΔIW+9; Righter et al., 2011). The overall heavier $\delta^{53/52}$Cr of OIBs compared to MORBs, thereby creating an overall positive relationship between $\delta^{53/52}$Cr and $(Gd/Yb)_{PM}$ defined by the MORB-OIB array, can thus be qualitatively explained by garnet in the source of OIBs (Figure 4.11a). However, calculated Cr isotopic compositions of garnet peridotite melts are only ~0.02 ‰ heavier than melts generated by partial melting of spinel-peridotite (Jerram et al., 2022). This is in agreement with the indistinguishable $\delta^{53/52}$Cr of Al-depleted komatiites compared to Al-undepleted komatiites (Wagner et al., 2021; Chapter 2). Therefore, the observed range for OIBs from $\delta^{53/52}$Cr of -0.227 $\pm$ 0.018 ‰ (transitional basalt J2-309-R1,

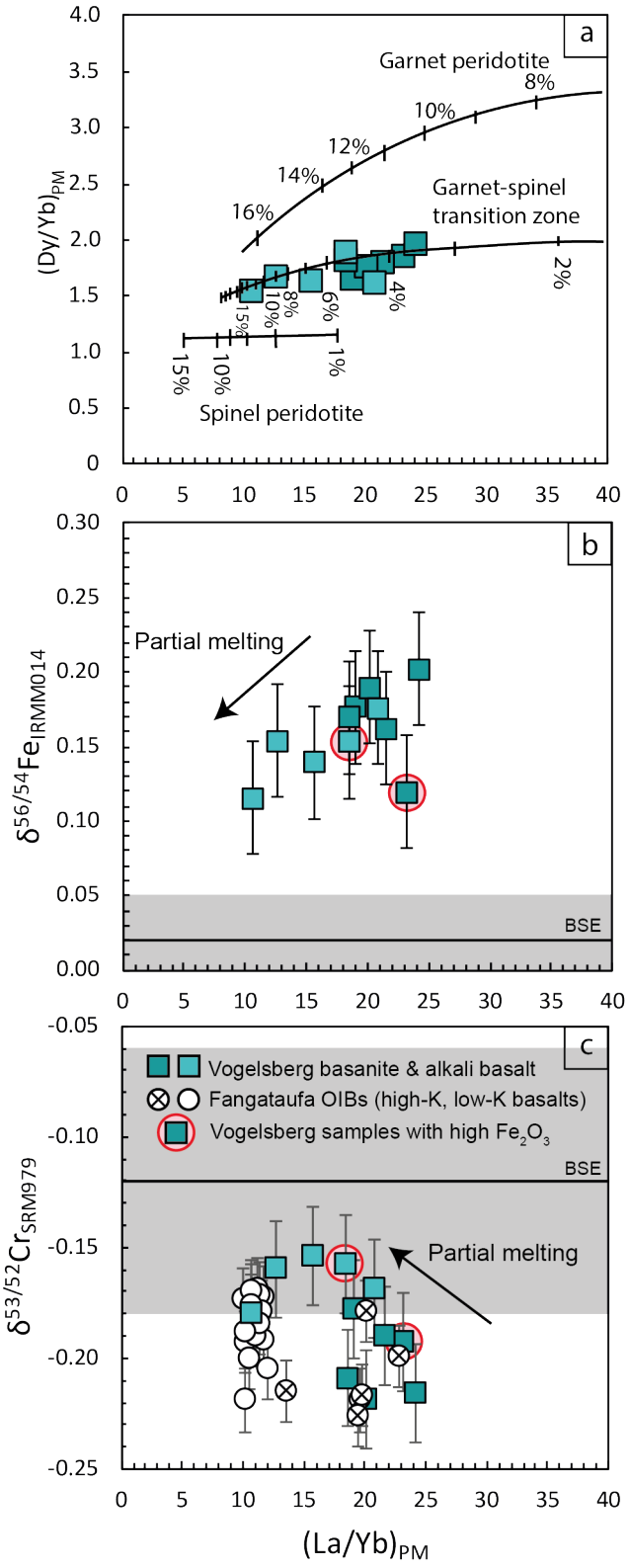

Figure 4.12: **a)** Variations of $(Dy/Yb)_{PM}$ vs. $(La/Yb)_{PM}$ for Vogelsberg basanites and alkali basalts show that basanites are generated at lower partial melting degrees than alkali basalts in the garnet-spinel transition zone. Modeled melting curves are from Bogaard and Woerner (2003). Tick marks with numbers indicate the degree of melting in %; **b)** Basanites and alkali basalts follow a trend of decreasing $\delta^{56/54}$Fe with decreasing $(La/Yb)_{PM}$ in line with partial melting control; **c)** $\delta^{53/52}$Cr increase with decreasing $(La/Yb)_{PM}$. Comparison with literature $\delta^{53/52}$Cr data from Fangataufa Island, in which high-K and low-K basalts display low- and high-degree melts, respectively (Bonnand et al. 2020), show a similar trend supporting the proposed partial melting control for this dataset. Errors on $\delta^{53/52}$Cr and $\delta^{56/54}$Fe as used in Figure 4.1.

Lō'ihi) to -0.094 ± 0.017 ‰ (tholeiitic basalt J2-243-1A-R2, Lō'ihi) and the difference between the average $\delta^{53/52}$Cr of MORBs (-0.237 ± 0.050 ‰, 2SD, n=19; Chapter 3) compared to average $\delta^{53/52}$Cr of OIBs (-0.153 ± 0.072 ‰, 2SD, n=39) may not fully be accounted by melting induced Cr isotopic fractionation of garnet vs. spinel bearing peridotite. Moreover, the absence of positive correlations between $\delta^{53/52}$Cr and $(Gd/Yb)_{PM}$ within each volcano or island group suggests that garnet does not exert a primary control on $\delta^{53/52}$Cr.

In particular, Vogelsberg basanites and alkali basalts display a negative correlation between $\delta^{53/52}$Cr and $(Gd/Yb)_{PM}$. Trace element modeling showed that Vogelsberg volcanic rocks were generated within the garnet-spinel transition zone, whereas basanites are generated at lower melting degrees compared to alkali basalts (Figure 4.12a; Bogaard and Wörner, 2003). Moreover, low SiO_2 saturation in primitive magmas indicate higher melting pressures, which suggests that basanites are generated at higher average melting depths compared to alkali basalts and is in agreement with observations from alkaline volcanic rocks from the Siebengebirge (Jung et al., 2012; Kolb et al., 2012). Thus, slightly higher $(Gd/Yb)_{PM}$ ratios (Figure 4.11), high CaO/Al_2O_3 and V/Sc ratios (not shown) in basanites compared to alkali basalts point to a higher influence of garnet. However, the lower $\delta^{53/52}$Cr of basanites compared to alkali basalts is in conflict with garnet peridotite melting controlling the $\delta^{53/52}$Cr in the light of model calculations by Jerram et al. (2022). Hence, a different process may control the $\delta^{53/52}$Cr of the Vogelsberg suite and possibly OIBs in general. Although, the positive correlations between $\delta^{56/54}$Fe and $(Gd/Yb)_{PM}$ (and V/Sc) ratios are in agreement with melting within a continuous spectrum of decreasing garnet control from Vogelsberg basanites to alkali basalts (Figure 4.11b), the observed $\delta^{56/54}$Fe variations within the Vogelsberg rock suite of ∼0.086 ‰ are much greater than can be accounted for by partial melting of garnet peridotite alone as indicated by theoretical partial melting model calculations (Gleeson et al., 2020; Soderman et al., 2021; Sossi and O'Neill, 2017).

In summary, the lighter $\delta^{53/52}$Cr and heavier $\delta^{56/54}$Fe compositions of OIBs compared to MORBs and the BSE value are in agreement with the general behavior of Cr and Fe isotopes during partial melting of garnet-peridotite. However, the observed isotopic variation is much greater than predicted by melting models published so far (For Cr: Jerram et al., 2022; for Fe: Gleeson et al., 2020; Sossi and O'Neill, 2017). As suggested for Fe isotopes in previous studies (Gleeson et al., 2020; Konter et al., 2016; Nebel et al., 2019; Soderman et al., 2021; Sossi and O'Neill, 2017; Teng et al., 2013; Williams and Bizimis, 2014), the large variations of $\delta^{53/52}$Cr in OIBs may be explained by melting of a lithological heterogeneous source.

4.5.2.2 Tracing the oceanic crust

Although the on average higher $\delta^{53/52}$Cr values of OIBs compared to MORB are qualitatively consistent with partial melting of garnet peridotite compared to melting in the spinel stability field, the $\delta^{53/52}$Cr of OIBs show a greater variation than is anticipated by current melting models (Jerram et al., 2022). Following, a lithologically heterogeneous mantle with possibly including heterogeneous $\delta^{53/52}$Cr source compositions, may cause the observed $\delta^{53/52}$Cr range in OIBs. This is in principle supported by the large range of $\delta^{53/52}$Cr exhibited by (subcontinental) lithospheric mantle xenoliths (Jerram et al., 2022; Xia et al., 2017).

A heterogeneous mantle has been traditionally inferred from the diverse composi-

tions of oceanic basalts in radiogenic isotope space (Sr-Nd-Hf-Pb; Hofmann, 1997; White et al., 2000) and linked to the recycling of crustal components. The different components are referred to as the depleted mantle, EM1, EM2, HIMU and PREMA and also exhibit specific characteristic in major element and trace element compositions suggesting varying origins of these crustal components (Jackson and Dasgupta, 2008; Jackson et al., 2012; Willbold and Stracke, 2006). Therein, recycling of crustal components such as oceanic crust is mostly associated with the HIMU and PREMA components whereas EM1 and EM2 are associated with an additional continentally derived component (e.g., Stracke, 2012; Stracke et al., 2005; Willbold and Stracke, 2006).

Moreover, this compositional diversity has often been linked to a lithological heterogeneity, encompassing variously depleted peridotite lithologies as well as enriched mafic and ultramafic lithologies such as eclogite or pyroxenite. Eclogite, the high-P and low-T derivate of basalt, is formed during subduction of oceanic crust. This eclogite may undergo partial melting during subduction or during later ascent in a plume and form a range of pyroxenite compositions by reacting with ambient peridotite (e.g., silica-excess and silica-deficient pyroxenite, respectively; Lambart et al., 2016). In addition, low degree melts of peridotite that metasomatize the ambient mantle may form pyroxenite lithologies or crystallize as pyroxenitic veins near or within the lithosphere and may thus be unrelated to recycling of oceanic crust (Downes, 2007; Halliday et al., 1995).

Stable Fe isotopes have been used previously to identify recycled source material (Gleeson et al., 2020; Konter et al., 2016; Nebel et al., 2019; Soderman et al., 2021; Williams and Bizimis, 2014), and have been linked to relatively high $\delta^{56/54}$Fe in OIBs or MORBs. The sensitivity of stable Fe isotopes is mainly based on mineral-specific fractionation factors of pyroxene enhancing the magnitude of isotopic fractionation. Thereby, higher melt $\delta^{56/54}$Fe values are generated, if pyroxenites are present in the source compared to melting of peridotite (Soderman et al., 2021; Williams and Bizimis, 2014). Similarly, partial melting of eclogites leads to higher $\delta^{56/54}$Fe in the melt due to preferential melting of pyroxene and retention of light Fe isotopes in garnet (Sossi and O'Neill, 2017). Moreover, this effect is enhanced, if the pyroxene-rich lithology or eclogite has a crustal origin and thus presumably carries a higher $\delta^{56/54}$Fe signature than pure peridotite with a BSE-like signature of +0.02 $\pm$ 0.03 ‰ (Weyer and Ionov, 2007). In this context, pyroxenite or eclogite components exhibit a $\delta^{56/54}$Fe signature represented by average MORB ($\delta^{56/54}$Fe = +0.107 $\pm$ 0.055 ‰, 2SD; compiled from Chen et al., 2019; Richter et al., 2021; Weyer and Ionov, 2007). More recently, mineralogical control on stable isotope fractionation of various non-traditional isotope systems (Fe-Mg-Ca-V-Cr) during partial melting have been explored by theoretical phase equilibria calculations by Soderman et al. (2022). Therein, stable Cr and Fe isotopes emerge as a lithological tracer, especially for pyroxenites, in the source of basalts. Similar to Fe isotopes, the sensitivity of stable Cr isotopes to different lithologies is based on mineral-specific fractionation factors during melting (Berry et al., 2021a; Shen et al., 2018a). The combination of relatively high Cr concentrations and positive isotopic differences between source and melt ($\Delta^{53/52}Cr_{source\text{-}melt}$; Shen et al., 2020) make clinopyroxene, together with spinel, crucial mineral phases during partial melting. Additionally, a pyroxenite component representing recycled oceanic crust has a presumably lower $\delta^{53/52}$Cr than peridotite with a BSE-like composition of $\delta^{53/52}$Cr = -0.12 $\pm$ 0.06 ‰, as suggested

by the recently discovered low $\delta^{53/52}$Cr of MORBs (Ma et al., 2022; Chapter 3) with an $\delta^{53/52}$Cr average of -0.237 $\pm$ 0.050 ‰ (2SD; Chapter 3). Thus, a pyroxenitic component contributing to the melt will enhance the bulk magnitude of Cr isotopic fractionation and result in overall lower melt $\delta^{53/52}$Cr compared to melting of a pure peridotitic source (Soderman et al., 2022). However, Cr isotope data for natural pyroxenite lithologies are scarce. For example, two garnet pyroxenites from the sub-arc mantle exhibit variable bulk $\delta^{53/52}$Cr of -0.10 $\pm$ 0.04 ‰ and -0.20 $\pm$ 0.05 ‰ and relatively low Cr concentrations of 194 μg g^{-1} and 164 μg g^{-1}, respectively (Shen et al., 2015). Furthermore, significant $\delta^{53/52}$Cr variations for subcontinental lithospheric mantle xenoliths have been observed, in which pyroxenitic veins formed from trapped melt were shown to exhibit exceptional light $\delta^{53/52}$Cr as a result of kinetic diffusion processes (Jerram et al., 2022; Xia et al., 2017). Although these samples may not be directly representative for pyroxenites derived from subduction induced crustal recycling, the variable but predominantly light $\delta^{53/52}$Cr values hint at possible complex behavior of Cr isotopes involved in pyroxenite formation.

Combining radiogenic isotopes evidencing crustal components in the source of OIBs with stable Fe isotopes showed that both proxies often correlate, which was interpreted to indicate a mixing relationship of different source components with variable $\delta^{56/54}$Fe (Gleeson et al., 2020; Nebel et al., 2019; Soderman et al., 2021; Sun et al., 2020; Zhong et al., 2021). Therein, the high $\delta^{56/54}$Fe component was attributed to pyroxenite/eclogite having a crustal origin. Similarly, positive correlations between radiogenic ^{143}Nd/^{144}Nd ratios and $\delta^{53/52}$Cr values in basalts from Fangataufa Island (French Polynesia) suggest an enriched component with a low $\delta^{53/52}$Cr in the source of these basalts, although this interpretation is potentially masked by high degrees of fractional crystallization and varying degrees of partial melting (Figure 4.13b; Bonnand et al., 2020b).

Here, the observed correlations of ^{87}Sr/^{86}Sr and ^{143}Nd/^{144}Nd ratios with $\delta^{53/52}$Cr between MORB and OIB may indeed reflect a simple mixing relationship between mantle components exhibiting different $\delta^{53/52}$Cr and sampled by oceanic basalts (Figure 4.13). Therein, MORBs represent one mixing endmember, whereas OIBs with more radiogenic ^{87}Sr/^{86}Sr isotopic signatures trend towards BSE-like $\delta^{53/52}$Cr. Interestingly, OIBs with HIMU- or PREMA-affinity (i.e., samples from Austral islands and sample FP15GA7 from Mangareva Island (French Polynesia), Vogelsberg basanites, transitional Lō'ihi glasses and literature data for Fangataufa Island (French Polynesia); Bonnand et al., 2020b) show lower $\delta^{53/52}$Cr values compared to the $\delta^{53/52}$Cr BSE value. As PREMA and HIMU mantle components are suggested to contain recycled oceanic crust of variable age, the low $\delta^{53/52}$Cr may be the result of mixing of MORB-like $\delta^{53/52}$Cr into the melting sources of the aforementioned samples and possibly present as lithologies with "different physico-chemically properties" (pyroxenite/eclogite) as suggested for the PREMA component in particular (Stracke, 2012).

When compared with the trend observed for Cr isotopes, Fe isotopic compositions do not correlate as well with ^{87}Sr/^{86}Sr or ^{143}Nd/^{144}Nd ratios (Figure 4.13c, d). However, relatively high $\delta^{56/54}$Fe values of the Vogelsberg suite, one HIMU sample from French Polynesia or Lō'ihi transitional glasses support the general model of recycled crustal components present as isotopically heavier pyroxenite/eclogite in the source of OIBs leading towards higher melt $\delta^{56/54}$Fe values (Gleeson et al., 2020; Nebel et al., 2019; Soderman et al., 2021; Williams and Bizimis, 2014). Consistently,

Réunion basalts, which are derived from a peridotite source considered to be free of recycled materials (e.g., Gleeson and Gibson, 2019), display BSE-like $\delta^{53/52}$Cr and $\delta^{56/54}$Fe values (Figure 4.13). In contrast to the observed positive relationship between $\delta^{53/52}$Cr and εNd for Fangataufa basalts (Bonnand et al., 2020b), no such trend is observed for OIBs in general or individual OIB suites in this study. Except for EM2 related basalts from French Polynesia, this may be ascribed to the small

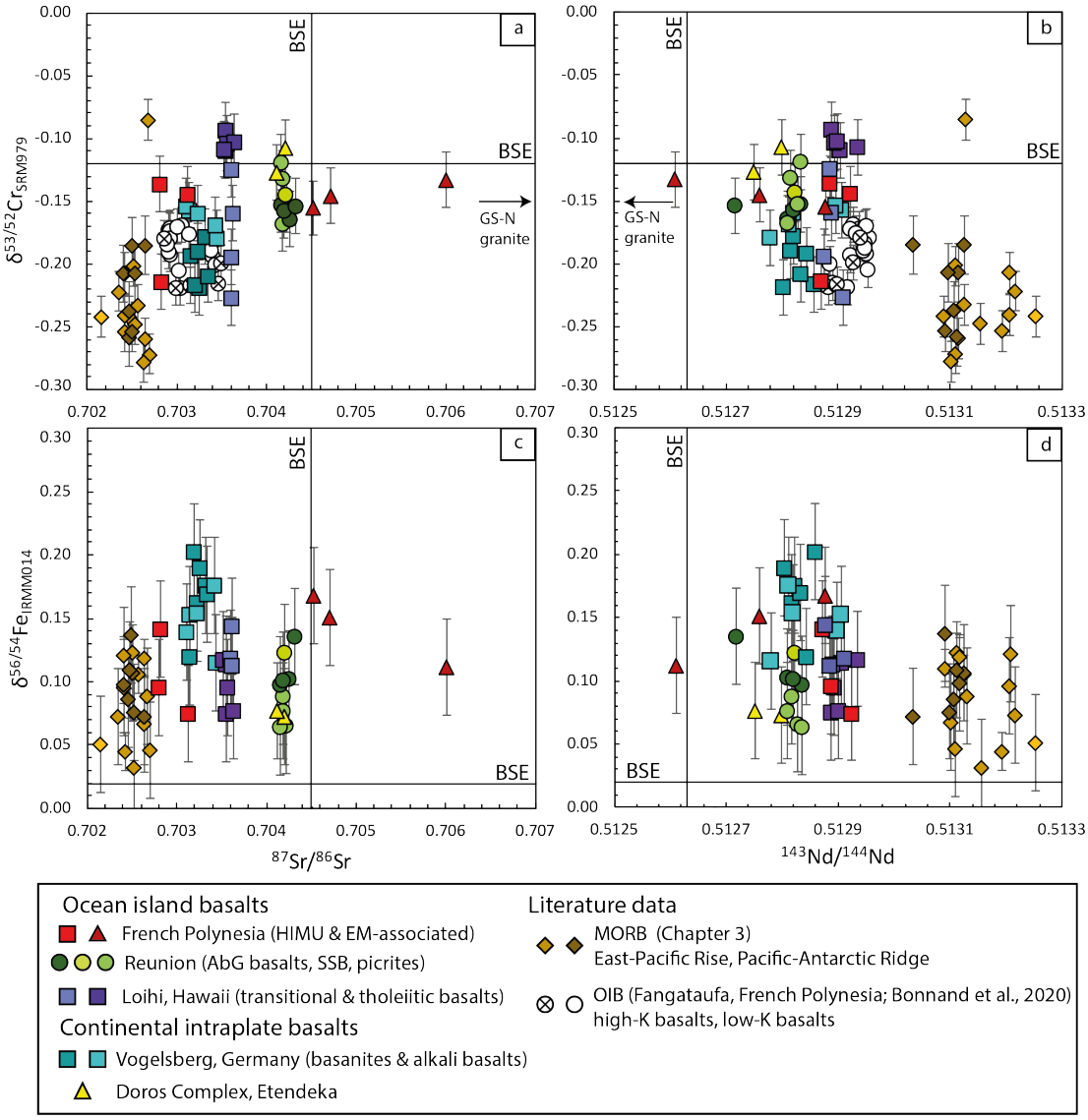

Figure 4.13: Cr and Fe isotopic composition vs. radiogenic Sr and Nd isotope compositions. Samples representative for HIMU- and PREMA-type OIBs exhibit relatively low $\delta^{53/52}$Cr and high $\delta^{56/54}$Fe in line with recycling of oceanic crust with a MORB-like isotope composition in the source of these OIBs, possibly present as pyroxenitic lithologies. Decreasing $\delta^{56/54}$Fe with increasing radiogenic Sr isotope compositions is in contrast with pyroxenititc components, but suggest a carbonated mantle sampled by EM2 associated basalts from French Polynesia controlling the Fe isotope compositions. Conclusively, the increase in $\delta^{53/52}$Cr with $^{87}Sr/^{86}Sr$ ratios for these samples suggests that carbonated mantle metasomatism causes high $\delta^{53/52}$Cr. Data for Fangataufa OIBs from Bonnand et al. (2020b). BSE-values for $\delta^{53/52}$Cr from Wagner et al. (2021), for $\delta^{56/54}$Fe from Weyer and Ionov (2007), and for radiogenic Sr and Nd isotope compositions from DePaolo and Wasserburg (1976) and Bouvier et al. (2008), respectively. Errors on $\delta^{53/52}$Cr and $\delta^{56/54}$Fe as used in Figure 4.1.

spread in radiogenic isotope compositions within each OIB suite (e.g., Réunion, Lō'ihi, or Doros complex). EM2 related basalts from French Polynesia show a relatively large spread in radiogenic Sr and Nd (Figure 4.13) and to lesser extent Pb (not shown). Interestingly, radiogenic isotopic compositions of these samples show strong correlations with $\delta^{53/52}$Cr and $\delta^{56/54}$Fe, the origin of which is discussed in the following.

4.5.2.2.1 Constraints from Vogelsberg basanites and alkali basalts Based on radiogenic Sr-Nd-Pb isotope and trace element compositions the source of basanites and alkali basalts include both asthenospheric and lithospheric components (Bogaard and Wörner, 2003), whereas source characteristics of both have been related to the subduction related recycling during the Variscan orogeny (e.g., Wilson and Downes, 1991). The asthenospheric component with a Sr-Nd-Pb composition similar to the EAR and PREMA (Figure 4.2), suggests the presence of recycled oceanic crust (Stracke, 2012; Stracke et al., 2005; Wörner et al., 1986). Moreover, the importance of residual eclogite has been suggested for alkaline lavas from the Siebengebirge Volcanic Field based on high Zr/Hf (Kolb et al., 2012). High Zr/Hf ratios in OIBs and continental intraplate basalts have been ascribed to a two-stage melting process, in which high Zr/Hf is initially generated during subduction involving slab-melting of eclogite. In a second stage, the eclogite becomes incorporated into the source of alkaline basalts imparting its high Zr/Hf to primary alkaline melts (Klemme et al., 2002; Kolb et al., 2012; Pfänder et al., 2007). Basanites from the Vogelsberg display Zr/Hf ratios ranging between 43 to 48, which are higher than observed for alkali basalts (Zr/Hf = 42 to 44) and the chondritic value of 34.2 (Figure 4.14; Münker et al., 2003). Fractionation of Zr/Hf ratios towards higher values may also be achieved by fractional crystallization of clinopyroxene as well as carbonatite metasomatism. As described in Section 4.5.1.2 clinopyroxene crystallization as the cause for high Zr/Hf is unlikely based on the fact that basanites represent near primary melts. Additionally, Sc contents increase with decreasing MgO within basanites, thus, indicating minor clinopyroxene crystallization (Figure C.2.7). Carbonatite-like metasomatism of the source has been shown to also increase Nb/Ta ratios of volcanic rocks above the range typically observed for MORBs (Nb/Ta = 11.5 to 16.6; Büchl et al., 2002) as shown for Etna volcanic rocks with Nb/Ta ratios between ∼21 to ∼25 (Bragagni et al., 2022) or continental basalts from Central Germany, including Vogelsberg, Eifel and Rhön, with Nb/Ta ratios of up to 19.1 (Pfänder et al., 2012). Based on the comparably low Nb/Ta ratios of Vogelsberg basanites and alkali basalts ranging between 14.3 and 15.9 (one sample with Nb/Ta of 18.1), carbonatite metasomatism as the cause for high Zr/Hf ratios in Vogelsberg rocks is considered unlikely. In agreement with observations made by Kolb et al. (2012), decreasing Zr/Hf with decreasing MgO (Figure 4.14) can thus be interpreted as a decreasing influence of eclogitic components from basanites to alkali basalt, and is also supported by higher $(Gd/Yb)_{PM}$ in basanites (Figure 4.11). This is corroborated by the fact that these phases have a lower solidus and contribute more readily at initial stages of melting becoming more diluted with increasing degree of melting (Kolb et al., 2012). The combination of high Zr/Hf and on average higher $\delta^{56/54}$Fe values of basanites compared to alkali basalts are thus in agreement with the presence of recycled crust (as eclogite) in the mantle source (Figure 4.14c; Soderman et al., 2021; Sossi and O'Neill, 2017). A similar effect can be observed for $\delta^{53/52}$Cr with basanites exhibiting lower

$\delta^{53/52}$Cr values than alkali basalts (Figure 4.14a) indicating that an eclogitic component in the source may lead towards lower $\delta^{53/52}$Cr in the melt. This observation is in agreement with model calculations showing that melting of a source consisting of peridotite and eclogitic pyroxenite (silica-excess pyroxenite, G2) generates lower melt $\delta^{53/52}$Cr compared to melting of a pure peridotitic source (Soderman et al., 2022). The correlation between $\delta^{53/52}$Cr and $(Gd/Yb)_{PM}$ ratios may thus be interpreted in the light of recycled oceanic crust present as eclogite (Figure 4.11).

Although the homogeneous radiogenic Sr-Nd-Pb isotope compositions of basanites

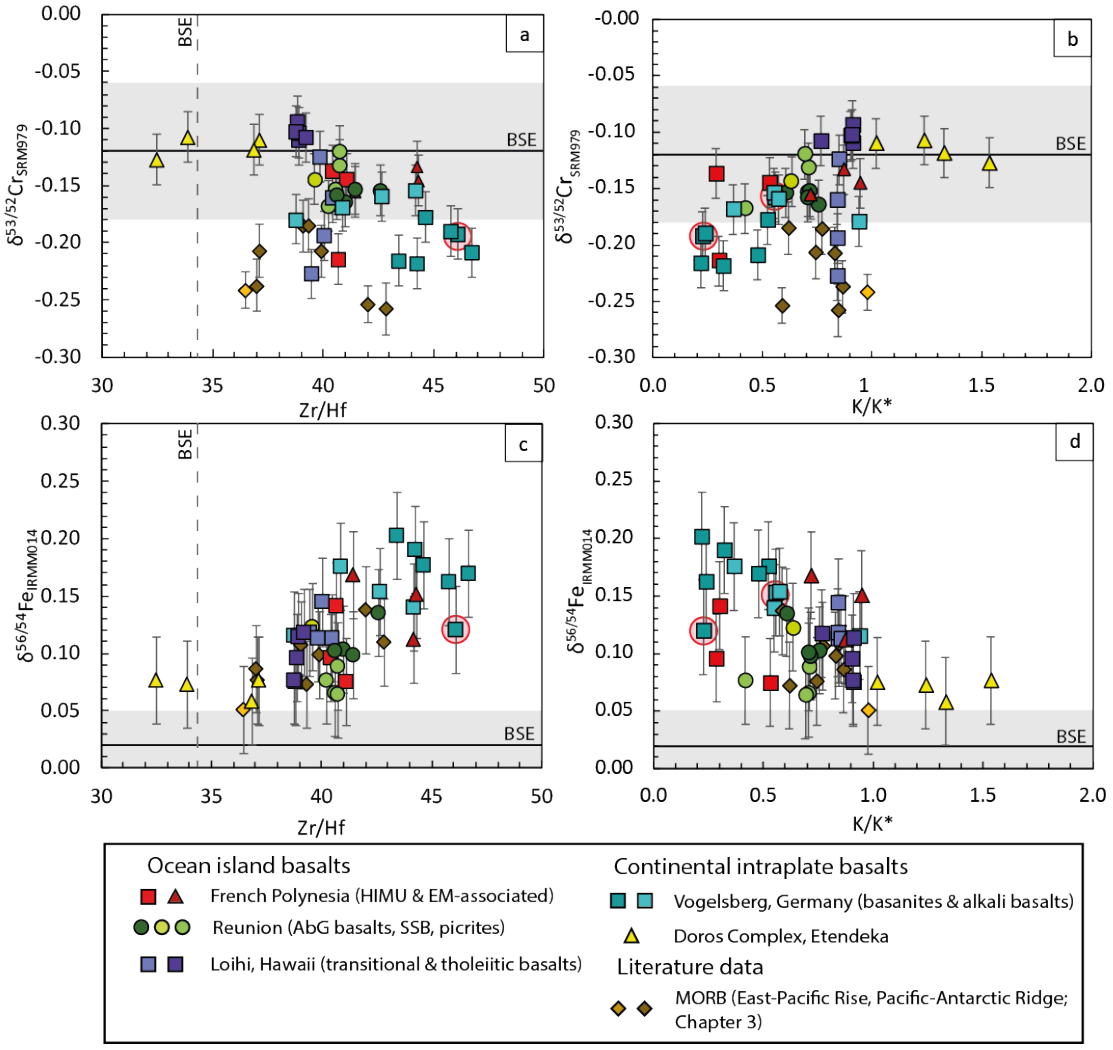

Figure 4.14: **a)** Cr and **c)** Fe isotopic compositions vs. Zr/Hf ratios for all OIBs in this study. Of special interest are Vogelsberg basanites, which have higher Zr/Hf (43-48) than alkali basalts (42-44), and can be attributed to eclogite in the source of basanites possibly leading towards higher Fe and lower Cr isotope values (see text for more discussion). EM2 related basalts from French Polynesia also show high Zr/Hf ratios likewise suggesting an eclogitic component. **b)** Cr and **d)** Fe isotope compositions vs. K/K* (representing the negative K-anomaly observed on PM-normalized trace element patterns; Figure 4.5; see text for calculation) showing that a lithospheric hydrous component, consisting of pyroxenite-rich layers or veins and K-bearing phases, contribute to the high $\delta^{56/54}$Fe and low $\delta^{53/52}$Cr of Vogelsberg basalts. We note that highly incompatible trace element compositions (e.g., Zr/Hf ratios) of Doros samples need to be taken with caution as they represent intrusive rocks. BSE value for $\delta^{53/52}$Cr and $\delta^{56/54}$Fe after Wagner et al. (2021) and Weyer and Ionov (2007), respectively. Zr/Hf ratio of BSE in a) and c) after Münker et al. (2003). Errors on $\delta^{53/52}$Cr and $\delta^{56/54}$Fe as used in Figure 4.1.

and alkali basalts highlight the predominance of an asthenospheric source component, a lithospheric component cannot be neglected based on the strong K-depletions on PM normalized trace element patterns (Figure 4.5d), which can also be expressed as K/K* ($K/K^* = K_{PM}/(U_{PM} \times Nb_{PM})^{0.5}$; normalizing values after Palme and O'Neill, 2014). The precipitation of hydrous K-bearing clinopyroxenite layers or veins preceding partial melting during Cenozoic magmatism has been linked to the Variscan orogeny leading to a metasomatized subcontinental lithospheric mantle beneath the CEVP (Jung et al., 2011). A decrease in K/K* ratios with decreasing MgO (not shown) thus suggest a decreasing influence of the lithospheric contribution with increasing degree of melting represented by alkali basalt and is in agreement with observations made for alkali basalts from other localities of the CEVP (Kolb et al., 2012). Following, the trend between K/K* and $\delta^{53/52}$Cr observed for Vogelsberg volcanic rocks suggests that increasing lithospheric mantle contributions may lead towards lower melt $\delta^{53/52}$Cr as observed for basanites (Figure 4.14b). The negative trend between $\delta^{56/54}$Fe and K/K* supports the possible effect of metasomatized lithospheric mantle contribution to result in heavy melt $\delta^{56/54}$Fe. This is supported by general observations made for subcontinental mantle xenoliths, in which the formation of secondary clinopyroxenes by melt-rock reactions has been shown to drive the $\delta^{56/54}$Fe towards higher values (Weyer and Ionov, 2007). The heavy $\delta^{56/54}$Fe of Vogelsberg basanites compared to alkali basalt may thus be readily explained by melting a metasomatized source containing secondary clinopyroxene such as has been proposed to be present beneath the CEVP and mantle source region of the Vogelsberg volcano (Bogaard and Wörner, 2003; Hartmann and Wedepohl, 1990; Jung et al., 2011). So far, only one sample exhibiting secondary clinopyroxene formed by melt-rock reaction has been measured for its Cr isotope composition and reveals a relatively heavy $\delta^{53/52}$Cr of -0.06 ‰ compared to the BSE value (Jerram et al., 2022). On the other hand, clinopyroxenite and websterite veins formed by trapped melt within lithospheric mantle xenoliths show variable $\delta^{53/52}$Cr ranging between -1.39 to -0.05 ‰ (Jerram et al., 2022; Xia et al., 2017), and may thus contribute to the low $\delta^{53/52}$Cr observed for Vogelsberg basanites.

Although melting of eclogite lenses and pyroxenite veins within the subcontinental lithospheric mantle can both explain the shift towards lower $\delta^{53/52}$Cr and higher $\delta^{56/54}$Fe of Vogelsberg rocks suite, the distinction between the two remains enigmatic. Based on the absence of clear correlations between $\delta^{53/52}$Cr and $\delta^{56/54}$Fe with radiogenic isotope (and also Zr/Hf ratios) within the Vogelsberg rock suite, but comparable well-defined trends with K/K* (Figure 4.14b-d), the latter model is preferred for the origin of heavy $\delta^{56/54}$Fe and light $\delta^{53/52}$Cr of Vogelsberg rocks. We note that one Vogelsberg basanite (VB96-08) plots towards lower $\delta^{56/54}$Fe diverging from the observed trends in Figure 4.13b. This sample has elevated Fe_2O_3 contents, similar to a Vogelsberg alkali basalt (VB96-16), which however does not show anomalous $\delta^{56/54}$Fe. Although the oxidation of Fe^{2+} to Fe^{3+} could indeed affect the isotopic composition of the two samples, both samples have FeO_{total} contents indicating negligible Fe loss, which in turn may impede significant isotopic fractionation (Figure C.2.7).

4.5.2.2.2 Constraints from Lō'ihi, Hawaii Compositional heterogeneity of the Hawaiian plume has been the subject of many geochemical studies investigating the major, trace and isotope compositions of Hawaiian lavas (Abouchami et al., 2005; Hauri, 1996; Jackson et al., 2012; Lassiter and Hauri, 1998). Especially, the presence of enriched mafic to ultramafic lithologies (eclogite/pyroxenite) contributing to the composition of Hawaiian lavas is debated (Herzberg, 2011; Putirka et al., 2011; Sobolev et al., 2007; Sobolev et al., 2005). Therein, most compositional characteristics can be explained by three components, i.e., Lō'ihi, Kea and Koolau (Jackson et al., 2012). The Koolau component has been suggested to be influenced by a mafic SiO_2-rich component (eclogite) in order to explain the high SiO_2 contents and low CaO contents together with relatively enriched radiogenic isotope signatures. Although a mafic component may be present in the source for Kea dominated lavas, the source has been proposed to consist predominantly of depleted peridotite. For Lō'ihi, contrasting observations suggest either a predominantly peridotitic source (Sobolev et al., 2005) or a mixture of peridotite and a SiO_2-poor mafic component (silica-deficient pyroxenite; Herzberg, 2011; Jackson et al., 2012). In this study, two geochemically distinct groups can be distinguished within Lō'ihi lavas based on petrography, major and trace element compositions as well as stable Cr and Fe isotope compositions. Transitional glasses exhibit $\delta^{53/52}$Cr values extending from a BSE-like value of -0.124 $\pm$0.016 ‰ (2SE; n=1) towards $\delta^{53/52}$Cr values as low as -0.227 $\pm$0.018 ‰ (2SE; n=1) displaying an average $\delta^{53/52}$Cr of -0.176 $\pm$0.089 ‰ (2SD; n=4 after filtering). Interestingly, these samples display high $\delta^{56/54}$Fe values with an average $\delta^{56/54}$Fe of +0.122 $\pm$0.030 ‰ (2SD; n=4 after filtering). In contrast, tholeiitic Lō'ihi glasses display a high $\delta^{53/52}$Cr average of -0.104 $\pm$0.013 ‰ (2SD; n=5) and are associated with low $\delta^{56/54}$Fe values displaying a $\delta^{56/54}$Fe average of +0.096 $\pm$0.040 ‰ (2SD; n=5) (Figure 4.1). It has been suggested that the compositional differences in major and trace element compositions between alkali and tholeiitic basalts are generated by different degrees of partial melting (Garcia et al., 1995; Garcia et al., 1993). However, partial melting alone cannot generate the large spread in $\delta^{53/52}$Cr and $\delta^{56/54}$Fe observed for Lō'ihi glasses (Section 4.5.2.1). Although both groups are overlapping in $\delta^{53/52}$Cr and $\delta^{56/54}$Fe within uncertainty, the observed contrasting stable Cr and Fe isotope compositions of the two groups are alike to Vogelsberg basanites (low $\delta^{53/52}$Cr and high $\delta^{56/54}$Fe) and alkali basalts (high $\delta^{53/52}$Cr and low $\delta^{56/54}$Fe) and may therefore display local source heterogeneities.
In general, high CaO, TiO_2 concentrations and CaO/Al_2O_3 ratios and low SiO_2 concentrations of Lō'ihi glasses in this study support the presence of an enriched pyroxenitic lithology in the source of Lō'ihi lavas (Figure 4.5b-d; Jackson et al., 2012; Prytulak and Elliott, 2007). Based on these features a hybrid mixture of a silica-deficient pyroxenite and peridotite is favoured over a silica-excess eclogite component (Jackson et al., 2012). Based on model calculations by Soderman et al. (2022) the observed low $\delta^{53/52}$Cr and high $\delta^{56/54}$Fe of Lō'ihi transitional glasses compared to Lō'ihi tholeiitic glasses suggests a pyroxene-rich component in Lō'ihi transitional glasses. In this context, Lō'ihi tholeiitic glasses would sample a source with smaller contributions from a pyroxenite component, and hence display more BSE-like $\delta^{53/52}$Cr and $\delta^{56/54}$Fe. As for the Vogelsberg suite, low $\delta^{53/52}$Cr and high $\delta^{56/54}$Fe of transitional basalts may be derived from pyroxene-rich lithologies incorporated in the lithospheric mantle and possibly present as veins or dykes, or from within the plume source, enclosing recycled components present as eclogitic or py-

roxenitic lithologies. In contrast to the Vogelsberg suite, the absence of negative K-anomalies on PM-normalized trace element patterns does not support a lithospheric imprint neither on transitional nor tholeiitic Lō'ihi glasses (Figure 4.5c). Moreover, according to Jackson et al. (2012), melt-rock reaction within the lithospheric mantle results in high SiO_2 and CaO/Al_2O_3 of the melt as pyroxene is dissolved and olivine is precipitated. However, the opposite is observed for transitional Lō'ihi glasses, which display both lower SiO_2 (Figure 4.3) and CaO/Al_2O_3 compared to tholeiitic Lō'ihi glasses (Figure 4.6d). Therefore, low $\delta^{53/52}$Cr and high $\delta^{56/54}$Fe of Lō'ihi transitional glasses is suggested to be caused by mixing of variable proportions of a low-SiO_2 mafic component, for example a silica-deficient pyroxenite melt, with a peridotite-derived melt. This is further supported by higher TiO_2 contents of Lō'ihi transitional glasses compared to tholeiitic glasses (Figure 4.5c) proposed to mirror the contribution of an enriched pyroxenitic component (Prytulak and Elliott, 2007). In contrast, Lō'ihi tholeiitic glasses may simply sample a pure peridotitic source, which has been previously suggested for Lō'ihi lavas based on petrologic models (Herzberg, 2011; Putirka et al., 2011). A homogeneous peridotitic source for tholeiitic glasses would also be in agreement with the observed lower average $\delta^{56/54}$Fe value compared to Lō'ihi transitional glasses as well as exhibiting $\delta^{56/54}$Fe values similar to those of the peridotite sourced Réunion lavas with an average of +0.095 $\pm$ 0.048 ‰ (2SD; n=9 after filtering).
High ^{3}He/^{4}He (R_A up to 32.2; Kurz et al., 1983; Mundl et al., 2017) in Lō'ihi lavas suggest a primordial, undegassed, lower mantle component. Although Réunion lavas have been shown to exhibit ^{3}He/^{4}He higher than MORB, they only show moderately high ^{3}He/^{4}He (R_A up to 17; Jackson et al., 2020) compared to Lō'ihi lavas (White, 2010). As Réunion samples exhibit BSE-like $\delta^{53/52}$Cr values, this may tentatively suggest that the high-^{3}He^{4}He component is not anomalous in its $\delta^{53/52}$Cr composition and that low $\delta^{53/52}$Cr in transitional Lō'ihi lavas are indeed due to pyroxenitic components in the melt source. On the other hand, lower mantle phases may contain significant amounts of Cr^{2+} (Eeckhout et al., 2007; Kagi et al., 2013; Odake et al., 2008) possibly indicating a low $\delta^{53/52}$Cr reservoir in the lower mantle. The absence of He isotope data for, in particular, these samples preclude detailed investigations of the effect of the high-^{3}He/^{4}He lower mantle component on the Cr isotopic composition of OIBs. Recently, the combination of ^{3}He/^{4}He ratios and the short-lived ^{182}Hf-^{182}W isotope system (i.e., μ^{182}W) has been used extensively to constrain this lower mantle component and further investigations involving these isotope systems coupled with stable Cr and Fe isotopes may provide further clues to this debate (Jackson et al., 2020; Mundl et al., 2017; Mundl-Petermeier et al., 2020; Mundl-Petermeier et al., 2019; Rizo et al., 2019; Williams et al., 2021).

4.5.2.2.3 Constraints from French Polynesia Ocean island basalts from French Polynesia are known to be highly heterogeneous sampling a source with different components encompassing HIMU, EM2, EM1 and PREMA. The French Polynesian samples in this study have typical HIMU and EM2 signatures, whereas sample FP15GA7 from the EM1 related Gambier island chain plots close to the PREMA field in Sr-Nd-Pb isotope space (Figure 4.2). Sample FP2RU2 from Rurutu Island showing the typical Austral-PREMA isotopic signature was excluded based on its relatively low MgO contents.
In this study, two samples from Austral islands (i.e., Tubuai) show very variable

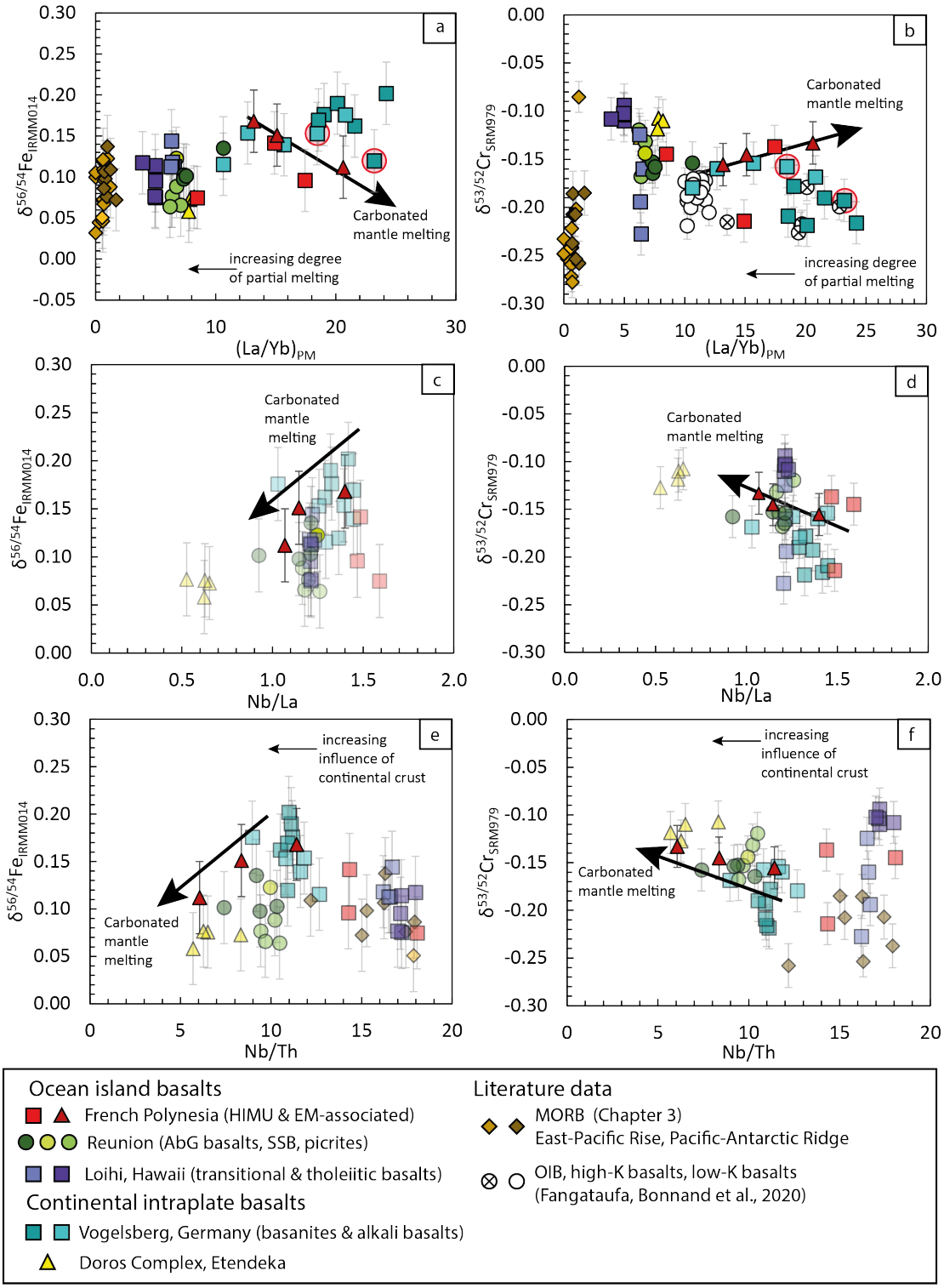

Figure 4.15: **a)** and **b)** Fe and Cr isotopic compositions vs. $(La/Yb)_{PM}$. Arrows indicate that with increasing degree of partial melting $(La/Yb)_{PM}$ decreases. Fe isotopic compositions are in general agreement with partial melting control, although variations are too large to be generated from a homogenous source. For Cr isotopes, MORBs are offset from the general trend towards BSE like values. Moreover EM2-associated basalts from French Polynesia show opposite trends associated with carbonated mantle melting. Open circles in b. represent basalts from Fangataufa by Bonnand et al. (2020). Normalizing values from Palme and O'Neill (2004); **c)** and **d)** Decreasing Nb/La ratios with decreasing Fe isotope and increasing Cr isotope compositions showing the effect of carbonated mantle melting of EM2 associated basalts in particular. **e)** and **f)** Fe and Cr isotopic compositions of Nb/Th as an indicator for crustal influence. We note that the incompatible element compositions of Doros samples need to be taken with caution as they represent intrusive rocks. All samples but EM2 related basalts are shown in transparent to highlight the observed trends.

Cr and Fe isotope compositions, which is in contrast with their homogeneous major, trace and radiogenic compositions showing typical HIMU characteristics (Figure 4.2, 4.4 and 4.6). The HIMU mantle component is commonly associated with ancient subducted oceanic crust based on the extremely high $^{206}Pb/^{204}Pb$ derived from an initially high amount of ^{238}U, which has evolved over >2 Ga (Chauvel et al., 1992; Dupuy et al., 1993; Hart, 1984; Hofmann and White, 1982). During subduction oceanic crust transforms into eclogite or pyroxenite, which may thus inherit the lower $\delta^{53/52}Cr$ and heavier $\delta^{56/54}Fe$ of MORB. In the case of HIMU samples in this study, relatively high CaO contents, low SiO_2 (not shown) and high CaO/Al_2O_3 ratios (Figure 4.4a) support the presence of a silica-deficient mafic (pyroxenitic) component in the source, which would be in agreement with previous studies (Chauvel et al., 1992; Jackson and Dasgupta, 2008; Jackson et al., 2012; Kogiso et al., 2003; Kogiso et al., 1997). However, only sample FP5TU1 ($^{206}Pb/^{204}Pb$ = 21.094; Figure 4.2) exhibits a $\delta^{53/52}Cr$ value significantly lower than the BSE range (-0.214 $\pm$ 0.040 ‰, 2SD; n=3, one digest) accompanied by a comparable high $\delta^{56/54}Fe$ value of +0.142 $\pm$ 0.026 ‰ (2SE; n=1; Figure 4.13). Together this may support a contribution of pyroxenite derived from recycled crust generating the low Cr and heavy Fe isotope compositions in this sample (Soderman et al., 2022). In contrast, HIMU sample FP8TU4 ($^{206}Pb/^{204}Pb$ = 21.080; Figure 4.2) displays comparable high $\delta^{53/52}Cr$ (-0.137 $\pm$ 0.022 ‰, 2SD; n=3, one digest) and lower $\delta^{56/54}Fe$ (+0.096 $\pm$ 0.027 ‰; 2SE, n=1). The BSE like $\delta^{53/52}Cr$ of this sample is not easily explained, but it is suggested to be due to local $\delta^{53/52}Cr$ heterogeneity of the source. This may be related to different formation mechanisms for the HIMU component. For example, the HIMU source of Tubuai Island has been inferred to be influenced by carbonated fluids (Hauri et al., 1993), which has been also suggested to have affected the source of the younger volcanic stage of Rurutu lavas (sample FP2RU2) (Chauvel et al., 1992). We note here that sample FP2RU2, which was initially not considered based on possible fractional crystallization effects, also displays a higher $\delta^{53/52}Cr$ than expected for PREMA associated basalts.

In general, the EM2 component has been attributed to a continental origin based on its high $^{87}Sr/^{86}Sr$ ratios, for example continental crust or continental crust derived sediments (Jackson et al., 2007; White, 2015). Additionally, the relatively high Pb isotopic compositions of EM2 basalts also indicate the contribution of oceanic crust, which together is commonly interpreted as subducted recycled oceanic crust with terrigenous sediments as the cause for the EM2 radiogenic isotopic signature (Weaver, 1991; Willbold and Stracke, 2006). Here, EM2 associated samples display relatively high SiO_2 and low FeO_{total} contents, in agreement with the contribution of a silica-excess eclogite (Jackson et al., 2012). This is further supported by relatively high Zr/Hf ratios indicating the presence of eclogite (Figure 4.14a, c; Pfänder et al., 2007). Moreover, EM2-type samples show typical low Ce/Pb, Nb/Th and Nb/Ba ratios indicating a recycled component of continental origin (Willbold and Stracke, 2006).

Interestingly, EM2 related basalts show increasing $\delta^{53/52}Cr$ and decreasing $\delta^{56/54}Fe$ with increasing $^{87}Sr/^{86}Sr$ (Figure 4.13a, c). The negative correlation between $\delta^{56/54}Fe$ and $^{87}Sr/^{86}Sr$ is in contrast with a recycled component present as pyroxenite or eclogite causing these variations (Nebel et al., 2019; Soderman et al., 2021; Williams and Bizimis, 2014). Moreover, the relatively high $\delta^{53/52}Cr$ for EM2 basalts suggest minor incorporation of MORB-like $\delta^{53/52}Cr$ values as they seem to converge towards the

$\delta^{53/52}$Cr BSE value (Figure 4.13). Although published $\delta^{53/52}$Cr analyses of highly differentiated high-Si rocks are scarce, $\delta^{53/52}$Cr values of -0.164 $\pm$0.037 ‰ (2SD, n=2; granite GS-N; Schoenberg et al., 2016; Schoenberg et al., 2008) and -0.14 $\pm$0.03 ‰ (2SE; 554 Ma tonalite; Berger and Frei, 2014) may be taken as representative values for $\delta^{53/52}$Cr of continental crust (Figure 4.1). Recycled continental crust, or thereof derived sediments, in the source of EM2 basalts would thus have a negligible effect due to the similarity of isotopic compositions when compared to the $\delta^{53/52}$Cr BSE value. Moreover, the Cr content of continental crust is low ($\sim$82 μg g^{-1}; Rudnick and Gao, 2014), thus suggesting a minor influence of continental material on the $\delta^{53/52}$Cr of basalts sampling EM2 components. It is noteworthy that BSE-like signatures of EM-like OIBs do not exclude eclogitic components derived from subducted sediments or continental crust in their source, but this signature may not surface in Cr isotopes based on mass balance considerations. To further understand the contribution of EM-like components in OIBs, a detailed study of $\delta^{53/52}$Cr of the continental crust is needed. The strong correlations of $\delta^{53/52}$Cr and $\delta^{56/54}$Fe with radiogenic isotope compositions suggest a source process controlling stable Cr and Fe isotopes. This is supported by very good correlations ($R^2 > 0.90$) of $\delta^{53/52}$Cr and $\delta^{56/54}$Fe with $(La/Yb)_{PM}$ (Figure 4.15a, b), Zr/Nb (not shown), Th/Nb (Figure 4.15e, f) and slightly less well correlations with Nb/La for these three samples ($R^2 > 0.75$; Figure 4.15c, d). Based on the typically low $\delta^{56/54}$Fe (-0.5 to 0 ‰) of carbonatite melts (Johnson et al., 2010), decreasing $\delta^{56/54}$Fe with increasing $^{87}Sr/^{86}Sr$ may indicate melting of a carbonated source generating the low $\delta^{56/54}$Fe and high $^{87}Sr/^{86}Sr$ for EM2 basalts. Melt source regions metasomatized by carbonated melts have been shown to have low Nb/La (Ionov et al., 1993). Positive correlations between Nb/La and $\delta^{56/54}$Fe, thus further support a carbonated source for EM2 related basalts (Figure 4.15c, d). We note however, that Nb/La ratios are not fractionated relative to other OIBs in this study. A carbonated peridotite source as the origin for EM2 related basalts has been highlighted recently by Adams et al. (2021) and evidence for carbonatite metasomatism for Tubuai in particular has been constrained from trace element analysis in xenoliths (Hauri et al., 1993). Moreover, high $\delta^{66/64}$Zn values detected in these samples (pers. comm. C. Rosca) are in agreement with carbonated peridotite melting in general (Beunon et al., 2020). So far, there have been no studies on the Cr isotope composition of carbonatite melts. However, Jerram et al. (2022) observed an increase in $\delta^{53/52}$Cr with increasing $(La/Yb)_N$ for mantle xenoliths that have been affected by carbonatite metasomatism, during which Cr isotopic fractionation is mostly driven by a chemical gradient between ambient peridotite and carbonatite melts. Hence, subsequent melting of these high $\delta^{53/52}$Cr mantle regions affected by carbonatite metasomatism would imprint its isotope composition and may thus lead to the observed relationships between $\delta^{53/52}$Cr and Nb/La and $(La/Yb)_{PM}$ (Figure 4.15).

4.6 Conclusions

In this study 45 OIBs and continental intraplate basalts from various locations encompassing a range of mantle components identified by radiogenic Sr-Nd-Pb isotope compositions were analyzed for $\delta^{53/52}$Cr and $\delta^{56/54}$Fe. Concluding remarks can be summarized as follows:

- The effect of fractional crystallization on stable Cr isotope fractionation is variable and calls for careful examination. For OIBs, large degrees of olivine + Cr-spinel accumulation may lead towards increasing $\delta^{53/52}$Cr with increasing MgO as seen for picrites from Piton de la Fournaise, La Réunion. Fractional crystallization of olivine and clinopyroxene, however, has no systematic effect on the $\delta^{53/52}$Cr, which is in contrast to $\delta^{56/54}$Fe values that follow trends as previously suggested. The greatest effect of magmatic differentiations can be seen for Doros intrusive rocks which show remarkable similar trends compared to the 3.5 Ga Barberton komatiite-tholeiite suite and the recently erupted Kilauea Iki lava lake suite. This tentatively suggest that neither temperature or pressure of melting, which are distinct in modern and Archean melting regimes, control stable Cr isotope fractionation.

- Despite filtering samples for possible effects of fractional crystallization the range of $\delta^{53/52}$Cr recorded in intraplate basalts remains too large to be caused by melting of a homogeneous garnet-bearing peridotite.

- Correlations between radiogenic Sr and Nd isotope compositions with $\delta^{53/52}$Cr suggest that Cr isotope composition of intraplate basalts are controlled by source compositions. Basalts representing HIMU- or PREMA-type mantle components, based on radiogenic isotope compositions, have on average lower $\delta^{53/52}$Cr compared to basalts sampling a source free of recycled material, namely Réunion displaying BSE-like $\delta^{53/52}$Cr values.

- The low $\delta^{53/52}$Cr of HIMU and/or PREMA-type OIBs is suggested to be derived from recycled oceanic crust present in the source of these samples and implies that the low $\delta^{53/52}$Cr signature of oceanic crust, which is recycled back into the mantle and sampled by deep-rooted plume derived melts, is preserved. If these source components are present as lithologically distinct components such as pyroxenite or eclogite in the mantle source of OIBs remains enigmatic. However, combined major element, trace element and radiogenic isotope compositions with stable Cr and Fe isotope compositions provide compelling evidence for pyroxenitic source components in the melt sources of Vogelsberg basanites and Lō'ihi transitional basalts. Moreover, there is strong evidence that the low $\delta^{53/52}$Cr of Vogelsberg basanites is due to melting of pyroxene-rich lithologies incorporated during melting of lithospheric mantle components previously modified by subduction zone processes.

- Using Cr isotope compositions of OIBs to trace continental components are limited based on mass balance considerations, and may be the cause for the convergence of EM related basalts from French Polynesia towards BSE-like values.

- EM2-type basalts from French Polynesia, known to have a continental derived source component, show strong trends between $\delta^{53/52}$Cr and incompatible trace element ratios such as Nb/La, Nb/Th and La/Yb and radiogenic Sr isotope compositions. Accompanied by strong correlations of decreasing $\delta^{56/54}$Fe with increasing radiogenic ^{87}Sr/^{86}Sr ratios, it is suggested that EM2 basalts sample a source metasomatized by carbonate melts. This is in agreement with the recently proposed effect of carbonatite metasomatism on $\delta^{53/52}$Cr, which is suggested to imprint a high $\delta^{53/52}$Cr onto the metasomatized peridotite. Thus,

it is proposed here that in the case of EM2 basalts from French Polynesia the strong correlations between $\delta^{53/52}$Cr and radiogenic $^{87}Sr/^{86}Sr$ are due to melting of a carbonated source imprinting its relatively high $\delta^{53/52}$Cr on the melt.

Acknowledgments

LJW acknowledges financial support from the German Research Council (DFG) project SCHO1071/9-1 to RS. Elmar Reitter and Bernd Steinhilber for general technical and analytical support. Analytical support from S. Staude and T. Wenzel for electron microprobe analysis at the University of Tuebingen are greatly appreciated. G. Wörner is thanked for providing samples from the Vogelsberg volcano and La Réunion. T. Owen-Smith is thanked for providing samples from the Doros Complex. O. Rouxel is thanked for sharing samples from Lō'ihi volcano and S. Koenig is thanked for providing samples from French Polynesia.

References

Abouchami, W., Hofmann, A., Galer, S., Frey, F., Eisele, J. and Feigenson, M. 2005. Lead isotopes reveal bilateral asymmetry and vertical continuity in the Hawaiian mantle plume. Nature. 434, 851-856.

Adam, J. and Green, T. 1994. The effects of pressure and temperature on the partitioning of Ti, Sr and REE between amphibole, clinopyroxene and basanitic melts. Chemical Geology. 117, 219-233.

Adams, J.V., Jackson, M.G., Spera, F.J., Price, A.A., Byerly, B.L., Seward, G. and Cottle, J.M. 2021. Extreme isotopic heterogeneity in Samoan clinopyroxenes constrains sediment recycling. Nature communications. 12, 1234.

Albarède, F., Luais, B., Fitton, G., Semet, M., Kaminski, E., Upton, B., Bachelery, P. and Cheminée, J.-L. 1997. The geochemical regimes of Piton de la Fournaise volcano (Réunion) during the last 530 000 years. Journal of Petrology. 38, 171-201.

Albut, G., Babechuk, M.G., Kleinhanns, I.C., Benger, M., Beukes, N.J., Steinhilber, B., Smith, A.J.B., Kruger, S.J. and Schoenberg, R. 2018. Modern rather than Mesoarchaean oxidative weathering responsible for the heavy stable Cr isotopic signatures of the 2.95 Ga old Ijzermijn iron formation (South Africa). Geochimica et Cosmochimica Acta. 228, 157-189.

Allègre, C.J. and Turcotte, D.L. 1986. Implications of a two-component marble-cake mantle. Nature. 323, 123-127.

Arevalo Jr, R. and McDonough, W.F. 2010. Chemical variations and regional diversity observed in MORB. Chemical Geology. 271, 70-85.

Babechuk, M.G., Weimar, N.E., Kleinhanns, I.C., Eroglu, S., Swanner, E.D., Kenny, G.G., Kamber, B.S. and Schoenberg, R. 2019. Pervasively anoxic surface conditions at the onset of the Great Oxidation Event: New multi-proxy constraints from the Cooper Lake paleosol. Precambrian Research. 323, 126-163.

Bai, Y., Su, B.X., Xiao, Y., Chen, C., Cui, M.M., He, X.Q., Qin, L.P. and Charlier, E.N.R. 2019. Diffusion-driven chromium isotope fractionation in ultramafic cumulate minerals: Elemental and isotopic evidence from the Stillwater Complex. Geochimica et Cosmochimica Acta. 263, 167-181.

Bartlett, R.J. and James, B. 1988. Mobility and bioavailability of chromium in soils, in: Nriagu J.O., Nieboer, E. (Eds.), Chromium in the natural and human environments. Wiley, New York, 20, pp. 267-304.

Beard, B.L. and Johnson, C.M. 2004. Inter-mineral Fe isotope variations in mantle-derived rocks and implications for the Fe geochemical cycle. Geochimica et Cosmochimica Acta. 68, 4727-4743.

Berger, A. and Frei, R. 2014. The fate of chromium during tropical weathering: A laterite profile from Central Madagascar. Geoderma. 213, 521-532.

Berry, A.J., Miller, L.A., O'Neill, H.S.C. and Foran, G.J. 2021a. The coordination of Cr^{2+} in silicate glasses and implications for mineral-melt fractionation of Cr isotopes. Chemical Geology. 586, 120483.

Berry, A.J. and O'Neill, H.S.C. 2004. A XANES determination of the oxidation state of chromium in silicate glasses. American Mineralogist. 89, 790-798.

Berry, A.J., O'Neill, H.S.C. and Foran, G.J. 2021b. The effects of temperature and pressure on the oxidation state of chromium in silicate melts. Contributions to Mineralogy and Petrology. 176, 14.

Berry, A.J., O'Neill, H.S.C., Scott, D.R., Foran, G.J. and Shelley, J.M.G. 2006. The effect of composition on Cr^{2+}/Cr^{3+} in silicate melts. American Mineralogist. 91, 1901-1908.

Beunon, H., Mattielli, N., Doucet, L.S., Moine, B. and Debret, B. 2020. Mantle heterogeneity through Zn systematics in oceanic basalts: Evidence for a deep carbon cycling. Earth-Science reviews. 205, 103174.

Bilenker, L.D., Simon, A.C., Reich, M., Lundstrom, C.C., Gajos, N., Bindeman, I., Barra, F. and Munizaga, R. 2016. Fe–O stable isotope pairs elucidate a high-temperature origin of Chilean iron oxide-apatite deposits. Geochimica et Cosmochimica Acta. 177, 94-104.

Bogaard, P. 2000. Temporal evolution of the Vogelsberg volcano, central Germany. Mantle sources, melting processes and magma differentiation, reconstructed from the 'Forschungsbohrung Vogelsberg 1996', Department of Geosciences. Georg August Universität Göttingen, Göttingen.

Bogaard, P. and Wörner, G. 2003. Petrogenesis of basanitic to tholeiitic volcanic rocks from the Miocene Vogelsberg, Central Germany. Journal of Petrology. 44, 569-602.

Boivin, P. and Bachèlery, P. 2009. Petrology of 1977 to 1998 eruptions of Piton de la Fournaise, La Réunion Island. Journal of Volcanology and Geothermal Research. 184, 109-125.

Bonnand, P., Bruand, E., Matzen, A.K., Jerram, M., Schiavi, F., Wood, B.J., Boyet, M. and Halliday, A.N. 2020a. Redox control on chromium isotope behaviour in

silicate melts in contact with magnesiochromite. Geochimica et Cosmochimica Acta. 288, 282-300.

Bonnand, P., Doucelance, R., Boyet, M., Bachelery, P., Bosq, C., Auclair, D. and Schiano, P. 2020b. The influence of igneous processes on the chromium isotopic compositions of Ocean Island basalts. Earth and Planetary Science Letters. 532, 116028.

Bonnand, P., Williams, H.M., Parkinson, I.J., Wood, B.J. and Halliday, A.N. 2016. Stable chromium isotopic composition of meteorites and metal-silicate experiments: Implications for fractionation during core formation. Earth and Planetary Science Letters. 435, 14-21.

Bosch, D., Blichert-Toft, J., Moynier, F., Nelson, B.K., Telouk, P., Gillot, P.-Y. and Albarède, F. 2008. Pb, Hf and Nd isotope compositions of the two Réunion volcanoes (Indian Ocean): a tale of two small-scale mantle "blobs"? Earth and Planetary Science Letters. 265, 748-765.

Botha, B. and Hodgson, F. 1976. Karoo dolerites in northwestern Damaraland. South African Journal of Geology. 79, 186-190.

Boudoire, G., Brugier, Y.-A., Di Muro, A., Wörner, G., Arienzo, I., Metrich, N., Zanon, V., Braukmüller, N., Kronz, A. and Le Moigne, Y. 2019. Eruptive activity on the western flank of Piton de la Fournaise (La Réunion Island, Indian Ocean): insights on magma transfer, storage and evolution at an oceanic volcanic island. Journal of Petrology. 60, 1717-1752.

Bouvier, A., Vervoort, J.D. and Patchett, P.J. 2008. The Lu–Hf and Sm–Nd isotopic composition of CHUR: constraints from unequilibrated chondrites and implications for the bulk composition of terrestrial planets. Earth and Planetary Science Letters. 273, 48-57.

Bragagni, A., Mastroianni, F., Münker, C., Conticelli, S. and Avanzinelli, R. 2022. A carbon-rich lithospheric mantle as a source for the large CO_2 emissions of Etna volcano (Italy). Geology. 50, 486-490.

Büchl, A., Münker, C., Mezger, K. and Hofmann, A. 2002. High-precision Nb/Ta and Zr/Hf ratios in global MORB, Geochimica et Cosmochimica Acta. 66 (15A), A108-A108.

Burns, R.G. 1975. Crystal field effects in chromium and its partitioning in the mantle. Geochimica et Cosmochimica Acta. 39, 857-864.

Caroff, M., Maury, R., Guille, G., Bellon, H. and Cotten, J. 1993. Les basaltes de l'Archipel des Gambier (Polynésie française). Comptes rendus de l'Académie des sciences. Série 2, Mécanique, Physique, Chimie, Sciences de l'univers, Sciences de la Terre. 317, 359-366.

Cebria, J. and Wilson, M. 1995. Cenozoic mafic magmatism in Western/Central Europe: a common European asthenospheric reservoir. Terra Nova. 7, 162.

Chauvel, C., Hofmann, A.W. and Vidal, P. 1992. HIMU-EM: the French Polynesian connection. Earth and Planetary Science Letters. 110, 99-119.

Chauvel, C., McDonough, W., Guille, G., Maury, R. and Duncan, R. 1997. Contrasting old and young volcanism in Rurutu Island, Austral chain. Chemical Geology. 139, 125-143.

Chen, L.-M., Song, X.-Y., Zhu, X.-K., Zhang, X.-Q., Yu, S.-Y. and Yi, J.-N. 2014. Iron isotope fractionation during crystallization and sub-solidus re-equilibration: Constraints from the Baima mafic layered intrusion, SW China. Chemical Geology. 380, 97-109.

Chen, S., Niu, Y.L., Guo, P.Y., Gong, H.M., Sun, P., Xue, Q.Q., Duan, M. and Wang, X.H. 2019. Iron isotope fractionation during mid-ocean ridge basalt (MORB) evolution: Evidence from lavas on the East Pacific Rise at 10° 30' N and its implications. Geochimica et Cosmochimica Acta. 267, 227-239.

Collerson, K.D., Kamber, B.S. and Schoenberg, R. 2002. Applications of accurate, high-precision Pb isotope ratio measurement by multi-collector ICP-MS. Chemical Geology. 188, 65-83.

Dauphas, N., Craddock, P.R., Asimow, P.D., Bennett, V.C., Nutman, A.P. and Ohnenstetter, D. 2009. Iron isotopes may reveal the redox conditions of mantle melting from Archean to Present. Earth and Planetary Science Letters. 288, 255-267.

DePaolo, D. and Wasserburg, G. 1976. Inferences about magma sources and mantle structure from variations of $^{143}Nd/^{144}Nd$. Geophysical Research Letters. 3, 743-746.

Desonie, D.L., Duncan, R.A. and Natland, J. 1993. Temporal and geochemical variability of volcanic products of the Marquesas hotspot. Journal of Geophysical Research: Solid Earth. 98, 17649-17665.

Dixon, J.E. and Clague, D.A. 2001. Volatiles in basaltic glasses from Loihi Seamount, Hawaii: Evidence for a relatively dry plume component. Journal of Petrology. 42, 627-654.

Downes, H. 2007. Origin and significance of spinel and garnet pyroxenites in the shallow lithospheric mantle: Ultramafic massifs in orogenic belts in Western Europe and NW Africa. Lithos. 99, 1-24.

Duncan, R., Backman, J., Peterson, L. and Party, T.S.S. 1989. Reunion hotspot activitity through tertiary time: Initial results from the ocean drilling program, leg 115. Journal of Volcanology and Geothermal Research. 36, 193-198.

Duncan, R.A. and McDougall, I. 1976. Linear volcanism in French polynesia. Journal of Volcanology and Geothermal Research. 1, 197-227. Dupré, B. and Allègre, C.J. 1983. Pb–Sr isotope variation in Indian Ocean basalts and mixing phenomena. Nature. 303, 142-146.

Dupuy, C., Vidal, P., Maury, R. and Guille, G. 1993. Basalts from Mururoa, Fangataufa and Gambier islands (French Polynesia): Geochemical dependence on the age of the lithosphere. Earth and Planetary Science Letters. 117, 89-100.

Eeckhout, S.G., Bolfan-Casanova, N., McCammon, C., Klemme, S. and Amiguet, E. 2007. XANES study of the oxidation state of Cr in lower mantle phases: Periclase and magnesium silicate perovskite. American Mineralogist. 92, 966-972.

Elderfield, H. 1970. Chromium speciation in sea water. Earth and Planetary Science Letters. 9, 10-16.

Fontaine, F.R., Barruol, G., Tkalčić, H., Wölbern, I., Rümpker, G., Bodin, T. and Haugmard, M. 2015. Crustal and uppermost mantle structure variation beneath La Réunion hotspot track. Geophysical Journal International. 203, 107-126.

Fourny, A., Weis, D. and Scoates, J.S. 2016. Comprehensive Pb-Sr-Nd-Hf isotopic, trace element, and mineralogical characterization of mafic to ultramafic rock reference materials. Geochemistry, Geophysics, Geosystems. 17, 739-773.

Fretzdorff, S. and Haase, K. 2002. Geochemistry and petrology of lavas from the submarine flanks of Réunion Island (western Indian Ocean): implications for magma genesis and the mantle source. Mineralogy and Petrology. 75, 153-184.

Frey, F.A. and Clague, D.A. 1983. Geochemistry of diverse basalt types from Loihi Seamount, Hawaii: petrogenetic implications. Earth and Planetary Science Letters. 66, 337-355.

Gale, A., Dalton, C.A., Langmuir, C.H., Su, Y.J. and Schilling, J.G. 2013. The mean composition of ocean ridge basalts. Geochemistry, Geophysics, Geosystems. 14, 489-518.

Garcia, M.O., Caplan-Auerbach, J., Eric, H., Kurz, M.D. and Becker, N. 2006. Geology, geochemistry and earthquake history of Lō'ihi Seamount, Hawai'i's youngest volcano. Geochemistry. 66, 81-108.

Garcia, M.O., Foss, D.J., West, H. and Mahoney, J.J. 1995. Geochemical and isotopic evolution of Loihi Volcano, Hawai'i. Journal of Petrology. 36, 1647-1674.

Garcia, M.O., Jorgenson, B.A., Mahoney, J.J., Ito, E. and Irving, A.J. 1993. An evaluation of temporal geochemical evolution of Loihi summit lavas: results from Alvin submersible dives. Journal of Geophysical Research: Solid Earth. 98, 537-550.

Garcia, M.O., Rubin, K.H., Norman, M.D., Rhodes, J.M., Graham, D.W., Muenow, D.W. and Spencer, K. 1998. Petrology and geochronology of basalt breccia from the 1996 earthquake swarm of Loihi seamount, Hawaii: magmatic history of its 1996 eruption. Bulletin of Volcanology. 59, 577-592.

Gleeson, M.L. and Gibson, S.A. 2019. Crustal controls on apparent mantle pyroxenite signals in ocean-island basalts. Geology. 47, 321-324.

Gleeson, M.L., Gibson, S.A. and Williams, H.M. 2020. Novel insights from Fe-isotopes into the lithological heterogeneity of Ocean Island Basalts and plume-influenced MORBs. Earth and Planetary Science Letters. 535, 116114.

Graham, D., Lupton, J., Albarède, F. and Condomines, M. 1990. Extreme temporal homogeneity of helium isotopes at Piton de la Fournaise, Réunion Island. Nature. 347, 545-548.

Halliday, A.N., Lee, D.-C., Tommasini, S., Davies, G.R., Paslick, C.R., Fitton, J.G. and James, D.E. 1995. Incompatible trace elements in OIB and MORB and source enrichment in the sub-oceanic mantle. Earth and Planetary Science Letters. 133, 379-395.

Hanyu, T., Dunai, T.J., Davies, G.R., Kaneoka, I., Nohda, S. and Uto, K. 2001. Noble gas study of the Reunion hotspot: evidence for distinct less-degassed mantle sources. Earth and Planetary Science Letters. 193, 83-98.

Hart, S.R. 1984. A large-scale isotope anomaly in the Southern Hemisphere mantle. Nature. 309, 753-757.

Hartmann, G. and Wedepohl, K.H. 1990. Metasomatically altered peridotite xenoliths from the Hessian Depression (Northwest Germany). Geochimica et Cosmochimica Acta. 54, 71-86.

Hauri, E.H. 1996. Major-element variability in the Hawaiian mantle plume. Nature. 382, 415-419.

Hauri, E.H., Shimizu, N., Dieu, J.J. and Hart, S.R. 1993. Evidence for hotspot-related carbonatite metasomatism in the oceanic upper mantle. Nature. 365, 221-227.

Hawkins, J. and Melchior, J. 1983. Petrology of basalts from Loihi seamount, Hawaii. Earth and Planetary Science Letters. 66, 356-368.

Herzberg, C. 2011. Identification of source lithology in the Hawaiian and Canary Islands: Implications for origins. Journal of Petrology. 52, 113-146.

Hofmann, A.W. 1997. Mantle geochemistry: the message from oceanic volcanism. Nature. 385, 219-229.

Hofmann, A.W. and White, W.M. 1982. Mantle plumes from ancient oceanic crust. Earth and Planetary Science Letters. 57, 421-436.

Ionov, D.A., Dupuy, C., O'Reilly, S.Y., Kopylova, M.G. and Genshaft, Y.S. 1993. Carbonated peridotite xenoliths from Spitsbergen: implications for trace element signature of mantle carbonate metasomatism. Earth and Planetary Science Letters. 119, 283-297.

Irvine, T.N. and Baragar, W.R.A. 1971. A guide to the chemical classification of the common volcanic rocks. Canadian journal of earth sciences. 8, 523-548.

Jackson, M.G., Blichert-Toft, J., Halldórsson, S.A., Mundl-Petermeier, A., Bizimis, M., Kurz, M.D., Price, A.A., Hartardóttir, S., Willhite, L.N. and Breddam, K. 2020. Ancient helium and tungsten isotopic signatures preserved in mantle domains least modified by crustal recycling. Proceedings of the National Academy of Sciences. 117, 30993-31001.

Jackson, M.G. and Dasgupta, R. 2008. Compositions of HIMU, EM1, and EM2 from global trends between radiogenic isotopes and major elements in ocean island basalts. Earth and Planetary Science Letters. 276, 175-186.

Jackson, M.G., Hart, S.R., Koppers, A.A., Staudigel, H., Konter, J., Blusztajn, J., Kurz, M. and Russell, J.A. 2007. The return of subducted continental crust in Samoan lavas. Nature. 448, 684-687.

Jackson, M.G., Weis, D. and Huang, S. 2012. Major element variations in Hawaiian shield lavas: Source features and perspectives from global ocean island basalt (OIB) systematics. Geochemistry, Geophysics, Geosystems. 13, Q09009.

Jerram, M., Bonnand, P., Harvey, J., Ionov, D. and Halliday, A.N. 2022. Stable chromium isotopic variations in peridotite mantle xenoliths: Metasomatism versus partial melting. Geochimica et Cosmochimica Acta. 317, 138-154.

Jerram, M., Bonnand, P., Kerr, A.C., Nisbet, E.G., Puchtel, I.S. and Halliday, A.N. 2020. The δ^{53}Cr isotope composition of komatiite flows and implications for the composition of the bulk silicate Earth. Chemical Geology. 551, 119761.

Johnson, C.M., Bell, K., Beard, B.L. and Shultis, A.I. 2010. Iron isotope compositions of carbonatites record melt generation, crystallization, and late-stage volatile-transport processes. Mineralogy and Petrology. 98, 91-110.

Jung, S., Pfänder, J., Brauns, M. and Maas, R. 2011. Crustal contamination and mantle source characteristics in continental intra-plate volcanic rocks: Pb, Hf and Os isotopes from central European volcanic province basalts. Geochimica et Cosmochimica Acta. 75, 2664-2683.

Jung, S., Vieten, K., Romer, R., Mezger, K., Hoernes, S. and Satir, M. 2012. Petrogenesis of Tertiary alkaline magmas in the Siebengebirge, Germany. Journal of Petrology. 53, 2381-2409.

Kagi, H., Odake, S., Ishibashi, H., Shozugawa, K., Matsuo, M., Satake, W. and Mikouchi, T. 2013. Oxygen fugacity and valence state of chromium in ferropericlase: Can Cr^{2+} be a redox indicator for the deep mantle? Journal of Mineralogical and Petrological Sciences. 108, 172-177.

Kang, J.-T., Ionov, D.A., Zhu, H.-L., Liu, F., Zhang, Z.-F., Liu, Z. and Huang, F. 2019. Calcium isotope sources and fractionation during melt-rock interaction in the lithospheric mantle: Evidence from pyroxenites, wehrlites, and eclogites. Chemical Geology. 524, 272-282.

Karner, J.M., Papike, J.J., Sutton, S.R., Shearer, C.K., McKay, G., Le, L. and Burger, P. 2007. Valence state partitioning of Cr between pyroxene-melt: Effects of pyroxene and melt composition and direct determination of Cr valence states by XANES. Application to Martian basalt QUE 94201 composition. American Mineralogist. 92, 2002-2005.

Klemme, S., Blundy, J.D. and Wood, B.J. 2002. Experimental constraints on major and trace element partitioning during partial melting of eclogite. Geochimica et Cosmochimica Acta. 66, 3109-3123.

Kogiso, T., Hirschmann, M.M. and Frost, D.J. 2003. High-pressure partial melting of garnet pyroxenite: possible mafic lithologies in the source of ocean island basalts. Earth and Planetary Science Letters. 216, 603-617.

Kogiso, T., Tatsumi, Y., Shimoda, G. and Barsczus, H.G. 1997. High μ (HIMU) ocean island basalts in southern Polynesia: new evidence for whole mantle scale recycling of subducted oceanic crust. Journal of Geophysical Research: Solid Earth. 102, 8085-8103.

Kolb, M., Paulick, H., Kirchenbaur, M. and Münker, C. 2012. Petrogenesis of mafic to felsic lavas from the Oligocene Siebengebirge volcanic field (Germany): implications for the origin of intracontinental volcanism in Central Europe. Journal of Petrology. 53, 2349-2379.

Konter, J.G., Pietruszka, A.J., Hanan, B.B., Finlayson, V.A., Craddock, P.R., Jackson, M.G. and Dauphas, N. 2016. Unusual δ^{56}Fe values in Samoan rejuvenated lavas generated in the mantle. Earth and Planetary Science Letters. 450, 221-232.

Kurz, M.D., Jenkins, W.J., Hart, S.R. and Clague, D. 1983. Helium isotopic variations in volcanic rocks from Loihi Seamount and the Island of Hawaii. Earth and Planetary Science Letters. 66, 388-406.

Kurzweil, F., Wille, M., Gantert, N., Beukes, N.J. and Schoenberg, R. 2016. Manganese oxide shuttling in pre-GOE oceans–evidence from molybdenum and iron isotopes. Earth and Planetary Science Letters. 452, 69-78.

Lambart, S., Baker, M.B. and Stolper, E.M. 2016. The role of pyroxenite in basalt genesis: Melt-PX, a melting parameterization for mantle pyroxenites between 0.9 and 5 GPa. Journal of Geophysical Research: Solid Earth. 121, 5708-5735.

Lassiter, J. and Hauri, E. 1998. Osmium-isotope variations in Hawaiian lavas: evidence for recycled oceanic lithosphere in the Hawaiian plume. Earth and Planetary Science Letters. 164, 483-496.

Le Bas, M.J., LE Maitre, R.W., Streckeisen, A. and Zanettin, B. 1986. A Chemical Classification of Volcanic Rocks Based on the Total Alkali-Silica Diagram. Journal of Petrology. 27, 745-750.

Leitzke, F.P., Fonseca, R.O., Michely, L.T., Sprung, P., Münker, C., Heuser, A. and Blanchard, H. 2016. The effect of titanium on the partitioning behavior of high-field strength elements between silicates, oxides and lunar basaltic melts with applications to the origin of mare basalts. Chemical Geology. 440, 219-238.

Lénat, J.-F., Bachèlery, P. and Merle, O. 2012. Anatomy of Piton de la Fournaise volcano (La Réunion, Indian Ocean). Bulletin of Volcanology. 74, 1945-1961.

Li, C.-F., Chen, F. and Li, X.-H. 2007. Precise isotopic measurements of subnanogram Nd of standard reference material by thermal ionization mass spectrometry using the NdO^+ technique. International Journal of Mass Spectrometry. 266, 34-41.

Liu, P.-P., Zhou, M.-F., Luais, B., Cividini, D. and Rollion-Bard, C. 2014. Disequilibrium iron isotopic fractionation during the high-temperature magmatic differentiation of the Baima Fe–Ti oxide-bearing mafic intrusion, SW China. Earth and Planetary Science Letters. 399, 21-29.

Lustrino, M. and Wilson, M. 2007. The circum-Mediterranean anorogenic Cenozoic igneous province. Earth-Science Reviews. 81, 1-65.

Ma, H., Xu, L.-J., Shen, J., Liu, S.-A. and Li, S. 2022. Chromium isotope fractionation during magmatic processes: Evidence from mid-ocean ridge basalts. Geochimica et Cosmochimica Acta. 327, 79-95.

MacDonald, G.A. and Katsura, T. 1964. Chemical Composition of Hawaiian Lavas. Journal of Petrology. 5, 82-133.

Mallmann, G. and O'Neill, H.S.C. 2009. The Crystal/Melt Partitioning of V during Mantle Melting as a Function of Oxygen Fugacity Compared with some other

Elements (Al, P, Ca, Sc, Ti, Cr, Fe, Ga, Y, Zr and Nb). Journal of Petrology. 50, 1765-1794.

Marsh, J., Duncan, A. and Miller, R. 2008. Doros gabbroic complex. The geology of Namibia. 3, 18-75.

McCoy-West, A.J., Fitton, J.G., Pons, M.L., Inglis, E.C. and Williams, H.M. 2018. The Fe and Zn isotope composition of deep mantle source regions: Insights from Baffin Island picrites. Geochimica et Cosmochimica Acta. 238, 542-562.

McDonough, W.F. and Sun, S.-S. 1995. The composition of the Earth. Chemical geology. 120, 223-253.

Michon, L., Ferrazzini, V., Di Muro, A., Villeneuve, N. and Famin, V. 2015. Rift zones and magma plumbing system of Piton de la Fournaise volcano: How do they differ from Hawaii and Etna? Journal of Volcanology and Geothermal Research. 303, 112-129.

Moore, J.G., Clague, D. and Normark, W. 1982. Diverse basalt types from Loihi seamount, Hawaii. Geology. 10, 88-92.

Moynier, F., Yin, Q.Z. and Schauble, E. 2011. Isotopic Evidence of Cr Partitioning into Earth's Core. Science. 331, 1417-1420.

Mundl, A., Touboul, M., Jackson, M.G., Day, J.M., Kurz, M.D., Lekic, V., Helz, R.T. and Walker, R.J. 2017. Tungsten-182 heterogeneity in modern ocean island basalts. Science. 356, 66-69.

Mundl-Petermeier, A., Walker, R., Fischer, R., Lekic, V., Jackson, M. and Kurz, M. 2020. Anomalous ^{182}W in high ^{3}He/^{4}He ocean island basalts: Fingerprints of Earth's core? Geochimica et Cosmochimica Acta. 271, 194-211.

Mundl-Petermeier, A., Walker, R., Jackson, M., Blichert-Toft, J., Kurz, M. and Halldórsson, S.A. 2019. Temporal evolution of primordial tungsten-182 and ^{3}He/^{4}He signatures in the Iceland mantle plume. Chemical Geology. 525, 245-259.

Münker, C., Pfänder, J.A., Weyer, S., Büchl, A., Kleine, T. and Mezger, K. 2003. Evolution of planetary cores and the Earth-Moon system from Nb/Ta systematics. Science. 301, 84-87.

Nebel, O., Sossi, P.A., Bénard, A., Arculus, R.J., Yaxley, G.M., Woodhead, J.D., Davies, D.R. and Ruttor, S. 2019. Reconciling petrological and isotopic mixing mechanisms in the Pitcairn mantle plume using stable Fe isotopes. Earth and Planetary Science Letters. 521, 60-67.

Norman, M.D. and Garcia, M.O. 1999. Primitive magmas and source characteristics of the Hawaiian plume: petrology and geochemistry of shield picrites. Earth and Planetary Science Letters. 168, 27-44.

O'Neill, H.S.C. and Berry, A.J. 2021. The oxidation state of chromium in basaltic silicate melts. Geochimica et Cosmochimica Acta. 306, 304-320.

Odake, S., Fukura, S., Arakawa, M., Ohta, A., Harte, B. and Kagi, H. 2008. Divalent chromium in ferropericlase inclusions in lower-mantle diamonds revealed by micro-XANES measurements. Journal of Mineralogical and Petrological Sciences. 103,

350-353.

Owen-Smith, T. and Ashwal, L. 2015a. Evidence for multiple pulses of crystal-bearing magma during emplacement of the Doros layered intrusion, Namibia. Lithos. 238, 120-139.

Owen-Smith, T. and Ashwal, L. 2015b. Geology of the early Cretaceous Doros layered mafic intrusion, Namibia: Complexity on a small scale. South African Journal of Geology. 118, 185-211.

Owen-Smith, T., Ashwal, L., Sudo, M. and Trumbull, R. 2017. Age and petrogenesis of the Doros Complex, Namibia, and implications for early plume-derived melts in the Paraná–Etendeka LIP. Journal of Petrology. 58, 423-442.

Palme, H. and O'Neill, H. 2014. Cosmochemical Estimates of Mantle Composition, in: Turekian, K., Holland, H. (Eds.), Treatise on Geochemistry, 2 ed. Elsevier, Amsterdam, pp. 1-39.

Papike, J.J., Karner, J.M. and Shearer, C.K. 2005. Comparative planetary mineralogy: Valence state partitioning of Cr, Fe, Ti, and V among crystallographic sites in olivine, pyroxene, and spinel from planetary basalts. American Mineralogist. 90, 277-290.

Papike, J.J., Simon, S.B., Burger, P.V., Bell, A.S., Shearer, C.K. and Karner, J.M. 2016. Chromium, vanadium, and titanium valence systematics in Solar System pyroxene as a recorder of oxygen fugacity, planetary provenance, and processes. American Mineralogist. 101, 907-918.

Peters, B.J., Carlson, R.W., Day, J. and Horan, M.F. 2018. Hadean silicate differentiation preserved by anomalous $^{142}Nd/^{144}Nd$ ratios in the Réunion hotspot source. Nature. 555, 89-93.

Peters, B.J., Shahar, A., Carlson, R.W., Day, J.M. and Mock, T.D. 2019. A sulfide perspective on iron isotope fractionation during ocean island basalt petrogenesis. Geochimica et Cosmochimica Acta. 245, 59-78.

Pfänder, J.A., Jung, S., Münker, C., Stracke, A. and Mezger, K. 2012. A possible high Nb/Ta reservoir in the continental lithospheric mantle and consequences on the global Nb budget–Evidence from continental basalts from Central Germany. Geochimica et Cosmochimica Acta. 77, 232-251.

Pfänder, J.A., Münker, C., Stracke, A. and Mezger, K. 2007. Nb/Ta and Zr/Hf in ocean island basalts - implications for crust-mantle differentiation and the fate of Niobium. Earth and Planetary Science Letters. 254, 158-172.

Pichavant, M., Brugier, Y. and Muro, A.D. 2016. Petrological and experimental constraints on the evolution of Piton de la Fournaise magmas, in: Bachelery, P., Lenat, J.F., Di Muro, A., Michon, L. (Eds.) Active Volcanoes of the Southwest Indian Ocean. Springer, Berlin, Heidelberg, pp. 171-184.

Pietruszka, A.J., Hauri, E.H. and Blichert-Toft, J. 2009. Crustal contamination of mantle-derived magmas within Piton de la Fournaise Volcano, Réunion Island. Journal of Petrology. 50, 661-684.

Pietruszka, A.J., Keyes, M.J., Duncan, J.A., Hauri, E.H., Carlson, R.W. and Garcia, M.O. 2011. Excesses of seawater-derived ^{234}U in volcanic glasses from Loihi Seamount due to crustal contamination. Earth and Planetary Science Letters. 304, 280-289.

Plank, T. 2014. The chemical composition of subducting sediments, in: Turekian, K., Holland, H. (Eds.), Treatise on Geochemistry, 2 ed. Elsevier, Amsterdam, pp. 607-629.

Polyakov, V., Clayton, R., Horita, J. and Mineev, S. 2007. Equilibrium iron isotope fractionation factors of minerals: reevaluation from the data of nuclear inelastic resonant X-ray scattering and Mössbauer spectroscopy. Geochimica et Cosmochimica Acta. 71, 3833-3846.

Polyakov, V.B. and Mineev, S.D. 2000. The use of Mössbauer spectroscopy in stable isotope geochemistry. Geochimica et Cosmochimica Acta. 64, 849-865.

Prytulak, J. and Elliott, T. 2007. TiO_2 enrichment in ocean island basalts. Earth and Planetary Science Letters. 263, 388-403.

Putirka, K., Ryerson, F., Perfit, M. and Ridley, W.I. 2011. Mineralogy and composition of the oceanic mantle. Journal of Petrology. 52, 279-313.

Raczek, I., Jochum, K.P. and Hofmann, A.W. 2003. Neodymium and strontium isotope data for USGS reference materials BCR-1, BCR-2, BHVO-1, BHVO-2, AGV-1, AGV-2, GSP-1, GSP-2 and eight MPI-DING reference glasses. Geostandards Newsletter. 27, 173-179.

Renne, P.R., Glen, J.M., Milner, S.C. and Duncan, A.R. 1996. Age of Etendeka flood volcanism and associated intrusions in southwestern Africa. Geology. 24, 659-662.

Richter, M., Nebel, O., Schwindinger, M., Nebel-Jacobsen, Y. and Dick, H.J.B. 2021. Competing effects of spreading rate, crystal fractionation and source variability on Fe isotope systematics in mid-ocean ridge lavas. Scientific Reports. 11, 4123.

Righter, K., Sutton, S., Danielson, L., Pando, K., Schmidt, G., Yang, H., Berthet, S., Newville, M., Choi, Y. and Downs, R.T. 2011. The effect of fO_2 on the partitioning and valence of V and Cr in garnet/melt pairs and the relation to terrestrial mantle V and Cr content. American Mineralogist. 96, 1278-1290.

Rizo, H., Andrault, D., Bennett, N., Humayun, M., Brandon, A., Vlastélic, I., Moine, B., Poirier, A., Bouhifd, M.A. and Murphy, D. 2019. ^{182}W evidence for core-mantle interaction in the source of mantle plumes. Geochemical Perspective Letters. 11, 6-11.

Rouxel, O., Toner, B., Germain, Y. and Glazer, B. 2018. Geochemical and iron isotopic insights into hydrothermal iron oxyhydroxide deposit formation at Loihi Seamount. Geochimica et Cosmochimica Acta. 220, 449-482.

Rudnick, R., Gao, S., 2014. Composition of the continental crust, in: Turekian, K.K., Holland, H.D. (Eds.), Treatise on Geochemistry, 2 ed. Elsevier, pp. 1-51.

Salaün, A., Villemant, B., Semet, M. and Staudacher, T. 2010. Cannibalism of olivine-rich cumulate xenoliths during the 1998 eruption of Piton de la Fournaise

(La Réunion hotspot): Implications for the generation of magma diversity. Journal of Volcanology and Geothermal Research. 198, 187-204.

Salters, V.J.M. and Stracke, A. 2004. Composition of the depleted mantle. Geochemistry, Geophysics, Geosystems. 5, Q05B07.

Schiller, M. 2019. Geochemical constraints on Sources of Ocean Island Basalts from French Polynesia, Department of Geosciences. University of Tübingen, Tübingen.

Schipper, C.I., White, J.D., Houghton, B.F., Shimizu, N. and Stewart, R.B. 2010. "Poseidic" explosive eruptions at Loihi seamount, Hawaii. Geology. 38, 291-294.

Schoenberg, R., Merdian, A., Holmden, C., Kleinhanns, I.C., Haßler, K., Wille, M. and Reitter, E. 2016. The stable Cr isotopic compositions of chondrites and silicate planetary reservoirs. Geochimica et Cosmochimica Acta. 183, 14-30.

Schoenberg, R., Zink, S., Staubwasser, M. and von Blanckenburg, F. 2008. The stable Cr isotope inventory of solid Earth reservoirs determined by double spike MC-ICP-MS. Chemical Geology. 249, 294-306.

Schuessler, J.A., Schoenberg, R. and Sigmarsson, O. 2009. Iron and lithium isotope systematics of the Hekla volcano, Iceland - Evidence for Fe isotope fractionation during magma differentiation. Chemical Geology. 258, 78-91.

Shahar, A., Young, E.D. and Manning, C.E. 2008. Equilibrium high-temperature Fe isotope fractionation between fayalite and magnetite: An experimental calibration. Earth and Planetary Science Letters. 268, 330-338.

Shen, J., Li, S.-G., Wang, S.-J., Teng, F.-Z., Li, Q.-L. and Liu, Y.-S. 2018a. Subducted Mg-rich carbonates into the deep mantle wedge. Earth and Planetary Science Letters. 503, 118-130.

Shen, J., Liu, J., Qin, L., Wang, S.J., Li, S., Xia, J., Ke, S. and Yang, J. 2015. Chromium isotope signature during continental crust subduction recorded in metamorphic rocks. Geochemistry, Geophysics, Geosystems. 16, 3840-3854.

Shen, J., Qin, L.P., Fang, Z.Y., Zhang, Y.N., Liu, J., Liu, W., Wang, F.Y., Xiao, Y., Yu, H.M. and Wei, S.Q. 2018b. High-temperature inter-mineral Cr isotope fractionation: A comparison of ionic model predictions and experimental investigations of mantle xenoliths from the North China Craton. Earth and Planetary Science Letters. 499, 278-290.

Shen, J., Xia, J.X., Qin, L.P., Carlson, R.W., Huang, S.C., Helz, R.T. and Mock, T.D. 2020. Stable chromium isotope fractionation during magmatic differentiation: Insights from Hawaiian basalts and implications for planetary redox conditions. Geochimica et Cosmochimica Acta. 278, 289-304.

Sobolev, A.V., Hofmann, A.W., Kuzmin, D.V., Yaxley, G.M., Arndt, N.T., Chung, S.-L., Danyushevsky, L.V., Elliott, T., Frey, F.A. and Garcia, M.O. 2007. The amount of recycled crust in sources of mantle-derived melts. Science. 316, 412-417.

Sobolev, A.V., Hofmann, A.W., Sobolev, S.V. and Nikogosian, I.K. 2005. An olivine-free mantle source of Hawaiian shield basalts. Nature. 434, 590-597.

Soderman, C.R., Matthews, S., Shorttle, O., Jackson, M.G., Ruttor, S., Nebel, O.,

Turner, S., Beier, C., Millet, M.A., Widom, E., Humayun, M. and Williams, H.M. 2021. Heavy δ^{57}Fe in ocean island basalts: A non-unique signature of processes and source lithologies in the mantle. Geochimica et Cosmochimica Acta. 292, 309-332.

Soderman, C.R., Shorttle, O., Matthews, S. and Williams, H.M. 2022. Global trends in novel stable isotopes in basalts: theory and observations. Geochimica et Cosmochimica Acta. 318, 388-414.

Sossi, P.A., Foden, J.D. and Halverson, G.P. 2012. Redox-controlled iron isotope fractionation during magmatic differentiation: an example from the Red Hill intrusion, S. Tasmania. Contributions to Mineralogy and Petrology. 164, 757-772.

Sossi, P.A. and O'Neill, H.S.C. 2017. The effect of bonding environment on iron isotope fractionation between minerals at high temperature. Geochimica et Cosmochimica Acta. 196, 121-143.

Staudigel, H., Park, K.-H., Pringle, M., Rubenstone, J., Smith, W. and Zindler, A. 1991. The longevity of the South Pacific isotopic and thermal anomaly. Earth and Planetary Science Letters. 102, 24-44.

Stracke, A. 2012. Earth's heterogeneous mantle: A product of convection-driven interaction between crust and mantle. Chemical geology. 330, 274-299.

Stracke, A., Hofmann, A.W. and Hart, S.R. 2005. FOZO, HIMU, and the rest of the mantle zoo. Geochemistry, Geophysics, Geosystems. 6, Q05007.

Stracke, A., Tipper, E., Klemme, S. and Bizimis, M. 2018. Mg isotope systematics during magmatic processes: Inter-mineral fractionation in mafic to ultramafic Hawaiian xenoliths. Geochimica et Cosmochimica Acta. 226, 192-205.

Sun, P., Niu, Y., Guo, P., Duan, M., Chen, S., Gong, H., Wang, X. and Xiao, Y. 2020. Large iron isotope variation in the eastern Pacific mantle as a consequence of ancient low-degree melt metasomatism. Geochimica et Cosmochimica Acta. 286, 269-288.

Teng, F.-Z., Dauphas, N., Helz, R.T., Gao, S. and Huang, S. 2011. Diffusion-driven magnesium and iron isotope fractionation in Hawaiian olivine. Earth and Planetary Science Letters. 308, 317-324.

Teng, F.Z., Dauphas, N. and Helz, R.T. 2008. Iron isotope fractionation during magmatic differentiation in Kilauea Iki Lava Lake. Science. 320, 1620-1622.

Teng, F.Z., Dauphas, N., Huang, S.C. and Marty, B. 2013. Iron isotopic systematics of oceanic basalts. Geochimica et Cosmochimica Acta. 107, 12-26.

Upton, B. and Wadsworth, W. 1966. The basalts of Reunion Island, Indian Ocean. Bulletin Volcanologique. 29, 7-23.

Valer, M., Schiano, P. and Bachèlery, P. 2017. Geochemical characteristics of the La Réunion mantle plume source inferred from olivine-hosted melt inclusions from the adventive cones of Piton de la Fournaise volcano (La Réunion Island). Contributions to Mineralogy and Petrology. 172, 1-20.

Villeneuve, N. and Bachèlery, P. 2006. Revue de la typologie des éruptions au Piton de La Fournaise, processus et risques volcaniques associés. Cybergeo: European

Journal of Geography. 336.

Vlastélic, I., Deniel, C., Bosq, C., Télouk, P., Boivin, P., Bachèlery, P., Famin, V. and Staudacher, T. 2009. Pb isotope geochemistry of Piton de la Fournaise historical lavas. Journal of Volcanology and Geothermal Research. 184, 63-78.

Vlastélic, I., Lewin, E. and Staudacher, T. 2006. Th/U and other geochemical evidence for the Reunion plume sampling a less differentiated mantle domain. Earth and Planetary Science Letters. 248, 379-393.

Wagner, L.J., Kleinhanns, I.C., Weber, N., Babechuk, M.G., Hofmann, A. and Schoenberg, R. 2021. Coupled stable chromium and iron isotopic fractionation tracing magmatic mineral crystallization in Archean komatiite-tholeiite suites. Chemical Geology. 576, 120121.

Wang, X.L., Planavsky, N.J., Reinhard, C.T., Zou, H.J., Ague, J.J., Wu, Y.B., Gill, B.C., Schwarzenbach, E.M. and Peucker-Ehrenbrink, B. 2016. Chromium isotope fractionation during subduction-related metamorphism, black shale weathering, and hydrothermal alteration. Chemical Geology. 423, 19-33.

Weaver, B.L. 1991. The origin of ocean island basalt end-member compositions: trace element and isotopic constraints. Earth and Planetary Science Letters. 104, 381-397.

Weis, D., Garcia, M.O., Rhodes, J.M., Jellinek, M. and Scoates, J.S. 2011. Role of the deep mantle in generating the compositional asymmetry of the Hawaiian mantle plume. Nature Geoscience. 4, 831-838.

Weis, D., Harrison, L.N., McMillan, R. and Williamson, N.M. 2020. Fine-Scale Structure of Earth's Deep Mantle Resolved Through Statistical Analysis of Hawaiian Basalt Geochemistry. Geochemistry, Geophysics, Geosystems. 21, e2020GC009292.

Weis, D., Kieffer, B., Maerschalk, C., Barling, J., De Jong, J., Williams, G.A., Hanano, D., Pretorius, W., Mattielli, N. and Scoates, J.S. 2006. High-precision isotopic characterization of USGS reference materials by TIMS and MC-ICP-MS. Geochemistry, Geophysics, Geosystems. 7.

Weyer, S. and Ionov, D.A. 2007. Partial melting and melt percolation in the mantle: The message from Fe isotopes. Earth and Planetary Science Letters. 259, 119-133.

White, W.M. 2010. Oceanic island basalts and mantle plumes: the geochemical perspective. Annual Review of Earth and Planetary Sciences. 38, 133-160.

White, W.M. 2015. Probing the Earth's deep interior through geochemistry. Geochemical Perspectives. 4. White, W.M., Albarède, F. and Télouk, P. 2000. High-precision analysis of Pb isotope ratios by multi-collector ICP-MS. Chemical Geology. 167, 257-270.

Willbold, M. and Stracke, A. 2006. Trace element composition of mantle end-members: Implications for recycling of oceanic and upper and lower continental crust. Geochemistry, Geophysics, Geosystems. 7.

Williams, H.M. and Bizimis, M. 2014. Iron isotope tracing of mantle heterogeneity within the source regions of oceanic basalts. Earth and Planetary Science Letters. 404, 396-407.

Williams, H.M., Matthews, S., Rizo, H. and Shorttle, O. 2021. Iron isotopes trace primordial magma ocean cumulates melting in Earth's upper mantle. Science Advances. 7, eabc7394.

Williams, H.M., Nielsen, S.G., Renac, C., Griffin, W.L., O'Reilly, S.Y., McCammon, C.A., Pearson, N., Viljoen, F., Alt, J.C. and Halliday, A.N. 2009. Fractionation of oxygen and iron isotopes by partial melting processes: implications for the interpretation of stable isotope signatures in mafic rocks. Earth and Planetary Science Letters. 283, 156-166.

Williams, H.M., Peslier, A.H., McCammon, C., Halliday, A.N., Levasseur, S., Teutsch, N. and Burg, J.-P. 2005. Systematic iron isotope variations in mantle rocks and minerals: the effects of partial melting and oxygen fugacity. Earth and Planetary Science Letters. 235, 435-452.

Wilson, M. and Downes, H. 1991. Tertiary—Quaternary extension-related alkaline magmatism in western and central Europe. Journal of Petrology. 32, 811-849. Woodhead, J.D. and Hergt, J.M. 2000. Pb-isotope analyses of USGS reference materials. Geostandards Newsletter. 24, 33-38.

Workman, R.K. and Hart, S.R. 2005. Major and trace element composition of the depleted MORB mantle (DMM). Earth and Planetary Science Letters. 231, 53-72.

Wörner, G., Zindler, A., Staudigel, H. and Schmincke, H.-U. 1986. Sr, Nd, and Pb isotope geochemistry of Tertiary and Quaternary alkaline volcanics from West Germany. Earth and Planetary Science Letters. 79, 107-119.

Wu, G., Zhu, J.-M., Tan, D., Han, G., Zhang, L. and Ren, K. 2017. Accurate and precise determination of lead isotope composition in selected geochemical reference materials. Acta Geochimica. 36, 421-425.

Xia, J.X., Qin, L.P., Shen, J., Carlson, R.W., Ionov, D.A. and Mock, T.D. 2017. Chromium isotope heterogeneity in the mantle. Earth and Planetary Science Letters. 464, 103-115.

Yi, W., Halliday, A.N., Alt, J.C., Lee, D.C., Rehkämper, M., Garcia, M.O., Langmuir, C. and Su, Y. 2000. Cadmium, indium, tin, tellurium, and sulfur in oceanic basalts: Implications for chalcophile element fractionation in the Earth. Journal of Geophysical Research: Solid Earth. 105, 18927-18948.

Young, E.D., Manning, C.E., Schauble, E.A., Shahar, A., Macris, C.A., Lazar, C. and Jordan, M. 2015. High-temperature equilibrium isotope fractionation of non-traditional stable isotopes: Experiments, theory, and applications. Chemical Geology. 395, 176-195.

Zhong, Y., Zhang, G.-L., Lv, W.-X. and Huang, F. 2021. Iron isotope constraints on the lithological heterogeneity of the upper mantle in the South China Sea. Journal of Asian Earth Sciences. 220, 104934.

Zindler, A. and Hart, S. 1986. Chemical geodynamics. Annual Review of Earth and Planetary sciences. 14, 493-571.

Chapter 5

Summary and Outlook

5.1 Summary

This thesis has shown that stable Cr isotopic compositions of basalts from different tectonic settings (MORB/OIB) show significant variability reflecting the influence of a combination of magmatic processes and source chemical and mineralogical compositions. The investigation of two komatiite-tholeiite suites from the 3.55 to 3.22 Ga Barberton Greenstone Belt (South Africa and Eswatini) and the 2.9 to 2.7 Ga Belingwe Greenstone Belt (Zimbabwe) highlighted the effect of fractional crystallization on Cr isotope systematics under terrestrial mantle conditions. Therein, the combination of Fe and Cr isotope systematics showed that the Cr-Fe isotope proxy provides valuable insights into magmatic differentiation by tracing the crystallizing phases olivine, Cr-spinel, and/or pyroxene. Moreover, based on the investigated komatiites, which represent large degree mantle melts of up to ∼30 %, the Cr isotopic composition of the BSE was determined to be -0.12 ± 0.06 ‰, identical to previous estimates and thus stressing its robustness.
To explore the impact of magmatic processes on the Cr isotopic compositions of modern basalts, mid-ocean ridge basalts were analyzed and found to be consistently lighter than the Cr isotope value of the BSE. The effect of fractional crystallization in typical MORB suites were found to be negligible, as no significant Cr isotopic variations over a large range of MgO contents from 4.52 to 9.00 wt. % could be identified. A theoretical partial melting model using thermodynamical constraints from the software MELTS combined with published mineral-melt fractionation factors constrained Cr isotopic fractionation during partial melting in a mid-ocean ridge setting to an upper estimate of ∼ 0.07 ‰. The considerably lower Cr isotopic composition of MORBs is attributed to a pyroxene-rich lithology in addition to peridotite in the MORB melt source, which is in accordance with the slightly heavier stable Fe isotopic composition of MORBs. This supported recent model approaches showing that Cr and Fe isotopes may be used as a tracer for source lithology.
To explore the influence of variable source compositions and possibly different source lithologies on stable Cr isotope compositions of basalts 45 intraplate basalts were studied. These samples include ocean island basalts and continental intraplate basalts encompassing variable sources of Earth's heterogeneous mantle inferred from radiogenic Sr-Nd-Pb isotopic compositions. A well-defined correlation between stable Cr and radiogenic Sr and Nd isotopic compositions reveal that stable Cr isotope

variability is most probably controlled by source compositions. Therein, basalts carrying a radiogenic isotope signature akin to prevalent mantle (PREMA) or high-μ (HIMU) show lower Cr isotopic compositions than the BSE value indicative of recycling of oceanic crust possibly present as pyroxenitic components. In accordance, basalts from La Réunion, representing a source with no influence of crustal recycling, show higher Cr isotopic compositions closer to the BSE value. Samples from French Polynesia representing an EM2-type mantle source, display positive and negative correlations of Sr isotope signatures with stable Cr and Fe isotopic compositions, respectively, thereby providing strong evidence that a carbonated mantle is contributing to EM2-type basalts.

5.2 Outlook

Considerable Cr isotope fractionation during magmatic differentiation has been shown for two komatiite-tholeiite suites in this study and for ocean island basalts in previous studies (Bonnand et al., 2020b; Shen et al., 2020). Yet, studies investigating Cr isotopic fractionation during fractional crystallization in highly evolved melts are scarce and published values encompass one granite (Schoenberg et al., 2016; Schoenberg et al., 2008) and one tonalite (Berger and Frei, 2014). Investigating highly differentiated high-Si rocks may provide additional constraints on Cr isotope fractionation during fractional crystallization involving variable mineral assemblages, which may include Cr-bearing phases such as rutile, amphibole, and Fe-Ti oxides, all of which are unexplored to date. A better understanding of the Cr isotopic composition of the continental crust will also aid the investigation of using Cr isotopes as a tracer for recycled more evolved components in the mantle.
Moreover, using Cr isotopes as a tracer for recycled components is based on the assumption that the Cr isotope signature of the recycled component is preserved during subduction-recycling back into the mantle. However, it needs to be evaluated whether processes such as dehydration, high-pressure metamorphism, and in some cases slab melting are associated with Cr isotope fractionation. A detailed study investigating a comprehensive island arc basalt suite may indirectly trace the effects of these processes on Cr isotopic compositions. An ideal suite for investigating subduction processes would be the Izu-Bonin fore-arc suite comprising fore-arc basalts followed stratigraphically by boninites. These two contrasting lithologies are closely related in space and time and allow for the evaluation of the effect of subduction components changing from slab melting to fluid fluxed melting on the Cr isotope compositions of these melts. Additionally, exploring fore-arc basalts and boninites from the Izu Bonin fore-arc may provide insights into the behavior of Cr isotopes during progressive melt depletion and thus be able to provide an alternative view on the contrasting results obtained so far from theoretical calculations (Jerram et al., 2022) vs. natural data (Xia et al., 2017). The effect of subduction zone processes on Cr isotopes may be elucidated by the combination of arc lavas with a well-studied suite of rocks representing the subducting slab, such as low temperature-high pressure metamorphic derivates of oceanic crust (i.e., blueschists and eclogites found in western Alps ophiolites or Syros Island, Greece).
Last but not least, the understanding of the extent and magnitude of Cr isotope fractionation during magmatic processes may be advanced substantially by experimental studies carried out under controlled temperature, pressure and fO_2 condi-

tions. So far, Cr isotope fractionation between silicate melt and metal (Bonnand et al., 2016b) and silicate melt and Cr-spinel (Bonnand et al. 2020) were investigated, but experimentally determined Cr isotope fractionation between silicate melt and other silicate minerals such as orthopyroxene, clinopyroxene, olivine, and garnet are not conducted yet. The derived isotope fractionation factors may further help to understand Cr isotope fractionation during partial melting and fractional crystallization. In the light of this study, the effect of pressure and composition on Cr isotopic fractionation during clinopyroxene fractionation would be of special interest. Moreover, as the available data on garnet-melt fractionation factors are limited, experiments involving garnet may give valuable insights into Cr isotope fractionation during melting of garnet-bearing vs. spinel-bearing peridotite, and by extension also of garnet-pyroxenite and eclogite melting.
Overall, each of these proposed topics have significant potential to contribute to the further understanding of stable Cr isotopic cycle of the deep Earth.

References

Berger, A., Frei, R., 2014. The fate of chromium during tropical weathering: A laterite profile from Central Madagascar. Geoderma 213, 521-532.

Bonnand, P., Doucelance, R., Boyet, M., Bachelery, P., Bosq, C., Auclair, D., Schiano, P., 2020. The influence of igneous processes on the chromium isotopic compositions of Ocean Island basalts. Earth and Planetary Science Letters 532, 116028.

Shen, J., Xia, J.X., Qin, L.P., Carlson, R.W., Huang, S.C., Helz, R.T., Mock, T.D., 2020. Stable chromium isotope fractionation during magmatic differentiation: Insights from Hawaiian basalts and implications for planetary redox conditions. Geochimica et Cosmochimica Acta 278, 289-304.

Schoenberg, R., Merdian, A., Holmden, C., Kleinhanns, I.C., Haßler, K., Wille, M., Reitter, E., 2016. The stable Cr isotopic compositions of chondrites and silicate planetary reservoirs. Geochimica et Cosmochimica Acta 183, 14-30.

Schoenberg, R., Zink, S., Staubwasser, M., von Blanckenburg, F., 2008. The stable Cr isotope inventory of solid Earth reservoirs determined by double spike MC-ICP-MS. Chemical Geology 249, 294-306.

Appendix A

Appendix Chapter 2
Coupled stable chromium and iron isotopic fractionation tracing magmatic mineral crystallization in Archean komatiite-tholeiite suites

A.1 Supplementary Figures and Tables

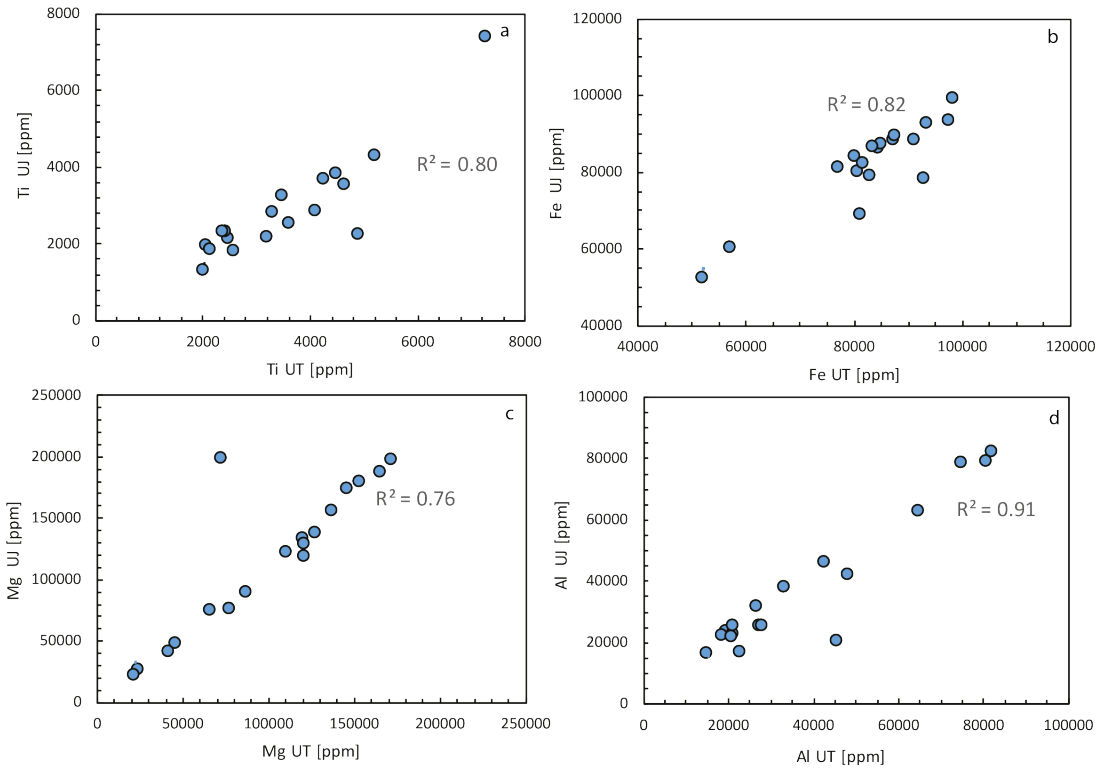

Figure A.1.1: Comparison of major element data derived from a portable x-ray fluorescence (pXRF) device at the University of Johannesburg (UJ; South Africa) and a instrumental wavelength dispersive Bruker AXS S4 Pioneer x-ray fluorescence (XRF) spectrometer at the University of Tuebingen (UT; Germany). Deviations of concentration data are inferred to be caused by the coarse-grained whole-rock surface when using pXRF, which is avoided when analyzing fused glass beads using the conventional XRF method at the University of Tuebingen.

Table A.1.1: Major element determinations carried out at the University Tuebingen (UT) compared with values obtained using a portable XRF (pXRF) at the University of Johannesburg (UJ).

Sample ID	60.70	66.70	109.22	221.64	229.40	240.66	242.47	255.50	261.02	262.00	269.65	290.65	315.55	315.91	342.57	345.29	360.23	372.13
	XRF University Tuebingen (UT)																	
wt. %																		
SiO_2	49.54	45.35	44.06	47.36	52.83	50.06	48.54	46.60	49.09	50.53	47.56	46.87	53.47	53.93	48.08	46.31	44.04	44.05
TiO_2	0.82	0.34	0.35	1.21	0.58	0.71	0.41	0.40	0.43	0.78	0.87	0.55	0.75	0.69	0.60	0.54	0.36	0.40
Al_2O_3	8.63	2.87	3.71	12.29	6.30	8.08	4.34	3.99	4.04	9.10	14.16	5.20	15.55	15.26	5.09	5.28	3.55	3.97
Fe_2O_3	13.27	11.01	11.59	14.06	11.54	13.96	11.85	12.06	12.16	13.35	11.46	12.49	8.17	7.44	12.51	13.03	11.68	11.94
MnO	0.23	0.17	0.19	0.24	0.24	0.23	0.23	0.21	0.21	0.21	0.20	0.24	0.19	0.20	0.22	0.23	0.20	0.21
MgO	12.07	22.79	25.40	7.59	14.42	12.85	21.18	24.18	19.96	11.03	6.96	20.09	4.02	3.65	18.35	20.08	28.53	27.46
CaO	8.16	10.63	5.65	10.79	9.23	9.17	9.09	6.17	9.50	8.82	7.37	8.74	4.49	5.14	9.45	8.32	2.85	4.00
Na_2O	2.86	0.10	0.30	3.15	2.69	2.61	0.25	0.19	0.38	3.51	5.45	0.50	7.66	7.80	0.80	0.40	0.27	0.35
K_2O	2.48	0.01	0.04	0.03	0.11	0.08	0.01	0.01	0.22	0.20	0.73	0.26	0.51	0.55	0.48	0.49	0.21	0.17
P_2O_5	0.07	0.03	0.04	0.09	0.06	0.07	0.04	0.03	0.04	0.06	0.10	0.05	0.32	0.30	0.06	0.05	0.03	0.03
	XRF University Tuebingen (UT) - recalculated to no oxides																	
$\mu g\, g^{-1}$																		
Si	231588	212002	205940	221360	246929	233991	226872	217808	229447	236188	222314	219084	249926	252076	224740	216480	205874	205912
Ti	4892	2020	2074	7272	3483	4257	2482	2416	2572	4652	5204	3303	4490	4107	3609	3207	2140	2374
Al	45690	15168	19641	65024	33359	42763	22969	21133	21361	48162	74937	27542	82304	80743	26928	27960	18773	21017
Fe	92801	76980	81064	98333	80722	97620	82862	84380	85044	93402	80162	87324	57172	52031	87464	91101	81708	83526
Mn	1460	1055	1207	1529	1523	1447	1441	1302	1340	1327	1270	1485	1207	1245	1397	1466	1283	1321
Mg	72792	137408	153177	45795	86976	77484	127711	145790	120354	66527	41995	121126	24242	22023	110657	121066	172040	165600
Ca	58341	75994	40402	77088	65931	65502	64931	44061	67925	63058	52681	62472	32083	36764	67539	59456	20362	28588
Na	21232	749	2233	23361	19919	19392	1832	1380	2812	26032	40453	3680	56819	57835	5942	2938	2025	2604
K	20579	100	357	224	872	623	75	100	1860	1652	6027	2175	4217	4533	3960	4093	1718	1395
P	319	148	161	406	240	301	170	144	153	275	436	205	1375	1292	253	196	127	140
	pXRF University of Johannesburg (UJ)																	
$\mu g\, g^{-1}$																		
Si	215054	222470	229908	236595	254777	232962	243703	239217	238853	244765	239779	213905	255930	248402	226184	228932	226725	215702
Ti	2238	1295	1953	7396	3254	3668	2116	2293	1805	3512	4274	2805	3829	2859	2514	2157	1843	2293
Al	20346	16259	23451	62775	37838	46092	16754	22675	25166	41876	78466	25267	81987	78954	31420	25258	22241	21914
Fe	78233	80999	68799	99157	79942	93304	78856	85975	87177	92424	83736	88166	60182	52243	89253	88367	81961	86536

Continued on next page

Table A.1.1 – *Continued from previous page*

Sample ID	60.70	66.70	109.22	221.64	229.40	240.66	242.47	255.50	261.02	262.00	269.65	290.65	315.55	315.91	342.57	345.29	360.23	372.13
Mn	1689	890	1170	1614	1539	1536	1458	1332	1333	1403	1312	1518	1093	1045	1605	1557	1313	1403
Mg	198386	155702	179606	48504	89788	76120	138201	174097	133819	75423	41748	118654	26921	22023	122153	128556	197953	187606
Ca	20613	69211	41029	78692	61564	62883	68542	41916	63677	70098	47690	57834	27351	34421	68434	64139	18141	27838
K	n.d.	n.d.	n.d.	n.d.	n.d.	n.d.	n.d.	n.d.	268	n.d.	3104	266	1616	1758	1529	1756	633	n.d.
P	n.d.	n.d.	n.d.	173	n.d.	n.d.	n.d.	n.d.	n.d.	n.d.	106	n.d.	1573	1052	n.d.	n.d.	n.d.	n.d.

Table A.1.2: Mean XRF abundance data (wt. %) and uncertainty (± r.s.d) of United States Geological Survey (USGS) rock powder reference material BHVO-2 measured at the University of Tuebingen (UT) over the course of this study and compared with recommended values.

	BHVO-2			
	UT		USGS	
wt. %		bias %		RSD %
SiO_2	49.47	0.9	49.9	0.6
TiO_2	2.82	3.2	2.73	0.04
Al_2O_3	13.43	0.5	13.5	0.2
Fe_2O_3	11.94	2.9	12.3	0.2
MnO	0.21			
MgO	7.45	3.0	7.23	0.12
CaO	11.29	1.0	11.4	0.2
Na_2O	2.28	2.5	2.22	0.08
K_2O	0.52	0.4	0.52	0.01
P_2O_5	0.27	1.5	0.27	0.02

Table A.1.3: FeO concentrations (wt. %) of single measurements along with mean FeO concentrations (wt. %) and uncertainties (± 1SD) of United States Geological Survey (USGS) rock powder reference material BIR-1a and International Association of Geoanalysts (IAG) reference material OKUM (= OPY-1) measured at the University of Tuebingen over the course of this study and compared with literature and recommended values.

Sample	**FeO [wt. %]**	**1SD**
BIR1-100-1	8.03	
BIR1-150-1	8.13	
BIR1-100-2	7.69	
BIR1-150-2	8.20	
BIR1-100-3	7.69	
BIR1-150-3	8.16	
BIR1-100-4	7.73	
BIR1-150-4	8.04	
BIR1-100-5	7.78	
BIR1-150-5	8.04	
Average	**7.95**	**± 0.20**
Literature[a]	**8.25**	**± 0.42**
OKUM-100-1	8.24	
OKUM-150-1	8.42	
OKUM-100-2	8.05	
OKUM-150-2	8.16	
OKUM-100-3	8.11	
OKUM-150-3	8.27	
Average	**8.21**	**± 0.13**
Certified[b]	**8.47**	**± 0.46**

[a]Value from Babechuk et al. 2019. Precambrian Research, 323.
[b]Value from Webb et al. 2007. GeoPT20. IAG Report.

Table A.1.4: Mean Q-ICP-MS abundance data (ng g^{-1}) and uncertainty (± r.s.d) for two United States Geological Survey (USGS) rock powder reference materials (BIR-1a, BHVO-2) measured at the University of Tuebingen over the course of this study and compared with literature, recommended and compiled values.

Standard	**BIR-1a**								**BHVO-2**						
Source		**University Tuebingen**		**Laurentian University**[a]			**GeoReM**[b]		**University Tuebingen**		**Laurentian University**[a]			**GeoReM**[b]	
	W2-A calibration values	**Average 5** [c] **7** [d]	**%RSD**	Value	%RSD	UT/LU	Value	UT/GeoReM	**Average 7** [c] **9** [d]	**%RSD**	Value	%RSD	UT/LU	Value	UT/GeoReM
Li	9158	3106	0.7	3136	1.2	0.99	3203	0.97	4482	0.9	4496	0.7	1.00	4500	1.00
Be	617.5	91	3.2	93.4	3.5	0.98	102	0.89	997	2.1	1004	3.5	0.99	1076	0.93
Sc	36074	43669	4.6	44500	1.4	0.98	43210	1.01	30030	13.9	32120	1.1	0.93	31830	0.94
Ti	6354611	5701875	1.0	5790000	1.2	0.98	5746000	0.99	16011000	1.4	16480000	1.1	0.97	16370000	0.98
V	261597	329225	2.9	322500	1.1	1.02	320600	1.03	325720	3.0	314800	1.2	1.03	318200	1.02
Cr	92791	404725	2.1	410600	1.8	0.99	392900	1.03	298240	2.2	299100	1.4	1.00	287200	1.04
Co	44526	53155	0.4	53330	1.1	1.00	52220	1.02	45176	0.8	45300	1.3	1.00	44890	1.01
Ni	69993	169050	0.8	171200	1.9	0.99	168900	1.00	117550	1.0	117900	1	1.00	119800	0.98
Cu	103000	117857	1.1	119500	1.7	0.99	120700	0.98	124790	0.8	125500	2.1	0.99	129300	0.97
Zn	77000	70029	1.9	70730	2.3	0.99	70400	0.99	101960	1.6	102400	3	1.00	103900	0.98
Ga	17424	15289	0.5	15430	1	0.99	15460	0.99	20987	0.8	21090	0.8	1.00	21370	0.98
Rb	19803	189	3.8	193.8	3	0.98	210	0.90	9149	0.7	9161	1	1.00	9261	0.99
Sr	194828	108075	0.4	109500	1	0.99	108600	1.00	395390	0.7	394900	1.1	1.00	394100	1.00
Y	20113	14593	0.5	14660	1.1	1.00	15600	0.94	24112	1.9	24300	0.7	0.99	25910	0.93
Zr	87866	14041	2.1	14600	2.3	0.96	14800	0.95	168230	1.6	169600	1.6	0.99	171200	0.98
Nb	7275	537	1.5	534.8	1.2	1.00	553	0.97	18434	0.9	18300	0.9	1.01	18100	1.02
Cd	77.0	62	5.6	65.17	7.5	0.95	77	0.81	119	4.7	115.2	5.7	1.04	152	0.79
Sn	1950	803	21.7	815.3	9	0.98	701	1.15	1956	2.2	1928	5.6	1.01	1776	1.10
Cs	888	5	7.3	5.054	4.9	0.98	6	0.77	96	1.6	96.67	1.7	0.99	99.6	0.96
Ba	169680	6459	0.9	6599	3.5	0.98	6750	0.96	130900	0.8	131300	0.7	1.00	130900	1.00
La	10521	597	0.7	604.3	1.2	0.99	627	0.95	15070	1.9	15190	0.7	0.99	15200	0.99
Ce	23216	1885	0.8	1900	1.4	0.99	1920	0.98	37510	1.6	37760	1	0.99	37530	1.00
Pr	3025	373	1.0	378.2	1.1	0.99	372	1.00	5337	1.5	5383	0.7	0.99	5339	1.00
Nd	12911	2369	0.9	2382	1.1	0.99	2397	0.99	24225	1.3	24360	0.6	0.99	24270	1.00

Continued on next page

Table A.1.4 – *Continued from previous page*

Standard		**BIR-1a**							**BHVO-2**						
Source		**University Tuebingen**		**Laurentian University[a]**			**GeoReM[b]**		**University Tuebingen**		**Laurentian University[a]**			**GeoReM[b]**	
	W2-A	**Average**	**%RSD**	Value	%RSD	UT/LU	Value	UT/GeoReM	**Average**	**%RSD**	Value	%RSD	UT/LU	Value	UT/GeoReM
Sm	3266	1090	1.3	1099	1.1	0.99	1113	0.98	6018	1.3	6059	0.6	0.99	6023	1.00
Eu	1094	520	0.9	524.6	0.8	0.99	520	1.00	2040	1.6	2050	0.6	1.00	2043	1.00
Tb	615	366	1.2	365.4	0.9	1.00	1809	0.20	933	1.3	934	0.7	1.00	6207.0	0.15
Gd	3708	1847	1.1	1874	1.1	0.99	362	5.10	6174	1.9	6210	0.7	0.99	939.2	6.57
Dy	3808	2525	1.1	2543	1.1	0.99	2544	0.99	5214	1.1	5228	0.7	1.00	5280	0.99
Ho	803	582	0.5	583.2	1	1.00	572	1.02	992	1.0	997.8	0.6	0.99	988.7	1.00
Er	2222	1715	1.8	1701	0.9	1.01	1680	1.02	2488	1.2	2502	0.6	0.99	2511	0.99
Tm	327	257	0.9	258.5	0.9	1.00	256	1.01	338	1.2	338.7	0.7	1.00	334.9	1.01
Yb	2058	1649	0.9	1663	0.9	0.99	1631	1.01	1969	1.2	1984	0.6	0.99	1994	0.99
Lu	301	246	0.4	248.2	1	0.99	248	0.99	272	1.3	273.9	0.7	0.99	275.4	0.99
Hf	2356	552	2.2	570.7	1.4	0.97	582	0.95	4278	1.3	4335	1.2	0.99	4470	0.96
Tl	94.0	1	10.8	1.251	7.5	1.13	2	0.67	20	4.2	19.33	1.1	1.06	22.4	0.91
Pb	7528	3202	9.2	3268	15	0.98	3037	1.05	1513	6.3	1530	11	0.99	1653	0.92
Th	2104	29	2.8	29.37	4	0.99	33	0.88	1179	4.5	1179	1.1	1.00	1224	0.96
U	505	10	2.4	10.09	2.1	1.04	11	0.99	429	1.4	420.5	1	1.02	412	1.04

[a] Values from Laurentian University (LU) determined on a Thermo XSeriesII; compiled from: Kamber (2009); Babechuk et al. (2010; 2015); Babechuk and Kamber (2011).
[b] Reference or information values from GeoReM as reported in Jochum et al. (2016).
[c]Number of digestions.
[d]Number of analyses.

Kamber, B.S. 2009. Geochemical fingerprinting: 40 years of analytical development and real world applications. Appl. Geochem. 24, 1074-1086.
Babechuk, M.G., Kamber, B.S., Greig, A., Canil, D. and Kodolanyi, J. 2010. The behaviour of tungsten during mantle melting revisited with implications for planetary differentiation time scales. Geochimica et Cosmochimica Acta 74, 1448-1470.
Babechuk, M.G., Widdowson, M., Murphy, M. and Kamber, B.S. 2015. A combined Y/Ho, high field strength element (HFSE) and Nd isotope perspective on basalt weathering, Deccan Traps, India. Chemical Geology. 396, 25-41.
Babechuk, M.G., Kamber, B.S. 2011. An estimate of 1.9 Ga mantle depletion using the high-field-strength elements and Nd–Pb isotopes of ocean floor basalts, Flin Flon Belt, Canada. Precambrian Research, 189, 114-139.
Jochum, K.P., Weis, U., Schwager, B., Wilson, S.A., Haug, G.H., Andreae, M.O. and Enzweiler, J. 2016. Reference Values following ISO guidelines for Frequently Requested Rock Reference Materials. Geostandards and Geoanalytical Research. 40, 333-350.

Table A.1.5: Stable Cr isotopic data for United States Geological Survey (USGS) rock reference material BHVO-2. Compilation of single runs from 22 measurement sessions over the course of four years. For each measurement session new BHVO-2 dilutions from partly new digests with indivdual sample : double spike mixes were prepared either by bomb (b) or table top digestion (tt).

session #	**digestion #**	**digestion method b = high-P bomb tt = low-P table top**	**run #**	**$\delta^{53/52}$Cr [‰]**	**2SE**	**data pooling**	**n=5**	**n=4**	**n=3**	**n=2**	**n=1**
							$\delta^{53/52}$Cr	**$\delta^{53/52}$Cr**	**$\delta^{53/52}$Cr**	**$\delta^{53/52}$Cr**	**$\delta^{53/52}$Cr**
						average	**-0.145**	**-0.144**	**-0.145**	**-0.145**	**-0.145**
						2 SD	**0.016**	**0.014**	**0.016**	**0.019**	**0.023**
						N	**18**	**22**	**30**	**45**	**90**
1	**1**	**b**	1	**-0.135**	0.013		-0.142	-0.144	-0.148	-0.146	-0.135
		b	2	**-0.156**	0.014						-0.156
		b	3	**-0.152**	0.014					-0.143	-0.152
2	**2**	**tt**	1	**-0.135**	0.011				-0.138		-0.135
		tt	2	**-0.135**	0.012			-0.140		-0.139	-0.135
		tt	3	**-0.144**	0.012		-0.145				-0.144
		tt	4	**-0.143**	0.011				-0.142	-0.141	-0.143
		tt	5	**-0.139**	0.012						-0.139
3	**2**	**tt**	1	**-0.146**	0.013			-0.159		-0.149	-0.146
		tt	2	**-0.152**	0.012				-0.164		-0.152
4	**3**	**b**	1	**-0.171**	0.017		-0.167			-0.169	-0.171
		b	2	**-0.168**	0.021						-0.168
		b	3	**-0.181**	0.019			-0.158	-0.165	-0.172	-0.181
		b	4	**-0.162**	0.021						-0.162
		b	5	**-0.152**	0.020					-0.144	-0.152
5	**4**	**b**	1	**-0.137**	0.012		-0.141		-0.140		-0.137
		b	2	**-0.135**	0.011			-0.142		-0.141	-0.135
		b	3	**-0.147**	0.013						-0.147
		b	4	**-0.144**	0.012				-0.140	-0.142	-0.144
		b	5	**-0.141**	0.011						-0.141
6	**5**	**b**	1	**-0.135**	0.017		-0.135	-0.136		-0.140	-0.135
		b	2	**-0.144**	0.017				-0.137		-0.144
		b	3	**-0.127**	0.018					-0.133	-0.127

Continued on next page

Table A.1.5 – *Continued from previous page*

session #	digestion #	digestion method b = high-P bomb t = low-P table top	run #	$\delta^{53/52}$Cr [‰]	2SE	data pooling	n=5	n=4	n=3	n=2	n=1
							$\delta^{53/52}$Cr	$\delta^{53/52}$Cr	$\delta^{53/52}$Cr	$\delta^{53/52}$Cr	$\delta^{53/52}$Cr
						average	**-0.145**	**-0.144**	**-0.145**	**-0.145**	**-0.145**
						2 SD	**0.016**	**0.014**	**0.016**	**0.019**	**0.023**
						N	**18**	**22**	**30**	**45**	**90**
		b	4	**-0.140**	0.016						-0.140
		b	5	**-0.128**	0.021			-0.149	-0.153	-0.140	-0.128
7	**5**	**b**	1	**-0.151**	0.019		-0.155				-0.151
		b	2	**-0.181**	0.023					-0.159	-0.181
8	**6**	**b**	1	**-0.138**	0.015				-0.148		-0.138
		b	2	**-0.153**	0.017			-0.148		-0.153	-0.153
		b	3	**-0.152**	0.018						-0.152
		b	4	**-0.136**	0.016		-0.138		-0.139	-0.144	-0.136
		b	5	**-0.152**	0.017						-0.152
9	**7**	**tt**	1	**-0.128**	0.013			-0.140		-0.130	-0.128
		tt	2	**-0.132**	0.012				-0.144		-0.132
		tt	3	**-0.142**	0.014					-0.151	-0.142
		tt	4	**-0.159**	0.012		-0.146				-0.159
		tt	5	**-0.147**	0.011			-0.142	-0.145	-0.148	-0.147
10	**7**	**tt**	1	**-0.149**	0.012						-0.149
		tt	2	**-0.140**	0.014					-0.137	-0.140
		tt	3	**-0.133**	0.014				-0.140		-0.133
		tt	4	**-0.144**	0.012		-0.140	-0.140		-0.143	-0.144
		tt	5	**-0.142**	0.011						-0.142
11	**7**	**tt**	1	**-0.150**	0.012				-0.138	-0.138	-0.150
12	**7**	**tt**	1	**-0.126**	0.010						-0.126
		tt	2	**-0.137**	0.013			-0.138		-0.137	-0.137
		tt	3	**-0.137**	0.010		-0.139		-0.139		-0.137
		tt	4	**-0.144**	0.012					-0.139	-0.144
		tt	5	**-0.134**	0.012						-0.134
13	**7**	**tt**	1	**-0.135**	0.012			-0.144	-0.143	-0.139	-0.135

Continued on next page

Table A.1.5 – *Continued from previous page*

session #	digestion #	digestion method b = high-P bomb t = low-P table top	run #	$\delta^{53/52}$Cr [‰]	2SE	data pooling	n=5	n=4	n=3	n=2	n=1
							$\delta^{53/52}$Cr	$\delta^{53/52}$Cr	$\delta^{53/52}$Cr	$\delta^{53/52}$Cr	$\delta^{53/52}$Cr
						average	**-0.145**	**-0.144**	**-0.145**	**-0.145**	**-0.145**
						2 SD	**0.016**	**0.014**	**0.016**	**0.019**	**0.023**
						N	**18**	**22**	**30**	**45**	**90**
		tt	2	**-0.142**	0.011						-0.142
		tt	3	**-0.152**	0.011		-0.147			-0.150	-0.152
		tt	4	**-0.147**	0.013				-0.143		-0.147
		tt	5	**-0.136**	0.012			-0.141		-0.141	-0.136
14	**8**	**tt**	1	**-0.146**	0.011						-0.146
		tt	2	**-0.152**	0.011				-0.138	-0.142	-0.152
		tt	3	**-0.131**	0.012		-0.138				-0.131
		tt	4	**-0.130**	0.013			-0.140		-0.132	-0.130
		tt	5	**-0.134**	0.013				-0.144		-0.134
15	**8**	**tt**	1	**-0.147**	0.014					-0.149	-0.147
		tt	2	**-0.151**	0.015						-0.151
		tt	3	**-0.152**	0.013		-0.142	-0.145	-0.148	-0.156	-0.152
		tt	4	**-0.161**	0.014						-0.161
		tt	5	**-0.130**	0.014					-0.134	-0.130
16	**8**	**tt**	1	**-0.138**	0.011				-0.130		-0.138
		tt	2	**-0.129**	0.012			-0.137		-0.127	-0.129
		tt	3	**-0.124**	0.012		-0.139				-0.124
		tt	4	**-0.148**	0.011				-0.143	-0.148	-0.148
		tt	5	**-0.149**	0.012						-0.149
17	**8**	**tt**	1	**-0.131**	0.013			-0.136		-0.136	-0.131
		tt	2	**-0.141**	0.011				-0.137		-0.141
		tt	3	**-0.124**	0.011		-0.139			-0.135	-0.124
		tt	4	**-0.145**	0.012						-0.145
		tt	5	**-0.133**	0.012			-0.144	-0.142	-0.139	-0.133
18	**8**	**tt**	1	**-0.144**	0.014						-0.144
		tt	2	**-0.150**	0.015					-0.149	-0.150

Continued on next page

Table A.1.5 – *Continued from previous page*

session #	digestion #	digestion method b = high-P bomb t = low-P table top	run #	$\delta^{53/52}$Cr [‰]	2SE	data pooling	n=5	n=4	n=3	n=2	n=1
							$\delta^{53/52}$Cr	$\delta^{53/52}$Cr	$\delta^{53/52}$Cr	$\delta^{53/52}$Cr	$\delta^{53/52}$Cr
						average	**-0.145**	**-0.144**	**-0.145**	**-0.145**	**-0.145**
						2 SD	**0.016**	**0.014**	**0.016**	**0.019**	**0.023**
						N	**18**	**22**	**30**	**45**	**90**
		tt	3	**-0.148**	0.013		-0.149		-0.148		-0.148
		tt	4	**-0.156**	0.012			-0.149		-0.147	-0.156
		tt	5	**-0.139**	0.014						-0.139
19	**9**	**b**	1	**-0.149**	0.013				-0.154	-0.150	-0.149
20	**10**	**b**	1	**-0.152**	0.011						-0.152
		b	2	**-0.162**	0.012		-0.158	-0.159		-0.162	-0.162
		b	3	**-0.162**	0.011				-0.158		-0.162
		b	4	**-0.148**	0.011					-0.156	-0.148
		b	5	**-0.164**	0.013						-0.164
21	**10**	**b**	1	**-0.153**	0.011			-0.144	-0.143	-0.147	-0.153
		b	2	**-0.142**	0.013		-0.145				-0.142
		b	3	**-0.135**	0.013					-0.142	-0.135
		b	4	**-0.148**	0.012				-0.150		-0.148
		b	5	**-0.145**	0.014					-0.151	-0.145
22	**10**	**b**	1	**-0.157**	0.011						-0.157

Table A.1.6: Stable Fe isotopic data for in-house standard solution Tueb-Fe. Compilation of single runs from 10 measurement sessions over the course of five years. For each measurement session new Tueb-Fe dilutions with individual sample : double spike mixes were prepared.

session #	**run #**	**$\delta^{56/54}$Fe [‰]**	**2SE**	**data pooling**	**n=5**	**n=4**	**n=3**	**n=2**	**n=1**
					$\delta^{56/54}$Fe	**$\delta^{56/54}$Fe**	**$\delta^{56/54}$Fe**	**$\delta^{56/54}$Fe**	**$\delta^{56/54}$Fe**
				average	**-0.377**	**-0.377**	**-0.377**	**-0.377**	**-0.377**
				2 SD	**0.018**	**0.018**	**0.025**	**0.025**	**0.041**
				N	**13**	**16**	**22**	**33**	**67**
1	1	**-0.353**	0.032		-0.364	-0.373	-0.382	-0.382	-0.353
	2	**-0.410**	0.031						-0.410
2	1	**-0.384**	0.026					-0.364	-0.384
	2	**-0.343**	0.028				-0.354		-0.343
	3	**-0.328**	0.028			-0.357		-0.359	-0.328
3	1	**-0.390**	0.034		-0.371				-0.390
	2	**-0.403**	0.031				-0.353	-0.355	-0.403
	3	**-0.308**	0.032						-0.308
	4	**-0.349**	0.019			-0.375		-0.377	-0.349
	5	**-0.406**	0.020				-0.384		-0.406
4	1	**-0.372**	0.019		-0.372			-0.373	-0.372
	2	**-0.374**	0.019						-0.374
5	1	**-0.390**	0.023			-0.379	-0.372	-0.376	-0.390
	2	**-0.362**	0.018						-0.362
	3	**-0.363**	0.021					-0.382	-0.363
6	1	**-0.400**	0.019		-0.379		-0.388		-0.400
	2	**-0.389**	0.018			-0.374		-0.382	-0.389
	3	**-0.375**	0.021						-0.375
7	1	**-0.363**	0.023				-0.379	-0.366	-0.363
	2	**-0.369**	0.025						-0.369
	3	**-0.405**	0.027		-0.383	-0.380		-0.384	-0.405
8	1	**-0.364**	0.019				-0.372		-0.364
9	1	**-0.368**	0.023					-0.376	-0.368
10	1	**-0.384**	0.022						-0.384

Continued on next page

Table A.1.6 – *Continued from previous page*

session #	run #	$\delta^{56/54}$Fe [‰]	2SE	data pooling	n=5	n=4	n=3	n=2	n=1
					$\delta^{56/54}$Fe	$\delta^{56/54}$Fe	$\delta^{56/54}$Fe	$\delta^{56/54}$Fe	$\delta^{56/54}$Fe
				average	**-0.377**	**-0.377**	**-0.377**	**-0.377**	**-0.377**
				2 SD	**0.018**	**0.018**	**0.025**	**0.025**	**0.041**
				N	**13**	**16**	**22**	**33**	**67**
	2	**-0.392**	0.023			-0.388	-0.381	-0.374	-0.392
11	1	**-0.356**	0.026		-0.381				-0.356
	2	**-0.394**	0.025					-0.403	-0.394
12	1	**-0.411**	0.021				-0.384		-0.411
13	1	**-0.373**	0.015			-0.367		-0.370	-0.373
14	1	**-0.368**	0.015						-0.368
	2	**-0.361**	0.016		-0.368		-0.372	-0.364	-0.361
15	1	**-0.367**	0.020						-0.367
16	1	**-0.389**	0.016			-0.373		-0.378	-0.389
	2	**-0.366**	0.021				-0.368		-0.366
	3	**-0.356**	0.022					-0.369	-0.356
	4	**-0.381**	0.021		-0.375				-0.381
	5	**-0.381**	0.018			-0.373	-0.379	-0.385	-0.381
17	1	**-0.389**	0.016						-0.389
	2	**-0.366**	0.021					-0.361	-0.366
	3	**-0.356**	0.022				-0.373		-0.356
	4	**-0.381**	0.021		-0.387	-0.384		-0.381	-0.381
	5	**-0.381**	0.018						-0.381
18	1	**-0.391**	0.023				-0.391	-0.386	-0.391
19	1	**-0.381**	0.018						-0.381
	2	**-0.401**	0.019			-0.382		-0.390	-0.401
20	1	**-0.380**	0.013		-0.379		-0.375		-0.380
	2	**-0.378**	0.016					-0.373	-0.378
21	1	**-0.368**	0.013						-0.368
	2	**-0.380**	0.012			-0.391	-0.387	-0.384	-0.380
	3	**-0.387**	0.015						-0.387
	4	**-0.394**	0.015		-0.384			-0.399	-0.394

Continued on next page

Table A.1.6 – *Continued from previous page*

session #	run #	$\delta^{56/54}$Fe [‰]	2SE	data pooling	n=5	n=4	n=3	n=2	n=1
					$\delta^{56/54}$Fe	$\delta^{56/54}$Fe	$\delta^{56/54}$Fe	$\delta^{56/54}$Fe	$\delta^{56/54}$Fe
				average	**-0.377**	**-0.377**	**-0.377**	**-0.377**	**-0.377**
				2 SD	**0.018**	**0.018**	**0.025**	**0.025**	**0.041**
				N	**13**	**16**	**22**	**33**	**67**
	5	**-0.404**	0.013				-0.383		-0.404
22	1	**-0.375**	0.022			-0.385		-0.373	-0.375
	2	**-0.370**	0.019						-0.370
	3	**-0.378**	0.018				-0.409	-0.398	-0.378
	4	**-0.418**	0.017		-0.393				-0.418
	5	**-0.432**	0.021			-0.387		-0.404	-0.432
23	1	**-0.377**	0.023				-0.372		-0.377
	2	**-0.384**	0.019					-0.370	-0.384
24	1	**-0.356**	0.021						-0.356
	2	**-0.356**	0.018		-0.364	-0.367	-0.369	-0.369	-0.356
25	1	**-0.382**	0.025						-0.382
	2	**-0.369**	0.023					-0.366	-0.369
	3	**-0.363**	0.023				-0.361		-0.363
26	1	**-0.352**	0.019					-0.361	-0.352
27	1	**-0.370**	0.024						-0.370
	2	**-0.371**	0.024						-0.371

Appendix B

Appendix Chapter 3
Consistently light stable chromium isotopic compositions in mid-ocean ridge basalts: Implications for the mantle source composition

B.1 Methods

Major and trace elements as well as radiogenic Sr and Nd compositions for sample 267ROV-5 from the Mid-Atlantic Ridge (MAR) were analyzed at the Isotope Geochemistry laboratories of the University of Tuebingen and were determined as described below (Section B.1.1 and B.1.2). All samples in this study were analyzed for their Cr and Fe isotopic compositions and information about analytical precision and reproducibility are given in Section B.1.3.

B.1.1 Major elements

An aliquot of 1.5 g of powdered sample was mixed with 7.5 g of Merck Spectromelt A12, melted at 1200° C and quenched to a glass bead. Analyses were performed with a wavelength dispersive Bruker AXS S4 Pioneer XRF spectrometer (Rh-tube at 4kW) with 32 standardized samples at the University of Tuebingen. Matrix effects were corrected using the standard Spectra software provided by Bruker AXS. To complement the determination of major constituents, loss on ignition (LOI) was determined on a separate aliquot of 1 g that was heated to 1000° C for 1 hour.

B.1.2 Trace elements and radiogenic Sr and Nd isotopes

For determination of trace element and radiogenic Sr and Nd isotope compositions, 30 mg of sample powder were mixed with 2 ml HF (∼27 M) and 0.4 ml HNO_3 (∼14.5 M) and heated in closed Savillex vials to 120° C on a hotplate for four days. Following evaporation, the sample was re-dissolved in 2 mL 6 M HCl and heated to 120° C for one day to ensure complete destruction of fluorides. Subsequent evaporation of the sample solution was followed by the removal of any excess Cl^- by repeated evaporation to incipient dryness with HNO_3 (65 %). The sample residue was re-dissolved in 1 mL 5 M HNO_3 and a stock solution (2 % HNO_3) with a nominal

dilution factor of ∼1000 was created gravimetrically.

B.1.2.1 Trace elements

Determination of trace element concentration is based on a method originally described by Eggins et al. (1997) and incorporating subsequent modifications (Albut et al., 2018; Babechuk et al., 2010; Kamber et al., 2005), with measurement via solution quadrupole ICP-MS (S-Q-ICP-MS) on a ThermoFisher Scientific iCAP-Qc. This study followed the most recent method adaptation by Wagner et al. (2021) and is described in detail by Albut et al. (2018). In brief, prepared stock solutions (Section B.1.2) were further diluted to a nominal, gravimetric dilution factor of 10000 to 15000, yielding a final 2 % HNO_3 solution ready for measurement. To account for sensitivity and instrumental drift, an internal standard carrying ^{6}Li, In, Re and Bi was added to procedural blanks, calibration standards, quality control reference materials, sample unknowns and external drift monitor samples. Drift-corrected instrument intensities were further corrected for procedural and instrumental background and analytical interferences (e.g., polyatomic and doubly charged species) as described elsewhere (e.g., Ulrich et al., 2010). External calibration was carried out using the averaged intensities at three different dilution factors of the natural USGS reference material W-2a. A combination of independent USGS reference materials AGV-2, BIR-1a and BHVO-2 were measured to provide a monitor of method precision and accuracy. Mean trace element concentrations for reference material BIR-1a and BHVO-2, which underwent the same geochemical procedure as sample 267ROV-5, agree well with previous studies applying the same method (i.e., better than 5 %), and the 1 r.s.d suggest a full method precision better than 5 %. Primitive mantle (PM) normalized rare earth element (REE) pattern of sample 267ROV-5 are shown in Figure B.1.1 (normalizing values from Palme and O'Neill, 2014) and compared to already published REE abundances of EPR and PAR samples used in this study (Bach et al., 1994; Yierpan et al., 2019) as well as to average REE abundances of normal mid-ocean ridge basalt (N-MORB), depleted MORB and enriched MORB (Gale et al., 2013).

B.1.2.2 Radiogenic Sr and Nd isotopes

Sample 267ROV-5 was analyzed for its Sr and Nd isotope composition via ion-exchange chromatography and TIMS (FinniganMAT 262). An adequate aliquot was taken from the prepared stock solution (Section B.1.2) and converted to chloride form and subsequently dissolved in 1 ml of 2.5 M HCl. In brief, Sr and light rare earth elements were separated using BioRad cation exchange resin AG 50W-X8 and subsequent Sr purification was carried out using Eichrom Sr spec resin. Purification of Nd was achieved by using Eichrom Ln resin. Total procedural blanks were < 55 pg for Sr and < 8 pg for Nd.
Sr separates were loaded on a Re single filaments and isotope ratio measurements were performed in automatic dynamic mode. A $^{88}Sr/^{86}Sr$ ratio of 8.375209 and exponential law were used to correct for mass fractionation. Repeated measurement of NBS SRM 987 yielded an $^{87}Sr/^{86}Sr$ of 0.710265 $\pm$ 0.000018 (2SD; n=6), which is in good agreement with the long-term reproducibility of 0.710251 $\pm$ 0.000019 (2SD;

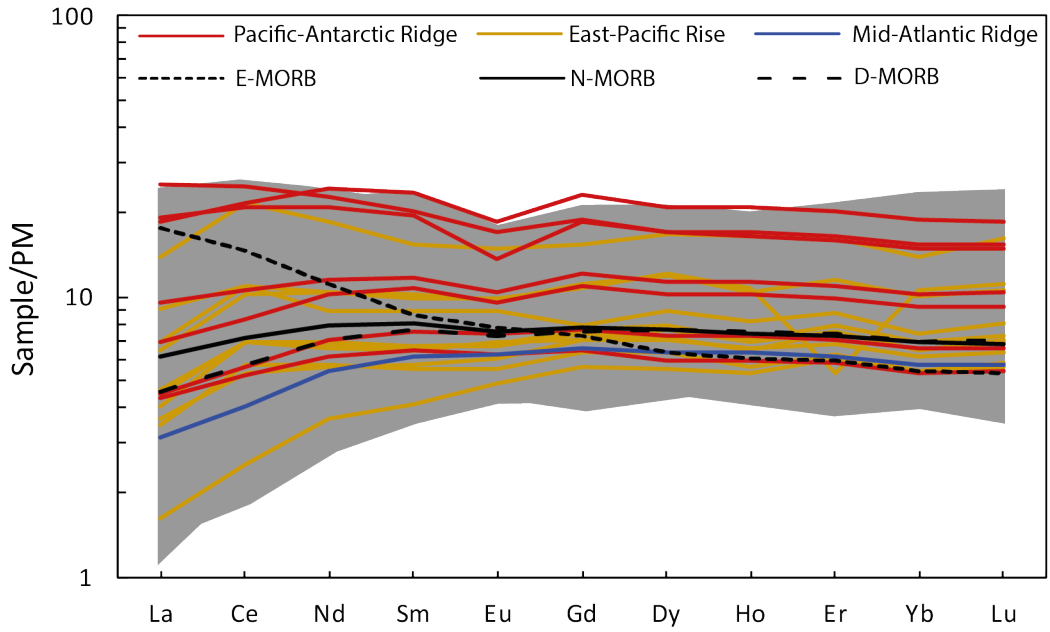

Figure B.1.1: Rare earth element (REE) patterns normalized to Primitive Manlte (PM) abundances from Palme and O'Neill (2014) for samples from the Pacific-Antarctic Ridge (PAR; Yierpan et al., 2019), East-Pacific Rise (EPR, Bach et al., 1994) and Mid-Atlantic Ridge (this study). Also shown are averages of PM-normalized REE concentrations of enriched MORB (E-MORB), normal MORB (N-MORB) and depleted MORB (D-MORB) by Gale et al. (2013). The grey field denotes the range of PM-normalized REE compositions from the PAR and southern EPR as compiled by Gale et al. (2013).

n=334). Accuracy was checked through digestion of rock reference standard materials BHVO-2 and BIR-1a, which gave $^{87}Sr/^{86}Sr$ ratios of 0.703493 ± 0.000010 (2SE) and 0.703115 ± 0.000010 (2SE), respectively.
Nd was loaded as phosphate on Re double filaments and measured in manual static multiple collector mode. Analytical mass fractionation was corrected with $^{146}Nd/^{144}Nd$ of 0.7219 using exponential law. εNd values were calculated using $^{143}Nd/^{144}Nd_{CHUR}$ of 0.512630 (Bouvier et al., 2008). Repeated measurements of the LaJolla Nd and J-Ndi standards gave $^{143}Nd/^{144}Nd$ ratios of 0.511817 ± 0.000024 (2SD; n=5) and 0.512075 ± 0.000022 (2SD; n=8), respectively. These values are in good agreement with the long-term reproducibility of 0.511830 ± 0.000041 (2SD; n=173) and 0.512075 ± 0.000073 (2SD; n=71), respectively. Standard rock reference material BHVO-2 and BIR-1a were measured to check for accuracy and yielded values of 0.512911 ± 0.000023 and 0.513030 ± 0.000011 (2SE), respectively.

B.1.3 Cr and Fe isotope compositions

Over the combined analytical sessions for this study, the compiled $\delta^{53/52}$Cr values of NIST SRM979 and in-house Merck Cr(III) standard solutions are 0.000 ± 0.018 ‰ (2SD; n=84) and -0.428 ± 0.019 ‰ (2SD; n=49), respectively. These values are in excellent agreement with previous studies (Albut et al., 2018; Babechuk et al., 2018; Schoenberg et al., 2016; Schoenberg et al., 2008; Wagner et al., 2021; Zink et al., 2010). The long-term reproducibility of $\delta^{53/52}$Cr values for single measurements of

NIST SRM979 and Cr(III) of our laboratory since May 2014 is 0.000 ± 0.020 ‰ (2SD; n=526) and -0.429 ± 0.023 ‰ (2SD; n=338), respectively. Accuracy of natural sample materials was assessed by measuring the USGS rock reference materials BHVO-2 and BIR-1a along with sample unknowns, which yielded $\delta^{53/52}$Cr values of -0.142 ± 0.012 ‰ (2SD; n=8, 3 digests) and -0.151 ± 0.015 ‰ (2SD; n=8, 3 digests), respectively, and are in excellent agreement with the long-term averages of -0.144 ± 0.023 ‰ (2SD; n=96, 14 digests) and -0.150 ± 0.025 ‰ (2SD; n=94, 13 digests), respectively. These values are in good agreement with previously reported values (D'Arcy et al., 2016; Li et al., 2016; Sossi et al., 2018; Xia et al., 2017). For most samples, the Cr isotope composition was determined at least five times from at least two digests from the same sample powder (Table 3.1). For these samples, accuracy was assessed by pooled 2SD based on replicate measurements of standard reference material BHVO-2, which equals ±0.016 ‰ and has been described in detail by Wagner et al. (2021). The reported uncertainty of sample unknowns analyzed once equals the long-term reproducibility of single measurements of natural reference material BHVO-2 of ± 0.023 ‰. Full procedural blanks were < 8.6 ng, contributing less than 0.5 % to the recovered amount of Cr, and were thus deemed negligible.
For Fe isotope analyses, IRMM-014 yielded a $\delta^{56/54}$Fe value of 0.000 ± 0.032 ‰ (2SD, n=21) throughout this study matching the long-term reproducibility of 0.000 ± 0.035 ‰ (2SD, n=299) of our laboratory since 2015. The in-house standards Han-Fe and Tueb-Fe gave $\delta^{56/54}$Fe values of +0.283 ± 0.051 ‰ (2SD, n=8) and -0.379 ± 0.056 ‰ (2SD, n=5), respectively, being in excellent agreement with previous studies (Babechuk et al., 2019; Eroglu et al., 2018; Swanner et al., 2015; Wagner et al., 2021; Wu et al., 2017) and the long-term reproducibility of +0.289 ± 0.039 ‰ (2SD, n=131) and -0.377 ± 0.038 ‰ (2SD, n=96), respectively. Furthermore, analytical accuracy was determined by measuring USGS reference materials BHVO-2 and BIR-1a, which were run together with processed samples, and yielded a $\delta^{56/54}$Fe of +0.099 ± 0.034 ‰ (2SD; n=6, two digest) and +0.065 ± 0.025 ‰ (2SD, n=2, one digest), respectively, agreeing well with published values (e.g., Barrat et al., 2015; Craddock et al., 2013; Millet et al., 2012; Nebel et al., 2015). The external reproducibility for samples from this study measured one time is equal to the long-term reproducibility of single measurements of the in-house Tueb-Fe standard solution equal to ± 0.038 ‰. For samples that have been measured multiple times, their accuracy is assessed by the pooled 2SD of five single measurements of Tueb-Fe, equal to ± 0.015 ‰. Procedural blanks were < 1.93 ng, contributing less than ∼0.01 % to the processed amount of sample Fe and thus considered negligible.

B.2 Influence of seafloor alteration on $\delta^{53/52}$Cr and $\delta^{56/54}$Fe of mid-ocean ridge basalts

The original Fe and Cr isotope signatures of MORBs may potentially be altered by non-magmatic processes such as hydrothermal fluid assimilation during and/or after storage in crustal magma chambers and post-eruptive seawater alteration. Samples in this study exhibit low H_2O contents ranging from 0.1 to 0.48 wt. % and from 0.18 to 0.78 wt. % for East-Pacific Rise (EPR) and Pacific-Antarctic Ridge (PAR) glasses, respectively (Bach et al., 1994; Clog et al., 2013). The MORB sample from the MAR displays a comparable low value with combined H_2O and CO_2 content (determined

as LOI at 1200° C) of 0.73 wt. %. These H_2O contents are within the typical range for MORB (H_2O = 2300 +3500/-1600 $\mu g\,g^{-1}$) and as discussed by Clog et al. (2013), are primarily controlled by igneous processes in the PAR suite. Furthermore, alteration by seawater is not likely to be responsible for the shift of MORBs towards lighter $\delta^{53/52}$Cr values compared to Bulk Silicate Earth (BSE) value ($\delta^{53/52}$Cr = 0.12 ± 0.06 ‰; Wagner et al., 2021) due to very low Cr contents and generally positive $\delta^{53/52}$Cr values for modern seawater of 64 to 1102 ng kg^{-1} and 0.412 to 1.55 ‰, respectively (Bonnand et al., 2013; Scheiderich et al., 2015). Moreover, Farkas et al. (2013) observed an increase towards heavy $\delta^{53/52}$Cr in hydrothermally altered ultramafic samples, which is opposite to the overall light $\delta^{53/52}$Cr of MORBs in this study. This is in accordance with the lack of a correlation between H_2O concentrations and $\delta^{53/52}$Cr values for all MORB glasses in this study (Figure B.2.1a). Despite this evidence for limited alteration, the PAR MORBs have been shown to be affected by contamination of Cl-rich brines and assimilation of hydrothermal sulfides during low-P magmatic differentiation and transport through the oceanic crust (Clog et al., 2013; Labidi et al., 2014). Evidence for the influence of Cl-rich fluids for some of the PAR MORBs is provided by higher Cl/K ratios than that of average MORB (Cl/K < 0.08; Michael and Cornell, 1998), whereas hydrothermal sulfide assimilation leads to δ^{34}S values higher than -0.5 ‰ compared to average PAR MORB (δ^{34}S = -0.89 ± 0.11 ‰; n=28; Figure B.2.2a; Clog et al., 2013; Labidi et al., 2014). Although Cr present as Cr^{3+} is generally regarded as insoluble and immobile, recent experiments simulating crustal and upper mantle conditions (T > 400° C; P > 0.3 GPa) indicated Cr^{3+} mobility in Cl-rich fluids (Klein-BenDavid et al., 2011; Spandler et al., 2011; Watenphul et al., 2014). Moreover, alteration by oxidizing fluids may oxidize Cr^{3+} to Cr^{6+}, which is highly soluble and mobile. The apparent correlation between Cl/K ratios and Cr concentrations (Figure B.2.2b) may indicate Cr loss during increasing magma-fluid interaction, which in turn may induce Cr isotope fractionation. However, while samples with the highest Cl contamination (PAC-Dr10-1g and PAC-Dr20-1) display the lowest $\delta^{53/52}$Cr, the difference in Cr isotopic compositions of these samples to uncontaminated ones is analytically not resolvable (Figure B.2.2c). Additionally, the average $\delta^{53/52}$Cr of these two samples ($\delta^{53/52}$Cr = -0.256 ± 0.006 ‰; 2SD) is well within the average $\delta^{53/52}$Cr of all N-MORBs, including EPR and MAR MORBs, from this study ($\delta^{53/52}$Cr = -0.237 ± 0.050 ‰; 2SD, n=19). Loss of Cr during alteration has been observed for serpentinized ultramafic peridotites (Wang et al., 2016; Xia et al., 2017) and the 1.85 Ga Flin Flon paleosol (Babechuk et al., 2017). Although the nature of Cr isotope fractionation remains a matter of debate, in both cases, Cr loss was associated with an increase in $\delta^{53/52}$Cr. Moreover, as noted by previous studies (Clog et al., 2013; Labidi et al., 2014), Cl contamination increases with increasing magmatic differentiation due to longer residence times in crustal magma chambers for more differentiated samples. The correlation of Cr with Cl/K may therefore reflect magmatic differentiation instead of Cr loss during interaction with Cl-rich fluids (Figure B.2.2b, c). Furthermore, limited Cr isotope variation during mild alteration of upper oceanic basaltic crust from ODP Hole 504, covering alteration temperatures from < 150 to > 500° C and varying redox conditions (oxidative vs. non-oxidative), point to a negligible effect of alteration on the $\delta^{53/52}$Cr of basaltic oceanic crust (Wang et al., 2016). The similarity of the average $\delta^{53/52}$Cr of evidently altered oceanic crust (-0.18 ± 0.1 ‰; Wang et al. 2016) compared to the average $\delta^{53/52}$Cr of N-MORBs (-0.237 ± 0.050 ‰) further support

this notion (Figure 3.3 in Chapter 3). Thus, the light $\delta^{53/52}$Cr values of MORBs compared to the BSE cannot be explained by interaction with hydrothermal fluids. Additionally, some PAR MORBs (n=3) were exposed to hydrothermal sulfide assimilation indicated by a relative increase of ^{34}S abundance (δ^{34}S > -0.5 ‰; Figure B.2.2a; Labidi et al., 2014). However, no systematic shift towards higher or lower values is observed in samples with a similar degree of sulfide assimilation (i.e., PAC1-Dr10 1g displays a $\delta^{34}S_{V\text{-}CTD}$ and $\delta^{53/52}$Cr values of -0.14 ‰ and -0.258 ‰, respectively, whereas sample PAC2-Dr27-1 has a $\delta^{34}S_{V\text{-}CTD}$ value of -0.1 ‰ and a $\delta^{53/52}$Cr value of -0.185 ‰; Figure B.2.2d). Sulfide deposits within the oceanic crust originate from sulfate reduction by the interaction of seawater sulfate with ferrous iron-bearing minerals. This process has been proposed to trigger efficient Cr removal from hydrothermal fluids, imparting a heavy Cr isotope signature on serpentinized peridotites (Farkas et al., 2013; Wang et al., 2016). So far, $\delta^{53/52}$Cr analyses of volcanogenic massive sulfides are not available and prevent further evaluation of the impact of sulfide assimilation on our MORB $\delta^{53/52}$Cr values.

Iron mobilization during seafloor alteration results in the preferential loss of light

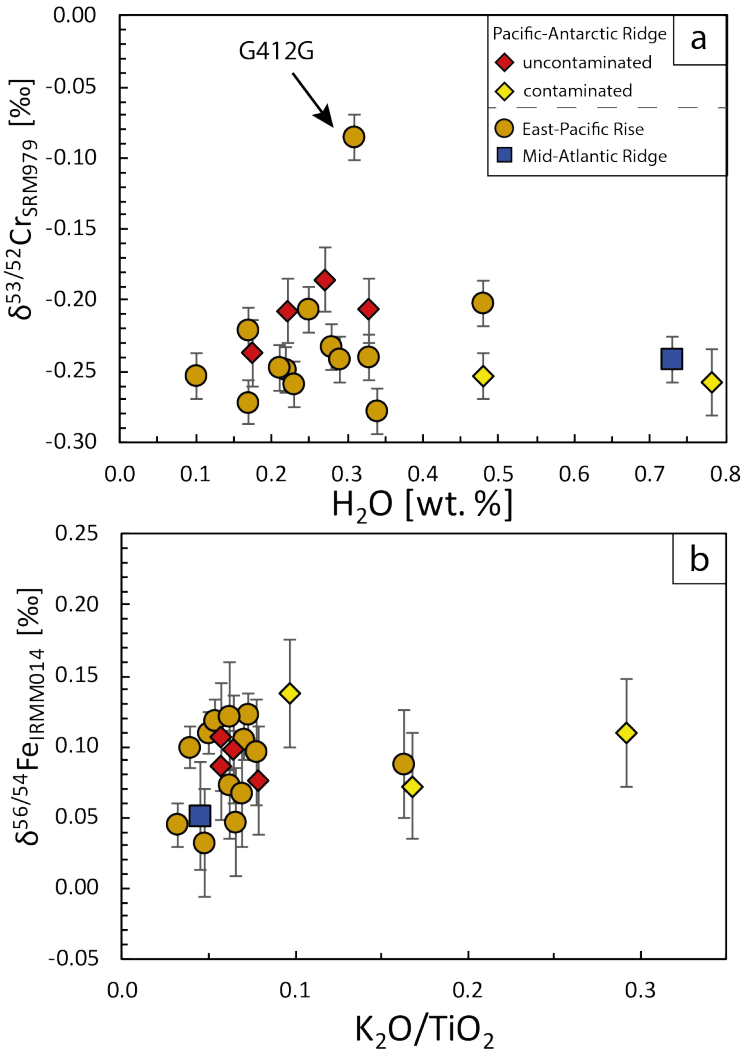

Figure B.2.1: a) Cr isotope compositions ($\delta^{53/52}$Cr) vs. H_2O content in samples from the Pacific-Antarctic Ridge and the East-Pacific Rise. Sample 267ROV-5 displays H_2O + CO_2 content. b) Fe isotope compositions ($\delta^{56/54}$Fe) vs. K_2O/TiO_2 ratios.

Fe isotopes, being partly responsible for the shift towards lower $\delta^{56/54}$Fe in hydrothermal fluids compared to the residual igneous rock. In particular, high- and low-temperature fluids from basaltic hosted systems display a restricted $\delta^{56/54}$Fe range from -0.67 to -0.21 ‰ (Beard et al., 2003; Bennett et al., 2009; Rouxel et al., 2008; Sharma et al., 2001), whereas the altered basalts show $\delta^{56/54}$Fe values of up to +1.36 ‰ (Rouxel et al., 2003). These high $\delta^{56/54}$Fe values in altered basalts are associated with extensive leaching of Fe from the rock. Iron loss is not observed in basaltic glasses from this study, which display high FeO_{total} contents of 8.6 to 14.13 wt. % (Figure 3.2c in Chapter 3). Moreover, altered oceanic basalts are highly oxidized with $Fe^{3+}/\Sigma Fe$ ratios ($\Sigma Fe = Fe^{2+} + Fe^{3+}$) reaching up to 0.86, which is mainly associated with the removal of soluble Fe^{2+} by fluids (Rouxel et al., 2003). EPR basalts display $Fe^{3+}/\Sigma Fe$ ratio of 0.15 (Bach et al., 1994), more comparable to the $Fe^{3+}/\Sigma Fe$ ratio of 0.07 of unaltered basalts (Christie et al., 1986) than to the average $Fe^{3+}/\Sigma Fe$ ratio of altered oceanic crust of 0.55 (Rouxel et al., 2003; Staudigel et al., 1996). Due to the high FeO_{total} content of MORBs, the Fe isotope signature should be resistant to minor loss of Fe, which is in accordance with $\delta^{56/54}$Fe values observed for MORBs in this study well within the range for non-altered MORBs reported in the literature (Figure 3.4c in Chapter 3; Chen et al., 2019; Richter et al., 2021; Teng et al., 2013) and similar $\delta^{56/54}$Fe values within uncertainty for non-altered vs. altered samples within this study (Figure B.2.2e). High $\delta^{56/54}$Fe values of altered oceanic crust are often associated with enrichment in K_2O due to the precipitation of secondary K-rich minerals (Rouxel et al., 2003). However, samples that show a K-enrichment, as indicated by high K_2O/TiO_2 ratios, cannot be distinguished in $\delta^{56/54}$Fe values from those with low K_2O/TiO_2 (Figure B.2.1b). Similarly, the samples affected most by hydrothermal sulfide assimilation ($\delta^{34}S >$ -0.5 ‰) exhibit similar $\delta^{56/54}$Fe values within uncertainty compared to uncontaminated samples ($\delta^{34}S <$ -0.5 ‰; Figure B.2.2f). Hydrothermal sulfides have been shown to exhibit lighter or similar $\delta^{56/54}$Fe compared to the hydrothermal fluids from which they precipitated (Rouxel et al., 2003; Rouxel et al., 2004; Rouxel et al., 2008; Sharma et al., 2001), indicating that hydrothermal sulfide assimilation cannot be responsible for the high $\delta^{56/54}$Fe in the most contaminated compared to uncontaminated samples and at maximum mute the high $\delta^{56/54}$Fe of the most contaminated samples. The similar range in $\delta^{56/54}$Fe values of EPR and MAR MORBs compared to PAR MORBs suggests that similar processes are also unlikely to have affected $\delta^{56/54}$Fe values of EPR and MAR MORBs.

B.3 Modeling Cr isotope fractionation during non-modal partial melting

To investigate the behavior of Cr isotopes during partial melting beneath mid-ocean ridges, we used a simplified model of isothermal decompression melting using the thermodynamic model pMELTS (Ghiorso et al., 2002) and the Excel-based GUI (Gualda and Ghiorso, 2015) with the update of April 2018. As a starting composition of the mantle source, we used the major element composition of the depleted mantle (DM) with a nominal water content of 0.0116 wt. % H_2O by Salters and Stracke (2004), excluding MnO and NiO as these components are not calibrated

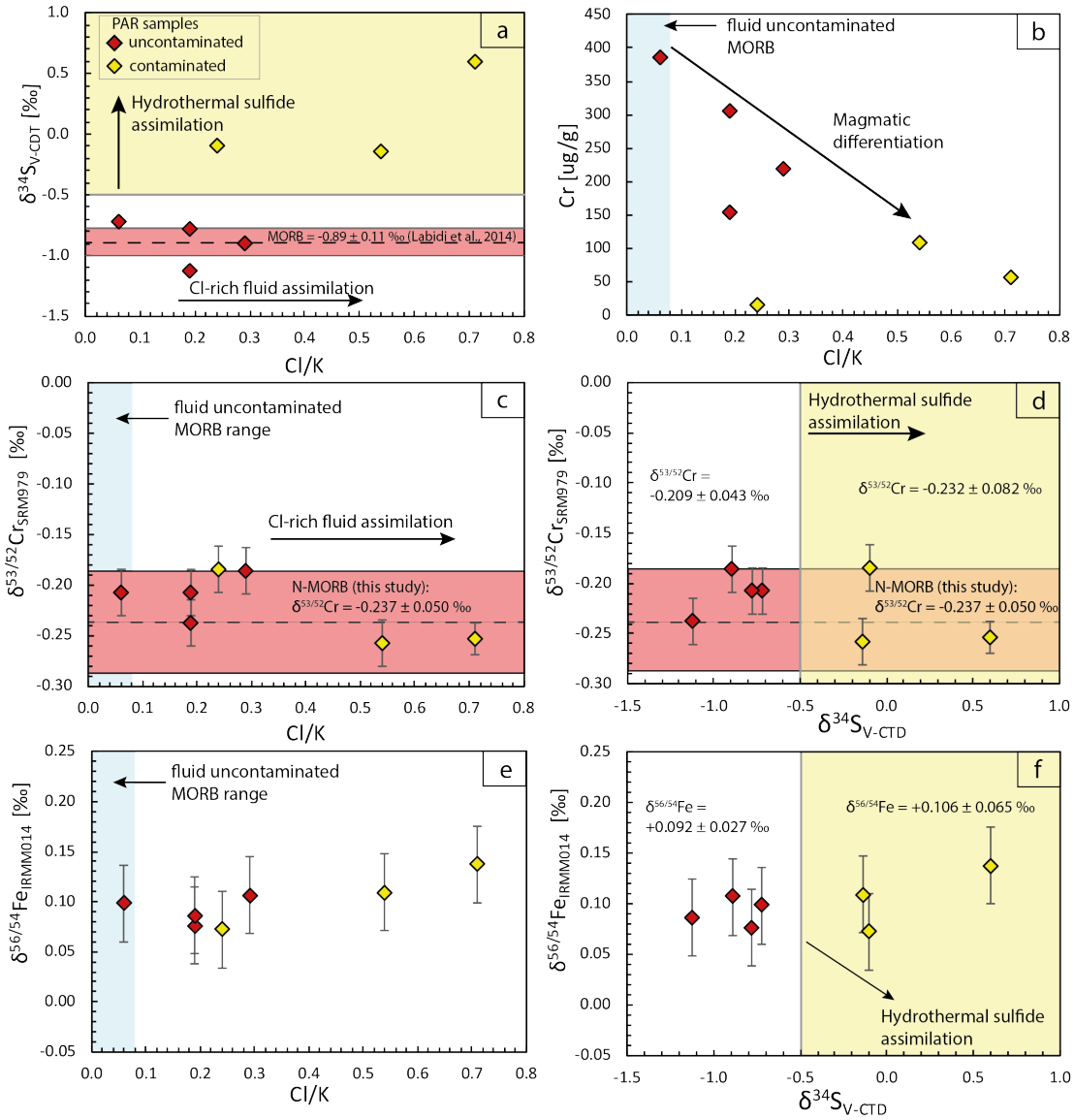

Figure B.2.2: a) Sulfur isotope compositions (δ^{34}S) vs. Cl/K ratios for PAR glasses. PAR samples, which are not affected by hydrothermal fluid assimilation, are shown in red, whereas samples that were shown to be affected by hydrothermal sulfide assimilation (δ^{34}S > -0.5 ‰) are shown in yellow (Labidi et al., 2014); b) Cr concentrations vs. Cl/K ratios, whereas decreasing Cr concentrations with increasing Cl/K ratios is interpreted as the result of magmatic differentiation; c) Cr isotope compositions ($\delta^{53/52}$Cr) vs. Cl/K ratios show that the samples affected most by fluid assimilation are within the range observed for all N-MORBs from the PAR, EPR and MAR (this study) as denoted by the red field; c) Sulfide assimilation does not affect $\delta^{53/52}$Cr of MORBs, as average $\delta^{53/52}$Cr values of contaminated samples cannot be distinguished from uncontaminated samples within uncertainty; e) Fe isotope compositions ($\delta^{56/54}$Fe) vs. Cl/K ratios showing no clear trend with increasing fluid contamination; f) $\delta^{56/54}$Fe vs. δ^{34}S. Hydrothermal fluid assimilation would drive $\delta^{56/54}$Fe of MORBs towards lower $\delta^{56/54}$Fe and lower δ^{34}S, which cannot be observed.

within pMELTS. Equilibration and mantle redox conditions were calculated around the Fayalite-Magnetite-Quartz (FMQ) mineral redox buffer at ΔFMQ +0.2 shown by O'Neill et al. (2018) to be relatively constant over the range of MORB melting conditions. The model starts with melting within the spinel stability field at 2 GPa. Decompression melting is simulated by releasing pressure in 0.1 kbar steps until 0.9 GPa at constant temperatures of 1350° C, which is close to the mean po-

tential temperature at a mid-ocean ridge setting (Herzberg et al., 2007; Lee et al., 2009). In general, the model follows the known behavior of incongruent non-modal melting, including preferential clinopyroxene consumption and olivine crystallization at low pressures. Exhaustion of clinopyroxene is achieved at ∼23 % of partial melting in accordance with previous models (Hirschmann et al., 1998). A limitation of pMELTS is that it considers Cr only in spinel and excludes Cr in mantle phases such as olivine, clinopyroxene and orthopyroxene, which may thus overestimate the stability of spinel during melting. Computed non-modal melting models presented in this study apply the modal residual mineralogy based on pMELTS to calculate Cr bulk partition coefficients ($D_{\text{mantle-melt}}$) for each melting increment. Based on changing modal mineralogy of the source with increasing degree of partial melting, $D_{\text{mantle-melt}}$ also varies with the partial melting degree. Partition coefficients between mineral and melt ($D_{\text{mineral-melt}}$) were compiled from Mallmann and O'Neill (2009) and Shen et al. (2018) and were assumed to be constant (Table B.3.1). Considering both oxidation states of Cr, bulk $D_{\text{mineral-melt}}$ were calculated for $Cr^{2+}/Cr_{\text{total}} = 0.15$ according to:

$$D_{Cr}^{mineral-melt} = D_{Cr^{2+}} \times \frac{Cr^{2+}}{Cr_{total}} + D_{Cr^{3+}} \times \frac{Cr^{3+}}{Cr_{total}} \tag{B.1}$$

Different melting models were considered, such as 1) batch melting (Equation B.2 and 2) aggregated fractional melting (Equation B.3; Shaw, 1970). Batch melting can be expressed by:

$$C_L = \frac{C_0}{F + D^{mantle-melt} \times (1 - F)} \tag{B.2}$$

where C_L represents the concentration of Cr in the liquid, C_0 represents the Cr concentration in the initial source, F the melt degree, and $D_{\text{mantle-melt}}$ the Cr bulk partition coefficient. Accordingly, the aggregated fractional melt is expressed by:

$$C_L = \frac{C_0}{F} \times [1 - (1 - F)^{\frac{1}{D^{mantle-melt}}}] \tag{B.3}$$

Due to the compatible behavior of Cr during partial mantle melting, Cr concentrations are rather insensitive to the first 20 % of partial melting as well as to the melting model. In order to evaluate $\delta^{53/52}$Cr of the melt with varying degrees of partial melting, the bulk isotopic difference between source and melt ($\Delta^{53/52}Cr_{\text{source-melt}}$) was calculated using the Cr content of the bulk source and the modal abundance of each mineral alongside with its Cr concentration at each melt increment, according to the following equation:

$$\begin{aligned} \Delta^{53/52}Cr_{source-melt} = C_{Cr,Mineral1} \times \frac{M_{Mineral1}}{Cr_{Cr,source}} \times \Delta^{53/52}Cr_{Mineral1-melt} + \\ C_{Cr,MineralX} \times \frac{M_{MineralX}}{Cr_{Cr,source}} \times \Delta^{53/52}Cr_{MineralX-melt} + [...] \end{aligned} \tag{B.4}$$

where M is the modal abundance of the mineral and $C_{\text{Cr,source}}$ and $C_{\text{Cr,MineralX}}$ are the Cr concentrations in the bulk source and mineral, respectively (modified from

Chen et al. (2021); Figure 3.5a in Chapter 3). Two different sets of mineral-melt isotopic differences ($\Delta^{53/52}Cr_{mineral\text{-}melt}$) were used: 1) Shen et al. (2020) and 2) Berry et al. (2021a). The data sets are based on a melt Cr^{2+}/Cr_{total} ratio of 0.55 (Shen et al., 2020) and 0.50 (Berry et al., 2021a) and temperatures of 1150° C. Berry et al. (2021a) proposed a systematic shift of 0.03 ‰ for $\Delta^{53/52}Cr_{olivine\text{-}melt}$ and $\Delta^{53/52}Cr_{spinel\text{-}melt}$. For this study, we assume this constant shift also applies to the isotopic difference between clinopyroxene and melt to present a coherent dataset yielding a $\Delta^{53/52}Cr_{cpx\text{-}melt}$ of 0.072 ‰ (Table B.3.1). Moreover, based on similar $\delta^{53/52}Cr_{cpx}$ and $\delta^{53/52}Cr_{opx}$ of equilibrated mineral pairs from mantle xenoliths and ionic model calculations, which predict $\delta^{53/52}Cr_{cpx} \leq \delta^{53/52}Cr_{opx}$ (Shen et al., 2018), each dataset treats $\Delta^{53/52}Cr_{cpx\text{-}melt}$ equal to $\Delta^{53/52}Cr_{opx\text{-}melt}$. Since mineral-melt fractionations are expected to decrease with temperature ($\sim 1/T^2$), $\Delta^{53/52}Cr_{mineral\text{-}melt}$ in this model are upper estimates as melting at temperatures of 1350 °C is expected. In the model presented here, no temperature correction has been applied.

Table B.3.1: Partition coefficients and $\Delta^{53/52}Cr_{mineral\text{-}melt}$ for olivine, orthopyroxene, clinopyroxene and spinel used for the non-modal batch and aggregated fractional melting models.

	Olivine	Orthopyroxene	Clinopyroxene	Spinel
$D_{mineral\text{-}melt}$ $(Cr^{3+})^*$	0.85	3.52	12.6	220
$D_{mineral\text{-}melt}$ $(Cr^{2+})^*$	0.85	0.843	0.587	0
Bulk $D_{mineral\text{-}melt}{}^\dagger$ Cr^{2+}/C_{total}=0.15	0.85	3.12	10.80	187
$\Delta^{53/52}Cr_{mineral\text{-}melt}{}^\ddagger$ Shen et al. (2020)	-0.086	0.046	0.046	0.063
$\Delta^{53/52}Cr_{mineral\text{-}melt}{}^\ddagger$ Berry et al. (2021a)	-0.050	0.076	*0.076*	0.087

*Partition coefficients for olivine, orthopyroxene and clinopyroxene compiled from Mallman and O'Neill (2009) and for spinel from the Supplementary Information of Shen et al. (2018).
†Bulk $D_{mineral\text{-}melt}$ for Cr is calculated for Cr^{2+}/Cr_{total} of 0.15 following Equation B.1, which represents an estimate for partial melting beneath a mid-ocean ridge (Berry et al., 2021b).
$^\ddagger\Delta^{53/52}Cr_{mineral\text{-}melt}$ are compiled from Shen et al. (2020) and Berry et al. (2021a), whereas the constant shift of 0.03 ‰ shown for spinel and olivine (Berry et al., 2021a) between the two datasets is applied to clinopyroxene and marked in italic (see also text).

The Cr bulk isotopic difference between source and melt changes with each melting increment, as it is governed by the changing modal mineralogy and hence, Cr concentrations of the source. The differences between model results for the two different data sets of Shen et al. (2020) and Berry et al. (2021a) can be attributed to larger isotopic differences for pyroxene and spinel reported by Berry et al. (2021a) compared to the values from Shen et al. (2020), sequestering the heavy Cr^{3+} in the source to larger amounts, and thus leading to overall larger isotopic differences between source and melt.
Ultimately, the $\delta^{53/52}Cr$ of the melt for batch and aggregated fractional melting models were calculated based on mass balance according to Equation B.5 (modified from Chen et al. (2021)):

$$\delta^{53/52}Cr_{melt} = \delta^{53/52}Cr_{source} - (1 - C_{Cr,melt} \times \frac{F}{C_{Cr,source}}) \times \Delta^{53/52}Cr_{source-melt} \quad \text{(B.5)}$$

using the corresponding calculated Cr concentration of the melt ($C_{Cr,melt}$) and $\Delta^{53/52}Cr_{source\text{-}melt}$ at each melting increment taken from Equation B.4 and the Cr concentration of the source. The starting composition of the source was set to $C_{Cr,source} = 2500\,\mu g\,g^{-1}$ (Salters and Stracke, 2004) and $\delta^{53/52}$Cr = -0.12 ‰ (Wagner et al., 2021). The modeled $\delta^{53/52}$Cr of the melt is lowest at low degrees of melting and increases with increasing degree of F in agreement with previous model results by Shen et al. (2020) and Jerram et al. (2022) (Figure 3.5b in Chapter 3). $\delta^{53/52}$Cr varies by 0.016 ‰ within the first 20 % of melting and shows limited variation for batch and aggregated fractional in accordance with the compatible behavior of Cr.

References

Albut, G., Babechuk, M.G., Kleinhanns, I.C., Benger, M., Beukes, N.J., Steinhilber, B., Smith, A.J.B., Kruger, S.J. and Schoenberg, R. 2018. Modern rather than Mesoarchaean oxidative weathering responsible for the heavy stable Cr isotopic signatures of the 2.95 Ga old Ijzermijn iron formation (South Africa). Geochim. Cosmochim. Ac. 228, 157-189.

Babechuk, M.G., Kamber, B.S., Greig, A., Canil, D. and Kodolanyi, J. 2010. The behavior of tungsten during mantle melting revisited with implications for planetary differentiation time scales. Geochim. Cosmochim. Ac. 74, 1448-1470.

Babechuk, M.G., Kleinhanns, I.C., Reitter, E. and Schoenberg, R. 2018. Kinetic stable Cr isotopic fractionation between aqueous Cr(III)-Cl-H_2O complexes at 25° C: Implications for Cr(III) mobility and isotopic variations in modern and ancient natural systems. Geochim. Cosmochim. Ac. 222, 383-405.

Babechuk, M.G., Kleinhanns, I.C. and Schoenberg, R. 2017. Chromium geochemistry of the ca. 1.85 Ga Flin Flon paleosol. Geobiology. 15, 30-50.

Babechuk, M.G., Weimar, N.E., Kleinhanns, I.C., Eroglu, S., Swanner, E.D., Kenny, G.G., Kamber, B.S. and Schoenberg, R. 2019. Pervasively anoxic surface conditions at the onset of the Great Oxidation Event: New multi-proxy constraints from the Cooper Lake paleosol. Precambrian Res. 323, 126-163.

Bach, W., Hegner, E., Erzinger, J. and Satir, M. 1994. Chemical and isotopic variations along the superfast spreading East Pacific Rise from 6 to 30° S. Contrib. Mineral. Petrol. 116, 365-380.

Barrat, J.A., Rouxel, O., Wang, K., Moynier, F., Yamaguchi, A., Bischoff, A. and Langlade, J. 2015. Early stages of core segregation recorded by Fe isotopes in an asteroidal mantle. Earth Planet. Sc. Lett. 419, 93-100.

Beard, B.L., Johnson, C.M., Von Damm, K.L. and Poulson, R.L. 2003. Iron isotope constraints on Fe cycling and mass balance in oxygenated Earth oceans. Geology. 31, 629-632.

Bennett, S.A., Rouxel, O., Schmidt, K., Garbe-Schonberg, D., Statham, P.J. and German, C.R. 2009. Iron isotope fractionation in a buoyant hydrothermal plume, 5° S Mid-Atlantic Ridge. Geochim. Cosmochim. Ac. 73, 5619-5634.

Berry, A.J., Miller, L.A., O'Neill, H.S.C. and Foran, G.J. 2021a. The coordination of Cr^{2+} in silicate glasses and implications for mineral-melt fractionation of Cr isotopes. Chem. Geol. 586, 120483.

Berry, A.J., O'Neill, H.S.C. and Foran, G.J. 2021b. The effects of temperature and pressure on the oxidation state of chromium in silicate melts. Contrib. Mineral. Petrol. 176, 40.

Bonnand, P., James, R.H., Parkinson, I.J., Connelly, D.P. and Fairchild, I.J. 2013. The chromium isotopic composition of seawater and marine carbonates. Earth Planet. Sc. Lett. 382, 10-20.

Bouvier, A., Vervoort, J.D. and Patchett, P.J. 2008. The Lu–Hf and Sm–Nd isotopic composition of CHUR: constraints from unequilibrated chondrites and implications for the bulk composition of terrestrial planets. Earth Planet. Sc. Lett. 273, 48-57.

Chen, S., Niu, Y.L., Guo, P.Y., Gong, H.M., Sun, P., Xue, Q.Q., Duan, M. and Wang, X.H. 2019. Iron isotope fractionation during mid-ocean ridge basalt (MORB) evolution: Evidence from lavas on the East Pacific Rise at 10° 30' N and its implications. Geochim. Cosmochim. Ac. 267, 227-239.

Chen, Y.H., Niu, Y.L., Duan, M., Gong, H.M. and Guo, P.Y. 2021. Fractional crystallization causes the iron isotope contrast between mid-ocean ridge basalts and abyssal peridotites. Commun. Earth Environ. 2, 65.

Christie, D.M., Carmichael, I.S.E. and Langmuir, C.H. 1986. Oxidations-states of midocean ridge basalt glasses. Earth Planet. Sc. Lett. 79, 397-411.

Clog, M., Aubaud, C., Cartigny, P. and Dosso, L. 2013. The hydrogen isotopic composition and water content of southern Pacific MORB: A reassessment of the D/H ratio of the depleted mantle reservoir. Earth Planet. Sc. Lett. 381, 156-165.

Craddock, P.R., Warren, J.M. and Dauphas, N. 2013. Abyssal peridotites reveal the near-chondritic Fe isotopic composition of the Earth. Earth Planet. Sc. Lett. 365, 63-76.

D'Arcy, J., Babechuk, M.G., Dossing, L.N., Gaucher, C. and Frei, R. 2016. Processes controlling the chromium isotopic composition of river water: Constraints from basaltic river catchments. Geochim. Cosmochim. Ac. 186, 296-315.

Eggins, S.M., Woodhead, J.D., Kinsley, L.P.J., Mortimer, G.E., Sylvester, P., McCulloch, M.T., Hergt, J.M. and Handler, M.R. 1997. A simple method for the precise determination of ≥40 trace elements in geological samples by ICPMS using enriched isotope internal standardisation. Chem. Geol. 134, 311-326.

Eroglu, S., Schoenberg, R., Pascarelli, S., Beukes, N.J., Kleinhanns, I.C. and Swanner, E.D. 2018. Open ocean vs. continetally-derived iron cycles along the Neoarchean

Campbellrand-Malmani carbonate platform, South Africa. Am. J. Sci. 318, 367-408.

Farkas, J., Chrastny, V., Novak, M., Cadkova, E., Pasava, J., Chakrabarti, R., Jacobsen, S.B., Ackerman, L. and Bullen, T.D. 2013. Chromium isotope variations ($\delta^{53/52}Cr$) in mantle-derived sources and their weathering products: Implications for environmental studies and the evolution of $\delta^{53/52}Cr$ in the Earth's mantle over geologic time. Geochim. Cosmochim. Ac. 123, 74-92.

Gale, A., Dalton, C.A., Langmuir, C.H., Su, Y.J. and Schilling, J.G. 2013. The mean composition of ocean ridge basalts. Geochem. Geophys. Geosyst. 14, 489-518.

Ghiorso, M.S., Hirschmann, M.M., Reiners, P.W. and Kress, V.C. 2002. The pMELTS: A revision of MELTS for improved calculation of phase relations and major element partitioning related to partial melting of the mantle to 3 GPa. Geochem. Geophys. Geosyst. 3, 5, 1-36.

Gualda, G.A.R. and Ghiorso, M.S. 2015. MELTS-Excel: A Microsoft Excel-based MELTS interface for research and teaching of magma properties and evolution. Geochem. Geophys. Geosyst. 16, 315-324.

Herzberg, C., Asimow, P.D., Arndt, N., Niu, Y.L., Lesher, C.M., Fitton, J.G., Cheadle, M.J. and Saunders, A.D. 2007. Temperatures in ambient mantle and plumes: Constraints from basalts, picrites, and komatiites. Geochem. Geophys. Geosyst. 8, Q02006.

Hirschmann, M.M., Ghiorso, M.S., Wasylenki, L.E., Asimow, P.D. and Stolper, E.M. 1998. Calculation of peridotite partial melting from thermodynamic models of minerals and melts. I. Review of methods and comparison with experiments. J. Petrol. 39, 1091-1115.

Jerram, M., Bonnand, P., Harvey, J., Ionov, D. and Halliday, A.N. 2022. Stable chromium isotopic variations in peridotite mantle xenoliths: Metasomatism versus partial melting. Geochim. Cosmochim. Ac. 317, 138-154.

Kamber, B.S., Greig, A. and Collerson, K.D. 2005. A new estimate for the composition of weathered young upper continental crust from alluvial sediments, Queensland, Australia. Geochim. Cosmochim. Ac. 69, 1041-1058.

Klein-BenDavid, O., Pettke, T. and Kessel, R. 2011. Chromium mobility in hydrous fluids at upper mantle conditions. Lithos. 125, 122-130.

Labidi, J., Cartigny, P., Hamelin, C., Moreira, M. and Dosso, L. 2014. Sulfur isotope budget (^{32}S, ^{33}S, ^{34}S and ^{36}S) in Pacific-Antarctic ridge basalts: A record of mantle source heterogeneity and hydrothermal sulfide assimilation. Geochim. Cosmochim. Ac. 133, 47-67.

Lee, C.T.A., Luffi, P., Plank, T., Dalton, H. and Leeman, W.P. 2009. Constraints on the depths and temperatures of basaltic magma generation on Earth and other terrestrial planets using new thermobarometers for mafic magmas. Earth Planet. Sc. Lett. 279, 20-33.

Li, C.F., Feng, L.J., Wang, X.C., Chu, Z.Y., Guoa, J.H. and Wilde, S.A. 2016. Precise measurement of Cr isotope ratios using a highly sensitive Nb_2O_5 emitter by

thermal ionization mass spectrometry and an improved procedure for separating Cr from geological materials. J. Anal. Atom. Spectrom. 31, 2375-2383.

Mallmann, G. and O'Neill, H.S.C. 2009. The Crystal/Melt Partitioning of V during Mantle Melting as a Function of Oxygen Fugacity Compared with some other Elements (Al, P, Ca, Sc, Ti, Cr, Fe, Ga, Y, Zr and Nb). J. Petrol. 50, 1765-1794.

Michael, P.J. and Cornell, W.C. 1998. Influence of spreading rate and magma supply on crystallization and assimilation beneath mid-ocean ridges: Evidence from chlorine and major element chemistry of mid-ocean ridge basalts. J. Geophys. Res.-Sol. Ea. 103, 18325-18356.

Millet, M.A., Baker, J.A. and Payne, C.E. 2012. Ultra-precise stable Fe isotope measurements by high resolution multiple-collector inductively coupled plasma mass spectrometry with a ^{57}Fe-^{58}Fe double spike. Chem. Geol. 304, 18-25.

Nebel, O., Sossi, P.A., Benard, A., Wille, M., Vroon, P.Z. and Arculus, R.J. 2015. Redox-variability and controls in subduction zones from an iron-isotope perspective. Earth Planet. Sc. Lett. 432, 142-151.

O'Neill, H.S.C., Berry, A.J. and Mallmann, G. 2018. The oxidation state of iron in Mid-Ocean Ridge Basaltic (MORB) glasses: Implications for their petrogenesis and oxygen fugacities. Earth Planet. Sc. Lett. 504, 152-162.

Palme, H. and O'Neill, H.S.C. 2014. Cosmochemical Estimates of Mantle Composition., in: Turekian, K., Holland, H. (Eds.), Treatise on Geochemistry, 2 ed. Elsevier, pp. 1-39.

Richter, M., Nebel, O., Schwindinger, M., Nebel-Jacobsen, Y. and Dick, H.J.B. 2021. Competing effects of spreading rate, crystal fractionation and source variability on Fe isotope systematics in mid-ocean ridge lavas. Sci. Rep. 11, 4123.

Rouxel, O., Dobbek, N., Ludden, J. and Fouquet, Y. 2003. Iron isotope fractionation during oceanic crust alteration. Chem. Geol. 202, 155-182.

Rouxel, O., Fouquet, Y. and Ludden, J.N. 2004. Subsurface processes at the Lucky Strike hydrothermal field, Mid-Atlantic Ridge: Evidence from sulfur, selenium, and iron isotopes. Geochim. Cosmochim. Ac. 68, 2295-2311.

Rouxel, O., Shanks, W.C., Bach, W. and Edwards, K.J. 2008. Integrated Fe- and S-isotope study of seafloor hydrothermal vents at East Pacific rise 9-10° N. Chem. Geol. 252, 214-227.

Salters, V.J.M. and Stracke, A. 2004. Composition of the depleted mantle. Geochem. Geophys. Geosyst. 5, Q05B07.

Scheiderich, K., Amini, M., Holmden, C. and Francois, R. 2015. Global variability of chromium isotopes in seawater demonstrated by Pacific, Atlantic, and Arctic Ocean samples. Earth Planet. Sc. Lett. 423, 87-97.

Schoenberg, R., Merdian, A., Holmden, C., Kleinhanns, I.C., Hassler, K., Wille, M. and Reitter, E. 2016. The stable Cr isotopic compositions of chondrites and silicate planetary reservoirs. Geochim. Cosmochim. Ac. 183, 14-30.

Schoenberg, R., Zink, S., Staubwasser, M. and von Blanckenburg, F. 2008. The

stable Cr isotope inventory of solid Earth reservoirs determined by double spike MC-ICP-MS. Chem. Geol. 249, 294-306.

Sharma, M., Polizzotto, M. and Anbar, A.D. 2001. Iron isotopes in hot springs along the Juan de Fuca Ridge. Earth Planet. Sc. Lett. 194, 39-51.

Shaw, D.M. 1970. Trace element fractionation during anatexis. Geochim. Cosmochim. Ac. 34, 237-243.

Shen, J., Qin, L.P., Fang, Z.Y., Zhang, Y.N., Liu, J., Liu, W., Wang, F.Y., Xiao, Y., Yu, H.M. and Wei, S.Q. 2018. High-temperature inter-mineral Cr isotope fractionation: A comparison of ionic model predictions and experimental investigations of mantle xenoliths from the North China Craton. Earth Planet. Sc. Lett. 499, 278-290.

Shen, J., Xia, J.X., Qin, L.P., Carlson, R.W., Huang, S.C., Helz, R.T. and Mock, T.D. 2020. Stable chromium isotope fractionation during magmatic differentiation: Insights from Hawaiian basalts and implications for planetary redox conditions. Geochim. Cosmochim. Ac. 278, 289-304.

Sossi, P.A., Moynier, F. and van Zuilen, K. 2018. Volatile loss following cooling and accretion of the Moon revealed by chromium isotopes. Proc. Natl. Acad. Sci. 115, 10920-10925.

Spandler, C., Pettke, T. and Rubatto, D. 2011. Internal and External Fluid Sources for Eclogite-facies Veins in the Monviso Meta-ophiolite, Western Alps: Implications for Fluid Flow in Subduction Zones. J. Petrol. 52, 1207-1236.

Staudigel, H., Plank, T., White, B. and Schmincke, H.-U. 1996. Geochemical fluxes during seafloor alteration of the basaltic upper oceanic crust: DSDP Sites 417 and 418. Washington DC American Geophysical Union Geophysical Monograph Series. 96, 19-38.

Swanner, E.D., Wu, W.F., Schoenberg, R., Byrne, J., Michel, F.M., Pan, Y.X. and Kappler, A. 2015. Fractionation of Fe isotopes during Fe(II) oxidation by a marine photoferrotroph is controlled by the formation of organic Fe-complexes and colloidal Fe fractions. Geochim. Cosmochim. Ac. 165, 44-61.

Teng, F.Z., Dauphas, N., Huang, S.C. and Marty, B. 2013. Iron isotopic systematics of oceanic basalts. Geochim. Cosmochim. Ac. 107, 12-26.

Ulrich, T., Kamber, B.S., Woodhead, J.D. and Spencer, L.A. 2010. Long-Term Observations of Isotope Ratio Accuracy and Reproducibility Using Quadrupole ICP-MS. Geostand. Geoanal. Res. 34, 161-174.

Wagner, L.J., Kleinhanns, I.C., Weber, N., Babechuk, M.G., Hofmann, A. and Schoenberg, R. 2021. Coupled stable chromium and iron isotopic fractionation tracing magmatic mineral crystallization in Archean komatiite-tholeiite suites. Chem. Geol. 576, 120121.

Wang, X.L., Planavsky, N.J., Reinhard, C.T., Zou, H.J., Ague, J.J., Wu, Y.B., Gill, B.C., Schwarzenbach, E.M. and Peucker-Ehrenbrink, B. 2016. Chromium isotope fractionation during subduction-related metamorphism, black shale weathering, and hydrothermal alteration. Chem. Geol. 423, 19-33.

Watenphul, A., Schmidt, C. and Jahn, S. 2014. Cr(III) solubility in aqueous fluids at high pressures and temperatures. Geochim. Cosmochim. Ac. 126, 212-227.

Wu, W.F., Swanner, E.D., Kleinhanns, I.C., Schoenberg, R., Pan, Y.X. and Kappler, A. 2017. Fe isotope fractionation during Fe(II) oxidation by the marine photoferrotroph Rhodovulum iodosum in the presence of Si - Implications for Precambrian iron formation deposition. Geochim. Cosmochim. Ac. 211, 307-321.

Xia, J.X., Qin, L.P., Shen, J., Carlson, R.W., Ionov, D.A. and Mock, T.D. 2017. Chromium isotope heterogeneity in the mantle. Earth Planet. Sc. Lett. 464, 103-115.

Yierpan, A., König, S., Labidi, J. and Schoenberg, R. 2019. Selenium isotope and S-Se-Te elemental systematics along the Pacific-Antarctic ridge: Role of mantle processes. Geochim. Cosmochim. Ac. 249, 199-224.

Zink, S., Schoenberg, R. and Staubwasser, M. 2010. Isotopic fractionation and reaction kinetics between Cr(III) and Cr(VI) in aqueous media. Geochim. Cosmochim. Ac. 74, 5729-5745.

B.4 Supplementary data

Table B.4.1: Compilation of major and trace element and radiogenic Sr-Nd isotope compositions for sample 267ROV-5 determined in this study together with major and trace element as well as stable and radiogenic isotope compositions compiled from the literature for normal MORB (N-MORB) and transitional MORB (T-MORB) from the Pacific-Antarctic Ridge. Dredingt depths are given in m below sea level (mbsl). Stable Cr and Fe isotopic compositions determined in this study are given again for completeness of the dataset.

Sample	267ROV-5	PAC1-CV03-g	PAC1-DR06-g	PAC1-DR10-1g	PAC2-DR05-2g	PAC2-DR20-1	PAC2-DR27-1	PAC2-DR38-1
Type	N-MORB	N-MORB	N-MORB	N-MORB	N-MORB	N-MORB	T-MORB	N-MORB
Latitude (S)	04°48.161'	64°31.8'	60°56.4'	57°53.4'	50°58.8'	49°43.98'	48°10.92'	41°48.0'
Longitude (W)	12°22.330'	171°52.8'	153°12.6'	148°30.0'	117°54.0'	113°46.98'	113°20.52'	111°20.4'
Dredging Depth (mbsl)	2987	2576	2527	2319	2784	2441	2359	2524
Radiogenic isotopes								
$^{87}Sr/^{86}Sr$	0.702154	*0.702406*	*0.702502*	*0.702473*	*0.702524*	*0.702493*	*0.702643*	*0.702465*
$^{143}Nd/^{144}Nd$	0.513253	*0.513117*	*0.513126*	*0.513112*	*0.513098*	*0.513092*	*0.513035*	*0.513108*
$^{176}Hf/^{177}Hf$		*0.283170*		*0.283149*	*0.283135*	*0.283126*	*0.283094*	*0.283125*
$^{3}He/^{4}He$ (R/R_A)			*8.0*		*7.5*	*7.1*	*6.1*	*7.2*
$^{206}Pb/^{204}Pb$		*18.497*	*18.504*	*18.435*	*18.634*	*18.749*	*19.174*	*18.671*
$^{207}Pb/^{204}Pb$		*15.498*	*15.505*	*15.510*	*15.504*	*15.540*	*15.585*	*15.533*
$^{208}Pb/^{204}Pb$		*38.093*	*37.987*	*37.968*	*38.024*	*38.168*	*38.634*	*38.039*
Major elements (wt. %)								
SiO_2	49.2	*50.7*	*51.0*	*53.8*	*49.9*	*51.2*	*49.8*	*49.1*
TiO_2	1.17	*1.24*	*2.08*	*1.65*	*2.28*	*2.58*	*3.16*	*1.47*
Al_2O_3	15.1	*15.53*	*13.99*	*14.10*	*13.65*	*13.90*	*12.90*	*15.70*
FeO_T	8.61	*8.60*	*11.2*	*10.8*	*12.1*	*12.8*	*14.1*	*9.72*
Fe_2O_3								
FeO								
MnO	0.19	*0.16*	*0.20*	*0.21*	*0.22*	*0.24*	*0.26*	*0.18*
MgO	8.37	*8.57*	*6.93*	*4.83*	*6.52*	*4.60*	*4.52*	*8.35*
CaO	11.9	*11.9*	*10.6*	*8.59*	*10.4*	*9.35*	*8.80*	*11.7*
Na_2O	2.69	*2.53*	*2.86*	*3.43*	*2.74*	*3.34*	*3.37*	*2.67*
K_2O	0.05	*0.08*	*0.12*	*0.48*	*0.18*	*0.25*	*0.53*	*0.09*
P_2O_5	0.10				*0.24*	*0.42*	*0.46*	*0.14*
CO_2								
H_2O^*	0.73	*0.22*	*0.27*	*0.78*	*0.33*	*0.48*		*0.18*

Continued on next page

Table B.4.1 – *Continued from previous page*

Sample	267ROV-5	PAC1-CV03-g	PAC1-DR06-g	PAC1-DR10-1g	PAC2-DR05-2g	PAC2-DR20-1	PAC2-DR27-1	PAC2-DR38-1
Trace elements (μg g^{-1})								
Li	5.33	*4.88*	*7.89*	*11.63*	*8.45*	*11.16*	*11.40*	*5.54*
Be	0.346	*0.38*	*0.60*	*1.36*	*0.62*	*1.25*	*1.30*	*0.40*
Sc	41	*38*	*41*	*32*	*42*	*36*	*38*	*40*
Ti	4989	*7428*	*12451*	*9863*	*13690*	*15485*	*18926*	*8824*
V	184	*261*	*375*	*217*	*391*	*290*	*414*	*285*
Cr	319	*413*	*232*	*106*	*163*	*58*	*18*	*322*
Co	43	*41*	*43*	*31*	*42*	*36*	*41*	*46*
Ni	79	*123*	*77*	*29*	*63*	*30*	*21*	*124*
Cu	80	*65*	*50*	*49*	*47*	*40*	*39*	*68*
Zn	73	*68*	*100*	*99*	*104*	*120*	*135*	*75*
Ga	15	*15*	*19*	*19*	*18*	*22*	*23*	*16*
Rb	0.50	*0.81*	*1.09*	*5.70*	*2.24*	*2.72*	*8.15*	*0.58*
Sr	114	*132*	*107*	*124*	*113*	*126*	*170*	*127*
Y	25	*25*	*43*	*67*	*45*	*82*	*66*	*29*
Zr	65	*76*	*132*	*323*	*142*	*342*	*265*	*86*
Nb	1.16	*2.42*	*3.57*	*12.26*	*6.38*	*10.28*	*21.66*	*2.32*
Mo	0.14	*0.19*	*0.38*	*1.09*	*0.45*	*0.97*	*1.22*	*0.29*
Cd	0.09	*0.09*	*0.13*	*0.21*	*0.15*	*0.22*	*0.21*	*0.10*
Sn	0.61	*0.88*	*1.53*	*3.45*	*1.53*	*3.27*	*2.79*	*0.99*
Sb	0.005	*0.009*	*0.011*	*0.025*	*0.014*	*0.025*	*0.041*	*0.030*
Cs	0.007	*0.009*	*0.012*	*0.062*	*0.024*	*0.027*	*0.085*	*0.007*
Ba	6.07	*9.49*	*11.65*	*47.21*	*25.32*	*28.83*	*92.44*	*7.52*
La	2.14	*2.98*	*4.68*	*13.05*	*6.50*	*12.72*	*17.27*	*3.07*
Ce	7.10	*9.14*	*14.65*	*36.30*	*18.58*	*38.04*	*43.61*	*9.89*
Pr	1.30	*1.55*	*2.54*	*5.62*	*3.02*	*6.27*	*6.41*	*1.74*
Nd	7.31	*8.20*	*13.66*	*27.84*	*15.52*	*32.38*	*30.53*	*9.44*
Sm	2.67	*2.78*	*4.64*	*8.48*	*5.12*	*10.16*	*8.82*	*3.26*
Eu	1.04	*1.03*	*1.58*	*2.25*	*1.72*	*3.07*	*2.84*	*1.23*
Gd	3.85	*3.75*	*6.36*	*10.87*	*7.08*	*13.46*	*11.06*	*4.47*

Continued on next page

Table B.4.1 – *Continued from previous page*

Sample	267ROV-5	PAC1-CV03-g	PAC1-DR06-g	PAC1-DR10-1g	PAC2-DR05-2g	PAC2-DR20-1	PAC2-DR27-1	PAC2-DR38-1
Tb	0.70	*0.67*	*1.12*	*1.87*	*1.23*	*2.32*	*1.90*	*0.80*
Dy	4.62	*4.31*	*7.37*	*12.29*	*8.15*	*15.04*	*12.24*	*5.26*
Ho	1.01	*0.95*	*1.62*	*2.70*	*1.81*	*3.34*	*2.63*	*1.15*
Er	2.87	*2.72*	*4.61*	*7.74*	*5.14*	*9.50*	*7.47*	*3.29*
Tm	0.43	*0.40*	*0.69*	*1.15*	*0.76*	*1.38*	*1.12*	*0.49*
Yb	2.72	*2.57*	*4.38*	*7.32*	*4.84*	*8.93*	*7.11*	*3.13*
Lu	0.40	*0.38*	*0.65*	*1.08*	*0.73*	*1.31*	*1.04*	*0.46*
Hf	1.79	*1.92*	*3.37*	*7.53*	*3.84*	*8.14*	*6.73*	*2.33*
Ta	0.06	*0.15*	*0.23*	*0.72*	*0.39*	*0.65*	*1.36*	*0.16*
W	0.92	*0.09*	*0.09*	*0.14*	*0.06*	*0.15*	*0.23*	*0.02*
Tl	0.006	*0.007*	*0.009*	*0.026*	*0.010*	*0.016*	*0.027*	*0.008*
Pb	0.51	*0.34*	*0.47*	*1.01*	*0.54*	*0.81*	*1.16*	*0.34*
Th	0.07	*0.16*	*0.22*	*1.01*	*0.37*	*0.63*	*1.44*	*0.13*
U	0.04	*0.05*	*0.09*	*0.37*	*0.13*	*0.24*	*0.47*	*0.06*
Se (ng g^{-1})		*158*	*177*	*170*	*176*	*193*	*219*	*180*
1 s.d. (ng g^{-1})		*1*	*2*	*3*	*4*	*4*	*4*	*1*
Te (ng g^{-1})		*3.19*	*1.61*	*2.68*	*1.43*	*1.68*	*1.16*	*3.12*
1 s.d. (ng g^{-1})		*0.10*	*0.05*	*0.08*	*0.04*	*0.05*	*0.03*	*0.09*
S (μg g^{-1})		*938*	*1351*	*1047*	*1339*	*1550*	*1755*	*1244*
1 s.d. (ng g^{-1})		*42*	*48*	*39*	*47*	*50*	*14*	*36*
Cl (μg g^{-1})		*38*	*290*	*2163*	*292*	*1475*	*1047*	*141*
Cl/K		*0.06*	*0.29*	*0.54*	*0.19*	*0.71*	*0.24*	*0.19*
Stable isotopes								
$\delta^{53/52}Cr_{SRM979}$ (‰)	-0.242	-0.208	-0.186	-0.258	-0.207	-0.254	-0.185	-0.237
2SD/2SE for n= 1	0.010	0.011	0.011	0.011	0.010	0.014	0.011	0.011
n	7	1	1	1	1	6	1	1
Cr (μg g^{-1})†	303	385	218	108	155	55.89	16.12	305
$\delta^{56/54}Fe_{IRMM014}$ (‰)	0.051	0.098	0.106	0.109	0.076	0.137	0.072	0.086
2SD/2SE for n= 1	0.030	0.025	0.024	0.022	0.029	0.023	0.024	0.026
n	1	1	1	1	1	1	1	1
Fe (μg g^{-1})†	67279	62901	84097	82506	87684	95584	101957	70916

Continued on next page

Table B.4.1 – *Continued from previous page*

Sample	267ROV-5	PAC1-CV03-g	PAC1-DR06-g	PAC1-DR10-1g	PAC2-DR05-2g	PAC2-DR20-1	PAC2-DR27-1	PAC2-DR38-1
$\delta^{82/76}Se_{SRM\ 3149}$ (‰)		*-0.19*	*-0.30*	*-0.24*	*-0.06*	*-0.15*	*-0.14*	*-0.16*
2 s.d. (‰)		*0.09*	*0.09*	*0.09*	*0.09*	*0.09*	*0.09*	*0.09*
$\delta^{34}S_{V\text{-}CDT}$ (‰)		*-0.72*	*-0.89*	*-0.14*	*-0.78*	*0.60*	*-0.10*	*-1.12*
1 s.d. (‰)d		*0.02*	*0.05*	*0.03*	*0.04*	*0.10*	*0.08*	*0.02*
$\delta^{98}Mo_{SRM\text{-}3134}$ (‰)		*-0.22*				*-0.15*	*-0.13*	*-0.18*
2 s.d. (‰)		*0.05*				*0.02*	*0.05*	*0.06*

Note: All literature data are shown in italics.
* H_2O content of 267ROV-5 represents loss on ignition value at 1200° C.
† Concentrations from MC-ICP-MS measurements.
Pacifc-Antarctic Ridge: dredging depths and major element data from Vlastélic et al. (2000) and Hamelin et al. (2010); H_2O contents from Clog et al. (2013); Trace element data are from Yierpan et al. (2019); Radiogenic isotope data are from Vlastélic et al. (2000), Moreira et al. (2008) and Hamelin et al. (2010, 2011); S and Cl concentrations and stable S isotope data are from Labidi et al. (2014); Se and Te concentrations and stable Se isotope data are from Yierpan et al. (2019); Stable Mo isotope data are from Bezard et al. (2016).

Bezard, R., Fischer-Gödde, M., Hamelin, C., Brennecka, G.A. and Kleine, T. 2016. The effects of magmatic processes and crustal recycling on the molybdenum stable isotopic composition of Mid-Ocean Ridge Basalts. Earth Planet. Sc. Lett. 453, 171-181.
Clog, M., Aubaud, C., Cartigny, P. and Dosso, L. 2013. The hydrogen isotopic composition and water content of southern Pacific MORB: A reassessment of the D/H ratio of the depleted mantle reservoir. Earth Planet. Sc. Lett. 381, 156-165.
Hamelin, C., Dosso, L., Hanan, B., Barrat, J.A. and Ondreas, H. 2010. Sr-Nd-Hf isotopes along the Pacific Antarctic Ridge from 41 to 53° S. Geophys. Res. Lett. 37, L10303.
Hamelin, C., Dosso, L., Hanan, B.B., Moreira, M., Kositsky, A.P. and Thomas, M.Y. 2011. Geochemical portray of the Pacific Ridge: New isotopic data and statistical techniques. Earth Planet. Sc. Lett. 302, 154-162.
Labidi, J., Cartigny, P., Hamelin, C., Moreira, M. and Dosso, L. 2014. Sulfur isotope budget (^{32}S, ^{33}S, ^{34}S and ^{36}S) in Pacific-Antarctic ridge basalts: A record of mantle source heterogeneity and hydrothermal sulfide assimilation. Geochim. Cosmochim. Ac. 133, 47-67.
Moreira, M.A., Dosso, L. and Ondréas, H. (2008). Helium isotopes on the Pacific-Antarctic ridge (52.5°–41.5°S). Geophysical Research Letters, 35(10).
Vlastelic, I., Dosso, L., Bougault, H., Aslanian, D., Geli, L., Etoubleau, J., Bohn, M., Joron, J.L. and Bollinger, C. 2000. Chemical systematics of an intermediate spreading ridge: The Pacific-Antarctic Ridge between 56° S and 66° S. J. Geophys. Res.-Sol. Ea. 105, 2915-2936.
Yierpan, A., König, S., Labidi, J. and Schoenberg, R. 2019. Selenium isotope and S-Se-Te elemental systematics along the Pacific-Antarctic ridge: Role of mantle processes. Geochim. Cosmochim. Ac. 249, 199-224.

Table B.4.2: Compilation of major and trace element as well as radiogenic isotopic compositions for East-Pacific Ridge glasses from the literature. Dredging depths are given in m below sea level (mbsl). Stable Cr and Fe isotopic compositions determined for this study are given again for completeness of the dataset.

Sample	G128G	G148G	G243G	G258G	G264G	G287G	G312G	G319G	G324G	G343G	G371G	G407G	G412G
Type	N-MORB	N-MORB	N-MORB	N-MORB	N-MORB	N-MORB	N-MORB	N-MORB	N-MORB	N-MORB	N-MORB	N-MORB	T-MORB
Latitude (S)	22°59.35'	21°29.44'	27°46.08'	48°45.26'	29°46.35'	17°23.39'	16°42.51'	16°26.39'	15°46.39'	13°59.12'	11°52.44'	07°23.71'	07°23.69'
Longitude (W)	114°30.77'	114°16.75'	113°16.40'	112°59.24'	111°43.61'	113°11.64'	113°04.10'	113°03.01'	112°56.90'	112°28.79'	110°43.40'	107°47.44'	107°47.43'
Dredging Depth (mbsl)	*3003*	*2764*	*1983*	*2350*	*2500*	*2610*	*2651*	*2674*	*2627*	*2637*	*2598*	*2740*	*2717*
Radiogenic isotopes													
$^{87}Sr/^{86}Sr$	*0.702422*		*0.702569*	*0.702512*	*0.702473*	*0.702642*	*0.702703*	*0.702531*	*0.702411*	*0.702414*	*0.702351*	*0.702635*	*0.702672*
$^{143}Nd/^{144}Nd$	*0.513193*		*0.513125*	*0.513111*	*0.51309*	*0.513117*	*0.51311*	*0.513156*	*0.513208*	*0.513206*	*0.513217*	*0.513102*	*0.51313*
$^{176}Hf/^{177}Hf$													
$^{3}He/^{4}He$ (R/R_A)													
$^{206}Pb/^{204}Pb$	*18.24*		*18.665*	*18.524*	*18.601*	*18.634*	*18.619*	*18.275*	*18.085*	*18.138*	*18.064*	*18.41*	*18.566*
$^{207}Pb/^{204}Pb$	*15.496*		*15.519*	*15.503*	*15.54*	*15.504*	*15.526*	*15.457*	*15.422*	*15.552*	*15.42*	*15.496*	*15.496*
$^{208}Pb/^{204}Pb$	*37.688*		*38.059*	*37.917*	*38.033*	*38.13*	*38.236*	*37.734*	*37.499*	*37.57*	*37.466*	*37.95*	*18.092*
Major elements (wt. %)													
SiO_2	*50.9*	*51.2*	*49.9*	*49.7*	*50.7*	*50.0*	*50.4*	*50.5*	*50.4*	*50.4*	*49.9*	*50.6*	*50.8*
TiO_2	*0.93*	*1.80*	*2.00*	*3.16*	*1.62*	*1.48*	*1.38*	*1.46*	*2.27*	*1.55*	*1.28*	*2.33*	*1.84*
Al_2O_3	*15.6*	*14.1*	*13.8*	*12.3*	*14.2*	*14.6*	*15.1*	*14.9*	*13.5*	*14.7*	*15.6*	*13.2*	*14.0*
FeO_T	*8.66*	*11.4*	*12.6*	*16.1*	*10.9*	*10.0*	*9.81*	*10.0*	*12.8*	*10.3*	*9.18*	*13.7*	*11.2*
Fe_2O_3	*0.65*	*2.37*	*2.43*	*2.71*	*1.84*	*1.41*	*1.42*	*1.72*	*2.42*	*1.73*	*1.49*	*2.65*	*2.55*
FeO	*8.08*	*9.24*	*10.4*	*13.7*	*9.23*	*8.72*	*8.53*	*8.44*	*10.6*	*8.70*	*7.84*	*11.3*	*8.86*
MnO	*0.16*	*0.21*	*0.22*	*0.27*	*0.20*	*0.19*	*0.18*	*0.18*	*0.22*	*0.18*	*0.17*	*0.24*	*0.20*
MgO	*9.00*	*7.19*	*6.61*	*4.87*	*7.35*	*7.82*	*8.17*	*8.00*	*6.41*	*7.69*	*8.07*	*5.94*	*7.05*
CaO	*12.7*	*11.2*	*11.2*	*8.91*	*11.7*	*12.1*	*12.0*	*12.0*	*10.6*	*11.7*	*12.2*	*10.0*	*11.2*
Na_2O	*2.18*	*2.79*	*2.89*	*3.19*	*2.62*	*2.43*	*2.41*	*2.49*	*2.82*	*2.72*	*2.69*	*3.01*	*2.88*
K_2O	*0.03*	*0.07*	*0.14*	*0.23*	*0.08*	*0.08*	*0.09*	*0.07*	*0.14*	*0.12*	*0.08*	*0.16*	*0.30*
P_2O_5	*0.07*	*0.15*	*0.17*	*0.38*	*0.12*	*0.12*	*0.11*	*0.11*	*0.20*	*0.14*	*0.11*	*0.21*	*0.21*
CO_2	*0.03*	*0.06*	*0.04*	*0.05*	*0.05*	*0.04*	*0.04*	*0.05*	*0.05*	*0.04*	*0.03*	*0.04*	*0.03*
H_2O^*	*0.10*	*0.22*	*0.28*	*0.48*	*0.29*	*0.23*	*0.17*	*0.21*	*0.33*	*0.25*	*0.17*	*0.34*	*0.31*
Trace elements ($\mu g\ g^{-1}$)													
Li													

Continued on next page

Table B.4.2 – *Continued from previous page*

Sample	G128G	G148G	G243G	G258G	G264G	G287G	G312G	G319G	G324G	G343G	G371G	G407G	G412G
Be	*0.18*	*0.55*											
Sc													
Ti													
V													
Cr	*394*	*179*	*138*	*84*	*215*	*363*	*297*	*339*	*149*	*281*	*315*	*71*	*199*
Co	*42*	*56*	*53*	*54*	*49*		*46*	*45*	*48*	*44*	*43*	*53*	
Ni	*108*	*61*	*53*	*28*	*65*	*84*	*95*	*95*	*52*	*82*	*92*	*33*	*55*
Cu													
Zn	*68*	*107*	*107*	*160*	*91*	*86*	*79*	*82*	*115*	*86*	*73*	*123*	*101*
Ga	*16*		*18*	*20*	*17*	*17*	*16*	*16*	*18*	*16*	*16*	*20*	*17*
Rb													
Sr	*75*	*92*	*123*	*112*	*100*	*102*	*103*	*99*	*99*	*119*	*133*	*110*	*141*
Y	*25*	*37*	*40*	*74*	*36*	*33*	*30*	*3*	*50*	*33*	*28*	*50*	*41*
Zr	*56*		*136*	*283*	*106*	*99*	*90*	*101*	*164*	*108*	*96*	*166*	*135*
Nb													
Mo													
Cd													
Sn													
Sb													
Cs													
Ba													
La	*1.1*			*9.5*	*3.1*	*2.8*	*2.5*		*4.4*	*3.2*	*2.4*	*4.7*	*6.2*
Ce	*4.4*			*38*	*12*	*12*	*9.3*		*18*	*12*	*10*	*19*	*19*
Pr													
Nd	*4.9*			*25*	*9.3*	*8.8*	*7.6*		*14*	*9*	*7.7*	*14*	*12*
Sm	*1.8*			*6.7*	*2.9*	*2.8*	*2.5*		*4.3*	*2.9*	*2.4*	*4.4*	*3.9*
Eu	*0.82*			*2.46*	*1.12*	*1.14*	*1*		*1.65*	*1.1*	*0.92*	*1.6*	*1.47*
Gd	*3.3*			*9*	*4.5*	*4.1*	*4.1*		*6.3*	*4.3*	*3.7*	*6.5*	*4.6*
Tb													
Dy	*4*			*12*	*5.7*	*5.5*	*5.1*		*8.7*	*5.2*	*4.6*	*8.6*	*6.4*
Ho	*0.86*			*2.64*	*1.12*	*1.11*	*1.05*		*1.71*	*1.02*	*0.89*	*1.65*	*1.3*

Continued on next page

Table B.4.2 – *Continued from previous page*

Sample	G128G	G148G	G243G	G258G	G264G	G287G	G312G	G319G	G324G	G343G	G371G	G407G	G412G
Er	*2.8*			*7.6*	*3.7*	*3.5*	*3.2*		*2.5*	*3.5*	*2.9*	*5.4*	*4.1*
Tm													
Yb	*2.6*			*6.6*	*3.3*	*3.1*	*2.9*		*5*	*3.1*	*2.6*	*4.8*	*3.5*
Lu	*0.4*			*1.14*	*0.51*	*0.5*	*0.45*		*0.78*	*0.49*	*0.41*	*0.75*	*0.57*
Hf													
Ta													
W													
Tl													
Pb													
Th													
U													
Se (ng g^{-1})													
1 s.d. (ng g^{-1})													
Te (ng g^{-1})													
1 s.d. (ng g^{-1})													
S (μg g^{-1})	*900*	*1300*	*1500*	*2000*	*1300*	*1200*	*1200*	*1100*	*1700*	*1300*	*1000*	*1500*	*1500*
1 s.d. (ng g^{-1})													
Cl (μg g^{-1})													
Cl/K													
Stable isotopes													
$\delta^{53/52}Cr_{SRM979}$ (‰)	-0.253	-0.248	-0.233	-0.202	-0.242	-0.259	-0.272	-0.248	-0.241	-0.207	-0.222	-0.278	-0.085
2SD/2SE for n= 1	0.020	0.012	0.020	0.006	0.021	0.015	0.024	0.021	0.013	0.023	0.024	0.019	0.024
n	7	7	7	5	6	7	7	7	8	7	7	6	9
Cr (μg g^{-1})†	411	183	98.59	20.45	184	320	272	328	103	251	324	23.97	159
$\delta^{56/54}Fe_{IRMM014}$ (‰)	0.045	0.100	0.106	0.123	0.110	0.119	0.046	0.032	0.121	0.096	0.073	0.067	0.088
2SD/2SE for n= 1	0.037	0.026	0.041	0.017	0.035	0.025	0.025	0.024	0.021	0.023	0.023	0.023	0.025
n	5	5	5	5	5	5	1	1	1	1	1	1	1
Fe (μg g^{-1})†	62389	82094	100627	108615	78077	75601	70899	74333	93363	74941	69339	100424	82170

Note: All literature data are shown in italics. Sample locations, dredging depths, major, trace and radiogenic isotope data are from Bach et al. (1994).
† Concentrations from MC-ICP-MS measurements.

Appendix C

Appendix Chapter 4
Heterogeneous Cr and Fe isotope compositions of Earth's silicate mantle: Constraints from intraplate basalts

C.1 Cr isotope measurements

Due to a failing MQ system at the day of chemical separation of Cr from the matrix, blank contribution for one batch of Réunion and French Polynesian samples was exceptional high and contributed 2 % of the total processed Cr (i.e., 40 ng Cr blank contribution on 2000 ng processed Cr). Following, a second aliquot from the prepared stock solution was taken and chemically purified via the three-column chromatography again, with standard blank contribution of 8 ng. This Cr cut was measured two times in two separate measurement sessions and compared with the high blank Cr cut in Figure C.2.10. Although it should be noted that low blanks are a prerequisite for successful Cr isotope data in this case repeated measurements show that samples with high blanks reproduce within external reproducibility of ± 0.022 ‰. Only one measurement of sample REU-14-57 with high blank contribution seems to be offset, although still within reproducibility, compared to the two replicate measurements of REU-14-57 with low blank contribution. However, this variability may be due to analytical variability as replicate measurements for samples FP5TU1 and FP2RU2 indicate. Both times, replicates with low blanks are offset compared to the other two replicate measurements including the replicate with high blank contribution. However, in general all replicate measurements are indistinguishable within the reported reproducibility.

C.2 Supplementary Figures and Tables

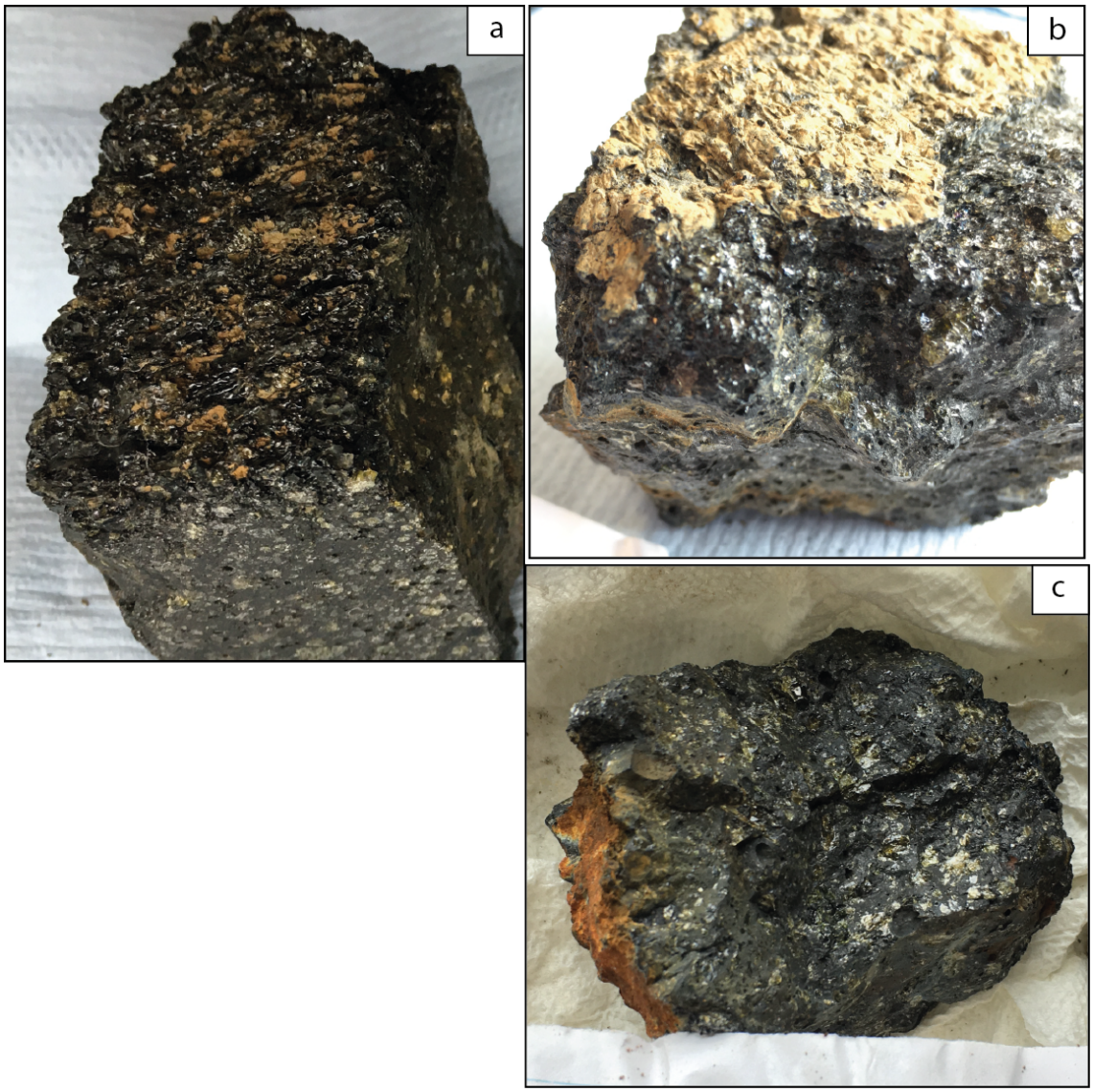

Figure C.2.1: Highly olivine-bearing samples from Lō'ihi, Hawaii: **a)** J2-246-R3D; **b)** J2-309-R1-B from the low -temperature hydrothermal site called Ula Nui at the southern rift zone; **c)** J2-307-R2-C. All three samples show large olivine phenocrysts in the whole-rock matrix and within the quenched glass. Variable, but in general thin, sediment covers are also observed. All samples are approximately 7 cm in size.

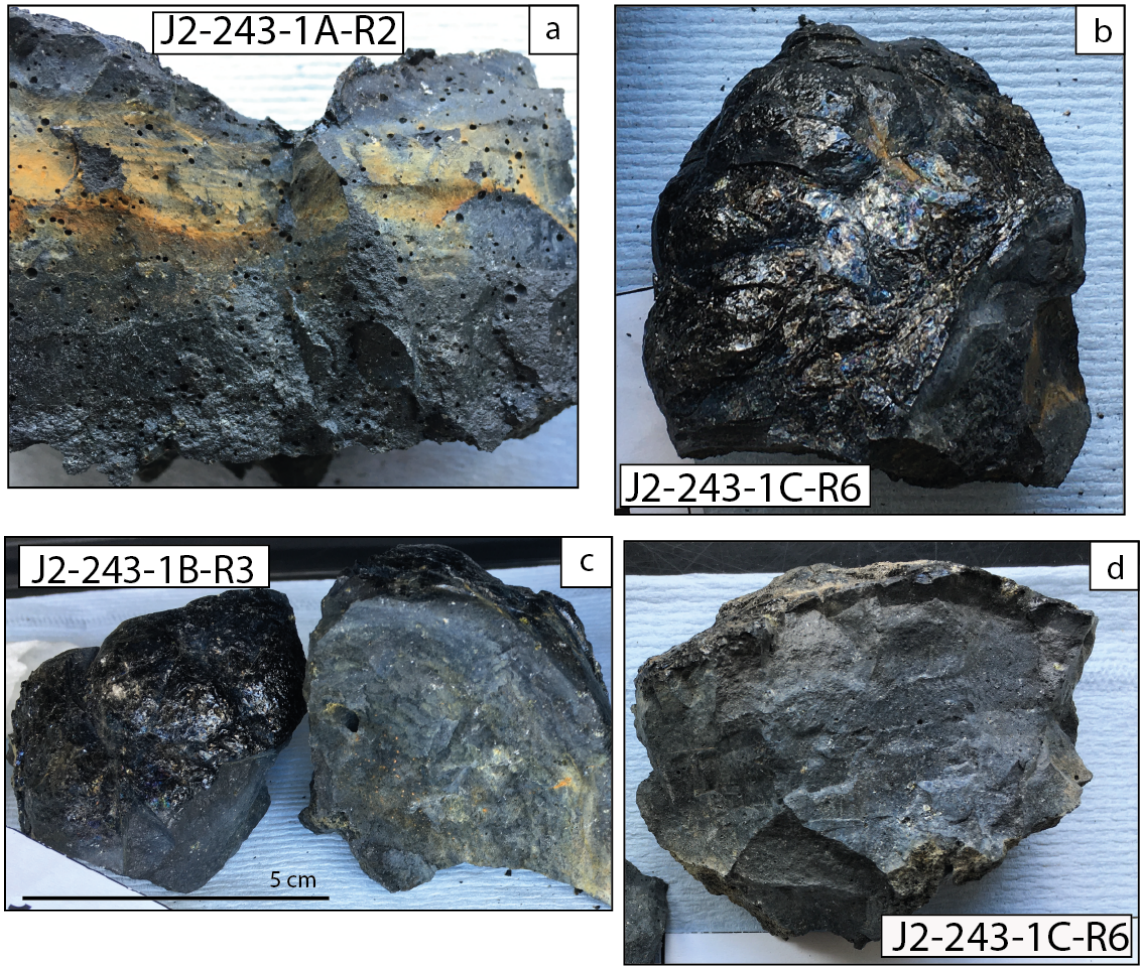

Figure C.2.2: Sparsley olivine-bearing to aphyric samples from Lō'ihi, Hawaii: **a)** J2-243-1A-R2 – mostly aphyric matrix with some plagioclase phenocrysts visible, thin glassy crust on top of fresh basalt within Fe oxidation seen on surface. Sample is 15 cm in size with photo showing a 10 cm wide sample section; **b)** J2-243-1C-R6 - view of the very fresh quenched glass. Sample is 7 cm in size; **c)** J2-243-1B-R3 - pillow structured basalt with relatively thick quenched glassy crust. Sample is 5cm in size; **d)** J2-243-1C-R6 - view of aphyric fine-grained matrix of pillow basalt.

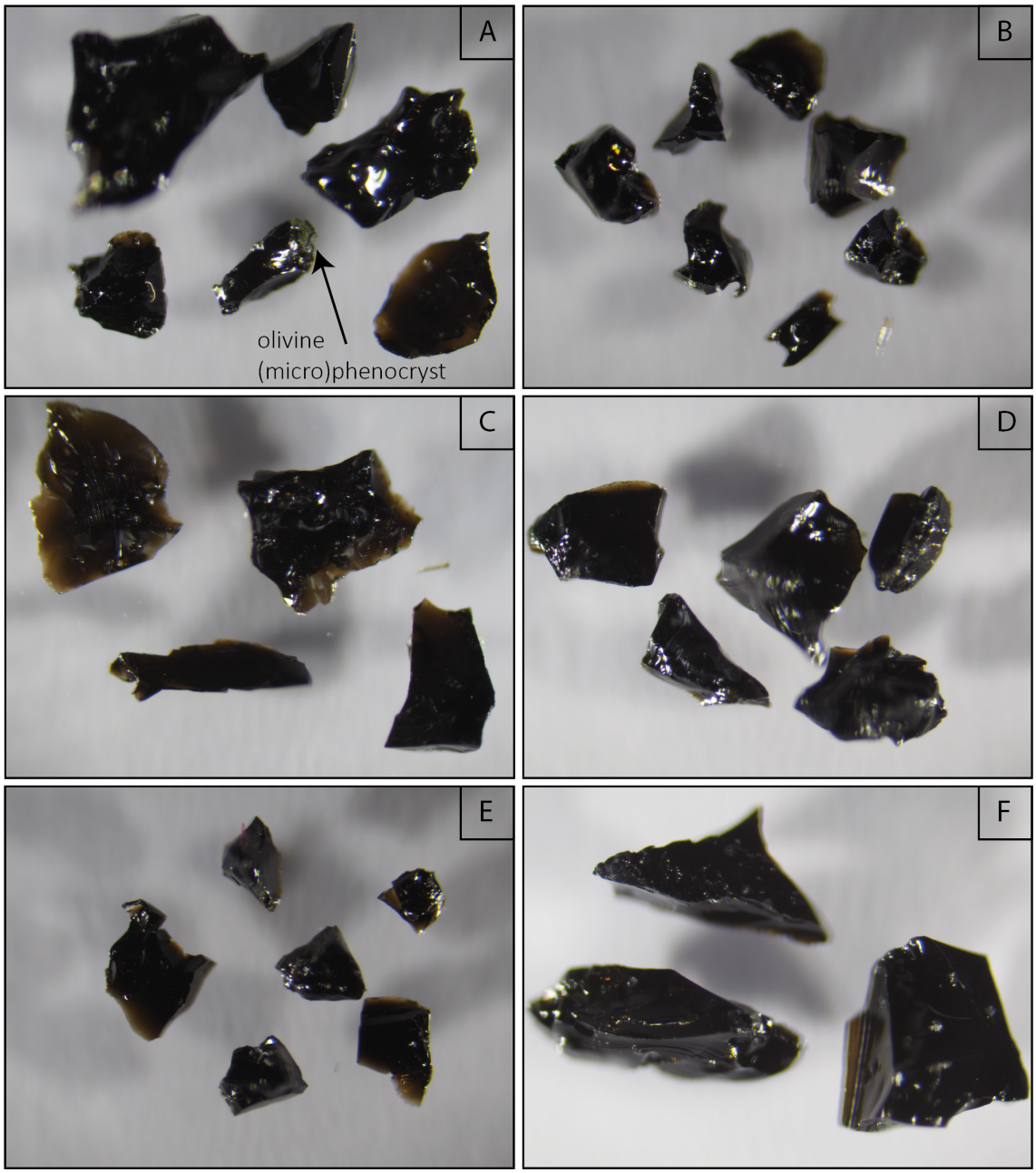

Figure C.2.3: Selection of handpicked and cleaned glass chips of Lō'ihi basalts. Individual glass chips are 0.5 to 1 mm wide. **A)** J2-309-R1 and **B)** J2-307-R2-C, both highly olivine-phyric basalts. In A. olivine phenocryst is visible in the center piece. **C)** J2-243-1B-R3, **D)** J2-243-1J-R20, **E)** J2-243-1C-R6, **F)** J2-241-2-R9, C. to F. represent sparsley olivine-phyric to aphyric basalts.

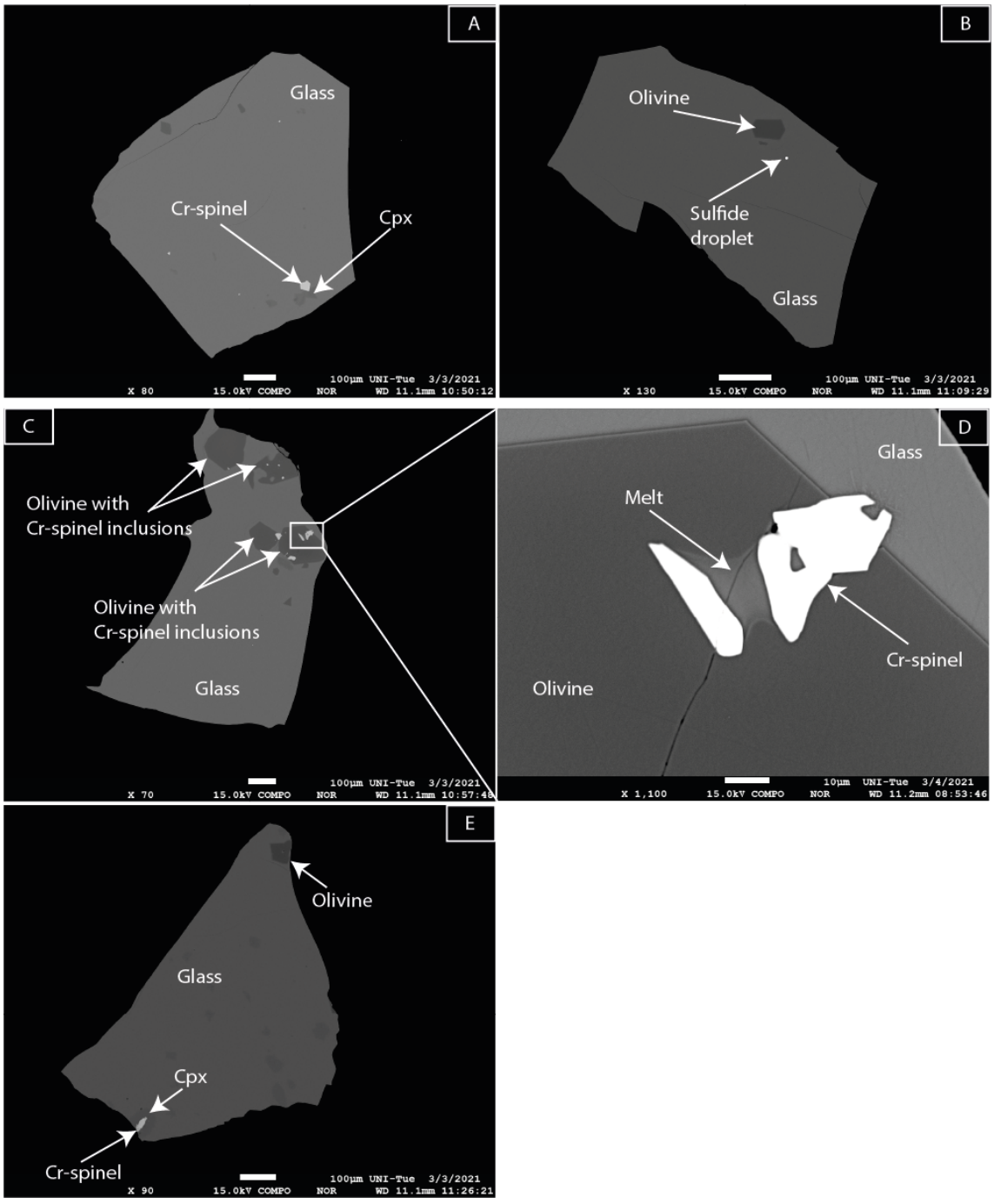

Figure C.2.4: Backscattered electron images of glass chips of sample J2-243-1C-R6. **A)** Relatively homogenous glass with Cr-spinel and Clinopyroxene (Cpx) microphenocrysts indicating concurrent growth; **B)** Homogenous glass with large, idiomorphic, unzoned olivine microphenocryst and small sulfide droplet; **C)** Glass chip with many olivine microphenocrysts with Cr-spinel inclusions. White rectangle represents zoom-in shown in **D)** Cr-spinel inclusion present in olivine. Melt is present in between Cr-spinel crystals, which was not replaced by olivine growth based on good adhesion of the melt to the Cr-spinel crystal. **E)** Olivine microphenocryst as well as Cr-spinel microphenocryst surrounded by incipient Cpx growth indicating rapid quenching.

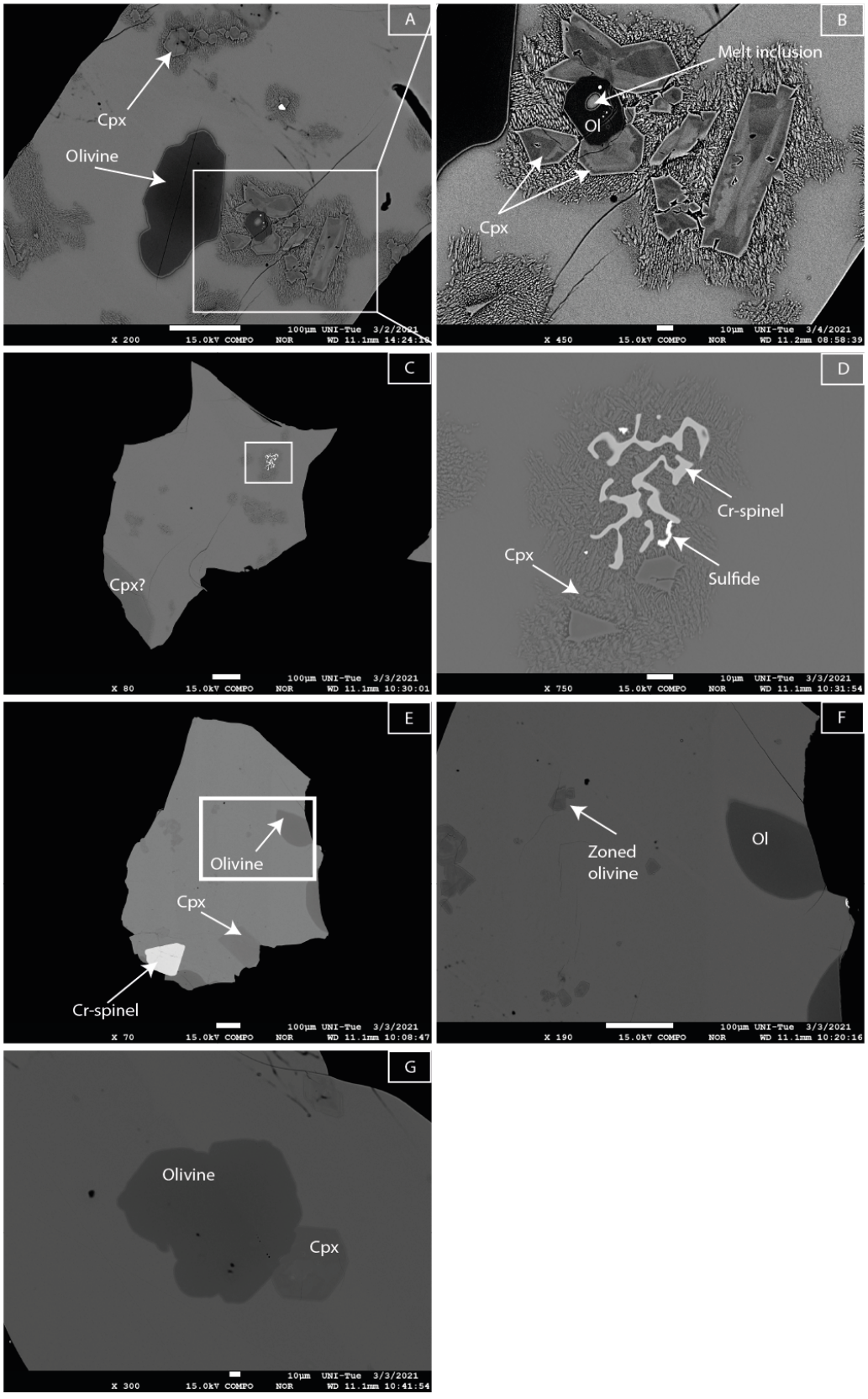

Figure C.2.5: Backscattered electron images of glass chips of sample J2-246-R3D. **A)** Relative heterogeneous glass chip with large idiomorphic olivine microphenocrysts adjacent to clinopyroxenes (Cpx) and smaller olivine microphenocrysts with Cr-spinel inclusions shown as a zoom-in in **B)** Olivine microphenocrysts with melt and Cr-spinel inclusion. Cpx microphenocrysts are zoned; **C)** Glass chip with large Cpx microphenocryst in left corner and skeletal Cr-spinel and sulfide surronded by Cpx microphenocrysts shown in more detail in **D)** Skeletal habitus of Cr-spinel indicates fast growth and heterogenous nucleation probably caused by quenching; **E)** Glass chip with olivine, Cpx and large Cr-spinel microphenocrysts. Cpx is homogenous and does not show zoning. More detail is shown in **F)** Small olivine microphenocrysts are often zoned; **G)** Cpx microphenocryst grew on surface of olivine microphenocryst indicating a crystallization sequence of olivine followed by Cpx.

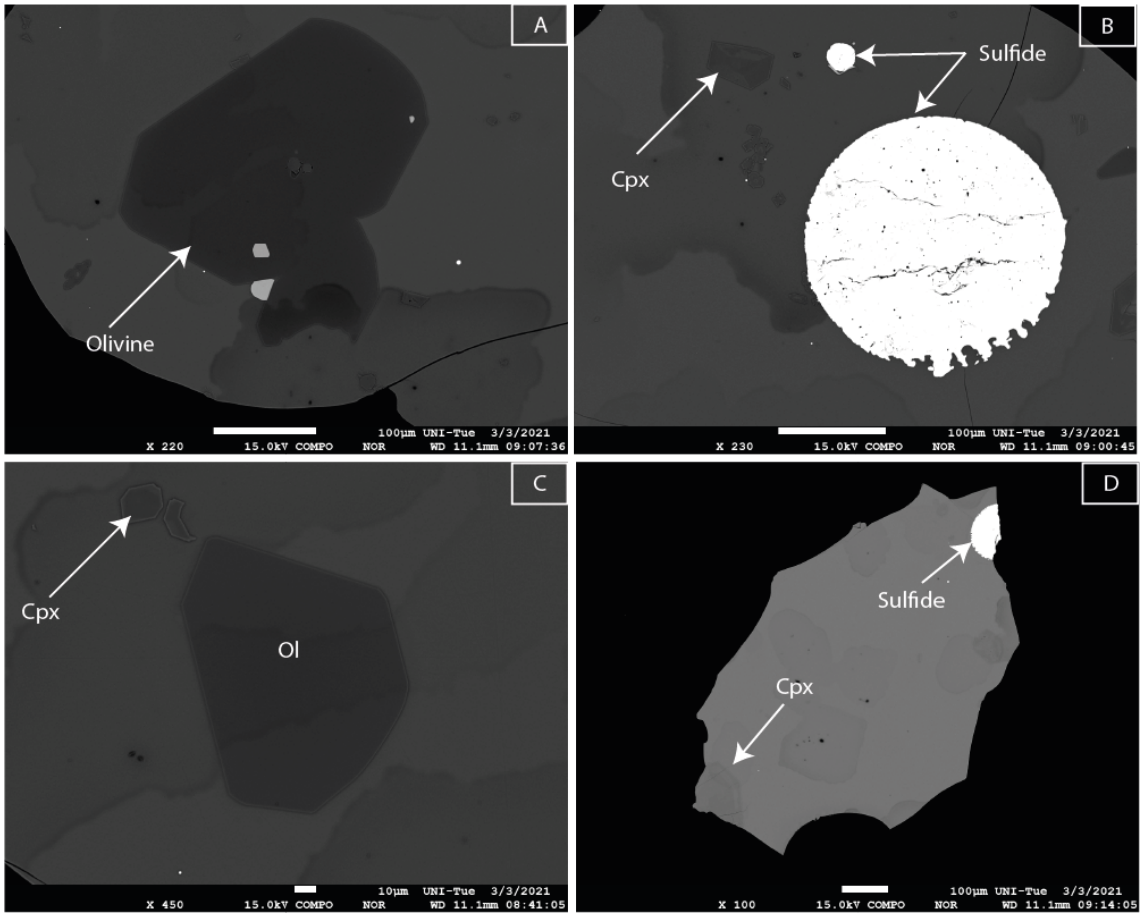

Figure C.2.6: Backscattered electron images of glass chips of sample J2-307-R2C. **A)** Large idiomorphic olivine microphenocryst with Cr-spinel inclusions; **B)** Large and smaller sulfide droplets adjacent to Cpx microphenocrysts with augitic composition. **C)** Glass chip with olivine and Cpx microphenocrysts not indicating any particular crystallization sequence; **D)** Sulfide and Cpx microphenocrysts. Stains in A.-D. from acetone used for surface cleaning before analyses.

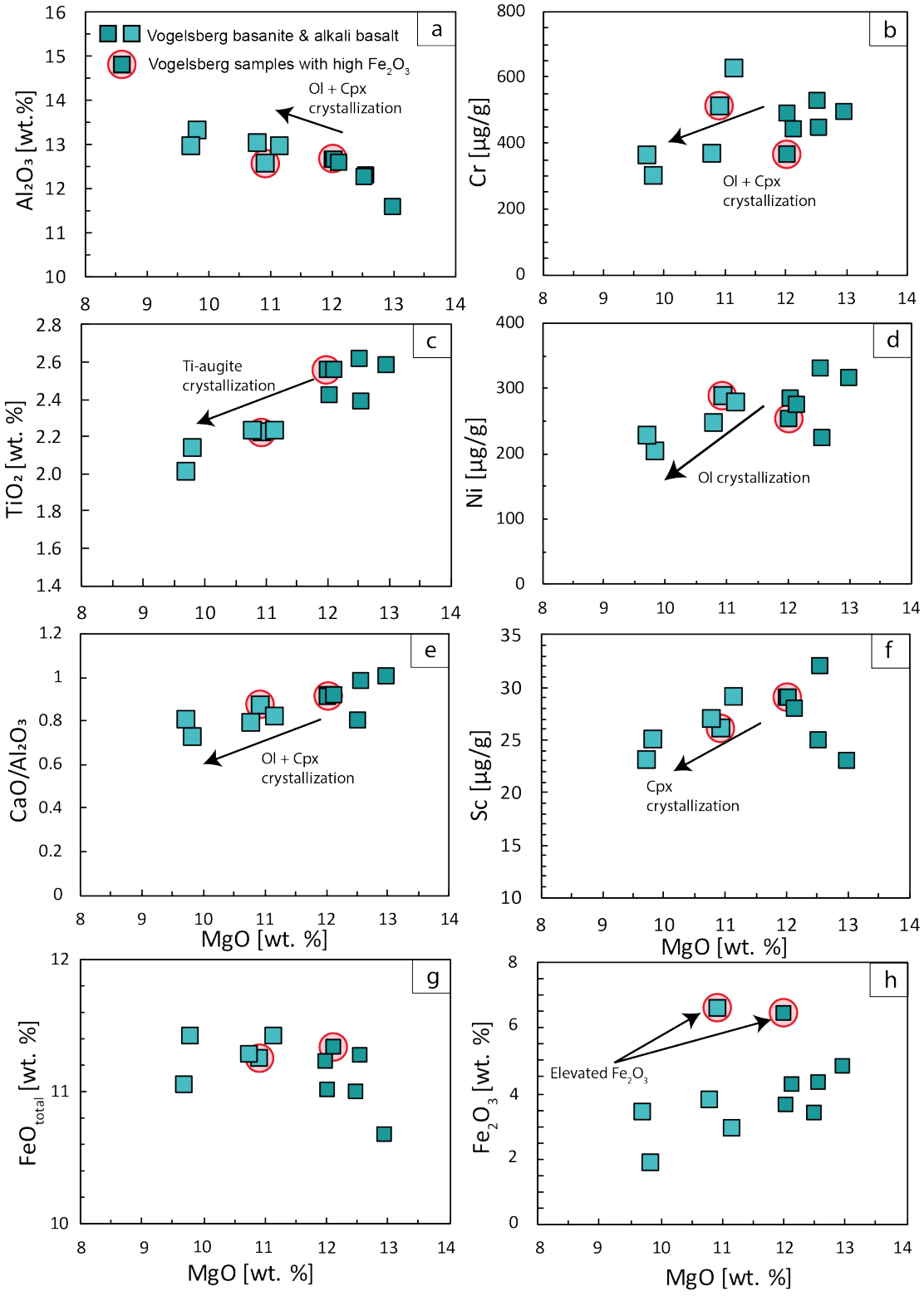

Figure C.2.7: **a) - f)** Major element variations for Vogelsberg volcanics from (Bogaard and Wörner, 2003). Alkali basalts have overall lower MgO (and SiO_2) contents compared to near-primary basanites, which indicates greater fractionation of phases such as olivine (Ol) and Ti-rich augite (Ti-augite or Cpx) in alkali basalts (Bogaard and Woerner, 2003) indicated by arrows. **h)** Two samples have elevated Fe_2O_3 and low FeO (not shown), but show negligible total FeO loss in **g)**. These two samples are highlighted by red eclipse in a) to h) and also Figures 4.14 and 4.15.

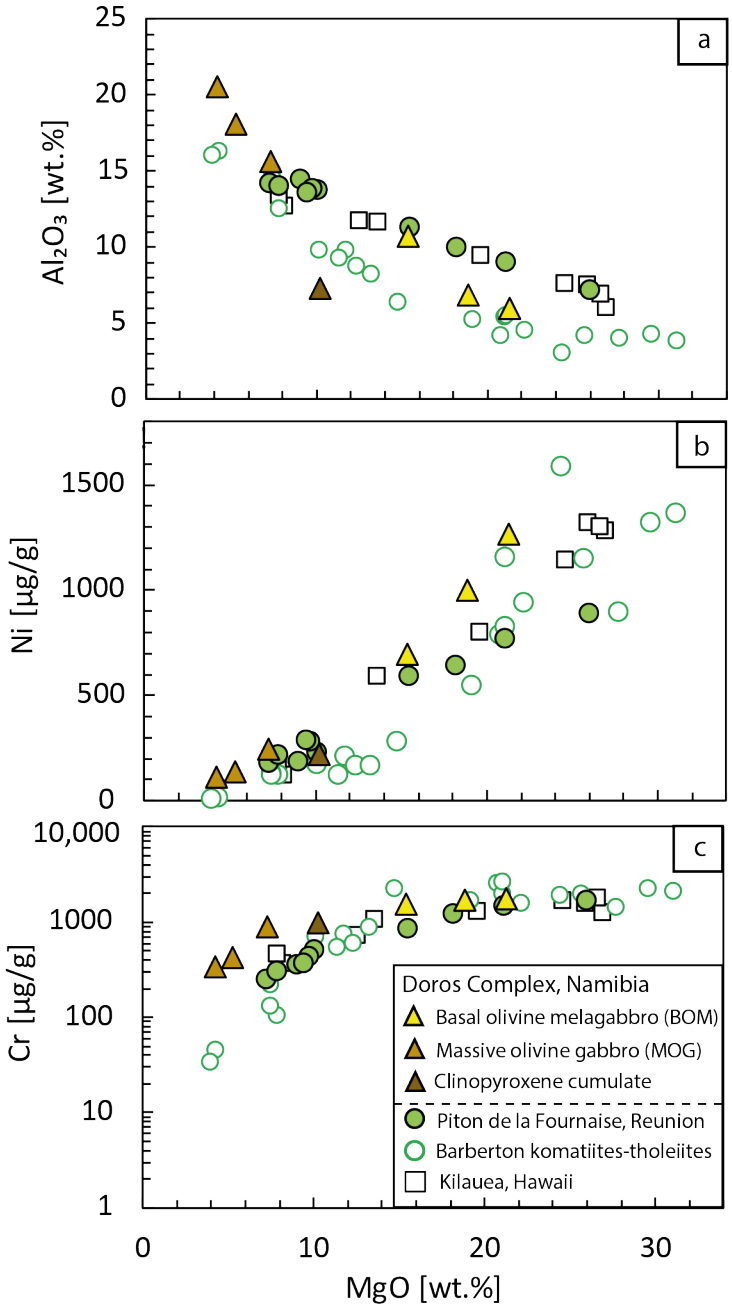

Figure C.2.8: Major element variations for Doros Complex intrusive rocks, i.e., basal olivine melagabbros and massive olivine gabbros and one clinopyroxene cumulate. Also shown are major element variations of Piton de la Fournaise basalts, Réunion as well as the komatiite-tholeiite suite from the Barberton greenstone belt (Wagner et al., 2021; Chapter 3). Also shown are Kilauea Iki lava lake samples used by Shen et al. (2020) for Cr isotopic meaurements with major element variations from Helz (1987). Major elements for Doros Complex intrusives from Owen-Smith and Ashwal (2015).

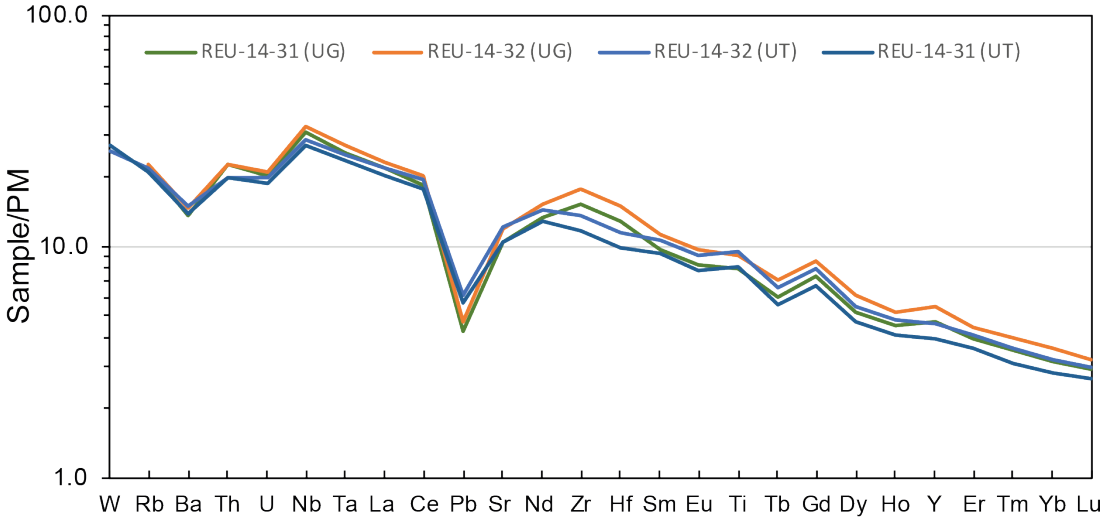

Figure C.2.9: Comparison of Primitive Mantle (PM)-normalized trace element patterns for two samples, REU-14-31 and REU-14-32, measured at the University of Goettingen (UG) and University of Tuebingen (UT). Primitive Mantle values after Palme and O'Neill (2014).

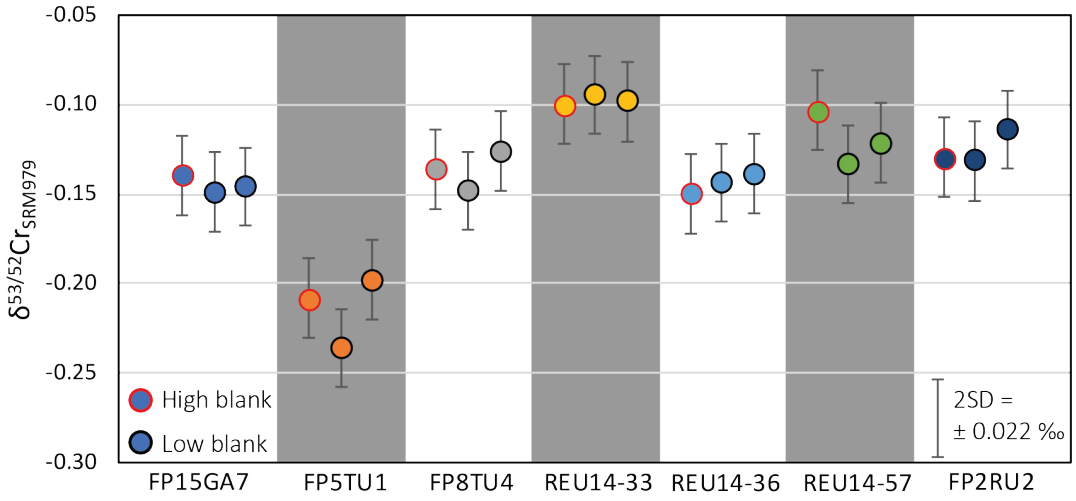

Figure C.2.10: Compilation of single measurements for samples, which experienced high blank contribution (highlighted in red for each sample), compared to a replicate with low blank contribution measured two times in two different sessions. Samples with unusual high blank cannot be distinguished within the long-term reproducibility of ± 0.022 ‰ represented by the error bars for each measurement.

Table C.2.1: Mean Q-ICP-MS abundance data (wt. %) and uncertainty (± r.s.d) for two rock powder reference materials (BIR-1a, BHVO-2) measured at the University of Tuebingen (UT) over the course of this study and compared with recommended values. Moreover, one sample previously measured by XRF at the University of Tuebingen and compared with values from Q-ICP-MS is also shown.

Sample	**BIR-1a**					**BHVO-2**					**SO267-ROV5**	
Source	**UT**		**GeoReM***		**UT/GeoReM**	**UT**		**GeoReM***		**UT/GeoReM**	**UT**	**UT (XRF)**
	Average	%RSD	Value	2SD	Ratio	Average	%RSD	Value	2SD	Ratio		
# digestions	3					2						
# analyses	4					2						
SiO_2			47.79	0.16				49.6	0.14			49.17
Al_2O_3	15.39	1.52	15.51	0.07	0.99	13.71	0.46	13.44	0.06	1.02	15.32	15.08
Fe_2O_{3T}	11.22	1.69	11.4	0.05	0.98	12.36	0.42	12.39	0.09	1.00	8.09	9.56
MnO	0.17	1.49	0.1731	0.0016	0.98	0.17	0.56	0.169	0.0019	0.99	0.17	0.19
MgO	9.49	1.58	9.689	0.052	0.98	7.29	0.54	7.257	0.042	1.00	8.26	8.37
CaO	12.93	1.30	13.29	0.06	0.97	11.28	0.04	11.40	0.06	0.99	11.99	11.93
Na_2O	1.75	1.61	1.832	0.022	0.96	2.20	0.69	2.219	0.048	0.99	2.65	2.69
K_2O	0.03	24.94	0.029	0.003	0.95	0.50	1.02	0.513	0.0037	0.97	0.08	0.05
TiO_2	0.94	2.11	0.9587	0.0066	0.98	2.72	0.15	2.731	0.018	1.00	0.53	1.17
P_2O_5	0.03	20.68	0.03	0.0043	0.98	0.30	0.97	0.2685	0.005	1.12	0.06	0.10

* GeoReM values are recommended values after Jochum et al. (2016)[a]. All major oxide data in Jochum et al. (2016) are derived byx-ray fluorescence (XRF).

[a]Jochum, K.P., Weis, U., Schwager, B., Wilson, S.A., Haug, G.H., Andreae, M.O. and Enzweiler, J. 2016. Reference Values following ISO guidelines for Frequently Requested Rock Reference Materials. Geostandards and Geoanalytical Research. 40, 333-350.

Table C.2.2: Mean Q-ICP-MS abundance data (ng g^{-1}) and uncertainty ± r.s.d) for two rock powder reference materials (BIR-1a, BHVO-2) measured at the University of Tuebingen (UT) over the course of this study and compared with recommended values.

Standard	**BIR-1a**				**BHVO-2**			
Source	**University Tuebingen this study**		**GeoReM***		**University Tuebingen this study**		**GeoReM***	
	Average	**%RSD**	Value	UT/GeoReM	**Average**	**%RSD**	Value	UT/GeoReM
# digestion	4				3			
# analyses	5				4			
Li	3120	0.3	3203	0.97	4487	0.3	4500	1.00
Be	90	5.4	102	0.88	1010	3.1	1076	0.94
Sc	44806	0.5	43210	1.04	32343	0.6	31830	1.02
Ti	5832600	1.2	5746000	1.02	16685000	0.4	16370000	1.02
V	328920	0.9	320600	1.03	320925	0.1	318200	1.01
Cr	413800	1.3	392900	1.05	300775	0.7	287200	1.05
Co	52966	0.5	52220	1.01	44940	0.2	44890	1.00
Ni	169740	0.6	168900	1.00	117450	0.5	119800	0.98
Cu	118200	0.9	120700	0.98	124600	0.4	129300	0.96
Zn	71462	1.2	70400	1.02	101375	1.6	103900	0.98
Ga	15418	0.7	15460	1.00	20845	0.4	21370	0.98
Rb	195	2.9	210	0.93	9133	0.4	9261	0.99
Sr	108800	0.5	108600	1.00	393375	0.6	394100	1.00
Y	14748	0.5	15600	0.95	24368	0.4	25910	0.94
Zr	14436	0.8	14800	0.98	168550	0.5	171200	0.98
Nb	538	0.8	553	0.97	18393	0.3	18100	1.02
Cd	60	1.8	77	0.77	114	2.2	152	0.75
Sn	841	7.5	701	1.20	1911	6.5	1776	1.08
Cs	5	4.0	6	0.76	96	1.2	99.6	0.96
Ba	6451	0.4	6750	0.96	130100	0.2	130900	0.99
La	598	0.3	627	0.95	14998	0.1	15200	0.99
Ce	1888	0.7	1920	0.98	37170	0.1	37530	0.99
Pr	374	0.4	372	1.01	5324	0.3	5339	1.00
Nd	2353	0.6	2397	0.98	24075	0.5	24270	0.99

Continued on next page

Table C.2.2 – *Continued from previous page*

Standard	**BIR-1a**				**BHVO-2**			
Source	**University Tuebingen**		**GeoReM***		**University Tuebingen**		**GeoReM***	
Sm	1093	0.4	1113	0.98	6026	0.4	6023	1.00
Eu	518	0.3	520	1.00	2038	0.4	2043	1.00
Tb	363	0.5	1809	0.20	928	0.6	6207.0	0.15
Gd	1865	0.4	362	5.15	6172	0.6	939.2	6.57
Dy	2548	0.8	2544	1.00	5207	0.8	5280	0.99
Ho	583	0.4	572	1.02	993	0.6	988.7	1.00
Er	1695	0.5	1680	1.01	2485	0.6	2511	0.99
Tm	258	0.5	256	1.01	336	0.8	334.9	1.00
Yb	1651	0.3	1631	1.01	1937	0.3	1994	0.97
Lu	247	1.0	248	0.99	268	0.5	275.4	0.97
Hf	566	0.8	582	0.97	4292	0.4	4470	0.96
Ta	35	1.7	41	0.84	1145	0.6	1154	0.99
Tl	2	8.2	2	0.86	20	1.1	22.4	0.91
Pb	3139	8.3	3037	1.03	1684	11.6	1653	1.02
Th	29	0.6	33	0.89	1199	0.2	1224	0.98
U	10	1.4	11	0.98	427	1.0	412	1.04

* GeoReM values are recommended values after Jochum et al. (2016)[a].

[a]Jochum, K.P., Weis, U., Schwager, B., Wilson, S.A., Haug, G.H., Andreae, M.O. and Enzweiler, J. 2016. Reference Values following ISO guidelines for Frequently Requested Rock Reference Materials. Geostandards and Geoanalytical Research. 40, 333-350.

Table C.2.3: Mean Q-ICP-MS abundance data (μg g^{-1}) for two samples from Reunion (REU-14-31 and REU-14-32) measured at the University of Tuebingen (UT) and at the University of Goettingen (UG). Reproducibility is shown as the ratio of the two values measured at each laboratory.

Sample	**REU-14-31**			**REU-14-32**		
Source	UT	UG	UT/UG	UT	UG	UT/UG
$\mu g\ g^{-1}$			ratio			ratio
Li	3.993	4.44	0.90	4.266	4.73	0.90
Be	0.714			0.802		
Sc	23.32	28.96	0.81	24.51	30.98	0.79
Ti	10250			11960		
V	209.8			228.8		
Cr	1554			1292		
Co	95.46	94.34	1.01	85.48	84.82	1.01
Ni	772.1	751.55	1.03	644.9	649.71	0.99
Cu	63.66	74.76	0.85	68.72	81.71	0.84
Zn	100.9	101.84	0.99	104.0	107.99	0.96
Ga	12.89	12.4	1.04	14.89	14.5	1.03
Rb	12.63	13.31	0.95	13.05	13.75	0.95
Sr	230.6			265.3		
Y	16.36	19.3	0.85	19.03	22.42	0.85
Zr	119.8	156.61	0.76	140.8	183.3	0.77
Nb	16.21	18.42	0.88	17.25	19.46	0.89
Mo	1.044			1.077		
Cd	0.083	0.06	1.38	0.095	0.08	1.19
Sn	1.240	1.27	0.98	1.455	1.54	0.94
Sb	0.05	0.06	0.87	0.056	0.06	0.93
Cs	0.183	0.18	1.01	0.191	0.2	0.96
Ba	95.38	93.33	1.02	102.0	99.62	1.02
La	13.77	14.72	0.94	14.81	15.8	0.94
Ce	30.79	32.08	0.96	33.72	35.17	0.96
Pr	4.033	4.24	0.95	4.491	4.75	0.95
Nd	17.01	17.95	0.95	19.38	20.51	0.94
Sm	4.011	4.2	0.96	4.648	4.91	0.95
Eu	1.317	1.38	0.95	1.529	1.62	0.94
Tb	0.605	0.65	0.93	0.715	0.76	0.94
Gd	3.981	4.31	0.92	4.681	5.04	0.93
Dy	3.432	3.77	0.91	4.001	4.43	0.90
Ho	0.662	0.72	0.92	0.772	0.83	0.93
Er	1.684	1.85	0.91	1.947	2.1	0.93
Tm	0.231	0.24	0.96	0.265	0.27	0.98
Yb	1.357	1.51	0.90	1.538	1.71	0.90
Lu	0.190	0.21	0.91	0.213	0.23	0.92
Hf	2.952	3.86	0.76	3.454	4.51	0.77
Ta	1.007	1.09	0.92	1.069	1.17	0.91
W	0.326			0.310		
Tl	0.023			0.021		
Pb	1.047	0.8	1.31	1.126	0.87	1.29
Th	1.674	1.9	0.88	1.690	1.93	0.88
U	0.430	0.46	0.93	0.450	0.48	0.94

Table C.2.4: Radiogenic Sr and Nd isotope composition of rock reference materials BHVO-2 and BIR-1a measured during the course of this study. The average and 2SD is given for BHVO-2, which has been measured two times on two separate digests.

Rock standard	$^{87}Sr/^{86}Sr$	2SE	$^{143}Nd/^{144}Nd$	2SE
BHVO-2	0.703500	11	0.512925	16
	0.703493	10	0.512911	
Average (2SD)	**0.703497**	**10**	**0.512918**	**20**
BIR-1a	0.703115	10	0.513030	11

Table C.2.5: Compilation of rock reference materials BHVO-2 and BIR-1a measured since 2018 at the University of Tuebingen. Single runs consist of 90 to 120 cycles with 4.2 s integration time. In-run precision is reported as 2SE and reproducibility of all measurements of each sample is given as 2SD.

digest #	run #	Sample	$\delta^{56/54}Fe_{IRMM014}$ [‰]	2 SE	^{56}Fe [V]
1	1	BHVO-2	0.120	0.019	10.67
1	2	BHVO-2	0.112	0.022	8.93
1	3	BHVO-2	0.089	0.024	8.98
1	4	BHVO-2	0.133	0.022	11.13
2	1	BHVO-2	0.115	0.018	12.42
2	2	BHVO-2	0.084	0.016	12.67
2	3	BHVO-2	0.120	0.018	12.43
2	4	BHVO-2	0.112	0.016	12.45
2	5	BHVO-2	0.110	0.017	12.49
3	1	BHVO-2	0.087	0.025	8.240
3	2	BHVO-2	0.088	0.028	8.53
3	3	BHVO-2	0.102	0.026	8.20
3	4	BHVO-2	0.094	0.022	8.20
3	5	BHVO-2	0.089	0.029	8.18
4	1	BHVO-2	0.131	0.022	10.64
5	1	BHVO-2	0.104	0.025	7.29
6	1	BHVO-2	0.153	0.028	8.56
7	1	BHVO-2	0.075	0.028	7.97
5	1	BHVO-2	0.122	0.025	8.12
8	1	BHVO-2	0.136	0.025	5.75
9	1	BHVO-2	0.141	0.026	5.56
		average	**0.110**		
		2 SD	**0.042**		
		N	***21***		
1	1	BIR-1a	0.054	0.018	11.88
1	2	BIR-1a	0.051	0.016	11.99
1	3	BIR-1a	0.045	0.017	11.93
1	4	BIR-1a	0.057	0.017	11.86
1	5	BIR-1a	0.059	0.017	11.57
2	1	BIR-1a	0.074	0.023	8.53
2	2	BIR-1a	0.056	0.026	8.64
3	1	BIR-1a	0.090	0.020	10.17
3	1	BIR-1a	0.058	0.025	9.67
4	1	BIR-1a	0.041	0.024	8.37
5	1	BIR-1a	0.117	0.027	8.74
6	1	BIR-1a	0.063	0.028	5.63
7	1	BIR-1a	0.080	0.026	5.72
8	1	BIR-1a	0.091	0.028	5.68
		average	**0.067**		
		2 SD	**0.042**		
		N	***14***		

Table C.2.6: Compilation of radiogenic isotope compositions, major element and trace element compositions, and stable Cr and Fe isotopic compositions alongside with Cr concentrations acquired by isotope dilution for samples from La Réunion. Also given are sampling height in m above NN.

Sample	**REU-14-28**	**REU-14-31***	**REU-14-32***	**REU-14-33**	**REU-14-36**	**REU-14-45***	**REU-14-48***	**REU-14-57**	**REU-14-67**	**REU-14-76**
Rock type	Picrite	Picrite	Picrite	SSB	SSB	AbG basalt	AbG basalt	Picrite	AbG basalt	AbG basalt
Latitude	21° 11.345' S	21° 09.647' S	21° 13.175' S	21° 14.259' S	21° 18.056' S	21° 11.948' S	21° 10.931' S	21° 15.724' S	21° 12.615' S	21° 13.227' S
Longitude	55° 38.560' E	55° 49.243' E	55° 48.420' E	55° 47.977' E	55° 48.047' E	55° 34.287' E	55° 35.543' E	55° 47.647' E	55° 38.589' E	55° 40.401' E
Altitude (m NN)	2142	-	100	120	150	1588	1695	179	2332	2394
Radiogenic isotopes										
$^{87}Sr/^{86}Sr$	0.70418	0.70423	0.70418	0.70418	0.70421	0.70425	0.70415	0.70416	0.70419	0.70432
2SE	0.0000097	0.0000105	0.0000094	0.0000093	0.0000095	0.0000102	0.0000092	0.0000100	0.0000087	0.0000099
$^{143}Nd/^{144}Nd$	0.512810	0.512828	0.512817	0.512861	0.512823	0.512811	0.512835	0.512834	0.512820	0.512717
2SE	0.000005	0.000007	0.000009	0.000009	0.000007	0.000006	0.000006	0.000005	0.000006	0.000035
εNd	3.51	3.87	3.65	4.50	3.77	3.52	4.00	3.99	3.71	1.71
$^{206}Pb/^{204}Pb$	18.947	18.939	18.890	18.867	18.928	18.887	18.925	18.886	18.936	18.940
$^{207}Pb/^{204}P$	15.605	15.608	15.601	15.599	15.606	15.596	15.603	15.599	15.604	15.602
$^{208}Pb/^{204}P$	39.036	39.057	38.997	38.974	39.031	38.989	39.018	38.982	39.039	39.054
Major elements (wt. %)										
SiO_2	*46.35*	*45.2*	*45.35*	*49.53*	*48.61*	*47.22*	*47.28*	*43.63*	*47.17*	*46.79*
TiO_2	*2.211*	*1.68*	*1.925*	*2.615*	*2.673*	*2.651*	*2.623*	*1.342*	*2.679*	*2.838*
Al_2O3	*11.35*	*9.01*	*9.98*	*14.23*	*14.01*	*13.81*	*14.49*	*7.17*	*13.87*	*13.62*
FeO_T	*11.93*	*12.75*	*12.40*	*11.20*	*11.25*	*11.86*	*11.80*	*13.55*	*11.90*	*11.89*
MnO	*0.18*	*0.19*	*0.184*	*0.176*	*0.175*	*0.179*	*0.177*	*0.196*	*0.179*	*0.186*
MgO	*15.42*	*21.04*	*18.14*	*7.19*	*7.76*	*9.99*	*8.97*	*25.94*	*9.67*	*9.38*
CaO	*9.24*	*7.5*	*8.13*	*11.24*	*11.31*	*10.07*	*9.37*	*5.8*	*9.69*	*9.77*
Na_2O	*1.91*	*1.61*	*1.87*	*2.62*	*2.62*	*2.57*	*2.89*	*1.25*	*2.67*	*3.08*
K_2O	*0.39*	*0.5*	*0.53*	*0.68*	*0.78*	*0.82*	*0.83*	*0.39*	*0.81*	*1.14*
P_2O_5	*0.246*	*0.203*	*0.235*	*0.306*	*0.322*	*0.333*	*0.383*	*0.164*	*0.354*	*0.509*
LOI	*n.d.*	*n.d.*	*n.d.*	*n.d.*	*n.d.*	*n.d.*	*0.022*	*n.d.*	*n.d.*	*0.046*
Trace elements (μg g^{-1})										
Li	*4.92*	3.993	4.266	*6.01*	*6.18*	5.531	6.473	*3.68*	*5.6*	*7.09*
Be		0.714	0.802			1.168	1.275			
Sc	*31.98*	23.32	24.51	*39.29*	*39.54*	28.93	26.31	*22.18*	*30.27*	*27.37*

Continued on next page

Table C.2.6 – *Continued from previous page*

Sample	REU-14-28	REU-14-31*	REU-14-32*	REU-14-33	REU-14-36	REU-14-45*	REU-14-48*	REU-14-57	REU-14-67	REU-14-76
Ti		10250	11960			16420	16040			
V		209.8	228.8			296.5	266.1			
Cr		1554	1292			533.5	366.0			
Co	*72.69*	95.46	85.48	*46.25*	*48.53*	57.76	52.93	*106.92*	*53.96*	*50.93*
Ni	*595.33*	772.1	644.9	*184.61*	*219.32*	232.0	193.3	*895.77*	*285.62*	*293.83*
Cu	*102.64*	63.66	68.72	*124.16*	*133.43*	69.89	60.70	*61.15*	*87.6*	*103.84*
Zn	*108.35*	100.9	104.0	*113.67*	*114.4*	105.1	107.0	*99.13*	*115.54*	*119.82*
Ga	*15.84*	12.89	14.89	*20.74*	*19.95*	19.57	20.31	*9.41*	*18.59*	*19.74*
Rb	*8.51*	12.63	13.05	*17.15*	*21.48*	16.85	18.49	*10.24*	*22.49*	*34.1*
Sr	*295*	230.6	265.3	*346*	*363*	389.6	388.1	*178*	*394*	*492*
Y	*25.58*	16.36	19.03	*30.98*	*31.99*	25.02	27.38	*15.18*	*31.52*	*32.81*
Zr	*202.02*	119.8	140.8	*238.96*	*242.74*	192	220	*118.18*	*262.04*	*351.35*
Nb	*21.51*	16.21	17.25	*23.72*	*29.15*	25.83	27.25	*13.41*	*23.45*	*42.8*
Mo		1.044	1.077			1.235	1.174			
Cd	*0.09*	0.083	0.095	*0.1*	*0.1*	0.111	0.134	*0.04*	*0.08*	*0.09*
Sn	*1.69*	1.240	1.455	*2.12*	*2.1*	1.923	2.093	*0.99*	*2.16*	*2.54*
Sb	*0.06*	0.052	0.056	*0.08*	*0.1*	0.058	0.058	*0.04*	*0.09*	*0.11*
Cs	*0.14*	0.183	0.191	*0.25*	*0.31*	0.202	0.137	*0.15*	*0.3*	*0.5*
Ba	*112.06*	95.38	102	*122.25*	*150.58*	182.5	171.6	*74.59*	*166.03*	*258.35*
La	*17.96*	13.77	14.81	*19.58*	*23.36*	21.36	23.78	*10.64*	*25.37*	*35.31*
Ce	*39.64*	30.79	33.72	*44.15*	*50.87*	48.55	53.30	*23.93*	*55.49*	*74.94*
Pr	*5.31*	4.033	4.491	*6.02*	*6.72*	6.360	6.964	*3.24*	*7.36*	*9.6*
Nd	*22.94*	17.01	19.38	*26.16*	*28.55*	26.68	29.13	*13.68*	*31*	*39.23*
Sm	*5.49*	4.011	4.648	*6.47*	*6.92*	6.262	6.798	*3.33*	*7.33*	*8.37*
Eu	*1.81*	1.317	1.529	*2.17*	*2.33*	2.056	2.253	*1.12*	*2.43*	*2.78*
Gd	*5.72*	3.981	4.681	*6.78*	*6.95*	6.212	6.728	*3.37*	*7.16*	*8.19*
Tb	*0.86*	0.605	0.715	*1.04*	*1.07*	0.931	1.026	*0.51*	*1.07*	*1.19*
Dy	*5.05*	3.432	4.001	*6.11*	*6.21*	5.246	5.760	*2.96*	*6.2*	*6.61*
Ho	*0.95*	0.662	0.772	*1.15*	*1.18*	1.009	1.118	*0.56*	*1.16*	*1.19*
Er	*2.39*	1.684	1.947	*2.92*	*2.99*	2.549	2.830	*1.45*	*2.91*	*3.04*
Tm	*0.31*	0.231	0.265	*0.37*	*0.39*	0.349	0.389	*0.19*	*0.38*	*0.37*
Yb	*1.97*	1.357	1.538	*2.38*	*2.43*	2.033	2.274	*1.2*	*2.35*	*2.32*

Continued on next page

Table C.2.6 – *Continued from previous page*

Sample	REU-14-28	REU-14-31*	REU-14-32*	REU-14-33	REU-14-36	REU-14-45*	REU-14-48*	REU-14-57	REU-14-67	REU-14-76
Lu	*0.26*	0.190	0.213	*0.32*	*0.33*	0.282	0.317	*0.16*	*0.32*	*0.31*
Hf	*5.02*	2.952	3.454	*5.92*	*6.13*	4.684	5.308	*2.9*	*6.45*	*8.25*
Ta	*1.24*	1.007	1.069	*1.42*	*1.73*	1.620	1.742	*0.79*	*0.36*	*1.66*
W		0.326	0.310			0.469	0.448			
Tl		0.023	0.021			0.034	0.022			
Pb	*1.01*	1.047	1.126	*1.21*	*1.34*	1.693	1.911	*0.51*	*1.56*	*2.67*
Th	*2.28*	1.674	1.69	*2.35*	*2.93*	2.503	2.903	*1.28*	*3.17*	*4.66*
U	*0.56*	0.430	0.450	*0.6*	*0.72*	0.632	0.687	*0.33*	*0.78*	*1.15*
Stable isotopes (‰)										
$\delta^{53/52}Cr_{SRM979}$	-0.168	-0.153	-0.132	-0.098	-0.144	-0.164	-0.153	-0.119	-0.158	-0.154
2SD/2SE if n= 1	0.015	0.010	0.010	0.005	0.011	0.012	0.011	0.030	0.014	0.014
n	1	1	1	3	3	1	1	3	1	1
Cr (μg g^{-1})	873.48	1515.35	1256.17	254.76	308.70	512.37	358.93	1728.46	442.30	377.23
$\delta^{56/57}Fe_{IRMM014}$	0.077	0.066	0.089	0.133	0.123	0.103	0.098	0.064	0.101	0.135
2SD/2SE if n= 1	0.027	0.027	0.025	0.025	0.024	0.026	0.024	0.026	0.028	0.025
n	1	1	1	1	1	1	1	1	1	1

Note: All data shown in italics were measured at the University of Goettingen.

*Trace element compositions were determined at the Isotope Geochemistry laboratory of the University Tuebingen.

Table C.2.7: Compilation of radiogenic isotope compositions, major element and trace element compositions, and stable Cr and Fe isotopic compositions alongside with Cr concentrations acquired by isotope dilution for samples from Lōi'hi. Sampling coordinates were not available.

Sample	**J2-243-1A-R2**	**J2-243-1B-R3**	**J2-243-1C-R6**	**J2-243-1J-R20**	**J2-244-1-R2**	**J2-246-R3D**	**J2-241-2-R9**	**J2-316-R1**	**J2-309-R1**	**J2-307-R2-C**
Rock type	Tholeiite	Tholeiite	Tholeiite	Tholeiite	Transitional basalt	Transitional basalt	Tholeiite	Transitional basalt	Transitional basalt	Transitional basalt
Radiogenic isotopes										
$^{87}Sr/^{86}Sr$	0.703545	0.703549	0.703567	0.703634	0.703620	0.703609	0.703518	0.703562	0.703607	0.703614
2SE	0.000010	0.000013	0.000010	0.000019	0.000009	0.000012	0.000009	0.000011	0.000011	0.000011
$^{143}Nd/^{144}Nd$	0.512888	0.512906	0.512893	0.512900	0.512889	0.512877	0.512935	0.512879	0.512911	0.512886
2SE	0.000015	0.000012	0.000010	0.000015	0.000013	0.000012	0.000023	0.000012	0.000012	0.000020
εNd	*5.04*	*5.38*	*5.13*	*5.27*	*5.05*	*4.81*	*5.96*	*4.85*	*5.48*	*5.00*
Major elements[a] (wt. %)										
SiO_2	-	-	-	-	-	-	-	-	-	-
TiO_2	2.30	2.30	2.32	2.34	2.72	2.77	2.52	2.85	2.66	2.68
Al_2O_3	12.48	12.39	12.56	12.53	12.75	13.00	12.89	13.50	12.76	12.90
FeO_T	11.85	11.63	11.70	11.82	11.13	11.01	11.64	11.72	11.79	11.36
MnO	0.18	0.17	0.18	0.18	0.16	0.16	0.18	0.17	0.17	0.16
MgO	9.27	8.59	8.91	8.70	8.61	8.33	7.34	6.38	9.73	9.20
CaO	11.63	11.56	11.70	11.83	10.80	11.29	11.10	11.01	10.52	10.68
Na_2O	2.26	2.25	2.29	2.27	2.60	2.61	2.29	2.76	2.57	2.60
K_2O	0.47	0.48	0.48	0.48	0.66	0.65	0.41	0.64	0.63	0.65
P_2O_5	0.25	0.25	0.26	0.25	0.33	0.34	0.28	0.36	0.33	0.33
Trace elements (μg g^{-1})										
Li	4.593	4.581	4.607	4.646	5.236	5.193	4.351	5.67	5.102	5.158
Be	0.848	0.848	0.839	0.840	1.132	1.128	0.879	1.187	1.088	1.089
Sc	34.37	34.15	33.99	34.45	29.58	31.48	34.02	30.60	28.43	29.67
Ti	14420	14510	14420	14650	17100	17220	16120	17980	16310	16780
V	342.6	344.0	342.4	346.4	363.8	367.2	369.4	376.5	356.6	361.5
Cr	568.6	475.6	509.7	481.3	1023	1063	317.7	217.8	3896	2860
Co	56.29	53.78	54.49	55.02	51.90	50.62	49.99	45.66	58.14	53.55
Ni	200.3	168.5	180.5	198.3	239.6	236.9	115.0	87.29	425.6	271.0
Cu	159.8	146.5	146.9	205.3	115.8	161.8	119.4	139.1	346.9	128.9

Continued on next page

Table C.2.7 – *Continued from previous page*

Sample	J2-243-1A-R2	J2-243-1B-R3	J2-243-1C-R6	J2-243-1J-R20	J2-244-1-R2	J2-246-R3D	J2-241-2-R9	J2-316-R1	J2-309-R1	J2-307-R2-C
Zn	111.7	110.1	111.9	110.4	108.3	108.1	110.7	119.4	113.0	110.2
Ga	19.29	19.23	19.19	19.46	20.56	20.94	20.40	22.11	20.42	20.70
Rb	9.176	9.191	9.220	9.272	13.44	13.32	8.047	12.50	12.79	13.14
Sr	368.2	369.1	368.9	372.5	465.4	467.2	357.7	442.3	447.7	454.1
Y	20.6	20.66	20.58	20.82	23.17	23.79	25.26	25.52	22.47	23.33
Zr	117.6	119.1	119	120.3	160.1	160.4	140.5	168.5	153.8	157.6
Nb	14.54	14.59	14.57	14.74	21.62	21.39	14.81	20.63	20.53	20.91
Mo	0.714	0.721	0.727	0.727	1.009	0.994	0.751	0.998	0.962	0.984
Cd	0.115	0.119	0.115	0.121	0.129	0.132	0.123	0.138	0.141	0.134
Sn	1.381	1.350	1.387	1.315	1.669	1.398	1.301	1.042	1.585	1.653
Sb	0.022	0.025	0.026	0.027	0.037	0.034	0.030	0.027	0.041	0.034
Cs	0.099	0.100	0.100	0.100	0.141	0.138	0.082	0.132	0.134	0.138
Ba	133.2	133.6	133.6	135.0	186.1	182.3	112.4	167.8	179.0	179.3
La	12.00	12.07	12.04	12.15	17.81	17.54	12.03	16.80	17.05	17.26
Ce	28.86	29.06	28.89	29.24	41.81	41.38	29.99	40.14	40.14	40.56
Pr	4.068	4.109	4.077	4.131	5.707	5.663	4.335	5.583	5.501	5.572
Nd	18.24	18.43	18.28	18.5	24.56	24.64	20.04	24.77	23.93	24.25
Sm	4.638	4.663	4.632	4.699	5.796	5.855	5.288	6.095	5.671	5.765
Eu	1.603	1.614	1.605	1.628	1.931	1.952	1.819	2.060	1.877	1.917
Gd	4.950	4.948	4.924	5.003	5.862	5.963	5.782	6.338	5.710	5.839
Tb	0.756	0.760	0.755	0.766	0.878	0.893	0.896	0.958	0.857	0.880
Dy	4.333	4.348	4.338	4.407	4.949	5.033	5.221	5.406	4.835	4.961
Ho	0.836	0.839	0.837	0.845	0.940	0.962	1.021	1.030	0.923	0.944
Er	2.110	2.114	2.115	2.141	2.373	2.422	2.639	2.603	2.324	2.385
Tm	0.292	0.292	0.292	0.296	0.328	0.335	0.368	0.359	0.321	0.330
Yb	1.682	1.696	1.689	1.721	1.901	1.940	2.154	2.090	1.866	1.922
Lu	0.237	0.237	0.237	0.241	0.268	0.273	0.306	0.292	0.264	0.270
Hf	3.029	3.060	3.059	3.104	3.957	4.006	3.582	4.180	3.897	3.956
Ta	0.897	0.900	0.899	0.909	1.331	1.321	0.924	1.275	1.296	1.305
W	0.151	0.152	0.156	0.158	0.228	0.225	0.150	0.214	0.219	0.229
Tl	0.023	0.024	0.024	0.024	0.031	0.031	0.022	0.030	0.031	0.033
Pb	1.171	1.171	1.174	1.212	1.552	1.566	1.039	1.478	1.631	1.539

Continued on next page

Table C.2.7 – *Continued from previous page*

Sample	**J2-243-1A-R2**	**J2-243-1B-R3**	**J2-243-1C-R6**	**J2-243-1J-R20**	**J2-244-1-R2**	**J2-246-R3D**	**J2-241-2-R9**	**J2-316-R1**	**J2-309-R1**	**J2-307-R2-C**
Th	0.845	0.849	0.850	0.868	1.303	1.282	0.824	1.202	1.268	1.267
U	0.260	0.262	0.264	0.267	0.390	0.385	0.263	0.374	0.380	0.386
Stable isotopes (‰)										
$\delta^{53/52}Cr_{SRM979}$	-0.094	-0.110	-0.104	-0.102	-0.160	-0.194	-0.108	-0.152	-0.227	-0.124
2SE	0.017	0.017	0.019	0.016	0.018	0.019	0.017	0.020	0.018	0.016
n	1	1	1	1	1	1	1	1	1	1
Cr (μg g^{-1})	523.12	443.59	475.41	452.44	969.47	1012.5	299.18	204.19	3920.5	2852.9
$\delta^{56/54}Fe_{IRMM14}$	0.075	0.114	0.095	0.077	0.113	0.144	0.117	0.146	0.118	0.113
2SE	0.026	0.024	0.030	0.026	0.026	0.021	0.021	0.022	0.025	0.027
n	1	1	1	1	1	1	1	1	1	1

[a]Major element concentrations determined by solution Q-ICP-MS at the University of Tuebingen.

Table C.2.8: Compilation of radiogenic isotope compositions, major element and trace element compositions, and stable Cr and Fe isotopic compositions alongside with Cr concentrations acquired by isotope dilution for samples from French Polynesia. Also shown are associated specific mantle components based on radiogenic isotopic Sr-Nd-Pb compositions.

Sample	FP2RU2	FP5TU1	FP8TU4	FP15GA7	FP24NU5	FP26HU1	FP27HU2
Island	Rurutu	Tubuai	Tubuai	Mangareva	Nuku Hiva	Huahine	Huahine
Island Group	Austral	Austral	Austral	Gambier	Marquesas	Society	Society
Rock type	Basanit/Tephrit	Picrobasalt	Picrobasalt	Basalt	Trachybasalt	Basalt	Basanit
Characteristics	PREMA	HIMU	HIMU	PREMA/EM1	EM2	EM2	EM2
Latitude (°S)	22° 29.530' S	23° 21.343' S	23° 22.033' S	23° 07.365' S	08° 53.890' S	15° 46.370' S	16° 47.255' S
Longitude (°W)	151° 19.760' W	149° 27.602' W	149° 28.520' W	134° 58.560' W	140° 05.977' W	151° 02.470' W	150° 57.523' W
Radiogenic isotopes[a]							
$^{87}Sr/^{86}Sr$	*0.703319*	*0.702819*	*0.702804*	*0.703125*	*0.704708*	*0.706009*	*0.704521*
2SE	*0.000009*	*0.000010*	*0.000009*	*0.000009*	*0.000010*	*0.000040*	*0.000009*
$^{143}Nd/^{144}Nd$	*0.512871*	*0.512872*	*0.512887*	*0.512923*	*0.512761*	*0.512610*	*0.512878*
2SE	*0.000008*	*0.000009*	*0.000010*	*0.000005*	*0.000006*	*0.000010*	*0.000007*
εNd	*4.55*	*4.56*	*4.85*	*5.57*	*2.40*	*-0.54*	*4.67*
$^{206}Pb/^{204}Pb$	*20.298*	*21.094*	*21.080*	*19.163*	*19.022*	*19.160*	*18.949*
$^{207}Pb/^{204}Pb$	*15.683*	*15.759*	*15.758*	*15.560*	*15.596*	*15.634*	*15.573*
$^{208}Pb/^{204}Pb$	*39.788*	*40.229*	*40.270*	*39.123*	*39.119*	*38.987*	*38.685*
Major elements[a] (wt. %)							
SiO_2	*43.46*	*44.16*	*41.90*	*48.24*	*47.45*	*46.99*	*42.67*
TiO_2	*3.25*	*2.56*	*2.31*	*2.18*	*2.40*	*2.69*	*2.61*
Al_2O_3	*14.93*	*12.79*	*8.71*	*15.58*	*14.52*	*12.87*	*9.89*
FeO_T	*13.67*	*12.16*	*12.90*	*9.96*	*9.61*	*10.46*	*12.06*
Fe_2O_3							
FeO							
MnO	*0.28*	*0.24*	*0.24*	*0.20*	*0.22*	*0.20*	*0.22*
MgO	*6.08*	*9.15*	*17.80*	*7.87*	*8.54*	*10.73*	*17.06*
CaO	*8.50*	*12.67*	*10.60*	*11.50*	*9.22*	*9.05*	*9.88*
Na_2O	*5.13*	*2.48*	*2.05*	*2.22*	*3.23*	*2.17*	*2.38*
K_2O	*1.57*	*0.65*	*0.47*	*0.47*	*2.19*	*2.25*	*1.09*
P_2O_5	*1.41*	*0.41*	*0.34*	*0.30*	*0.55*	*0.51*	*0.36*

Continued on next page

Table C.2.8 – *Continued from previous page*

Sample	FP2RU2	FP5TU1	FP8TU4	FP15GA7	FP24NU5	FP26HU1	FP27HU2
LOI	*-0.27*	*1.21*	*0.41*	*-0.25*	*0.7*	*0.71*	*-0.16*
Trace elements[a] (μg g^{-1})							
Li	*7.816*	*6.753*	*5.528*	*3.726*	*6.682*	*7.501*	*5.762*
Be	*2.818*	*1.716*	*1.407*	*1.006*	*1.666*	*1.925*	*1.335*
Sc	*11.63*	*30.03*	*17.05*	*26.07*	*19.20*	*20.75*	*15.28*
Ti	*19784*	*15830*	*13946*	*13083*	*14781*	*16535*	*16030*
V	*160.8*	*301.5*	*249.1*	*234.3*	*191.6*	*207.5*	*269.3*
Cr	*29.29*	*273.56*	*1719.71*	*285.06*	*594.27*	*527.10*	*933.38*
Co	*40.91*	*55.21*	*82.97*	*44.51*	*39.68*	*57.36*	*77.64*
Ni	*66.37*	*134.6*	*460.7*	*127.8*	*167.4*	*308.1*	*572.7*
Cu	*50.85*	*162.5*	*103.1*	*60.57*	*45.20*	*44.23*	*61.01*
Zn	*154.9*	*109.7*	*107.8*	*91.58*	*101.3*	*117.6*	*113.0*
Ga	*22.63*	*18.90*	*14.22*	*18.54*	*18.34*	*19.43*	*16.53*
Rb	*36.35*	*16.06*	*10.49*	*5.614*	*57.09*	*51.01*	*27.12*
Sr	*1281.1*	*521.5*	*416.4*	*373.3*	*663.1*	*661.6*	*608.1*
Y	*39.94*	*23.74*	*17.04*	*18.26*	*24.48*	*23.33*	*19.55*
Zr	*396.9*	*178.0*	*138.9*	*139.9*	*251.1*	*302.9*	*169.9*
Nb	*98.82*	*60.04*	*45.49*	*29.52*	*49.91*	*53.53*	*36.95*
Mo	*3.630*	*1.624*	*1.818*	*0.732*	*1.940*	*2.118*	*1.654*
Cd	*0.227*	*0.119*	*0.084*	*0.110*	*0.168*	*0.183*	*0.112*
Sn	*2.810*	*1.805*	*1.481*	*1.417*	*1.958*	*2.671*	*1.797*
Sb	*0.113*	*0.055*	*0.046*	*0.020*	*0.080*	*0.124*	*0.050*
Cs	*0.387*	*0.165*	*0.163*	*0.046*	*0.625*	*0.480*	*1.233*
Ba	*435.1*	*260.2*	*202.0*	*158.2*	*570.4*	*646.5*	*413.4*
La	*80.72*	*40.44*	*30.99*	*18.56*	*43.56*	*50.11*	*26.39*
Ce	*187.6*	*83.65*	*64.28*	*40.70*	*91.28*	*103.5*	*56.96*
Pr	*21.50*	*9.953*	*7.844*	*5.301*	*10.851*	*12.086*	*7.345*
Nd	*84.38*	*38.33*	*30.49*	*22.27*	*41.65*	*46.27*	*30.50*
Sm	*15.81*	*7.560*	*6.092*	*5.034*	*7.774*	*8.774*	*6.604*
Eu	*4.790*	*2.377*	*1.901*	*1.700*	*2.421*	*2.570*	*2.097*
Gd	*13.44*	*6.918*	*5.490*	*4.788*	*6.851*	*7.397*	*6.217*
Tb	*1.779*	*0.979*	*0.758*	*0.719*	*0.980*	*1.027*	*0.873*

Continued on next page

Table C.2.8 – *Continued from previous page*

Sample	FP2RU2	FP5TU1	FP8TU4	FP15GA7	FP24NU5	FP26HU1	FP27HU2
Dy	*9.016*	*5.239*	*3.983*	*3.957*	*5.249*	*5.258*	*4.518*
Ho	*1.619*	*0.972*	*0.713*	*0.749*	*0.995*	*0.933*	*0.803*
Er	*3.867*	*2.376*	*1.665*	*1.913*	*2.489*	*2.239*	*1.902*
Tm	*0.507*	*0.319*	*0.220*	*0.254*	*0.340*	*0.298*	*0.246*
Yb	*2.927*	*1.897*	*1.242*	*1.532*	*2.014*	*1.699*	*1.401*
Lu	*0.402*	*0.256*	*0.166*	*0.214*	*0.276*	*0.226*	*0.186*
Hf	*8.435*	*4.373*	*3.437*	*3.405*	*5.664*	*6.849*	*4.099*
Ta	*5.549*	*3.332*	*2.522*	*1.705*	*3.009*	*2.971*	*2.108*
W	*1.028*	*0.465*	*0.501*	*0.197*	*0.647*	*0.931*	*0.342*
Tl	*0.033*	*0.027*	*0.006*	*0.008*	*0.087*	*0.065*	*0.031*
Pb	*3.424*	*2.503*	*1.697*	*1.167*	*3.481*	*5.797*	*2.325*
Th	*7.519*	*4.190*	*3.187*	*1.634*	*5.965*	*8.837*	*3.237*
U	*2.190*	*1.095*	*0.818*	*0.359*	*1.486*	*1.725*	*0.862*
Stable isotopes (‰)							
$\delta^{53/52}Cr_{SRM979}$	-0.125	-0.214	-0.137	-0.145	-0.145	-0.133	-0.155
2SD/2SE if n= 1	0.019	0.040	0.022	0.009	0.015	0.012	0.016
n	3	3	3	3	1	1	1
Cr (μg g^{-1})	3.084	273.7	1694.5	272.6	555.9	490.5	857.8
$\delta^{56/54}Fe_{IRMM14}$	0.127	0.142	0.096	0.075	0.151	0.112	0.168
2SD/2SE if n= 1	0.024	0.026	0.027	0.026	0.027	0.026	0.026
n	1	1	1	1	1	1	1

Note: All literature data are shown in italics.

[a]Major element, trace element and radiogenic isotopic compositions are from Schiller (2019)*.

*Schiller, M. Geochemical constraints on Sources of Ocean Island Basalts from French Polynesia, Department of Geosciences. University of Tübingen, Tübingen.

Table C.2.9: Compilation of radiogenic isotope compositions, major element and trace element compositions, and stable Cr and Fe isotopic compositions alongside with Cr concentrations acquired by isotope dilution for samples from Vogelsberg volcano, Germany. Also shown are sampling localities: FBV ("Forschungsbohrung Vogelsberg") for drill core samples and locations for outcrop samples. For drill core samples associated sampling depths are also given in m.

Sample	VB96-08	VB96-14	VB96-23	VB96-26	VB97-100	VB97-101	VB96-16	VB96-18	VB96-40	VB97-102	VB97-103
Rock type	basanite	basanite	basanite	basanite	basanite	basanite	alk. Basalt	alk. Basalt	alk. Basalt	alk. Basalt	alk. Basalt
Locationa	FBV	FBV	FBV	FBV	Taufstein	Ortenberg	FBV	FBV	FBV	Ortenheim	Bergheim
Depth (m)	20.86	49.88	77.1	94.4	-	-	55.91	64.54	229	-	-
Radiogenic isotopes[a, b]											
$(^{87}Sr/^{86}Sr)_i$	*0.703146*	*0.703230*	*0.703316*	*0.703256*	*0.703192*	*0.703344*	*0.703142*	*0.703106*	*0.703226*	*0.703437*	*0.703424*
2SE	*14*	*12*	*16*	*12*	*18*	*16*	*15*	*12*	*12*	*11*	*11*
$(^{143}Nd/^{144}Nd)_i$	*0.512844*	*0.512816*	*0.512822*	*0.512803*	*0.512858*	*0.512833*	*0.512906*	*0.512897*	*0.512820*	*0.512780*	*0.512813*
2SE	*6*	*5*	*5*	*6*	*10*	*10*	*12*	*7*	*3*	*10*	*13*
$(\varepsilon Nd)_i$	*3.98*	*3.28*	*4.32*	*3.30*	*4.31*	*4.04*	*4.94*	*5.23*	*3.63*	*2.93*	*3.67*
$^{206}Pb/^{204}Pb$	*19.415*		*19.403*					*19.271*	*19.129*		
$^{207}Pb/^{204}Pb$	*15.637*		*15.608*					*15.601*	*15.598*		
$^{208}Pb/^{204}Pb$	*39.231*		*39.144*					*38.939*	*38.817*		
Major elements[a] (wt. %)											
SiO_2	*41.12*	*42.20*	*43.29*	*42.76*	*40.30*	*43.30*	*44.91*	*45.14*	*45.54*	*46.20*	*45.90*
TiO_2	*2.56*	*2.39*	*2.42*	*2.56*	*2.58*	*2.62*	*2.22*	*2.23*	*2.23*	*2.13*	*2.01*
Al_2O_3	*12.69*	*12.32*	*12.69*	*12.60*	*11.62*	*12.27*	*12.58*	*12.95*	*13.05*	*13.33*	*12.95*
FeO_T	*11.24*	*11.29*	*11.01*	*11.34*	*10.68*	*11.01*	*11.25*	*11.42*	*11.28*	*11.41*	*11.05*
Fe_2O_3	*6.43*	*4.32*	*3.67*	*4.26*	*4.85*	*3.42*	*6.57*	*2.95*	*3.77*	*1.87*	*3.39*
FeO	*5.45*	*7.40*	*7.71*	*7.51*	*6.32*	*7.93*	*5.34*	*8.77*	*7.89*	*9.73*	*8.00*
MnO	*0.20*	*0.19*	*0.20*	*0.20*	*0.18*	*0.22*	*0.18*	*0.18*	*0.18*	*0.17*	*0.17*
MgO	*12.01*	*12.55*	*12.02*	*12.12*	*12.97*	*12.51*	*10.94*	*11.16*	*10.79*	*9.83*	*9.72*
CaO	*11.69*	*12.09*	*11.52*	*11.52*	*11.65*	*9.86*	*10.92*	*10.53*	*10.31*	*9.63*	*10.35*
Na_2O	*3.18*	*1.90*	*2.84*	*2.93*	*2.25*	*3.12*	*2.69*	*3.26*	*2.34*	*2.45*	*2.78*
K_2O	*0.76*	*0.71*	*1.54*	*0.95*	*0.74*	*1.35*	*1.26*	*1.30*	*1.04*	*1.39*	*1.01*
P_2O_5	*0.79*	*0.76*	*0.67*	*0.72*	*0.72*	*0.61*	*0.51*	*0.52*	*0.49*	*0.42*	*0.79*
LOI	*2.85*	*3.31*	*1.00*	*1.57*	*3.93*	*1.50*	*1.72*	*1.20*	*2.88*	*1.23*	*1.43*
Trace elements[a] ($\mu g\ g^{-1}$)											
Li	*7.55*	*6.72*	*6.57*	*7.4*	*6.29*	*8.03*	*6.73*	*7.45*	*6.30*	*6.63*	*7.34*

Continued on next page

Table C.2.9 – *Continued from previous page*

Sample	VB96-08	VB96-14	VB96-23	VB96-26	VB97-100	VB97-101	VB96-16	VB96-18	VB96-40	VB97-102	VB97-103
Be	*1.60*	*1.37*	*1.41*	*1.49*	*1.74*	*1.82*	*1.10*	*1.25*	*1.03*	*1.12*	*1.30*
Sc	*29*	*32*	*29*	*28*	*23*	*25*	*26*	*29*	*27*	*25*	*23*
Ti											
V	*258*	*257*	*255*	*262*	*248*	*235*	*222*	*217*	*220*	*215*	*189*
Cr	*371*	*430*	*462*	*446*	*486*	*515*	*495*	*473*	*368*	*294*	*356*
Co	*57*	*52*	*54*	*59*	*55*	*59*	*57*	*61*	*52*	*56*	*56*
Ni	*255*	*226*	*285*	*276*	*317*	*332*	*288*	*279*	*248*	*203*	*228*
Cu											
Zn	*100*	*101*	*96*	*106*	*89*	*101*	*143*	*111*	*108*	*107*	*115*
Ga	*17*	*17*	*17*	*18*	*16*	*16*	*18*	*18*	*18*	*21*	*18*
Rb	*89*	*99*	*43*	*30*	*54*	*31*	*41*	*43*	*39*	*32*	*28*
Sr	*922*	*1164*	*813*	*909*	*872*	*762*	*727*	*661*	*721*	*622*	*895*
Y	*30*	*27*	*29*	*27*	*25*	*24*	*25*	*25*	*26*	*25*	*27*
Zr	*212*	*212*	*203*	*219*	*222*	*255*	*169*	*167*	*151*	*147*	*161*
Nb	*87*	*76*	*78*	*76*	*84*	*68*	*56*	*61*	*48*	*38*	*62*
Mo	*2.66*	*3.01*	*4.28*	*2.58*	*1.33*	*2.68*	-	*3.4*	*1.89*	*1.41*	*2.76*
Cd											
Sn	*2.23*	*0.58*	*1.38*	*1.15*	*1.51*	*1.67*	*0.81*	*1.47*	*0.80*	*1.15*	*1.69*
Sb											
Cs	*0.9*	*1.07*	*0.87*	*1.06*	*0.74*	*0.93*	*0.54*	*0.67*	*0.59*	*0.36*	*0.47*
Ba	*762*	*746*	*727*	*696*	*775*	*568*	*678*	*588*	*514*	*439*	*588*
La	*63.73*	*58.95*	*58.82*	*57.58*	*59.23*	*46.99*	*44.60*	*42.19*	*34.45*	*29.38*	*60.17*
Ce	*125.37*	*123.12*	*118.61*	*118.41*	*116.74*	*97.12*	*87.10*	*86.21*	*73.43*	*63.79*	*117.24*
Pr	*13.28*	*13.01*	*12.22*	*12.46*	*12.60*	*10.75*	*8.96*	*8.75*	*8.07*	*7.38*	*12.18*
Nd	*50.26*	*48.89*	*46.25*	*48.29*	*47.34*	*41.73*	*36.46*	*34.26*	*32.93*	*29.27*	*43.47*
Sm	*9.55*	*9.34*	*8.62*	*9.16*	*8.45*	*7.96*	*7.75*	*6.83*	*6.93*	*6.33*	*7.88*
Eu	*2.89*	*2.71*	*2.71*	*2.79*	*2.96*	*2.72*	*2.32*	*2.23*	*2.15*	*2.21*	*2.67*
Gd	*7.73*	*7.22*	*7.06*	*7.12*	*6.92*	*6.27*	*6.07*	*6.01*	*5.71*	*5.28*	*6.72*
Tb	*1.06*	*1.02*	*1.01*	*1.01*	*1.06*	*0.99*	*0.88*	*0.90*	*0.89*	*0.88*	*1.04*
Dy	*5.37*	*5.18*	*5.40*	*5.33*	*5.09*	*4.89*	*4.85*	*4.66*	*4.80*	*4.52*	*4.95*
Ho	*0.92*	*0.94*	*0.94*	*0.95*	*0.86*	*0.86*	*0.84*	*0.83*	*0.88*	*0.85*	*0.89*
Er	*2.47*	*2.46*	*2.69*	*2.58*	*2.26*	*2.27*	*2.32*	*2.34*	*2.39*	*2.40*	*2.55*

Continued on next page

Table C.2.9 – *Continued from previous page*

Sample	VB96-08	VB96-14	VB96-23	VB96-26	VB97-100	VB97-101	VB96-16	VB96-18	VB96-40	VB97-102	VB97-103
Tm	*0.33*	*0.33*	*0.33*	*0.32*	*0.27*	*0.29*	*0.30*	*0.31*	*0.32*	*0.30*	*0.32*
Yb	*1.92*	*1.91*	*2.16*	*2.00*	*1.71*	*1.77*	*1.69*	*1.88*	*1.90*	*1.93*	*2.02*
Lu	*0.27*	*0.29*	*0.32*	*0.30*	*0.23*	*0.25*	*0.25*	*0.26*	*0.28*	*0.27*	*0.29*
Hf	*4.60*	*4.63*	*4.55*	*4.95*	*5.11*	*5.46*		*3.78*	*3.54*	*3.79*	*3.94*
Ta	*5.82*	*4.94*	*5.44*	*4.97*	*5.32*	*4.27*		*4.15*	*3.26*	*2.50*	*3.43*
W	*1.71*	*1.22*	*4.96*	*1.08*	*0.95*	*0.96*		*1.58*	*0.89*	*0.74*	*2.06*
Tl											
Pb	*3.33*	*3.71*	*3.18*	*3.36*			*2.33*	*2.62*	*2.27*		
Th	*7.97*	*7.23*	*6.98*	*6.84*	*7.65*	*6.23*	*5.18*	*5.25*	*4.06*	*3.00*	*6.92*
U	*1.81*	*1.62*	*1.55*	*1.58*	*1.88*	*1.63*	*1.27*	*1.27*	*0.95*	*0.80*	*1.71*
Stable isotopes (‰)											
$\delta^{53/52}Cr_{SRM979}$	-0.193	-0.190	-0.178	-0.219	-0.216	-0.209	-0.157	-0.154	-0.160	-0.179	-0.168
2SE	0.012	0.014	0.013	0.010	0.013	0.012	0.012	0.011	0.012	0.012	0.013
n	1	1	1	1	1	1	1	1	1	1	1
Cr (μg g^{-1})	367.6	446.9	490.4	445.9	497.0	528.3	509.7	625.1	367.0	302.3	361.5
$\delta^{56/54}Fe_{IRMM14}$	0.120	0.162	0.176	0.190	0.202	0.169	0.153	0.139	0.154	0.115	0.176
2SE	0.022	0.025	0.027	0.026	0.025	0.028	0.022	0.024	0.028	0.027	0.025
n	1	1	1	1	1	1	1	1	1	1	1

Note: All literature data are shown in italics.

[a] Major element, trace element and radiogenic isotope data are from Bogaard and Wörner (2003)*.

[b] Radiogenic Sr and Nd isotope data are age corrected to initial values at ∼18 Ma (Bogaard and Wörner, 2003)*.

*Bogaard, P. and Wörner, G. 2003. Petrogenesis of basanitic to tholeiitic volcanic rocks from the Miocene Vogelsberg, Central Germany. Journal of Petrology. 44, 569-602.

Table C.2.10: Compilation of radiogenic isotope compositions, major element and trace element compositions, and stable Cr and Fe isotopic compositions alongside with Cr concentrations acquired by isotope dilution for Doros Complex intrusive rocks, Namibia. BOM = basal olivine melagabbro, MOG = massive olivine gabbro, cpx = clinopyroxene.

Sample	TOD-39	TOD-40	TOD-43	TOD-63	TOD-68A	TOD-71	TOD-77
Rock type	BOM	BOM	MOG	BOM	MOG	MOG	Cpx cumulate
Radiogenic isotopes[a]							
$(^{87}Sr/^{86}Sr)_i$	*0.704209*	*0.706843*			*0.704449*	*0.704144*	*0.704115*
	20	*27*			*45*	*40*	*28*
$(^{143}Nd/^{144}Nd)_i$	*0.512799*	*0.512731*			*0.512674*	*0.512669*	*0.512751*
2SE	*18*	*22*			*14*	*15*	*18*
$(\varepsilon Nd)_i$	*6.5*	*5.1*			*4.0*	*3.9*	*5.5*
$(^{206}Pb/^{204}Pb)_i$	*17.9961*	*18.0711*			*18.1425*	*18.1363*	*18.0627*
$(^{207}Pb/^{204}Pb)_i$	*15.5548*	*15.5647*			*15.5733*	*15.5746*	*15.5596*
$(^{208}Pb/^{204}Pb)_i$	*37.7499*	*37.8554*			*37.9785*	*37.9601*	*37.7950*
Major elements[b] **(wt. %)**							
SiO_2	*45.66*	*44.15*	*49.36*	*43.46*	*50.58*	*49.49*	*49.72*
TiO_2	*1.39*	*1.46*	*1.64*	*1.15*	*1.40*	*1.21*	*1.99*
Al_2O_3	*10.69*	*6.86*	*18.10*	*5.99*	*15.62*	*20.52*	*7.31*
FeO_T	*11.8*	*15.5*	*7.5*	*16.6*	*6.5*	*6.1*	*8.9*
Fe_2O_3							
FeO							
MnO	*0.17*	*0.22*	*0.12*	*0.23*	*0.11*	*0.10*	*0.16*
MgO	*15.34*	*18.82*	*5.25*	*21.26*	*7.24*	*4.17*	*10.18*
CaO	*10.63*	*7.71*	*12.71*	*7.19*	*12.80*	*13.28*	*17.45*
Na_2O	*1.26*	*1.02*	*2.23*	*0.88*	*2.47*	*2.42*	*1.15*
K_2O	*0.32*	*0.39*	*0.54*	*0.35*	*0.69*	*0.45*	*0.45*
P_2O_5	*0.10*	*0.14*	*0.15*	*0.12*	*0.18*	*0.11*	*0.13*
CO_2							
LOI	*0.69*	*0.61*	*0.80*	*-0.01*	*0.75*	*0.72*	*0.99*
Trace elements[b] **($\mu g\ g^{-1}$)**							
Li	*3.63*	*5.83*	*3.66*	*5.21*	*3.46*	*4.00*	*2.10*
Be							

Continued on next page

Table C.2.10 – *Continued from previous page*

Sample	TOD-39	TOD-40	TOD-43	TOD-63	TOD-68A	TOD-71	TOD-77
Sc	*24.4*	*21.8*	*18.5*	*21.1*	*26.9*	*17.0*	*63.9*
Ti							
V	*327*	*326*	*293*	*275*	*274*	*256*	*590*
Cr	*1705*	*1923*	*385*	*2073*	*998*	*357*	*1120*
Co	*82.1*	*109*	*28.8*	*126.2*	*34.7*	*25.0*	*40.3*
Ni	*697*	*1004*	*140*	*1267*	*248*	*116*	*220*
Cu	*51.5*	*98.7*	*90.5*	*69.4*	*254*	*71.2*	*28.9*
Zn	*82.4*	*116*	*59.1*	*120*	*51.7*	*54.9*	*62.9*
Ga							
Rb	*4.65*	*7.87*	*7.86*	*6.39*	*10.8*	*7.24*	*6.39*
Sr	*457*	*443*	*715*	*216*	*623*	*807*	*306*
Y	*8.57*	*11.3*	*10.9*	*8.90*	*14.5*	*9.64*	*16.0*
Zr	*59.2*	*85.7*	*84.3*	*59.0*	*107.0*	*62.4*	*89.9*
Nb	*5.06*	*7.03*	*7.42*	*5.04*	*9.11*	*5.52*	*5.83*
Ba	*112*	*138*	*159*	*106*	*230*	*154*	*135*
La	*7.76*	*11.2*	*11.4*	*8.09*	*15.5*	*9.75*	*11.1*
Ce	*18.9*	*26.7*	*26.9*	*19.1*	*36.1*	*22.6*	*28.7*
Pr	*2.57*	*3.51*	*3.50*	*2.48*	*4.55*	*2.90*	*4.02*
Nd	*11.4*	*15.3*	*15.1*	*10.8*	*19.8*	*12.6*	*18.7*
Sm	*2.62*	*3.36*	*3.24*	*2.45*	*4.24*	*2.79*	*4.49*
Eu	*0.988*	*1.05*	*1.25*	*0.784*	*1.52*	*1.09*	*1.40*
Gd	*2.55*	*3.26*	*3.22*	*2.46*	*4.17*	*2.72*	*4.59*
Tb	*0.349*	*0.449*	*0.440*	*0.348*	*0.576*	*0.378*	*0.637*
Dy	*2.01*	*2.57*	*2.48*	*1.99*	*3.26*	*2.17*	*3.66*
Ho	*0.348*	*0.457*	*0.448*	*0.355*	*0.578*	*0.378*	*0.635*
Er	*0.911*	*1.19*	*1.14*	*0.919*	*1.46*	*0.974*	*1.62*
Tm	*0.113*	*0.154*	*0.149*	*0.119*	*0.182*	*0.122*	*0.202*
Yb	*0.692*	*0.955*	*0.885*	*0.729*	*1.09*	*0.76*	*1.23*
Lu	*0.097*	*0.131*	*0.121*	*0.105*	*0.142*	*0.103*	*0.164*
Hf	*1.75*	*2.31*	*2.26*	*1.60*	*2.86*	*1.72*	*2.77*
Ta	*0.264*	*0.361*	*0.422*	*0.265*	*0.480*	*0.298*	*0.324*
W							

Continued on next page

Table C.2.10 – *Continued from previous page*

Sample	TOD-39	TOD-40	TOD-43	TOD-63	TOD-68A	TOD-71	TOD-77
Tl							
Pb	*1.34*	*1.96*	*2.12*	*1.54*	*3.04*	*1.83*	*1.45*
Th	*0.608*	*1.08*	*1.04*	*0.885*	*1.59*	*0.939*	*0.930*
U	*0.179*	*0.296*	*0.237*	*0.195*	*0.347*	*0.202*	*0.202*
Stable isotopes (‰)							
$\delta^{53/52}Cr_{SRM979}$	-0.107	-0.110	-0.138	-0.119	-0.154	-0.186	-0.127
2SE	0.012	0.013	0.014	0.014	0.010	0.013	0.013
n	1	1	1	1	1	1	1
Cr (μg g^{-1})	1537.199654	1720.797113	421.6115085	1746.999007	886.4059036	341.7651148	998.8769308
$\delta^{56/54}Fe_{IRMM14}$	0.073	0.076	0.118	0.058	0.138	0.130	0.077
2SE	0.025	0.025	0.027	0.028	0.028	0.030	0.029
n	1	1	1	1	1	1	1

Note: All literature data are shown in italics.
Rock type abbrevations: BOM, Basal olivine melagabbro; MOG, massive olivine gabbro; Cpx cumulate, clinopyroxene cumulate.
[a]Radiogenic isotope data are from Owen-Smith et al. (2017)[*]. Sr, Nd, and Pb Isotopic ratios are age corrected and give initial values at 132 Ma.
[b]Major and trace element composition are from Owen-Smith and Ashwal (2015)[#].

[*]Owen-Smith, T., Ashwal, L., Sudo, M. and Trumbull, R. 2017. Age and petrogenesis of the Doros Complex, Namibia, and implications for early plume-derived melts in the Paraná–Etendeka LIP. Journal of Petrology. 58, 423-442.
[#]Owen-Smith, T. and Ashwal, L. 2015. Evidence for multiple pulses of crystal-bearing magma during emplacement of the Doros layered intrusion, Namibia. Lithos. 238, 120-139.

List of Figures